

UNIVERZITA PALACKÉHO V OLMOUCI  
Přirodovědecká fakulta

**From Crystallography to Quantum Crystallography of  
Magnetically Bistable Materials**

Habilitační práce

**Ivan Nemeč, PhD**

**2023**

# Contents

Introduction .....	2
Chapter 1: Magnetically Bistable Materials.....	3
1.2 Semi-coordination and single-ion magnets .....	8
1.3 Spin crossover .....	12
CHAPTER 4: SINGLE-ION MAGNETS.....	18
4.1 Co(II)-based Single-Ion Magnets with 1,1'-ferrocenediyl-bis(diphenylphosphine) metalloligands .....	18
4.2 Halogen bonding in new dichloride-cobalt(II) complex with iodo-substituted chalcone ligands . and Deposition of Tetracoordinate Co(II) Complex with Chalcone Ligands on Graphene .....	21
4.3 Trigonally distorted hexacoordinate Co(II) single-ion magnets .....	25
4.4 Weak antiferromagnetic interaction in Cu(II) complex with semi-coordination exchange pathway .....	27
4.5 Neutral Cobalt(II)-Bis(Benzimidazole)Pyridine Field-Induced Single-Ion Magnets for Surface Deposition .....	30
Chapter 4.6 Tetracoordinate Co(II) Complexes with Semi-Coordination as Stable Single-Ion Magnets for Deposition on Graphene .....	32
CHAPTER 5: SPIN-CROSSOVER.....	38
5.1 Spin crossover in three mononuclear iron (III) Schiff-base complexes .....	38
5.2 Ion-pair complexes of Schiff base Fe(III) cations and complex anions.....	40
5.3 Variation of Spin-Transition Temperature in the Iron (III) Complex Induced by Different Compositions of the Crystallization Solvent .....	42
CHAPTER 6: CONCLUSION AND PERSPECTIVE .....	49
REFERENCES .....	50

## Introduction

The world of magnetically bistable materials is as fascinating as it is complex. The interplay of atomic arrangements, bonding, and magnetism paints a picture that underpins many technological applications, from memory devices to potential quantum computing components. My scientific journey, closely connected to magnetically bistable molecular materials, has evolved over the years in tandem with advancements in the field of material science and the evolving methodologies used to understand these intricate materials.

Formerly, my work was primarily focused on crystallography. This traditional method has been crucial for understanding the atomic structures of various materials. Using crystallography, my goal was to clarify the crystal structures of magnetically bistable materials and relate these structures to their magnetic properties. My research, starting with a study on hydrogen bonding's effect on spin crossover phenomena published in 2015,<sup>1</sup> highlighted the limitations of traditional crystallography, particularly in addressing the quantum aspects of these materials. It was at this juncture that the need for a more advanced approach became evident, leading me to quantum crystallography. By merging principles from both classical structural analysis and quantum mechanics, quantum crystallography offered a richer and more nuanced exploration of magnetically bistable materials. Over the course of the last five years, I have integrated this approach into my standard research procedures, which have produced encouraging outcomes. As I will explore in subsequent sections, this integration has also had noteworthy consequences for enhancing the design of coordination compounds.

This habilitation thesis documents this methodological shift. It is not aimed at comprehensive review of the state-of-art in the field of magnetically bistable molecular materials. Rather it compiles my publications from the past five years, charting the transition from purely crystallographic techniques to integrated quantum crystallographic investigations. Each publication marks a stage in this journey, showcasing my personal advancements and deeper insights into magnetically bistable materials. The overarching goal is to underscore the importance and potential of quantum crystallography in the domain of magnetically bistable molecular materials. The prospects for future work will be presented in the concluding chapter.

At the end of this chapter, I would like to express my gratitude to all my exceptional students and colleagues from Olomouc and Brno who have significantly contributed to both my professional and personal growth. In the context of this habilitation, my heartfelt thanks go particularly to my colleague, frequent co-author, and friend, Radovan Herchel, for our enlightening discussions about molecular magnetism and his invaluable guidance in introducing me to *ab initio* calculations. However, my deepest appreciation is reserved for my family: my parents, who continued to believe in me through the wilder parts of my life, and most importantly, my wife, Pavla. Her presence in my life, her dedication to our family, and her love have made our world a much better place.

## Chapter 1: Magnetically Bistable Materials

At its core, bistability is a phenomenon observed in certain dynamical systems. Simply put, a system displaying bistability has two stable equilibrium states. This means that the system can rest in either of these states without being easily pushed to another state. When this concept is applied to the realm of magnetism, we encounter the term 'magnetic bistability'. Just as with general bistability, a magnetically bistable system can remain in two distinct magnetic states. These states can be swapped via external stimuli like temperature, pressure, or light. Because of this unique property, magnetic bistability has become a focal point of interest, especially when considering its potential uses in magnetic memory devices, sensors, and advanced quantum computing components.<sup>2</sup>

Magnetically ordered materials, especially ferro- and ferrimagnets, are fundamental in the realm of magnetic bistability. Their importance is not merely historical; these materials have revolutionized various sectors of technology. They form the backbone of many modern applications including memory devices, which depend on their ability to retain magnetic states. Magnetically ordered materials play also a significant role in numerous other traditional and modern applications. They are integral to the functioning of many electric devices, particularly electric generators, but their relevance also extends also to the automotive industry, highlighting their widespread utility in contemporary technology. The fundamental concepts essential for comprehending their characteristics include magnetic anisotropy and the presence of magnetic domains.<sup>3</sup>

Magnetic anisotropy dictates how magnetic properties in ordered materials vary with direction, primarily influenced by magnetocrystalline anisotropy. This variation stems from the material's crystal structure: certain crystallographic directions promote easy magnetization, while others resist it. A specific subtype, uniaxial anisotropy, highlights this dependency on direction. The energy required for magnetization is influenced by the material's orientation to a single axis, determined by its inherent crystal structure. Magnetic domains are fundamental to the understanding of magnetically ordered materials. These materials comprise multiple small regions, termed domains, wherein the local magnetization achieves saturation. Notably, the magnetization direction can differ between domains. Boundary regions, known as domain walls, delineate these domains. As magnetization begins, domains favorably aligned with the applied magnetic field grow, dominating the misaligned ones. As the field intensifies, magnetization may orient toward the closest easy axis, particularly if the anisotropic energy threshold is surpassed. At peak field strengths, domains universally align with the field, irrespective of their intrinsic axes. Central to this discussion is the concept of hysteresis, evident in the magnetization's delayed response to magnetic field shifts. This phenomenon arises as was discussed above from the domain structure of the ordered materials, and also from interactions between and within magnetic domains, shaping the material's magnetic characteristics and its bistable behavior.<sup>4</sup>

Ordered materials can be categorized based on their magnetic exchange interactions. These interactions can either be ferromagnetic or antiferromagnetic in nature. The distinction arises due to the alignment of the magnetic moments within the material. The interaction mechanisms responsible for these alignments are diverse. They can be direct, dipolar, superexchange, double exchange, or RKKY (Ruderman-Kittel-Kasuya-Yosida) in conductive materials, among others. Each mechanism results in a specific manner of orientation of the magnetic moments. For instance, when the magnetic moments align in parallel to each other, the outcome is ferromagnetic alignment. A material demonstrating this type of alignment, upon



cooling down, can undergo a transformation, forming its magnetic domain structure and eventually transitioning into a ferromagnetic ordered state once it reaches a critical temperature, referred to as the Curie temperature. Antiferromagnetic ordering is distinguished by the antiparallel orientation of neighboring magnetic moments which under critical temperature (Neel temperature) corresponds to a vanishing total magnetization. There are instances where the crystal structure of a material is made up of two “sublattices”, each having magnetic moments of different magnitudes. This introduces a change in the scenario. A prime example of such a situation is the compound  $\text{Fe}_3\text{O}_4$ . Here, the value of  $S$  is 2 for Fe(II) and 5/2 for Fe(III),  $S$  stands for spin quantum number. Although there is a complex magnetic exchange situation involving a combination of super and double exchange mechanisms, the antiparallel orientation of the magnetic moments produced by the Fe(III) ions results in the material having a net magnetic moment produced by the Fe(II) ions. Once these materials achieve an ordered state, they are referred to as ferrimagnets.<sup>4</sup>

Due to the topic of this habilitation, we must address the behavior of magnetically ordered materials when their particle size diminishes. One key phenomenon that becomes pronounced with decreasing particle size is superparamagnetism. As particles near the superparamagnetic limit—a distinct small size—their magnetic moments become highly sensitive to thermal fluctuations, thereby overcoming the anisotropy barrier. This results in these moments fluctuating between antiparallel directions, leading to an inability to retain permanent magnetization without an external magnetic field. This behavior contrasts with ferro/ferrimagnetic materials, which can maintain their magnetization on their own. There exists a blocking temperature ( $T_B$ ), a specific temperature threshold, below which superparamagnetic particles begin to behave more like their larger, magnetically stable counterparts. Under this temperature, the fluctuations of particles’ magnetic moments are slower than the shortest measurement time, causing them to appear “blocked”.<sup>4</sup>

In the context of this habilitation, it is pertinent to emphasize that magnetic ordering is not confined solely to standard inorganic materials. Indeed, molecular materials can also showcase this intriguing property. There are specific subclasses of coordination polymers that stand out in this regard. For instance, the Prussian blue analogues<sup>5</sup> have been identified as materials that exhibit such magnetic ordering. Moreover, 2D polymers, in which metal ions are interconnected by radical pyrazine ligands,<sup>6</sup> offer another example. Notably, these materials retain their ordered magnetic state even when exposed to ambient conditions, which showcase potential industry applicability.

In this habilitation, two kinds of magnetic bistability are discussed. The first kind is somewhat reminiscent of the previously discussed topic and can be conceptualized as magnetically ordered materials that have been reduced to the size of a single molecule. However, this tempting analogy is misleading. To add complexity, such a molecule might consist of multiple metal centers that engage in either ferromagnetic or antiferromagnetic exchange interactions. Nonetheless, as will be discussed in Chapter 1.1, these materials are termed single-molecule magnets (SMMs) and unlike ferro/ferri/antiferromagnets, they do not show magnetic ordering. However, they still can display hallmarks of magnetic bistability, namely magnetic field hysteresis.<sup>7</sup>

The second type of bistable material under discussion in this thesis also exhibits magnetic hysteresis. In this instance, it is the thermal hysteresis of magnetic moment/susceptibility. In materials exhibiting Spin Crossover (SCO), a transition occurs between at least two phases, low-spin (LS) and high-spin (HS) phase. As implied by their names, these phases produce different magnetic moments due to their distinct ground spin states, with ( $S_{LS} < S_{HS}$ ). When SCO occurs and there are significant changes in the crystal structures of these phases, hysteresis is observed. Specifically, when the differences in the crystal structures of LS and HS phases are pronounced due to changes in the metal-ligand bond lengths and also the influence of non-covalent interactions, temperature-induced transitions between them result in distinct critical temperatures ( $T_{1/2\uparrow}$  when heated,  $T_{1/2\downarrow}$  upon cooling). Such thermal hysteresis is a hallmark of magnetic bistability. This phenomenon will be briefly discussed in chapter 1.2.<sup>8</sup>

## 1.1 Single-molecule magnets

Single-Molecule Magnets (SMMs) exhibit slow-relaxation of magnetization and behaviors characteristic of superparamagnets, displaying magnetic hysteresis below their blocking temperature,  $T_B$ . An essential parameter defining SMMs is their spin-reversal barrier ( $U_{\text{eff}}$ ), which manifests as the barrier between the  $\pm M_S$  states. This arises from the total ground spin state of molecule  $S$  and the axial anisotropy zero-field splitting (ZFS) parameter of magnetic anisotropy, referred to as  $D$ .  $D$  can manifest as either negative (axial magnetic anisotropy, easy axis) or positive (equatorial magnetic anisotropy, easy-plane). Molecules exhibiting a negative  $D$  value possess maximal  $|M_S|$  states that adopt the lowest energy. Conversely, in compounds featuring a positive  $D$  value, the spin-reversal barrier is absent, typically leading to the absence of slow magnetization relaxation. The well-established relationship defines  $U_{\text{eff}}$  for integer  $S$  as  $U_{\text{eff}} = |D| \times S^2$  and for non-integer  $S$  s as  $U_{\text{eff}} = |D| \times (S^2 - 1/4)$ . While several deviations from this pattern have been documented, particularly within the realm of SMMs containing a single paramagnetic center so called 3d-based Single-Ion Magnets (SIMs),<sup>9</sup> these exceptions often find explanations rooted in alternative relaxation mechanisms than Orbach relaxation process (overcoming the spin reversal barrier). Another option comprises a unique combinations of the ZFS parameters ( $E/D$  close to  $1/3$ ,  $E$  stands for rhombicity parameter), which eventually leads to axial anisotropy even in the scenarios with positive value of the  $D$  parameter. The spin Hamiltonian involving ZFS terms reads as follows:

$$\hat{H}_{ZFS} = D \left( \hat{S}_z^2 - \frac{1}{3} \hat{S}^2 \right) - E (\hat{S}_x^2 - \hat{S}_y^2) \quad (1)$$

The Orbach relaxation process, depicted by the red arrows in **Fig. 1**, illustrates how the magnetic moment surmounts the spin-reversal barrier and progressively aligns with the system's  $M_S$  levels.<sup>10</sup> However, multiple other relaxation processes also merit consideration and are briefly expounded upon below. The direct relaxation process can occur between the non-degenerate  $\pm M_S$  states. The Raman relaxation process, illustrated by the orange arrows in **Fig. 1**, employs virtual states to surmount the spin-reversal barrier. Quantum Tunneling of Magnetization (QTM), represented by the green arrow in **Fig. 1**, arises when the magnetic moment traverses the energy barrier between two degenerate states via quantum tunneling phenomena.

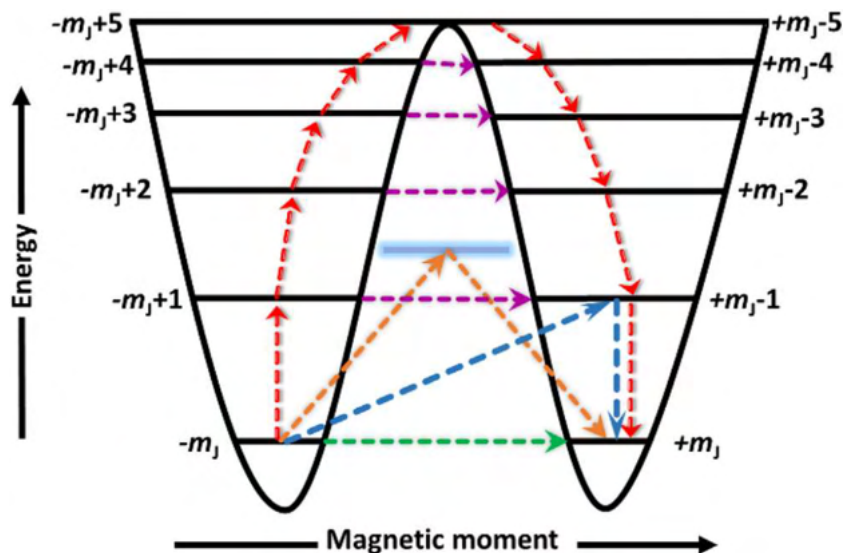


**Figure 1** Depiction of different relaxation processes. The red and blue arrows represent the Orbach process, green represents QTM, purple indicates thermally assisted QTM, and orange represents the Raman process. Adapted from ref.10

When the Quantum Tunneling of Magnetization QTM process is predominant, the complex does not demonstrate slow relaxation of magnetization in the absence of an external magnetic field. However, upon the application of an external magnetic field, the QTM process is suppressed. As a result, these compounds then exhibit what is termed as "field-induced relaxation of magnetization". Within the group of 3d transition metal-based SIMs, it is noteworthy that complexes displaying slow relaxation of magnetization without any external magnetic field are relatively scarce. Such instances are exceptional and pertain to only a handful of documented cases and these are termed zero-field SIMs (ZF-SIMs). Of note is that ZF-SIMs are complexes possessing huge axial magnetic anisotropy and negligible rhombicity. Conversely, a significant number of field-induced SIMs have been reported in scientific literature to date. The relaxation mechanisms in SMMs are not the central focus of this habilitation, so they will not be discussed in depth. However, for those interested, an excellent introductory review on this topic, recently written by J. Zadrozny et al., is recommended.<sup>11</sup>

Magnetic anisotropy plays a pivotal role in the functionality of SMMs. Beyond simply defining the spin reversal barrier, it provides the foundation to engineer SMMs with significantly elevated spin reversal barriers, as highlighted through a brief historical journey. In 1993, R. Sessoli and colleagues<sup>12</sup> made a breakthrough with the discovery of the renowned  $Mn_{12}$  acetate compound, the very first SMM. This particular compound was characterized by a large ground spin state and a relatively small axial anisotropy constant ( $D = -0.46 \text{ cm}^{-1}$ ,  $S = 10$ ). The discovery of  $Mn_{12}$  acetate spurred a rapid influx of research into polynuclear SMMs in the subsequent decade. Initial enthusiasm in this direction, however, was met with unforeseen challenges. Contrary to the anticipated behavior deduced from the energy barrier equation, it was later established that  $S^2$  inversely affects  $D$ .<sup>13</sup> Moreover, the magnetic moments of individual paramagnetic centers do not align parallelly.<sup>14</sup> As a result, the cumulative anisotropy – a summation of all the components – remains limited. Upon this revelation, researchers discerned the pivotal role played by magnetic anisotropy. This insight revolutionized the approach towards SMMs design, steering it towards the synthesis of SMMs possessing a single paramagnetic center (SIMs) accompanied by pronounced magnetic and axial anisotropy.

In a groundbreaking study in 2003, N. Ishikawa et al.<sup>15</sup> demonstrated for the first time that coordination compounds, even those with just a single paramagnetic center like Tb(III), could exhibit slow relaxation of magnetization. This discovery had a profound impact, paving the way for subsequent investigations into 3d-based SIMs.

S. Karasawa et al.<sup>16</sup> made significant progress with the unveiling of the first 3d-based SIM, a Co(II) complex. Intriguingly, while the cobalt atom takes center stage in this compound, it is not the lone contributor to the magnetic moment. This is evident as the Co(II) atom is coordinated by four carbene ligands, each endowed with two unpaired electrons. The advances in Co(II) compounds were followed by the discovery of the Fe(II) SIMs by D. E. Freedman et al. in 2010.<sup>17</sup> After these key events, lots of research started focusing on SIMs, showing a big change in how we think about magnetism in molecular materials.

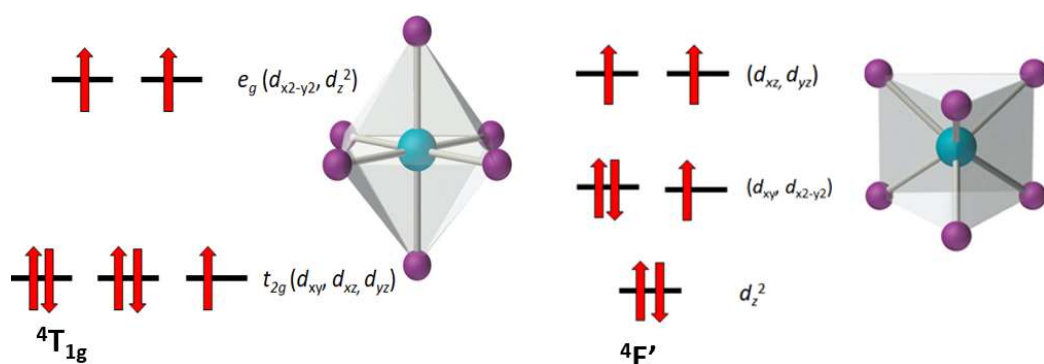


**Figure 2** Illustration of electron configuration of the ground state for Co(II) complexes with octahedral (left) and trigonal prismatic (right) geometry of coordination polyhedron. Ligand field terms are emphasized in bold. Red arrows represent electrons.

When considering the design of high-performing SMMs, a primary question arises: How can one attain pronounced and axial magnetic anisotropy? The key rests in the careful design of the coordination sphere of the complex molecule. By ensuring the appropriate symmetry, one can foster significant magnetic anisotropy.

In general, magnetic anisotropy can be induced via first-order or second-order effects. It is worth noting that immense axial anisotropies often result from first-order effects, stemming directly from the spin-orbit coupling's contribution to the ground state. A fitting illustration of this concept can be observed in Co(II) complexes. In instances where the coordination geometry assumes a regular octahedral form, the ground state is represented by the  ${}^4T_{1g}$  crystal field term (**Fig.2**). Under these conditions, the angular momentum predominantly contributes to ZFS. This arises since the spin-orbit coupling operator transforms under  $t_{1g}$ , allowing a direct mixing with the ground state. Consequently, this induces substantial magnetic anisotropy but of the easy-plane type.<sup>18</sup> In such scenario, the conventional spin Hamiltonian description becomes less applicable, and low-lying excited states emerge.<sup>19</sup> However, for the creation of highly anisotropic magnetic molecules, alterations in the standard octahedral geometry are essential. These changes can manifest through elongation/compression of the metal-ligand bonds or even through trigonal distortion. Both forms of distortion can yield double orbitally degenerate ground states ( ${}^4E_g$  for a compressed octahedron with  $D_{4h}$  symmetry and  ${}^4E'$  for a trigonal prism with  $D_{3h}$  symmetry). Once again, these states are characterized by a significant influence of the

spin-orbit coupling on the ground state. However, it is crucial to recognize that, unlike the  ${}^4T_{1g}$  state, the anisotropy associated with E-states exhibits an axial nature.<sup>20</sup> This is very important for preparation of ZF-SIMs which typically exhibit large axial anisotropy and negligible rhombicity.

In addition to the aforementioned instances, E-states can also be identified in Co(II) complexes that adopt various low-coordinate geometries. Examples include the square pyramidal configuration, characterized by  $C_{4v}$  symmetry ( ${}^4E$ ), and the linear geometry ( ${}^4I_1$ ). In the case of the latter, the influence of spin-orbit coupling is so predominant that it can lead to the observation of non-Aufbau ground states.<sup>21</sup> While the Co(II) compounds serve as notable examples of SIMs with E ground states, there are other instances within 3d metal-based ZF-SIMs worth highlighting. Specifically, instances such as linear two-coordinate Fe(I)<sup>22,23</sup> and pentacoordinate Fe(III) SIMs<sup>24</sup> have been documented. Additionally, it is important to emphasize that ZF-SIMs have been identified in tetracoordinate Co(II) complexes, which intriguingly, do not always exhibit E ground states.<sup>25,26, 27</sup>

Eliseo Ruiz et al.<sup>28</sup> proposed a qualitative model to generalize changes in magnetic anisotropy based on proximity to the E-term. This model emphasizes several key considerations:

(i) The sign of  $D$  hinges on the comparative magnitudes of  $D_{zz}$  and  $(D_{xx} + D_{yy})/2$ . Specifically, when  $|D_{zz}|$  surpasses  $|(D_{xx} + D_{yy})/2|$ ,  $D$  is negative. Conversely, if the latter is greater,  $D$  is positive.

The magnitude of the  $D_{ii}$  components is largely influenced by two factors:

(ii)  $m_l$  of the orbitals involved in the integrals with the angular momentum operator.

(iii) The energy gap between these orbitals can be approximated at the extended-Hückel level, accounting solely for excitations of the same multiplicity. Notably, significant contributions to the integrals with the z-component of the angular momentum operator,  $l_z$ , arise when the two orbitals involved in the initial excitations have identical  $|m_l|$  values, such as  $d_{xy}$  and  $d_{x^2-y^2}$  (where  $m_l = \pm 2$ ) or  $d_{xz}$  with  $d_{yz}$  (where  $m_l = \pm 1$ ). For the  $D_{xx}$  and  $D_{yy}$  terms, the larger integral values correspond to orbitals with  $m_l$  changes of  $\pm 1$ . For the integrals associated with the z-component of the angular momentum operator,  $l_z$ , significant contributions emerge when the orbitals involved in the initial excitations share the same absolute  $m_l$  value. Specifically, this occurs with the orbitals  $d_{xy}$  and  $d_{x^2-y^2}$  (where  $m_l = \pm 2$ ) or with  $d_{xz}$  and  $d_{yz}$  (where  $m_l = \pm 1$ ).

## ***1.2 Semi-coordination and single-ion magnets***

A semicoordination bond (SB),<sup>29</sup> often viewed as the non-covalent counterpart of the coordination bond, remains relatively elusive in the literature. However, its presence is distinct, especially in metal centers with labile coordination numbers, such as Cu(II). This captivating bonding phenomenon, has not been explored as deeply as other non-covalent interactions involving metal atoms, like regium and spodium bonding. This existing knowledge gap motivated our initial exploration of semi-coordination in conjunction with SIMs. It subsequently led us to introduce and harness this phenomenon in designing novel classes of Co(II) SIMs.

The term 'semicoordination' was coined by Brown et al. in 1967.<sup>30</sup> In their research, they delved into the structure of the copper(II) complex  $[\text{Cu}(\text{en})_2](\text{BF}_4)_2$  (en = ethane-1,2-diamine). Through their analysis, the authors identified weak  $\text{Cu}\cdots\text{F}$  interactions, classifying these unique interactions as semi-coordination. They described it as a bond that is intermediate, situating somewhere between typical coordination and very weak coordination. This type of bond was interpreted as an edge case of axial elongation in the Cu coordination octahedron, an effect attributed to the Jahn-Teller distortion. An intriguing observation was made by the authors: despite the significant  $\text{Cu}\cdots\text{F}$  separation the contact had a noticeable impact on the IR spectra of the complexes. This spectral shift suggested a minor distortion of  $\text{BF}_4^-$ , confirming the existence of a subtle yet discernible  $\text{Cu}\cdots\text{F}$  interaction.

Currently, semi-coordination is understood as a type of non-covalent contact. It occurs between an electrophilic region associated with the metal atom and nucleophilic region of the non-metal part of the same or another molecule. To identify semi-coordination, one can look at the distance between the metal (M) and the non-metal (X) atoms. This distance should be shorter than the total sum of their van der Waals radii. Yet, it should still be longer than the regular bond length when both M and X have their usual formal oxidation states. Interactions between transition metal atoms and electron-donor non-metal centers are typically characterized as coordination bonds. Their strengths can vary widely, ranging from a mere few to several dozen  $\text{kcal mol}^{-1}$ . Though the term "semi-coordination bonding" lacks a formal definition, it is generally understood to cover noncovalent interactions dominated by electrostatic forces, with minor influences from charge polarization and charge transfer (CT). Differentiating between conventional and weak coordination bonds is often based on structural criteria. Specifically, the distance between the metal (M) and electron-donor atom (X) in semi-coordination should be longer than the sum of relevant covalent radii but shorter than the combined van der Waals radii.<sup>29</sup>

The Quantum Theory of Atoms in Molecules (QTAIM)<sup>31</sup> offers a real-space method to probe bonding diatomic interactions with significant exchange energy contributions, enabling the construction of atomic connectivity graphs. Characteristics of these bonding descriptors, like interatomic surfaces and (3,-1) critical points (CPs) of electron density  $\rho(\mathbf{r})$ , act as reference points for assessing diatomic interactions concerning charge distribution and energy contributions. For example, topographical analysis of  $\rho(\mathbf{r})$  in metal complexes often signifies  $\text{M}\cdots\text{X}$  bonding interactions, evident from a (3, -1) CP and a bond path connecting M and X nuclei. According to QTAIM, most noncovalent interactions, like semi-coordination bonds, lean towards being closed-shell types. This indicates a notable electronic charge depletion between atoms, primarily supported by the kinetic energy of electrons, i.e. at specific CPs,  $\nabla^2\rho(\mathbf{r}) > 0$ , full energy density of electrons  $h_e(\mathbf{r}) > 0$ . In contrast, traditional coordination bonds typically align with an intermediate interaction type (at the CP,  $\nabla^2\rho(\mathbf{r}) > 0$ ,  $h_e(\mathbf{r}) < 0$ ). It is worth noting that, due to potential inaccuracies in computing  $h_e(\mathbf{r})$  values, this criterion remains as formal as the geometric one, mainly highlighting the presence of covalent contributions.<sup>32</sup>

Another useful criterion is a ratio of electron potential ( $V_e$ ) and kinetic ( $G_e$ ) energy densities, calculated at CP. Interpreting  $V_e$  and  $G_e$  as the pressures exerted on and by the electrons at CP, a ratio  $V_e/G_e > 1$  indicates that the interaction is stabilized by a localized charge concentration. Upon the formation of a bond molecular orbital (BMO), the redistribution of  $\rho(\mathbf{r})$  within the internuclear region allows for an increase in both the quantity of electrons and their localized concentration. Conversely, a pure closed-shell interaction upon strengthening results in a depletion of the increased charge. In summary, three  $V_e/G_e$  regions can be identified<sup>32</sup>:

- (I) pure closed-shell interactions, characterized by  $V_e/G_e < 1$  and  $h_e(\mathbf{r}) > 0$ ,
- (II) closed shell interactions with some degree of covalency, where  $V_e/G_e = 1-2$  and  $h_e(\mathbf{r}) < 0$ . Of note is that within this region, there is a pronounced increase in charge associated with BMO,
- (III) shared shell interactions,  $V_e/G_e > 2$ ,  $h_e(\mathbf{r}) \ll 0$ .

The interaction energy of non-covalent interactions can be estimated from the virial by calculating  $E_{\text{int}} = V_e/2$ .

Two significant examples stand out when considering the interaction between semi-coordination and magnetism. Firstly, Nelyubina et al.<sup>33</sup> suggested that even relatively long and weak interatomic contacts in  $\text{Na}_2\text{Cu}(\text{CO}_3)_2$  ( $d(\text{Cu}\cdots\text{O}) = 3.6 \text{ \AA}$ ), can form magnetic super-exchange pathways, in the current case antiferromagnetic exchange was observed (**Fig.3**). This confirms the possibility of weak interactions even at such distances. Another instance<sup>34</sup> highlights the mediation of a weak antiferromagnetic exchange interaction by a  $\text{Cu}\cdots\text{S}$  semi-coordination bond in the copper(II) 1,3-dithiole-2-thione-4,5-dithiolate complex, where  $d(\text{Cu}\cdots\text{S}) = 3.144(1) \text{ \AA}$  (**Fig.3**).

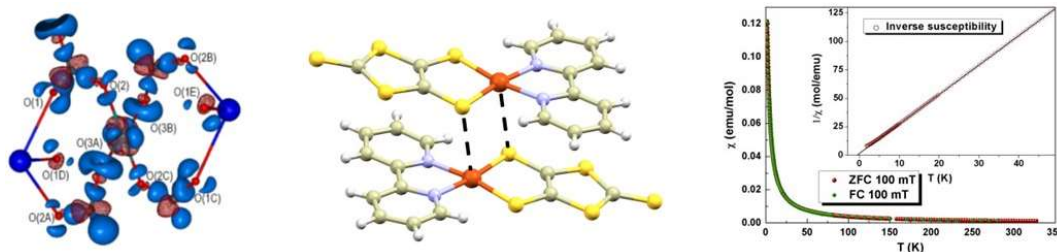


**Figure 3** Experimental deformation electron density in selected fragment of  $\text{Na}_2\text{Cu}(\text{CO}_3)_2$  (left). The fragment of the crystal structure of copper(II) 1,3-dithiole-2-thione-4,5-dithiolate complex highlighting  $\text{Cu}\cdots\text{S}$  interaction (black dashed line, middle) and magnetic properties measured for this complex (right).

We first delved<sup>35</sup> into the study of semi-coordination bonds in SMM compounds, publishing our results in 2016. Complex  $[\text{Co}(\text{dpt})(\text{NCS})_2]$ , with dpt being bis(3-aminopropyl)amine. This compound, previously prepared and described by J. Boeckmann et al.,<sup>36</sup> has a molecular structure that features the dpt ligand coordinating tridentately to the Co(II) atom, with two  $\text{NCS}^-$  ligands coordinating in a monodentate manner. The primary amine groups in the compound form two shorter Co–N bonds, measured at 2.076(1) and 2.082(1)  $\text{\AA}$ , respectively. In contrast, the secondary amine group gives rise to a longer Co–N bond of 2.197(2)  $\text{\AA}$ . The isothiocyanato ligands connect to the Co(II) atom at two distinct Co–N distances: 2.004(1) and 2.120(2)  $\text{\AA}$ . Evaluating the structure using the Addison parameter,<sup>37</sup> the chromophore geometry is positioned almost midway between the ideal SPY ( $\tau = 0$ ) and TBY ( $\tau = 1$ ) geometries, with  $\tau = 0.46$ . The crystal structure consists of  $[\text{Co}(\text{dpt})(\text{NCS})_2]_2$  supramolecular dimers connected by weak N–H $\cdots$ S hydrogen bonds, measured at  $d(\text{N}\cdots\text{S}) = 3.590(1) \text{ \AA}$ , between the secondary amine groups and thiocyanato ligands. Within the dimer, there appears to be a potential  $\text{Co}\cdots\text{N}$  interaction at  $d(\text{Co}\cdots\text{N}) = 3.541(1) \text{ \AA}$  with thiocyanido ligand of the adjacent molecule of the dimer (**Fig. 4A**). Given the  $\text{NCS}^-$  ligand's primary role as a sigma donor, a direct  $\text{Co}\cdots\text{N}$  interaction from this already coordinated atom is questionable. Another notable feature in  $[\text{Co}(\text{dpt})(\text{NCS})_2]$  is the short distance, 3.550  $\text{\AA}$ , between the Co(II) atom and the centroid of the N–C bond on the  $\text{NCS}^-$  ligand. Hirschfield surface analysis using CrystalExplorer<sup>38</sup> shows electron density between the carbon and nitrogen atoms interacting



with the Co(II) atom (**Fig. 4B**), suggesting a  $\text{Co}\cdots\pi$  interaction where the  $\text{NCS}^-$  ligands donate  $\pi$  electrons.

Magnetic data were assessed based on temperature and field variations of the magnetic moment. **Fig. 4C** displays the temperature dependence of the effective magnetic moment ( $\mu_{\text{eff}}$ ) and the field-related magnetization ( $M_{\text{mol}}$ ) of  $[\text{Co}(\text{dpt})(\text{NCS})_2]$ . At 300 K, the  $\mu_{\text{eff}}$  value is  $4.56 \mu_{\text{B}}$ , surpassing the spin-only value for  $S = 3/2$  and  $g = 2.0$  ( $3.87 \mu_{\text{B}}$ ). This suggests notable spin-orbit coupling, indicating  $g > 2.0$ . The  $\mu_{\text{eff}}$  remains mostly steady until 100 K, after which it gradually decreases, indicating prominent magnetic anisotropy due to ZFS. Around 10 K, a shift in  $\mu_{\text{eff}}$  is noted, with values rising from about  $3.88$  to  $3.96 \mu_{\text{B}}$  (**Fig. 4C**). This behavior is characteristic of weak ferromagnetic interactions in the crystal structure. The magnetic data was fitted utilizing a spin Hamiltonian that incorporated isotropic magnetic exchange ( $-J\vec{S}_1\vec{S}_2$ ) and ZFS terms. This resulted in the following set of the parameters with positive value of isotropic exchange constant  $J$ :  $J = +0.27 \text{ cm}^{-1}$ ,  $g = 2.34$ ,  $D = +36.2 \text{ cm}^{-1}$ ,  $E/D = 0.33$ .

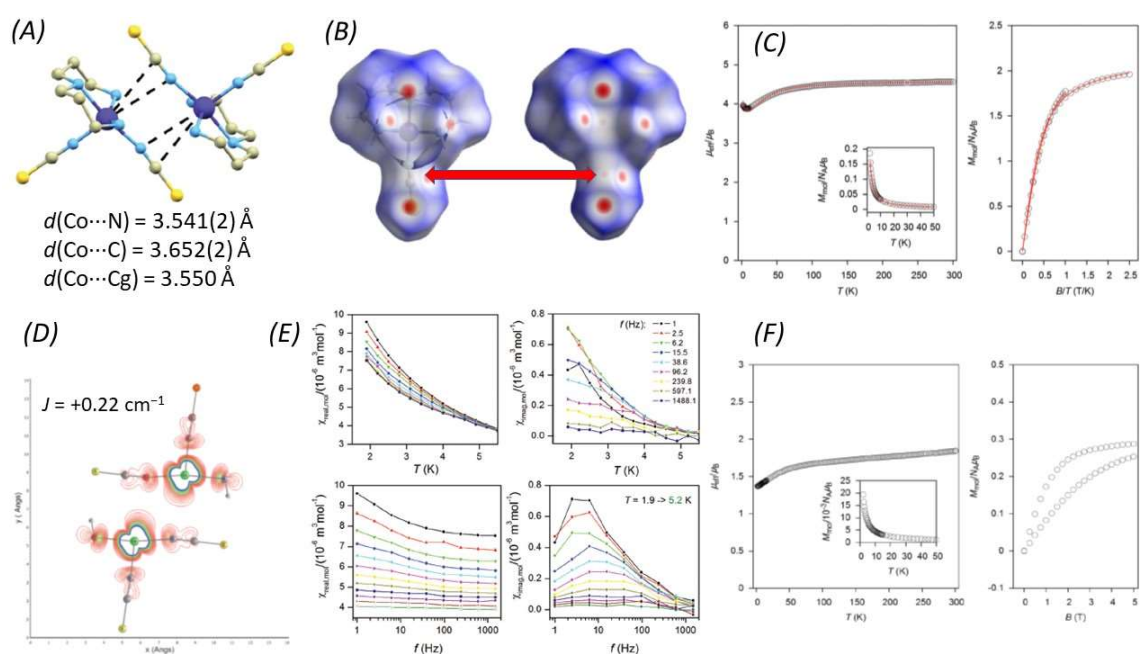


**Figure 4** A Perspective view of a centrosymmetric supramolecular dimer,  $\{\text{Co}(\text{dpt})(\text{NCS})_2\}_2$  (A), with highlighted shortest  $\text{Co}\cdots\text{C}$  and  $\text{Co}\cdots\text{N}$  distances (indicated by black dashed lines). Hirschfeld surface of the  $[\text{Co}(\text{dpt})(\text{NCS})_2]$  molecule mapped with  $d_{\text{norm}}$ . Red areas represent non-covalent interactions where the distance between specific atoms is shorter than the sum of their van der Waals radii, (B). Static magnetic data measured for  $[\text{Co}(\text{dpt})(\text{NCS})_2]$ , (C). Spin density contour plot in the  $\{\text{Co}-\text{C}-\text{Co}-\text{C}\}$  plane of supramolecular dimer,  $\{\text{Co}(\text{dpt})(\text{NCS})_2\}_2$ , where C belongs to the thiocyanate ligand calculated by B3LYP/ZORA/-def2-TZVP(-f), (D). Dynamic magnetic data measured for  $[\text{Co}(\text{dpt})(\text{NCS})_2]$  and its Zn diluted derivative (E, Co on left, Zn diluted right column). Static magnetic data measured for Zn diluted derivative (F).

Theoretical *ab initio* calculations further confirmed these values. Using Broken-Symmetry Density Functional Theory (BS-DFT) allowed us to investigate magnetic coupling within the supramolecular dimer and we revealed at B3LYP/ZORA/-def2-TZVP level of theory<sup>39</sup> that magnetic coupling is indeed of ferromagnetic nature and the value of the  $J$  is in excellent agreement with the experiment ( $J = +0.22 \text{ cm}^{-1}$ ). Furthermore, these calculations helped us to explore the exchange pathway mediating magnetic exchange interaction. Three magnetic orbitals facilitate this exchange between the cobalt atoms. The most overlapping orbitals are orthogonal, contributing to the ferromagnetic exchange. These orbitals align with the direction of the  $\text{Co}\cdots\pi$  interaction. This is further evident in **Fig. 4D**, which displays the



spin density in the Co–NCS⋯Co–NCS section. The calculation results strongly support the presence of the superexchange pathway through the Co⋯π interactions. Measurements of AC susceptibility (**Fig. 4E**) revealed that this compound acts as field induced SIM. The slow-relaxation of magnetization noticeably differs between the bulk compound and the Zn-diluted sample (Co:Zn = 1:9). Distinct static magnetic properties of the Zn-diluted sample were further confirmed through measurements, which showed that, upon dilution, the ferromagnetic exchange interaction is no longer evident (**Fig. 4F**). This is consistent with the low likelihood of both central atoms in the supramolecular dimer being occupied by the Co(II) atom. All these findings underscore the influence of the Co⋯π interaction on both static and dynamic magnetic properties within this complex.

This paper was foundational for our subsequent research on Co(II) SIMs. We realized that semi-coordination offers a unique avenue to explore the magnetic anisotropy of complexes with atypical coordination geometries, especially those that sit on the boundary between formal coordination numbers (e.g., between 4 and 5 or 4 and 6). Additionally, semi-coordination, being an attractive non-covalent interaction, might aid in stabilizing coordination geometries that lead to E-ground states. As discussed previously, while these are intriguing for creating systems with significant axial magnetic anisotropy, they are scarcely reported, because the Jahn-Teller effect tends to significantly alter or disrupt their coordination geometry.

Another crucial realization was that, when properly designed, semi-coordination could stabilize low-coordinate species, which often display large axial anisotropies. The semi-coordination may help stabilize low coordinate molecules by protecting the formally unoccupied sites of the metal atom without destroying their unique magnetic properties. This strategy could pave the way toward our ultimate objective: depositing SIMs on functional surfaces as chemically stable mono- or sub-monolayer thick films.

### 1.3 Spin crossover

Compounds exhibiting specific kind of spin transitions, so called SCO materials, belong to a special class of magnetic materials. Transition metal complexes of the fourth period, with an electron configuration of  $3d^4$ - $3d^7$ , can in certain cases form two distinct spin isomers: high-spin (HS) and low-spin (LS).<sup>40</sup> By "crossover", we mean the thermodynamic transition between these two isomers, hence the possibility of the coexistence of both states in certain situations. The condition for the mole fraction of the low-spin and high-spin fraction must always be met:  $x_{LS} + x_{HS} = 1$ . The equilibrium could be disrupted by temperature, pressure, and electromagnetic radiation. This transformation is an entropy-driven process where  $\Delta H > 0$  and  $\Delta S > 0$ . The critical temperature at which  $x_{HS} = 0.5$  ( $\Delta G = 0$ ) is expressed by the relationship:

$$T_{1/2} = \Delta H / \Delta S \quad (2)$$

The Ligand Field Theory (LFT) provides an appropriate foundation for interpreting the magnetic properties of SCO complexes. A primary condition is the electron configuration of  $3d^4$ - $3d^7$  and typically also (pseudo)octahedral coordination geometry. For central metal atoms of the first transition series, the strength of ligands is essential in the context of the spectrochemical series of ligands. In the case of octahedral symmetry of the coordination polyhedron, the valence 3d orbitals split into two sets:  $t_{2g}$  and  $e_g$ . These are separated by an energy equivalent to the ligand field strength,  $\Delta$ . If the strength of the ligand field they create is greater than the inter-electron repulsion  $P$ , then the  $t_{2g}$  and  $e_g$  behave according to the Aufbau principle as two distinct orbitals, and the configuration of the central atom is LS. When  $\Delta < P$ , in line with Hund's rule of maximum multiplicity, the number of unpaired electrons is

"maximized", and the configuration of the central atom is HS. If the strength of the ligand field satisfies the condition

$$|\Delta-P| \approx kT \quad (3)$$

then these two states can coexist in thermal equilibrium, and SCO can occur.<sup>41</sup>

The spin transition is most commonly characterized by the dependence of the molar fraction of the high-spin fraction on temperature:  $x_{HS}=f(T)$ . This dependence is called the conversion curve, and the fraction  $x_{HS}$  is defined by the relationship.

$$x_{HS} = \frac{n_{HS}}{n_{HS}+n_{LS}} \quad (4)$$

With the change in spin state, structural parameters of molecules also change, such as bond lengths, intramolecular volume, distortion of the coordination polyhedron, and lattice parameters. The transition of two electrons from the non-bonding  $t_{2g}$  orbital to the anti-bonding  $e_g$  results in a decrease in bond order, thus weakening the bonds and extending the bond distances of the coordination polyhedron. This implies a change in characteristics dependent on these parameters: vibrational and electron spectra change, and since the strength of the ligand field also changes, there is a change in electron configuration. This often results in a change in the color of the compound - thermochromism is observed (**Fig.5**). SCO has been observed mainly in the solid phase of coordination compounds of Fe(II), Fe(III), Cr(II), and Co(II), and in some complex compounds even in solution.

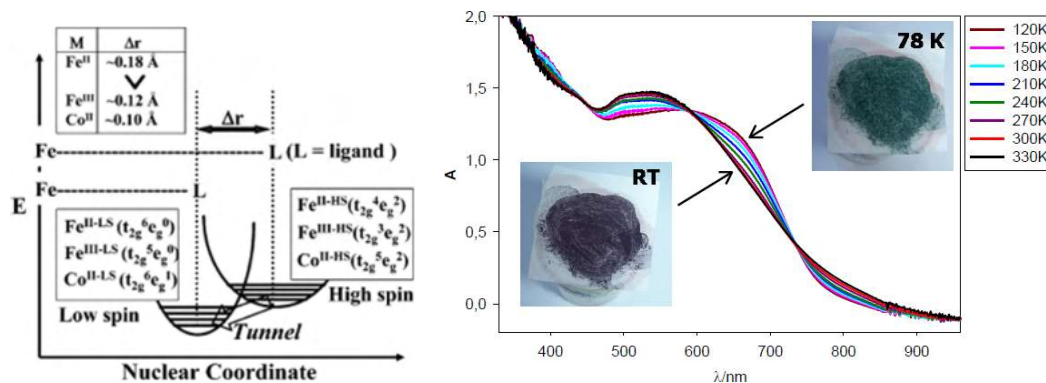


**Figure 5** Differences of metal-ligand bond distances among spin isomers of Fe(II), Fe(III), and Co(II) SCO complexes (left).<sup>42</sup> An example of thermochromism is observed in the Fe(III) Schiff base complex, which is accompanied by solid-state, temperature-dependent UV-VIS measurements.<sup>43</sup>

An essential characteristic for solid substances exhibiting SCO is cooperativity.<sup>44</sup> It determines the "steepness" of the conversion curve and also the presence of hysteresis. By cooperativity, we mean the ability of molecules to "sense" each other in the crystal lattice of a solid, essentially forming a certain kind of domains where there is a simultaneous change in the spin state. The larger the average volume of such domains, the steeper the transition. This is conditioned by the presence of intermolecular interactions such as hydrogen bonds (between complex molecules or through a solvent) or close interaction of benzene cores of the nearest neighbors, known as " $\pi$ - $\pi$  stacking." Simplified, it can be said that the more interactions there are, the more delayed the change in spin state will be; however, the steeper the conversion curve will be. SCO hysteresis refers to the phenomenon where the transition from a LS state to a HS

state (and *vice versa*) does not follow the same path upon heating as it does upon cooling. Essentially, the temperature at which a compound transitions from one spin state to another during heating can differ from the temperature at which it transitions during cooling.

The presence of hysteresis in SCO systems<sup>45</sup> is closely related to cooperativity. As a molecule undergoes a spin transition, it can induce its neighboring molecules to experience the same transition due to significant intermolecular interactions. This chain reaction results in the creation of domains or regions with molecules sharing the same spin state. As the system undergoes heating or cooling, these domains expand or contract, albeit not necessarily at identical rates or starting points. The system's history (whether previously heated or cooled) can affect the size and distribution of these domains, producing the observed hysteresis effect.

Another crucial factor in the manifestation of SCO hysteresis is the structural changes that accompany the spin transitions. When molecules transition between low-spin and high-spin states, they often undergo concomitant structural adjustments. These changes can alter bond lengths, molecular shapes and volumes, and even the overall crystal structure. Such structural transformations can introduce additional energy barriers or stabilize specific configurations, making it more challenging for the system to revert to its original state. These structural changes, combined with the energy barriers between the HS and LS states, can further enhance the hysteresis phenomenon.

In our studies prior to 2018, our primary focus was on the magnetic behavior of mononuclear or dinuclear Fe(III) Schiff base complexes. Schiff base ligands are an excellent choice for systematic research in this area. Their structures are straightforward and cost-effective to modify. This ease of modification allows for systematic tuning of the magnetic properties of the complexes. By making subtle changes to the Schiff base ligands, we can fine-tune and understand the resulting magnetic behavior in greater detail.

I would like to emphasize two of our studies published earlier that are of notable significance. In 2012, we reported on a series of iron(III) SCO compounds formed with hexadentate Schiff-base ligands.<sup>46</sup> Interestingly, these ligands, commonly used in preparing Fe(II) and Fe(III) SCO complexes, arise from reactions between variously substituted aromatic 2-hydroxy-aldehydes and triethylenetetramine. While these ligands are often abbreviated as H<sub>2</sub>saltrien and Hsal<sub>2</sub>trien in literature, we will refer to them using the abbreviation H<sub>2</sub>R-L6 here, with 'R' indicating the aromatic ring substitution. Our research ambition was to expand the number of intermolecular interactions and therefore, we made modifications to the Schiff base ligand by incorporating peripheral hydroxy groups at the fourth position. This led to the creation of a series of isostructural compounds represented by the formula [Fe(4OH-L6)]X, where 'X' stands for the Cl<sup>-</sup>, Br<sup>-</sup>, or I<sup>-</sup> anions.

The compounds in the studied series are isomorphous, crystallizing in the *P2/c* space group. They possess one-dimensional zig-zag chains of the [Fe(4OH-L6)]<sup>+</sup> cations. These chains are stabilized by N-H···O hydrogen bonds between the amino nitrogen atoms and peripheral hydroxy oxygen atoms, as well as by offset  $\pi$ - $\pi$  stacking interactions between the phenyl rings of neighboring cations. Furthermore, the zig-zag chains are interconnected via O-H···X hydrogen bonds with halide anions. Static magnetic data (**Fig. 6**) revealed weak antiferromagnetic interactions at lower temperatures, with the strength of the interaction increasing for smaller halide anion volumes. At higher temperatures (> 300K), the onset of SCO is observed, where a smaller anion volume results in a higher critical SCO temperature. An analysis of structural and magnetic data indicates that both the centroid-centroid distances in the ring-ring stacking interactions and the O-H···X hydrogen bond distances play a crucial role in mediating the exchange interaction. Remarkably, when compounds under study were dissolved, dark brown solutions formed at room temperature. Cooling these with liquid nitrogen changed their color to bright blue, as shown in **Fig. 6**. This reversible process indicates a spin crossover phenomenon with thermochromism between 77–300 K in solution which was studied

by EPR (Fig. 6). In summary, this series demonstrates that compounds with  $[\text{Fe}(\text{4OH-L6})]^+$  cations can exhibit SCO. Their magnetic properties are notably influenced by non-covalent interactions and the selected counter anion. While this behavior is observed in other SCO complexes, the peripheral hydroxy group in this case facilitates the intentional design of diverse supramolecular architectures which can result in exciting magnetic behavior.

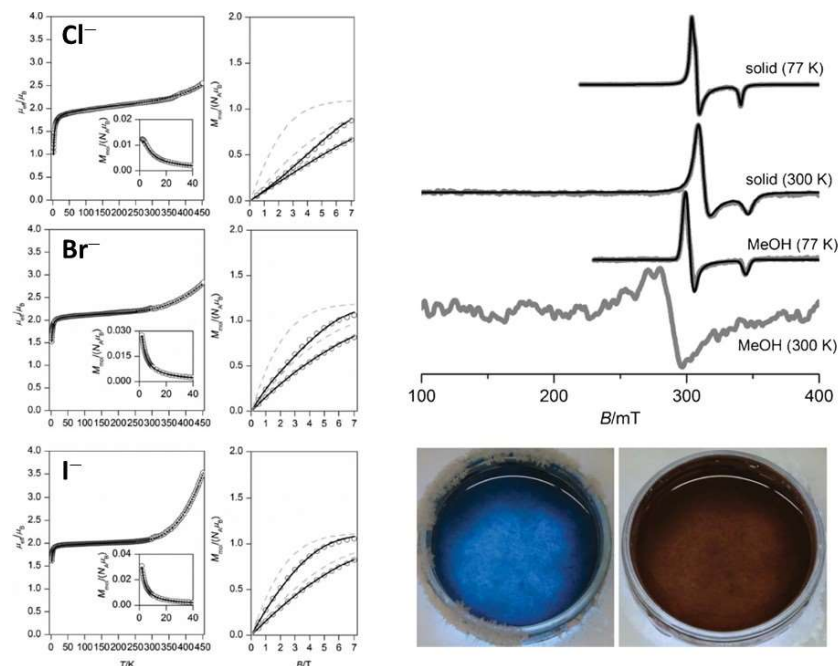


**Figure 6** Static magnetic properties of  $[\text{Fe}(\text{4OH-L6})]\text{X}$  compounds ( $\text{X} = \text{Cl}^-, \text{Br}^-, \text{I}^-$ , left). The powder and solution X-band EPR spectra of iodide compounds at different temperatures (above right). The thermochromism for the methanolic solution of iodide compound (below right, room temperature, below left, cooled down closely to the freezing point of the solution).

Another notable previous work focused on a series of solvatomorphs of the  $[\text{Fe}(\text{napet})(\text{NCS}/\text{Se})]$  complex, where  $\text{H}_2\text{napet}$  represents  $\text{N,N}'$ -bis(2-hydroxy-naphthylidene)-1,6-diamino-4-azahexane.<sup>1</sup> Eight such complexes were synthesized. Their crystal structures showed they are isostructural, comprising  $[\text{Fe}(\text{napet})(\text{NCS}/\text{Se})]$  and Solv molecules (Solv = tetrahydrofuran (THF), methanol (MeOH) and 0.5 pyrazine (PYZ), butanone (MEK),  $\text{N,N}'$ -dimethylformamide (DMF), dimethyl sulfoxide (DMSO), 0.5MeOH and 0.5 MEK acetone). These assemble into a three-dimensional framework through  $\text{C-H}\cdots\text{O}$  and  $\text{C-H}\cdots\pi$  interactions. Central to this framework is a centrosymmetric dimer, formed by two adjacent  $[\text{Fe}(\text{napet})(\text{NCS}/\text{Se})]$  molecules. These are linked by a  $\text{C-H}\cdots\text{O}$  contact between the C-H group of the naphthalene ring and the phenolic oxygen atom. An additional stabilization inside the dimer arises from an offset stacking of the naphthalene rings. Solv molecules are placed into cavities located between these dimeric structures and each cavity is occupied by two same guest molecules in most of the cases, as depicted in Fig. 7 (top left). The static magnetic properties of the entire series categorize the compounds into two subgroups: purely HS complexes and SCO complexes. Remarkably, if one inspects the relationship between the length of the  $\text{N-H}\cdots\text{O}$  contact and occurrence of SCO, or even more, its correlation with  $T_{1/2}$ , a possible association can be found (Fig. 7, top right). It is apparent that SCO occurs only in the compound with the donor $\cdots$ acceptor ( $\text{D}\cdots\text{A}$ ) distance shorter than ca. 3.0 Å and moreover, the compounds with the shortest  $\text{D}\cdots\text{A}$  distance have the highest  $T_{1/2}$ . Furthermore, two complexes from the series exhibited SCO accompanied with thermal hysteresis.

To assess the N–H···O contact's influence on SCO behavior and specifically on the critical temperature  $T_{1/2}$ , we examined the bond properties between  $[\text{Fe}(\text{napet})(\text{NCS}/\text{Se})]$  and solvent molecules in  $\{[\text{Fe}(\text{napet})(\text{NCS}/\text{Se})]\cdots\text{Solv}\}$  units, using coordinates as obtained from experimental X-ray structures. We employed the non-covalent interaction (NCI) index using NCIPLOT<sup>47</sup> to visualize both attractive (like hydrogen bonding) and repulsive (steric) interactions.

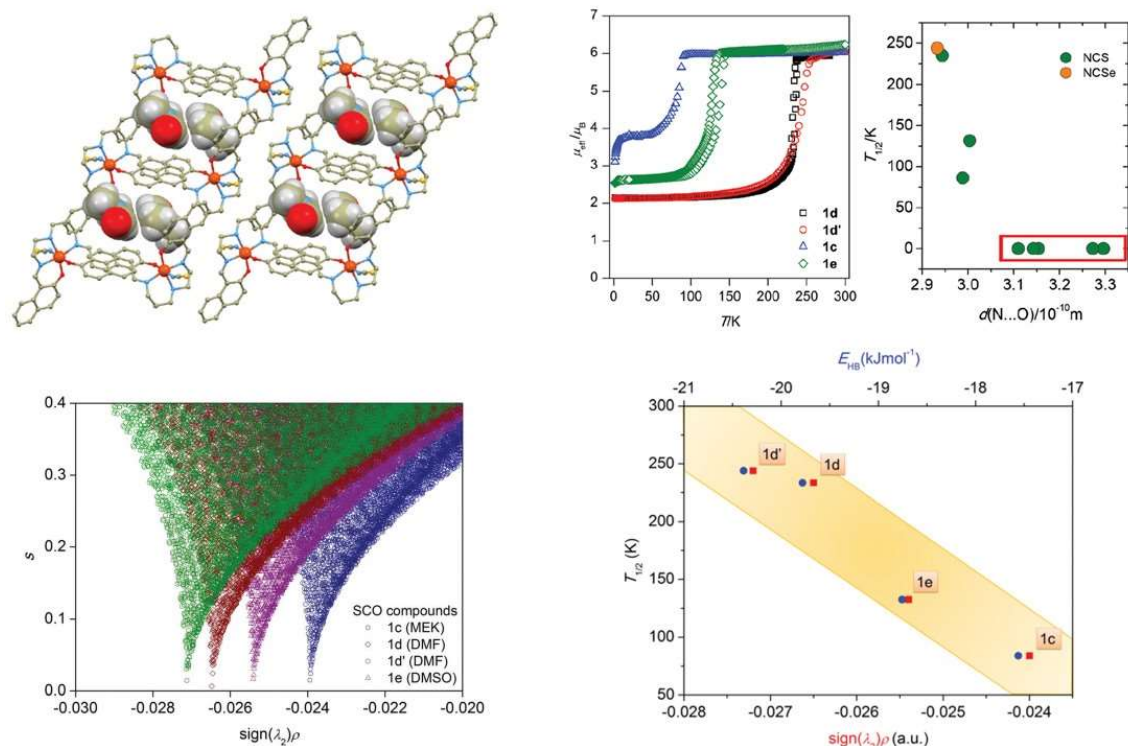


**Figure 7** Top left: Perspective view illustrating supramolecular dimers in the crystal structures of the  $[\text{Fe}(\text{napet})(\text{NCS}/\text{Se})]\cdots\text{Solv}$  complexes, with the guest molecules highlighted using a space-fill model. Top middle: temperature dependence of  $\mu_{\text{eff}}/\mu_{\text{B}}$ , showing the SCO behavior of  $[\text{Fe}(\text{napet})(\text{NCS}/\text{Se})]\cdots\text{Solv}$  complexes. Top right: Plot depicting possible  $T_{1/2}$  dependence on the hydrogen bond length between the amine group and the acceptor atom from the guest solvent molecule. The  $T_{1/2}$  values for purely HS compounds are set to zero and highlighted with a red rectangle. Bottom left: NCI analysis of SCO compounds zoomed to focus on the N–H···O contact region. Bottom right: Plot showcasing the spin transition temperature  $T_{1/2}$  of SCO compounds as a function of the strength of N–H···O contacts. Quantification is done either through  $\text{sign}(\lambda_2)\rho$  via NCI analysis (represented by red squares) or by the potential energy density  $V(r)$  calculated at particular CPs ( $E_{\text{HB}} = V(r)/2$ , represented by blue circles).

A notable change in the reduced gradient of density ( $s$ ) emerges from weak molecular interactions, resulting in critical density points between interacting moieties. These points are displayed in 2D plots as  $s$  vs.  $\rho$  plots. The sign of the eigenvalue  $\lambda_2$  of the electron density Hessian matrix determines the nature of these interactions—negative for bonding interactions (e.g., hydrogen bonds) and positive for non-bonded ones (e.g., steric repulsions). Essentially, troughs in the density gradient  $s$  identify non-covalent contacts, with the value and sign of  $(\lambda_2)\rho$  indicating their strength and type. In SCO compounds, the most pronounced N–H···O interactions lie in the range of  $-0.027 < \text{sign}(\lambda_2)\rho < -0.024$ , and these values align with  $T_{1/2}$  as shown in Fig. 7 (bottom left). The significance of the N–H···O contacts becomes evident when comparing the  $\text{sign}(\lambda_2)\rho$  values of SCO compounds with those of HS compounds. The absence of troughs in the range of  $-0.027 < \text{sign}(\lambda_2)\rho < -0.024$ , indicates a lack of strong N–H···O

contacts in the HS compounds. The strongest such interaction in HS compounds has a  $\text{sign}(\lambda_2)\rho$  value of  $-0.020$ , but its strength does not trigger SCO behavior.

To deepen our understanding of the role of the N–H···O contact in SCO behavior across the presented series of complexes, we adopted a topological analysis. This analysis utilized the total molecular electronic density,  $\rho(\mathbf{r})$ , and its Laplacian  $\nabla^2\rho(\mathbf{r})$ , based on QT-AIM calculations. We identified (3,–1) CPs in the N–H···O contacts. At these points, we calculated the potential energy density,  $V(\mathbf{r})$ . As previously discussed, the energy of hydrogen bonds ( $E_{\text{HB}}$ ) can be approximated from the virial theorem. The findings illustrated in **Fig. 7** (bottom right) confirm that the energy of the N–H···O hydrogen bonds within the series of SCO compounds correlates with  $T_{1/2}$ . Essentially, a stronger N–H···O hydrogen bond in the HS X-ray structure corresponds to a higher observed  $T_{1/2}$ . In conclusion, both theoretical methods, based on *ab initio* calculations, identify the strength (energy) of the N–H···O hydrogen bond as the primary determinant for observing SCO in the isostructural series of the  $[\text{Fe}(\text{napet})(\text{NCS}/\text{Se})]\cdot\text{Solv}$  complexes.

## CHAPTER 4: SINGLE-ION MAGNETS

### 4.1 Co(II)-based Single-Ion Magnets with 1,1'-ferrocenediyl-bis(diphenylphosphine) metalloligands

In this study, we explored the potential of the compound [CoCl<sub>2</sub>(dppf)] as a SIM candidate, where dppf stands for 1,1'-ferrocenediyl-bis(diphenylphosphine). The complex is synthesized through the reaction of dppf with CoCl<sub>2</sub>. Both the ligand dppf and the resulting compound [CoCl<sub>2</sub>(dppf)] are well-documented and extensively studied in various areas, excluding their magnetic properties. They are also available as commercial coordination compounds. The crystal structure of [CoCl<sub>2</sub>(dppf)] was reported in 1999,<sup>48</sup> revealing a tetracoordinate {CoP<sub>2</sub>Cl<sub>2</sub>} arrangement of coordination polyhedron.

A significant aspect of [CoCl<sub>2</sub>(dppf)] is its crystal structure, which is stabilized solely by very weak C–H···π and C–H···Cl non-covalent interactions. More effective interactions often lead to a reduction in  $U_{\text{eff}}$ , introducing other relaxation channels.<sup>49</sup> Owing to the bulkiness of the dppf metalloligand, these interactions are organized in a way that precludes the efficient transmission of even the weakest exchange interactions. The minimal Co···Co separations exceed 9.6 Å, ensuring that dipolar interactions between the Co(II) atoms are minimal. Therefore, good SIM behaviour could be expected. We synthesized also its bromido [CoBr<sub>2</sub>(dppf)], and iodido [CoI<sub>2</sub>(dppf)] counterparts and we determined crystal structures for all these complexes. Our research then shifted focus to their static and dynamic magnetic properties. We utilized also High-Frequency and -Field Electron Spin Resonance (HF-ESR) measurements to accurately determine the magnetic anisotropy parameters. We further supported our experimental data with *ab initio* calculations using the CASSCF/NEVPT2<sup>50,51</sup> method using Orca 4.2.1 computational package.<sup>52</sup> Additionally, we explored the effectiveness of depositing thick films of Cl and Br derivatives on surfaces, employing both thermal sublimation and wet-chemistry-based approaches.

X-ray diffraction analysis has shown that all three complexes possess dinuclear [CoX<sub>2</sub>(dppf)] molecules within their crystal structures. In these complexes, the Fe(II) centers are bonded to two cyclopentadienyl rings (Cp) in an almost eclipsed geometry. The dppf metalloligand coordinates with the Co(II) center via two diphenylphosphine groups. Together, with the coordination of two additional halido ligands, this results in the formation of a P<sub>2</sub>X<sub>2</sub> coordination sphere (**Fig. 8A**). The geometry surrounding the Co(II) centers is best described as distorted tetrahedral, with continuous shape measure indexes<sup>53</sup> for T<sub>d</sub> being 0.356 in (Cl), 0.399 (Br), and 0.637 in (I). Angles such as P–Co–P, P–Co–X, and X–Co–X deviate significantly from those of an ideal tetrahedron. The bond lengths between Co and P in [CoX<sub>2</sub>(dppf)] range from 2.35 to 2.37 Å. Meanwhile, the Co–X bond lengths exhibit considerable variation across the series: 2.2229(10) and 2.2353(9) in (Cl), 2.3874(6) and 2.3640(6) in (Br), and 2.5596(6) and 2.5581(6) in (I). The non-covalent interactions in [CoX<sub>2</sub>(dppf)] are predominantly weak, represented solely by the C–H···X and C–H···π contacts.

Magnetic data, contingent on temperature and field, were compiled and evaluated for both the chlorido and bromide compounds. Unfortunately, we did not succeed in procuring a pure phase of the iodide compound. This conclusion is supported by results from elemental analysis, X-ray powder diffraction, and magnetic data. The observed reddish-brown outer and green inner colors of the crystals suggest possible partial decomposition of the iodide compound. The temperature-dependent effective magnetic moment ( $\mu_{\text{eff}}/\mu_{\text{B}}$ ) exhibits similarities between the (Cl) and (Br) compounds, with values (4.4–4.5) surpassing the spin-



only value for Co(II) with an  $e^4 t_2^3$  configuration in the tetrahedral symmetry of the coordination polyhedron ( $g = 2.0$ ,  $S = 3/2$ ,  $\mu_{\text{eff}}/\mu_B = 3.87$ ). The magnetic data were fitted using a spin Hamiltonian involving both axial and rhombic ZFS terms. From a simultaneous analysis of both temperature and field-dependent magnetization data, the following set of parameters were obtained: for (Cl),  $g = 2.20$ ,  $D = -11.0 \text{ cm}^{-1}$ ,  $E/D = 0.00$ ,  $\chi_{\text{TIP}} = 10.1 \times 10^{-9} \text{ m}^3 \text{ mol}^{-1}$  and for (Br),  $g = 2.24$ ,  $D = -8.7 \text{ cm}^{-1}$ ,  $E/D = 0.24$ ,  $\chi_{\text{TIP}} = 6.1 \times 10^{-9} \text{ m}^3 \text{ mol}^{-1}$  (**Fig.8B**). HF-EPR measurements (**Fig.8D**) unveiled analogous parameters. For (Cl), the most accurate fit was determined with  $D = -12.0 \text{ cm}^{-1}$ ,  $E/D = 0.106$ , and the g-values being  $g_x = 2.20$ ,  $g_y = 2.20$ , and  $g_z = 2.28$ . Meanwhile, for (Br), the optimal fit was observed with  $D = -11.2 \text{ cm}^{-1}$ ,  $E/D = 0.090$ , and g-values of  $g_x = 2.22$ ,  $g_y = 2.22$ , and  $g_z = 2.31$ . These parameters align well with theoretical calculations:  $D = -13.2 \text{ cm}^{-1}$ ,  $E/D = 0.130$  for (Cl),  $D = -10.1 \text{ cm}^{-1}$ ,  $E/D = 0.106$  for (Br). All these results confirm axial magnetic anisotropy in both compounds.

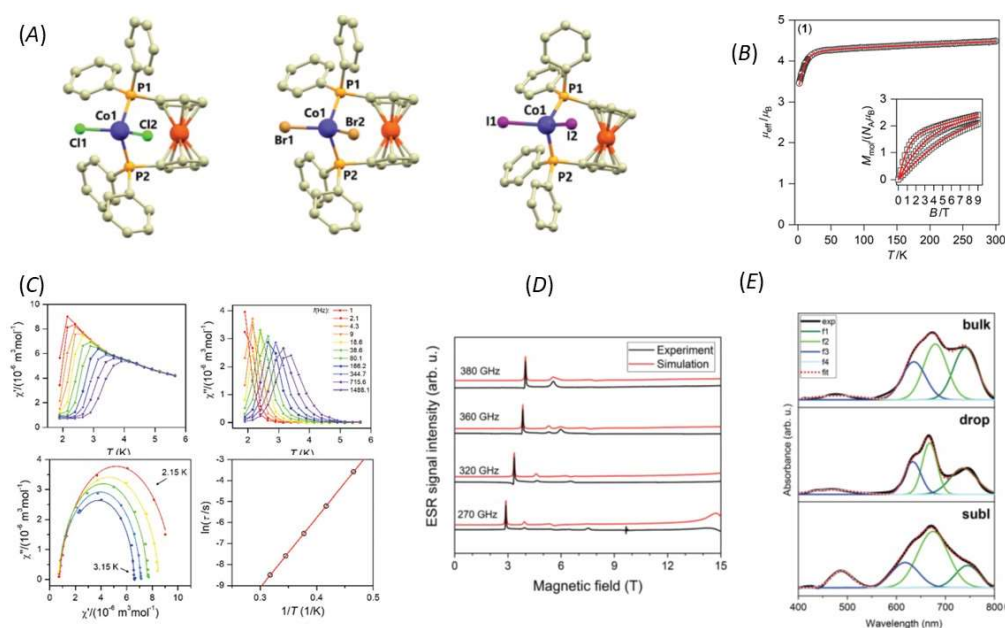


**Figure 8** (A): Perspective view illustrating crystal structures of the  $[\text{CoX}_2(\text{dppf})]$ -complexes ( $X = \text{Cl}^-$ ,  $\text{Br}^-$ ,  $\text{I}^-$ ). (B): Static magnetic data displayed as the temperature dependence of the effective magnetic moment, and the isothermal molar magnetisation measured at  $T = 2, 5$ , and  $10 \text{ K}$  is in the inset. The empty symbols represent the experimental data; red full lines represent the fitted data. (C): AC susceptibility data for the  $[\text{CoCl}_2(\text{dppf})]$ : in-phase  $\chi'$  and out-of-phase  $\chi''$  molar susceptibilities at the applied external magnetic field  $B_{\text{DC}} = 0.1 \text{ T}$ , the Argand (Cole–Cole) plot with full lines fitted and the fit of resulting relaxation times  $\tau$  with Arrhenius law (red line). (D): HF-EPR spectra for  $[\text{CoCl}_2(\text{dppf})]$  of a pressed powder pellet recorded at  $5 \text{ K}$  and four frequencies as indicated. The black solid line represents experimental data and the red solid line is the simulation. (E): UV-VIS spectra of  $[\text{CoBr}_2(\text{dppf})]$  as a bulk powder (above), drop-cast layer on glass (middle) and sublimated layer on acetate substrate (below).

The measurements of AC susceptibility confirmed that both (Cl) and (Br) compounds behave as field-induced SIMs (**Fig.8C**). We explored the deposition of (Br) on surfaces using two distinct methods: drop-casting in an inert nitrogen atmosphere (referred to as 'drop') and thermal sublimation in a high-vacuum environment (referred to as 'subl'). **Fig.8E** compares the UV-VIS spectra of (Br) in its bulk powder form, its drop-cast deposit on glass, and a 30 nm thick film produced by sublimation onto an acetate substrate. All three solid samples display two primary absorptions in the visible spectrum range: a peak near 480 nm linked to the  $e_2-e_1$



transition in the ferrocenyl unit (approximately in  $D_{5h}$  symmetry) and a set of peaks between roughly 600–800 nm attributable to the d–d transition bands of the tetracoordinate  $3d^7$  central ion. Although the same absorption bands are present in all three samples, distinct spectral profiles are noticeable. For instance, the 'subl' spectra exhibit broader bands and a more pronounced  $e_2-e_1$  transition compared to the 'bulk' and 'drop' samples. We conclude that these variations might stem from the partial decomposition of (Br) into the metalloligand dppf during the sublimation process, leading to a higher concentration of dppf in the deposit.

In this study, we presented the synthesis, crystal structures, and both static and dynamic magnetic properties of Co(II) SIMs with halogenido and 1,1'-ferrocenediyl-bis(diphenylphosphine) metalloligands. Through combining static magnetic properties, HF-EPR, and theoretical calculations, we confirmed the axial magnetic anisotropy of these compounds. The static magnetic data further confirmed their behavior as field-induced SIMs under an external magnetic field of 0.1T. We explored both high-vacuum sublimation and drop-casting as methods to deposit (Br) on selected surfaces. Despite the moisture sensitivity of (Br), it was successfully deposited using drop-casting in an inert nitrogen atmosphere. However, during the thermal sublimation process, partial decomposition of the complex was observed, suggesting that (Br) may not be stable enough for thermal evaporation deposition.

## 4.2 Halogen bonding in new dichloride-cobalt(II) complex with iodo-substituted chalcone ligands .

and

### Deposition of Tetracoordinate Co(II) Complex with Chalcone Ligands on Graphene

In this chapter, we will discuss the findings presented in two distinct papers. While both studies primarily focus on the use of chalcone ligands in synthesizing Co(II) complexes with intriguing magnetic properties, their specific areas of investigation differ. The first paper delves into the uncommon halogen bonding observed between the coordinated ligand and a diethylether molecule. The second paper explores the potential of depositing a tetracoordinated Co(II) complex onto graphene, leveraging extended aromatic ligand systems to bolster the interaction strength between the complex molecules and the substrate.

Chalcones are a subset of  $\alpha,\beta$ -unsaturated ketones (**Fig.9A**) and are crucial in the world of organic chemistry and plant biochemistry.<sup>54</sup> These compounds serve as the biogenetic precursors to flavonoids and isoflavonoids, which are prolific in plant structures. Structurally, chalcones can manifest in both the trans (E) and cis (Z) isomeric forms. However, the Z conformer tends to be less stable, primarily due to the steric hindrance between ring A (**Fig.9A**) and the carbonyl group. A distinct feature of chalcones is the continuous conjugation between the two aromatic rings and the electrophilic  $\alpha,\beta$ -unsaturated carbonyl system, providing them with unique chemical properties. The synthesis of chalcones typically involves the Claisen-Schmidt condensation reaction,<sup>55</sup> which is an aldol condensation process between an aromatic aldehyde and an acetophenone in the presence of a base. This reaction yields an  $\alpha,\beta$ -unsaturated ketone, which is the core structure of chalcones. The simplicity and efficiency of this synthetic route have made it an essential in organic chemistry laboratories and a valuable tool in generating a diverse array of chalcone derivatives for various applications.

The chalcone ligand 4I-L was synthesized via the aldol condensation of 4'-(imidazol-1-yl)acetophenone with 4-iodobenzaldehyde, as depicted in **Fig.9B**. The initial complex was formed through the reaction of  $\text{CoCl}_2 \cdot 6\text{H}_2\text{O}$  and 4I-L in a 1:2 molar ratio in methanol, yielding a blue precipitate. Elemental CHN analysis aligns closely with the formula  $[\text{Co}(4\text{I-L})_2\text{Cl}_2]$ , a finding further corroborated by ESI mass spectrometry. The complex displays negligible solubility in water, methanol, ethanol, and acetone, but is soluble in DMF and DMSO. Recrystallization of the complex from a  $\text{CH}_3\text{OH}/\text{DMF}$  mixture, followed by slow diethyl ether ( $\text{Et}_2\text{O}$ ) diffusion, produced light blue crystals. X-ray diffraction of a selected crystal confirmed the hexacoordinate nature of the complex, comprising four 4I-L and two chlorido ligands coordinated to a Co(II) center. The 4I-L ligands, in E-configuration, bind to the Co(II) via the nitrogen donors of the imidazolyl units, forming an equatorial plane with varied Co–N bond lengths: 2.121(3) and 2.162(3) Å. Two chlorido ligands occupy the axial positions with elongated Co–Cl bonds of 2.4880(9) Å. The complex's geometry can best be described as an axially elongated octahedron, stabilized by various weak intermolecular interactions. Notably, two symmetry-independent iodine substituents on the 4I-L ligands engage in interesting non-covalent interactions. One forms I $\cdots$ O interaction, being capped by a co-crystallized  $\text{Et}_2\text{O}$  molecule at a distance of 3.264(4) Å (**Fig.9C**). The second iodine interacts with two adjacent functional groups on the 4I-L ligand: one with the iodine substituent at 4.1676(5) Å and another with a C–H group at 3.918(5) Å (**Fig.9D**).

The interactions were probed theoretically using a combination of DFT and QT-AIM calculations. Initially, QT-AIM was employed to compute interaction energies from the virial. For the molecular fragment  $\{(4\text{I-L})\cdots(\text{Et}_2\text{O})\}$ , as depicted in **Fig.9C**, the calculated interaction

energy ( $E_{\text{int}}$ ) amounted to  $-4.401$  kcal/mol. Subsequently, we examined the  $\text{I}\cdots\text{I}$  type interaction (**Fig.9D**) between two 4I-L ligands  $\{(4\text{I-L})\cdots(4\text{I-L})\}$  from distinct complex entities, yielding an  $E_{\text{int}}$  of  $-2.212$  kcal/mol. Based on these results, combined with NCI calculations, we infer that the interactions are attractive and can be ranked in increasing strength as:  $\text{I}\cdots\text{I} < \text{C-H}\cdots\text{I} \approx \text{O}\cdots\text{I}$ .

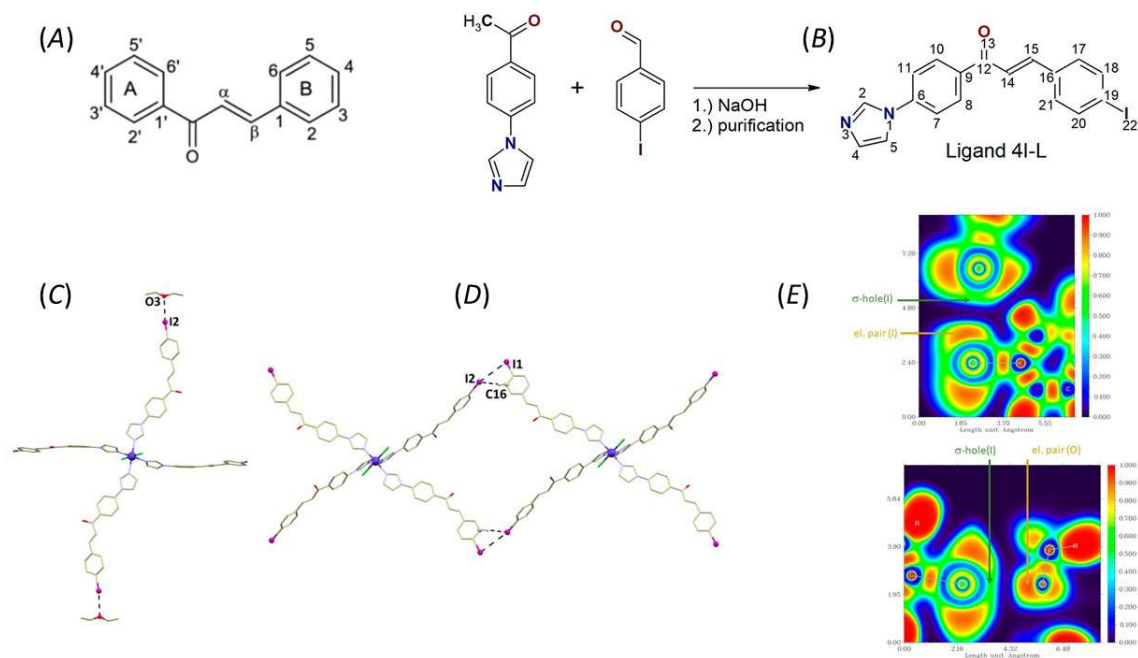


**Figure 9** (A): Depiction of the chalcone molecular structure. (B): Synthetic route for preparation of 4I-L. (C): A perspective view illustrating the  $\text{I}\cdots\text{O}$  halogen bonding and  $\text{C-H}\cdots\text{I}$  non-covalent interactions (D). (E): Calculated ELF for the molecular fragments  $\{(4\text{I-L})\cdots(4\text{I-L})\}$  (left) and  $\{(4\text{I-L})\cdots(\text{Et}_2\text{O})\}$  (right) showing halogen bonds of the types  $\text{I}\cdots\text{I}$  and  $\text{O}\cdots\text{I}$ .

It is well established that halogen bonds are characterized by the formation of  $\sigma$ -holes<sup>56</sup> on heavy halogen atoms, which can engage with an electron pair of the electron-donating atom. To gain deeper insights into this phenomenon, we employed the Multiwfn package<sup>57</sup> to compute the Electron Localization Function (ELF). ELF, introduced by Becke and Edgecombe<sup>58</sup> and further elucidated by Lu and Chen<sup>59</sup> in the context of electronic structure study, aids in understanding electron localization. Color-mapped figures were generated, as shown in **Fig.9E**, to outline the electron density distribution via ELF. Notably, in both  $\text{I}\cdots\text{I}$  and  $\text{O}\cdots\text{I}$  halogen bonding instances, the  $\sigma$ -holes on the iodine atoms are visible, accompanied by the corresponding electron donor pairs of either iodine or oxygen atoms.

In summary, we synthesized the chalcone ligand 4I-L and used it to produce the tetracoordinate complex  $[\text{Co}(4\text{I-L})_2\text{Cl}_2]$ , which upon recrystallization transformed into the hexacoordinate complex  $[\text{Co}(4\text{I-L})_4\text{Cl}_2]\cdot 2\text{Et}_2\text{O}$ . The structure of the latter is supported by weak non-covalent interactions, predominantly  $\text{C-H}\cdots\text{O}$ ,  $\text{C-H}\cdots\text{Cl}$ , and  $\pi$ - $\pi$  stacking, along with interactions from iodine substituents on the 4I-L ligands. These interactions, particularly the halogen bond in the  $\text{I}\cdots\text{O}$  contact, were validated through DFT, NCI, QT-AIM, and ELF calculations.

Building upon the previous work we delved into another study involving chalcogen-type ligands, specifically focusing on leveraging their rich aromatic systems for deposition onto substrates like graphene. These substrates primarily engage only in weak non-covalent

interactions, notably  $\pi$ - $\pi$  and C-H $\cdots\pi$ . In this context, we synthesized the chalcone ligand 4MeO-L through the aldol condensation of 4'-(imidazol-1-yl)benzaldehyde and 4-methoxyacetophenone. The complex was formed by reacting CoCl<sub>2</sub>·6H<sub>2</sub>O with 4MeO-L in a 1:2 molar ratio in methanol, producing a blue microcrystalline precipitate. Recrystallization from methanol yielded pale blue crystals suitable for single-crystal X-ray diffraction, revealing tetracoordinate [Co(4MeO-L)<sub>2</sub>Cl<sub>2</sub>] entities (**Fig.10A**). Here, the 4MeO-L<sub>4</sub> ligands coordinate to the Co center through imidazolyl nitrogen atoms with Co-N bond lengths of 2.014(4) and 2.016(4) Å. The chlorido ligands have bond lengths of 2.255(2) and 2.257(2) Å. Overall, the structure exhibits a distorted tetrahedral geometry with C<sub>2v</sub> pseudosymmetry (continuous shape measure index for T<sub>d</sub>: 1.356). Notably, the 4MeO-L ligands, remain in an *E* configuration, and planar even when coordinated. The crystal structure of [Co(4MeO-L)<sub>2</sub>Cl<sub>2</sub>] is stabilized primarily by a plethora of weak hydrogen bonds such as C-H $\cdots$ Cl and C-H $\cdots$ O. Notably, the expansive aromatic systems of the 4MeO-L ligands engage in  $\pi$ - $\pi$  stacking interactions, which contribute significantly to the stabilization of supramolecular chains along the b crystallographic axis.

**Fig. 10B** depicts the HF-EPR spectra of bulk compound [Co(4MeO-L)<sub>2</sub>Cl<sub>2</sub>], acquired at four distinct frequencies (380, 415, 456, and 490 GHz). The magnetic field was swept from 0 to 15 T at a temperature of 5 K. For simulating the experimental data, we employed an effective spin Hamiltonian that incorporated a ZFS term. The optimal fit was derived from the following spin Hamiltonian parameters:  $D = +14.6 \text{ cm}^{-1}$ ,  $E/D = 0.235$ ,  $g_x = 2.32$ ,  $g_y = 2.38$ , and  $g_z = 2.16$ . To further support the HF-EPR spectra analysis, CASSCF/NEVPT2 calculations were performed. Through the application of effective Hamiltonian theory, spin Hamiltonian parameters were extracted, resulting in a ZFS parameter set:  $S = 3/2$ ,  $D = +14.5 \text{ cm}^{-1}$ ,  $E/D = 0.15$ . The anisotropy of the g-tensor components was calculated as  $g_x = 2.325$ ,  $g_y = 2.378$ ,  $g_z = 2.163$ , and  $g_{av} = 2.289$  which aligns well with the HF-EPR spectroscopy results.

To prepare thin films of the complex on graphene, we utilized CVD graphene on a Si/SiO<sub>2</sub> substrate. Optical images of the hybrid materials, in conjunction with Raman spectroscopy, can be observed in **Fig.10D**, a comparison between the bulk compound, drop-cast and two samples sublimated at temperatures of 75 and 265°C. Molecules which were deposited via drop-casting formed tiny droplets with heights up to 50 nanometers. Conversely, molecules in sublimated samples generated microcrystals with heights reaching into the hundreds of nanometers. The Raman spectrum (**Fig.10D**) of the bulk compound, when placed on the Si/SiO<sub>2</sub> substrate, displayed distinct peaks at 964, 1186, 1366, and 1603 cm<sup>-1</sup>, in addition to the peaks from Si/SiO<sub>2</sub>. For the drop-cast sample, many of these distinctive peaks were obscured by the peaks of both graphene and Si/SiO<sub>2</sub>, with the exception of the peak at 1190 cm<sup>-1</sup>. In contrast, the Raman spectra for the sublimated samples consistently presented prominent peaks. This is likely due to measurements taken on larger specimens, which yielded stronger signals.

XPS was employed to investigate the chemical composition of all phases, assessing alterations from the XPS spectrum observed for the bulk phase. For the drop-cast sample, there was a noticeable decline in the graphitic nitrogen component relative to the bulk compound. Additionally, there was an apparent division of chlorine peaks between inorganic and organic forms. The drop-cast sample presented a faint Co 2p signal on its surface, hinting at potential complex decomposition. Regarding the sublimated samples, no discernible Co 2p peaks were detected for either 75 or 265°C, even after extended acquisition periods. This lack of detection might be due to the partial decomposition of the complex or the inherent surface sensitivity of XPS. This absence led us to a semi-empirical quantitative analysis of the powder after each sublimation and revealed an increased amount of cobalt and chlorine in the powder from the

crucible compared to the bulk powder. This finding, combined with the identification of organic chlorine, implies potential chlorination of the graphene, suggesting partial complex decomposition during both deposition techniques.

In summary, we reported a synthesis, crystal structure and HF-EPR spectra for tetracoordinate Co(II) complex with two chalcone ligands. Depositions on graphene were attempted by both drop-casting in an inert nitrogen atmosphere and by the thermal sublimation of the bulk compound in a high vacuum. In both cases, we observed organic chlorine components, suggesting either the partial decomposition of the complex or possible chlorination of the graphene. This underscores the importance of ensuring sufficient stability of SIMs used for depositions on surfaces.

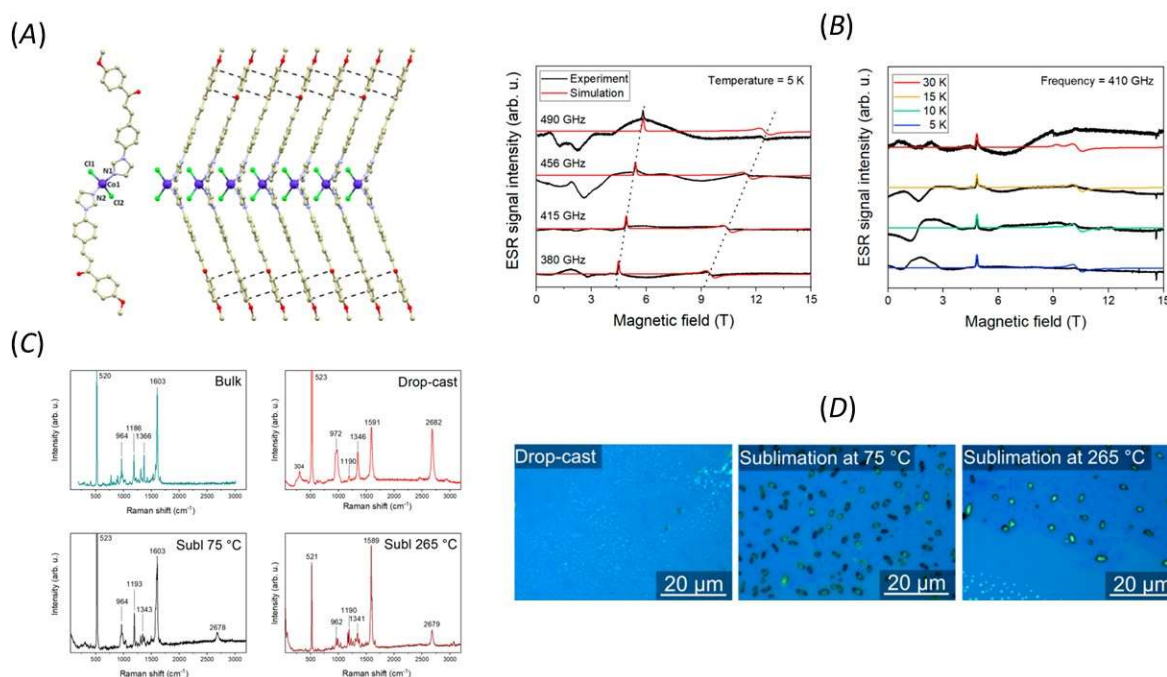


**Figure 10** (A): Drawing of the molecular structure of [Co(4MeO-L)2Cl2] and a perspective view of the packing of the [Co(4MeO-L)2Cl2] molecules along the crystallographic b-axis. Observed π-π stacking interactions are visualized by depicting the shortest C···C distances using black dashed lines. (B) HF-EPR spectra for four different frequencies at 5 K. The dotted line is guidance for Zeeman splitting. temperature dependence acquired at 410 GHz. Black line in both is experimental, and red/colored line is the simulation. (C): Comparison of Raman spectra of bulk compound, drop-cast, and sublimations at 75 and 265 °C. (D): Images from the optical microscope of the samples after drop-casting and sublimations at 75 and 265 °C.

### 4.3 Trigonal distorted hexacoordinate Co(II) single-ion magnets

In the introductory section of this habilitation, we highlighted the importance of E-term anisotropy for achieving significant axial magnetic anisotropy. However, to realize this, one must employ specific, rigid ligands that ensure the 'correct' symmetry of coordination polyhedron. This is because E-terms are affected by the Jahn-Teller effect, which introduces distortions that remove state degeneracy. As a result, it is not common to easily produce complexes with geometries resulting into the E-term using straightforward synthesis and basic mono- or bidentate ligands. However, we discovered a method to substantially increase magnetic anisotropy by introducing large trigonal distortions in simple coordination compounds that consist of carboxylate and neocuproine (neo) ligands. Our initial findings were published in 2018,<sup>60</sup> focusing on two polymorphs of the [Co(neo)(PhCOO)<sub>2</sub>] complex. The subsequent study on this topic is presented here.

We synthesized a series of [Co(neo)(RCOO)<sub>2</sub>] complexes, which exhibited notable changes in the trigonality of their coordination polyhedra when different carboxylate ligands were used. Here, RCOO<sup>-</sup> stands for carboxylate ligands such as acetate, pivalate, and 4-hydroxybenzoate. The resulting compounds crystallized as violet crystals, which diffracted rather well enabling us to determine their crystal structures using single-crystal X-ray diffraction. All compounds are comprised of the [Co(neo)(RCOO)<sub>2</sub>] complex molecules (**Fig. 11A**). However, in the 4-hydroxybenzoate complex, two additional co-crystallized methanol molecules are found within the asymmetric unit. Each complex molecule is hexacoordinate, with all ligands binding to the Co atom bidentately. The Co–N bond lengths range from 2.08 to 2.13 Å, while Co–O bond lengths vary between 2.04 and 2.20 Å. We assessed the shapes of the coordination polyhedra using CSMs) and the analysis showed that all the complex molecules have significant distortions from ideal geometries. The pivalate and 4-hydroxybenzoate complexes lean more towards regular octahedral (O<sub>h</sub>) rather than trigonal prismatic (D<sub>3h</sub>) geometries, with respective CSMs (O<sub>h</sub>, D<sub>3h</sub>) of 7.650, 9.801 and 6.352, 10.110. In contrast, the acetate complex displays the most pronounced trigonal distortion, aligning closely with a trigonal prism geometry (CSMs: 11.893, 3.761).

The magnetic properties of all the studied complexes, measured in a static magnetic field. Notably, the profile of  $\mu_{\text{eff}}$  versus  $T$  varies across the series, a result of differences in the geometry of the coordination polyhedra and the corresponding ligand field. We analyzed the magnetic data using the L-S Hamiltonian, as per the models of Griffith and Figgis. This approach describes the splitting of the <sup>4</sup>T<sub>1g</sub> term, which originates from the <sup>4</sup>F atomic term in symmetries lower than O<sub>h</sub>. Our analysis indicates that all the complexes demonstrate significant splittings (> 140 cm<sup>-1</sup>) between the Kramers doublets. This finding was further corroborated by CASSCF/NEVPT2 calculations. These findings suggest that the d-orbital splitting for the acetate complex closely resembles the pattern typical of a trigonal prism ligand field (**Fig. 11B**). In contrast, the splitting observed for the pivalate and 4-hydroxybenzoate complexes deviates more significantly from this trigonal prism pattern. This observation aligns well with the varying degree of trigonality observed in each individual complex and effectively illustrates the progressive shift in ligand field symmetry throughout the series.

AC magnetic susceptibility measurements revealed that all the studied compounds show slow magnetization relaxation under weak applied magnetic fields, classifying them as field-induced SIMs. In the case of the acetate complex, a faint imaginary susceptibility signal ( $\chi''$ ) was also detected, indicating that it functions as a zero-field SIM. These findings align well with ab initio calculations of magnetization blocking barriers carried out using the SINGLE\_ANISO module.<sup>61</sup> Specifically, the matrix element of the transverse magnetic moment between ground states with opposite magnetization is close to 0.5 for the pivalate and

4-hydroxybenzoate complexes. This value exceeds 0.1, suggesting a high tendency for quantum tunneling of magnetization (**Fig. 11C**). In contrast, the acetate complex shows a value of 0.08, implying a preference for quenched tunneling channel and, consequently, slow magnetization relaxation in the absence of an external magnetic field (**Fig. 11D**).

In summary, a series of hexacoordinate Co(II) complexes, characterized by significant trigonal distortion, function as field-induced SIMs. Remarkably, even with a straightforward synthesis employing basic, easily accessible bidentate ligands, the resulting compounds exhibit pronounced axial magnetic anisotropy and E-term based magnetism. In one instance, we even detected zero-field slow magnetization relaxation.

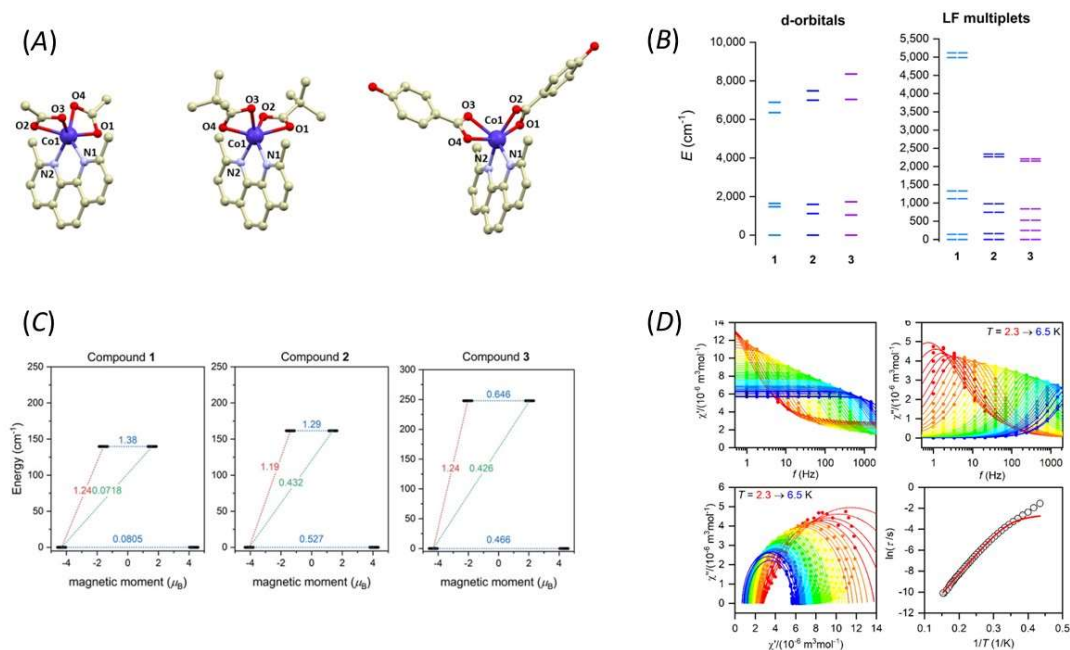


**Figure 11** (A): Drawing of molecular structures of complex molecules. (B): The outcome of the CASSCF/NEVPT2 calculations for studied complexes. Plot of the d-orbitals splitting calculated by *ab initio* ligand field theory (AILFT), and ligand-field multiplets (LFM). (C): The outcome of SINGLE\_ANISO CASSCF/NEVPT2 calculations for studied complexes. The numbers presented in the plots represent the corresponding matrix element of the transversal magnetic moment (for values larger than 0.1, an efficient relaxation mechanism is expected). Dashed lines refer to (temperature-assisted) quantum tunneling (blue), Orbach/Raman mechanisms (red), and direct/Raman mechanisms (green). (D): The AC magnetic data for acetate compound. Temperature dependence of the real ( $\chi'$ ) and imaginary ( $\chi''$ ) components of the AC susceptibility at the applied external magnetic field BDC = 0.1 T for frequencies from 1 to 1500 Hz (full lines are only guides for eyes). Legend: 1 stands for acetate complex, 2 for pivalate and 3 for 4-hydroxybenzoate complex.



#### 4.4 Weak antiferromagnetic interaction in Cu(II) complex with semi-coordination exchange pathway

This study builds upon the research introduced earlier in which we conducted a detailed analysis of the crystal structure and magnetic properties of the  $[\text{Co}(\text{dpt})(\text{NCS})_2]$  complex. This complex acts as a SIM and also displays ferromagnetic exchange interactions. We demonstrated that these interactions are mediated by a unique  $\text{Co}\cdots\pi$  interaction, which influences both static and dynamic magnetic properties. A summary of this can be found in chapter 2.1. In the study from 2022 we present results for the  $[\text{Cu}(\text{dpt})(\text{NCS})_2]$  complex, which is isomorphous to the  $[\text{Co}(\text{dpt})(\text{NCS})_2]$  complex.

The crystal structure of the Cu compound is isomorphous to that of the Co complex (**Fig. 12A**), as previously mentioned. However, the difference in the central atom brings about notable structural variations. In the Cu compound, the metal center is pentacoordinate, exhibiting a coordination geometry approximating square pyramidal as evident from the Addison parameter value ( $\tau = 0.33$ ). The  $\tau$  value calculated for the Cu compound is lower than its Co counterpart ( $\tau = 0.46$ ). Comparing metal-ligand bond lengths, the nitrogen atom bonds of the dpt ligand to the Cu central atom are shorter than the equivalent Co–N bonds in the Co complex:  $d(\text{M}-\text{N})$  in Å for Cu [Co] are 2.0145(13) [2.076(1)], 2.0757(13) [2.197(2)], and 2.0280(13) [2.062(1)]. Conversely, the M–N bonds involving the isothiocyanato ligands are longer in the Cu complex:  $d(\text{M}-\text{N})$  in Å for Cu [Co] are 2.0373(14), 2.1458(14) compared to [2.004(1), 2.120(2)] in the Co complex.

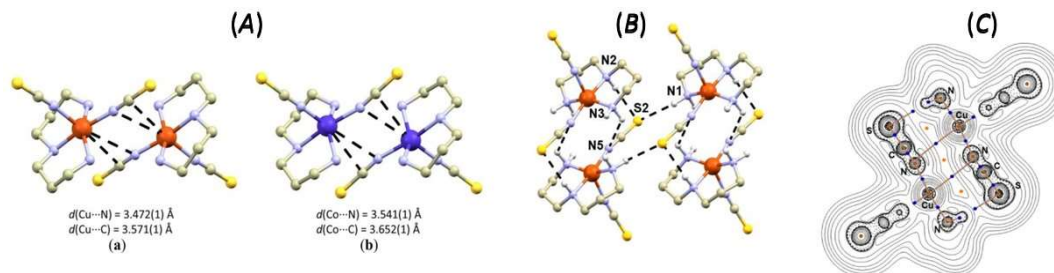


**Figure 12** (A): A perspective view of the centrosymmetric supramolecular dimer in  $[\text{Cu}(\text{dpt})(\text{NCS})_2]$  (a) and  $[\text{Co}(\text{dpt})(\text{NCS})_2]$  (b). The hydrogen atoms were omitted for clarity. The Co/Cu...C/N interactions were depicted as black dashed lines. (B): A perspective view of the fragment in the Cu complex crystal structure with showed N–H...S hydrogen bonding. (C): The  $\nabla^2\rho(r)$  contour plot in the  $\{\text{Cu}-\text{NCS1}\}_2$  plane of the dimeric fragment in the Cu complex crystal structure.

Similarly to the Co complex, the crystal structure of the Cu complex also features a centrosymmetric supramolecular dimer  $\{[\text{Cu}(\text{dpt})(\text{NCS})_2]_2\}$ . This is stabilized by a weak N–H...S interaction (**Fig. 12B**) between the secondary amine group of the dpt ligand and the sulfur atom of the NCS ligand from another molecule, with a distance of  $d(\text{N2}\cdots\text{S2}) = 3.564(1)$  Å. Within this dimer, short non-covalent contacts can be observed:  $\text{Cu}\cdots\text{N}$  ( $d(\text{Cu}\cdots\text{N}) = 3.472(1)$  Å,  $\sum R_{\text{vdw}}(\text{Cu},\text{N}) = 3.60$  Å) and  $\text{Cu}\cdots\text{C}$  ( $d(\text{Cu}\cdots\text{C}) = 3.571(1)$  Å,  $\sum R_{\text{vdw}}(\text{Cu},\text{C}) = 3.70$  Å) as shown in **Fig. 12A**. Remarkably, an interesting difference between Cu and Co complex is in the way how the NCS ligands providing the aforementioned interaction (NCS1) coordinate the metal atoms. In Cu complex, the Cu–N<sub>NCS1</sub> distance is much shorter (2.0373(14) Å) than that for the other NCS ligand (2.1458(14) Å). On the contrary, in Co complex, the Co–N<sub>NCS1</sub> distance is the longer one (2.120(2) vs. 2.004(1) Å).



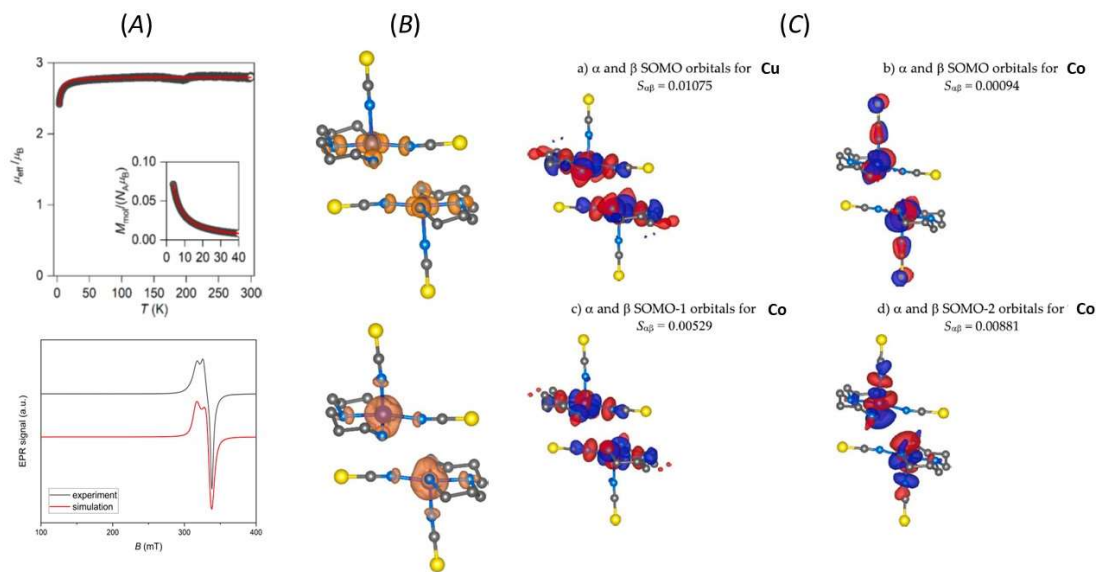


**Figure 13** (A): The temperature dependence of the effective magnetic moment), X-band EPR powder spectrum of Cu complex in the solid state at room temperature. The black dots represent experimental values, red line is a simulation for  $g_x = 2.012$ ,  $g_y = 2.013$  and  $g_z = 2.135$  (below). (B) The HS calculated spin density distribution using ZORA/B3LYP/ZORA-def2-TZVP for  $\{[\text{Cu}(\text{dpt})(\text{NCS})_2]_2\}$  (above) and  $\{[\text{Co}(\text{dpt})(\text{NCS})_2]_2\}$  (below). (C) The non-orthogonal magnetic orbitals of the BS spin state visualized for  $\{[\text{Cu}(\text{dpt})(\text{NCS})_2]_2\}$  and  $\{[\text{Co}(\text{dpt})(\text{NCS})_2]_2\}$ . The values of overlap  $S_{\alpha\beta}$  between the corresponding orbitals are listed too. The molecular orbitals are represented by dark blue/red surfaces calculated with a cutoff value of  $0.02 e\text{-bohr}^{-3}$ . Hydrogen atoms were omitted for clarity.

Non-covalent interactions in both compounds were assessed using theoretical methods. The wavefunctions were calculated using DFT with the B3LYP exchange–correlation functional through single-point calculations for two distinct fragments from the crystal structures of Cu complex (supramolecular dimer and the fragment illustrated **Fig. 12A**). The topology and energetics of electron density  $\rho(\mathbf{r})$  were examined employing the QT-AIM approach. For the analysis of non-covalent interactions, it should be fulfilled that at the relevant CPs, both the Laplacian of electron density (**Fig. 12C**),  $\nabla^2\rho(\mathbf{r})$ , and the total energy density of electrons,  $h_e(\mathbf{r})$ , should manifest positive values. In contrast, coordination bonds and covalent bonds at their CPs display either  $\nabla^2\rho(\mathbf{r}) > 0$ ,  $h_e(\mathbf{r}) < 0$  (pertaining to coordination bonds, termed as the intermediate interaction type) or  $\nabla^2\rho(\mathbf{r}) < 0$ ,  $h_e(\mathbf{r}) < 0$  (typical of strong covalent bonds).<sup>32</sup> It was observed that all the Cu–N coordination bonds complex conformed to the anticipated intermediate interactions nature. The interaction energies of all Cu–N bonds are of similar value ( $E_{\text{int}} = -33$  to  $-40$  kcal/mol) except for the longest Cu–N<sub>NCS2</sub> bond ( $E_{\text{int}} = -26.8$  kcal/mol). The N–H $\cdots$ S hydrogen bonds exhibited notably reduced  $E_{\text{int}}$  values, spanning between  $-1.8$  to  $-2.9$  kcal/mol. Topological analysis of the Cu complex disclosed that within the centrosymmetric dimer  $\{[\text{Cu}(\text{dpt})(\text{NCS})_2]_2\}$ , there is a bond path and a (3,-1) CP between the Cu atom and the nitrogen atom of the NCS1 ligand from the neighboring complex molecule, as depicted in **Fig. 12C**. Both  $\nabla^2\rho(\mathbf{r})$  and  $h_e(\mathbf{r})$  have positive small values. This suggests a non-covalent nature for this interaction. Furthermore,  $E_{\text{int}}$  is rather low ( $-1.02$  kcal/mol). Additionally, the  $|V(\mathbf{r})|/G(\mathbf{r})$  criterium further confirms the non-covalent character of this contact given its relatively low value (0.89). Thus, it can be concluded that this interaction exhibits a non-covalent nature and aligns with the criteria for semi-coordination. Similar calculations were performed also for Co complex. A bond path and a (3,-1) CP are present between the Co atom and the nitrogen atom of the NCS1 ligand from the adjacent complex molecule. Topological and energetic properties calculated at this CP indicate a non-covalent character for this interaction, with  $\nabla^2\rho(\mathbf{r}) > 0$ ,  $h_e(\mathbf{r})$

$> 0$ , and  $|V(\mathbf{r})/G(\mathbf{r})| < 1$ .  $E_{\text{int}}$  calculated for this interaction is marginally lower (-0.79 kcal/mol) than that computed for Cu complex.

The magnetic properties of the Cu complex were investigated by examining the temperature dependence (ranging from 2-300 K) of the magnetic moment. At room temperature,  $\mu_{\text{eff}}$  for the  $\{[\text{Cu}(\text{dpt})(\text{NCS})_2]\}_2$  supramolecular dimer is  $2.5 \mu_{\text{B}}$ . This closely matches the expected spin-only value for two spins with  $S = 1/2$  and  $g = 2.0023$ , equating to  $2.45 \mu_{\text{B}}$ . The  $\mu_{\text{eff}}$  value remains steady until around 10 K, after which it decreases to  $1.8 \mu_{\text{B}}$ . This decrease might suggest the presence of an antiferromagnetic interaction between the Cu(II) atoms. However, this interaction seems to be rather weak since no maximum was observed in the  $\chi T$  plot (**Fig. 13A**). For a more comprehensive understanding of the magnetic properties, the collected data were fitted using a spin Hamiltonian that includes an isotropic exchange term. The resulting parameters correspond with antiferromagnetic exchange interaction ( $J = -2.24 \text{ cm}^{-1}$ ,  $g = 2.29$ ). The electronic structure of the Cu complex in its solid-state was further examined using X-band EPR spectroscopy at room temperature (**Fig.13A**). The pattern observed indicates a rhombic distorted axial symmetry, with  $g_x$  being approximately equal to  $g_y$  but different from  $g_z$ . Utilizing the EasySpin software<sup>62</sup> for fitting the experimental data yielded g-tensor values of  $g_x = 2.012$ ,  $g_y = 2.013$ , and  $g_z = 2.135$ . BS-DFT calculations were used to rationalize the magnetic exchange between the paramagnetic ions present in the supramolecular dimers of both complexes. For this purpose, well-established B3LYP hybrid functional with DFT-NL variant to account for van der Waals interactions were used. The isotropic exchange, denoted as  $J$ , was determined for the  $H = -J(S_1S_2)$  spin Hamiltonian via the Ruiz<sup>63</sup> and Yamaguchi formulations.<sup>64</sup> Observations underscore the spin delocalization from the metal ion to the donor atoms. Notably, this spin density transfer is more pronounced in the Cu complex. A significant portion of the spin density is discernible on the nitrogen atom of the NCS1 ligand, which is in close proximity to the spin density of the Cu atom in neighboring molecules of the supramolecular dimer (**Fig. 13B**). Such an observation highlights the pivotal role of the  $\text{Cu}\cdots\pi$  interaction in establishing the magnetic exchange. Furthermore, the visualization of the non-orthogonal magnetic orbitals, or single-occupied molecular orbitals (SOMOs), is provided in **Fig.13C**. As anticipated for a square pyramid configuration, the magnetic orbital for Cu complex predominantly involves a metal-based  $3d_{x^2-y^2}$  orbital situated in the equatorial plane, as shown **Fig. 13C**. For Co complex, three distinctive magnetic orbitals emerge: SOMO orbitals based in  $d_{yz}$  Co(II) orbitals with minimal overlap  $S_{\alpha\beta}$ , SOMO-1 orbitals rooted in  $3d_{x^2-y^2}$  Co(II) orbitals with moderate overlap  $S_{\alpha\beta}$  and SOMO-2 orbitals rooted in  $d_{z^2}$  Co(II) orbitals with maximum overlap  $S_{\alpha\beta}$  (**Fig.13C**). These variations in  $S_{\alpha\beta}$  amid the magnetic orbitals, combined with the energy gap  $\Delta$ , explain the opposing types of magnetic exchange in Cu and Co complexes.

In summary, we investigated the bonding and magnetic properties of two isomorphous complexes:  $[\text{Cu}(\text{dpt})(\text{NCS})_2]$  and  $[\text{Co}(\text{dpt})(\text{NCS})_2]$ . Using QT-AIM, we examined the non-covalent interactions present between the central atom and the thiocyanide group on the neighboring molecule in both complexes. Our analysis supports the conclusion that these interactions are non-covalent and can be described as semi-coordination. The magnetic properties of the Cu complex revealed an antiferromagnetic exchange interaction, in contrast to the ferromagnetic exchange observed for the Co complex. This difference was explained using BS-DFT calculations.

#### 4.5 Neutral Cobalt(II)-Bis(Benzimidazole)Pyridine Field-Induced Single-Ion Magnets for Surface Deposition

The research presented in this chapter was conducted in collaboration with various institutions, with primary contributions from Dr. Ivan Salitros's laboratory at FCHP STU Bratislava, Slovakia and CEITEC BUT, Brno, Czechia. My principal role involved the theoretical analysis of the magnetic and structural properties, making this the primary emphasis of this chapter.

We thoroughly examined the crystal structure of two new Co(II) complexes (**Fig.14A**), their magnetic characteristics, X-band EPR spectroscopy, and HF-EPR/FIRMS spectroscopy. A noteworthy development was the enhancement of tridentate ligand solubility in non-polar and volatile solvents, facilitated by the introduction of alkyl chains. This proved beneficial for lithographical deposition processes. However, we assume that the weak halogenido coordination bonds contributed to the observed thermal instability in the neutral pentacoordinate Co(II)-SIMs, which consequently obstructed their effective surface deposition via sublimation.

X-ray diffraction of single crystals indicated that both compounds crystallize in the triclinic  $P\bar{1}$  space group. The asymmetric unit in each structure comprises neutral complex molecules, depicted by the formulas  $[\text{Co}(\text{C8-L})(\text{NO}_3)_2]$  and  $[\text{Co}(\text{C12-L})(\text{NO}_3)_2]$ , where C8-L represents 2,6-bis(1-octyl-1H-benzimidazol-2-yl)pyridine and C12-L stands for 2,6-bis(1-dodecyl-1H-benzimidazol-2-yl)pyridine (**Fig.14B-C**). In both entities, the Co(II) atom interacts with three nitrogen atoms from the related tridentate ligand and three oxygen atoms: one from a chelating nitrate anion and another from a terminal nitrate anion. At 100 K, the Co–N bond lengths in the compounds are between 2.088(1) and 2.103(1) Å, extending slightly to 2.100(3)–2.117(2) Å at room temperature. Notably, the Co–O bonds with terminal  $\text{NO}_3^-$  anions are shorter ( $d_{\text{avg}} = 2.04$  Å for C8-L complex and  $d_{\text{avg}} = 2.05$  Å for C12-L complex) than those associated with chelating  $\text{NO}_3^-$  anions (2.11 Å for C8-L complex; 2.10 Å for C12-L complex). Additionally, in both complexes, the second oxygen atom of the terminal  $\text{NO}_3^-$  anion is oriented towards the central atom, exhibiting relatively long Co $\cdots$ O distances: 3.013(1) Å for the C8-L complex and 2.997(1) Å for the C12-L complex at 100 K.

To understand the connection between the magnetic anisotropy and the structural properties of the compounds we conducted a computational analysis with several objectives. Initially, we looked at the role of the nitrate ligand that coordinates to the Co(II) atom in a monodentate manner, which might affect static and dynamic magnetic properties. We carried out a QT-AIM electron density analysis using wavefunctions from single-point DFT (B3LYP and def2-SVP) calculations, based on coordinates from single-crystal diffraction data. Our findings showed that the (3,-1) bond CPs were present only in regular metal-ligand bonds and not for the longer Co $\cdots$ O contact. Further, by assessing the values of the NCI index, we found these interactions to have a weak van der Waals character. Therefore, we conclude that the second oxygen atom likely does not have a significant impact on the Co(II) center.

Next, we directed our efforts towards analyzing the magnetic anisotropy of both compounds and computing the ZFS parameters using the state average complete active space self-consistent field (SA-CASSCF) complemented by the N-electron valence second-order perturbation theory (NEVPT2). We based our calculations on experimentally determined molecular structures, with the positions of hydrogen atoms optimized for input coordinates. Our active space was specified by seven electrons in five d-orbitals of Co(II) (CAS(7e,5o)), including all possible multiplets: 10 quartets and 40 doublets. To determine the ligand field

parameters, we incorporated ab initio ligand field theory (AILFT) calculations.<sup>65</sup> The findings for both complexes displayed marked similarities. The d-orbital splitting mirrored the distorted octahedral geometry of the coordination polyhedron, specifically with the proximity of the  $d_{xz}$  and  $d_{xy}$  orbitals and with  $d_{yz}$  having marginally elevated energy by approximately  $1000\text{ cm}^{-1}$  (**Fig. 14D-F**). The other d-orbitals presented substantially elevated energy levels:  $d_{z^2}$  ( $\sim 7700\text{ cm}^{-1}$ ),  $d_{x^2-y^2}$  ( $\sim 9000\text{ cm}^{-1}$ ). Thus, the electronic configuration of the d-valence shell for both complexes is  $d_{xz}^2, d_{xy}^2, d_{yz}^1, d_{z^2}^1, d_{x^2-y^2}^1$ . Within this configuration, the energy difference for the first excitation between orbitals sharing the same  $|m_l|$  value ( $d_{xz} \rightarrow d_{yz}, |m_l| = \pm 1$ ) slightly exceeds that for excitations altering  $m_l$  by 1 ( $d_{xy} \rightarrow d_{yz}$ ). As a result, a relatively large and positive  $D$  values can be expected for both complexes. The calculated ZFS parameters for both complexes showed very similar values:  $D = +25.6\text{ cm}^{-1}$  and  $E/D = 0.146$  for C8-L complex and  $+25.4\text{ cm}^{-1}$  and  $E/D = 0.138$  for C12-L complex. Additionally, the effective spin Hamiltonian g-tensors for both compounds were almost identical, indicating a pronounced easy-plane anisotropy (where  $g_x$  is roughly equal to  $g_y$  and both are much greater than  $g_z$ ). Furthermore, the analysis of the first Kramers doublet, by utilizing an effective spin,  $S_{\text{eff}} = 1/2$ , resulted in effective g-factors consistent with the easy-plane anisotropy ( $g_{x,\text{eff}} \ll g_{y,\text{eff}} \ll g_{z,\text{eff}}$ ) for both complexes. The results of theoretical calculations are in excellent agreement with the experimentally determined values of ZFS parameters (by combination of HF-EPR and FIRMS):  $D = +23.7\text{ cm}^{-1}$  and  $E/D = 0.184$  for C8-L complex and  $+24.2\text{ cm}^{-1}$  and  $E/D = 0.162$  for C12-L complex.

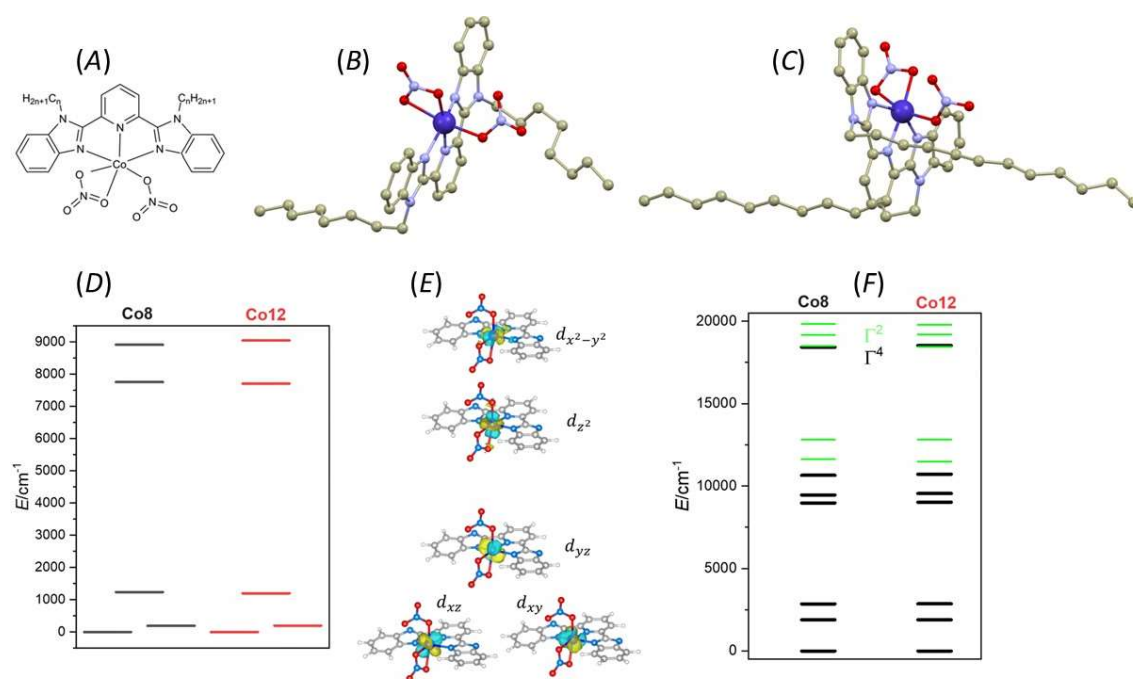


**Figure 14** (A): Drawing of molecular structure together with figures of molecular structures determined by X-ray diffraction of C8-L (B) and C12-L (C) complexes. The outcome of the CASSCF/NEVPT2 calculations for complexes C8-L and C12-L. Plot of the d-orbital splitting calculated by ab initio ligand field theory (AILFT) (D), visualizations of the d-orbitals (E) and low-lying ligand-field terms (F). Note: different multiplicities of LFT are shown in different colours.

## Chapter 4.6 Tetracoordinate Co(II) Complexes with Semi-Coordination as Stable Single-Ion Magnets for Deposition on Graphene

This study represents the current apex of our efforts to integrate magnetochemistry, especially its SIMs category, and quantum crystallography. The foundational concept originates from our prior, unsuccessful endeavors to synthesize SIMs that are amenable to the formation of hybrid materials by their deposition on functional surfaces, as detailed in Sections 4.1 and 4.2. Past experiments strongly advised against the utilization of monodentate ligands when designing complexes for thermal deposition applications. In such cases, we encountered challenges related to the stability of these complex molecules under ambient conditions. Even under a controlled, protective atmosphere, the tetracoordinate Co(II) complexes could not be deposited in an unaltered state. In light of these findings, we chose to employ bidentate ligands, specifically bidentate Schiff base ligands, which are renowned for forming mononuclear Co(II) complexes with field-induced or zero-field slow relaxation of magnetization. To further enhance the stability of these Co(II) complexes, we modified the Schiff base ligands by incorporating a 2-pyridyl substituent to their structure. This addition supplies an extra nitrogen atom that is sterically hindered, preventing it from forming a conventional coordination bond with the metal atom. Nevertheless, this nitrogen atom can engage in non-covalent interactions with adjacent metal centers. As we have previously proposed, such non-covalent interactions between donor atoms with free electron pairs (such as nitrogen or oxygen) and metal atoms can augment the stability of the complex without significantly impacting the metal center's magnetic anisotropy.

For our deposition experiments, we selected Co(II) compounds featuring a specialized class of Schiff base ligands synthesized via the condensation of aromatic 2-hydroxobenzaldehydes and 2-amino-6-picoline (**Fig. 15A**). The crystal structure of the Co(II) compound incorporating the Hsalapi ligand (Hsalapi = 2-methyl-6-(2'-oxybenzylideneamino)pyridin) has been reported in earlier studies. In its crystal structure, deposited in Cambridge Structural Database (CSD) under code MIFWUU,<sup>66</sup> two deprotonated salapi<sup>-</sup> ligands are observed to coordinate the Co(II) atom in a bidentate fashion, resulting in the formation of the [Co(salapi)<sub>2</sub>] molecule. Notably, the pyridine nitrogen atoms are oriented toward the metal center, but the Co···N distances are relatively long, measuring 2.625(14) and 2.708(14) Å. Given these characteristics, these contacts may be potentially classified as semi-coordination within the framework of structural coordination chemistry, due to their non-covalent nature and significant electrostatic contributions.

Although both studied complexes display strikingly similar crystal structures, they are not isostructural. Compound [Co(salapi)<sub>2</sub>] crystallizes within the monoclinic *I2/a* space group, while [Co(me-salapi)<sub>2</sub>] belongs to the orthorhombic *Pbcn* space group. Notably, the crystal structures of both compounds are solely comprised of the complex molecules. In each structure, the cobalt atom occupies a position along a two-fold rotational axis, making only half of the complex molecule symmetrically independent. Both compounds feature two bidentate ligands that coordinate to the central Co(II) atom: each ligand attaches *via* one phenolate oxygen atom having distances of  $d(\text{Co1-O1})=1.9527(16)$  Å for [Co(salapi)<sub>2</sub>] and  $d(\text{Co1-O1})=1.9613(7)$  Å for [Co(me-salapi)<sub>2</sub>] - as well as through an imine nitrogen atom (N1) with distances  $d(\text{Co1-N1})=1.9913(18)$  Å and  $d(\text{Co1-N1})=1.9923(9)$  Å in [Co(salapi)<sub>2</sub>] and [Co(me-salapi)<sub>2</sub>], respectively. The Co···N distance concerning the pyridine nitrogen atoms (N2) is more extended, measuring 2.6908(19) Å and 2.6951(9) Å for [Co(salapi)<sub>2</sub>] and [Co(me-salapi)<sub>2</sub>], respectively (**Fig. 15B**). Therefore, both compounds can be formally classified as tetracoordinate.

The analysis of coordination polyhedra coordinates using CSMs indicates that the coordination polyhedron resembles a distorted tetrahedron, with CSMs( $T_d$ ) values of 2.857 and 2.531 for  $[\text{Co}(\text{salapi})_2]$  and  $[\text{Co}(\text{me-salapi})_2]$ , respectively. However, the distortion from an ideal see-saw geometry is relatively small, as evidenced by CSMs( $C_{2v}$ ) values of 3.800 and 4.723.

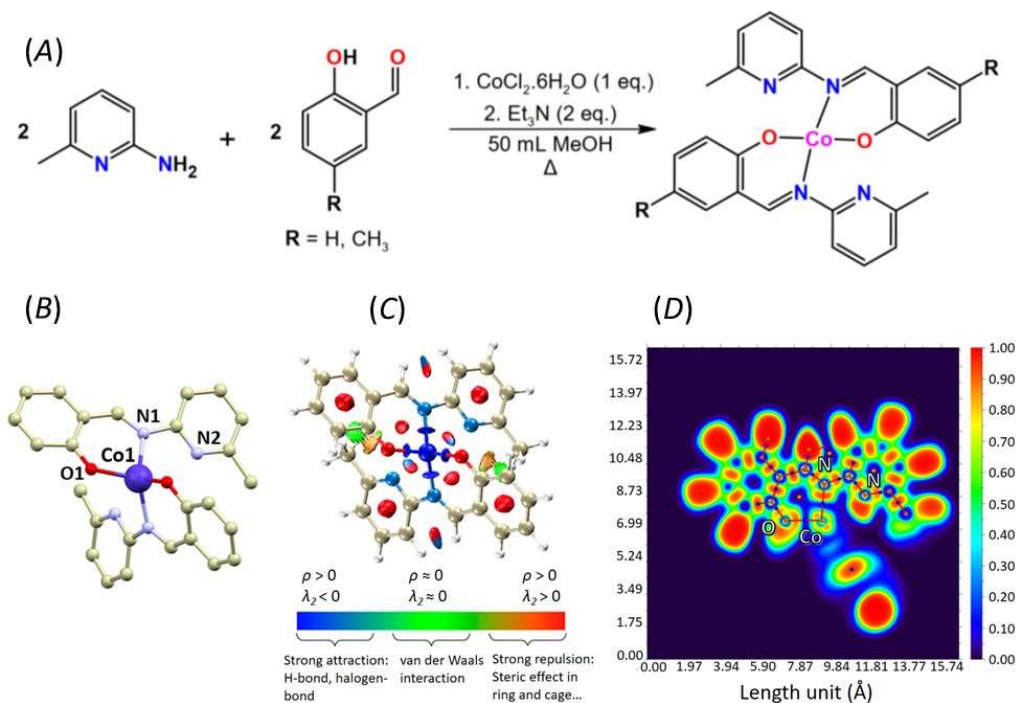


**Figure 15** (A): Preparation scheme of compounds  $[\text{Co}(\text{salapi})_2]$ ,  $R = \text{H}$ , and  $[\text{Co}(\text{me-salapi})_2]$ ,  $R = \text{CH}_3$ . (B): perspective view of the structure of the  $[\text{Co}(\text{salapi})_2]$  molecule. The hydrogen atoms were omitted for clarity. Color code: carbon (light brown), cobalt (dark blue), nitrogen (light blue), and oxygen (red). (C): NCI plot calculated for  $[\text{Co}(\text{salapi})_2]$ . (D) Visualization of the ELF for  $[\text{Co}(\text{salapi})_2]$ .

To delve into the nature of the  $\text{Co} \cdots \text{N}$  interactions, we employed QT-AIM for topological analysis of the electron density. Initial steps involved single-point DFT calculations, using the molecular coordinates of both complexes as derived from X-ray diffraction experiments. To refine the positions of hydrogen atoms reliably, Hirshfeld atom refinement<sup>67</sup> was implemented for both structures. Subsequently, topological analysis of the electron density,  $\rho(\mathbf{r})$  was performed using the Multiwfn software suite. Interestingly, we did not identify critical points between the Co1 and N2 atoms, as evidenced by the Laplacian of electron density,  $\nabla^2\rho(\mathbf{r})$ . This absence of CPs is attributed to the orientation of the pyridyl moiety, which modulates the topology  $\nabla^2\rho(\mathbf{r})$  between the Co and N atoms, thereby precluding the establishment of a bond path or (3,-1) CP. To further scrutinize the  $\text{Co} \cdots \text{N}$  interaction, we employed the NCI method. Visualization of the molecular interactions revealed that the  $\text{Co} \cdots \text{N}$  interaction manifests as a composite of steric repulsion between neighboring nitrogen atoms (indicated in red) and an attractive force between the Co and N atoms (indicated in blue, **Fig. 15C**). To achieve a more nuanced visualization, we computed the Electron Localization Function. Although this method is not well-established for multi-reference systems, we based our conclusions on a comparative analysis. Specifically, we compared the results obtained for Co(II) complexes with those acquired for Zn(II) analogues, finding considerable similarity between the two. **Fig. 15D** illustrates that the electron pair of the pyridine is well-localized and directed towards the more electropositive cobalt atom. In summary, despite the absence of a



CPs, our analysis indicates that the Co···N interaction possesses an attractive non-covalent character. This is attributed to the interplay between the pyridyl electron pair and the cobalt atom. Accordingly, we categorize this interaction as semi-coordination.

DC magnetic measurements were measured over a range of 2 to 300 Kelvin, and a field-dependent magnetic moment, recorded between 0 and 7 Tesla at a temperature of 2 Kelvin. The crystal structures of both compounds are made up of individual complexes that interact through  $\pi$ - $\pi$  stacking interactions, which could serve as non-covalent magnetic exchange pathways. To rigorously analyze the magnetic data, initial theoretical calculations were conducted. For this purpose, we selected dimeric structural fragments, as depicted in **Fig. 16A**, and performed BS-DFT calculations. These were aimed at estimating the isotropic exchange parameter  $J$  in the spin Hamiltonian, defined as  $\hat{H} = -J\hat{S}_1\hat{S}_2$ . The energy difference  $\Delta = E_{BS} - E_{HS}$ , between the high-spin (HS,  $S_{1\uparrow} \dots S_{2\uparrow}$ ) and broken-symmetry (BS,  $S_{1\uparrow} \dots S_{2\downarrow}$ ) spin states, was used to calculate  $J$ , following the formulas established by Ruiz and Yamaguchi. All approaches predicted a weak antiferromagnetic coupling within the dimer for both compounds. A slightly stronger antiferromagnetic exchange ( $J = -0.27 \text{ cm}^{-1}$ ) was predicted for  $[\text{Co}(\text{me-salapi})_2]$ , which is consistent with its shorter C···C and C···N distances between the  $\pi$ - $\pi$  stacked ligands of the neighboring molecules compared to those in compound  $[\text{Co}(\text{salapi})_2]$ , ( $J = -0.25 \text{ cm}^{-1}$ ).

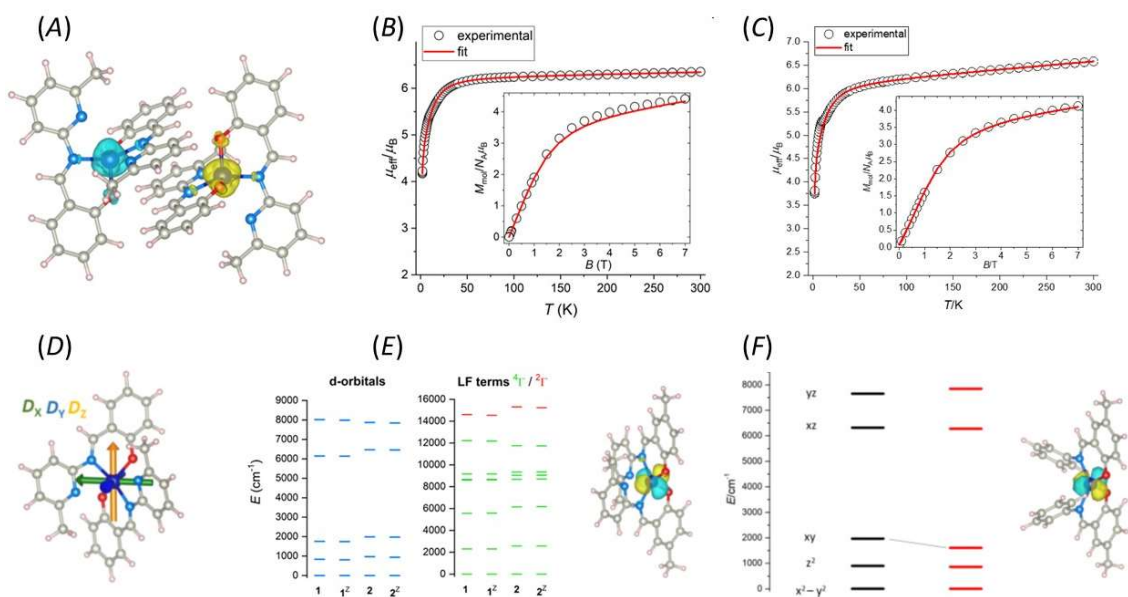


**Figure 16** (A): The outcome of the BS-DFT calculations for  $[\text{Co}(\text{salapi})_2]$ , with visualization of the spin density isosurface. Temperature dependence of  $\mu_{\text{eff}}/\mu_B$  acquired for  $[\text{Co}(\text{salapi})_2]$ , (B), and  $[\text{Co}(\text{me-salapi})_2]$ , (C), in the range from 2 K to 300 K with external magnetic field 0.1 T, and the isothermal magnetization data measured at 2 K shown in the inset. (D): Visualization of the D-tensor axes overlaid over the molecular structure of  $[\text{Co}(\text{salapi})_2]$ . (E) AILFT-calculated d-orbital splitting (left) and ligand field terms (right). (F): The orbital splitting resulting from the AILFT (NEVPT2) calculations is shown for molecular structures  $[\text{Co}(\text{me-salapi})_2]$  (left) and  $[\text{Co}(\text{me-salapi})_2]'$  (right). The d-orbitals are represented as black bars for  $[\text{Co}(\text{me-salapi})_2]$  and red bars for  $[\text{Co}(\text{me-salapi})_2]'$ . The decrease in  $d_{xy}$  energy is highlighted by the black line.

The effective magnetic moment ( $\mu_{\text{eff}}/\mu_B$ ) for both compounds remained largely constant down to a temperature of 30 Kelvin (**Fig. 16B-C**). At this point, a decrease was observed, moving from a value of 4.1 to 3.7 at 2 Kelvin. This decline suggests the potential existence of intermolecular magnetic exchange interactions or ZFS. A noticeable absence of maxima in the susceptibility curve ( $\chi=f(T)$ ) allows us to conclude that the magnetic interactions mediated through intermolecular non-covalent interactions among the molecules are relatively weak.

However, it proved impossible to fit the magnetic data without considering exchange coupling interactions. Consequently, considering these challenges and the findings from the BS-DFT calculations, we employed a spin Hamiltonian model incorporating both axial ZFS terms, as well as isotropic exchange coupling. The experimental magnetic data were analyzed using the EasySpin software package, taking into account both temperature-dependent and field-dependent measurements concurrently. Optimal fits were achieved with the following parameter sets: for [Co(salapi)<sub>2</sub>], the isotropic exchange constant  $J$  was found to be  $-0.19\text{ cm}^{-1}$ , the isotropic g-factor  $g_{\text{iso}}$  was 2.272,  $D = -15.3\text{ cm}^{-1}$ ,  $E/D = 0.012$ . For [Co(me-salapi)<sub>2</sub>],  $J = -0.27\text{ cm}^{-1}$ ,  $g_{\text{iso}} = 2.213$ ,  $D = -17.5\text{ cm}^{-1}$ , and  $E/D = 0.044$ . These results confirm the existence of significant axial magnetic anisotropy in both complexes.

The computational results reveal that the <sup>4</sup>F atomic term is split into seven ligand field multiplets. This is consistent with the low-symmetry characteristics of the coordination polyhedron in both compounds. Moreover, the energy of the first excited state exceeds  $1000\text{ cm}^{-1}$  (**Fig. 16E**), making the spin Hamiltonian formalism an appropriate tool for the analysis of the magnetic data. The observed splitting of the d-orbitals is indicative of a distorted tetrahedral geometry, with the lowest energy state corresponding to the  $d_{x^2-y^2}$  orbital. The electronic configurations for both complexes are specified as follows:  $d_{x^2-y^2}^2, d_{z^2}^2, d_{xy}^1, d_{xz}^1, d_{yz}^1$  (**Fig. 16E**). In such an arrangement, the energy difference for the first excitation between d-orbitals with the same  $|m_l|$  value ( $d_{x^2-y^2}^2 \rightarrow d_{xy}^1, |m_l| = 2$ ) is smaller than the energy difference for the first excitation with  $\Delta|m_l| = 1$  ( $d_{z^2}^2 \rightarrow d_{xz}^1$ ). This indicates a relatively large and axial magnetic anisotropy. Further validation of this assumption comes from CASSCF-NEVPT2 calculations of the ZFS parameters, which yielded  $D = -25.3\text{ cm}^{-1}$  and  $E/D = 0.084$  for compound [Co(salapi)<sub>2</sub>], and  $D = -28.3\text{ cm}^{-1}$  and  $E/D = 0.107$  for [Co(me-salapi)<sub>2</sub>].

We assessed the effects of pyridine nitrogen atoms on the electronic structure and magnetic anisotropy of both compounds by substituting 6-methyl-pyridine groups with phenyl rings. The DFT calculations were employed to optimize the positions of these phenyl rings while maintaining the positions of other atoms constant. The resultant structures, referred to as [Co(salapi)<sub>2</sub>]' and [Co(me-salapi)<sub>2</sub>]', were then subjected to CASSCF-NEVPT2 calculations. This method allowed us to maintain the ligand field strength and symmetry from the regular donor atoms ( $\{\text{NO}\}_2$ ) while eliminating any influence of the pyridine nitrogen atoms. The CASSCF-NEVPT2 calculations for [Co(salapi)<sub>2</sub>]' and [Co(me-salapi)<sub>2</sub>]' yielded ligand field term structures that closely resembled those of the parent complexes, however, the energy of the lowest quartet decreased. The calculated ZFS parameters were also different: the  $D$  values increased, registering  $-40.3\text{ cm}^{-1}$  and  $-38.1\text{ cm}^{-1}$  for [Co(salapi)<sub>2</sub>]' and [Co(me-salapi)<sub>2</sub>]', respectively. The  $E/D$  values decreased substantially to 0.055 and 0.039 in [Co(salapi)<sub>2</sub>]' and [Co(me-salapi)<sub>2</sub>]', respectively. Thus, the magnetic anisotropy in [Co(salapi)<sub>2</sub>]' and [Co(me-salapi)<sub>2</sub>]' is more pronounced and less rhombic than in the parent complexes.

Interestingly, the same d-orbital splitting patterns and similar orbital energies were observed for both the original and modified compounds. However, the most notable energy decrease occurred in the  $d_{xy}$  orbital (**Fig. 16F**). This change aligns with the spatial orientation of this orbital relative to the position of the pyridyl rings in compounds [Co(salapi)<sub>2</sub>] and [Co(me-salapi)<sub>2</sub>]. It should be highlighted that this decrease in  $d_{xy}$  energy was greater in [Co(me-salapi)<sub>2</sub>]' than in [Co(salapi)<sub>2</sub>]', correlating with the shorter Co...N distance—and thus, greater destabilization of  $d_{xy}$  in [Co(me-salapi)<sub>2</sub>] ( $2.6592(9)\text{ \AA}$ ) compared to [Co(me-salapi)<sub>2</sub>] ( $2.6901(11)\text{ \AA}$ ). The lower  $d_{xy}$  energy thereby leads to reduced  $d_{x^2-y^2}^2 \rightarrow d_{xy}^1$  excitations and larger  $|D|$  values. In summary, CASSCF-NEVPT2 calculations showed that while the interaction between the Co(II) atom and pyridyl nitrogen atoms does not significantly alter the



overall ligand field, it does influence the  $d_{xy}$  orbital and consequently the ZFS parameters. Specifically, interactions with the lone pairs of nitrogen atoms contribute to the smaller  $|D|$  values observed in complexes featuring  $\text{Co}\cdots\text{N}$  interactions.

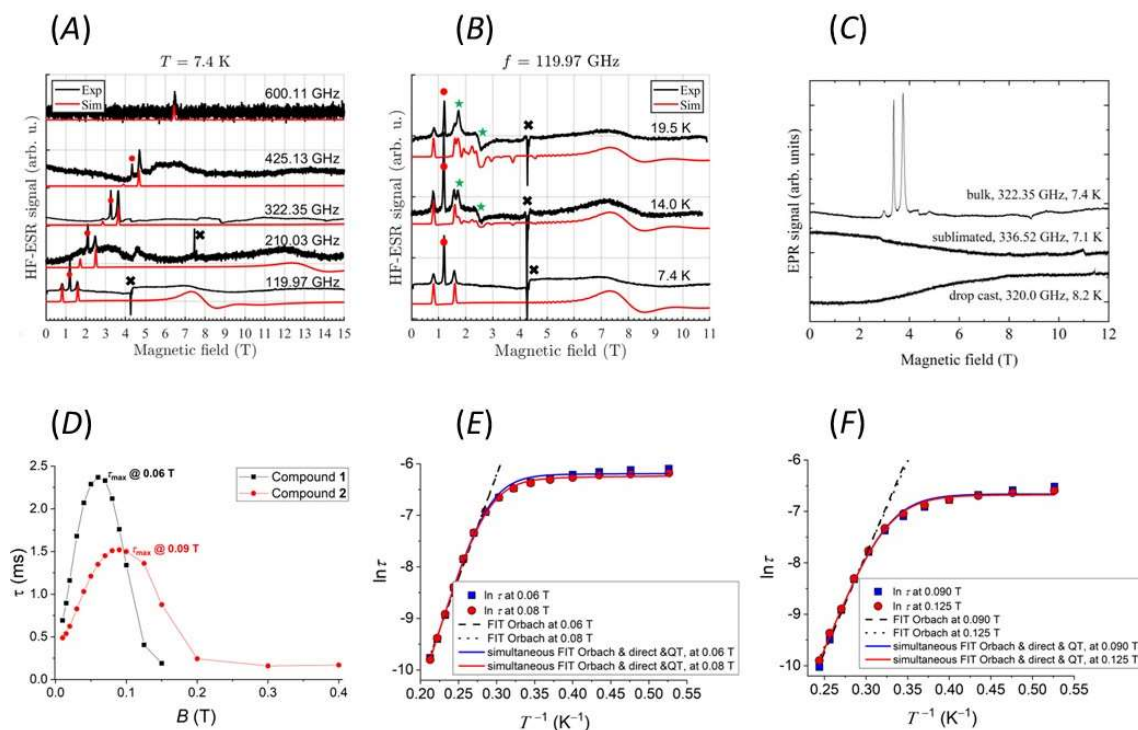


**Figure 17** Frequency dependence of the HF-EPR spectra of compound 1 at 7.4 K. (A) Temperature dependence of the HF-ESR spectra of  $[\text{Co}(\text{salapi})_2]$  compound at 119.97 GHz. The parameters in the simulated spectra (with offset for more clarity) were  $D = -20 \text{ cm}^{-1}$ ,  $g_x = 2.20$ ,  $g_y = 2.15$ ,  $g_z = 2.40$ ,  $E/D = 0.122$ , and  $J = -0.3 \text{ cm}^{-1}$ . Green stars correspond to thermally activated transitions ascribed to the excited  $S = 1/2$  doublet, black crosses indicate an ESR signal from an impurity in the sample holder's mirror, and red dots indicate a spurious signal not considered in the simulation. (C): Comparison of HF-EPR spectra of  $[\text{Co}(\text{salapi})_2]$  compound in bulk state (powder spectra) and deposited on graphene by dropcast and thermal sublimation, at frequency around 320 GHz. (D):  $\tau$  vs. BDC dependencies for compounds 1 ( $[\text{Co}(\text{salapi})_2]$ ) and 2 ( $[\text{Co}(\text{mesalapi})_2]$ ). (E, F)  $\ln \tau$  vs.  $1/T$  plots for compounds 1 (E) and 2 (F), respectively, obtained from AC susceptibility measurements recorded at two different DC magnetic fields. The blue and red solid lines result from simultaneous fits of two  $\ln \tau$  vs.  $1/T$  dependencies at two different DC magnetic fields for each compound.

Further investigation of the magnetic properties of  $[\text{Co}(\text{salapi})_2]$  was conducted using HF-EPR, **Fig.17A-B**). We also carried out HF-EPR measurements on compounds that were deposited on graphene. Unfortunately, these measurements did not yield a discernible signal which we attribute to the insufficient amounts of the deposited material. From the analysis of temperature-dependent spectra, prominent thermally activated transitions were identified, ascribed to the  $S = 1/2$  doublet. These transitions are indicated by green stars in the spectral data and confirm that the ground state possesses a spin of  $3/2$ . Consequently, it can be inferred that the  $D$  parameter is negative. Nonetheless, transitions between the ground-state ( $S = 3/2$ ) and the excited state ( $S = 1/2$ ) were not observed within the energy range accessible through our experiments. Therefore, due to the limitations of our spectrometer, we did not observe the mentioned transition in the spectrum. This suggests that the  $|D|$  value exceeds 600 GHz or  $20 \text{ cm}^{-1}$ . Simulations conducted with the following parameters -  $g_x = 2.20$ ,  $g_y = 2.15$ ,  $g_z = 2.40$ ,  $D = -20 \text{ cm}^{-1}$ ,  $E/D = 0.122$ , and an exchange term  $J = -0.3 \text{ cm}^{-1}$  - largely succeeded in replicating most of the spectral features. These simulations also suggest the presence of intermolecular

antiferromagnetic coupling which aligns with the results from BS-DFT calculations and is consistent with findings obtained through magnetometry. AC measurements confirmed that both compounds behave as field-induced SIMs as slow relaxation of magnetization was observed in small external magnetic field (**Fig.17D-F**).

Both studied compounds demonstrated remarkable thermal and chemical stability, with high melting points 261°C for [Co(salapi)<sub>2</sub>] and 299°C for [Co(me-salapi)<sub>2</sub>], respectively. These properties allowed their deposition on Chemical Vapor Deposition (CVD) graphene layered on Si/SiO<sub>2</sub> via both drop-casting and thermal sublimation methods. Optical microscopy confirmed the successful deposition of both complexes (**Fig.18A**). Atomic Force Microscopy (AFM) was employed to investigate the topography of the deposited samples. The results indicated that drop-casting led to the formation of crystals with heights of a few micrometers, while thermal sublimation produced nanoscale islands with heights reaching up to 150 nm for both complexes (**Fig.18A**). To confirm the chemical identity of the deposited compounds, Raman spectroscopy and X-ray Photoelectron Spectroscopy (XPS) were utilized. These analyses verified that the chemical composition of the molecules remained unaltered after both drop-casting and thermal sublimation. A detailed comparative study involving XPS and Raman spectroscopy was conducted, affirming these results against a bulk reference (**Fig.18B**).

In summary, we successfully developed molecular systems that not only exhibit slow magnetization relaxation but also maintain sufficient stability for surface deposition through various methods. This achievement was made possible due to their specific structural features, including a semi-coordination bond that protects the low-coordinate complex molecule from decomposition.

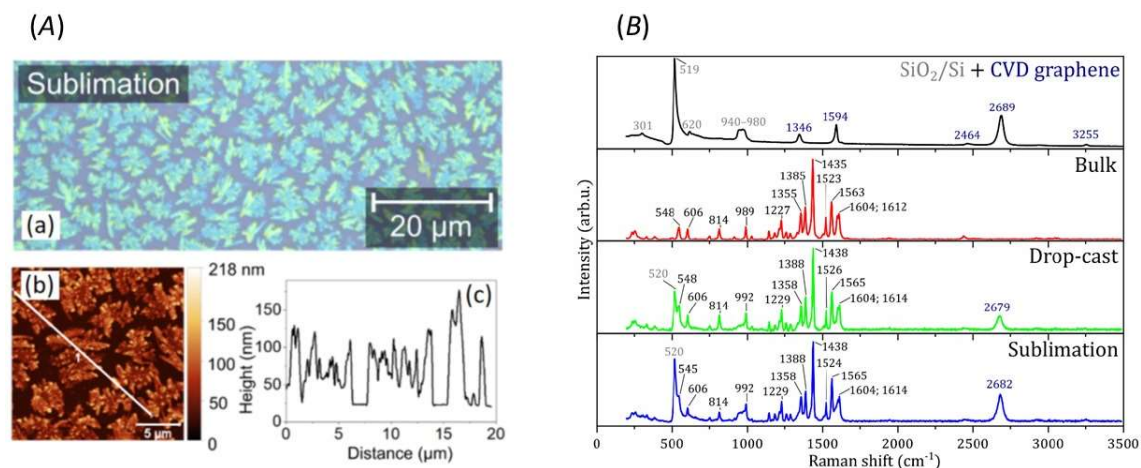


**Figure 18** (A) (a) Optical image of deposited compound [Co(salapi)<sub>2</sub>] (in green) on CVD graphene (dark blue) by thermal sublimation. (b) AFM image of deposited compound [Co(salapi)<sub>2</sub>] on CVD graphene by sublimation. (c) The height profile along the white line indicated in the AFM image. (B): Comparison of Raman spectra of the [Co(salapi)<sub>2</sub>] compound, from top to bottom, of Si/SiO<sub>2</sub> substrate (Raman shift values marked in grey) and CVD graphene (marked in dark blue), bulk, and deposited by drop-cast and by thermal sublimation.

## CHAPTER 5: SPIN-CROSSOVER

### 5.1 Spin crossover in three mononuclear iron (III) Schiff-base complexes

Non-covalent interactions play a significant role in a theoretical explanations of SCO characteristics. Furthermore, it is widely accepted that a careful choice of ligands and thus also of peripheral groups they are bearing could help in design of interesting SCO systems. In this work, we investigated crystal structures and magnetic properties of the Fe(III) complexes with pentadentate Schiff bases originating from reactions between derivatives of various ortho-hydroxy salicylaldehydes and aliphatic triamines such as bis(3-aminopropyl)amine or its methylated derivative 3,3'-Diamino-N-methyldipropylamine. This leads to a preparation of what are termed "symmetric" Schiff bases, which frequently display SCO when conforming to the structural formula:  $[\text{Fe}(\text{R-LA})(\text{L1})](\text{BPh}_4)$ . Here,  $\text{R-LA}^{2-}$  represents a pentadentate Schiff base ligand, and L1 is a monodentate heterocyclic ligand (**Fig.19A**). Generally, the transitions observed in these compounds were of a gradual nature or exhibited spin equilibrium. A notable exception was a mononuclear compound with R-LA constituted by bis(3-methoxysalicylideneiminopropyl)methylamine and L1 as 4-aminopyridine. This compound demonstrated cooperative SCO, possibly owing to its crystal packing which involved  $\text{N-H}\cdots\text{O}$  and  $\text{N-H}\cdots\pi$  non-covalent interactions between complex cations. In the current work, our aim was to transform this kind of complex systems into more cooperative ones. The main idea was to incorporate ligands that could induce a significant number of intermolecular interactions, thereby ensuring high cooperativity and potentially intriguing SCO transitions. We utilized benzimidazole (L1a) and 1-benzofuro[3,2-c]pyridine (L1b) in combination with two slightly different pentadentate ligands,  $\text{H}_2\text{LA}$  and  $\text{H}_2\text{3EtO-LA}$  (4-azaheptamethylene-1,7-bis(3-ethoxysalicylideneiminate), (**Fig.19**). Large and rigid monodentate ligands like L1a and L1b, which also bear substituents capable of forming hydrogen bonds (such as the NH group in L1a), were employed to enhance number of aromatic ring interactions, so called  $\pi$ - $\pi$  stacking. These, in conjunction with pentadentate ligands containing NH groups as hydrogen bond donors and phenolic and ethoxy oxygen atoms as acceptors, could potentially mitigate the steric hindrance imposed by bulky  $\text{BPh}_4^-$  anions that typically inhibit effective intermolecular interactions.

Three coordination compounds were synthesized:  $[\text{Fe}(\text{3EtO-LA})(\text{L1a})](\text{BPh}_4)$ ,  $[\text{Fe}(\text{3EtO-LA})(\text{L1b})](\text{BPh}_4)$ , and  $[\text{Fe}(\text{LA})(\text{L1b})](\text{BPh}_4)$ , abbreviated as 3EtO-LAL1a, 3EtO-LAL1b, and LAL1b, respectively. Single crystal X-ray diffraction analyses showed that all three compounds feature complex cations with a pentadentate Schiff base ligand coordinated to a central Fe(III) atom (**Fig.19B**). The sixth coordination site is filled by a monodentate N-donor heterocyclic ligand. The metal-ligand bond lengths, measured at temperatures of 100K for 3EtO-LAL1a, 190K for 3EtO-LAL1b, and 293K for LAL1b, closely match values typical for the LS state. Specifically, the longest bonds were observed between the iron atoms and the secondary nitrogen atoms of the pentadentate ligands, measuring 2.0293(19) Å in 3EtO-LAL1a, 2.0539(16) Å in 3EtO-LAL1b, and 2.0843(15) Å in LAL1b. Comparable lengths were noted for the nitrogen atom of the monodentate heterocyclic ligand (2.0105(18) Å for 3EtO-LAL1a, 2.0497(15) Å for 3EtO-LAL1b, and 2.0990(16) Å for LAL1b). The Fe-N bonds involving imino nitrogen atoms were relatively shorter, ranging from 1.98 to 2.01 Å for all three structures. The Fe-O bonds were even shorter (1.87 and 1.89 Å).

The crystal structures of 3EtO-LAL1a, 3EtO-LAL1b, and LAL1b do not exhibit hydrogen bonding of notable strength (**Fig.19C-E**). In 3EtO-LAL1a, the secondary amine group engages in an offset  $\text{N-H}\cdots\pi$  non-covalent interaction with the aromatic ring of the  $\text{BPh}_4^-$  anion. The shortest  $\text{N}\cdots\text{C}$  distance measures 3.446(3) Å. Additionally, the N-H group from benzimidazole forms an  $\text{N-H}\cdots\pi$  interaction with the aromatic ring of the  $\text{BPh}_4^-$  anion, where the  $\text{N}\cdots\text{C}_g$  distance is 3.227(4) Å ( $\text{C}_g$  denotes the centroid of the ring). In 3EtO-LAL1b,

complex cations interact through highly offset ring–ring interactions, featuring the shortest C···C distance of 3.192(3) Å. In LAL1b, the secondary amine group from the complex cation forms a weakly offset N–H··· $\pi$  interaction with the aromatic ring of the BPh<sub>4</sub><sup>−</sup> anion, where the shortest N···C distance is 3.713(3) Å.

The temperature-dependent behavior of the effective magnetic moment for 3EtO-LAL1a, 3EtO-LAL1b, and LAL1b is presented in **Fig.19F**. All three compounds experience SCO ( $S = 1/2 \rightarrow 5/2$ ), initiating at temperatures above approximately 150 K. Notably, this spin crossover is not complete even at 300 K, as evidenced by the room temperature values of the  $\mu_{\text{eff}}$  falling short of the theoretical spin-only value for  $S = 5/2$  and  $g = 2.0$  ( $5.93 \mu_{\text{B}}$ ). Additionally, the low-temperature values of  $\mu_{\text{eff}}$  range between approximately 2–3  $\mu_{\text{B}}$ . This suggests that a minor fraction of iron(III) complexes remain in the HS state at these temperatures, which was also confirmed by field dependent measurements of molar magnetizations. Analysis of the magnetic data confirms the low cooperativity of the observed transitions since the observed transitions display a gradual and incomplete character. Therefore, we can conclude that although we achieved high critical SCO temperatures in the compounds under study—specifically,  $T_{1/2} = 262$  K for 3EtO-LAL1a, 239 K for 3EtO-LAL1b, and 365 K for LAL1b—our design approach was not successful in inducing strong cooperativity among the molecules.

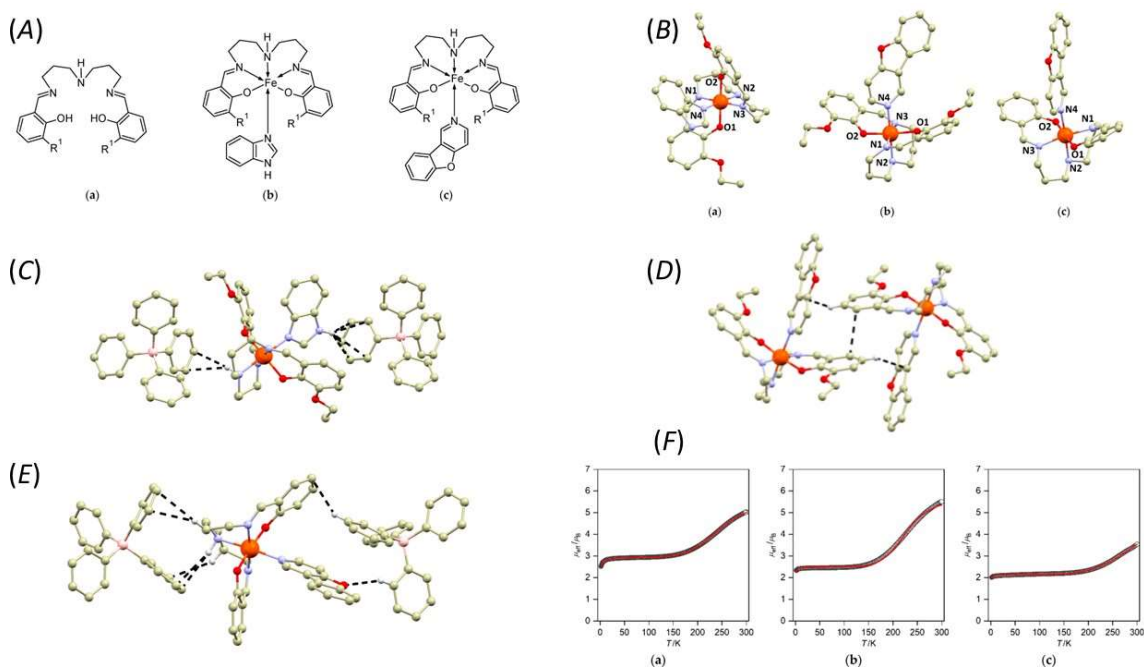


**Figure 19** (A) Structural formulas of (a) ligands H<sub>2</sub>LA ( $R_1 = H$ ) and H<sub>2</sub>3EtO-LA ( $R_1 = O-CH_2-CH_3$ ). (B) Depiction of the molecular structures of  $[Fe(3EtO-LA)(L1a)]^+$  (a),  $[Fe(3EtO-LA)(L1b)]^+$  (b) and  $[Fe(LA)(L1b)]^+$  (c). The non-covalent interactions (black dashed lines) in  $[Fe(3EtO-LA)(L1a)](BPh_4)$ , (C),  $[Fe(3EtO-LA)(L1b)](BPh_4)$ , (D) and  $[Fe(LA)(L1b)](BPh_4)$ , (E). Hydrogen atoms (except for those involved in non-covalent interactions) were omitted for clarity. (F): The temperature dependence of the effective magnetic moment for  $[Fe(3EtO-LA)(L1a)](BPh_4)$  (a),  $[Fe(3EtO-LA)(L1b)](BPh_4)$ , (b), and  $[Fe(LA)(L1b)](BPh_4)$  (c). The experimental data are displayed as empty circles, calculated data are displayed as full lines.

## 5.2 Ion-pair complexes of Schiff base Fe(III) cations and complex anions

As detailed in chapter 3.1, the cations of the form  $[\text{Fe}(\text{4OH-L6})]^+$  exhibit significant potential for the application of crystal engineering techniques aimed at modulating SCO phenomenon. In the current study, a variety of complex anions were employed to realize this objective. Additionally, deprotonated complex compounds comprising  $[\text{Fe}(\text{4OH-L6})_{\text{-H}}]$  molecules were synthesized. In this work we studied crystal structure and magnetic properties of the following complexes:  $[\text{Fe}(\text{4OH-L6})][\text{M}(\text{L3})_2] \cdot \text{H}_2\text{O}$  ( $\text{M} = \text{Co}(\text{III}), \text{Cr}(\text{III})$  and  $\text{Fe}(\text{III})$ ), further abbreviated as FeCo, FeCr and FeFe, respectively, and  $[\text{Fe}(\text{4OH-L6})][\text{Ag}(\text{CN})_2]$  (FeAg). The abbreviations H<sub>2</sub>-4OH-L6 and H<sub>2</sub>L3 stands for N,N'-bis[2,4-dihydroxy-(benzylideneamino)ethyl]ethane-1,2-diamine and = 2-{(E)-[(2-hydroxyphenyl)imino]methyl}phenol, respectively.

Our study focused on Fe(III) complexes with the H<sub>2</sub>-4OH-L6 ligand for their potential in SCO behavior and formation of  $[\text{Fe}(\text{4OH-L6})_{\text{-2H}}]^-$  anions. SCO anions are rare and could enable multifunctional materials with switchable properties. Despite using highly basic solutions, only a mono-deprotonated complex  $[\text{Fe}(\text{4OH-L6})_{\text{-H}}]$  was obtained, showing remarkable stability. This complex endured even in a 1:10 molar ratio with KOH and could be isolated as a unique product. Weaker bases produced a side product  $[\text{Fe}(\text{H-4OH-L6})_{\text{-H}}] \cdot 2\text{H}_2\text{O}$ , which could not be isolated as a pure phase. The complexes: FeCo, FeCr, FeFe and FeAg complexes were synthesized by substituting the chloride ion from  $[\text{Fe}(\text{4OH-L6})]\text{Cl}$  using the particular complex anions.

The crystal structures of all reported compounds exhibited bond lengths typical for the HS state. The longest M–L bonds are observed between the Fe(III) and secondary amine atoms, with distances Varying between 2.20 and 2.26 Å. In contrast, the imine nitrogen atoms form shorter Fe–N<sub>im</sub> bonds, measured at 2.02 Å and 2.12 Å. The shortest M–L bonds are established with the phenolic oxygen atoms, with bond lengths varying between 1.89 and 1.93 Å. The coordination polyhedrons in all studied compounds adopt rather distorted octahedral shapes with large angular distortions which is also typical for Fe(III) complexes in the HS state. The non-covalent interactions are in all compounds governed by dominant hydrogen bonding groups such as secondary amine and peripheral hydroxy groups. In both complexes containing triply deprotonate ligands  $(\text{4OH-L6})_{\text{-H}}^{3-}$  the complex molecules are organized via O–H···O hydrogen bonding (**Fig.20A**) and in  $[\text{Fe}(\text{4OH-L6})_{\text{-H}}]$  the supramolecular substructure is of chain type ( $d(\text{O} \cdots \text{O}) = 2.504(3)$  Å), while in  $[\text{Fe}(\text{4OH-L6})_{\text{-H}}] \cdot 2\text{H}_2\text{O}$  the helices along the a-axis (**Fig.20B**) are observed ( $d(\text{O} \cdots \text{O}) = 2.606(7)$  Å). The FeCo, FeCr and FeFe compounds are isostructural and their crystal structures are organized by formation of supramolecular centrosymmetric  $\{[\text{Fe}(\text{4OH-L6})]^+\}_2$  dimers held by  $\pi$ - $\pi$  stacking and N–H···O hydrogen bonding. The peripheral hydroxy groups are forming relatively strong O–H···O hydrogen bonding ( $d(\text{O} \cdots \text{O}) \sim 2.6$  Å) with phenolic oxygen atoms of the  $[\text{M}(\text{L3})_2]^-$  complex anions (**Fig.20C**). The overall supramolecular structure can be described as ladder-like with  $[\text{Fe}(\text{4OH-L6})]^+$  rungs. In the FeAg complex the  $[\text{Fe}(\text{H}_2\text{-4OH-L6})]^+$  cations are organized into two interpenetrating supramolecular networks (**Fig.20D**). Each network is formed by N–H···N and O–H···N hydrogen bonds in which the secondary amine and peripheral hydroxyl groups of the  $[\text{Fe}(\text{4OH-L6})]^+$  molecules act as hydrogen bonding donors, while the nitrogen atoms from the cyanido ligands act as acceptors of the bifurcated hydrogen bond. The O–H···N hydrogen bond is significantly stronger than N–H···N ( $d(\text{N} \cdots \text{N}) = 3.178(3)$  Å,  $d(\text{O} \cdots \text{N}) = 2.753(3)$  Å).

The magnetic revealed that in the range between 1.9-300K, either  $[\text{Fe}(\text{4OH-L6})_{\text{-H}}]$  molecules or  $[\text{Fe}(\text{4OH-L6})]^+$  cations remain in the HS state throughout the entire measured temperature range for all studied compounds. The magnetic data were fitted using a spin Hamiltonian that includes ZFS terms (**Fig.20E**). The results revealed that all Fe(III) molecules



possess very low magnetic anisotropy, exhibiting  $|D|$  values lower than  $1.2 \text{ cm}^{-1}$ . In the case of the FeCr and FeFe compounds, the magnetic anisotropy of the anionic counterparts is also very low. The BS-DFT calculations revealed that in the FeCr, FeFe and FeAg compounds, weak antiferromagnetic interactions ( $J = -0.05 - -1.84 \text{ cm}^{-1}$ ) mediated by non-covalent interactions could be observed. However, to achieve sufficiently good fit of the magnetic data, it was not necessary to involve exchange term. The CASSCF/NEVPT2 calculations correctly predicted spin states in the case of all the complexes and confirmed observation of only low magnetic anisotropy.

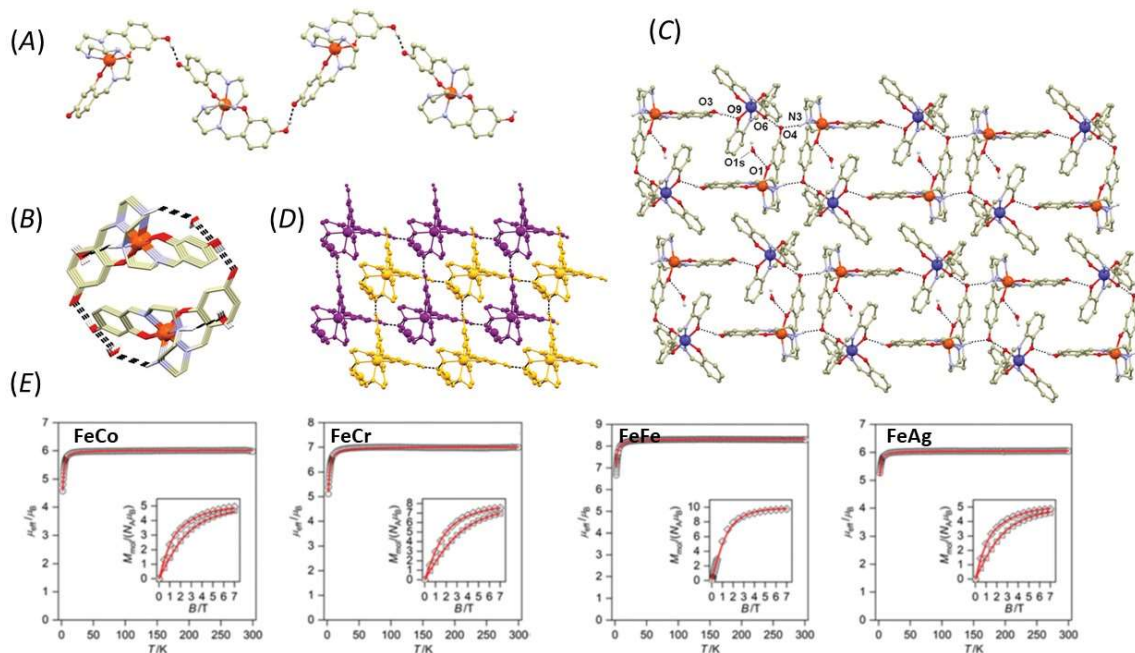


**Figure 20** (A) A perspective view of the chain crystal packing motif in  $[\text{Fe}(4\text{OH-L6})\text{-H}]$  complex. (B) helical chain substructure in  $[\text{Fe}(4\text{OH-L6})\text{-H}]\cdot 2\text{H}_2\text{O}$  compound. (C) Packing motifs in FeCo, FeCr and FeFe compounds. (D) Two interpenetrating supramolecular substructures (differentiated by violet and yellow colors) in FeAg compound. (E) Magnetic data measured for *te* FeCo, FeCr, FeFe and FeAg compounds.

### 5.3 Variation of Spin-Transition Temperature in the Iron (III) Complex Induced by Different Compositions of the Crystallization Solvent

The tunability of SCO materials is crucial for various applications. Key parameters such as thermal hysteresis width and transition temperature can be modified through strategies such as solvent changes, anion selection, side substituent choice, metal dilution, and post-synthetic anion metathesis. In this study, we focused on a new Fe(III) SCO complex with a pentadentate Schiff base ligand ( $H_23,5Cl-L5$ ,  $N,N'$ -bis(1-hydroxy-3,5-dichloro-2-benzylidene)-1,6-diamino-4-azahexane) that exhibited a 24 K wide thermal hysteresis. Our work primarily aimed to fill the research gap left by the original study, which did not delve into the noncovalent interactions during spin transition. We conducted extensive theoretical and experimental investigations on the LS and HS crystal structures of the complex to better understand the wide thermal hysteresis observed. In the crystal structure of the complex, a reorganization of noncovalent interactions ( $H\cdots Cl$  and  $Cl\cdots Cl$ ) occurs upon spin transition. This reorganization could potentially account for the wide thermal hysteresis observed. A comparison of the LS and HS structural fragments are illustrated in **Fig.21** and **Fig.22**.

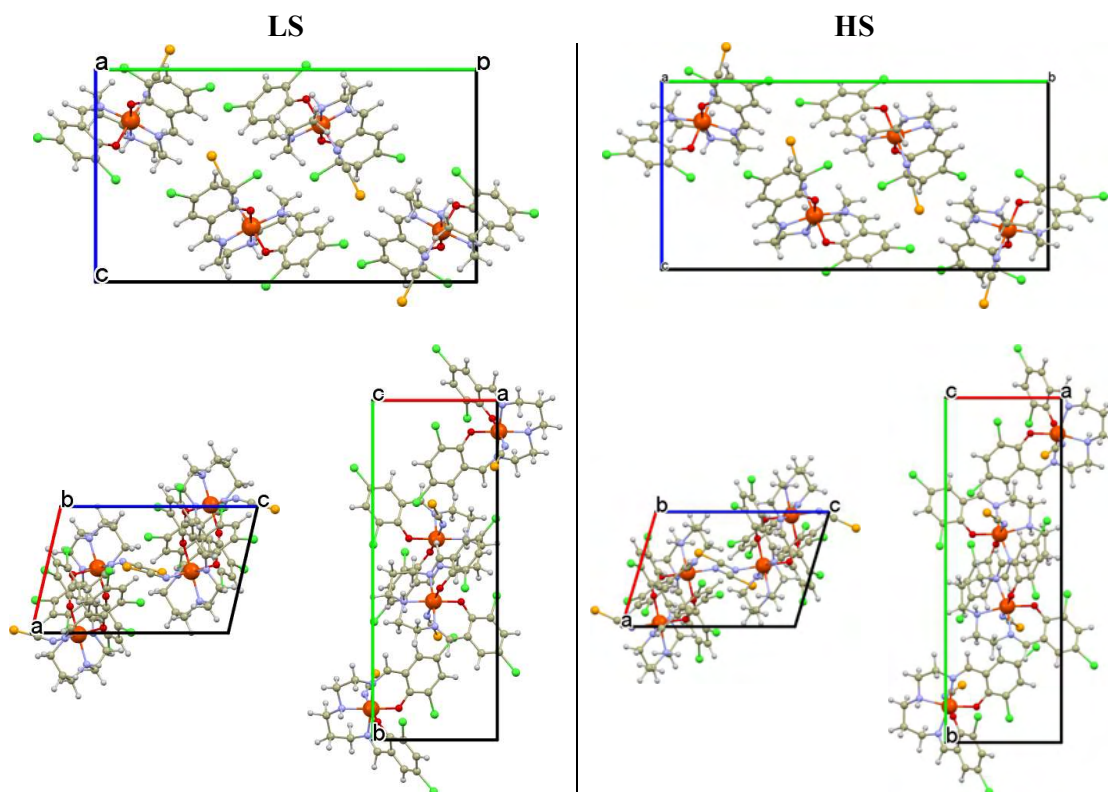


**Figure 21** A perspective view at views along particular axes of the Bravais cells in the LS (left column) and HS (right column) crystal structures of  $[Fe(3,5Cl-L5)(NCSe)]$  complex.

One can easily recognize with the naked eye the changes between the crystal structures of the LS and HS state. The complex molecule changes the angle SCO between the least square planes of the aromatic rings upon from  $78.0^\circ$  in the LS crystal structure to  $75.4^\circ$  in the HS crystal structure. Although this is a substantial change within the group of  $[Fe(L5)(L1)]$  SCO complexes, even more noticeable are the changes in interactions and the mutual positioning of the molecules in the crystal lattice. SCO in the studied compound does not result in symmetry



breaking, as both LS and HS phases retain the same space group ( $P2_1/n$ ). However, the changes observed in the crystal structures are attributable not only to the alteration of molecular shape but also to the rotation and movement of the complex molecules, as presented in **Fig.21**.

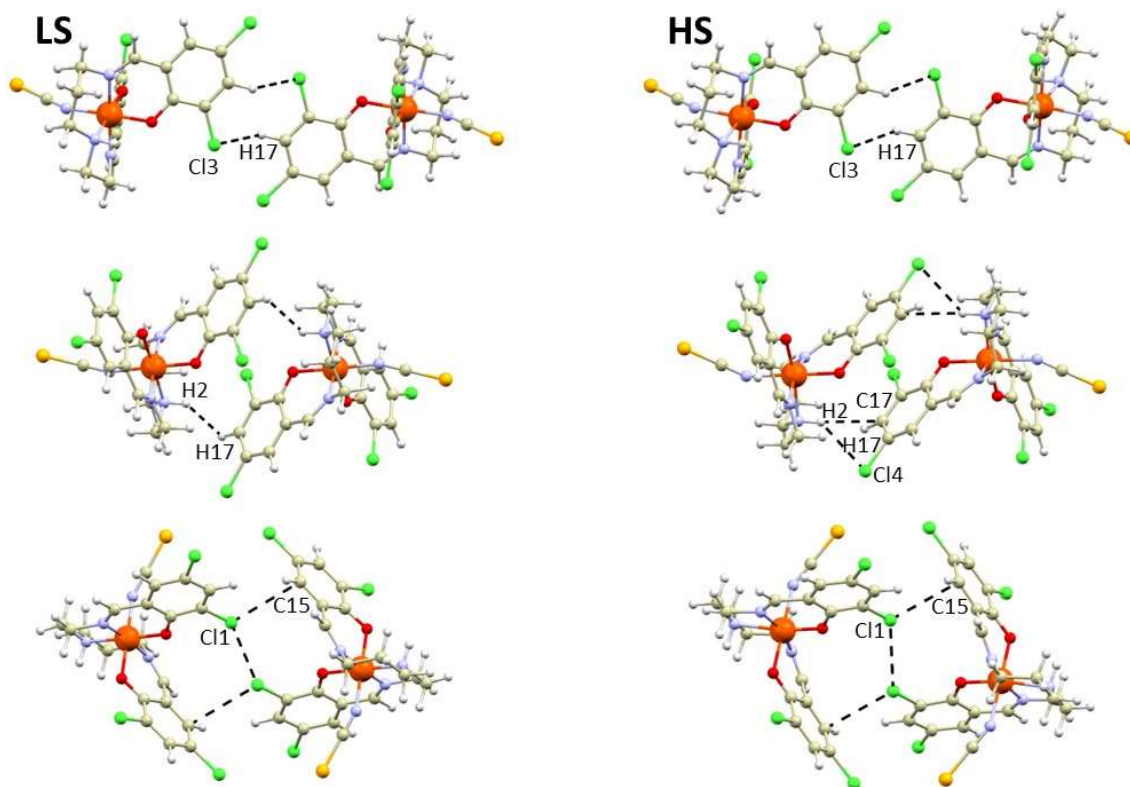


**Figure 22** A perspective view at selected structural fragments of the LS (left column) and HS (right column) crystal structures of the  $[Fe(3,5Cl-L5)(NCSe)]$  complex. Non-covalent interactions are depicted only for pairs of atoms adopting their distance shorter than sum of their van der Waals radii  $+0.1\text{\AA}$  and they were depicted by black dashed lines. Their selected distances (in  $\text{\AA}$ , LS;HS):  $d(H17\cdots Cl3) = 2.77(9)$ ;  $2.82(6)$ .  $d(H2\cdots H17) = 2.20(10)$ ;  $2.42(7)$ ,  $d(H2\cdots C17) = 2.63(9)$ ;  $2.77(5)$ ,  $d(H2\cdots Cl4) = 4.27(8)$ ;  $2.90(6)$ ,  $d(Cl1\cdots C15) = 3.447(8)$ ;  $3.509(5)$ ,  $d(Cl1\cdots Cl1) = 3.345(3)$ ;  $3.537(2)$ .

The changes in the intermolecular interactions between the LS and HS phases were studied by QT-AIM. Only the interactions in which the distance of the interacting atoms is equal or shorter than the sum of van der Waals radii  $+0.1\text{\AA}$  are shown in **Fig.22**. Indeed, the QT-AIM calculations revealed much richer interaction landscape, however, most of the interactions are of a rather weak character ( $E_{\text{int}} < 1\text{ kcal.mol}^{-1}$ ). All the interactions fulfill conditions for non-covalency as based on values of the topology and energetic parameters (existence of bond paths with (3,-1) CPs,  $\nabla^2\rho(\mathbf{r}) > 0$ ,  $h_c(\mathbf{r}) < 0$ ,  $V(\mathbf{r})/G(\mathbf{r}) < 1$ ) and the corresponding interaction energies were evaluated based on virial ( $E_{\text{int}} = V(\mathbf{r})/2$ ). The most pronounced changes were observed for supramolecular dimers formed by interactions involving secondary amine groups (**Fig.22** middle row) and mutual interactions of the peripheral Cl atoms (**Fig.22** below).

In the supramolecular dimer based on the hydrogen bonding of the secondary amine group in the HS state, the interaction with the largest  $E_{\text{int}}$  is that between the amine group and the chlorine atom at the fifth position ( $E_{\text{int}} = 1.22\text{ kcal.mol}^{-1}$ , **Fig.22** middle row right). In the

LS state this interaction is weaker ( $E_{\text{int}} = 0.87 \text{ kcal}\cdot\text{mol}^{-1}$ ) and due to the reorientation of the complex molecules, a different dominant interaction arises (**Fig.23A**), taking place between the amino group and the hydrogen atom attached to the carbon atom in the 4<sup>th</sup> position of the neighboring complex molecule ( $E_{\text{int}} = 1.54 \text{ kcal}\cdot\text{mol}^{-1}$ ). In the HS structure, the bond pathway occurs directly between the amine hydrogen atom and carbon atom in the 4<sup>th</sup> position, and the interaction is relatively weak ( $E_{\text{int}} = 0.88 \text{ kcal}\cdot\text{mol}^{-1}$ ). The N–H $\cdots$ Cl interaction is also present in the LS structure (**Fig.23A**), but remarkably not with chlorine atom in the fifth position, but in the third; this interaction is similarly weak ( $E_{\text{int}} = 0.87 \text{ kcal}\cdot\text{mol}^{-1}$ ).

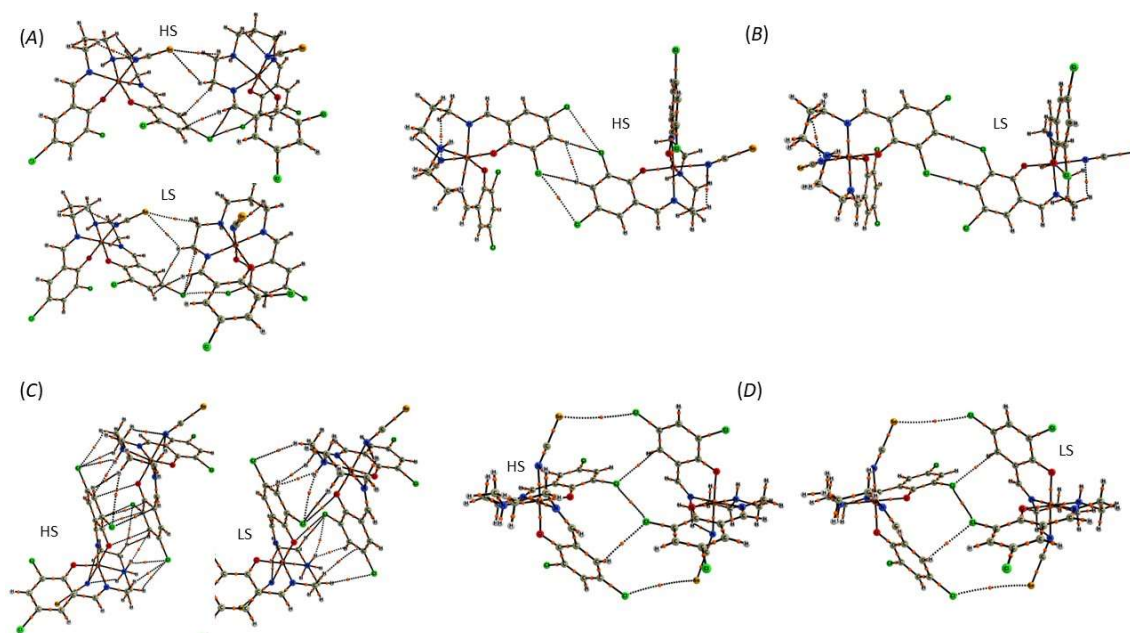


**Figure 23** The full atomic connectivity graphs of the selected fragments of the  $[\text{Fe}(3,5\text{Cl-L5})(\text{NCSe})]$  complex. The orange dots denote  $(3, -1)$  CPs of  $\sigma(\mathbf{r})$ . Bond paths of noncovalent interactions are shown by dashed lines.

Significant alterations are also noted in the interactions between the aromatic rings (**Fig.23C**). In the HS structure, the rings are offset, with bond paths forming between the carbon atoms at positions 2 and 3 ( $E_{\text{int}} = 0.65 \text{ kcal}\cdot\text{mol}^{-1}$ ), between the phenolic oxygen and the carbon atom at position 4 ( $E_{\text{int}} = 0.60 \text{ kcal}\cdot\text{mol}^{-1}$ ), and between the carbon atom at position 1 and the chlorine atom at position 3 ( $E_{\text{int}} = 0.85 \text{ kcal}\cdot\text{mol}^{-1}$ ). In contrast, the LS state exhibits only a single weak bond path between the chlorine atom at position 3 and phenolic oxygen atoms ( $E_{\text{int}} = 0.43 \text{ kcal}\cdot\text{mol}^{-1}$ ). Additional reorganization of non-covalent contacts upon SCO is evident in interactions involving chlorine atoms (**Fig.22**, top and bottom, **Fig.23B**). The hydrogen bonding that includes aromatic C–H groups at position 4 and chlorine atoms at position 3 forms a centrosymmetric pair of C–H $\cdots$ Cl hydrogen bonds in the LS phase ( $E_{\text{int}} = 1.50 \text{ kcal}\cdot\text{mol}^{-1}$ ). The HS state presents a more complex scenario (**Fig.23B**): these hydrogen bonds are slightly weaker ( $E_{\text{int}} = 1.50 \text{ kcal}\cdot\text{mol}^{-1}$ ), but new interactions emerge. The hydrogen atom at position 4 forms a weak H $\cdots$ H contact ( $E_{\text{int}} = 0.58 \text{ kcal}\cdot\text{mol}^{-1}$ ), and the chlorine atoms at positions 3 and 5 form an additional weak contact ( $E_{\text{int}} = 0.54 \text{ kcal}\cdot\text{mol}^{-1}$ ). Another case is the centrosymmetric Cl $\cdots$ Cl interaction between chlorine atoms at position 3 (**Fig.22**, bottom). This interaction weakens in the HS phase ( $0.74 \text{ kcal}\cdot\text{mol}^{-1}$ , **Fig.23D**) compared to the LS phase ( $1.30 \text{ kcal}\cdot\text{mol}^{-1}$ ). However, the formation of this interaction is associated in both states with the development of a Cl $\cdots$ C interaction involving the carbon atom of the aromatic ring, where the

trend is reversed ( $1.12 \text{ kcal}\cdot\text{mol}^{-1}$  in the HS phase versus  $0.82 \text{ kcal}\cdot\text{mol}^{-1}$  in the LS phase). When examining the non-centrosymmetric  $\text{Cl}\cdots\text{Cl}$  interaction between chlorine atoms at positions 3 and 5,  $E_{\text{int}}$  is higher in the LS phase ( $1.15 \text{ kcal}\cdot\text{mol}^{-1}$ ) than in the HS phase ( $0.87 \text{ kcal}\cdot\text{mol}^{-1}$ ).

In summary, the investigations conducted using QT-AIM topological and energetic analysis clearly demonstrate significant differences in the non-covalent interactions between the LS and HS phases. These distinctions are believed to be the underlying cause of the thermal hysteresis observed in the  $[\text{Fe}(3,5\text{-Cl-L5})(\text{NCSe})]$  complex and SCO compounds broadly. Employing such a method lays a solid foundation for the systematic study of cooperativity, a phenomenon that remains inadequately explained thus far. The findings reported herein are novel and will be included in a forthcoming publication that is currently under preparation.

Recently, we have already published another interesting feature of the  $[\text{Fe}(3,5\text{Cl-L5})(\text{NCSe})]$  complex. In the original report, the authors produced  $[\text{Fe}(3,5\text{-Cl-L5})(\text{NCSe})]$ , ( $\mathbf{1}^{\text{CICL}}$ ), through a reaction of  $[\text{Fe}(3,5\text{-Cl-L5})\text{Cl}]$  with  $\text{KNcSe}$  in pure methanol using an ultrasonic bath. We replicated these conditions but replaced the ultrasonic bath with a standard magnetic stirrer. This approach led to the formation of a brown microcrystalline powder, which we removed via filtration using a paper filter. To prepare single crystals suitable for X-ray diffraction, we used the mother liquor that was left after filtration and allowed it to crystallize at a constant temperature. After several days, we obtained thin, needle-like crystals. Initially, we collected diffraction data at 150 K to observe the high-spin state, and then we attempted to measure the low-spin state crystal structure at 90 K, as was performed in the original study. Upon measurement, to our surprise we discovered that the crystal structure determined at 90K exhibited the same metal-ligand bond lengths and unit cell parameters as those observed in the HS phase. This finding did not align with the previously reported magnetic properties. Consequently, we examined the temperature dependence of the magnetic moment ( $\mu_{\text{eff}}/\mu_{\text{B}}$ ) for both the needle-like crystals ( $\mathbf{1}^{\text{CICL}}_{\Phi 1}$ ) and the microcrystalline powder precipitate ( $\mathbf{1}^{\text{CICL}}_{\Phi 1p}$ ). These tests confirmed the existence of an SCO phenomenon with thermal hysteresis for both fractions; however, the critical temperatures for the transition between LS and HS states, as well as the magnetic profiles, differed between these two. The  $\mathbf{1}^{\text{CICL}}_{\Phi 1}$  batch exhibited much lower  $T_{1/2}$  ( $72\downarrow$  and  $96\uparrow$  K,  $\Delta T = 24$  K) than  $\mathbf{1}^{\text{CICL}}_{\Phi 1p}$  ( $106\downarrow$  and  $129\uparrow$  K,  $\Delta T = 23$  K). Powder X-ray diffraction undoubtedly confirmed that both samples were the same crystallographic phase identical to the HS structure of  $\mathbf{1}^{\text{CICL}}$ .

In response to this compelling discrepancy, we delved deeper into the investigation. Magnetic measurements indicated a lower  $T_{1/2}$  in crystals that had grown over a period exceeding five days, whereas the higher  $T_{1/2}$  corresponded to the precipitate. This led to the hypothesis that the varying  $T_{1/2}$  values might be linked to the crystallinity, which in turn is influenced by the crystallization duration. To explore this, we adjusted the crystallization time by changing the solvent composition from pure  $\text{CH}_3\text{OH}$  to mixtures increasingly rich in  $\text{CHCl}_3$ . The latter was chosen for its inability to form solvates with  $\mathbf{1}^{\text{CICL}}$  and for its excellent solubility of  $\mathbf{1}^{\text{CICL}}$ , as well as its high vapor pressure, which enables faster evaporation of solutions with  $\text{CHCl}_3$  compared to those with pure  $\text{CH}_3\text{OH}$ . Four different crystallization mixtures with a different volume fraction  $\Phi$  of  $\text{CH}_3\text{OH}$  were prepared ( $\Phi = 0.83, 0.50, 0.25$  and  $0.05$ ), and the corresponding crystalline samples ( $\mathbf{1}^{\text{CICL}}_{\Phi 0.83}$ ,  $\mathbf{1}^{\text{CICL}}_{\Phi 0.50}$ ,  $\mathbf{1}^{\text{CICL}}_{\Phi 0.25}$ ,  $\mathbf{1}^{\text{CICL}}_{\Phi 0.05}$ ) were obtained. In the case of the solutions with  $\Phi > 0.5$  also microcrystalline precipitates  $\mathbf{1}^{\text{CICL}}_{\Phi 0.83p}$  (besides already prepared  $\mathbf{1}^{\text{CICL}}_{\Phi 1p}$ ) were obtained and were included into this study.

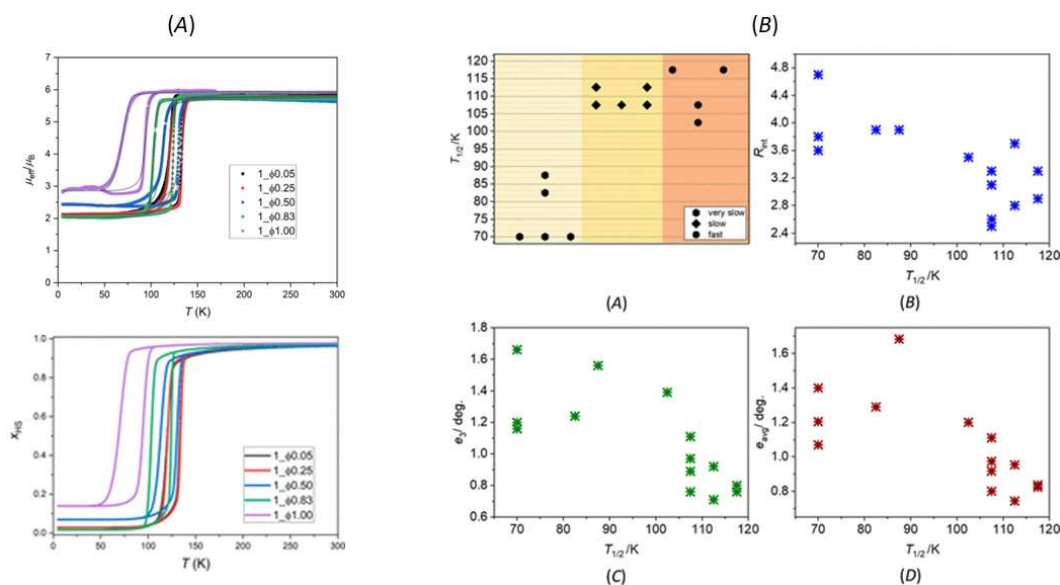


**Figure 24** (A) The temperature dependence of the effective magnetic moment measured for the crystalline samples of  $1^{CICl}$  (Top). Temperature dependence the high-spin molar fraction  $x_{HS}$  according to ISM (Bottom). (B) Plot of  $T_{1/2\downarrow}$  versus crystallization rate (A). The colored boxes are used to highlight the crystallization rate, with a lighter color indicating slower crystallization. The plots of  $R_{int}$  vs  $T_{1/2\downarrow}$  (B),  $e_3$  vs  $T_{1/2\downarrow}$  (C), and  $e_{avg}$  vs  $T_{1/2\downarrow}$  (D). The value of  $e_{avg}$  was calculated as the arithmetic average of components  $e_1$ ,  $e_2$ , and  $e_3$ . In all plots, the  $T_{1/2\downarrow}$  value of crystals that remained in the high spin phase down to 80 K was assigned as 70 K for visualization purposes.

The optimal quality crystals were yielded from batch  $1^{CICl}_{\Phi 0.25}$ . From this batch, we selected a single crystal to measure both the LS and HS crystal structures, employing single crystal X-ray diffraction to monitor the SCO phenomenon. Our experimental procedure started at 140 K, where we collected diffraction data sets at various temperatures during both cooling and heating cycles. A notable alteration in the diffraction quality was observed at 116 K during the cooling process, marking the  $T_{1/2\downarrow}$  temperature. The crystal structure of  $1^{CICl}_{\Phi 0.25}$  at 116 K ( $1^{CICl}_{\Phi 0.25@116K}$ ) revealed M-L bond lengths that were significantly shorter than those observed at higher temperatures, aligning closely with the LS structure of compound  $1^{CICl}$  reported in the original report. Subsequent cooling to 108 K did not yield significant changes in the M-L bond lengths or unit cell parameters, indicating that the complete HS to LS transition occurred between 116 K and 117 K. During the heating phase, the LS to HS transition was detected between 133 K (LS) and 135 K (HS), with data at 134 K proving unobtainable due to poor quality. An attempt to cycle another SCO thermal process was made; however, the crystal cracked upon further cooling. From these measurements, it was confirmed that  $1^{CICl}_{\Phi 0.25}$  undergoes a thermally induced SCO with an 18 K hysteresis width, presuming  $T_{1/2\uparrow}$  is at 134 K. This discovery does not corroborate the magnetic findings reported in the original paper, and it also shows discrepancies with the magnetic measurements taken for  $1^{CICl}_{\Phi 1p}$ .

Magnetic measurements (Fig.24A) were conducted on all prepared batches, confirming that each sample exhibited thermally induced SCO. Notably, batches synthesized using a methanol-rich mixture demonstrated hysteretic loops at lower temperatures, while those with greater proportions of  $CHCl_3$  displayed loops at higher temperatures. There was also an observable shift in the hysteretic loops between batches  $1^{CICl}_{\Phi 0.83}$  and  $1^{CICl}_{\Phi 1}$ ; however, their corresponding precipitates,  $1^{CICl}_{\Phi 0.83p}$  and  $1^{CICl}_{\Phi 1p}$ , did not exhibit a substantial difference in  $T_{1/2}$ . The loops for the batches with the highest  $CHCl_3$  content, specifically  $1^{CICl}_{\Phi 0.25}$  and  $1^{CICl}_{\Phi 0.05}$ , showed great similarity and had the highest recorded  $T_{1/2}$  values. Significantly, the atomic coordinates of the non-hydrogen atoms in the HS crystal

structure of **1<sup>CICL</sup>\_Φ1** at 90 K were almost identical to those in **1<sup>CICL</sup>\_Φ0.25** at 130 K, suggesting that the difference in  $T_{1/2}$  is not due to changes in the crystal structures.

The analysis of magnetic data was conducted using an Ising-like model (ISM) with a Gaussian distribution for the cooperativity parameter (**Fig.24A**). Additionally, we explored theoretically the influence of different solvents on the molecular geometry and the energy states of the LS and HS isomers of **1<sup>CICL</sup>** through DFT calculations. However, these theoretical investigations did not clarify the cause of the variations in magnetic behavior observed. Should the theoretical calculations hold true, it appears more plausible that the phenomena in question are not dictated by thermodynamic principles, but rather by the kinetics of crystal growth for compound **1<sup>CICL</sup>** in the presence of varying concentrations of chloroform and methanol in the crystallization solutions. Consequently, it seems that the crystalline material's quality and its SCO characteristics are indeed influenced by the solvent mixture, although the solvent molecules themselves do not become incorporated into the crystal structure.

To validate our hypothesis, which posits a correlation between parameters such as crystal mosaicity and the observed magnetic behavior, we initiated the preparation of various batches of **1<sup>CICL</sup>**, each crystallized at different rates. As previously mentioned, the best quality crystals were produced in the **1<sup>CICL</sup>\_Φ0.25 batch**. Nonetheless, batches that crystallized from solutions with a predominant chloroform fraction (Φ0.25 and Φ0.05) displayed nearly identical magnetic properties. Therefore, our strategy involved crystallizing **1<sup>CICL</sup>** from Φ0.5 and Φ0.83 solutions. It is important to note that the batches **1<sup>CICL</sup>\_Φ0.5** and **1<sup>CICL</sup>\_Φ0.83** exhibit different  $T_{1/2\downarrow}$  values (114 K for **1<sup>CICL</sup>\_Φ0.5** and 103 K for **1<sup>CICL</sup>\_Φ0.83**). Moreover, their spin transition upon cooling is within the operational range of standard commercial cryogenic equipment (above 80 K), making them suitable subjects for our study.

The crystals under investigation are exceptionally thin, with typical dimensions of approximately 0.05 mm in two axes, and they possess a needle-like morphology, often growing in clumps of overlapping individuals. These characteristics pose significant challenges in analyzing a statistically significant number of crystallites within a feasible timeframe for measurements. Consequently, we managed to perform measurements on a limited set of 14 single crystals. It is crucial to emphasize that the bulk of the crystals synthesized were not appropriate for single-crystal studies. Therefore, the results we present are representative solely of those select crystals that fulfilled the stringent requirements for such experiments.

The obtained findings corroborate our hypothesis that the rate of crystallization influences both the quality of the crystals and the  $T_{1/2\downarrow}$  values. Crystals that were crystallized under "fast" and "slow" conditions exhibited  $T_{1/2\downarrow}$  values exceeding 100 K. In contrast, those that crystallized "very slowly" demonstrated  $T_{1/2\downarrow}$  values below 90 K, with the majority presenting  $T_{1/2\downarrow}$  values even beneath 80 K.

The first approach to assess the quality of the crystals, we examined the internal agreement among symmetry-equivalent reflections (**Fig.24B**), referred to as  $R_{\text{int}}$ , within the crystals studied. While there does not appear to be a strong correlation between  $T_{1/2\downarrow}$  values and  $R_{\text{int}}$ , there is a noticeable trend where crystals with lower  $T_{1/2\downarrow}$  values tend to exhibit higher  $R_{\text{int}}$  values, and conversely, those with higher  $T_{1/2\downarrow}$  values tend to have lower  $R_{\text{int}}$  values. The CrysAlisPro software determines the mosaicity along three axes ( $e_1$ ,  $e_2$ , and  $e_3$ ) by applying a Gaussian function to the peak profile. Although these parameters do not provide a direct measurement of mosaicity, variations in  $e_1$ ,  $e_2$ , and  $e_3$  values can serve as indicators of changes in a crystal's mosaicity and, by extension, its overall quality. Our findings indicated a modest fluctuation in the  $e_2$  value across different measurements (ranging from 0.76 to 0.96 degrees), while more significant variations were seen for  $e_1$  (ranging from 0.75 to 2.61 degrees) and  $e_3$

(ranging from 0.71 to 1.66 degrees). Consistent with previous studies, we assessed mosaicity using the  $e_3$  value and the arithmetic mean ( $e_{\text{avg}}$ ) of the three components,  $e_1$ ,  $e_2$ , and  $e_3$ , as outlined in our earlier work. Similar to the observations with  $R_{\text{int}}$ , no strong linear correlation was evident between  $e_{\text{avg}}$  and  $e_3$  and the  $T_{1/2\downarrow}$  values; however, a general trend was observed where crystals with higher  $T_{1/2\downarrow}$  values exhibited lower mosaicity values for  $e_{\text{avg}}$  and  $e_3$ , and the reverse was true for crystals with lower  $T_{1/2\downarrow}$  values.

In conclusion, this study reveals solvent-driven variations in the spin-transition temperature of SCO for compound [Fe(3,5-Cl-L5)(NCSe)], a phenomenon not previously documented. Our research indicates that the crystallization rate significantly influences the SCO critical temperatures. Crystallization extending beyond seven days, particularly with  $\Phi 0.5$  and  $\Phi 0.83$  solutions, generates crystals with low SCO critical temperatures ( $T_{1/2\downarrow}$  under 90 K). Conversely, crystals formed within a shorter span, under four days, exhibit higher  $T_{1/2\downarrow}$  values, over 100 K. X-ray diffraction analysis implies that crystals with lower  $T_{1/2\downarrow}$  values tend to display increased mosaicity and  $R_{\text{int}}$ , suggesting inferior quality relative to those with elevated  $T_{1/2\downarrow}$  values. These findings pose a crucial question regarding the overarching relationship between crystal quality and SCO behavior. Should these observations be applicable across various SCO compounds, additional factors such as crystallization rate and crystal quality may need to be integrated into the analysis of magnetic behavior of such compounds.

## CHAPTER 6: CONCLUSION AND PERSPECTIVE

In this thesis, I aimed to illustrate my evolution from a magnetochemist with a solid foundation in crystallography to a researcher who employs methods of quantum crystallography in his research. To date, these methods have been theoretical; however, I plan to incorporate experimental techniques, such as experimental X-ray charge density studies, in my forthcoming research endeavors.

My scientific inquiries have focused on two types of magnetically bistable molecular materials: single ion magnets (SIMs) and spin crossover (SCO) compounds. Despite both types exhibiting magnetic bistability, their underlying mechanisms differ. In SIMs, the magnetic anisotropy, which is heavily influenced by the ligand field symmetry, plays a crucial role. On the other hand, SCO compounds' bistability arises from the dynamic balance between different spin states, which is highly responsive to external environmental conditions and molecular interactions within the crystal.

In the realm of SIMs, intermolecular interactions typically hinder magnetic relaxation, making the precise assessment of coordination bonds and non-covalent interactions imperative. The Quantum Theory of Atoms in Molecules (Q-TAIM) has proven indispensable for dissecting the coordination environment and for providing a deep understanding of the stabilizing interactions in these complexes. A novel strategy that emerged from our research is the integration of semi-coordination in SIM design, a concept born from initial experiments with a cobalt thiocyanido complex, as I discuss in Chapter 4.5. This discovery led to further explorations, such as our work on cobalt(II) nitrate complexes presented in Section 4.6, where we used QT-AIM to study variations in nitrate ligand binding modes and their impacts on the ligand field.

A significant development in our SIMs research has been the synthesis of stable Co(II) SIMs with semi-coordination to a pyridine nitrogen atom. These SIMs have been deposited as thin films by thermal evaporation, as outlined in section 4.7 of this thesis. Notably, these films exhibit chemical stability in the absence of an inert atmosphere, which facilitates extensive studies of SIM films on functional surfaces. This development is crucial, as it allows for an in-depth examination of the magnetic and electronic properties at the molecular scale, as well as the interactions of these molecules with various substrates. Insights gained from this research are fundamental for the progress of applications in areas such as memory storage, sensing devices, and quantum computing.

In the realm of SCO compounds, my research has been devoted to influencing the degree of cooperativity through chemical modification. Cooperativity is a key factor in determining the interaction strength between SCO molecules, with enhanced cooperativity resulting in more defined spin transitions and the presence of thermal hysteresis. Initially, I introduced bulky monodentate ligands to foster ring-ring interactions, which were thought to increase cooperativity in SCO systems. This hypothesis was tested on systems typically exhibiting non-cooperative behavior with the intention of inducing cooperative SCO properties. However, as documented in section 5.1, the results did not align with our expectations. Pursuing a different strategy, I engaged in crystal engineering to construct systems with peripheral hydroxy groups and complex anions, thereby creating a matrix rich in non-covalent interactions. Despite the promising design, the synthesized compounds did not demonstrate the anticipated SCO behavior, as described in section 5.2.



In chapter 5.3 of my thesis, the initial focus is on a QT-AIM study of non-covalent interactions and their varying strengths between the LS and HS states of an previously reported highly cooperative SCO complex. This section is distinctive within the thesis, as it diverges from reviewing previously published papers and instead introduces research that is forthcoming. The inclusion of this QT-AIM study underscores its potential to further our understanding of SCO cooperativity and the factors that contribute to thermal hysteresis. This approach, while demanding, promises to expand our comprehension of the intricate SCO phenomena in the years ahead.

Following this is a thorough investigation into the same system, which revealed that its magnetic properties are significantly influenced by the crystallization rate. This influence is observed as noticeable variations in the critical temperature of the spin transition and the width of thermal hysteresis. These findings suggest that factors such as crystallization rate and crystal quality may be crucial in the analysis of the magnetic characteristics of other SCO compounds.

## REFERENCES

- <sup>1</sup> Ivan Nemeč, Radovan Herchel, and Zdeněk Trávníček. 'The Relationship between the Strength of Hydrogen Bonding and Spin Crossover Behaviour in a Series of Iron(III) Schiff Base Complexes'. *Dalton Transactions* 44, no. 10 (19 January 2015): 4474–84. <https://doi.org/10.1039/c4dt03400g>.
- <sup>2</sup> Jiang, ShangDa, Karin Goß, Christian Cervetti, and Lapo Bogani. 'An Introduction to Molecular Spintronics'. *Science China Chemistry* 55, no. 6 (1 June 2012): 867–82. <https://doi.org/10.1007/s11426-012-4628-4>.
- <sup>3</sup> O. Gutfleisch, M.A. Willard, E. Brück, C.H. Chen, S.G. Sankar and J.P. Liu., *Magnetic Materials and Devices for the 21st Century: Stronger, Lighter, and More Energy Efficient*. *Adv. Mater.*, (2011), 23: 821-842. <https://doi.org/10.1002/adma.201002180>
- <sup>4</sup> Stephen J. Blundell, *Magnetism in Condensed Matter*, Oxford University Press, 2001
- <sup>5</sup> Huang, Yulong, and Shenqiang Ren. 'Multifunctional Prussian Blue Analogue Magnets: Emerging Opportunities'. *Applied Materials Today* 22 (1 March 2021): 100886. <https://doi.org/10.1016/j.apmt.2020.100886>.
- <sup>6</sup> Panagiota Perlepe, Itziar Oyarzabal, Aaron Mailman, Morgane Yquel, Mikhail Platunov, Iurii Dovgaliuk, Mathieu Rouzières, et al. 'Metal-Organic Magnets with Large Coercivity and Ordering Temperatures up to 242°C'. *Science* 370, no. 6516 (30 October 2020): 587–92. <https://doi.org/10.1126/science.abb3861>.
- <sup>7</sup> Richard Winpenny, *Single-Molecule Magnets and Related Phenomena, Structure and Bonding*, 2006, Springer Berlin, Heidelberg
- <sup>8</sup> Malcolm Halcrow, *Spin-Crossover Materials: Properties and Applications*, Wiley, 2013, ISBN: 978-1-119-99867-9
- <sup>9</sup> Gavin A. Craig and Mark Murrie. '3d Single-Ion Magnets'. *Chem. Soc. Rev.* 44, no. 8 (2015): 2135–47. <https://doi.org/10.1039/C4CS00439F>.
- <sup>10</sup> Aditya Borah and Ramaswamy Murugavel. 'Magnetic Relaxation in Single-Ion Magnets Formed by Less-Studied Lanthanide Ions Ce(III), Nd(III), Gd(III), Ho(III), Tm(II/III) and Yb(III)'. *Coordination Chemistry Reviews* 453 (15 February 2022): 214288. <https://doi.org/10.1016/j.ccr.2021.214288>.
- <sup>11</sup> Cassidy E. Jackson, Ian P. Moseley, Roxanna Martinez, Siyoung Sung, and Joseph M. Zadrozny. 'A Reaction-Coordinate Perspective of Magnetic Relaxation'. *Chemical Society Reviews* 50, no. 12 (2021): 6684–99. <https://doi.org/10.1039/D1CS00001B>.
- <sup>12</sup> Roberta Sessoli, Dante Gatteschi, A. Caneschi, and M. A. Novak. 'Magnetic Bistability in a Metal-Ion Cluster'. *Nature* 365, no. 6442 (1 September 1993): 141–43. <https://doi.org/10.1038/365141a0>.
- <sup>13</sup> O. Waldmann, A criterion for the anisotropy barrier in single-molecule magnets. *Inorg Chem.* 2007 Nov 26;46(24):10035-7. doi: 10.1021/ic701365t.
- <sup>14</sup> Frank Neese, D.A. Pantazis. What is not required to make a single molecule magnet. *Faraday Discuss.* 2011;148:229-38; discussion 299-314. doi: 10.1039/c005256f. PMID: 21322486.

- <sup>15</sup> Naoto Ishikawa, Miki Sugita, Tadahiko Ishikawa, Shin-ya Koshihara, and Youkoh Kaizu. 'Lanthanide Double-Decker Complexes Functioning as Magnets at the Single-Molecular Level'. *Journal of the American Chemical Society* 125, no. 29 (1 July 2003): 8694–95. <https://doi.org/10.1021/ja029629n>.
- <sup>16</sup> Satoru Karasawa, Guangyuan Zhou, Hiroshi Morikawa, and Noboru Koga. 'Magnetic Properties of Tetrakis[4-( $\alpha$ -Diazobenzyl)Pyridine]Bis(Thiocyanato-N)Cobalt(II) in Frozen Solution after Irradiation. Formation of a Single-Molecule Magnet in Frozen Solution'. *Journal of the American Chemical Society* 125, no. 45 (1 November 2003): 13676–77. <https://doi.org/10.1021/ja035478s>.
- <sup>17</sup> Danna E. Freedman, W. Hill Harman, T. David Harris, Gary J. Long, Christopher J. Chang, and Jeffrey R. Long. 'Slow Magnetic Relaxation in a High-Spin Iron(II) Complex'. *Journal of the American Chemical Society* 132, no. 4 (3 February 2010): 1224–25. <https://doi.org/10.1021/ja909560d>.
- <sup>18</sup> Roman Boča, *Theoretical Foundations of Molecular Magnetism*; Elsevier: Amsterdam, The Netherlands, 1999; p. 873.
- <sup>19</sup> Alexander A.Pavlov, Joscha Nehr Korn, Sergey V. Zubkevich, Matvey V. Fedin, Karsten Hollmack, Alexander Schnegg, and Valentin V. Novikov. 'A Synergy and Struggle of EPR, Magnetometry and NMR: A Case Study of Magnetic Interaction Parameters in a Six-Coordinate Cobalt(II) Complex'. *Inorganic Chemistry* 59, no. 15 (3 August 2020): 10746–55. <https://doi.org/10.1021/acs.inorgchem.0c01191>.
- <sup>20</sup> Silvia Gómez-Coca, Daniel Aravena, Roser Morales, and Eliseo Ruiz. 'Large Magnetic Anisotropy in Mononuclear Metal Complexes'. *Progress in Magnetochemistry* 289–290 (15 April 2015): 379–92. <https://doi.org/10.1016/j.ccr.2015.01.021>.
- <sup>21</sup> Philip C. Bunting, Mihail Atanasov, Emil Damgaard-Møller, Mauro Perfetti, Iris Crassee, Milan Orlita, Jacob Overgaard, Joris van Slageren, Frank Neese, and Jeffrey R. Long. 'A Linear Cobalt(II) Complex with Maximal Orbital Angular Momentum from a Non-Aufbau Ground State'. *Science* 362, no. 6421 (21 December 2018): eaat7319. <https://doi.org/10.1126/science.aat7319>.
- <sup>22</sup> Joseph M Zadrozny, Joshua Telser, and Jeffrey R Long. 'Slow Magnetic Relaxation in the Tetrahedral Cobalt(II) Complexes [Co(EPh)<sub>4</sub>]<sub>2</sub>– (EO, S, Se)'. *Polyhedron* 64 (2013): 209–17. <https://doi.org/10.1016/j.poly.2013.04.008>.
- <sup>23</sup> Gunnar C. Werncke, Philip C. Bunting, Carine Duhayon, Jeffrey R. Long, Sébastien Bontemps, and Sylviane Sabo-Etienne. 'Two-Coordinate Iron(I) Complex [Fe{N(SiMe<sub>3</sub>)<sub>2</sub>}<sub>2</sub>]<sup>–</sup>: Synthesis, Properties, and Redox Activity'. *Angewandte Chemie International Edition* 54, no. 1 (2 January 2015): 245–48. <https://doi.org/10.1002/anie.201408802>.
- <sup>24</sup> Susanne, Mossin, Ba L. Tran, Debashis Adhikari, Maren Pink, Frank W. Heinemann, Jörg Sutter, Robert K. Szilagyi, Karsten Meyer, and Daniel J. Mindiola. 'A Mononuclear Fe(III) Single Molecule Magnet with a 3/2 $\leftrightarrow$ 5/2 Spin Crossover'. *Journal of the American Chemical Society* 134, no. 33 (22 August 2012): 13651–61. <https://doi.org/10.1021/ja302660k>.
- <sup>25</sup> Yvonne Rechkemmer, , Frauke D. Breitgoff, Margarethe van der Meer, Mihail Atanasov, Michael Hakl, Milan Orlita, Petr Neugebauer, Frank Neese, Biprajit Sarkar, and Joris van Slageren. 'A Four-Coordinate Cobalt(II) Single-Ion Magnet with Coercivity and a Very High Energy Barrier'. *Nature Communications* 7, no. 1 (17 April 2016): 10467. <https://doi.org/10.1038/ncomms10467>.
- <sup>26</sup> Majed S. Fataftah, Joseph M. Zadrozny, Dylan M. Rogers, and Danna E. Freedman. 'A Mononuclear Transition Metal Single-Molecule Magnet in a Nuclear Spin-Free Ligand Environment'. *Inorganic Chemistry* 53, no. 19 (6 October 2014): 10716–21. <https://doi.org/10.1021/ic501906z>.
- <sup>27</sup> Shefali Vaidya, Subrata Tewary, Saurabh Kumar Singh, Stuart K. Langley, Keith S. Murray, Yanhua Lan, Wolfgang Wernsdorfer, Gopalan Rajaraman, and Maheswaran Shanmugam. 'What Controls the Sign and Magnitude of Magnetic Anisotropy in Tetrahedral Cobalt(II) Single-Ion Magnets?' *Inorganic Chemistry* 55, no. 19 (3 October 2016): 9564–78. <https://doi.org/10.1021/acs.inorgchem.6b01073>.
- <sup>28</sup> Silvia Gomez-Coca, Eduard Cremades, Núria Aliaga-Alcalde, and Eliseo Ruiz. 'Mononuclear Single-Molecule Magnets: Tailoring the Magnetic Anisotropy of First-Row Transition-Metal Complexes'. *Journal of the American Chemical Society* 135, no. 18 (8 May 2013): 7010–18. <https://doi.org/10.1021/ja4015138>.
- <sup>29</sup> Ivan V. Ananyev, Nadezhda A. Bokach, and Vadim Yu. Kukushkin. 'Structure-Directing Sulfur $\cdot$ metal Noncovalent Semicoordination Bonding'. *Acta Crystallographica Section B* 76, no. 3 (June 2020): 436–49. <https://doi.org/10.1107/S2052520620005685>.
- <sup>30</sup> Leo D Brown,, Kenneth N. Raymond, and Stephen Z. Goldberg. 'Preparation and Structural Characterization of Barium Decacyanodicobaltate(II) Tridecahydrate, Ba<sub>3</sub>[Co<sub>2</sub>(CN)<sub>10</sub>].13H<sub>2</sub>O, an Air-Stable Salt of the [Co<sub>2</sub>(CN)<sub>10</sub>]<sup>6-</sup> Ion'. *Journal of the American Chemical Society* 94, no. 22 (November 1972): 7664–74. <https://doi.org/10.1021/ja00777a010>.
- <sup>31</sup> Richard Bader, *Atoms in Molecules: A Quantum Theory*. USA: Oxford University Press. 1994, ISBN 978-0-19-855865-1.
- <sup>32</sup> Enrique Espinosa, Ibon Alkorta, José Elguero, and Elies Molins. 'From Weak to Strong Interactions: A Comprehensive Analysis of the Topological and Energetic Properties of the Electron Density Distribution

- Involving X–H···F–Y Systems’. *The Journal of Chemical Physics* 117, no. 12 (September 2002): 5529–42. <https://doi.org/10.1063/1.1501133>.
- <sup>33</sup> Yulia V. Nelyubina, Alexander A. Korlyukov, Ivan V. Fedyanin, and Konstantin A. Lyssenko. ‘Extremely Long Cu···O Contact as a Possible Pathway for Magnetic Interactions in Na<sub>2</sub>Cu(CO<sub>3</sub>)<sub>2</sub>’. *Inorganic Chemistry* 52, no. 24 (16 December 2013): 14355–63. <https://doi.org/10.1021/ic4024025>.
- <sup>34</sup> V.A. Starodub, S.V. Vitushkina, D. Kamenskyi, A.G. Anders, V.O. Cheranovskii, H. Schmidt, D. Steinborn, et al. ‘Peculiarities of Crystal Structures and Magnetic Properties of Cu(II) and Ni(II) Mixed-Ligand Complexes on the 1,3-Dithiole-2-Thione-4,5-Dithiolate Basis’. *Journal of Physics and Chemistry of Solids* 73, no. 2 (1 February 2012): 350–56. <https://doi.org/10.1016/j.jpcs.2011.10.001>.
- <sup>35</sup> Ivan Nemeč, Radovan Herchel, and Z. Trávníček. ‘Ferromagnetic Coupling Mediated by Co··· $\pi$  Non-Covalent Contacts in a Pentacoordinate Co(II) Compound Showing Field-Induced Slow Relaxation of Magnetization’. *Dalton Transactions* 45, no. 31 (2016): 12479–82. <https://doi.org/10.1039/c6dt01539e>.
- <sup>36</sup> J. Boeckmann and C. Nather, *Acta Crystallogr., Sect. E: Struct. Rep. Online*, 2011, 67, m1025–m1026
- <sup>37</sup> A. W. Addison, T. N. Rao, J. Reedijk, J. Vanriijn and G. C. Verschoor, *J. Chem. Soc., Dalton Trans.*, 1984, 1349–1356.
- <sup>38</sup> S. K. Wolff, D. J. Grimwood, J. J. McKinnon, M. J. Turner, D. Jayatilaka and M. A. Spackman, *CrystalExplorer (Version 3.1)*, University of Western Australia, 2012
- <sup>39</sup> F. Weigend Accurate Coulomb-fitting basis sets for H to Rn, *Phys. Chem. Chem. Phys.*, 2006, 8, 1057.
- <sup>40</sup> Philipp Gütllich and Harold A Goodwin. ‘Spin Crossover—An Overall Perspective’, 1–47, 2012. <https://doi.org/10.1007/b13527>.
- <sup>41</sup> Philipp Gütllich, Yann Garcia, and Harold A. Goodwin. ‘Spin Crossover Phenomena in Fe() Complexes’. *Chem. Soc. Rev.* 29, no. 6 (2000): 419–27. <https://doi.org/10.1039/B003504L>.
- <sup>42</sup> Osamu Sato, Optically switchable molecular solids: Photoinduced spin-crossover, photochromism, and photoinduced magnetization, *Acc. Chem. Res.*, ISSN 0001-4842, 2003, Vol. 36, 692-700
- <sup>43</sup> Ivan Nemeč, Roman Boča, Radovan Herchel, Zdeněk Trávníček, Milan Gembický, and Wolfgang Linert. ‘Dinuclear Fe(III) Complexes with Spin Crossover’. *Monatshefte Für Chemie - Chemical Monthly* 140, no. 7 (4 December 2009): 815–28. <https://doi.org/10.1007/s00706-008-0096-0>.
- <sup>44</sup> Ivan Šalitraš, N. T. Madhu, Roman Boča, Ján Pavlík, and Mario Ruben. ‘Room-Temperature Spin-Transition Iron Compounds’. *Monatshefte Für Chemie - Chemical Monthly* 140, no. 7 (1 July 2009): 695–733. <https://doi.org/10.1007/s00706-009-0128-4>.
- <sup>45</sup> Malcolm A. Halcrow, ‘Spin-Crossover Compounds with Wide Thermal Hysteresis’. *Chemistry Letters* 43, no. 8 (5 August 2014): 1178–88. <https://doi.org/10.1246/cl.140464>.
- <sup>46</sup> Ivan Nemeč, Radovan Herchel, Ivan Šalitraš, Zdeněk Trávníček, Ján Moncol, Hartmut Fuess, Mario Ruben, and Wolfgang Linert. ‘Anion Driven Modulation of Magnetic Intermolecular Interactions and Spin Crossover Properties in an Isomorphous Series of Mononuclear Iron(III) Complexes with a Hexadentate Schiff Base Ligand’. *CrystEngComm* 14, no. 20 (17 September 2012): 7015. <https://doi.org/10.1039/c2ce25862e>.
- <sup>47</sup> Julia Contreras-García, Erin R. Johnson, Shahar Keinan, Robin Chaudret, Jean-Philip Piquemal, David N. Beratan, and Weitao Yang. ‘NCIPLoT: A Program for Plotting Noncovalent Interaction Regions’. *Journal of Chemical Theory and Computation* 7, no. 3 (8 March 2011): 625–32. <https://doi.org/10.1021/ct100641a>.
- <sup>48</sup> T.-J. Park, S. Huh, Y. Kim and M.-J. Jun, *Acta Crystallogr., Sect. C: Cryst. Struct. Commun.*, 1999, 55, 848–850
- <sup>49</sup> Katie R. Meihaus, Jeffrey D. Rinehart, and Jeffrey R. Long. ‘Dilution-Induced Slow Magnetic Relaxation and Anomalous Hysteresis in Trigonal Prismatic Dysprosium(III) and Uranium(III) Complexes’. *Inorganic Chemistry* 50, no. 17 (5 September 2011): 8484–89. <https://doi.org/10.1021/ic201078r>.
- <sup>50</sup> P.Å. Malmqvist and B. O. Roos, The CASSCF state interaction method, *Chem. Phys. Lett.*, 1989, 155, 189
- <sup>51</sup> C. Angeli, R. Cimiraglia, S. Evangelisti, T. Leininger and J. P. Malrieu, N-electron valence state perturbation theory: a fast implementation of the strongly contracted variant, *J. Chem. Phys.*, 2001, 114, 10252
- <sup>52</sup> F. Weigend and R. Ahlrichs, The ORCA quantum chemistry program package, *Phys. Chem. Chem. Phys.*, 2005, 7, 3297.
- <sup>53</sup> Santiago Alvarez, ‘Polyhedra in (Inorganic) Chemistry’. *Dalton Trans.*, no. 13 (2005): 2209–33. <https://doi.org/10.1039/B503582C>.
- <sup>54</sup> Chunlin Zhuang, Wen Zhang, Chunquan Sheng, Wannian Zhang, Chengguo Xing, and Zhenyuan Miao. ‘Chalcone: A Privileged Structure in Medicinal Chemistry’. *Chemical Reviews* 117, no. 12 (28 June 2017): 7762–7810. <https://doi.org/10.1021/acs.chemrev.7b00020>.
- <sup>55</sup> Mohamad-Ali Tehfe, Frédéric Dumur, Pu Xiao, Marie Delgove, Bernadette Graff, Jean-Pierre Fouassier, Didier Gimes, and Jacques Lalevée. ‘Chalcone Derivatives as Highly Versatile Photoinitiators for Radical, Cationic, Thiol–Ene and IPN Polymerization Reactions upon Exposure to Visible Light’. *Polymer Chemistry* 5, no. 2 (2014): 382–90. <https://doi.org/10.1039/C3PY00922J>.

- 
- <sup>56</sup> Wang, Hui, Weizhou Wang, and Wei Jun Jin. 'σ-Hole Bond vs π-Hole Bond: A Comparison Based on Halogen Bond'. *Chemical Reviews* 116, no. 9 (11 May 2016): 5072–5104. <https://doi.org/10.1021/ACS.CHEMREV.5B00527>/ASSET/IMAGES/CR-2015-00527Q\_M005.GIF.
- <sup>57</sup> Tian Lu, and Feiwu Chen. 'Multiwfn: A Multifunctional Wavefunction Analyzer'. *Journal of Computational Chemistry* 33, no. 5 (15 February 2012): 580–92. <https://doi.org/10.1002/jcc.22885>.
- <sup>58</sup> Becke, A D, and K E Edgecombe. 'A Simple Measure of Electron Localization in Atomic and Molecular Systems'. *The Journal of Chemical Physics* 92, no. 9 (1 May 1990): 5397–5403. <https://doi.org/10.1063/1.458517>.
- <sup>59</sup> Tian, Lu, Fei-Wu Chen. Meaning and Functional Form of the Electron Localization Function[J]. *Acta Phys. - Chim. Sin.* 2011, 27(12), 2786-2792. doi: 10.3866/PKU.WHXB20112786
- <sup>60</sup> I., Nemeč, R. Herchel, and Z. Trávníček. 'Two Polymorphic Co(II) Field-Induced Single-Ion Magnets with Enormous Angular Distortion from the Ideal Octahedron'. *Dalton Transactions* 47, no. 5 (2018): 1614–23. <https://doi.org/10.1039/c7dt03992a>.
- <sup>61</sup> Frank Neese, Efficient and Accurate Approximations to the Molecular Spin-Orbit Coupling Operator and Their Use in Molecular g-Tensor Calculations. *J. Chem. Phys.* 2005, 122 (3), 034107. <https://doi.org/10.1063/1.1829047>.
- <sup>62</sup> Stefan Stoll, Arthur Schweiger EasySpin, a comprehensive software package for spectral simulation and analysis in EPR *J. Magn. Reson.* 178(1), 42-55 (2006).
- <sup>63</sup> E. Ruiz, J. Cano, S. Alvarez, P. Alemany. Broken symmetry approach to calculation of exchange coupling constants for homobinuclear and heterobinuclear transition metal complexes, *J. Comput. Chem.*, 20 (1999), pp. 1391-1400, [https://doi.org/10.1002/\(SICI\)1096-987X\(199910\)20:13<1391::AID-JCC6>3.0.CO;2-J](https://doi.org/10.1002/(SICI)1096-987X(199910)20:13<1391::AID-JCC6>3.0.CO;2-J)
- <sup>64</sup> T. Soda, Y. Kitagawa, T. Onishi, Y. Takano, Y. Shigeta, H. Nagao, Y. Yoshioka, K. Yamaguchi, Ab initio computations of effective exchange integrals for H-H, H-He-H and Mn 2 O 2 complex: comparison of broken-symmetry approaches, *Chem. Phys. Lett.*, 319 (2000), pp. 223-230, 10.1016/S0009-2614(00)00166-4
- <sup>65</sup> S. K. Singh , J. Eng , M. Atanasov and F. Neese , Covalency and chemical bonding in transition metal complexes: An ab initio based ligand field perspective, *Coord. Chem. Rev.*, 2017, 344 , 2
- <sup>66</sup> L.Xu, Yu.V.Mironov, X.Qi, S.-J.Kim, *Zhurnal Strukturnoi Khimii*, 2006, 47, 1003
- <sup>67</sup> Florian Kleemiss, Oleg V. Dolomanov, Michael Bodensteiner, Norbert Peyerimhoff, Laura Midgley, Luc J. Bourhis, Alessandro Genoni, et al. "Accurate Crystal Structures and Chemical Properties from NoSpherA2." *Chemical Science* 12, no. 5 (2021): 1675–92. <https://doi.org/10.1039/D0SC05526C>.

## Seznam příloh

- 1) Co(II)-Based single-ion magnets with 1,1'-ferrocenediyl-bis(diphenylphosphine) metalloligands
- 2) Halogen bonding in new dichloride-cobalt(II) complex with iodo-substituted chalcone ligands
- 3) Deposition of Tetracoordinate Co(II) Complex with Chalcone Ligands on Graphene
- 4) Trigonally Distorted Hexacoordinate Co(II) Single-Ion Magnets
- 5) Weak antiferromagnetic interaction in Cu(II) complex with semi-coordination exchange pathway
- 6) Neutral cobalt(II)-bis(benzimidazole)pyridine field-induced single-ion magnets for surface deposition
- 7) Tetracoordinate Co(II) complexes with semicoordination as stable single-ion magnets for deposition on graphene
- 8) Spin crossover in three mononuclear iron (III) Schiff-base complexes
- 9) Ion-pair complexes of Schiff base Fe(III) cations and complex anions.
- 10) Variation of Spin-Transition Temperature in the Iron (III) Complex Induced by Different Compositions of the Crystallization Solvent

Cite this: *Dalton Trans.*, 2020, **49**, 11697

## Co(II)-Based single-ion magnets with 1,1'-ferrocenediyl-bis(diphenylphosphine) metalloligands†

J. Hrubý,<sup>a</sup> D. Dvořák,<sup>b</sup> L. Squillantini,<sup>c</sup> M. Mannini,<sup>c</sup> J. van Slageren,<sup>d</sup> R. Herchel,<sup>b</sup> I. Nemeč<sup>\*a,b</sup> and P. Neugebauer<sup>a</sup>

Herein, we report on investigations of magnetic and spectroscopic properties of three heterobimetallic Fe(II)–Co(II) coordination compounds based on the tetracoordinate {CoP<sub>2</sub>X<sub>2</sub>} core encapsulated by dpfp metalloligand, where X = Cl (**1**), Br (**2**), I (**3**), dpfp = 1,1'-ferrocenediyl-bis(diphenylphosphine). The analysis of static magnetic data has revealed the presence of axial magnetic anisotropy in compounds (**1**) and (**2**) and this was further confirmed by high-frequency electron spin resonance (HF-ESR) spectroscopy. Dynamic magnetic data confirmed that (**1**) and (**2**) behave as field-induced Single-Ion Magnets (SIMs). Together with bulk studies, we have also tested the possibility of depositing (**2**) as thick films on Au(111), glass, and polymeric acetate by drop-casting as well as thermal sublimation, a key aspect for the development of future devices embedding these magnetic objects.

Received 24th April 2020,  
Accepted 20th July 2020

DOI: 10.1039/d0dt01512a

rsc.li/dalton

### Introduction

Single-Molecule Magnets (SMMs) feature magnetic bistability at low temperature<sup>1</sup> due to the intrinsic energy barrier ( $U$ ), which is a function of the total spin in the ground state ( $S$ ) and the axial parameter of the molecular anisotropy ( $D$ ):  $U = |D| \times S^2$  for integer spins and  $U = |D| \times (S^2 - 1/4)$  for non-integer spins, under the condition that the magnetic anisotropy is axial  $-D < 0$ . However, it has been reported that  $D$  is inversely dependent on  $S^2$  as can be extracted from the relationships describing spin-orbit contributions to  $D$ -tensor.<sup>2</sup> Therefore, in parallel with a growing interest in the use of SMM archetypes for the exploration of innovative devices for spintronics<sup>3</sup> and quantum computing,<sup>4</sup> research efforts in recent decades have been concentrated on maximising the magnetic anisotropy in novel molecular systems, and thus the

dynamic magnetic properties of transition metal-ion and rare-earth-based complexes.<sup>5</sup> As a result, a plethora of 3d or 4f SMMs with one paramagnetic metal centre, called Single-Ion Magnets (SIMs), have been reported,<sup>6</sup> including one with the highest blocking temperature, exceeding the temperature of liquid nitrogen.<sup>7</sup> Among the group of 3d SIMs, the Co(II) compounds are the most abundant and the SMM phenomenon was reported for a great variety of the coordination numbers and geometries such as tetracoordinate,<sup>8</sup> pentacoordinate,<sup>9</sup> hexacoordinate,<sup>10</sup> heptacoordinate<sup>11</sup> or even octacoordinate.<sup>12</sup> In these compounds, the ground spin state is split by strong spin-orbit coupling into two Kramers doublets ( $|3/2, \pm 1/2\rangle$  and  $|3/2, \pm 3/2\rangle$ ), which are separated by the energy equal to  $2\sqrt{D^2 + 3E^2}$ . In the case of tetracoordinate Co(II) compounds with the general formula  $[\text{Co}(\text{L}^{\text{N/P}})_2(\text{L}1)_2]$  or  $[\text{Co}(\text{L}^{\text{N/P}})(\text{L}1)_2]$ , where  $\text{L}^{\text{N/P}}$  represents mono or bidentate N- or P-donor ligands and L1 is halido or pseudohalido ligands, a magneto-structural correlation was established by Boča and co-workers in 2013.<sup>13</sup> It reads  $\delta = 2\alpha_{\text{Td}} - (\alpha)$ , where  $\alpha_{\text{Td}}$  is the angle of the ideal tetrahedron ( $109.5^\circ$ ),  $\alpha$  is the angle between the two Co–N/P bonds. Despite some limitations,<sup>14</sup> this relationship has proved to be successful in the prediction of sign and magnitude of  $D$ , such that more negative/positive  $\delta$  should lead to more negative/positive value of  $D$ . Therefore, our attention has focused on compounds with rather large and negative parameter  $\delta$  and these were further investigated for their static and dynamic magnetic properties.<sup>14,15</sup> Therefore, we opted to investigate the compound  $[\text{CoCl}_2(\text{dpfp})]$  as a suitable SIM candidate, where dpfp represents the 1,1'-ferrocenediyl-bis(diphenylphosphine). This complex can be prepared by the

<sup>a</sup>Central European Institute of Technology, CEITEC BUT, Purkyňova 656/123, 61200 Brno, Czech Republic. E-mail: ivan.nemec@ceitec.vutbr.cz

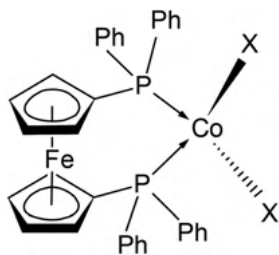
<sup>b</sup>Department of Inorganic Chemistry, Faculty of Science, Palacký University, 17. listopadu 12, 77147 Olomouc, Czech Republic

<sup>c</sup>Department of Chemistry "Ugo Schiff", University of Florence and INSTM Research Unit of Florence, via Lastruccia 3-13, 50019 Sesto Fiorentino, Italy

<sup>d</sup>Institute of Physical Chemistry, University of Stuttgart, Pfaffenwaldring 55, 70569 Stuttgart, Germany

† Electronic supplementary information (ESI) available: Crystallographic data, temperature dependence in HF-ESR spectra, static magnetic data measured for two batches of **3**, dynamic magnetic properties at zero magnetic field, Debye's model parameters, CASSCF/NEVPT2 calculations comparison, individual contributions to  $D$ -tensor, UV-VIS solution spectra comparison, XPS spectra comparison, XRPD data. CCDC 1998989–1998991. For ESI and crystallographic data in CIF or other electronic format see DOI: 10.1039/d0dt01512a





**Scheme 1** Drawing of the molecular structure of compounds 1–3, X stands for halido ligands (X = Cl in 1, Br in 2 and I in 3). Ph stands for the phenyl rings.

reaction between dppf and  $\text{CoCl}_2$  where both dppf and the resulting product  $[\text{CoCl}_2(\text{dppf})]$  are very well known, thoroughly studied (besides magnetic properties)<sup>16</sup> and even commercially available coordination compounds.<sup>17</sup> The crystal structure of  $[\text{CoCl}_2(\text{dppf})]$  was reported in 1999<sup>18</sup> and this compound has tetracoordinate  $\{\text{CoP}_2\text{Cl}_2\}$  arrangement with  $\delta = -4.8^\circ$ . Therefore, according to the magneto-structural correlation by Boča *et al.*,<sup>10</sup> it should possess negative  $D$ . Furthermore, having in mind influence of the intermolecular interactions which often effectively decrease  $U$ ,<sup>19</sup> giving also the rise to other relaxation channels,<sup>20</sup> another structural property of  $[\text{CoCl}_2(\text{dppf})]$  must be emphasised. The crystal structure of this compound is composed of the complex molecules connected only by weak C–H $\cdots\pi$  and C–H $\cdots\text{Cl}$  non-covalent interactions (Scheme 1).

Due to the bulkiness of the dppf metalloligand, these interactions are organised in a way (*vide infra*) that they cannot effectively transmit even very weak exchange interactions. The shortest Co $\cdots$ Co separations are longer than 9.6 Å assuring

that also dipolar interactions between the Co(II) atoms are negligible. Therefore, we decided to study the static and dynamic magnetic properties of the compound  $[\text{CoCl}_2(\text{dppf})]$ , (1), together with the bromido  $[\text{CoBr}_2(\text{dppf})]$ , (2) and iodido  $[\text{CoI}_2(\text{dppf})]$ , (3) analogues. The precise determination of the magnetic anisotropy parameters was performed by High-Frequency and -Field Electron Spin Resonance (HF-ESR) measurements. We also focused our synthetic strategy on the preparation of the single crystals of compounds 2 and 3 and the determination of their crystal structures by the X-ray diffraction. The analysis of the experimental data was supported by *ab initio* calculations (CASSCF/NEVPT2). Furthermore, we tested the deposition<sup>21</sup> of thick films of these complexes on surfaces *via* both thermal sublimation and wet-chemistry-based protocols.

## Results and discussion

### Crystal structure

Crystal structure of the compound 1 was reported previously ( $T = 293$  K),<sup>15</sup> here we report on its re-determination at a lower temperature ( $T = 150$  K) and determination of the new structures of the bromide (2) and iodide (3) analogues. Compounds 1 and 2 are isostructural, both crystallising in the triclinic space group  $P\bar{1}$  (see ESI, Table S1†). Compound 3 crystallises in the monoclinic space group  $P2_1$ . All three complexes contain dinuclear  $[\text{CoX}_2(\text{dppf})]$  molecules in their crystal structures. In these, the Fe(II) centres are coordinated by two cyclopentadienyl rings (Cp) in the almost eclipsed geometry (Fig. 1) and they are rotated by only  $9.3(2)^\circ$  (1),  $9.1(1)^\circ$  (2) and  $0.2(4)^\circ$  (3) as based on the P–C $\cdots$ C–P torsion angle of two Cp–P moieties. The Cp rings are tilted by  $6.3^\circ$  (1),  $6.3^\circ$  (2) and  $6^\circ$  (3). The dppf metalloligand coordinates the Co(II) centre by two

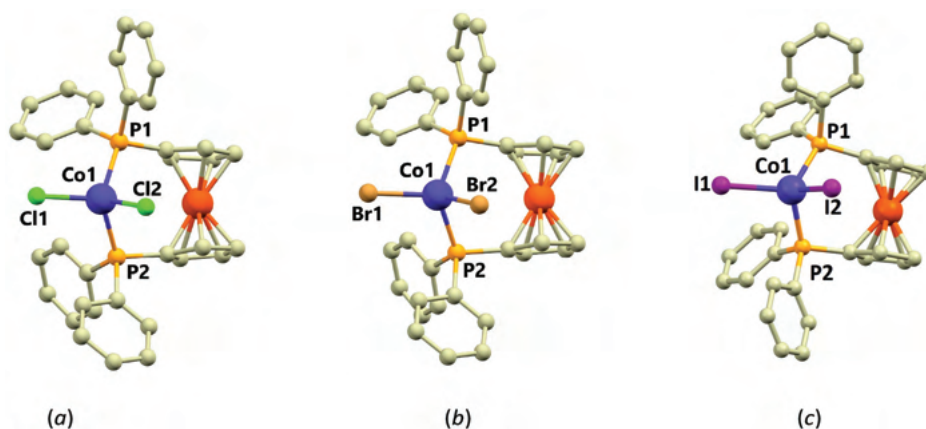


**Fig. 1** Molecular structures of 1 (a), 2 (b) and 3 (c). Selected metal–ligand bond distances (in Å) and angles (in  $^\circ$ ): in 1, Co1–P1 = 2.3632(10), Co1–P2 = 2.3517(10), Co1–Cl1 = 2.2353(9), Co1–Cl2 = 2.2229(10), Cl1–Co1–Cl2 =  $116.14(4)$ , P1–Co1–P2 =  $108.17(4)$ , Cl2–Co1–P2 =  $113.03(4)$ , Cl1–Co1–P2 =  $98.59(4)$ , Cl2–Co1–P1 =  $110.74(4)$ , Cl1–Co1–P1 =  $109.39(4)$ ; in 2, Co1–P1 = 2.3527(9), Co1–P2 = 2.3758(9), Co1–Br1 = 2.3874(6), Co1–Br2 = 2.3640(6), P1–Co1–P2 =  $108.65(2)$ , Br1–Co1–Br2 =  $114.874(19)$ , P1–Co1–Br2 =  $112.78(3)$ , Br2–Co1–P2 =  $111.16(2)$ , P1–Co1–Br1 =  $97.76(2)$ , P2–Co1–Br1 =  $110.81(3)$ ; in 3, Co1–P1 = 2.3648(13), Co1–P2 = 2.3423(13), Co1–I1 = 2.5596(6), Co1–I2 = 2.5581(6), P1–Co1–P2 =  $106.31(5)$ , I1–Co1–I2 =  $116.82(2)$ , P2–Co1–I2 =  $107.41(4)$ , P1–Co1–I2 =  $102.70(4)$ , P2–Co1–I1 =  $106.19(4)$ , P1–Co1–I1 =  $116.70(4)$ .





diphenylphosphine groups which together with coordination of two other halide ligands lead to the formation of the  $P_2X_2$  coordination sphere.

The geometry around the  $Co(II)$  centres can be described as distorted tetrahedral (continuous shape measures<sup>22</sup> for  $T_d$ : 0.356 in **1**, 0.399 in **2** and 0.637 in **3**) with the P–Co–P, P–Co–X and X–Co–X angles deviating significantly from the ideal tetrahedron with the largest deviation observed for the X–Co–X angles (in  $^\circ$ ): 116.14(4) in **1**, 114.87(2) in **2** and 116.82(4) in **3**. The P–Co–P angles are much closer to the ideal tetrahedral angle (109.5, all values in  $^\circ$ ): 108.17(4) in **1**, 108.65(2) in **2** and 106.31(5) in **3**. The distortion from ideal tetrahedron is not only of angular character, but also the bond lengths significantly differ. The Co–P bonds in **1–3** adopt lengths ranging from 2.35 to 2.37 Å, whereas the Co–X bond lengths vary within a series significantly (in Å): 2.2229(10) and 2.2353(9) in **1**, 2.3874(6) and 2.3640(6) in **2** and 2.5596(6) and 2.5581(6) in **3**. The non-covalent interactions in **1–3** are of very weak character represented only by the C–H...X and C–H... $\pi$  contacts. Furthermore, the closest Co...Co distances are 9.609(1) Å in **1**, 9.680(3) Å in **2** and 8.9206(8) Å in **3**. Therefore, the presence of the magnetic exchange or dipolar interactions cannot be expected.

### Electron spin resonance

We acquired HF-ESR spectra at four frequencies: 270 GHz, 320 GHz, 360 GHz, and 380 GHz while sweeping the magnetic field from 0–15 T at temperature of 5 K. By these measurements we were able to correlate  $g$ -tensor values and zero-field splitting parameters from *ab initio* simulations with HF-ESR measurements. The best fit for **1** (Fig. 2 top) was found for  $D = -12.0 \text{ cm}^{-1}$  with  $E/D = 0.106$ , and  $g_x = 2.20$ ,  $g_y = 2.20$ ,  $g_z = 2.28$ ; for **2** (Fig. 2 bottom) was found for  $D = -11.2 \text{ cm}^{-1}$  with  $E/D = 0.090$ , and  $g_x = 2.22$ ,  $g_y = 2.22$ ,  $g_z = 2.31$ . For **1** and **2** we have also acquired HF-ESR spectra at 10 K, 20 K, and 40 K (see ESI, Fig. S1 and S2†).

### Static magnetic properties

The temperature and field-dependent magnetic data were collected and analysed for compounds **1–2**. We were not successful in obtaining the pure phase of compound **3** as was confirmed by measurements of elemental analysis, X-ray powder diffraction and magnetic data (*vide infra*). We believe that partial decomposition of **3** occurred, as can be judged from outward reddish-brown and inner green colours of obtained crystals. Therefore, we briefly describe and discuss magnetic data of **3** only to draw the attention to potential issues with surprisingly large  $D$  parameters of  $Co(II)$  tetracoordinate complexes with iodide ligands.

The temperature dependencies of the effective magnetic moment ( $\mu_{\text{eff}}/\mu_B$ ) are similar for **1–2**, adopting values (4.4–4.5 $\mu_B$ ) larger than spin only value for  $Co(II)$  with  $e^4 t_2^3$  configuration in tetrahedral symmetry of the coordination polyhedron ( $g = 2.0$ ,  $S = 3/2$ ,  $\mu_{\text{eff}}/\mu_B = 3.87$ ). The  $\mu_{\text{eff}}$  value was almost constant to *ca.* 20 K and then decrease to *ca.* 3.5 (**1**) and 3.7 (**2**)  $\mu_B$  was observed. With respect to the crystal structures

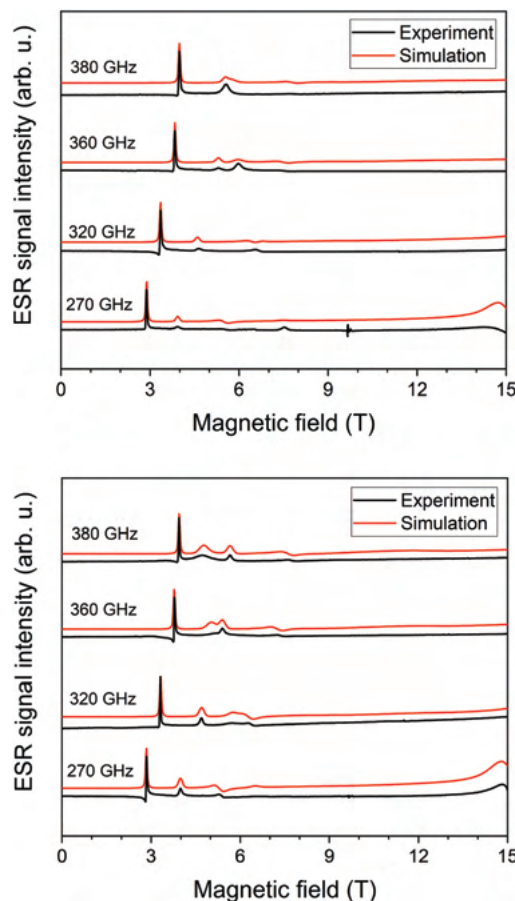


Fig. 2 HF-ESR spectra for **1** (top) and **2** (bottom) of a pressed powder pellet recorded at 5 K and four frequencies as indicated. The black solid line represents experimental data and the red solid line is the simulation.

of **1–2** compounds as discussed above, we can conclude that there are no covalent or non-covalent magnetic exchange pathways, which could be responsible for mediation of weak anti-ferromagnetic interactions. Hence, the observed decreases of  $\mu_{\text{eff}}$  can only be attributed to the occurrence of the zero-field splitting (ZFS), and thus magnetic anisotropy. Therefore, the magnetic data were fitted for spin Hamiltonian including axial and rhombic ZFS terms:

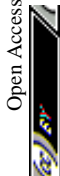
$$\hat{H} = D(\hat{S}_z^2 - \hat{S}^2/3) + E(\hat{S}_x^2 - \hat{S}_y^2) + \mu_B B g \hat{S}_a \quad (1)$$

where  $D$  and  $E$  are the single-ion axial and rhombic ZFS parameters and the last term is Zeeman term defined in the direction of a magnetic field as  $B_a = B(\sin(\theta) \cos(\varphi), \sin(\theta) \sin(\varphi), \cos(\theta))$  with the help of the polar coordinates.

Next, the molar magnetisation in  $a$ -direction of the magnetic field was numerically calculated as:

$$M_a = N_A k T \frac{d \ln Z}{d B_a} \quad (2)$$

where  $Z$  is the partition function constructed from the energy levels of the spin Hamiltonian. Then, the averaged molar mag-



netisation of the powder sample was calculated as the integral (orientational) average:<sup>23</sup>

$$M_{\text{mol}} = \frac{1}{4\pi} \int_0^{2\pi} \int_0^\pi M_a \sin \theta d\theta d\varphi. \quad (3)$$

Taking into account the fitting procedure for both temperature and field-dependent magnetisation data, the best fits were found for **1** with  $g = 2.20$ ,  $D = -11.0 \text{ cm}^{-1}$ ,  $E/D = 0.00$ ,  $\chi_{\text{TIP}} = 10.1 \times 10^{-9} \text{ m}^3 \text{ mol}^{-1}$  and for **2** with  $g = 2.24$ ,  $D = -8.7 \text{ cm}^{-1}$ ,  $E/D = 0.24$ ,  $\chi_{\text{TIP}} = 6.1 \times 10^{-9} \text{ m}^3 \text{ mol}^{-1}$  – Fig. 3. These parameters confirm that an axial magnetic anisotropy is present in both compounds **1** and **2**.

Static and dynamic magnetic data were measured for two different batches of **3** (see ESI, Fig. S3†). The first batch was crystallised for longer than 3 weeks and the analysis of magnetic data using eqn (1)–(3) resulted in a rather unsatisfactory fit with a rather large value of  $D = -29.2 \text{ cm}^{-1}$  (Fig. S3†). This can be explained by the occurrence of a decomposition process resulting in hexacoordinate Co(II) species and triiodide anion (deduced from the reddish-brown colour of contaminant). Hexacoordinate Co(II) complexes typically possess large

and positive values of  $D$  (i.e.  $>30 \text{ cm}^{-1}$ ),<sup>10</sup> while the compound **3** is expected to have ca. 3-times smaller and negative  $D$  value. Simultaneous fitting of both temperature and magnetic dependencies of the magnetic moment is then very sensitive to the occurrence of hexacoordinate contaminant, which might be a plausible explanation for very low fit quality observed for this batch of **3**.

The crystals of the second batch were collected immediately after the first crystals appeared and the surface of crystals was again reddish-brown coloured.

The magnetic data were analysed in the same manner as the first batch with a much better quality of fit and lower  $D$  value of  $-14.0 \text{ cm}^{-1}$ .

However, this value is inconsistent with expected lower  $|D|$  values for complexes with heavier halido ligands within this series as was corroborated by results from HF-ESR spectroscopy (comparison of **1** and **2**), and also supported by CASSCF calculations (Table 1). Furthermore, the results of X-ray powder diffraction obtained for both batches of **3** indicate that they contain small amount of impurity (see ESI† for details) Therefore, we decided not to include a detailed discussion of its magnetic properties in the paper.

### Dynamic magnetic properties

To further characterise compounds **1** and **2**, AC susceptibility was measured for both compounds. Unfortunately, there were no out-of-phase signals in zero static magnetic field, but the

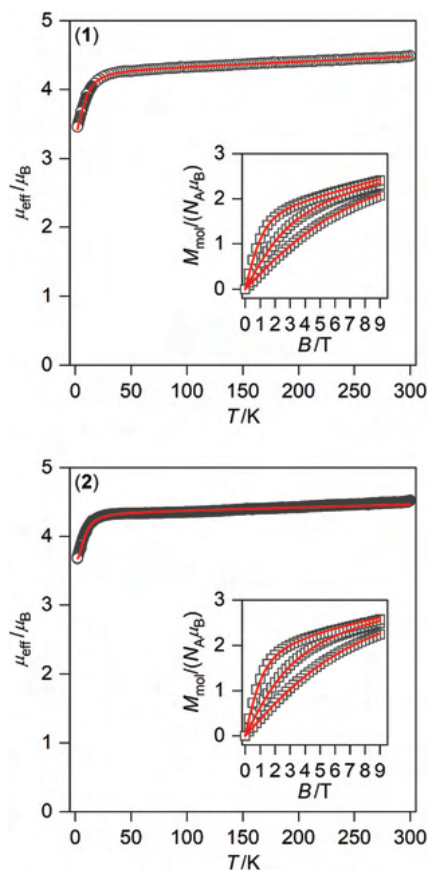
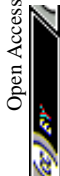


**Fig. 3** Magnetic data for **1** (top) and **2** (bottom) displayed as the temperature dependence of the effective magnetic moment, and the isothermal molar magnetisation measured at  $T = 2, 5$ , and  $10 \text{ K}$  is in the inset. The empty symbols represent the experimental data; red full lines represent the fitted data using eqn (1) and parameters listed in Table 1.

**Table 1** The comparison of the *ab initio* calculated and fitted experimental parameters for **1–3**<sup>a</sup>

	<b>1</b>	<b>2</b>	<b>3</b>
CASSCF/NEVPT2 with CAS(7,5)			
$D$ ( $\text{cm}^{-1}$ )	-13.2	-10.1	-7.44
$E/D$	0.130	0.106	0.119
$g_x$	2.215	2.233	2.256
$g_y$	2.188	2.215	2.239
$g_z$	2.331	2.321	2.318
$U_{\text{calc}}$ ( $\text{cm}^{-1}$ )	27.1	20.6	15.2
CASSCF/NEVPT2 with CAS(7,10)			
$D$ ( $\text{cm}^{-1}$ )	-15.0	-12.1	-9.59
$E/D$	0.116	0.102	0.146
$g_x$	2.238	2.264	2.296
$g_y$	2.207	2.241	2.275
$g_z$	2.374	2.373	2.382
$U_{\text{calc}}$ ( $\text{cm}^{-1}$ )	30.6	24.7	19.8
The best-fit of the experimental HF-ESR data			
$D$ ( $\text{cm}^{-1}$ )	-12.0	-11.2	
$E/D$	0.106	0.090	
$g_x$	2.20	2.22	
$g_y$	2.20	2.22	
$g_z$	2.28	2.31	
$U_{\text{calc}}$ ( $\text{cm}^{-1}$ )	24.0	22.4	
The best-fit of the experimental magnetic data			
$D$ ( $\text{cm}^{-1}$ )	-11.0	-8.7	
$E/D$	0.00	0.24	
$g$	2.20	2.24	
$\chi_{\text{TIP}}$ ( $10^{-9} \text{ m}^3 \text{ mol}^{-1}$ )	10.1	6.1	
$U_{\text{calc}}$ ( $\text{cm}^{-1}$ )	22.0	18.7	

<sup>a</sup>  $U_{\text{calc}}$  is the energy separation between the first two Kramers doublets arising from  $S = 3/2$ .



small static magnetic field was enough to suppress fast relaxations and the imaginary susceptibility became non-zero for both compounds (see ESI, Fig. S4 and 5†). Therefore, the AC susceptibility was measured at  $B_{DC} = 0.1$  T and revealed frequency-dependent maxima of the imaginary susceptibility, and thus confirming the slow relaxation of the magnetisation in **1** and **2**. Next, the one-component Debye's model was applied based on the equation:

$$\chi(\omega) = \frac{\chi_T - \chi_S}{1 + (i\omega\tau)^{1-\alpha}} + \chi_S \quad (4)$$

which resulted in isothermal ( $\chi_T$ ) and adiabatic ( $\chi_S$ ) susceptibilities, relaxation times ( $\tau$ ) and distribution parameters ( $\alpha$ ) for both **1** and **2** (see ESI, Tables S2 and S3).

The Argand (Cole-Cole) plots are depicted above (Fig. 4). The extracted relaxation times follow the Arrhenius law and subsequent analysis yielded these parameters:  $\tau_0 = 5.17 \times 10^{-9}$  s,  $U_{\text{eff}} = 33.3$  K ( $23.2$  cm $^{-1}$ ) for **1**, and  $\tau_0 = 1.80 \times 10^{-9}$  s,  $U_{\text{eff}} = 28.8$  K ( $20.0$  cm $^{-1}$ ) for **2**. The values of  $U_{\text{eff}}$  are very close to  $U_{\text{calc}}$  calculated with fitted parameters from the analysis of HF-ESR or experimental magnetic data – Table 1.

## Theoretical calculations

To support the analysis of the experimental magnetic and HF-ESR data, a multi-reference method based on the Spin-Averaged Complete Active Space Self Consistent Field (SA-CASSCF) was utilised to calculate all energy levels resulting from  $3d^7$  electronic configuration with the ORCA 4.0 computational package. The active space was defined as seven electrons in five d-orbitals, CAS(7,5) and dynamic electronic correlation was treated with the NEVPT2 method. The *ab initio* ligand field theory (AILFT)<sup>24</sup> was used to calculate the splitting of d-orbitals as shown in Fig. 5 (left). The overall pattern is similar to  $T_d$  symmetry of the ligand field, but the degeneracy of e and  $t_2$  orbitals is removed due to lower symmetry of the complexes under study. Moreover, the size of the d-orbitals splitting is decreasing from **1** to **2** according to the decrease of the ligand field of halogenido ligands ( $\text{Br}^- < \text{Cl}^-$ ), but in case of **3**, the splitting pattern of d-orbitals is slightly different due to larger change of the ligand field geometry evidenced by continuous shape measures indexes<sup>22</sup> (for  $T_d$ : 0.356 in **1**, 0.399 in **2** and 0.637 in **3**). Next, CASSCF/NEVPT2 calculations provided the energies of the ligand-field (LF) terms – Fig. 5 (middle), in which lowering the energies of first excited quartet state is observed from 3914 cm $^{-1}$  for **1** to 3227 cm $^{-1}$  for **3**. Next, due to

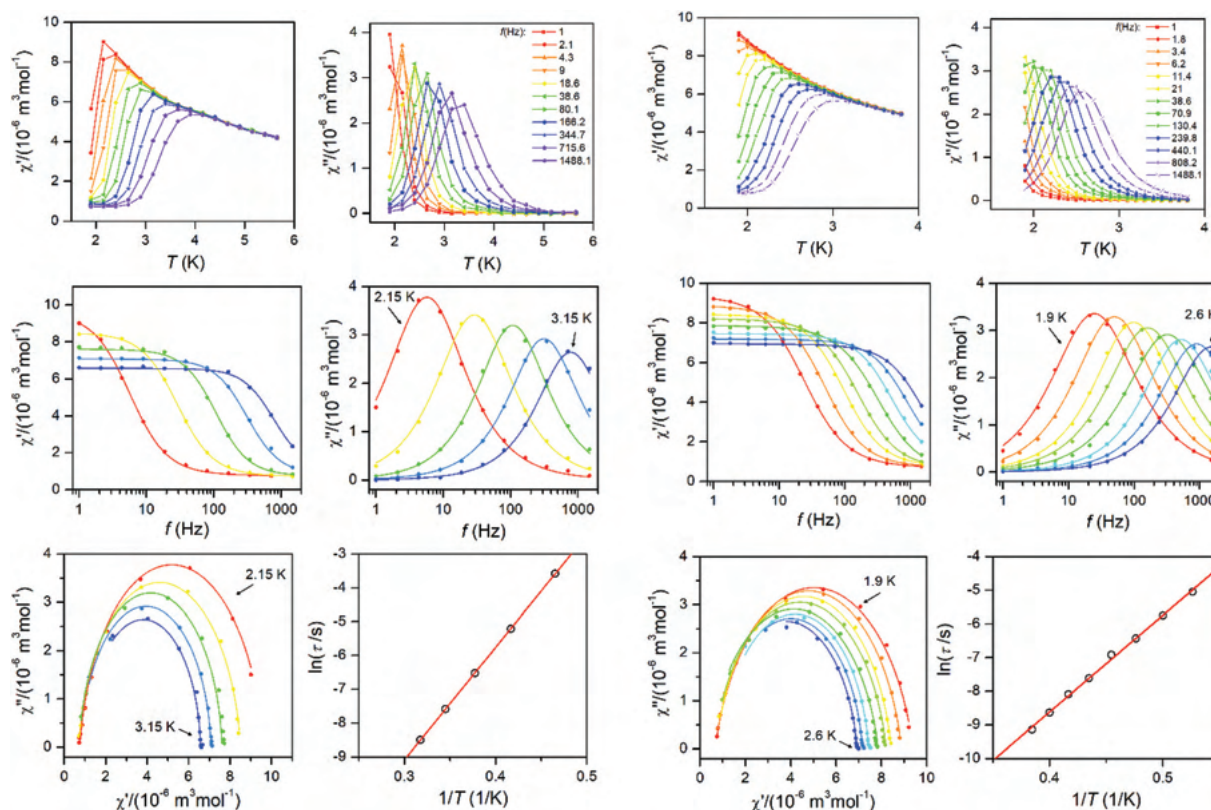


**Fig. 4** AC susceptibility data for **1** (left two columns) and **2** (right two columns). Top: In-phase  $\chi'$  and out-of-phase  $\chi''$  molar susceptibilities at the applied external magnetic field  $B_{DC} = 0.1$  T (full lines are only guides for eyes). Middle: Frequency dependence of in-phase  $\chi'$  and out-of-phase  $\chi''$  molar susceptibilities fitted with one-component Debye's model using eqn (4) (full lines). Bottom: The Argand (Cole-Cole) plot with full lines fitted with eqn (4) and the fit of resulting relaxation times  $\tau$  with Arrhenius law (red line).





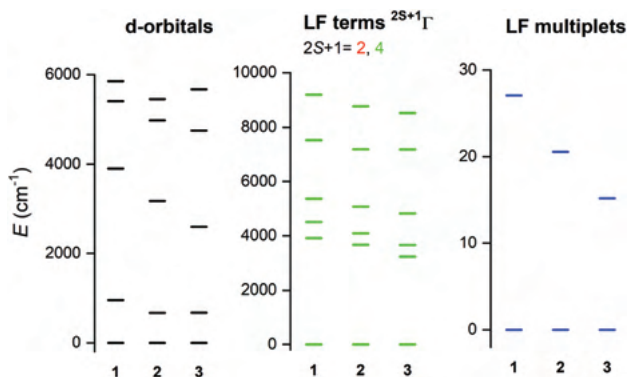


Fig. 5 The graphical output of the CASSCF/NEVPT2 calculations with CAS(7,5) for complexes 1–3. The plot of the d-orbitals splitting calculated by *ab initio* ligand field theory (AILFT) (left), low-lying ligand-field terms (middle), and ligand-field multiplets – Kramers doublets (right).

the spin–orbit coupling, the ligand-field terms (LFT) are split into the ligand-field multiplets (LFM) showing the ZFS into two Kramers doublets arising from  $S = 3/2$  ground spin state – Fig. 5 (right). The energy separation of these two doublets is decreasing from 1 to 3 which means that the axial ZFS parameter  $|D|$  is also decreasing in this order – Table 1. As the sign of  $D$  is negative for all complexes, they possess axial magnetic anisotropy. The spin-orbital interaction is responsible for the largest contribution of the first four excited states to the ZFS parameters as can be elucidated from Table S4.† Evidently, the size of the contributions of these excited states is varying across series 1–3 due to the changes of the ligand field strength and symmetry. Furthermore, the double-shell effect was encountered by enlarging the active space to ten d-orbitals, CAS(7,10). These calculations led to a small increase of  $|D|$  parameters preserving the rhombicity ( $E/D$ ) – see Table 1. To summarise, the theoretical calculations are in good quantitative and qualitative agreement with the parameters extracted from the experiments, which is also reflected in the good agreement of the calculated magnetic data from CASSCF/NEVPT2 calculations compared to the experimental data themselves – Fig. S6.†

### Surface depositions

Deposition of 2 on surfaces was also investigated by two distinct techniques: by drop-casting under an inert nitrogen atmosphere (drop hereafter) and by thermal sublimation in high-vacuum (subl hereafter). Fig. 6 shows a comparison of UV-VIS spectra of 2 as a bulk powder, the deposit obtained from the drop-casting on glass, and the 30 nm thick film obtained by the sublimation onto acetate substrate. Spectra of all three solid samples exhibited two dominant absorptions in the visible part of the spectra: the peak around 480 nm, which corresponds to the  $e_2-e_1$  transition in ferrocenyl moiety (in approximate  $D_{5h}$  symmetry)<sup>25</sup> and the cluster of peaks between ca. 600–800 nm, that can be assigned to d–d transitions of the

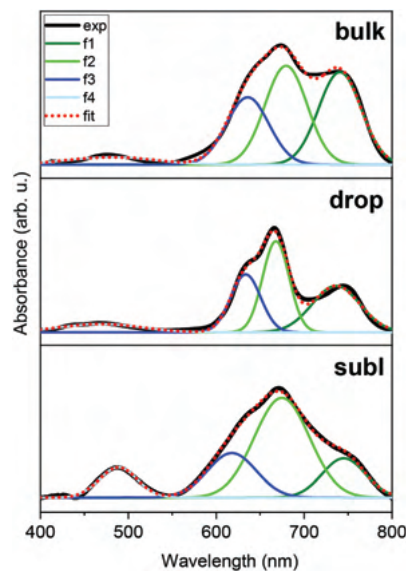
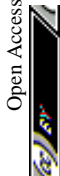


Fig. 6 UV-VIS spectra of 2 as a bulk powder (above), drop-cast layer on glass (middle) and sublimated layer on acetate substrate (below). The results of spectra fitting to four Gaussian primitives (f1 – olive, f2 – green, f3 – blue, f4 – light blue); bulk (top,  $\lambda_{max}$  in nm, absorbance in arb. u.): f1 = 741, 0.1795, f2 = 680, 0.1917, f3 = 636, 0.1295, f4 = 481, 0.012; drop-cast (middle): f1 = 736, 0.0578, f2 = 668, 0.1167, f3 = 634, 0.0730, f4 = 468, 0.0081; sublimated (bottom): f1 = 745, 0.0127, f2 = 675, 0.0326, f3 = 618, 0.0144, f4 = 489, 0.0097.

tetracoordinate  $3d^7$  central ion.<sup>26</sup> Despite the same absorption bands in all three spectra, it is apparent that profile of each spectrum is slightly different, e.g. the subl spectra show broader bands and more intense  $e_2-e_1$  transition band than in bulk and drop. Despite being aware of different samples' nature requiring different approaches in acquiring the UV-VIS data, we attempted to fit all three spectra to quantify the observed differences. Each spectrum (400–800 nm) was fitted using four Gaussian primitives, three peaks (olive – f1, green – f2, blue – f3) sufficiently reconstructed the d–d band,<sup>27</sup> while the fourth one (light blue – f4, Fig. 6) was used to fit the  $e_2-e_1$  transition. Three rather well separated components of the d–d band arising from  ${}^4A_2 \rightarrow {}^4T_1(P)$  transition (in ideal  $T_d$  symmetry)<sup>28</sup> reflect the lower symmetry of coordination polyhedron, because the parent term  ${}^4T_1(P)$  splits into three terms  $\{{}^4A_1 + {}^4B_1 + {}^4B_2\}$ <sup>29</sup> in more realistic  $C_{2v}$  symmetry.<sup>30</sup> The peak heights cannot be directly compared among the spectra, therefore we compared ratios of the peak heights derived for each spectrum.

The f1/f2 ratios are similar for drop (0.49) and subl (0.39) samples, while in the bulk f1/f2 is rather larger (0.94). On the other hand, the f4/f2 ratios are similar for bulk (0.06) and drop (0.07) samples, while f4/f2 is significantly larger in subl (0.30). From the presented UV-VIS data it is hard to determine if any variations among the spectra, such as one described by f1/f2 ratio, originate from chemical changes or different spectral resolution due to different nature of the measured sample. However, it must be noted that an increase of f4/f2 in subl



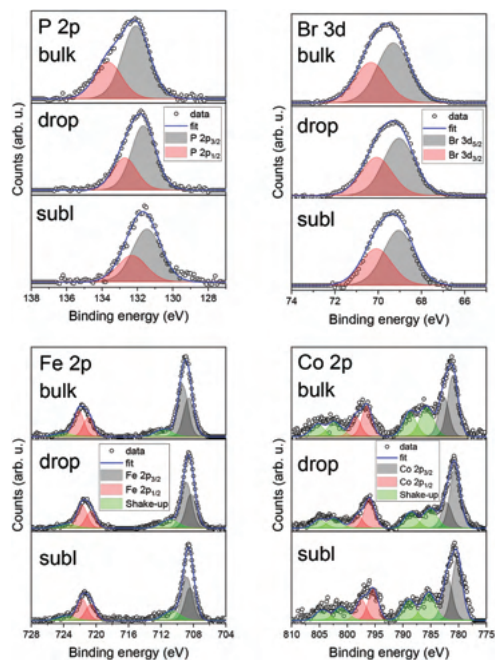


Fig. 7 Detailed XPS spectra comparison of **2** for bulk powder, drop-cast, and sublimation for P 2p, Br 3d, Fe 2p, and Co 2p photoelectron peaks.

spectrum can be reasonably explained by partial decomposition of **2** to metalloligand dppf during sublimation process resulting in a larger abundance of dppf in the deposit.

We have also investigated the chemical composition of bulk **1** and **2** by means of XPS (see ESI, Fig. S8 and S9†) and a survey comparison for **2** as a bulk powder, drop and subl deposits (see ESI, Fig. S10†). Detailed XPS spectra for depositions are shown in Fig. 7 along with a semi-quantitative determination of the elemental composition in Table 2. Carbon and oxygen contributions were considered not relevant since they may be affected by adventitious contaminations due to the *ex situ* preparation procedures. The quantitative analysis for an as-synthesised powder of **2** and drop-cast in nitrogen atmosphere of **2** suggests preserved stoichiometric composition structure, whereas, in the case of sublimated **2**, the amount of Co and Br was lower than expected, which could be attributed to partial chemical decomposition. In the case of Fe 2p and Co 2p, shake-up satellite features were present in all

Table 2 Semi-quantitative determination of the elemental composition

Element	Calculated <sup>a</sup>	1 bulk	2 bulk	2 drop	2 subl
Co	16.7%	12.5%	13.1%	12.3%	10.1%
Fe	16.7%	13.0%	13.1%	14.0%	19.3%
Br <sup>a</sup>	33.3%	—	34.5%	33.3%	21.6%
P	33.3%	37.1%	39.3%	40.4%	49.0%
Cl <sup>a</sup>	33.3%	37.4%	—	—	—

<sup>a</sup> Chlorine and Bromine content were evaluated respectively only in compound **1** and **2**.

three investigated samples as expected. No significant shift in binding energies among the different samples has been detected.

Iron 2p<sub>3/2</sub> peak positions were in good agreement with previous studies addressing the iron in ferrocene molecules (see ESI, Table S6†). This might be due to the intactness of ferrocene moiety on the surface, even after utilising high vacuum sublimation techniques. However, in the case of the film of **2** obtained by sublimation we observed a shift in binding energies of both elements which can be attributed to partial decomposition to the thermally stable dppf,<sup>31</sup> which serves as a precursor for synthesis. This finding agrees with decomposition hypothesis deduced from UV-VIS spectroscopy. These findings suggest that films obtained *via* sublimation are affected by a partial decomposition. Therefore, we may conclude, that the future deposition attempts should adopt preferentially wet-chemistry based protocols under inert atmosphere,<sup>32</sup> which have proven to provide chemically intact deposits of **2**.

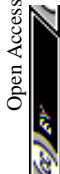
## Conclusions

In this paper, we reported on the crystal structure, magnetic properties and field-induced single-molecule magnet behaviour of series of Co(II) tetracoordinate compounds with 1,1'-ferrocenediyl-bis(diphenylphosphine) metalloligand (dppf) and with the general formula [Co(dppf)X<sub>2</sub>], where X = Cl (**1**), Br (**2**), I (**3**). The static and dynamic magnetic properties were thoroughly studied only for complexes **1–2** because magnetic properties of **3** were found to be very sensitive to even slight decomposition of the sample. Investigations by magnetometry and HF-ESR revealed that **1–2** possess relatively large and axial magnetic anisotropy ( $D = -12.0 \text{ cm}^{-1}$  in **1** and  $-11.2 \text{ cm}^{-1}$  in **2**) and significant rhombicity ( $E/D = 0.106$  in **1** and  $0.090$  in **2**), in good agreement with *ab initio* quantum chemical calculations. Measurements of dynamic AC susceptibility revealed that both compounds behave as field-induced single-ion magnets with predominant Orbach relaxation of magnetisation. Sublimation in high-vacuum and drop-casting were attempted in order to deposit **2** on selected surfaces (Au(111), glass, acetate). Despite the sensitivity to moisture, **2** was successfully deposited by drop-casting under inert nitrogen atmosphere, while attempting thermal sublimation, we observed a partial decomposition of the complex, and thus suggesting that nano-structuration of these systems should be operated by the introduction of functional groups allowing the chemisorption from diluted solution and promoting the formation of monolayers on surfaces.

## Experimental details

### Synthesis

All used chemicals and solvents were purchased from commercial sources and were used without any further purification.



Compounds **1–3** were synthesised similarly by adapting previously reported methods,<sup>33</sup> however, during attempts to prepare phase pure compound **3**, we modified the procedure as described below.

### Synthesis of **1** and **2**

0.5 mmol of  $\text{CoCl}_2$  (65 mg) or  $\text{CoBr}_2$  (108 mg) was dissolved in 10 mL of methanol and subsequently, solution of 0.5 mmol of dppf (277 mg) in 25 mL of  $\text{CH}_2\text{Cl}_2$  was slowly added. The colour of the solution turned green and it was stirred under heating to boiling for 20 min. Heating together with a stream of nitrogen gas led to a significant reduction of solution volume followed by precipitation of green powder which was filtered off. The mother liquor was crystallised by slow diffusion of diethyl ether and this led to precipitation of hexagonally shaped green crystals, which were filtered off and dried in a desiccator.

**1**: Anal. Calc. for  $\text{C}_{34}\text{H}_{28}\text{Cl}_2\text{CoFeP}_2$   $M_w = 684.22 \text{ g mol}^{-1}$ , (in %): C, 59.45; H, 4.33. Observed: C, 59.68; H, 4.12.

**2**: Anal. Calc. for  $\text{C}_{34}\text{H}_{28}\text{Br}_2\text{CoFeP}_2$   $M_w = 773.12 \text{ g mol}^{-1}$ , (in %): C, 52.89; H, 3.47. Observed: C, 52.82; H, 3.65. Thermal stability was investigated using DSC-TGA measurements and the compound is stable up to 260 °C.

Positions of peaks in powder diffraction patterns agree rather well with calculated patterns from the single-crystal structures (see ESI, Fig. S11†). Intensities of the diffraction peaks were strongly affected by texture with crystals preferentially oriented along (00 $l$ ) crystal planes.

### Synthesis of **3**

The first batch of **3** was synthesised in the same way as compounds **1** and **2**. 0.5 mmol of  $\text{CoI}_2$  (156 mg) was dissolved in 10 mL of methanol and subsequently, solution of 0.5 mmol of dppf (277 mg) in 25 mL of  $\text{CH}_2\text{Cl}_2$  was slowly added. The colour of the solution turned green brown and it was stirred under heating to boiling for 20 min. Heating together with a stream of nitrogen gas led to a significant reduction of solution volume followed by precipitation of brown powder which was filtered off. The mother liquor was crystallised by slow diffusion of diethyl ether and this led to precipitation of brown crystals, which were filtered off and dried in a desiccator.

The second batch of **3** was prepared in the same way as the first batch, with the crystallisation performed by slow diffusion of diethyl ether but in presence of a drying medium (pellets of KOH).<sup>34</sup> Brown crystals were isolated by filtration immediately after they appeared in a vial.

**3**: Anal. Calc. for  $\text{C}_{34}\text{H}_{28}\text{I}_2\text{CoFeP}_2$   $M_w = 867.14 \text{ g mol}^{-1}$ , (in %): C, 44.89; H, 2.82. Observed: C, 47.68; H, 4.12.

Positions of peaks in diffraction patterns of both batches of **3** agree well with the calculated pattern (see ESI, Fig. S11 and 12†). However, peaks originating from the presence of the contaminant are visible in the diffraction pattern of the first batch (e.g. at  $2\theta = 6.7, 9.3, 11.7$  deg.). Some of the contaminant peaks (e.g. at  $2\theta = 11.7$  deg.) are still visible in diffraction pattern of the second batch (Fig. S12 and 13†).

### Deposition techniques

For the preparation of thick films, we used a home-built high-vacuum sublimation chamber. For sublimations of **2**, a cleaned quartz crucible was used. The base chamber pressure during the sublimation was  $1 \times 10^{-7}$  mbar. We prepared a 30 nm thick molecular film on Au(111) surface deposited on muscovite mica previously treated with a hydrogen flame annealing treatment and a 30 nm thick film on acetate for UV-VIS measurements. The sublimation was performed at 225 °C with a growth rate of 1 Å per 9 min. This was carefully monitored by calibrated quartz crystal microbalance (STM-2, Inficon) placed at the same height as samples inside the vacuum chamber.

### UV-VIS

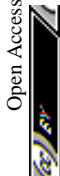
Absorption spectra were acquired using a JASCO V670 UV-VIS-NIR spectrophotometer. The bulk powder of **2** was grafted onto filtration paper, the wet deposition sample was prepared by drop-casting of 1 mL of a 5 mM DCM solution onto a cover glass substrate inside inert nitrogen atmosphere, and the 30 nm thick film obtained by the sublimation onto acetate substrate. All samples were put into the light beam of the UV-VIS spectrometer filled with nitrogen (Fig. 6). UV-VIS spectra of 1 mM solutions of **1** and **2** in dichloromethane (SigmaAldrich, 99.8%) were obtained in quartz 10 mm path-length cuvettes (see ESI, Fig. S7 and Table S5†).

### X-ray photoelectron spectroscopy (XPS)

XPS measurements were carried out at room temperature in a UHV chamber equipped with X-ray source (non-monochromatic Mg-K $\alpha$  source, 1253.6 eV) and hemispherical analyser by VSW mounting a 16-channel detector. The X-ray source mounted at 54.44° with respect to the analyser was operated at a power of 120 W (12 kV and 10 mA). Survey and detailed XPS spectra were acquired at normal emission with the fixed pass energy of 44 eV. All bulk powder spectra were referenced to the Cu 2p<sub>3/2</sub> peak at 932.7 eV, because it served as a substrate for investigated molecules, therefore, no change in position for this peak was expected. Drop-cast and evaporated samples were referenced to the Au 4f<sub>7/2</sub> peak at 84.0 eV. The inelastic backgrounds in spectra were subtracted according to Shirley method<sup>35</sup> except for Fe peaks, where a linear background was used. Data analysis was based on a standard deconvolution method using mixed Gaussian (G) and Lorentzian (L) line shape (G = 70% and L = 30%, Gaussian–Lorentzian product) for each component in the spectra. Elemental composition of the samples was evaluated using a semi-empirical approach. The integrated intensity of each component was corrected with the photoionization cross-section calculated for each atom, neglecting the differences in photoelectron escape length as a function of the kinetic energy.<sup>36</sup> Spectra were analysed using CasaXPS software (version 2.3.18).

### HF-ESR measurements

High-frequency ESR (HF-ESR) spectra at 5 K, 10 K, 20 K, and 40 K for four frequencies 270 GHz, 320 GHz, 360 GHz, and 380





GHz were recorded on a home-built spectrometer<sup>37</sup> featuring a VDI signal generator, a VDI amplifier-multiplier chain, a Thomas Keating quasi-optical bridge, an Oxford Instruments 15/17 T solenoid cryogenic magnet and a QMC Instruments InSb hot-electron bolometer. Both **1** and **2** samples were studied as pressed Teflon®-wrapped powder pellets. All spectra were simulated using the EasySpin toolbox for Matlab.<sup>38</sup>

### Physical methods

Temperature dependence of the magnetisation at  $B = 0.1$  T from 1.9 to 300 K and the isothermal magnetisations at  $T = 2.0, 5.0$  and  $10.0$  K up to  $B = 9$  T were measured using a PPMS Dynacool with a VSM option. The experimental data were corrected for diamagnetism and the signal of the sample holder. Measurements of AC susceptibility were carried out in a 3.8 Oe AC field oscillating at various frequencies from 1 to 1500 Hz and with various dc fields using a MPMS XL7 SQUID magnetometer. The DSC-TGA measurements were performed using a Thermal Analyzer SDT65.

### Crystallography

X-ray measurements on the selected crystal of **1** were performed on an Oxford Diffraction Xcalibur™<sup>2</sup> equipped with a Sapphire2 CCD detector using Mo-K $\alpha$  radiation. The CrysAlis program package (version 1.171.33.52, Oxford Diffraction) was used for data collection and reduction.<sup>39</sup> X-ray measurements on the single-crystals of **2** and **3** were performed on a Bruker D8 Quest diffractometer equipped with a Photon 100 CMOS detector using the Mo-K $\alpha$  radiation. Data collection, data reduction, and cell parameters refinements were performed using the Bruker Apex III software package.<sup>40</sup> The molecular structures were solved by direct methods SHELXS-2014 and all non-hydrogen atoms were refined anisotropically on  $F^2$  using full-matrix least-squares procedure SHELXL-2014.<sup>41</sup> All hydrogen atoms were found in differential Fourier maps and their parameters were refined using a riding model with  $U_{\text{iso}}(\text{H}) = 1.2(\text{CH})$  or  $1.5(\text{CH}_3)U_{\text{eq}}$ .

The X-ray powder diffraction patterns of all solid samples were recorded on an MiniFlex600 (Rigaku) instrument equipped with the Bragg–Brentano geometry, and with iron-filtered Cu K $\alpha_{1,2}$  radiation.

### Theoretical methods

All theoretical calculations were performed with the ORCA 4.0 computational package.<sup>42</sup> All the calculations employed the triple- $\zeta$  def2-TZVP basis functions<sup>43</sup> together with the auxiliary basis def2/JK<sup>44</sup> and also utilising the chain-of-spheres (RIJCOSX) approximation to exact exchange.<sup>45</sup> The ZFS and  $g$  tensors were calculated using self-consistent field (SA-CASSCF) wave functions<sup>46</sup> complemented by N-electron valence second-order perturbation theory (NEVPT2).<sup>47</sup> The active space of the CASSCF calculation was set to five d-orbitals of Co(II) (CAS(7,5)) or as a combination of 3d and 4d orbitals CAS(7,10). The ZFS parameters, based on dominant spin–orbit coupling contributions from excited states, were calculated through quasi-

degenerate perturbation theory (QDPT),<sup>48</sup> in which approximations to the Breit–Pauli form of the spin–orbit coupling operator (SOMF approximation)<sup>49</sup> and the effective Hamiltonian theory<sup>50</sup> were utilised.

## Conflicts of interest

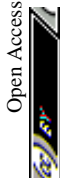
There are no conflicts to declare.

## Acknowledgements

The authors would like to thank to Martina Kubíková for TGA/DSC measurements. The presented work has been funded by: the EU (COST Action CA15128 MOLSPIN); the Ministry of Education, Youth and Sports of the Czech Republic under the projects: CEITEC 2020 (LQ1601), LO1305, LTAUSA19060 in the INTER-EXCELLENCE programme and GAČR 19-01536S; DFG SPP1601 (SL104/3-2, NE1900/3-2), INST41/863-1 and the Italian MIUR through the “Progetto Dipartimenti di Eccellenza 2018–2022 ref. B96C1700020008” allocated to Department of Chemistry “Ugo Schiff”, by the Fondazione Cassa di Risparmio di Firenze for the support to the CETECS activities. J. H. acknowledges Dominik Bloos and Michal Kern for help with HF-ESR measurements. I. N. and R. H. gratefully acknowledge the support received from the Department of Inorganic Chemistry, Palacký University Olomouc. This project has received funding from the ERC under the European Union’s Horizon 2020 research and innovation programme (GA No 714850). M. M., L. S., and J. H. acknowledge Brunetto Cortigiani for the technical support during XPS experiments.

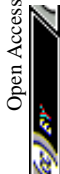
## Notes and references

- 1 D. Gatteschi, R. Sessoli and J. Villain, *Molecular nanomagnets*, Oxford University Press on Demand, 2006, vol. 5.
- 2 F. Neese and D. A. Pantazis, *Faraday Discuss.*, 2011, **148**, 229–238.
- 3 (a) M. Cinchetti, V. A. Dediu and L. E. Hueso, *Nat. Mater.*, 2017, **16**, 507–515; (b) R. Vincent, S. Klyatskaya, M. Ruben, W. Wernsdorfer and F. Balestro, *Nature*, 2012, **488**, 357–360; (c) G. Cucinotta, L. Poggini, A. Pedrini, F. Bertani, N. Cristiani, M. Torelli, P. Graziosi, I. Cimatti, B. Cortigiani, E. Otero, P. Ohresser, P. Sainctavit, A. Dediu, E. Dalcanale, R. Sessoli and M. Mannini, *Adv. Funct. Mater.*, 2017, **27**, 1703600.
- 4 (a) F. Meier, J. Levy and D. Loss, *Phys. Rev. Lett.*, 2003, **90**, 167204; (b) M. D. Jenkins, D. Zueco, O. Roubeau, G. Aromí, J. Majer and F. Luis, *Dalton Trans.*, 2016, **45**, 16682–16693; (c) E. Moreno-Pineda, C. Godfrin, F. Balestro, W. Wernsdorfer and M. Ruben, *Chem. Soc. Rev.*, 2018, **47**, 501–513; (d) C. Godfrin, A. Ferhat, R. Ballou, S. Klyatskaya, M. Ruben, W. Wernsdorfer and F. Balestro, *Phys. Rev. Lett.*, 2017, **119**, 187702.





- 5 (a) S. T. Liddle and J. van Slageren, *Chem. Soc. Rev.*, 2015, **44**, 6655–6669; (b) J. M. Frost, K. L. M. Harriman and M. Murugesu, *Chem. Sci.*, 2016, **7**, 2470–2491; (c) J.-L. Liu, Y.-C. Chen and M.-L. Tong, *Chem. Soc. Rev.*, 2018, **47**, 2431–2453; (d) E. Coronado, *Nat. Rev. Mater.*, 2020, **5**, 87–104.
- 6 N. Ishikawa, M. Sugita, T. Ishikawa, S. Y. Koshihara and Y. Kaizu, *J. Am. Chem. Soc.*, 2003, **125**, 8694–8695.
- 7 F.-S. Guo, B. M. Day, Y.-C. Chen, M.-L. Tong, A. Mansikkamäki and R. A. Layfield, *Science*, 2018, **362**, 1400–1403.
- 8 (a) Y.-Q. Zhai, Y.-F. Deng and Y.-Z. Zheng, *Dalton Trans.*, 2018, **47**, 8874–8878; (b) D.-K. Cao, J.-Q. Feng, M. Ren, Y.-W. Gu, Y. Song and M. D. Ward, *Chem. Commun.*, 2013, **49**, 8863–8865; (c) J. M. Zadrozny, J. Liu, N. A. Piro, C. J. Chang, S. Hill and J. R. Long, *Chem. Commun.*, 2012, **48**, 3927–3929; (d) J. M. Zadrozny and J. R. Long, *J. Am. Chem. Soc.*, 2011, **133**, 20732–20734; (e) M. Böhme, S. Ziegenbalg, A. Aliabadi, A. Schnegg, H. Görls and W. Plass, *Dalton Trans.*, 2018, **47**, 10861–10873; (f) T. Wu, Y.-Q. Zhai, Y.-F. Deng, W.-P. Chen, T. Zhang and Y.-Z. Zheng, *Dalton Trans.*, 2019, **48**, 15419–15426; (g) M. S. Fataftah, J. M. Zadrozny, D. M. Rogers and D. E. Freedman, *Inorg. Chem.*, 2014, **53**, 10716–10721; (h) F. Yang, Q. Zhou, Y. Zhang, G. Zeng, G. Li, Z. Shi, B. Wang and S. Feng, *Chem. Commun.*, 2013, **49**, 5289–5291; (i) S. Ziegenbalg, D. Hornig, H. Görls and W. Plass, *Inorg. Chem.*, 2016, **55**, 4047–4058; (j) Y. Rechkemmer, F. D. Breitgoff, M. van der Meer, M. Atanasov, M. Hakl, M. Orlita, P. Neugebauer, F. Neese, B. Sarkar and J. van Slageren, *Nat. Commun.*, 2016, **7**, 10467; (k) S. Vaidya, S. K. Singh, P. Shukla, K. Ansari, G. Rajaraman and M. Shanmugam, *Chem. – Eur. J.*, 2017, **23**, 9546–9559; (l) S. Vaidya, P. Shukla, S. Tripathi, E. Rivière, T. Mallah, G. Rajaraman and M. Shanmugam, *Inorg. Chem.*, 2018, **57**, 3371–3386; (m) S. Vaidya, S. Tewary, S. K. Singh, S. K. Langley, K. S. Murray, Y. Lan, W. Wernsdorfer, G. Rajaraman and M. Shanmugam, *Inorg. Chem.*, 2016, **55**, 9564–9578; (n) S. Vaidya, A. Upadhyay, S. K. Singh, T. Gupta, S. Tewary, S. K. Langley, J. P. S. Walsh, K. S. Murray, G. Rajaraman and M. Shanmugam, *Chem. Commun.*, 2015, **51**, 3739–3742.
- 9 (a) F. Habib, O. R. Luca, V. Vieru, M. Shiddiq, I. Korobkov, S. I. Gorelsky, M. K. Takase, L. F. Chibotaru, S. Hill, R. H. Crabtree and M. Murugesu, *Angew. Chem., Int. Ed.*, 2013, **52**, 11290–11293; (b) T. J. Woods, M. F. Ballesteros-Rivas, S. Gómez-Coca, E. Ruiz and K. R. Dunbar, *J. Am. Chem. Soc.*, 2016, **138**, 16407–16416; (c) S. S. Massoud, R. C. Fischer, F. A. Mautner, M. M. Parfait, R. Herchel and Z. Trávníček, *Inorg. Chim. Acta*, 2018, **471**, 630–639; (d) A. K. Mondal, J. Jover, E. Ruiz and S. Konar, *Chem. Commun.*, 2017, **53**, 5338–5341.
- 10 (a) V. Chandrasekhar, A. Dey, A. J. Mota and E. Colacio, *Inorg. Chem.*, 2013, **52**, 4554–4561; (b) Y.-Y. Zhu, C. Cui, Y.-Q. Zhang, J.-H. Jia, X. Guo, C. Gao, K. Qian, S.-D. Jiang, B.-W. Wang, Z.-M. Wang and S. Gao, *Chem. Sci.*, 2013, **4**, 1802–1806; (c) J. Vallejo, I. Castro, R. Ruiz-García, J. Cano, M. Julve, F. Lloret, G. De Munno, W. Wernsdorfer and E. Pardo, *J. Am. Chem. Soc.*, 2012, **134**, 15704–15707; (d) Y. Peng, V. Mereacre, C. E. Anson, Y. Zhang, T. Bodenstein, K. Fink and A. K. Powell, *Inorg. Chem.*, 2017, **56**, 6056–6066; (e) Y.-L. Wang, L. Chen, C.-M. Liu, Y.-Q. Zhang, S.-G. Yin and Q.-Y. Liu, *Inorg. Chem.*, 2015, **54**, 11362–11368; (f) A. Świtlicka-Olszewska, J. Palion-Gazda, T. Klemens, B. Machura, J. Vallejo, J. Cano, F. Lloret and M. Julve, *Dalton Trans.*, 2016, **45**, 10181–10193; (g) S. Roy, I. Oyarzabal, J. Vallejo, J. Cano, E. Colacio, A. Bauza, A. Frontera, A. M. Kirillov, M. G. B. Drew and S. Das, *Inorg. Chem.*, 2016, **55**, 8502–8513; (h) A. A. Pavlov, Y. V. Nelyubina, S. V. Kats, L. V. Penkova, N. N. Efimov, A. O. Dmitrienko, A. V. Vologzhanina, A. S. Belov, Y. Z. Voloshin and V. V. Novikov, *J. Phys. Chem. Lett.*, 2016, **7**, 4111–4116; (i) C. Villa-Pérez, I. Oyarzabal, G. A. Echeverría, G. C. Valencia-Urbe, J. M. Seco and D. B. Soria, *Eur. J. Inorg. Chem.*, 2016, **29**, 4835–4841; (j) M. A. Lemes, F. Magnan, B. Gabidullin and J. Brusso, *Dalton Trans.*, 2018, **47**, 4678–4684; (k) C. M. Klug, T. J. Ozumerzifon, I. Bhowmick, B. N. Livesay, A. K. Rappé and M. P. Shores, *Dalton Trans.*, 2019, **48**, 9117–9126.
- 11 (a) X.-C. Huang, C. Zhou, D. Shao and X.-Y. Wang, *Inorg. Chem.*, 2014, **53**, 12671–12673; (b) P. Antal, B. Drahoš, R. Herchel and Z. Trávníček, *Inorg. Chem.*, 2016, **55**, 5957–5972; (c) D. Shao, S.-L. Zhang, L. Shi, Y.-Q. Zhang and X.-Y. Wang, *Inorg. Chem.*, 2016, **55**, 10859–10869; (d) B. Drahoš, R. Herchel and Z. Trávníček, *Inorg. Chem.*, 2017, **56**, 5076–5088; (e) P. Antal, B. Drahoš, R. Herchel and Z. Trávníček, *Eur. J. Inorg. Chem.*, 2018, **38**, 4286–4297.
- 12 L. Chen, J. Wang, J.-M. Wei, W. Wernsdorfer, X.-T. Chen, Y.-Q. Zhang, Y. Song and Z.-L. Xue, *J. Am. Chem. Soc.*, 2014, **136**, 12213–12216.
- 13 J. Titiš, J. Miklovič and R. Boča, *Inorg. Chem. Commun.*, 2013, **35**, 72–75.
- 14 I. Nemeč, R. Herchel, M. Kern, P. Neugebauer, J. van Slageren and Z. Trávníček, *Materials*, 2017, **10**, 249.
- 15 I. Nemeč, R. Herchel and Z. Trávníček, *Sci. Rep.*, 2015, **5**, 10761.
- 16 B. Corain, B. Longato, G. Favero, D. Ajò, G. Pilloni, U. Russo and F. R. Kreissl, *Inorg. Chim. Acta*, 1989, **157**, 259–266.
- 17 CAS numbers: dppf, 12150-46-8; [CoCl<sub>2</sub>(dppf)], 67292-36-8.
- 18 T.-J. Park, S. Huh, Y. Kim and M.-J. Jun, *Acta Crystallogr., Sect. C: Cryst. Struct. Commun.*, 1999, **55**, 848–850.
- 19 K. R. Meihaus, J. D. Rinehart and J. R. Long, *Inorg. Chem.*, 2011, **50**, 8484–8489.
- 20 I. Nemeč, R. Herchel and Z. Trávníček, *Dalton Trans.*, 2016, **45**, 12479–12482.
- 21 (a) F. Ciccullo, M. Glaser, M. S. Sättele, S. Lenz, P. Neugebauer, Y. Rechkemmer, J. van Slageren and M. B. Casu, *J. Mater. Chem. C*, 2018, **6**, 8028–8034; (b) F. Ciccullo, A. Calzolari, K. Bader, P. Neugebauer, N. M. Gallagher, A. Rajca, J. van Slageren and M. B. Casu, *ACS Appl. Mater. Interfaces*, 2019, **11**, 1571–1578; (c) J. Rozbořil, Y. Rechkemmer, D. Bloos, F. Münz,





- C. N. Wang, P. Neugebauer, J. Čechal, J. Novák and J. van Slageren, *Dalton Trans.*, 2016, **45**, 7555–7558; (d) J. Hrubý, V. T. Santana, D. Kostiuik, M. Bouček, S. Lenz, M. Kern, P. Šiffalovič, J. van Slageren and P. Neugebauer, *RSC Adv.*, 2019, **9**, 24066–24073; (e) L. S. Marie, A. El Fatimy, J. Hrubý, I. Nemeč, J. Hunt, R. Myers-Ward, D. K. Gaskill, M. Kruskopf, Y. Yang, R. Elmquist, R. Marx, J. van Slageren, P. Neugebauer and P. Barbara, *J. Phys. Mater.*, 2020, **3**, 014013.
- 22 M. Llunell, D. Casanova, J. Cicera, P. Alemany and S. Alvarez, *SHAPE, Version 2.1*, Barcelona, Spain, 2013.
- 23 R. Boča and R. Herchel, *Program Polymagnet*, 2009–2019.
- 24 (a) M. Atanasov, D. Ganyushin, K. Sivalingam and F. Neese, in *Molecular Electronic Structures of Transition Metal Complexes II*, ed. D. M. P. Mingos, P. Day and J. P. Dahl, Springer Berlin Heidelberg, Berlin, Heidelberg, 2012, pp. 149–220; (b) S. K. Singh, J. Eng, M. Atanasov and F. Neese, *Coord. Chem. Rev.*, 2017, **344**, 2–25.
- 25 (a) B. Corain, B. Longato, G. Favero, D. Ajò, G. Pilloni, U. Russo and F. R. Kreissl, *Inorg. Chim. Acta*, 1989, **157**, 259–266; (b) U. Salzner, *J. Chem. Theory Comput.*, 2013, **9**, 4064–4073.
- 26 M. M. Rohmer, A. Veillard and M. H. Wood, *Chem. Phys. Lett.*, 1974, **29**, 466–468.
- 27 D. Lomjanský, F. Varga, C. Rajnák, J. Moncol, R. Boča and J. Titiš, *Nova Biotechnol. Chim.*, 2016, **15–2**, 200.
- 28 B. N. Figgis and M. A. Hitchman, *Ligand Field Theory and Its Applications, Special Topics in Inorganic Chemistry*, John Wiley, India, 2010.
- 29 M. Idešicová, J. Titiš, J. Krzystek and R. Boča, *Inorg. Chem.*, 2013, **52**, 9409–9417.
- 30 L. Masaryk, J. Moncol, R. Herchel and I. Nemeč, *Crystals*, 2020, **10**, 354.
- 31 C. M. Woodbridge, D. L. Pugmire, R. C. Johnson, N. M. Boag and M. A. Langell, *J. Phys. Chem. B*, 2000, **104**, 3085–3093.
- 32 M. Mannini and L. Poggini, in *Encyclopedia of Interfacial Chemistry*, Elsevier, 2018, pp. 538–546.
- 33 U. Casellato, D. Ajò, G. Valle, B. Corain, B. Longato and R. Graziani, *J. Crystallogr. Spectrosc. Res.*, 1988, **18**, 583–590.
- 34 I. Nemeč, R. Marx, R. Herchel, P. Neugebauer, J. Van Slageren and Z. Trávníček, *Dalton Trans.*, 2015, **44**, 15014–15021.
- 35 D. A. Shirley, *Phys. Rev. B: Solid State*, 1972, **5**, 4709–4714.
- 36 J. J. Yeh and I. Lindau, *At. Data Nucl. Data Tables*, 1985, **32**, 1–155.
- 37 P. Neugebauer, D. Bloos, R. Marx, P. Lutz, M. Kern, D. Aguilà, J. Vaverka, O. Laguta, C. Dietrich, R. Clérac and J. van Slageren, *Phys. Chem. Chem. Phys.*, 2018, **20**, 15528–15534.
- 38 S. Stoll and A. Schweiger, *J. Magn. Reson.*, 2006, **178**, 42–55.
- 39 *CrysAlis CCD and CrysAlis RED, Version 1.171.33.52*, Oxford Diffraction Ltd, England, 2009.
- 40 *Bruker. Apex3*, Bruker AXS Inc., Madison, Wisconsin, USA, 2015.
- 41 G. M. Sheldrick, *Acta Crystallogr., Sect. C: Struct. Chem.*, 2015, **71**, 3–8.
- 42 (a) F. Neese, *Wiley Interdiscip. Rev.: Comput. Mol. Sci.*, 2012, **2**, 73–78; (b) F. Neese, *Wiley Interdiscip. Rev.: Comput. Mol. Sci.*, 2018, **8**, e1327.
- 43 F. Weigend and R. Ahlrichs, *Phys. Chem. Chem. Phys.*, 2005, **7**, 3297–3305.
- 44 F. Weigend, *J. Comput. Chem.*, 2008, **29**, 167–175.
- 45 F. Neese, F. Wennmohs, A. Hansen and U. Becker, *Chem. Phys.*, 2009, **356**, 98–109.
- 46 P. A. Malmqvist and B. O. Roos, *Chem. Phys. Lett.*, 1989, **155**, 189–194.
- 47 (a) C. Angeli, R. Cimiraglia, S. Evangelisti, T. Leininger and J. P. Malrieu, *J. Chem. Phys.*, 2001, **114**, 10252–10264; (b) C. Angeli, R. Cimiraglia and J. P. Malrieu, *Chem. Phys. Lett.*, 2001, **350**, 297–305; (c) C. Angeli, R. Cimiraglia and J. P. Malrieu, *J. Chem. Phys.*, 2002, **117**, 9138–9153; (d) C. Angeli, S. Borini, M. Cestari and R. Cimiraglia, *J. Chem. Phys.*, 2004, **121**, 4043–4049; (e) C. Angeli, B. Bories, A. Cavallini and R. Cimiraglia, *J. Chem. Phys.*, 2006, **124**, 054108.
- 48 D. Ganyushin and F. Neese, *J. Chem. Phys.*, 2006, **125**, 024103.
- 49 F. Neese, *J. Chem. Phys.*, 2005, **122**, 034107.
- 50 R. Maurice, R. Bastardis, C. de Graaf, N. Suaud, T. Mallah and N. Guihéry, *J. Chem. Theory Comput.*, 2009, **5**, 2977–2984.



Article

# Halogen Bonding in New Dichloride-Cobalt(II) Complex with Iodo Substituted Chalcone Ligands

Lukáš Masaryk<sup>1</sup>, Ján Moncol<sup>2</sup>, Radovan Herchel<sup>1,\*</sup>  and Ivan Nemeč<sup>1,3,\*</sup> 

<sup>1</sup> Department of Inorganic Chemistry, Faculty of Science, Palacký University, 17. listopadu 12, 771 46 Olomouc, Czech Republic; lukas.masaryk01@upol.cz

<sup>2</sup> Department of Inorganic Chemistry, Faculty of Chemical and Food Technology, Slovak University of Technology in Bratislava, SK-81237 Bratislava, Slovakia; jan.moncol@stuba.sk

<sup>3</sup> Central European Institute of Technology, Brno University of Technology, Purkyňova 123, 61200 Brno, Czech Republic

\* Correspondence: radovan.herchel@upol.cz (R.H.); ivan.nemec@upol.cz (I.N.); Tel.: +420-58563-4435 (R.H.); +420-58563-4354 (I.N.)

Received: 7 April 2020; Accepted: 28 April 2020; Published: 30 April 2020



**Abstract:** The synthesis and properties of new chalcone ligand 4I-L ((2E)-1-[4-(1H-imidazol-1-yl)phenyl]-3-(4-iodophenyl)prop-2-en-1-one) and tetracoordinate Co(II) complex [Co(4I-L)<sub>2</sub>Cl<sub>2</sub>], (1a), are reported in this article. Upon recrystallization of 1a, the single crystals of [Co(4I-L)<sub>4</sub>Cl<sub>2</sub>]·2DMF·3Et<sub>2</sub>O (1b) were obtained and crystal structure was determined using X-ray diffraction. The non-covalent interactions in 1b were thoroughly analyzed and special attention was dedicated to interactions formed by the peripheral iodine substituents. The density functional theory (DFT), atoms in molecule (AIM) and noncovalent interaction (NCI) methods and electronic localization function (ELF) calculations were used to investigate halogen bond formed between the iodine functional groups and co-crystallized molecules of diethyl ether.

**Keywords:** dichloride cobalt complex; chalcone; halogen bonding; Hirshfeld surfaces

## 1. Introduction

In molecular crystals, the building blocks, molecules, are held together by various directional and non-directional non-covalent intermolecular interactions. Some of these interactions have been widely explored, such as hydrogen bonding, cation/anion... $\pi$  or  $\pi$ ... $\pi$  interactions [1–5], but non-conventional interactions such as tetrel [6], pnictogen [7], chalcogen [8] and halogen bonding [9,10] have been less extensively studied [11,12]. All the above-mentioned interactions can be used to control the supramolecular architectures [13] of the coordination compounds and thus to influence their, e.g., mechanical [14], optical [15], catalytic [16], photochemical [17], luminescent [18] and magnetic properties [19]. In our recent research we devoted a lot of attention to prominence of non-covalent interactions in properties of magnetically bistable materials. We studied magnetic exchange interactions mediated by hydrogen bonding [20],  $\pi$ ... $\pi$  interactions [21] or their combination [22]. We also discovered a new type of magnetic exchange pathway engaging Co... $\pi$  interactions [23] and revealed possible influence of hydrogen bonding on occurrence of spin-crossover phenomenon [24]. In this report we focused our attention on interplay between halogen bonding and structure of mononuclear Co(II) coordination compounds, despite being aware of unpredictable competitiveness of hydrogen and halogen bonding [25]. These have a great potential to behave as molecular nanomagnets, so-called Single Ion Magnets (SIMs), due to large magnetic anisotropy exhibited by their central atoms in various symmetries of the ligand fields [26]. An inevitable condition for preparation of SIMs exhibiting high blocking temperatures in a zero-external magnetic field is the axial type of magnetic anisotropy



possessed by their metal centers. This can be achieved by careful choice of coordination number and polyhedral symmetry. It is well established that, for Co(II) compounds, very interesting results can be achieved for tetracoordinate coordination compounds exhibiting large distortion from ideal tetrahedral geometry [27]. To achieve significant distortions of coordination geometry, one can assume two viable strategies: (a) use of polydentate and sufficiently rigid ligands, (b) use of monodentate bulky ligands. Both strategies exploit steric hindrance of the ligands, which in (a) may be further supported by predefined bite angles of the chelating ligands [28]. In this work we explored approach (b) by using bulky monodentate ligands derived from chalcones of 4'-(imidazol-1-yl)acetophenone containing peripheral groups allowing formation of non-covalent interactions such as hydrogen or halogen bonding [29,30]. Such interactions can either induce or stabilize distortions of molecular shapes [31] or coordination polyhedrons [32,33]. Here, we report on the first results obtained using the above-mentioned approach. We used ligand 4I-L ((2E)-1-[4-(1H-imidazol-1-yl)phenyl]-3-(4-iodophenyl)prop-2-en-1-one) prepared by the aldol condensation [34] in reaction with  $\text{CoCl}_2$  to obtain tetracoordinate complex  $[\text{Co}(\text{4I-L})_2\text{Cl}_2]$  in the powder form, (1a). Following recrystallization of 1a led to isolation of hexacoordinate complex  $[\text{Co}(\text{4I-L})_4\text{Cl}_2]\cdot 2\text{DMF}\cdot 3\text{Et}_2\text{O}$  (1b), ( $\text{Et}_2\text{O}$  stands for diethylether), the crystal structure of which was determined using single-crystal X-ray diffraction. The crystal structure of 1b contains rather weak non-covalent interactions, which were analyzed by calculating Hirshfeld surfaces and special attention was given to interactions provided by the peripheral iodine substituents. The  $\text{O}\cdots\text{I}$  halogen bond formed by co-crystallized molecule of  $\text{Et}_2\text{O}$  was thoroughly studied by modern theoretical calculations, because reports on  $\text{O}\cdots\text{I}$  halogen bonding involving  $\text{Et}_2\text{O}$  [35] or similar alkoxy compounds [36–41] are rare. Similarly, the crystal structures with short  $\text{O}\cdots\text{Cl}$  (e.g., [42,43]) and  $\text{O}\cdots\text{Br}$  (e.g., [44,45]) non-covalent interactions formed between halogen atoms and  $\text{Et}_2\text{O}$  molecules can be found in the Cambridge Structural Database (CSD version 2.0.4, [46]), but to the best of our knowledge, reports applying advanced theoretical calculations for better understanding the nature of this certain type of halogen bond are missing.

## 2. Experimental

### 2.1. Materials

$\text{CoCl}_2\cdot 6\text{H}_2\text{O}$  was purchased from Precious Metals Online, while other chemicals 4-iodobenzaldehyde, 4'-(imidazol-1-yl)acetophenone, NaOH, solvents (MeOH, diethyl ether ( $\text{Et}_2\text{O}$ ), EtOH, dimethylformamide (DMF) and dichloromethane (DCM)) and deuterated solvents for NMR experiments ( $\text{DMSO}-d_6$ ) were supplied by VWR International (Stříbrná Skalice, Czech Republic), Sigma-Aldrich (Prague, Czech Republic), Lach-Ner (Neratovice, Czech Republic) and Litolab (Chudobín, Czech Republic).

### 2.2. General Methods

Elemental analysis was performed by Flash 2000 CHNS Elemental Analyzer (Thermo Scientific, Waltham, MA, USA). Electrospray ionization mass spectrometry (ESI-MS; methanol solutions) was carried out with LCQ Fleet ion trap spectrometer (Thermo Scientific, Waltham, MA, USA; QualBrowser software, version 2.0.7) in both positive (ESI+) and negative (ESI-) ionization modes.  $^1\text{H}$  and  $^{13}\text{C}$  NMR spectroscopy, and  $^1\text{H}$ - $^{13}\text{C}$  gsHMQC and  $^1\text{H}$ - $^{13}\text{C}$  gsHMBC two dimensional correlation experiments were performed using  $\text{DMSO}-d_6$  (HA1) solution at 300 K using Varian spectrometer (Palo Alto, CA, USA) at 400.00 MHz (for  $^1\text{H}$  NMR) and 101.00 MHz (for  $^{13}\text{C}$  NMR); gs = gradient selected, HMQC = heteronuclear multiple quantum coherence, HMBC = heteronuclear multiple bond coherence.  $^1\text{H}$  and  $^{13}\text{C}$  NMR spectra were calibrated against the residual DMF  $^1\text{H}$  NMR (8.03, 2.92 and 2.75 ppm) and  $^{13}\text{C}$  NMR (163.2, 34.9 and 29.8 ppm) signals. The splitting of proton resonances in the reported  $^1\text{H}$  spectra is defined as s = singlet, d = doublet, dd = doublet of doublets, sep = septet, m = multiplet and bs = broad signal.



A Jasco FT/IR-4700 spectrometer (Jasco, Easton, MD, USA) was used for the collection of the infrared (IR) spectra of the studied ligand and complexes in the range of 400–4000  $\text{cm}^{-1}$  by using the attenuated total reflection (ATR) technique on a diamond plate. UV-VIS spectroscopy was performed using a Perkin-Elmer (Waltham, MA, USA) Lambda 35 spectrometer at 11,000–40,000  $\text{cm}^{-1}$ .

### 2.3. Crystal Structure Determination

Data collection and cell refinement of 1b were made by Stoe StadiVari (Stoe & Cie GmbH, Darmstadt, Germany) diffractometer using Pilatus3R 300K detector and microfocused X-ray source Incoatec I $\mu$ S 2.0 HB (Ag K $\alpha$  radiation). The structure was solved using SHELXT [47] program and refined by the full matrix least-squares procedure with Olex2.refine [48] in OLEX2 (version 1.3) [49]. The multi-scan absorption corrections were applied using the program Stoe LANA software [50]. The molecular structures and packing diagram were drawn with MERCURY [51]. Crystal Data for C<sub>90</sub>H<sub>96</sub>Cl<sub>2</sub>CoI<sub>4</sub>N<sub>10</sub>O<sub>9</sub> (M = 2099.19 g/mol): triclinic, space group  $P\bar{1}$  (no. 2),  $a = 8.5546(2)$  Å,  $b = 15.2289(3)$  Å,  $c = 18.6054(4)$  Å,  $\alpha = 110.729(2)^\circ$ ,  $\beta = 90.916(2)^\circ$ ,  $\gamma = 102.814(2)^\circ$ ,  $V = 2198.59(9)$  Å<sup>3</sup>,  $Z = 1$ ,  $T = 100(1)$  K,  $\mu(\text{AgK}\alpha) = 0.915$  mm<sup>-1</sup>,  $D_{\text{calc}} = 1.585$  g/cm<sup>3</sup>, 61909 reflections measured ( $2.110^\circ \leq 2\theta \leq 19.501^\circ$ ), 7765 unique ( $R_{\text{int}} = 0.0160$ ) which were used in all calculations. The final R1 was 0.0405 ( $I > 2\sigma(I)$ ) and  $wR_2$  was 0.1180 (all data). The highest peak: +1.03 (0.84 Å from I1), the deepest hole -0.98 (0.90 Å from I1). Crystal structure refinement: All non-hydrogen atoms were refined anisotropically. The hydrogen atoms were placed into the calculated positions and they were included into the riding-model approximation with  $U_{\text{iso}} = 1.2U_{\text{eq}}(\text{C})$  or  $1.5U_{\text{eq}}(\text{CH}_3)$  and  $d(\text{C}-\text{H}) = 0.95\text{--}0.98$  Å. Non-routine aspects of the refinement: one of the Et<sub>2</sub>O molecules is disordered over two positions with the oxygen atom lying on an inversion center.

### 2.4. Theoretical Calculations

The ORCA 4.2.1 computational package was employed for the presented calculations [52]. All the computations were based on the molecular fragments derived from the X-ray data, where only the positions of the hydrogen atoms were optimized using Density Functional Theory (DFT) with  $\omega$ B97X-D3BJ functional [53] comprising the atom-pairwise dispersion correction (D3BJ) [54,55] with Sapporo-TZP-2012 basis set for all atoms [56]. The calculations exploited the resolution of identity approximation with the auxiliary basis created by the AutoAux generation procedure [57] and the chain-of-spheres approximation to exact exchange (RIJCOSX) [58,59]. The integration grids were increased by setting Grid5 and Gridx5, and the convergence criteria were set to tight SCF (self-consistent field) in all calculations. Then, the interaction energies ( $E_{\text{int}}$ ) were calculated also taking into the account the basis set superposition error (BSSE). The further analysis was done with Multiwfn program [60,61]. The calculation of Hirshfeld [62] and shape index [63] surfaces were performed using the program Crystal Explorer 3.1 [64].

### 2.5. Synthesis of (2E)-1-[4-(1H-imidazol-1-yl)phenyl]-3-(4-iodophenyl)prop-2-en-1-one (4I-L)

A methanolic sodium hydroxide solution (40%; 1.2 mL) was added dropwise to a mixture of 4-iodobenzaldehyde (2 mmol, 0.464 g), 4'-(imidazol-1-yl)acetophenone (2 mmol, 0.370 g) and methanol (5 mL) over a period of 30–40 minutes with continuous stirring at room temperature until completion of the reaction (as indicated by TLC). The precipitates were filtered and washed with cold methanol–water mixture (1:10). Finally, the product was recrystallized from methanol [33].

Yellowish solid. Yield: 90%. <sup>1</sup>H NMR (400 MHz, DMSO-*d*<sub>6</sub>, 298 K, ppm)  $\delta$  8.42 (s, 1H, C2-H), 8.26 (d,  $J = 8.7$  Hz, 2H, C17-H, C21-H), 7.99 (d,  $J = 15.7$  Hz, 1H, C14-H), 7.88–7.80 (m, 5H, C5-H, C7-H, C11-H, C18-H, C20-H), 7.72–7.64 (m, 3H, C8-H, C10-H, C15-H), 7.12 (s, 1H, C4-H). <sup>13</sup>C NMR (101 MHz, DMSO-*d*<sub>6</sub>, 298 K, ppm)  $\delta$  188.24 (C12), 143.51 (C15-H), 140.77 (C6), 138.20 (C18-H, C20-H), 136.22 (C2-H), 135.88 (C9), 134.69 (C16), 131.21 (C8-H, C10-H), 130.98 (C17-H, C21-H), 130.85 (C4-H), 123.05 (C14-H), 120.30 (C7-H, C11-H), 118.24 (C5-H), 98.14 (C19-H). ESI+MS (MeOH, *m/z*): 401.17 (calc. 401.22; 100%; {4I-L+H}<sup>+</sup>), 423.05 (calc. 401.20; 32%; {4I-L+Na}<sup>+</sup>). IR (ATR,  $\nu$ ,  $\text{cm}^{-1}$ ): 408w, 463w,

507w, 538w, 594w, 652w, 677w, 727w, 812s, 830m, 960w, 981w, 1031w, 1060w, 1118w, 1165m, 1215m, 1289m, 1337w, 1428w, 1492w, 1512m, 1588s, 1652s, 2150w, 3118w.

### 2.6. Complex $[\text{Co}(\text{4I-L})_2(\text{Cl})_2]$ (1a)

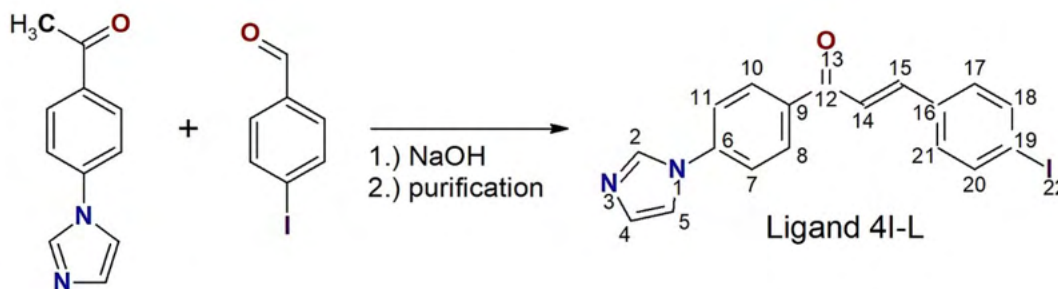
The solution of  $\text{CoCl}_2 \cdot 6\text{H}_2\text{O}$  (0.5 mmol, 0.119 g) in 5 mL of methanol was heated up to 50 °C and then 2 molar equiv. of 4I-L were added (2 mmol, 0.400 g). The solution was allowed to cool down and then the reaction mixture was stirred at ambient temperature for 2 hours. The obtained blue precipitate was collected by filtration and washed with water ( $2 \times 0.5$  mL) and  $\text{Et}_2\text{O}$  ( $2 \times 1$  mL). The blue solid product was dried in desiccator under reduced pressure (overnight). Compound 1b was prepared by recrystallization of 1a from DMF/ $\text{CH}_3\text{OH}$  solvent mixture by slow diffusion of  $\text{Et}_2\text{O}$  in closed flask. Only small amounts of light blue crystals of 1b was isolated and, therefore, no technique other than single-crystal diffraction was used for characterization of this compound.

Yield: 84%. Anal. Calcd. for  $\text{CoC}_{36}\text{H}_{26}\text{Cl}_2\text{N}_4\text{I}_2\text{O}_2$  (1a): C, 46.48; H, 2.82; N, 6.02%; found: C, 46.41; H, 2.72; N, 5.86%. ESI+MS (MeOH,  $m/z$ ): 401,14 (calc. 401.22; 30%;  $\{4\text{I-L}+\text{H}\}^+$ ), 567.09 (calc. 567.06; 100%;  $\{[\text{Co}(4\text{I-L})(\text{Cl})_2]+2\text{H}_2\text{O}+\text{H}\}^+$ ), 894.02 (calc. 893.91; 66%;  $\{[\text{Co}(4\text{I-L})(\text{Cl})_2]+2\text{H}_2\text{O}+\text{H}\}^+$ ). IR (ATR,  $\nu$ ,  $\text{cm}^{-1}$ ): 402w, 448w, 490w, 522w, 605w, 647w, 735w, 811s, 962w, 1002w, 1062w, 1119w, 1182w, 1213w, 1318m, 1395w, 1479w, 1519m, 1602s, 1657s, 2159w, 3131w.

## 3. Results and Discussion

### 3.1. Synthesis and Basic Characterizations

The chalcone ligand 4I-L was prepared by aldol condensation of 4'-(imidazol-1-yl)acetophenone with the 4-iodobenzaldehyde as is shown in Scheme 1. The purity and structure of 4I-L were confirmed by NMR spectroscopy and elemental analysis. The  $^1\text{H}$  NMR (see ESI, Figure S1),  $^{13}\text{C}$  NMR (see ESI, Figure S2), spectra of 4I-L in  $\text{DMSO}-d_6$  showed shifts characteristic for the aromatic functional groups (the list of all observed peaks can be found in the experimental chapter). The representative peak confirming the presence of the olefinic moiety resulting from aldol condensation (C14-H) was observed in  $^1\text{H}$  NMR spectra approximately at 7.99 ppm. In the  $^{13}\text{C}$  NMR spectra corresponding peak of C14-H was observed approximately at 123.05 ppm. The C-H groups were assigned by  $^1\text{H}$ - $^{13}\text{C}$  HMQC correlation experiments (Figure 1 left), while quaternary carbon atoms were assigned by  $^1\text{H}$ - $^{13}\text{C}$  HMBC correlation experiments.



**Scheme 1.** Preparation of ligand 4I-L with given atom numbering scheme.

The complex 1a was prepared by reaction between  $\text{CoCl}_2 \cdot 6\text{H}_2\text{O}$  and 4I-L (molar ratio 1:2) in methanolic solution as a blue precipitate. The elemental composition (CHN analysis) corresponds rather well with formula  $[\text{Co}(4\text{I-L})_2\text{Cl}_2]$ , and this assumption was further supported by the results of ESI+ mass spectroscopy, which revealed occurrence of peaks with suitable  $m/z$  isotopic distribution attributable to the  $\{[\text{Co}(4\text{I-L})_2(\text{Cl})]\}^+$  species (see ESI, Figure S3). The FTIR spectra showed valence vibration of the chalcone ketone group ( $\nu(\text{C}=\text{O})$ ) at ca.  $1600 \text{ cm}^{-1}$ . The UV-VIS spectroscopy of 1a measured in the solid state showed absorption bands centered at ca. 600 nm (Figure 1 right), which can be attributed to spin allowed  $d-d$  transitions characteristic for the tetracoordinate  $\text{Co}(\text{II})$  complexes [65].



The spectral band was fitted to three Gaussian primitives having peak maxima at 518 nm, 578 nm and 631 nm (Figure 1 right). The individual bands originate from  ${}^4A_2 \rightarrow {}^4T_1(P)$  transition in ideal  $T_d$  symmetry [66], although the  ${}^4T_1(P)$  term splits into three individual terms ( ${}^4A_2(P)$ ,  ${}^4B_1(P)$  and  ${}^4B_2(P)$ ) in lower symmetry (expected symmetry of coordination polyhedron of 1a is  $C_{2v}$ ). Thus, it may be concluded that compound 1a is tetracoordinate Co(II) complex with the formula  $[Co(4I-L)_2Cl_2]$ .

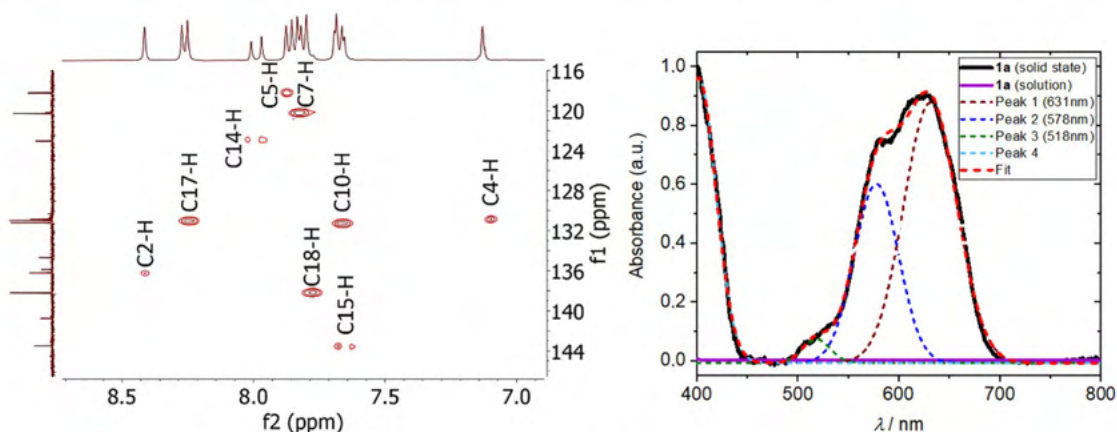


**Figure 1.** *Left*—HMQC NMR spectrum of the ligand 4I-L; DMSO- $d_6$  solutions. See Scheme 1 for the structural formula and atom numbering scheme. *Right*—UV-VIS absorption spectrum measured for 1a in the solid state (black line) and methanolic solution (violet line) in the range of 400–800 nm. Fit to four Gaussian primitives shown as dashed lines with peak maxima listed in the legend.

Complex 1a is only negligibly soluble in water, methanol, ethanol or acetone, but it is well soluble in DMF or DMSO. The UV-VIS spectrum measured for  $CH_3OH$  solution of 1a revealed no strong absorption bands in the range of 400–800 nm (Figure 1 right). Interestingly, upon recrystallization of 1a from  $CH_3OH/DMF$  solvent mixture, followed by slow diffusion of  $Et_2O$ , the small amount of light blue crystals precipitated. The selected single crystal was subjected to the X-ray diffraction analysis, which revealed that the prepared complex 1b is hexacoordinate (*vide infra*).

### 3.2. Crystal Structure

Compound 1b crystallizes in the triclinic crystal system with the space group  $P\bar{1}$ . The Co atom lies on a crystallographic inversion center (1h) and thus the asymmetric unit consists of the half of the complex molecule  $[Co(4I-L)_4Cl_2]$ , one DMF molecule and one and half  $Et_2O$  molecules, which altogether gives formula of  $[Co(4I-L)_4Cl_2] \cdot 2DMF \cdot 3Et_2O$ . The complex molecule is hexacoordinate and it consists of four 4I-L and two chlorido ligands coordinated to Co(II) center. The 4I-L ligands adopt *E*-configuration and coordinate the Co(II) atom by nitrogen donor atoms from the imidazolyl moieties forming equatorial plane with rather dissimilar Co–N bond lengths ( $d(Co-N) = 2.121(3)$  and  $2.162(3)$  Å). The axial coordination sites are occupied by two chlorido ligands with rather long Co–Cl bonds ( $d(Co-Cl) = 2.4880(9)$  Å). The overall geometry of the coordination polyhedron can be described best as an axially elongated octahedron (Figure 2).



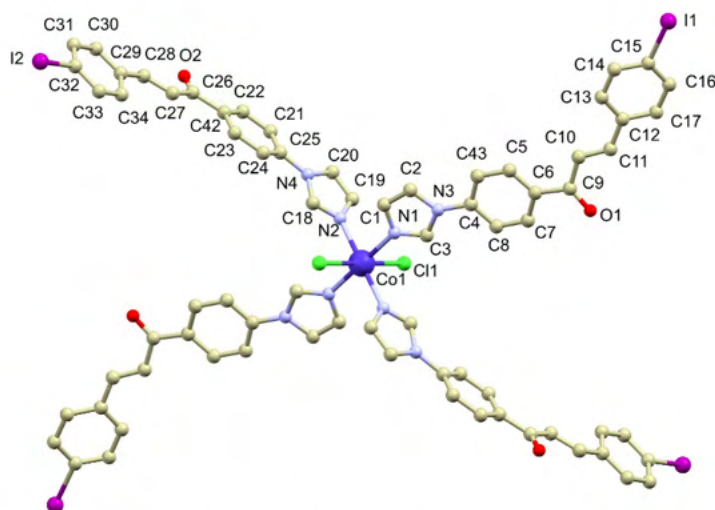


**Figure 2.** Molecular structure of 1b. Color code: grey (C), green (Cl), dark blue (Co), violet (I), light blue (N) and red (O). Hydrogen atoms are omitted for clarity. Selected bond lengths (in Å) and angles (deg.):  $d(\text{Co1-N1}) = 2.121(3)$ ,  $d(\text{Co1-N2}) = 2.162(3)$ ,  $d(\text{Co1-Cl1}) = 2.4880(9)$ ,  $\text{N1-Co1-N1}^i = \text{N2-Co1-N2}^i = \text{Cl1-Co1-Cl1}^i = 180.0$ ,  $\text{N1-Co1-N2} = 88.15(12)$ ,  $\text{N1-Co1-Cl1} = 92.26(9)$ ,  $\text{N1-Co1-Cl1}^i = 87.74(9)$ ,  $\text{N2-Co1-Cl1}^i = 90.14(9)$ ,  $\text{N2-Co1-Cl1} = 89.86(9)$ . Symmetry code: (i) = 1 -x, 1 -y, 1 -z.

The complex molecules are stabilized in the structure by plethora of weak intermolecular contacts and therefore analysis of the Hirshfeld surface was performed to identify them (Figures S4 and S5, the parameters of hydrogen bonds are listed in Table S1). The complex molecules are organized in supramolecular chains by bifurcated C–H...Cl hydrogen bonding between the aromatic C–H groups located on 1-phenyl-imidazolyl fragment of the 4I-L ligand from adjacent complex molecule ( $d(\text{C}\cdots\text{Cl}) = 3.466(5)$  and  $3.673(5)$ , Å Figure 3a). The chlorido ligand also acts as an acceptor of another C–H...Cl hydrogen bond involving C–H group from the DMF molecule ( $d(\text{C}\cdots\text{Cl}) = 3.807(4)$  Å). Interestingly, the DMF molecule is further stabilized in the crystal structure by set of three rather strong C–H...O hydrogen bonds between three C–H groups from the 4I-L ligand and oxygen atom of the DMF molecule ( $d(\text{C}\cdots\text{O}) = 3.324(6)$ ,  $3.388(5)$  and  $3.394(5)$  Å, Figure 3b).

One of the chalcone ligands forms offset  $\pi$ - $\pi$  stacking interactions with the adjacent counterpart related by operation of inversion. The shortest C...C distances are rather short ( $d(\text{C}\cdots\text{C}) = 3.290(5)$  and  $3.357(5)$  Å, Figure 4a). These interactions can be visualized best by calculating Hirshfeld surface followed by highlighting areas corresponding to C...C interactions (Figure 4c). Furthermore, by inspecting the shape-index surfaces we were able to confirm these interactions because of appearance of neighboring red and blue triangular map areas (red circles), which are characteristic for occurrence of  $\pi$ - $\pi$  stacking [67,68]. Both types of the supramolecular dimers, (a) and (b), are extended to chain substructures due to the inversion symmetry. The keto oxygen atoms are involved in the weak C–H...O hydrogen bonds, where one of the keto groups forms a pair of bifurcated hydrogen bonds with the C–H groups of the benzyl-imidazolyl moiety ( $d(\text{C}\cdots\text{O}) = 3.193(5)$  and  $3.420(4)$  Å, Figure 4a). The second keto group forms only weak C–H...O non-covalent contacts.

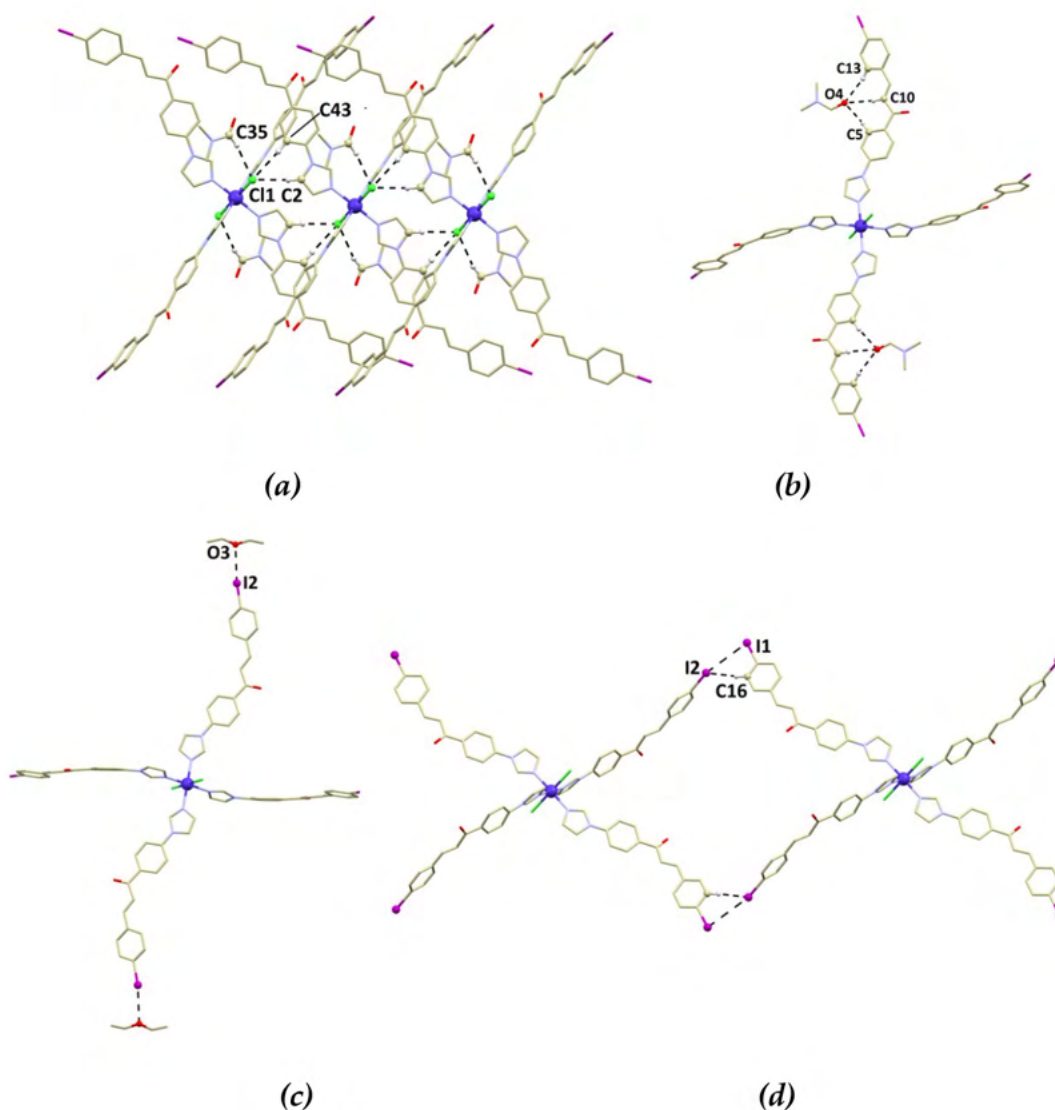


**Figure 3.** A perspective view on the non-covalent interactions in 1b. (a) Supramolecular chain formed by C–H...Cl hydrogen bonding:  $d(\text{C2}\cdots\text{Cl1}) = 3.466(5) \text{ \AA}$ ,  $d(\text{C35}\cdots\text{Cl1}) = 3.807(4) \text{ \AA}$ ,  $d(\text{C43}\cdots\text{Cl1}) = 3.673(5) \text{ \AA}$ . (b) Bifurcated C–H...O hydrogen bonding of the DMF molecule:  $d(\text{C5}\cdots\text{O4}) = 3.324(6) \text{ \AA}$ ,  $d(\text{C10}\cdots\text{O4}) = 3.388(5) \text{ \AA}$ ,  $d(\text{C13}\cdots\text{O4}) = 3.394(5) \text{ \AA}$ . A perspective view on the I...O halogen bonding (c) and C–H...I non-covalent interaction (d). Donor-acceptor distances of displayed interactions:  $d(\text{I2}\cdots\text{O3}) = 3.264(4) \text{ \AA}$ ,  $d(\text{C16}\cdots\text{I2}) = 3.918(4) \text{ \AA}$ ,  $d(\text{I1}\cdots\text{I2}) = 4.1676(5) \text{ \AA}$ . Hydrogen atoms (except for those involved in hydrogen bonding) were omitted for clarity. The non-covalent interactions were depicted as black dashed lines.

Two symmetry-independent iodine substituents on the 4I-L ligands form different types of the non-covalent interactions. One of them forms I...O type of the interaction, since it is capped by co-crystallized Et<sub>2</sub>O molecule at rather short distance:  $d(\text{I}\cdots\text{O}) = 3.264(4) \text{ \AA}$  (Figure 3c). The other one forms two weak contacts with two neighboring functional groups on the 4I-L ligand: one with the above-mentioned iodine substituent ( $d(\text{I}\cdots\text{I}) = 4.1676(5) \text{ \AA}$ ) and the second one with the neighboring C–H group ( $d(\text{C}\cdots\text{I}) = 3.918(5) \text{ \AA}$ , Figure 3d).



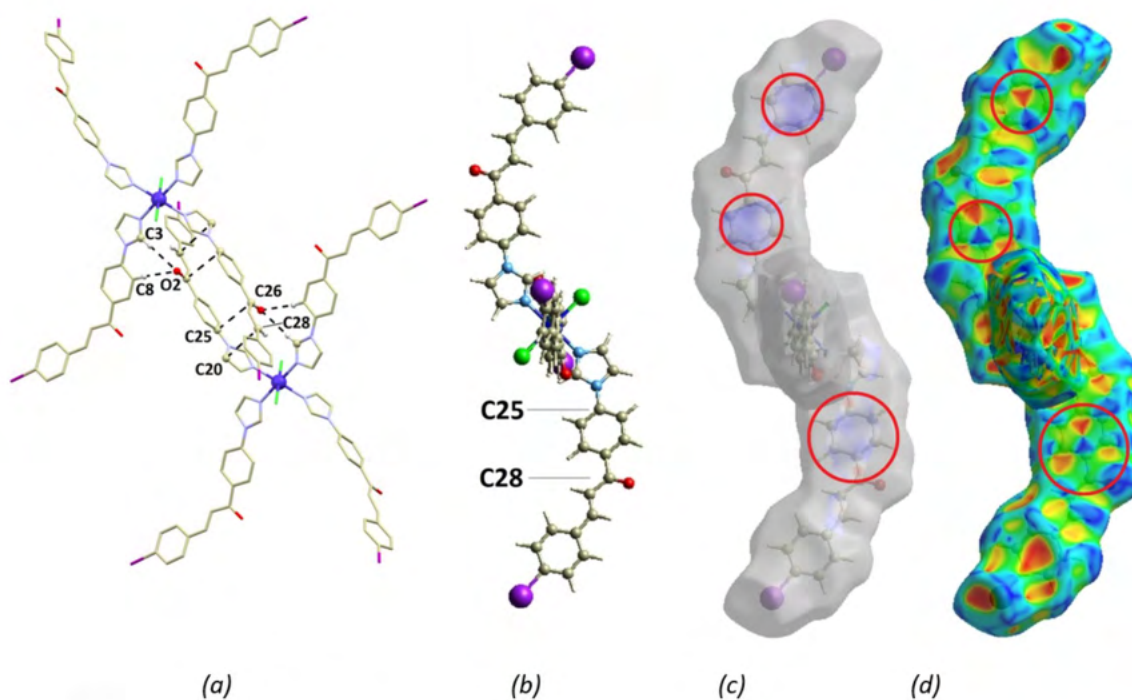


**Figure 4.** (a) A perspective view on  $\pi$ - $\pi$  stacking interactions and bifurcated C-H...O hydrogen bonding involving chalcone keto group. Donor-acceptor distances of displayed interactions:  $d(\text{C}20\cdots\text{C}28) = 3.357(5) \text{ \AA}$ ,  $d(\text{C}25\cdots\text{C}26) = 3.290(5) \text{ \AA}$ ,  $d(\text{C}3\cdots\text{O}2) = 3.421(6) \text{ \AA}$ ,  $d(\text{C}8\cdots\text{O}2) = 3.193(5) \text{ \AA}$ . The non-covalent interactions were depicted as black dashed lines. Hydrogen atoms (except for those involved in hydrogen bonding) were omitted for clarity. The drawing of molecular structure of 1b with the atom labels of the carbon atoms involved in short C...C contacts (b). Calculated Hirshfeld surfaces ( $d_{\text{norm}}$ ) with highlighted areas of the C...C interactions (colored maps in red circles, c) and shape-index surface with highlighted areas involved in  $\pi$ - $\pi$  stacking interactions (red circles, d).

### 3.3. Theoretical Studies

The DFT theory was employed together with ORCA program to evaluate the interaction energies for selected non-covalent contacts affecting the crystal packing with range-separated functional  $\omega$ B97X-D3BJ. First, the I...O type of the interaction between 4I-L ligand and co-crystallized  $\text{Et}_2\text{O}$  molecule was dealt with (Figure 3c). Thus, for the molecular fragment  $\{(4\text{I-L})\cdots(\text{Et}_2\text{O})\}$  shown in Figure 5, the computed interaction energy is  $E_{\text{int}} = -4.401 \text{ kcal/mol}$ . Next, the I...I type of the interaction (Figure 3d) between two 4I-L ligands  $\{(4\text{I-L})\cdots(4\text{I-L})\}$  from different complex moieties was inspected and the calculation resulted in  $E_{\text{int}} = -2.212 \text{ kcal/mol}$  (Figure 5). Moreover, these interactions were analyzed with the noncovalent interaction (NCI) method [69] with the help of Multiwfn software. This method is based on the analysis of the electron density ( $\rho$ ) by defining the reduced density gradient (RDG) function which helps to identify the weak intra/inter molecular interactions and the nature of these interactions, thus attractive vs repulsive, is analyzed by the sign of eigenvalue  $\lambda_2$  of the electron density Hessian matrix. These interactions were successfully visualized with VMD program [70] as  $\text{sign}(\lambda_2)\rho$  values in Figure 5. It is evident that in  $\{(4\text{I-L})\cdots(4\text{I-L})\}$  molecular fragment (Figure 5 top) two types of weak interactions are present, the hydrogen bond C-H...I and halogen bond I...I, whereas the second fragment  $\{(4\text{I-L})\cdots(\text{Et}_2\text{O})\}$ , (Figure 5 bottom), is dominated by O...I halogen bond. Indeed, the topological analysis based on the atoms in molecules (AIM) method [71] implemented in Multiwfn program identified the bond critical points (BCP) of the type (3,-1) as depicted in Figure 6 together with the bond paths, which follow the maximal gradient path connecting two BCPs. Next, the NCI  $\text{sign}(\lambda_2)\rho$  values were calculated in selected BCPs as  $-0.00529$  for I...I,  $-0.0103$  for C-H...I and  $-0.0102$  for O...I contacts.

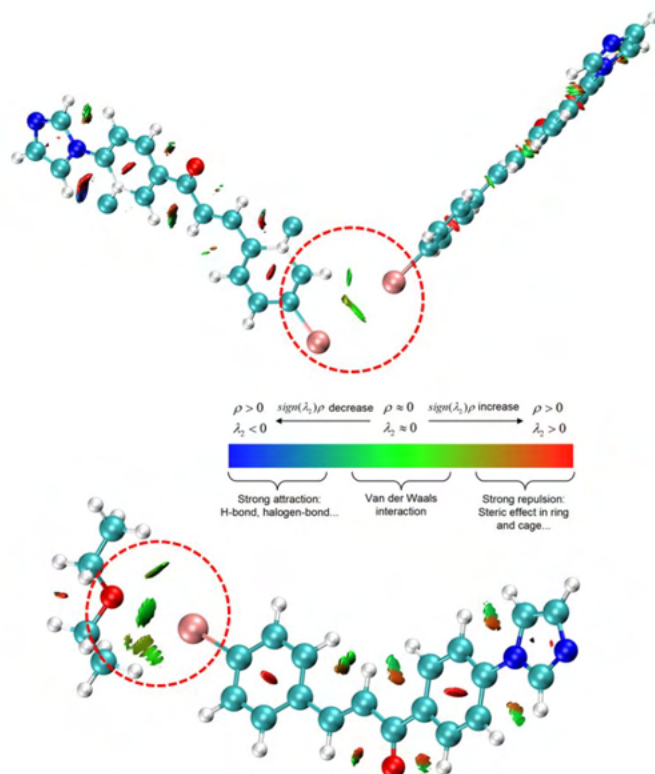


**Figure 5.** The molecular fragments  $\{(4I-L)\cdots(4I-L)\}$  (*top*) and  $\{(4I-L)\cdots(Et_2O)\}$  (*bottom*) used for the theoretical calculations of the interaction energies ( $E_{int}$ ) overlapped with NCI calculations showing weak intermolecular interactions of interest in red dashed circles.

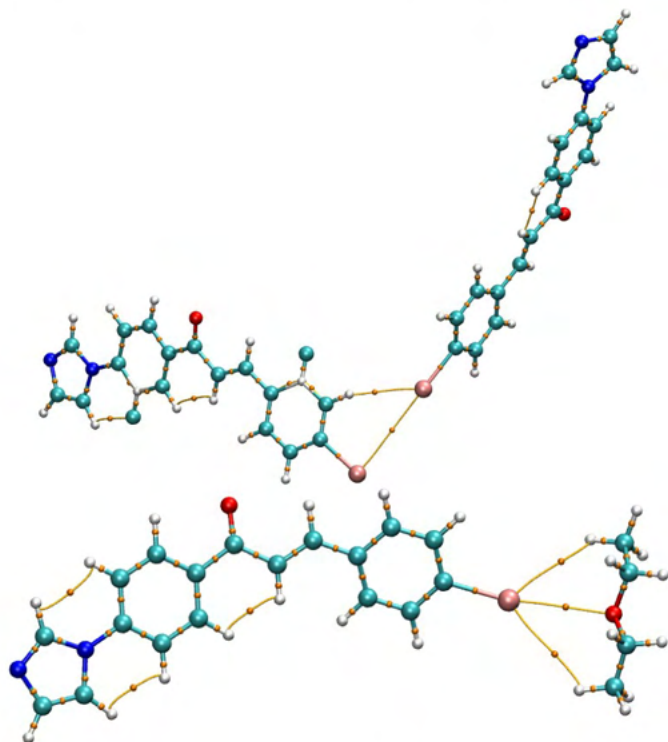


**Figure 6.** The molecular fragments  $\{(4I-L)\cdots(4I-L)\}$  (*top*) and  $\{(4I-L)\cdots(Et_2O)\}$  (*bottom*) showing the atoms in molecules (AIM) analysis indicating the position of the bond electron density critical points (BCP) of the type  $(3, -1)$  as small orange spheres together with calculated bond paths (yellow lines).



Thus, we can conclude that all these interactions are attractive and sort them by the increasing strength as  $I\cdots I < C-H\cdots I \approx O\cdots I$ , which agrees with the DFT calculated energies. It well known that halogen bonds are characteristic by formation of so-called  $\sigma$ -holes on heavy halogen atoms, which can interact with an electron pair of the electron donor atom. To better understand and visualize this phenomenon, Multiwfn package was used to calculate Electron Localization Function (ELF). The ELF was introduced by Becke and Edgecombe [72] and its application to the study of electronic structure is discussed by Lu and Chen [73]. Thus, the colored mapped figures were calculated as shown in Figure 7 to elucidate the distribution of electron density by ELF. Indeed, in both cases of  $I\cdots I$  (Figure 7 left) and  $O\cdots I$  (Figure 7 right) halogen bonds, the presence of  $\sigma$ -holes on I atoms is evident and the complementary donor electron pair of I or O atoms is present too. The detailed view of ELF along the particular AIM calculated bond paths (Figure 7) is also depicted in Figure S6.

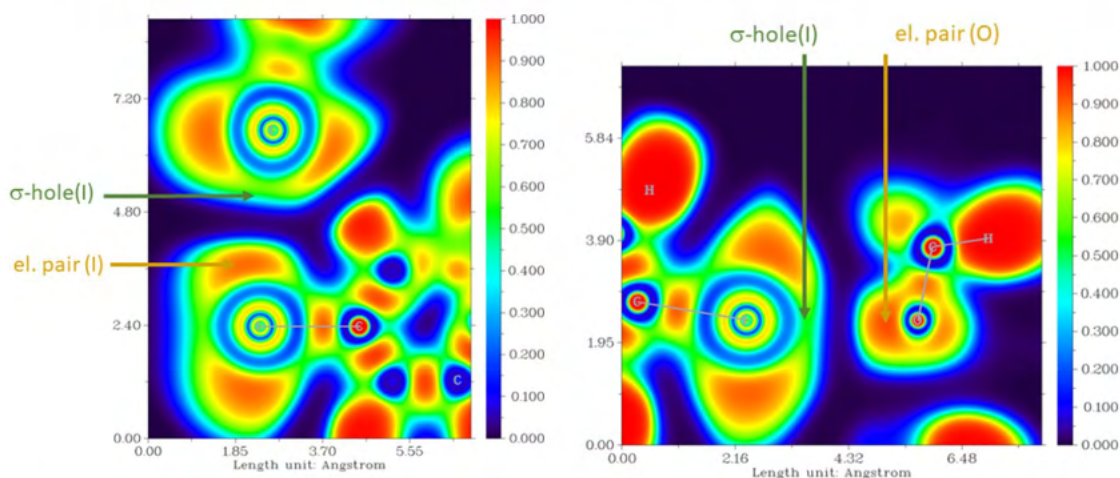


**Figure 7.** The calculated Electron localization function (ELF) for the molecular fragments  $\{(4I-L)\cdots(4I-L)\}$  (left) and  $\{(4I-L)\cdots(Et_2O)\}$  (right) showing halogen bonds of the types  $I\cdots I$  and  $O\cdots I$ .

#### 4. Conclusions

In this article, we reported on the synthesis of the chalcone ligand (2E)-1-[4-(1H-imidazol-1-yl)phenyl]-3-(4-iodophenyl)prop-2-en-1-one (4I-L), which was further used for synthesis of tetracoordinate complex  $[Co(4I-L)Cl_2]$ , (1a), which after recrystallization transformed into hexacoordinate complex  $[Co(4I-L)_4Cl_2]\cdot 2DMF\cdot 3Et_2O$ , (1b). Ligand and complex 1a were thoroughly characterized by spectroscopic techniques and for 1b, the crystal structure was determined by X-ray diffraction analysis. It was revealed that 1b is hexacoordinate Co(II) complex with chlorido ligands in the axial positions. The crystal structure of 1b is stabilized by a plethora of weak non-covalent interactions, mainly by  $C-H\cdots O$ ,  $C-H\cdots Cl$  and  $\pi-\pi$  stacking of aromatic rings. Furthermore, the peripheral iodine substituents on the 4I-L ligands form  $I\cdots O$ ,  $C-H\cdots I$  and  $I\cdots I$  non-covalent interactions. These were theoretically studied by the DFT, NCI, AIM and ELF calculations and all confirmed formation of halogen bond of significant strength in the case of the  $I\cdots O$  contact. The weak nature of the  $C-H\cdots I$  hydrogen bonding and  $I\cdots I$  interaction was confirmed.

**Supplementary Materials:** The following are available online at <http://www.mdpi.com/2073-4352/10/5/354/s1>, Figure S1:  $^1H$  NMR spectrum of ligand 4I-L in  $DMSO-d_6$ , Figure S2:  $^{13}C$  NMR spectrum of ligand 4I-L in  $DMSO-d_6$ , Figure S3: ESI-MS mass spectrum of complex 1a in methanol, Figure S4: 2D fingerprint plots generated for the complex molecule  $[Co(4I-L)_4Cl_2]$ , Figure S5: Hirshfeld surface calculated for the complex molecule  $[Co(4I-L)_4Cl_2]$ , Figure S6: The calculated Electron localization function (ELF) along calculated bond paths for the molecular fragments  $\{(4I-L)\cdots(4I-L)\}$  (top) and  $\{(4I-L)\cdots(Et_2O)\}$  (bottom) showing halogen bonds of the types  $I\cdots I$  and  $O\cdots I$ . The dotted line locates the BCP (3,-1, Table S1: summary of hydrogen bonding parameters).

**Author Contributions:** Conceptualization: L.M. and I.N.; Formal analysis: L.M., J.M., R.H., I.N.; Investigation: L.M., J.M.; Writing—original draft: I.N., R.H.; Writing—review & editing: L.M., J.M., I.N., R.H.; All authors have read and agreed to the published version of the manuscript.

**Funding:** This research was funded by Palacký University Olomouc (PrF\_2020\_016) and also supported by the Grant Agencies of the Slovak Republic, (VEGA 1/0639/18, APVV-18-0016) and MŠVVaŠ of the Slovak Republic within the Research and Development Operation Program for the project “University Science Park of STU Bratislava” (ITMS project no. 26240220084) cofounded by the European Regional Development Fund.

**Conflicts of Interest:** The authors declare no competing financial interests.

## References

1. Jeffrey, G.A. Hydrogen-Bonding: An update. *Crystallogr. Rev.* **2003**, *9*, 135–176. [[CrossRef](#)]
2. Steiner, T. C–H...O hydrogen bonding in crystals. *Crystallogr. Rev.* **2003**, *9*, 177–228. [[CrossRef](#)]
3. Tiekink, E.R.T.; Zukerman-Schpector, J. Gold... $\pi$  aryl interactions as supramolecular synthons. *CrystEngComm* **2009**, *11*, 1176. [[CrossRef](#)]
4. Chen, T.; Li, M.; Liu, J.  $\pi$ – $\pi$  Stacking Interaction: A Nondestructive and Facile Means in Material Engineering for Bioapplications. *Cryst. Growth Des.* **2018**, *18*, 2765–2783. [[CrossRef](#)]
5. Watt, M.M.; Collins, M.S.; Johnson, D.W. Ion– $\pi$  Interactions in Ligand Design for Anions and Main Group Cations. *Acc. Chem. Res.* **2012**, *46*, 955–966. [[CrossRef](#)]
6. Bauzá, A.; Seth, S.; Frontera, A. Tetrel bonding interactions at work: Impact on tin and lead coordination compounds. *Coord. Chem. Rev.* **2019**, *384*, 107–125. [[CrossRef](#)]
7. Alkorta, I.; Elguero, J.; Frontera, A. Not Only Hydrogen Bonds: Other Noncovalent Interactions. *Crystals* **2020**, *10*, 180. [[CrossRef](#)]
8. Gleiter, R.; Haberhauer, G.; Werz, D.B.; Rominger, F.; Bleiholder, C. From Noncovalent Chalcogen–Chalcogen Interactions to Supramolecular Aggregates: Experiments and Calculations. *Chem. Rev.* **2018**, *118*, 2010–2041. [[CrossRef](#)]
9. Cavallo, G.; Metrangolo, P.; Milani, R.; Pilati, T.; Priimagi, A.; Resnati, G.; Terraneo, G. The Halogen Bond. *Chem. Rev.* **2016**, *116*, 2478–2601. [[CrossRef](#)]
10. Kolář, M.H.; Hobza, P. Computer Modeling of Halogen Bonds and Other  $\sigma$ -Hole Interactions. *Chem. Rev.* **2016**, *116*, 5155–5187. [[CrossRef](#)]
11. Carreras, L.; Benet-Buchholz, J.; Franconetti, A.; Frontera, A.; Van Leeuwen, P.W.N.M.; Vidal-Ferran, A. Halogen bonding effects on the outcome of reactions at metal centres. *Chem. Commun.* **2019**, *55*, 2380–2383. [[CrossRef](#)] [[PubMed](#)]
12. Zhao, Y.; Cotelle, Y.; Sakai, N.; Matile, S. Unorthodox Interactions at Work. *J. Am. Chem. Soc.* **2016**, *138*, 4270–4277. [[CrossRef](#)] [[PubMed](#)]
13. Amabilino, D.B.; Smith, D.K.; Steed, J.W. Supramolecular materials. *Chem. Soc. Rev.* **2017**, *46*, 2404–2420. [[CrossRef](#)] [[PubMed](#)]
14. Chakrabarty, R.; Mukherjee, P.S.; Stang, P.J. Supramolecular Coordination: Self-Assembly of Finite Two- and Three-Dimensional Ensembles. *Chem. Rev.* **2011**, *111*, 6810–6918. [[CrossRef](#)]
15. El-Mellouhi, F.; Bentría, E.T.; Marzouk, A.; Rashkeev, S.N.; Kais, S.; Alharbi, F.H. Hydrogen bonding: A mechanism for tuning electronic and optical properties of hybrid organic–inorganic frameworks. *npj Comput. Mater.* **2016**, *2*, 16035. [[CrossRef](#)]
16. Raynal, M.; Ballester, P.; Vidal-Ferran, A.; Van Leeuwen, P.W.N.M. Supramolecular catalysis. Part 1: Non-covalent interactions as a tool for building and modifying homogeneous catalysts. *Chem. Soc. Rev.* **2014**, *43*, 1660–1733. [[CrossRef](#)]
17. Ramamurthy, V.; Sivaguru, J. Supramolecular Photochemistry as a Potential Synthetic Tool: Photocycloaddition. *Chem. Rev.* **2016**, *116*, 9914–9993. [[CrossRef](#)]
18. Mako, T.; Racicot, J.M.; Levine, M. Supramolecular Luminescent Sensors. *Chem. Rev.* **2018**, *119*, 322–477. [[CrossRef](#)]
19. Kahn, O. *Magnetism: A Supramolecular Function*; Springer: Dordrecht, The Netherlands, 1996; ISBN 978-94-015-8707-5.
20. Nemeč, I.; Herchel, R.; Šilha, T.; Trávníček, Z. Towards a better understanding of magnetic exchange mediated by hydrogen bonds in Mn(III)/Fe(III) salen-type supramolecular dimers. *Dalton Trans.* **2014**, *43*, 15602–15616. [[CrossRef](#)]

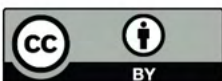


21. Nemeč, I.; Herchel, R.; Šalitroš, I.; Travnicek, Z.; Moncol, J.; Fuess, H.; Ruben, M.; Linert, W. Anion driven modulation of magnetic intermolecular interactions and spin crossover properties in an isomorphous series of mononuclear iron(III) complexes with a hexadentate Schiff base ligand. *CrystEngComm* **2012**, *14*, 7015. [[CrossRef](#)]
22. Herchel, R.; Nemeč, I.; Machata, M.; Travnicek, Z. Experimental and Theoretical Investigations of Magnetic Exchange Pathways in Structurally Diverse Iron(III) Schiff-Base Complexes. *Inorg. Chem.* **2015**, *54*, 8625–8638. [[CrossRef](#)] [[PubMed](#)]
23. Nemeč, I.; Herchel, R.; Travnicek, Z. Ferromagnetic coupling mediated by Co $\cdots\pi$  non-covalent contacts in a pentacoordinate Co(II) compound showing field-induced slow relaxation of magnetization. *Dalton Trans.* **2016**, *45*, 12479–12482. [[CrossRef](#)]
24. Nemeč, I.; Herchel, R.; Travnicek, Z. The relationship between the strength of hydrogen bonding and spin crossover behaviour in a series of iron(III) Schiff base complexes. *Dalton Trans.* **2015**, *44*, 4474–4484. [[CrossRef](#)] [[PubMed](#)]
25. Awwadi, F.F.; Taher, D.; Haddad, S.F.; Turnbull, M.M. Competition between Hydrogen and Halogen Bonding Interactions: Theoretical and Crystallographic Studies. *Cryst. Growth Des.* **2014**, *14*, 1961–1971. [[CrossRef](#)]
26. Gómez-Coca, S.; Aravena, D.; Morales, R.; Ruiz, E. Large magnetic anisotropy in mononuclear metal complexes. *Coord. Chem. Rev.* **2015**, *289*, 379–392. [[CrossRef](#)]
27. Nemeč, I.; Herchel, R.; Kern, M.; Neugebauer, P.; Van Slageren, J.; Travnicek, Z. Magnetic Anisotropy and Field-induced Slow Relaxation of Magnetization in Tetracoordinate Co<sup>II</sup> Compound [Co(CH<sub>3</sub>-im)<sub>2</sub>Cl<sub>2</sub>]. *Materials* **2017**, *10*, 249. [[CrossRef](#)]
28. Alvarez, S. Distortion Pathways of Transition Metal Coordination Polyhedra Induced by Chelating Topology. *Chem. Rev.* **2015**, *115*, 13447–13483. [[CrossRef](#)]
29. Siskos, M.G.; Choudhary, M.I.; Gerothanassis, I.P. Hydrogen Atomic Positions of O–H $\cdots$ O Hydrogen Bonds in Solution and in the Solid State: The Synergy of Quantum Chemical Calculations with 1H-NMR Chemical Shifts and X-ray Diffraction Methods. *Molecules* **2017**, *22*, 415. [[CrossRef](#)]
30. Sobczyk, L.; Chudoba, D.; Tolstoy, P.M.; Filarowski, A. Some Brief Notes on Theoretical and Experimental Investigations of Intramolecular Hydrogen Bonding. *Molecules* **2016**, *21*, 1657. [[CrossRef](#)]
31. Sen, S.; Kaseman, D.C.; Colas, B.; Jacob, D.; Clark, S. Hydrogen bonding induced distortion of CO<sub>3</sub> units and kinetic stabilization of amorphous calcium carbonate: Results from 2D 13C NMR spectroscopy. *Phys. Chem. Chem. Phys.* **2016**, *18*, 20330–20337. [[CrossRef](#)]
32. Fielden, J.; Long, D.L.; Speldrich, M.; Kögerler, P.; Cronin, L. [Co<sub>x</sub>Cu<sub>1-x</sub>(DDOP)(OH<sub>2</sub>)(NO<sub>3</sub>)](NO<sub>3</sub>): Hydrogen bond-driven distortion of cobalt(II) by solid solution ‘network mismatch’. *Dalton Trans.* **2012**, *41*, 4927. [[CrossRef](#)] [[PubMed](#)]
33. Dahl, E.W.; Szymczak, N.K. Hydrogen Bonds Dictate the Coordination Geometry of Copper: Characterization of a Square-Planar Copper(I) Complex. *Angew. Chem.* **2016**, *128*, 3153–3157. [[CrossRef](#)]
34. Hussain, T.; Siddiqui, H.L.; Zia-Ur-Rehman, M.; Yasinzai, M.M.; Parvez, M. Anti-oxidant, anti-fungal and anti-leishmanial activities of novel 3-[4-(1H-imidazol-1-yl) phenyl] prop-2-en-1-ones. *Eur. J. Med. Chem.* **2009**, *44*, 4654–4660. [[CrossRef](#)] [[PubMed](#)]
35. Bauman, V.T.; Shults, E.E.; Kononchuk, V.V.; Bagryanskaya, I.Y.; Shakirov, M.M.; Tolstikov, G.A. Synthetic Transformations of Isoquinoline Alkaloids. 1-Alkynyl-3,6-dimethoxy-N-methyl-4,5 $\alpha$ -epoxy-6,18-endoethenobenzo[*i*]isomorphinans and Their Transformations. *Russ. J. Org. Chem.* **2013**, *49*, 1502–1513. [[CrossRef](#)]
36. Cinčić, D.; Frišćić, T.; Jones, W. Isostructural Materials Achieved by Using Structurally Equivalent Donors and Acceptors in Halogen-Bonded Cocrystals. *Chem. A Eur. J.* **2008**, *14*, 747–753. [[CrossRef](#)]
37. Turunen, L.; Beyeh, N.K.; Pan, F.; Valkonen, A.; Rissanen, K. Tetraiodoethynyl resorcinarene cavitands as multivalent halogen bond donors. *Chem. Commun.* **2014**, *50*, 15920–15923. [[CrossRef](#)]
38. Bock, H.; Holl, S. Wechselwirkungen in Molekülkristallen, 167 [1,2]. Kristallzüchtung und Strukturbestimmung von  $\sigma$ -Donator/Akzeptor-Komplexen zwischen 1,4-Dioxan und den Polyiod-Molekülen I<sub>2</sub>, I<sub>2</sub>C=Cl<sub>2</sub>, (IC)<sub>4</sub>S sowie (IC)<sub>4</sub>NR (R = H, CH<sub>3</sub>)/Interaction in Molecular Crystals, 167 [1,2]. Crystallization and Structure Determination of  $\sigma$ -Donor/Acceptor Complexes between 1,4-Dioxane and the Polyiodine Molecules I<sub>2</sub>, I<sub>2</sub>C=Cl<sub>2</sub>, (IC)<sub>4</sub>S and (IC)<sub>4</sub>NR (R = H, CH<sub>3</sub>). *Z. Für Naturforsch. B* **2001**, *56*, 111–121. [[CrossRef](#)]



39. Turunen, L.; Pan, F.; Beyeh, N.K.; Trant, J.F.; Ras, R.H.A.; Rissanen, K. Bamboo-like Chained Cavities and Other Halogen-Bonded Complexes from Tetrahaloethynyl Cavities with Simple Ditopic Halogen Bond Acceptors. *Cryst. Growth Des.* **2017**, *18*, 513–520. [[CrossRef](#)]
40. Chu, Q.; Wang, Z.; Huang, Q.; Yan, C.; Zhu, S. Fluorine-containing donor-acceptor complexes: Crystallographic study of the interactions between electronegative atoms (N, O, S) and halogen atoms (I, Br). *New J. Chem.* **2003**, *27*, 1522. [[CrossRef](#)]
41. Roper, L.C.; Präsang, C.; Kozhevnikov, V.N.; Whitwood, A.C.; Karadakov, P.B.; Bruce, D. Experimental and Theoretical Study of Halogen-Bonded Complexes of DMAP with Di- and Triiodofluorobenzenes. A Complex with a Very Short N...I Halogen Bond. *Cryst. Growth Des.* **2010**, *10*, 3710–3720. [[CrossRef](#)]
42. Pearson, R.J.; Evans, K.M.; Slawin, A.M.Z.; Philp, D.; Westwood, N.J. Controlling the Outcome of an N-Alkylation Reaction by Using N-Oxide Functional Groups. *J. Org. Chem.* **2005**, *70*, 5055–5061. [[CrossRef](#)] [[PubMed](#)]
43. Kroke, E.; Schwarz, M.; Horath-Bordon, E.; Kroll, P.; Noll, B.; Norman, A.D. Tri-s-triazine derivatives. Part I. From trichloro-tri-s-triazine to graphitic C<sub>3</sub>N<sub>4</sub> structures. *New J. Chem.* **2002**, *26*, 508–512. [[CrossRef](#)]
44. Sun, W.; Zhu, G.; Wu, C.; Li, G.; Hong, L.; Wang, R. Organocatalytic Diastereo- and Enantioselective 1,3-Dipolar Cycloaddition of Azlactones and Methyleneindolinones. *Angew. Chemie Int. Ed.* **2013**, *52*, 8633–8637. [[CrossRef](#)] [[PubMed](#)]
45. Mustapha, A.; Reglinski, J.; Kennedy, A.R. The use of hydrogenated Schiff base ligands in the synthesis of multi-metallic compounds. *Inorg. Chim. Acta* **2009**, *362*, 1267–1274. [[CrossRef](#)]
46. Groom, C.; Bruno, I.J.; Lightfoot, M.; Ward, S.C. The Cambridge Structural Database. *Acta Crystallogr. Sect. B Struct. Sci. Cryst. Eng. Mater.* **2016**, *72*, 171–179. [[CrossRef](#)] [[PubMed](#)]
47. Sheldrick, G.M. SHELXT-Integrated space-group and crystal-structure determination. *Acta Crystallogr. Sect. A Found. Adv.* **2015**, *71*, 3–8. [[CrossRef](#)]
48. Bourhis, L.J.; Dolomanov, O.V.; Gildea, R.; Howard, J.A.K.; Puschmann, H. The anatomy of a comprehensive constrained, restrained refinement program for the modern computing environment Olex2 dissected. *Acta Crystallogr. Sect. A Found. Adv.* **2015**, *71*, 59–75. [[CrossRef](#)]
49. Dolomanov, O.; Bourhis, L.J.; Gildea, R.; Howard, J.A.; Puschmann, H. OLEX2: A complete structure solution, refinement and analysis program. *J. Appl. Crystallogr.* **2009**, *42*, 339–341. [[CrossRef](#)]
50. Koziskova, J.; Hahn, F.; Richter, J.; Kozisek, J. Comparison of different absorption corrections on the model structure of tetrakis ( $\mu$ 2-acetato)-diaquadicopper(II). *Acta Chim. Slovaca.* **2016**, *9*, 136–140. [[CrossRef](#)]
51. Macrae, C.F.; Sovago, I.; Cottrell, S.J.; Galek, P.T.A.; McCabe, P.; Pidcock, E.; Platings, M.; Shields, G.P.; Stevens, J.S.; Towler, M.; et al. Mercury 4.0: From visualization to analysis, design and prediction. *J. Appl. Crystallogr.* **2020**, *53*, 226–235. [[CrossRef](#)]
52. Neese, F. Software update: The ORCA program system, version 4. *Wiley Interdiscip. Rev. Comput. Mol. Sci.* **2017**, *8*, e1327. [[CrossRef](#)]
53. Najibi, A.; Goerigk, L. The Nonlocal Kernel in van der Waals Density Functionals as an Additive Correction: An Extensive Analysis with Special Emphasis on the B97M-V and  $\omega$ B97M-V Approaches. *J. Chem. Theory Comput.* **2018**, *14*, 5725–5738. [[CrossRef](#)] [[PubMed](#)]
54. Grimme, S.; Ehrlich, S.; Goerigk, L. Effect of the damping function in dispersion corrected density functional theory. *J. Comput. Chem.* **2011**, *32*, 1456–1465. [[CrossRef](#)]
55. Grimme, S.; Antony, J.; Ehrlich, S.; Krieg, H. A consistent and accurate ab initio parametrization of density functional dispersion correction (DFT-D) for the 94 elements H-Pu. *J. Chem. Phys.* **2010**, *132*, 154104. [[CrossRef](#)] [[PubMed](#)]
56. Noro, T.; Sekiya, M.; Koga, T. Segmented contracted basis sets for atoms H through Xe: Sapporo-(DK)-nZP sets (n = D, T, Q). *Theor. Chem. Acc.* **2012**, *131*, 131. [[CrossRef](#)]
57. Stoychev, G.L.; Auer, A.A.; Neese, F. Automatic Generation of Auxiliary Basis Sets. *J. Chem. Theory Comput.* **2017**, *13*, 554–562. [[CrossRef](#)] [[PubMed](#)]
58. Neese, F.; Wennmohs, F.; Hansen, A.; Becker, U. Efficient, approximate and parallel Hartree-Fock and hybrid DFT calculations. A “chain-of-spheres” algorithm for the Hartree-Fock exchange. *Chem. Phys.* **2009**, *356*, 98–109. [[CrossRef](#)]
59. Izsák, R.; Neese, F. An overlap fitted chain of spheres exchange method. *J. Chem. Phys.* **2011**, *135*, 144105. [[CrossRef](#)]

60. Lu, T.; Chen, F. Multiwfn: A multifunctional wavefunction analyzer. *J. Comput. Chem.* **2011**, *33*, 580–592. [[CrossRef](#)]
61. Lu, T.; Chen, F. Quantitative analysis of molecular surface based on improved Marching Tetrahedra algorithm. *J. Mol. Graph. Model.* **2012**, *38*, 314–323. [[CrossRef](#)]
62. Spackman, M.A.; McKinnon, J. Fingerprinting intermolecular interactions in molecular crystals. *CrystEngComm* **2002**, *4*, 378–392. [[CrossRef](#)]
63. Manna, P.; Seth, S.K.; Mitra, M.; Choudhury, S.R.; Bauzá, A.; Frontera, A.; Mukhopadhyay, S. Experimental and Computational Study of Counterintuitive  $\text{ClO}_4^- \dots \text{ClO}_4^-$  Interactions and the Interplay between and Anion + Interactions. *Cryst. Growth Des.* **2014**, *14*, 5812–5821. [[CrossRef](#)]
64. Wolff, S.K.; Grimwood, D.J.; McKinnon, J.J.; Jayatilaka, D.; Spackman, M.A. *CrystalExplorer 3.1*; University of Western Australia: Perth, Australia, 2007.
65. Osborne, S.; Wellens, S.; Felton, S.; Gunaratne, H.Q.N.; Nockemann, P.; Ward, C.; Bowman, R.; Binnemans, K.; Swadzba-Kwasny, M. Thermochromism and switchable paramagnetism of cobalt(ii) in thiocyanate ionic liquids. *Dalton Trans.* **2015**, *44*, 11286–11289. [[CrossRef](#)] [[PubMed](#)]
66. Lomjanský, D.; Varga, F.; Rajnák, C.; Moncol, J.; Boča, R.; Titis, J. Redetermination of Zero-Field Splitting in  $[\text{Co}(\text{qu})_2\text{Br}_2]$  and  $[\text{Ni}(\text{PPh}_3)_2\text{Cl}_2]$  Complexes. *Nova Biotechnol. Chim.* **2016**, *15*, 200–211. [[CrossRef](#)]
67. Manna, P.; Seth, S.K.; Mitra, M.; Das, A.; Singh, N.J.; Choudhury, S.R.; Kar, T.; Mukhopadhyay, S. A successive layer-by-layer assembly of supramolecular frameworks driven by a novel type of face-to-face  $\pi^+ - \pi^+$  interactions. *CrystEngComm* **2013**, *15*, 7879–7886. [[CrossRef](#)]
68. Mahmoudi, G.; Seth, S.; Zubkov, F.I.; Torres, E.S.L.; Bacchi, A.; Stilinović, V.; Frontera, A. Supramolecular Assemblies in Pb(II) Complexes with Hydrazido-Based Ligands. *Crystals* **2019**, *9*, 323. [[CrossRef](#)]
69. Johnson, E.R.; Keinan, S.; Mori-Sánchez, P.; Contreras-Garcia, J.; Cohen, A.; Yang, W. Revealing Noncovalent Interactions. *J. Am. Chem. Soc.* **2010**, *132*, 6498–6506. [[CrossRef](#)]
70. Humphrey, W.; Dalke, A.; Schulten, K. VMD: Visual molecular dynamics. *J. Mol. Graph.* **1996**, *14*, 33–38. [[CrossRef](#)]
71. Matta, C.F.; Boyd, R.J.; Becke, A. *The Quantum Theory of Atoms in Molecules: From Solid State to DNA and Drug Design*; Wiley-VCH: Weinheim, Germany, 2007.
72. Becke, A.D.; Edgecombe, K.E. A simple measure of electron localization in atomic and molecular systems. *J. Chem. Phys.* **1990**, *92*, 5397–5403. [[CrossRef](#)]
73. Lu, T.; Chen, F.W. Meaning and Functional Form of the Electron Localization Function. *Acta Phys. Chim. Sin.* **2011**, *27*, 2786–2792.



© 2020 by the authors. Licensee MDPI, Basel, Switzerland. This article is an open access article distributed under the terms and conditions of the Creative Commons Attribution (CC BY) license (<http://creativecommons.org/licenses/by/4.0/>).





Article

# Deposition of Tetracoordinate Co(II) Complex with Chalcone Ligands on Graphene

Jakub Hrubý<sup>1</sup> , Šárka Vavrečková<sup>1,2</sup>, Lukáš Masaryk<sup>3</sup>, Antonín Sojka<sup>1</sup>, Jorge Navarro-Giraldo<sup>1</sup>, Miroslav Bartoš<sup>1</sup>, Radovan Herchel<sup>3</sup> , Ján Moncol<sup>4</sup>, Ivan Nemeč<sup>1,3</sup>  and Petr Neugebauer<sup>1,\*</sup>

<sup>1</sup> Central European Institute of Technology, CEITEC BUT, Purkyňova 656/123, 61200 Brno, Czech Republic; Jakub.Hruby@ceitec.vutbr.cz (J.H.); 200777@vutbr.cz (S.V.); Antonin.Sojka@ceitec.vutbr.cz (A.S.); Jorge.Navarro@ceitec.vutbr.cz (J.N.-G.); Miroslav.Bartos@ceitec.vutbr.cz (M.B.); Ivan.Nemec@ceitec.vutbr.cz (I.N.)

<sup>2</sup> Institute of Physical Engineering, Faculty of Mechanical Engineering, Brno University of Technology, Technická 2, 61669 Brno, Czech Republic

<sup>3</sup> Department of Inorganic Chemistry, Faculty of Science, Palacký University, 17. listopadu 12, 77147 Olomouc, Czech Republic; lukas.masaryk01@upol.cz (L.M.); radovan.herchel@upol.cz (R.H.)

<sup>4</sup> Department of Inorganic Chemistry, Faculty of Chemical and Food Technology, Slovak University of Technology in Bratislava, 81237 Bratislava, Slovakia; jan.moncol@stuba.sk

\* Correspondence: petr.neugebauer@ceitec.vutbr.cz; Tel.: +42-054-114-9727

Academic Editor: Daniela Meroni

Received: 6 October 2020; Accepted: 28 October 2020; Published: 29 October 2020



**Abstract:** Studying the properties of complex molecules on surfaces is still mostly an unexplored research area because the deposition of the metal complexes has many pitfalls. Herein, we probed the possibility to produce surface hybrids by depositing a Co(II)-based complex with chalcone ligands on chemical vapor deposition (CVD)-grown graphene by a wet-chemistry approach and by thermal sublimation under high vacuum. Samples were characterized by high-frequency electron spin resonance (HF-ESR), XPS, Raman spectroscopy, atomic force microscopy (AFM), and optical microscopy, supported with density functional theory (DFT) and complete active space self-consistent field (CASSCF)/N-electron valence second-order perturbation theory (NEVPT2) calculations. This compound's rationale is its structure, with several aromatic rings for weak binding and possible favorable  $\pi$ - $\pi$  stacking onto graphene. In contrast to expectations, we observed the formation of nanodroplets on graphene for a drop-cast sample and microcrystallites localized at grain boundaries and defects after thermal sublimation.

**Keywords:** graphene; cobalt complexes; hybrid material; magneto-chemistry

## 1. Introduction

Nearly three decades have already passed since the first description of the slow relaxation of magnetization in the polynuclear cluster  $[\text{Mn}_{12}\text{O}_{12}(\text{O}_2\text{CCH}_3)_{16}(\text{H}_2\text{O})_4]$  known as  $\text{Mn}_{12}$  [1–3], which started the whole new research field of molecular magnetism [4]. These so-called Single-Molecule Magnets (SMMs) exhibit magnetic bistability up to a specific blocking temperature manifested by an intrinsic spin-reversal barrier energy ( $U_{\text{eff}}$ ). The barrier is a function of the total spin in the ground state ( $S$ ) and the axial component of magnetic dipole–dipole interaction ( $D$ ) as follows:  $U_{\text{eff}} = |D| \times S^2$  for integer spins and  $U_{\text{eff}} = |D| \times (S^2 - \frac{1}{4})$  for non-integer spins, respectively, in axial symmetry. This alone would imply that by increasing the number of magnetic centers, a better SMM would be obtained; however, there is a dependency of  $D \propto \frac{1}{S^2}$  that stems from spin-orbit contributions to the  $D$ -tensor [5]. This dependency shifted the interest from rather large molecules with many magnetic

atoms to Single-Ion Magnets (SIMs) [6]. Several challenges need to be addressed before fully utilizing these SIMs in real applications. One of the challenges is increasing the blocking temperature, which was recently found to be 80 K in dysprosium metallocene in 2018 [7]. This temperature, above the boiling point of liquid nitrogen (77 K), already holds promise for possible applications in spintronics [8], quantum computing [9], and molecular electronics [10]. The second challenge is finding the way from bulk material to functional surfaces.

The magnetic properties of magnetic molecules can be precisely measured by high-frequency electron spin resonance (HF-ESR) both in bulk [11–20] and on a surface [21–23]. Primarily, the Zeeman and zero-field-splitting (ZFS) contributions to the spin Hamiltonian with information about the intrinsic magnetic properties of a molecule can be determined. Today, the current effort is focused on making thin films, ordered arrays, or self-assembled monolayers that will lead to technological applications [24,25]. The key for this is to understand the behavior and adsorption of complex molecules on surfaces since their exposed surface offers many application possibilities but also brings many challenges, as these molecules can oxidize, decompose, or degrade in ambient conditions. There are two main ways to produce nanostructured magnetic thin films. They can be deposited onto a substrate via a wet-chemistry protocol from a solution [26–28] or by thermal sublimation in vacuum [29–34].

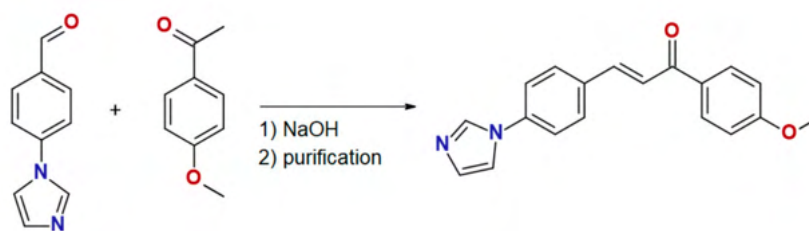
The electrical addressing of SMMs can be provided via a conductive substrate. A promising candidate is an atomically thin layer of graphite, known as graphene [35], which is an interesting substrate due to its high electron mobility [36,37], mechanical strength [38], and thermal conductivity [39]. The original preparation technique firstly used to prepare graphene in 2004 was micro-mechanical cleavage [40]. This method is suitable for tens-of-micrometers-large flakes; however, more industrial techniques for large and homogeneous surface coverage soon emerged, such as graphene production by chemical vapor deposition (CVD) [41], on silicon carbide [42], by liquid-phase exfoliation [43], or by large-scale roll-to-roll printing [44]. The perfect graphene is a zero-gap semiconductor, which helps the charge carrier mobility but also limits the applications.

Herein, we report on the synthesis, crystal structure, magnetic properties, and characterization of a new tetracoordinate complex  $[\text{Co}(\text{4MeO-L})_2\text{Cl}_2]$  (**1**) with the chalcone imidazole-derivative ligand  $\text{4MeO-L} = (2\text{E})\text{-3-[4-(1H-imidazol-1-yl)phenyl]-1-(4-methoxyphenyl)prop-2-en-1-on}$ . The determination of the crystal structure revealed that this compound is tetracoordinate, and its molecules possess a unique shape with a large angle between the coordinated  $\text{4MeO-L}$  ligands (vide infra). Tetracoordinate  $\text{Co(II)}$  compounds very often exhibit large easy-axis ( $D < 0$ ) or easy-plane ( $D > 0$ ) magnetic anisotropies [45]. Furthermore, the “flat” molecular shape involving the large aromatic system of the ligands might help to anchor complex molecules on surfaces such as graphene by non-covalent interactions. Therefore, we decided to thoroughly characterize the electronic structure of **1** by HF-ESR, to investigate both wet-chemistry and thermal sublimation depositions, and, thus, to produce a hybrid material composed of highly anisotropic  $\text{Co(II)}$ -based molecules and graphene. These samples were then characterized by Raman spectroscopy, X-ray photoelectron spectroscopy (XPS), and atomic force microscopy (AFM).

## 2. Results and Discussion

### 2.1. Synthesis and Crystal Structure of **1**

The chalcone ligand  $\text{4MeO-L}$  was prepared by the aldol condensation of 4'-(imidazol-1-yl)benzaldehyde with 4-methoxyacetophenone, as is shown in Scheme 1. The purity and structure of  $\text{4MeO-L}$  were confirmed by  $^1\text{H}$  and  $^{13}\text{C}$  NMR spectroscopy, mass spectrometry, and elemental analysis. The complex **1** was synthesized by a reaction between  $\text{CoCl}_2 \cdot 6\text{H}_2\text{O}$  and  $\text{4MeO-L}$  (molar ratio, 1:2) in methanolic solution, and it precipitated as a blue microcrystalline powder. Recrystallization from methanol led to the isolation of pale blue crystals suitable for single-crystal diffraction. The purity of **1** was confirmed by elemental analysis, and the phase purity, by powder diffraction experiments.



**Scheme 1.** Preparation of ligand 4MeO-L.

Compound **1** crystallizes in the monoclinic space group  $Pc$ , and it consists of tetracoordinate  $[\text{Co}(\text{4MeO-L})_2\text{Cl}_2]$  molecules (Figure 1). The 4MeO-L ligands coordinate to the Co atom by the imidazolyl nitrogen atoms forming the Co-N bonds ( $d(\text{Co-N}) = 2.014(4)$  and  $2.016(4)$  Å), while the chlorido ligands form longer bonds ( $d(\text{Co-Cl}) = 2.255(2)$  and  $2.257(2)$  Å). The overall shape of the coordination polyhedron can be described best as a significantly distorted tetrahedron adopting  $C_{2v}$  pseudosymmetry (continuous shape measures index [46,47] for  $T_d$ : 1.356 in 1). The 4MeO-L ligands adopt an *E* conformation and remain planar even after coordination (Figure 1). The N-Co-N angle is wider than the Cl-Co-Cl one:  $\angle(\text{N1-Co1-N2}) = 125.7(2)$  vs.  $\angle(\text{Cl1-Co1-Cl2}) = 119.44(6)$ .

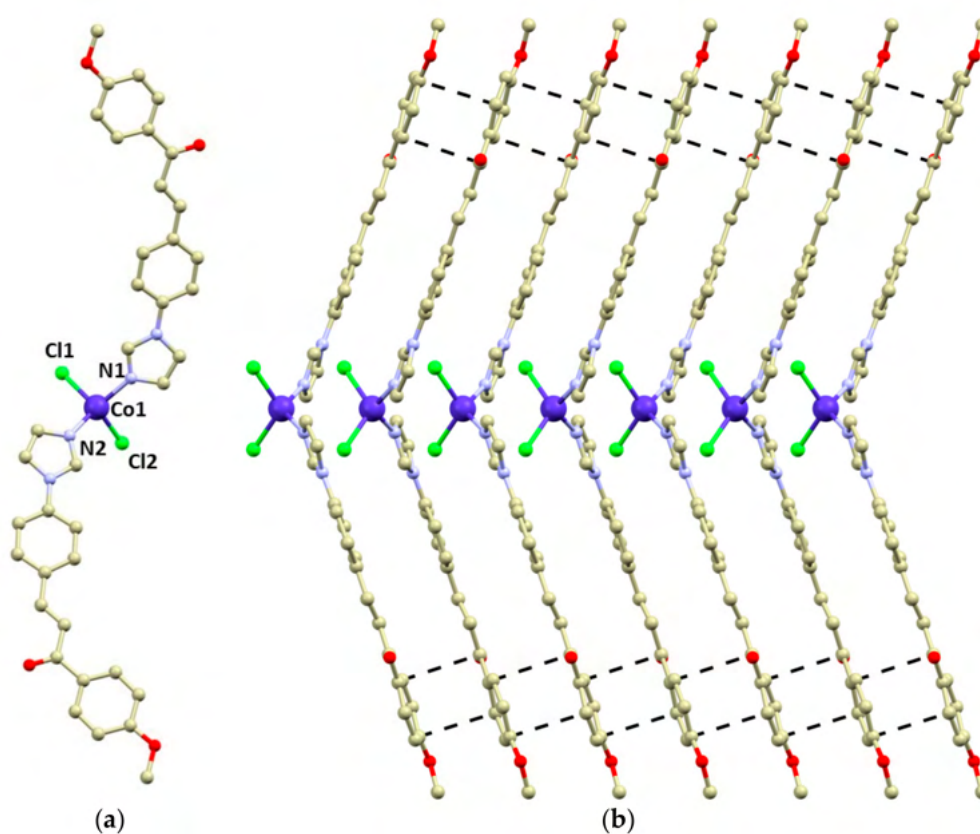


**Figure 1.** (a)—molecular structure of **1**. Selected bond lengths (Å) and angles (deg):  $d(\text{Co1-N1}) = 2.014(4)$ ,  $d(\text{Co1-N2}) = 2.016(4)$ ,  $d(\text{Co1-Cl1}) = 2.255(2)$ ,  $d(\text{Co1-Cl2}) = 2.257(2)$ ,  $\angle(\text{N1-Co1-N2}) = 125.7(2)$ , and  $\angle(\text{Cl1-Co1-Cl2}) = 119.44(6)$ . (b)—a perspective view of the packing of the  $[\text{Co}(\text{4MeO-L})_2\text{Cl}_2]$  molecules in the direction of the crystallographic *b*-axis. Observed  $\pi$ - $\pi$  stacking interactions were visualized by depicting the shortest C...C distances (black dashed lines). The hydrogen atoms are omitted for clarity.

The crystal packing in **1** is stabilized by a plethora of weak hydrogen bonds such as C-H...Cl and C-H...O. Remarkably, the large aromatic systems of the 4MeO-L ligands form  $\pi$ - $\pi$  stacking

interactions (the shortest C...C distances range between 3.27 and 3.45 Å), which stabilize the formation of supramolecular chains along the b crystallographic axis (Figure 1b).

## 2.2. Raman Vibrations

We used CVD graphene (Graphenea, San Sebastian, Spain) on a Si/SiO<sub>2</sub> substrate. Figure 2 shows the substrate Raman spectra that helped us to determine the defects involved in the graphene. The Si/SiO<sub>2</sub> Raman spectrum has a main strong phonon band at 520 cm<sup>-1</sup> and two medium peaks at 301 cm<sup>-1</sup> and in the region 946–976 cm<sup>-1</sup> [48,49]. A spectrum of CVD graphene exhibited the strong peaks D at 1347 cm<sup>-1</sup>, G at 1595 cm<sup>-1</sup>, and 2D at 2689 cm<sup>-1</sup>, with the weaker peaks D' at 1627 cm<sup>-1</sup> and D+D' at 2462 cm<sup>-1</sup>. The presence of a strong G peak and weak D' suggests CVD graphene with defects [50].

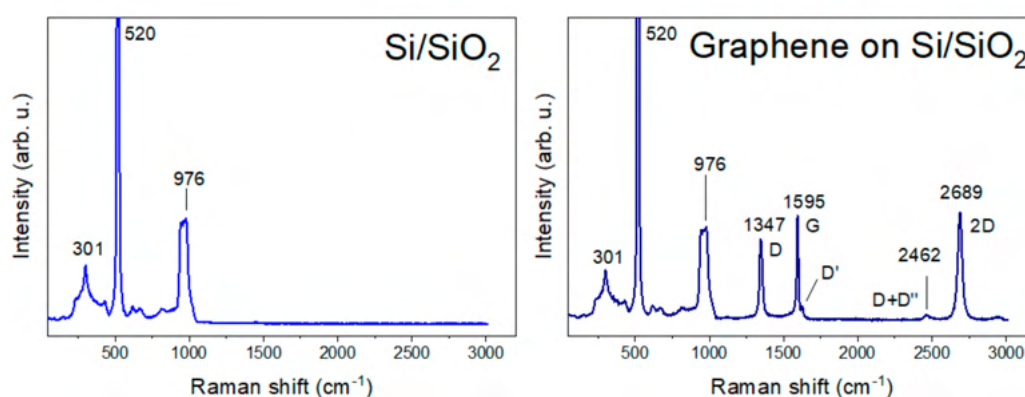


**Figure 2.** Raman spectra of Si/SiO<sub>2</sub> substrate and graphene on Si/SiO<sub>2</sub> substrate.

A comparison of bulk compound 1, drop-cast, and two sublimated samples at 75 and 265 °C is illustrated in Figure 3. The Raman spectrum of the bulk compound 1 on the Si/SiO<sub>2</sub> substrate consists of significant peaks (964, 1186, 1366, and 1603 cm<sup>-1</sup>) and peaks of Si/SiO<sub>2</sub>. In the case of the drop-cast sample, significant peaks were overlapped with the peaks of graphene and Si/SiO<sub>2</sub>, except one (1190 cm<sup>-1</sup>). By contrast, the Raman spectra of the sublimated samples all showed significant peaks due to measurements on a larger crystal and obtaining a stronger signal. The comparison tables of the Raman spectra can be found in Table S1.

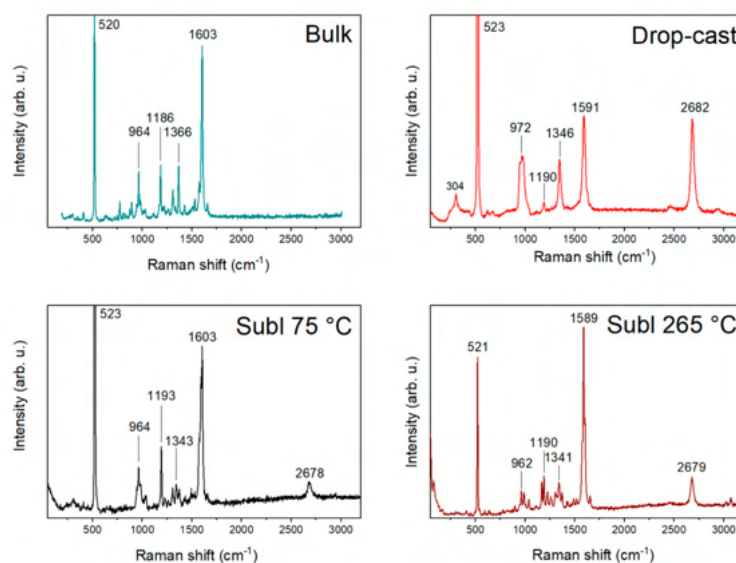


**Figure 3.** Comparison of Raman spectra of bulk compound 1, drop-cast, and sublimations at 75 and 265 °C.



Optical images of the hybrid material taken along with Raman spectroscopy are shown in Figure 4. The molecules deposited by drop-casting formed small droplets up to 50 nanometers high. On the contrary, the molecules on sublimated samples formed microcrystals hundreds of nanometers high (see ESI, Figure S1).

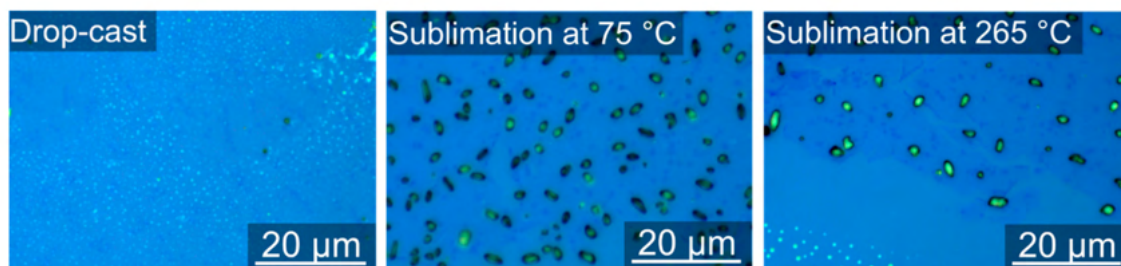


**Figure 4.** Images from the optical microscope of the samples after drop-casting and sublimations at 75 and 265 °C.

### 2.3. Chemical Composition and Bonds

The chemical composition was probed by XPS. Figure 5 shows spectra of bulk compound 1 together with the molecular structure.

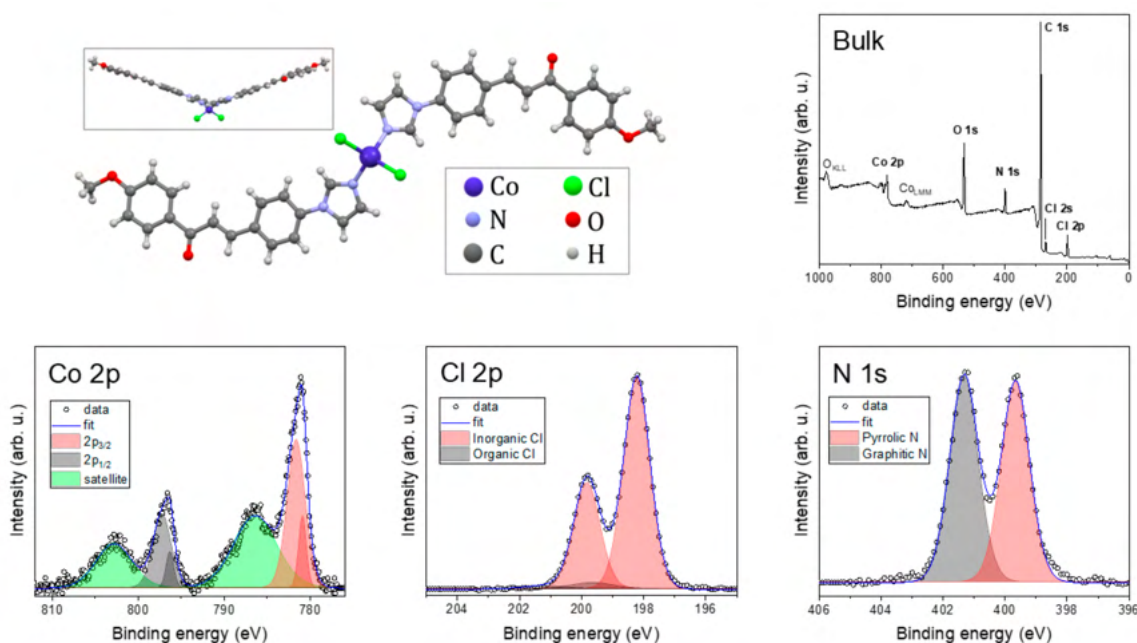


**Figure 5.** Molecular structure with survey XPS spectrum and detailed Co 2p, Cl 2p, and N 1s spectra.

The bulk compound 1 spectrum exhibited photoelectron peaks—Co 2p, Cl 2p, N 1s, C 1s, and O 1s—and Augers peaks:  $O_{KLL}$  and  $Co_{LMM}$ . The detailed spectra of the selected peaks revealed specific chemical bonds. The N 1s peak was deconvoluted to two components: graphitic N with three neighboring C atoms and pyrrolic N with two C atoms and one Co bond [51]. The photoelectron peaks emitted from the p, d, and f electronic levels are further split by spin-orbit interactions. This helped us to distinguish, in the Cl 2p spectrum, between organic (Cl–C and Cl–H) and inorganic (Cl–Co) components [52]. Co 2p exhibited two main components and shake-up satellites. The spin-orbit shift of the main components Co 2p<sub>3/2</sub> and Co 2p<sub>1/2</sub> depends on the oxidation state, and with 15.6 eV, the Co(II) high-spin state predominates [53].

Figure 6 shows the comparison of the hybrid samples with CVD graphene: drop-cast, and sublimated at 75 °C and at 265 °C, respectively. In the drop-cast sample, we observed a decrease in

the graphitic nitrogen component compared to bulk compound **1** and an apparent split of chlorine to inorganic and organic contributions. In the case of drop-casting, we detected a weak Co 2p signal on the surface, suggesting a possible complex decomposition (see ESI, Figure S2). In the case of the sublimated samples, even after several hours of acquisition, we did not obtain any convincing Co 2p peaks for 75 or 265 °C. This may be attributed to the possible partial decomposition of the complex or the surface sensitivity of XPS, with the complex outermost layers containing only a very few Co atoms or so-called “dead” layers with oxidized, spoiled molecules. This absence led us to a semi-empirical quantitative analysis of the powder after each sublimation (see ESI, Figure S3) and revealed an increased amount of cobalt and chlorine in the powder from the crucible compared to the bulk powder. This, along with the detected organic chlorine, suggests the possible partial chlorination of the graphene with a partial decomposition of the complex during both deposition processes. Carbon and oxygen contributions were discarded since they might be affected by adventitious contaminations due to the ex situ preparation procedures.

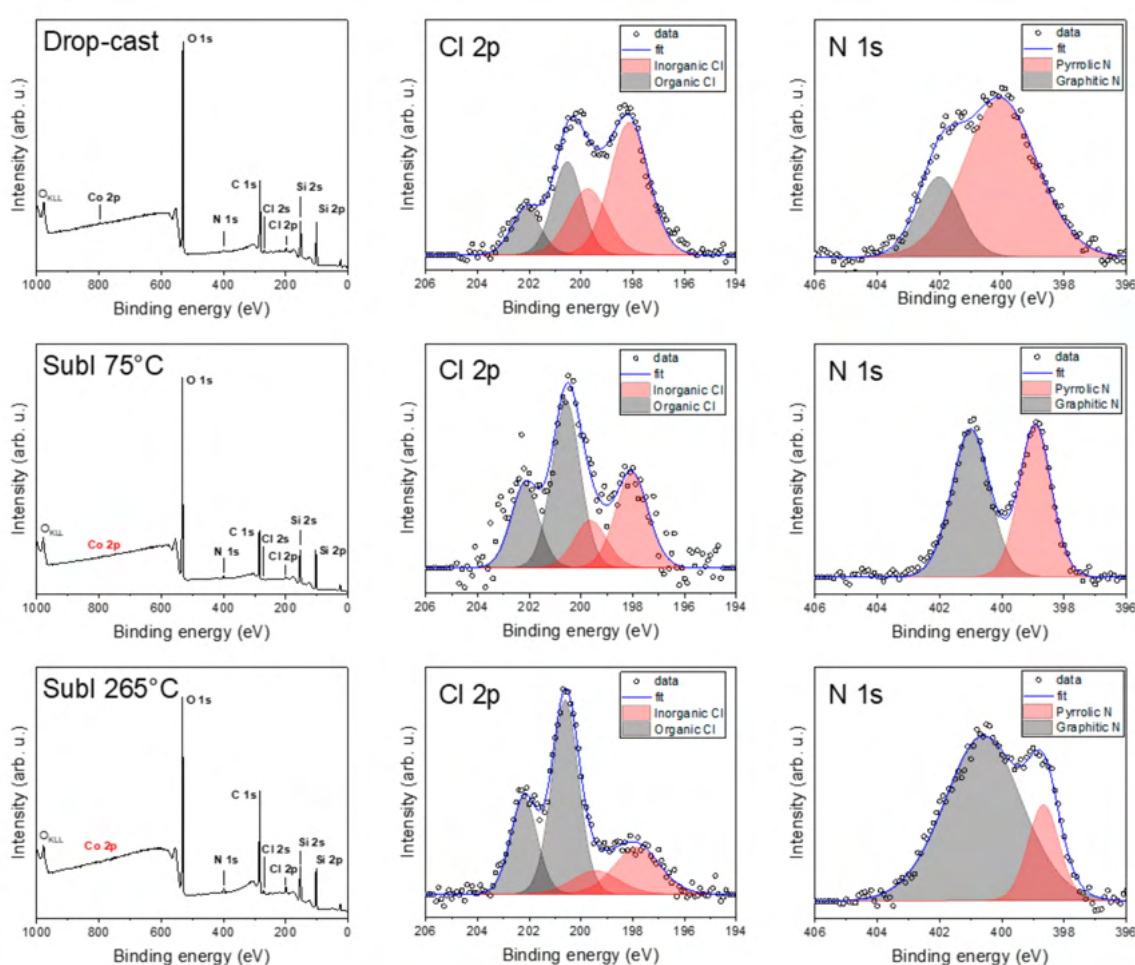


**Figure 6.** Comparison of detailed XPS spectra of drop-cast and sublimated samples at 75 and 265 °C.

#### 2.4. Molecular Adsorption by DFT

We investigated the adsorption of the molecule on graphene in the framework of density functional theory (DFT) using the Vienna Ab-Initio Simulation Package (VASP) [54–57]. The exchange–correlation potential was approximated by the generalized gradient approximation in Perdew–Burke–Ernzerhof (PBE) parametrization [58,59], the pseudopotential approach was used for the interaction between the valence electrons and ionic core, and Van der Waals forces were considered. Further details can be found in Section 3.

We performed a geometric relaxation calculation considering two possible geometries of the molecule relative to the graphene plane, as shown in Figure 7. The initial position of the molecule was chosen to mimic an AB-stacking configuration between the carbon rings of the molecule and the graphene substrate, as shown in Figure 7b,d, and also to take advantage of possible C–H $\cdots\pi$  hydrogen bonding between the hydrogen atoms of the molecule and  $\pi$  electrons of the carbon atoms in graphene. The molecule was placed manually on top of the substrate, such that the distances between the closest carbon atom of the molecule and the graphene plane was 3.13 and 3.20 Å for Geometries 1 and 2, respectively. During relaxation, the atoms of the molecule could move freely to their equilibrium positions, while the atoms of the substrate were kept fixed.

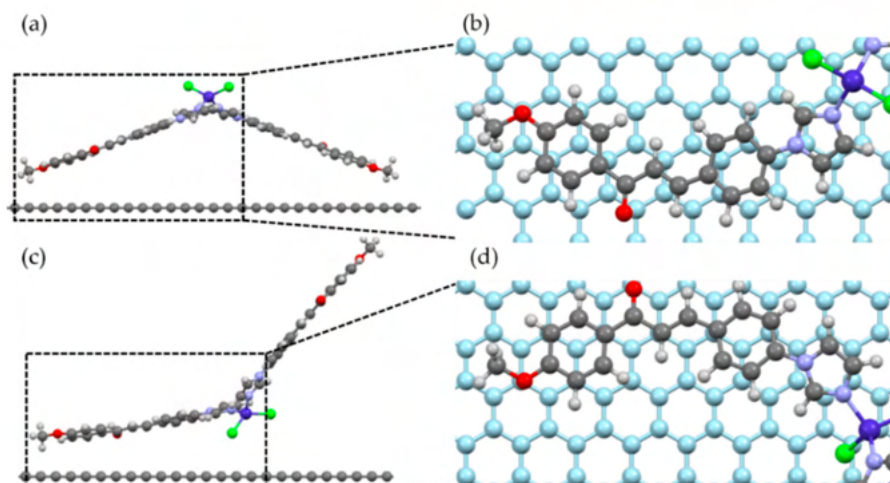


**Figure 7.** Initial position of the two geometries used for the simulation of molecular adsorption on graphene. As referred to in the text, (a) Geometry 1, (b) top view of the selected part of (a), with the graphene substrate in light blue; the closest carbon atom of the molecule to the substrate was placed in the center of one of the graphene rings. (c) Geometry 2, and (d) top view of the selected part of (c).

After relaxation, we found that the molecule bound to the substrate in both configurations, with distances of 3.31 Å (Geometry 1) and 3.29 Å (Geometry 2) between the closest carbon atom of the molecule and the graphene plane. Such distances correspond to the typical distances between  $\pi$ – $\pi$ -bonded carbon rings, and we found that there was no considerable change in the molecular shapes after the adsorption. The binding energies were 0.89 eV per molecule (85.4 kJ/mol) for Geometry 1, and 1.08 eV per molecule (104.0 kJ/mol) for Geometry 2, where the main contribution to this energy comes from the van der Waals interactions between the carbon atoms of the molecule and substrate. If van der Waals forces are not considered, the binding energies fall to the meV range, below the thermal energy at room temperature (25.8 meV at 300 K). Therefore, van der Waals forces play a crucial role in the adsorption of these cobalt-based molecules on graphene.

### 2.5. HF-ESR Spectroscopy

Figure 8 shows the HF-ESR spectra acquired for bulk compound **1** at four frequencies—380, 415, 456, and 490 GHz—while sweeping the magnetic field from 0 to 15 T at 5 K.

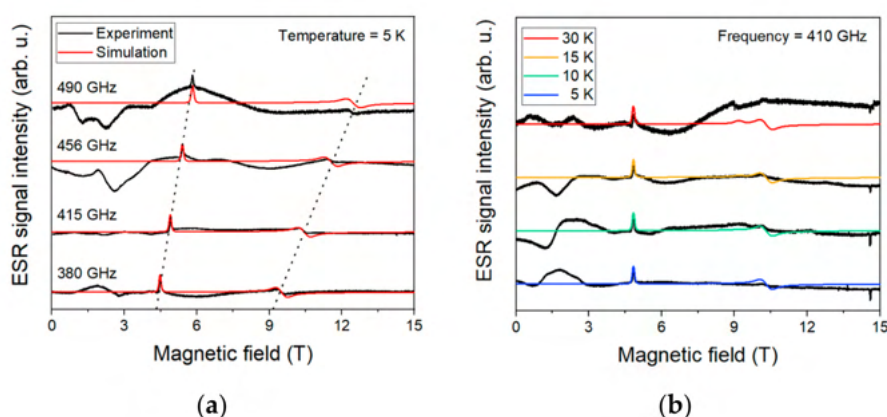


**Figure 8.** (a)—high-frequency electron spin resonance (HF-ESR) spectra for four different frequencies at 5 K. The dotted line is guidance for Zeeman splitting. (b)—temperature dependence acquired at 410 GHz. Black line in both is experimental, and red/colored line is the simulation.

The used effective spin Hamiltonian for the simulations is the following Equation (1):

$$\hat{H} = \hat{H}_{\text{Zeeman}} + \hat{H}_{\text{ZFS}} = \mu_B \mathbf{B} \cdot \mathbf{g} \cdot \hat{S} + D \left[ \hat{S}_z^2 - \frac{1}{3} S(S+1) \right] + E (\hat{S}_x^2 - \hat{S}_y^2) \quad (1)$$

where  $\mu_B$  is the Bohr magneton,  $\mathbf{B}$  is the external magnetic field,  $\mathbf{g}$  is a tensor linking the external magnetic field with spin vectors,  $\hat{S}$  is the electron spin operator, and  $D$  and  $E$  are axial and rhombic zero-field splitting parameters, respectively. The best fit was found for the spin Hamiltonian parameters as follows:  $D = 14.6 \text{ cm}^{-1}$  with  $E/D = 0.235$ , and  $g_x = 2.32$ ,  $g_y = 2.38$ , and  $g_z = 2.16$  (Table 1).

**Table 1.** Zero-field-splitting (ZFS) parameters obtained by complete active space self-consistent field (CASSCF)/N-electron valence second-order perturbation theory (NEVPT2) calculations compared to HF-ESR.

	$D/\text{cm}^{-1}$	$E/D$	$g_x$	$g_y$	$g_z$	$g_{av}$
<b>1</b>	+14.5	0.150	2.325	2.378	2.163	2.289
Geometry 1	+16.4	0.090	2.346	2.364	2.150	2.287
Geometry 2	+17.5	0.132	2.345	2.381	2.143	2.290
HF-ESR	+14.6	0.235	2.320	2.380	2.160	2.287

## 2.6. CASSCF Calculations

To support the analysis of the HF-ESR spectra of **1**, we performed complete active space self-consistent field (CASSCF) calculations complemented by N-electron valence second-order perturbation theory (NEVPT2) using an ORCA 4.2 computational package [60]. The details of the calculations are explained in Section 3—*Theoretical Methods*. The spin Hamiltonian parameters were extracted by utilizing the effective Hamiltonian theory and we obtained a set of the ZFS parameters—for  $S = 3/2$ ,  $D = +14.5 \text{ cm}^{-1}$  and  $E/D = 0.15$ —and the anisotropy of the  $g$ -tensor components was confirmed ( $g_x = 2.325$ ,  $g_y = 2.378$ ,  $g_z = 2.163$ , and  $g_{av} = 2.289$ ). These values are in good agreement with the values obtained by HF-ESR spectroscopy. Next, we performed additional calculations for the optimized Geometries 1 and 2 of the  $[\text{Co}(\text{4MeO-L})_2\text{Cl}_2]$  molecules deposited on the graphene surface as calculated by periodic DFT. The resulting ZFS parameters are, besides the slightly lower rhombicity, rather similar to those calculated for **1** (all the calculated values are summarized in Table 1). The visualizations of the calculated  $D$ -tensor principal axes overlaid over the structures of the complex molecules (Figure 9) underline the similarities among **1** and Geometries 1 and 2. The directions of  $D_z$  are practically the same in all the studied molecules. However, the directions of the  $D_x$  and  $D_y$  axes differ among the studied molecules (Figure 9).



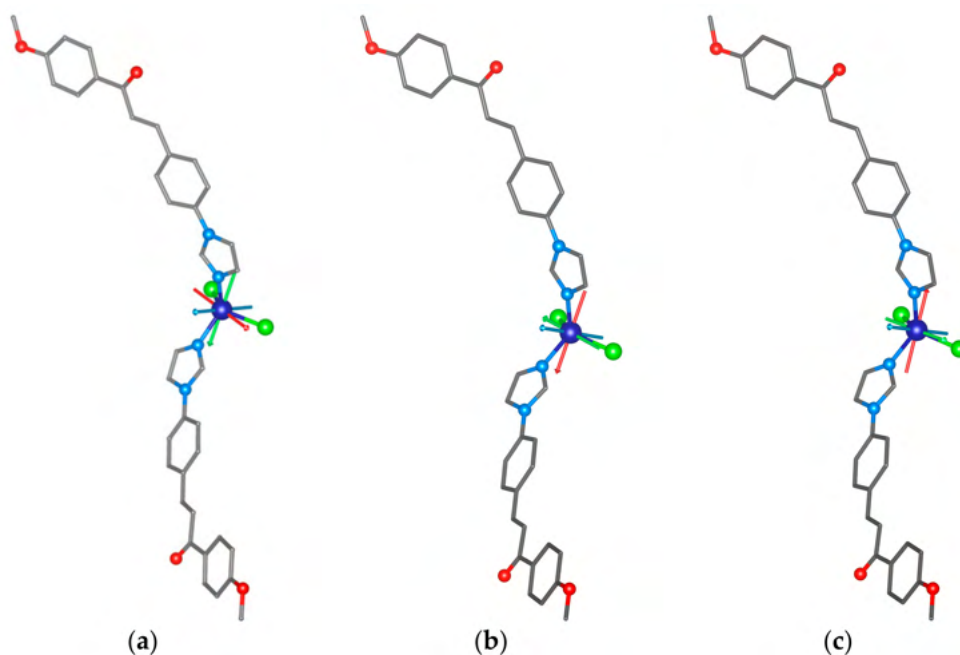


**Figure 9.** The CASSCF/NEVPT2 calculated principal axes of the  $D$ -tensor labeled  $D_X$  (red),  $D_Y$  (green), and  $D_Z$  (blue) visualized together with molecular structures of **1** (a), Geometry 1 (b), and Geometry 2 (c).

### 3. Materials and Methods

#### 3.1. Materials

$\text{CoCl}_2 \cdot 6\text{H}_2\text{O}$  was bought from PMRLab (Port Elizabeth, South Africa), and 4-(1H-imidazol-1-yl)benzaldehyde, 4-methoxyacetophenone, NaOH, and the solvents (methanol (MeOH), diethyl ether ( $\text{Et}_2\text{O}$ ), and the deuterated solvents for the NMR experiments (deuterated chloroform ( $\text{CDCl}_3$ ))) were purchased from VWR International (Stříbrná Skalice, Czech Republic), Sigma-Aldrich (Prague, Czech Republic), Lach-Ner (Neratovice, Czech Republic), and Litolab (Chudobín, Czech Republic).

#### 3.2. Synthesis

##### 3.2.1. (2E)-3-[4-(1H-imidazol-1-yl)phenyl]-1-(4-methoxyphenyl)prop-2-en-1-one (4MeO-L)

A methanolic sodium hydroxide solution (40%; 1.2 mL) was added dropwise to a mixture of 4-methoxybenzaldehyde (2 mmol, 0.300 g), 4'-(imidazol-1-yl)benzaldehyde (2 mmol, 0.377 g), and methanol (5 mL) over a period of 40 min. The resulting solution was stirred at room temperature until the completion of the reaction. The precipitate was filtered off and washed with a cold methanol–water mixture (1:10). The resulting product was recrystallized from methanol and dried in a desiccator under reduced pressure (overnight) [61].

Yellowish solid. Yield: 83%.  $^1\text{H}$  NMR (400 MHz, Chloroform-*d*, 298 K, ppm)  $\delta$  8.06 (d,  $J = 8.4$  Hz, 2H, C17-H, C21-H), 7.92 (s, 1H, C2-H), 7.84–7.74 (m, 3H, C8-H, C10-H, C13-H), 7.57 (d,  $J = 15.6$  Hz, 1H, C12-H), 7.46 (d,  $J = 8.1$  Hz, 2H, C7-H, C11-H), 7.34 (s, 1H, C5-H), 7.24 (s, 1H, C4-H), 7.00 (d,  $J = 8.4$  Hz, 2H, C18-H, C20-H), 3.91 (s, 3H, C23-H).  $^{13}\text{C}$  NMR (101 MHz, Chloroform-*d*, 298 K, ppm)  $\delta$  188.28 (C14), 163.59 (C19), 142.12 (C12-H), 138.43 (C6), 135.38 (C2-H), 134.23 (C16), 132.72 (C9), 130.87 (C4-H), 130.85 (C8-H, C10-H), 129.86 (C17-H, C21-H), 122.51 (C13-H), 121.45 (C7-H, C11-H), 117.84 (C5-H), 113.91 (C18-H, C20-H), 55.52 (C23-H). ESI+MS (MeOH,  $m/z$ ): 305.27 (calc. 305.12; 100%; {4MeO-L + H} $^+$ ), 327.11 (calc. 327.11; 79%; {4MeO-L + Na} $^+$ ), 630.81 (calc. 631.67; 88%; {2  $\times$  4MeO-L + Na} $^+$ ). IR

(ATR,  $\nu$ ,  $\text{cm}^{-1}$ ): 407w, 447w, 521w, 593w, 653w, 770w, 816s, 905w, 958w, 981w, 1015m, 1061w, 1120w, 1168m, 1225m, 1254w, 1309w, 1342w, 1433w, 1523s, 1588s, 1658m, 3103w.

### 3.2.2. Complex $[\text{Co}(\text{4MeO-L})_2(\text{Cl})_2]$ (**1**)

The solution of  $\text{CoCl}_2 \cdot 6\text{H}_2\text{O}$  (1 mmol, 0.237 g) in 5 mL of methanol was heated up to 50 °C, and then, 2 molar equiv. of 4MeO-L was added (2 mmol, 0.608 g). The solution was cooled down and stirred at ambient temperature for 2 h. The obtained blue precipitate was collected by filtration and washed with water ( $2 \times 0.5$  mL) and  $\text{Et}_2\text{O}$  ( $2 \times 1$  mL). The blue solid product was dried in a desiccator under reduced pressure (overnight) [62].

Blue solid. Yield: 92%. Anal. Calc. for  $\text{CoC}_{38}\text{H}_{32}\text{Cl}_2\text{N}_4\text{O}_4$  (**1**): C, 61.80; H, 4.37; N, 7.59%; found: C, 61.59; H, 4.31; N, 7.42%. ESI+MS (MeOH,  $m/z$ ): 305.34 (calc. 305.7; 10%;  $\{4\text{MeO-L} + \text{H}\}^+$ ), 471.07 (calc. 471.21; 100%;  $\{[\text{Co}(\text{4MeO-L})(\text{Cl})_2] + 2\text{H}_2\text{O} + \text{H}\}^+$ ), 702.21 (calc. 702.14; 71%;  $\{[\text{Co}(\text{4MeO-L})_2(\text{Cl})]\}^+$ ), 774.76 (calc. 775.13; 30%;  $\{[\text{Co}(\text{4MeO-L})_2(\text{Cl})] + 4\text{H}_2\text{O}\}^+$ ). IR (ATR,  $\nu$ ,  $\text{cm}^{-1}$ ): 399w, 412w, 476w, 501w, 517w, 589w, 612w, 646w, 729w, 809s, 969w, 1013w, 1059w, 1102w, 1134w, 1159w, 1212w, 1347w, 1401w, 1497w, 1534w, 1598s, 3129w. Thermal stability up to ca. 310 °C was confirmed by thermogravimetry measurement.

### 3.3. Deposited Samples

Drop-cast sample was prepared by dissolving the bulk compound **1** in dichloromethane (98%, Penta, Czech Republic) to make a final solution with a 100  $\mu\text{M}$  concentration. The actual drop-casting was conducted in a mobile glove bag (Merck, Germany) filled with inert nitrogen gas; 10  $\mu\text{L}$  was drop-cast onto a substrate. For the thermal sublimation, we used a home-built high-vacuum sublimation chamber equipped with a quartz crucible heated by tungsten wire, with a thermocouple in thermal contact with the crucible. The base chamber pressure during the sublimation was  $2 \times 10^{-7}$  mbar. The sublimations were performed at 75 and 265 °C, respectively.

### 3.4. Raman Spectroscopy (RS)

Raman spectra were acquired on a confocal Raman microscope WITec Alpha300 R+ (WITec, Ulm, Germany). All measurements were carried out with the excitation laser source with a 532 nm wavelength and 1 mW power output. Optical images were acquired with a 100 $\times$  objective (NA 0.9, WD 0.31 mm).

### 3.5. Atomic Force Microscopy (AFM)

All topography images and profiles were obtained with the scanning probe microscope Bruker Dimension Icon in tapping mode.

### 3.6. X-ray Photoelectron Spectroscopy (XPS)

X-ray photoelectron (XPS) measurements were carried out with a Kratos Axis Supra (Kratos Analytical, Manchester, United Kingdom) spectrometer at room temperature and under ultra-high vacuum (UHV) conditions. The instrument was equipped with a monochromatic Al  $K\alpha$  source of 1486.6 eV (15 mA, 15 kV) and a hemispherical analyzer with a hybrid magnetic and electrostatic lens for enhanced electron collection. Survey and detailed XPS spectra were acquired at normal emission with fixed pass energies of 160 and 20 eV, respectively. All spectra were calibrated to the hydrocarbon peak set to 284.8 eV. The Kratos charge neutralizer system was used on all specimens. The inelastic backgrounds in all the spectra were subtracted according to the Shirley method [63]. Data analysis was based on a standard deconvolution method using a mixed Gaussian (G) and Lorentzian (L) line shape (G = 70% and L = 30%, Gaussian–Lorentzian product) for each component in the spectra. The elemental composition of the samples was evaluated using a semi-empirical approach. The integrated intensity of each component was corrected with the photoionization cross-section calculated for each



atom, neglecting the differences in photoelectron escape length as a function of the kinetic energy [64]. The spectra were analyzed using the CasaXPS software (version 2.3.18).

### 3.7. High-Frequency Electron Spin Resonance (HF-ESR)

HF-ESR spectra were acquired on a newly home-built spectrometer featuring a signal generator (Virginia Diodes, Charlottesville, VA, USA), an amplifier–multiplier chain (Virginia Diodes, Charlottesville, USA), a quasi-optical bridge (Thomas Keating, Billingshurst, UK), and a 16 T solenoid cryomagnet (Cryogenic, London, UK) with heterodyne signal detection. The reference powder sample of the complex was studied as a pressed powder with a  $\varnothing$  5 mm pellet sample. All ESR spectra were simulated using EasySpin [65], a toolbox for Matlab.

### 3.8. Density Functional Theory (DFT)

The density functional calculations for molecular adsorption were performed with the Vienna Ab-Initio Simulation Package (VASP) [54–57] version 5.4.4, which uses a plane-wave basis for the Kohn–Sham orbitals, the Projector Augmented Wave (PAW) method [57,66], and pseudopotentials. The exchange–correlation potential was approximated by generalized gradient approximation in Perdew–Burke–Ernzerhof (PBE) parametrization [58,59]. Van der Waals corrections were calculated using the D2 method of Grimme [67]. In all calculations, the kinetic energy cut-off for the plane waves was 420 eV. For the calculation of the ground state energy of the system molecule+substrate and graphene substrate, a  $\Gamma$ -centered  $2 \times 2 \times 1$  Monkhorst–Pack mesh [68] was used to sample the Brillouin zone, while a  $\Gamma$ -point calculation was used for the ground-state energy of the molecule. We considered two different molecular geometries relative to the graphene plane. Geometry 1 lies on top of a  $17 \times 8$  graphene supercell, while a  $13 \times 7$  supercell was used for Geometry 2 ( $1 \times 1$  corresponds to graphene's unit cell). Since a plane-wave basis was used, the systems were periodic along each lattice vector; therefore, an array of infinite molecules was simulated, which in principle can interact with each other. Nevertheless, the distance between the closest atoms of neighboring molecules was no less than 9.0 Å for Geometry 1 and 5.8 Å for Geometry 2 (the distance between the closest Co atoms was 17.2 Å for Geometry 1, and 19.7 Å for Geometry 2); therefore, it was assumed that the molecules did not interact with each other. Geometry relaxation was performed until the forces were below 0.1 eV/Å.

### 3.9. Theoretical Methods (CASSCF/NEVPT2)

All the theoretical calculations were performed with the ORCA 4.2 computational package [69]. All the calculations employed the triple- $\zeta$  def2-TZVP basis functions for all atoms except for carbon and hydrogen, for which the def2-SVP basis set was applied [70]. Additionally, the def2/J and def2-TZVP/C auxiliary basis sets were utilized together with RIJCOSX approximation [71,72]. The multiconfigurational character of the studied Co(II) complexes was handled by calculations utilizing self-consistent field (SA-CASSCF) wave functions [73] with N-electron valence second-order perturbation theory (NEVPT2) [74]. The active space of the CASSCF calculation was set to five d-orbitals of Co(II) (CAS(7,5)). The *D*- and *g*-tensors, based on dominant spin–orbit coupling contributions from excited states, were calculated through quasi-degenerate perturbation theory (QDPT) [75]. We utilized approximations to the Breit–Pauli form of the spin-orbit coupling operator (SOMF approximation) [76] and effective Hamiltonian theory [77].

### 3.10. Elemental Analyses (EA)

Elemental analysis was carried out using a Flash 2000 CHNS Elemental Analyzer (Thermo Scientific, Waltham, MA, USA).

### 3.11. Mass Spectrometry (MS)

Electrospray ionization mass spectrometry (ESI-MS; methanol solutions) was performed with an LCQ Fleet ion trap spectrometer (Thermo Scientific, Waltham, MA, USA; QualBrowser software, version 2.0.7) in both positive (ESI+) and negative (ESI-) ionization modes.

### 3.12. NMR Spectroscopy

$^1\text{H}$  and  $^{13}\text{C}$  NMR spectroscopy, and  $^1\text{H}$ - $^{13}\text{C}$  gsHMQC and  $^1\text{H}$ - $^{13}\text{C}$  gsHMBC two-dimensional correlation experiments were performed using  $\text{CDCl}_3$  (4MeO-L) solution at 300 K using a Varian spectrometer (Palo Alto, CA, USA) at 400.00 MHz (for  $^1\text{H}$  NMR) and 101.00 MHz (for  $^{13}\text{C}$  NMR), where gs = the gradient selected, HMQC = the heteronuclear multiple quantum coherence, and HMBC = the heteronuclear multiple bond coherence.  $^1\text{H}$  and  $^{13}\text{C}$  NMR spectra were calibrated against the residual  $\text{CDCl}_3$   $^1\text{H}$  NMR (7.26 ppm) and  $^{13}\text{C}$  NMR (77.16 ppm) signals. The splitting of the proton resonances in the reported  $^1\text{H}$  spectra is defined as s = singlet, d = doublet, dd = doublet of doublets, sep = septet, m = multiplet, and bs = broad signal.

### 3.13. Infrared Spectroscopy

A Jasco FT/IR-4700 spectrometer (Jasco, Easton, MD, USA) was used for the collection of the infrared (IR) spectra of the studied ligand and complex in the range of 400–4000  $\text{cm}^{-1}$  by using the attenuated total reflection (ATR) technique on a diamond plate.

### 3.14. Crystallography

A single crystal of **1** was mounted on a Stoe StadiVari diffractometer possessing a Pilatus3R 300 K detector and microfocused sealed tube Xenocs Genix3D Cu HF ( $\lambda = 1.54186 \text{ \AA}$ ) at 100 K. The structure was solved using the program SuperFlip [78] and refined using the program ShelXL (ver. 2018/3) [79] in the crystallographic package Olex2 [80]. The structure was drawn using the Mercury program [81]. Crystal data for  $\text{CoC}_{38}\text{H}_{32}\text{Cl}_2\text{N}_4\text{O}_4$  ( $M = 738.50 \text{ g/mol}$ ): monoclinic, space group  $Pc$  (no. 7),  $a = 18.7700(3) \text{ \AA}$ ,  $b = 12.2910(4) \text{ \AA}$ ,  $c = 7.3969(6) \text{ \AA}$ ,  $\beta = 101.392(3)^\circ$ ,  $V = 1672.86(15) \text{ \AA}^3$ ,  $Z = 2$ ,  $T = 100(1) \text{ K}$ ,  $\mu(\text{CuK}\alpha) = 5.885 \text{ mm}^{-1}$ ,  $D_{\text{calc}} = 1.466 \text{ g/cm}^3$ , 31,686 reflections measured ( $3.596^\circ \leq 2\theta \leq 72.338^\circ$ ), 5367 unique ( $R_{\text{int}} = 0.0372$ ), used in all calculations. The final  $R_1$  was 0.0455 ( $I > 2\sigma(I)$ ), and the  $wR_2$  was 0.1211 (all data). The highest peak: +0.28; the deepest hole: −0.53. Crystal structure refinement: All atoms except for hydrogen were refined anisotropically. The hydrogen atoms were placed into the calculated positions, and they were included into the riding-model approximation with  $U_{\text{iso}} = 1.2U_{\text{eq}}(\text{C})$  or  $1.5U_{\text{eq}}(\text{CH}_3)$  and  $d(\text{C}-\text{H}) = 0.95\text{--}0.98 \text{ \AA}$ .

## 4. Conclusions

This paper reports on the synthesis, crystal structure, magnetic properties, and characterization of a new Co(II)-based complex with monodentate chalcone ligands and its deposition on graphene. The magnetic properties were determined from HF-ESR measurements and were found to be in fair agreement with CASSCF/NEVPT2 ab initio quantum chemical calculations. The spin Hamiltonian parameters are as follows:  $D = 14.6 \text{ cm}^{-1}$  with significant rhombicity  $E/D = 0.235$ , and  $g_x = 2.32$ ,  $g_y = 2.38$ , and  $g_z = 2.16$ . Depositions on graphene were attempted by both drop-casting in an inert nitrogen atmosphere and by the thermal sublimation of bulk compound **1** in a high vacuum. In both cases, we observed organic chlorine components, suggesting the partial decomposition of the complex or possible chlorination of graphene. On the contrary, the Raman spectra showed a good agreement of the peaks in bulk and on the graphene; however, a few peaks from the complex overlapped with the graphene peaks, which hindered the analysis. In the case of the drop-cast sample, we observed the formation of small nanodroplets about 50 nm high on the graphene. Samples prepared by thermal sublimations revealed the formation of microcrystallites formed mostly at the grain edges and defects on graphene. DFT simulations of the complex at two geometries on the graphene surface confirmed only weak

attraction to the graphene surface, with the crucial role of van der Waals forces in the adsorption on graphene. The outlook for the successful deposition of intact complexes on graphene surfaces requires the fine chemical tailoring of ligands, promoting adhesion on graphene, and utilizing chelation agents that protect the complex from detrimental effects such as atmospheric moisture, oxidation, and thermal decomposition. The next step after successful deposition is to obtain the magnetic properties of a thin film on the surface, which will be obtained from HF-ESR measurements or from X-ray magnetic circular dichroism (XMCD) at the synchrotron facility.

**Supplementary Materials:** The following are available online. Table S1: Comparison of Raman shift peaks (in  $\text{cm}^{-1}$ ) for drop-casting. Peak intensity is denoted as follows: strong—s, medium—m, and weak—w. Figure S1: AFM images from drop-cast and sublimated samples at 75 and 265 °C. Figure S2: Weak Co 2p peak from the drop-cast sample. Figure S3: Elemental percentage of atoms in powder from crucible after thermal sublimation at 75 and 265 °C. Deposition Number 2034425 (1) contains the supplementary crystallographic data for this paper.

**Author Contributions:** XPS, depositions, and writing—original manuscript, J.H.; AFM, Raman, and depositions, Š.V.; chemical synthesis and analytical characterization of ligand and complex, L.M.; HF-ESR experiments, A.S.; DFT calculations, J.N.-G.; graphene sample preparation, M.B.; CASSCF/NEVPT2, R.H.; crystal structure measurements, J.M.; XRD analysis and writing, I.N.; supervision, P.N. All authors have read and agreed to the published version of the manuscript.

**Funding:** This research was funded by the Ministry of Education, Youth and Sports of the Czech Republic: grant number CEITEC 2020 (LQ1601); LTAUSA19060 in the INTER-EXCELLENCE Programme; GAČR 19-01536S; the ERC under the European Union's Horizon 2020 Research and Innovation Programme (GA No. 714850); and an internal grant of Brno University of Technology CEITEC-VUT-J-20-6514, J.N.-G. is a holder of the Brno Ph.D. Talent Scholarship—Funded by the Brno City Municipality. R.H., I.N., and L.M. acknowledge financial support from the Palacký University Olomouc project IGA\_PrF\_2020\_016. J.M. acknowledges financial support for the structural analysis from the Grant Agencies of the Slovak Republic (VEGA 1/0639/18, APVV-19-0087).

**Acknowledgments:** J.H. acknowledges Tomáš Králevic Musálek and Radek Řihák (Activair, Czech Republic) for help with the design and manufacture of the custom UHV sublimation chamber. J.N.-G. acknowledges Davonne Henry and Amy Liu (Georgetown University, USA) for a fruitful discussion and support with DFT on surfaces.

**Conflicts of Interest:** The authors declare no conflict of interest.

## References

1. Caneschi, A.; Gatteschi, D.; Sessoli, R.; Barra, A.L.; Brunei, L.C.; Guillot, M. Alternating Current Susceptibility, High Field Magnetization, and Millimeter Band EPR Evidence for a Ground  $S=10$  State in  $[\text{Mn}_{12}\text{O}_{12}(\text{CH}_3\text{COO})_{16}(\text{H}_2\text{O})_4]\cdot 2\text{CH}_3\text{COOH}\cdot 4\text{H}_2\text{O}$ . *J. Am. Chem. Soc.* **1991**, *113*, 5873–5874. [[CrossRef](#)]
2. Sessoli, R.; Gatteschi, D.; Tsai, H.L.; Hendrickson, D.N.; Schake, A.R.; Wang, S.; Vincent, J.B.; Christou, G.; Folting, K. High-Spin Molecules:  $[\text{Mn}_{12}\text{O}_{12}(\text{O}_2\text{CR})_{16}(\text{H}_2\text{O})_4]$ . *J. Am. Chem. Soc.* **1993**, *115*, 1804–1816. [[CrossRef](#)]
3. Sessoli, R.; Gatteschi, D.; Caneschi, A.; Novak, M.A. Magnetic bistability in a metal-ion cluster. *Nature* **1993**, *365*, 141–143. [[CrossRef](#)]
4. Gatteschi, D.; Sessoli, R.; Villain, J. *Molecular Nanomagnets*, 1st ed.; Oxford University Press: Oxford, UK, 2007; ISBN 9780198567530.
5. Neese, F.; Pantazis, D.A. What is not required to make a single molecule magnet. *Faraday Discuss.* **2011**, *148*, 229–238. [[CrossRef](#)]
6. Ishikawa, N.; Sugita, M.; Ishikawa, T.; Koshihara, S.Y.; Kaizu, Y. Lanthanide double-decker complexes functioning as magnets at the single-molecular level. *J. Am. Chem. Soc.* **2003**, *125*, 8694–8695. [[CrossRef](#)]
7. Guo, F.-S.; Day, B.M.; Chen, Y.-C.; Tong, M.-L.; Mansikkamäki, A.; Layfield, R.A. Magnetic hysteresis up to 80 kelvin in a dysprosium metallocene single-molecule magnet. *Science* **2018**, *362*, 1400–1403. [[CrossRef](#)]
8. Wolf, S.A. Spintronics: A Spin-Based Electronics Vision for the Future. *Science* **2001**, *294*, 1488–1495. [[CrossRef](#)] [[PubMed](#)]
9. Leuenberger, M.N.; Loss, D. Quantum computing in molecular magnets. *Nature* **2001**, *410*, 789–793. [[CrossRef](#)]
10. Bogani, L.; Wernsdorfer, W. Molecular spintronics using single-molecule magnets. *Nat. Mater.* **2008**, *7*, 179–186. [[CrossRef](#)]

11. Barra, A.L.; Gatteschi, D.; Sessoli, R. High-frequency EPR spectra of a molecular nanomagnet: Understanding quantum tunneling of the magnetization. *Phys. Rev. B Condens. Matter Mater. Phys.* **1997**, *56*, 8192–8198. [[CrossRef](#)]
12. Barra, A.L.; Gatteschi, D.; Sessoli, R. High-frequency EPR spectra of [Fe<sub>8</sub>O<sub>2</sub>(OH)<sub>12</sub>(taCn)<sub>6</sub>]Br<sub>8</sub>: A critical appraisal of the barrier for the reorientation of the magnetization in single-molecule magnets. *Chem. Eur. J.* **2000**, *6*, 1608–1614. [[CrossRef](#)]
13. Barra, A.L. High-frequency EPR spectroscopy of single-molecule magnets: A case study. *Appl. Magn. Reson.* **2001**, *21*, 619–628. [[CrossRef](#)]
14. Krzystek, J.; Ozarowski, A.; Zvyagin, S.A.; Telser, J. High spin Co(I): High-frequency and -field EPR spectroscopy of CoX(PPh<sub>3</sub>)<sub>3</sub> (X = Cl, Br). *Inorg. Chem.* **2012**, *51*, 4954–4964. [[CrossRef](#)] [[PubMed](#)]
15. Rechkemmer, Y.; Fischer, J.E.; Marx, R.; Dörfel, M.; Neugebauer, P.; Horvath, S.; Gysler, M.; Brock-Nannestad, T.; Frey, W.; Reid, M.F.; et al. Comprehensive Spectroscopic Determination of the Crystal Field Splitting in an Erbium Single-Ion Magnet. *J. Am. Chem. Soc.* **2015**, *137*, 13114–13120. [[CrossRef](#)]
16. Realista, S.; Fitzpatrick, A.J.; Santos, G.; Ferreira, L.P.; Barroso, S.; Pereira, L.C.J.; Bandeira, N.A.G.; Neugebauer, P.; Hrubý, J.; Morgan, G.G.; et al. A Mn(III) single ion magnet with tridentate Schiff-base ligands. *Dalton Trans.* **2016**, *45*, 12301–12307. [[CrossRef](#)]
17. Kultaeva, A.; Biktagirov, T.; Neugebauer, P.; Bamberger, H.; Bergmann, J.; Van Slageren, J.; Krautscheid, H.; Pöpl, A. Multifrequency EPR, SQUID, and DFT Study of Cupric Ions and Their Magnetic Coupling in the Metal–Organic Framework Compound ∞<sup>3</sup>[Cu(prz-trz-ia)]. *J. Phys. Chem. C* **2018**, *122*, 26642–26651. [[CrossRef](#)]
18. Neugebauer, P.; Bloos, D.; Marx, R.; Lutz, P.; Kern, M.; Aguilà, D.; Vaverka, J.; Laguta, O.; Dietrich, C.; Clérac, R.; et al. Ultra-broadband EPR spectroscopy in field and frequency domains. *Phys. Chem. Chem. Phys.* **2018**, *20*, 15528–15534. [[CrossRef](#)]
19. Bucinsky, L.; Breza, M.; Malček, M.; Powers, D.C.; Hwang, S.J.; Krzystek, J.; Nocera, D.G.; Telser, J. High-Frequency and -Field EPR (HFEP) Investigation of a Pseudotetrahedral Cr IV Siloxide Complex and Computational Studies of Related Cr IV L<sub>4</sub> Systems. *Inorg. Chem.* **2019**, *58*, 4907–4920. [[CrossRef](#)]
20. Hrubý, J.; Dvořák, D.; Squillantini, L.; Mannini, M.; van Slageren, J.; Herchel, R.; Nemeč, I.; Neugebauer, P. Co(ii)-Based single-ion magnets with 1,1'-ferrocenediyl-bis(diphenylphosphine) metalloligands. *Dalton Trans.* **2020**, *2*, 11697–11707. [[CrossRef](#)]
21. Hrubý, J.; Santana, V.T.; Kostiučuk, D.; Bouček, M.; Lenz, S.; Kern, M.; Šiffalovič, P.; van Slageren, J.; Neugebauer, P. A graphene-based hybrid material with quantum bits prepared by the double Langmuir–Schaefer method. *RSC Adv.* **2019**, *9*, 24066–24073. [[CrossRef](#)]
22. Marie, L.S.; El Fatimy, A.; Hrubý, J.; Nemeč, I.; Hunt, J.; Myers-Ward, R.; Gaskill, D.K.; Kruskopf, M.; Yang, Y.; Elmquist, R.; et al. Nanostructured graphene for nanoscale electron paramagnetic resonance spectroscopy. *J. Phys. Mater.* **2020**, *3*, 014013. [[CrossRef](#)]
23. Ciccullo, F.; Glaser, M.; Sättele, M.S.; Lenz, S.; Neugebauer, P.; Rechkemmer, Y.; Van Slageren, J.; Casu, M.B. Thin film properties and stability of a potential molecular quantum bit based on copper(ii). *J. Mater. Chem. C* **2018**, *6*, 8028–8034. [[CrossRef](#)]
24. Holmberg, R.J.; Murugesu, M. Adhering magnetic molecules to surfaces. *J. Mater. Chem. C* **2015**, *3*, 11986–11998. [[CrossRef](#)]
25. Caneschi, A.; Gatteschi, D.; Totti, F. Molecular magnets and surfaces: A promising marriage. A DFT insight. *Coord. Chem. Rev.* **2015**, *289–290*, 357–378. [[CrossRef](#)]
26. Mannini, M.; Pineider, F.; Sainctavit, P.; Danieli, C.; Otero, E.; Sciancalepore, C.; Talarico, A.M.; Arrio, M.A.; Cornia, A.; Gatteschi, D.; et al. Magnetic memory of a single-molecule quantum magnet wired to a gold surface. *Nat. Mater.* **2009**, *8*, 194–197. [[CrossRef](#)]
27. Saywell, A.; Magnano, G.; Satterley, C.J.; Perdigão, L.M.A.; Britton, A.J.; Taleb, N.; Del Carmen Giménez-López, M.; Champness, N.R.; O’Shea, J.N.; Beton, P.H. Self-assembled aggregates formed by single-molecule magnets on a gold surface. *Nat. Commun.* **2010**, *1*, 75. [[CrossRef](#)]
28. Rozbořil, J.; Rechkemmer, Y.; Bloos, D.; Münz, F.; Wang, C.N.; Neugebauer, P.; Čechal, J.; Novák, J.; van Slageren, J. Magneto-optical investigations of molecular nanomagnet monolayers. *Dalton Trans.* **2016**, *45*, 7555–7558. [[CrossRef](#)]

29. Malavolti, L.; Lanzilotto, V.; Ninova, S.; Poggini, L.; Cimatti, I.; Cortigiani, B.; Margheriti, L.; Chiappe, D.; Otero, E.; Sainctavit, P.; et al. Magnetic bistability in a submonolayer of sublimated Fe<sub>4</sub> single-molecule magnets. *Nano Lett.* **2015**, *15*, 535–541. [[CrossRef](#)]
30. Kiefl, E.; Mannini, M.; Bernot, K.; Yi, X.; Amato, A.; Leviant, T.; Magnani, A.; Prokscha, T.; Suter, A.; Sessoli, R.; et al. Robust Magnetic Properties of a Sublimable Single-Molecule Magnet. *ACS Nano* **2016**, *10*, 5663–5669. [[CrossRef](#)]
31. Lanzilotto, V.; Malavolti, L.; Ninova, S.; Cimatti, I.; Poggini, L.; Cortigiani, B.; Mannini, M.; Totti, F.; Cornia, A.; Sessoli, R. The Challenge of Thermal Deposition of Coordination Compounds: Insight into the Case of an Fe<sub>4</sub> Single Molecule Magnet. *Chem. Mater.* **2016**, *28*, 7693–7702. [[CrossRef](#)]
32. Cañon-Mancisidor, W.; Miralles, S.G.; Baldoví, J.J.; Espallargas, G.M.; Gaita-Ariño, A.; Coronado, E. Sublimable Single Ion Magnets Based on Lanthanoid Quinolate Complexes: The Role of Intermolecular Interactions on Their Thermal Stability. *Inorg. Chem.* **2018**, *57*, 14170–14177. [[CrossRef](#)]
33. Miralles, S.G.; Bedoya-Pinto, A.; Baldoví, J.J.; Cañon-Mancisidor, W.; Prado, Y.; Prima-Garcia, H.; Gaita-Ariño, A.; Mínguez Espallargas, G.; Hueso, L.E.; Coronado, E. Sublimable chloroquinolate lanthanoid single-ion magnets deposited on ferromagnetic electrodes. *Chem. Sci.* **2018**, *9*, 199–208. [[CrossRef](#)]
34. Margheriti, L.; Mannini, M.; Sorace, L.; Gorini, L.; Gatteschi, D.; Caneschi, A.; Chiappe, D.; Moroni, R.; de Mongeot, F.B.; Cornia, A.; et al. Thermal Deposition of Intact Tetrairon(III) Single-Molecule Magnets in High-Vacuum Conditions. *Small* **2009**, *5*, 1460–1466. [[CrossRef](#)]
35. Geim, A.K.; Novoselov, K.S. The rise of graphene. *Nat. Mater.* **2007**, *6*, 183–191. [[CrossRef](#)]
36. Du, X.; Skachko, I.; Andrei, E.Y.; Barker, A. Approaching ballistic transport in suspended graphene. *Nat. Nanotechnol.* **2008**, *3*, 491–495. [[CrossRef](#)]
37. Neugebauer, P.; Orlita, M.; Faugeras, C.; Barra, A.L.; Potemski, M. How perfect can graphene be? *Phys. Rev. Lett.* **2009**, *103*, 136403. [[CrossRef](#)]
38. Lee, C.; Wei, X.; Kysar, J.W.; Hone, J. Measurement of the Elastic Properties and Intrinsic Strength of Monolayer Graphene. *Science* **2008**, *321*, 385–388. [[CrossRef](#)]
39. Seol, J.H.; Jo, I.; Moore, A.L.; Lindsay, L.; Aitken, Z.H.; Pettes, M.T.; Li, X.; Yao, Z.; Huang, R.; Broido, D.; et al. Two-dimensional phonon transport in supported graphene. *Science* **2010**, *328*, 213–216. [[CrossRef](#)]
40. Novoselov, K.S.S.; Geim, A.K.K.; Morozov, S.V.V.; Jiang, D.; Zhang, Y.; Dubonos, S.V.V.; Grigorieva, I.V.V.; Firsov, A.A.A. Electric Field Effect in Atomically Thin Carbon Films. *Science* **2004**, *306*, 666–669. [[CrossRef](#)]
41. Warner, J.H.; Mukai, M.; Kirkland, A.I. Atomic structure of ABC rhombohedral stacked trilayer graphene. *ACS Nano* **2012**, *6*, 5680–5686. [[CrossRef](#)]
42. VanMil, B.L.; Myers-Ward, R.L.; Tedesco, J.L.; Eddy, C.R., Jr.; Jernigan, G.G.; Culbertson, J.C.; Campbell, P.M.; McCrate, J.M.; Kitt, S.A.; Gaskill, D.K. Graphene Formation on SiC Substrates. *Mater. Sci. Forum* **2009**, *615–617*, 211–214. [[CrossRef](#)]
43. Coleman, J.N.; Lotya, M.; O'Neill, A.; Bergin, S.D.; King, P.J.; Khan, U.; Young, K.; Gaucher, A.; De, S.; Smith, R.J.; et al. Two-dimensional nanosheets produced by liquid exfoliation of layered materials. *Science* **2011**, *331*, 568–571. [[CrossRef](#)] [[PubMed](#)]
44. Bae, S.; Kim, H.; Lee, Y.; Xu, X.; Park, J.S.; Zheng, Y.; Balakrishnan, J.; Lei, T.; Ri Kim, H.; Song, Y.; et al. Roll-to-roll production of 30-inch graphene films for transparent electrodes. *Nat. Nanotechnol.* **2010**, *5*, 574–578. [[CrossRef](#)] [[PubMed](#)]
45. Atanasov, M.; Aravena, D.; Suturina, E.; Bill, E.; Maganas, D.; Neese, F. First principles approach to the electronic structure, magnetic anisotropy and spin relaxation in mononuclear 3d-transition metal single molecule magnets. *Coord. Chem. Rev.* **2015**, *289–290*, 177–214. [[CrossRef](#)]
46. *SHAPE, Version 2.1*; University of Barcelona: Barcelona, Spain, 2013.
47. Alvarez, S. Polyhedra in (inorganic) chemistry. *Dalton Trans.* **2005**, *13*, 2209–2233. [[CrossRef](#)]
48. Mankad, V.; Gupta, S.K.; Jha, P.K.; Ovsyuk, N.N.; Kachurin, G.A. Low-frequency Raman scattering from Si/Ge nanocrystals in different matrixes caused by acoustic phonon quantization. *J. Appl. Phys.* **2012**, *112*, 54318. [[CrossRef](#)]
49. Spizzirri, P.G.; Fang, J.H.; Rubanov, S.; Gauja, E.; Prawer, S. Nano-Raman spectroscopy of silicon surfaces. *arXiv* **2010**, arXiv:1002.2692.
50. Ferrari, A.C. Raman spectroscopy of graphene and graphite: Disorder, electron-phonon coupling, doping and nonadiabatic effects. *Solid State Commun.* **2007**, *143*, 47–57. [[CrossRef](#)]



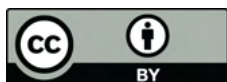
51. Akula, S.; Parthiban, V.; Peera, S.G.; Singh, B.P.; Dhakate, S.R.; Sahu, A.K. Simultaneous Co-Doping of Nitrogen and Fluorine into MWCNTs: An In-Situ Conversion to Graphene Like Sheets and Its Electro-Catalytic Activity toward Oxygen Reduction Reaction. *J. Electrochem. Soc.* **2017**, *164*, F568–F576. [[CrossRef](#)]
52. Fiedler, R.; Herzsuh, R. An XPS investigation of the effects of heat treatment on the chlorine surface chemistry of some lignites. *Fuel* **1993**, *72*, 1501–1505. [[CrossRef](#)]
53. Poneti, G.; Mannini, M.; Cortigiani, B.; Poggini, L.; Sorace, L.; Otero, E.; Sainctavit, P.; Sessoli, R.; Dei, A. Magnetic and spectroscopic investigation of thermally and optically driven valence tautomerism in thioether-bridged dinuclear cobalt-dioxolene complexes. *Inorg. Chem.* **2013**, *52*, 11798–11805. [[CrossRef](#)]
54. Kresse, G.; Hafner, J. Ab initio molecular dynamics for liquid metals. *Phys. Rev. B* **1993**, *47*, 558–561. [[CrossRef](#)]
55. Kresse, G.; Furthmüller, J. Efficiency of ab-initio total energy calculations for metals and semiconductors using a plane-wave basis set. *Comput. Mater. Sci.* **1996**, *6*, 15–50. [[CrossRef](#)]
56. Kresse, G.; Furthmüller, J. Efficient iterative schemes for ab initio total-energy calculations using a plane-wave basis set. *Phys. Rev. B Condens. Matter Mater. Phys.* **1996**, *54*, 11169–11186. [[CrossRef](#)] [[PubMed](#)]
57. Kresse, G.; Joubert, D. From ultrasoft pseudopotentials to the projector augmented-wave method. *Phys. Rev. B* **1999**, *59*, 1758–1775. [[CrossRef](#)]
58. Perdew, J.P.; Burke, K.; Ernzerhof, M. Generalized Gradient Approximation Made Simple. *Phys. Rev. Lett.* **1996**, *77*, 3865–3868. [[CrossRef](#)]
59. Perdew, J.P.; Burke, K.; Ernzerhof, M. Generalized Gradient Approximation Made Simple [Phys. Rev. Lett. *77*, 3865 (1996)]. *Phys. Rev. Lett.* **1997**, *78*, 1396. [[CrossRef](#)]
60. Neese, F. The ORCA program system. *Wiley Interdiscip. Rev. Comput. Mol. Sci.* **2012**, *2*, 73–78. [[CrossRef](#)]
61. Hussain, T.; Siddiqui, H.L.; Zia-ur-Rehman, M.; Masoom Yasinzi, M.; Parvez, M. Anti-oxidant, anti-fungal and anti-leishmanial activities of novel 3-[4-(1H-imidazol-1-yl) phenyl]prop-2-en-1-ones. *Eur. J. Med. Chem.* **2009**, *44*, 4654–4660. [[CrossRef](#)]
62. Masaryk, L.; Moncol, J.; Herchel, R.; Nemeč, I. Halogen Bonding in New Dichloride-Cobalt(II) Complex with Iodo Substituted Chalcone Ligands. *Crystals* **2020**, *10*, 354. [[CrossRef](#)]
63. Shirley, D.A. High-resolution x-ray photoemission spectrum of the valence bands of gold. *Phys. Rev. B* **1972**, *5*, 4709–4714. [[CrossRef](#)]
64. Yeh, J.J.; Lindau, I. Atomic subshell photoionization cross sections and asymmetry parameters:  $1 \leq Z \leq 103$ . *At. Data Nucl. Data Tables* **1985**, *32*, 1–155. [[CrossRef](#)]
65. Stoll, S.; Schweiger, A. EasySpin, a comprehensive software package for spectral simulation and analysis in EPR. *J. Magn. Reson.* **2006**, *178*, 42–55. [[CrossRef](#)]
66. Blöchl, P.E. Projector augmented-wave method. *Phys. Rev. B* **1994**, *50*, 17953–17979. [[CrossRef](#)] [[PubMed](#)]
67. Grimme, S. Semiempirical GGA-type density functional constructed with a long-range dispersion correction. *J. Comput. Chem.* **2006**, *27*, 1787–1799. [[CrossRef](#)]
68. Monkhorst, H.J.; Pack, J.D. Special points for Brillouin-zone integrations. *Phys. Rev. B* **1976**, *13*, 5188–5192. [[CrossRef](#)]
69. Neese, F. Software update: The ORCA program system, version 4.0. *Wiley Interdiscip. Rev. Comput. Mol. Sci.* **2018**, *8*, e1327. [[CrossRef](#)]
70. Weigend, F.; Ahlrichs, R. Balanced basis sets of split valence, triple zeta valence and quadruple zeta valence quality for H to Rn: Design and assessment of accuracy. *Phys. Chem. Chem. Phys.* **2005**, *7*, 3297–3305. [[CrossRef](#)]
71. Weigend, F. Accurate Coulomb-fitting basis sets for H to Rn. *Phys. Chem. Chem. Phys.* **2006**, *8*, 1057–1065. [[CrossRef](#)]
72. Hellweg, A.; Hättig, C.; Höfener, S.; Klopper, W. Optimized accurate auxiliary basis sets for RI-MP2 and RI-CC2 calculations for the atoms Rb to Rn. *Theor. Chem. Acc.* **2007**, *117*, 587–597. [[CrossRef](#)]
73. Malmqvist, P.Å.; Roos, B.O. The CASSCF state interaction method. *Chem. Phys. Lett.* **1989**, *155*, 189–194. [[CrossRef](#)]
74. Angeli, C.; Cimraglia, R.; Evangelisti, S.; Leininger, T.; Malrieu, J.P. Introduction of n-electron valence states for multireference perturbation theory. *J. Chem. Phys.* **2001**, *114*, 10252. [[CrossRef](#)]
75. Ganyushin, D.; Neese, F. First-principles calculations of zero-field splitting parameters. *J. Chem. Phys.* **2006**, *125*, 024103. [[CrossRef](#)] [[PubMed](#)]



76. Neese, F. Efficient and accurate approximations to the molecular spin-orbit coupling operator and their use in molecular g-tensor calculations. *J. Chem. Phys.* **2005**, *122*, 034107. [[CrossRef](#)] [[PubMed](#)]
77. Maurice, R.; Bastardis, R.; de Graaf, C.; Suaud, N.; Mallah, T.; Guihéry, N. Universal theoretical approach to extract anisotropic spin hamiltonians. *J. Chem. Theory Comput.* **2009**, *5*, 2977–2984. [[CrossRef](#)]
78. Palatinus, L.; Chapis, G. SUPERFLIP—A computer program for the solution of crystal structures by charge flipping in arbitrary dimensions. *J. Appl. Crystallogr.* **2007**, *40*, 786–790. [[CrossRef](#)]
79. Sheldrick, G.M. Crystal structure refinement with SHELXL. *Acta Crystallogr. Sect. C Struct. Chem.* **2015**, *71*, 3–8. [[CrossRef](#)]
80. Dolomanov, O.V.; Bourhis, L.J.; Gildea, R.J.; Howard, J.A.K.; Puschmann, H. OLEX2: A complete structure solution, refinement and analysis program. *J. Appl. Crystallogr.* **2009**, *42*, 339–341. [[CrossRef](#)]
81. MacRae, C.F.; Sovago, I.; Cottrell, S.J.; Galek, P.T.A.; McCabe, P.; Pidcock, E.; Platings, M.; Shields, G.P.; Stevens, J.S.; Towler, M.; et al. Mercury 4.0: From visualization to analysis, design and prediction. *J. Appl. Crystallogr.* **2020**, *53*, 226–235. [[CrossRef](#)]

**Sample Availability:** Samples are available from the authors upon request in limited amount.

**Publisher’s Note:** MDPI stays neutral with regard to jurisdictional claims in published maps and institutional affiliations.



© 2020 by the authors. Licensee MDPI, Basel, Switzerland. This article is an open access article distributed under the terms and conditions of the Creative Commons Attribution (CC BY) license (<http://creativecommons.org/licenses/by/4.0/>).

## Article

## Trigonally Distorted Hexacoordinate Co(II) Single-Ion Magnets

Ivan Nemeč<sup>1,2,\*</sup> , Ondřej F. Fellner<sup>1</sup> , Berenika Indruchová<sup>1</sup>  and Radovan Herchel<sup>1</sup> 

<sup>1</sup> Department of Inorganic Chemistry, Faculty of Science, Palacký University, 17. Listopadu 12, 77146 Olomouc, Czech Republic; ondrej.fellner01@upol.cz (O.F.F.); berenika.indruchova01@upol.cz (B.I.); radovan.herchel@upol.cz (R.H.)

<sup>2</sup> Central European Institute of Technology, Brno University of Technology, Purkynova 123, 61200 Brno, Czech Republic

\* Correspondence: ivan.nemec@upol.cz

**Abstract:** By simple reactions involving various cobalt(II) carboxylates (acetate and in situ prepared pivalate and 4-hydroxybenzoate salts) and neocuproine (neo), we were able to prepare three different carboxylate complexes with the general formula  $[\text{Co}(\text{neo})(\text{RCOO})_2]$  ( $\text{R} = -\text{CH}_3$  for **1**,  $(\text{CH}_3)_3\text{C}-$  for **2**, and  $4\text{OH}-\text{C}_6\text{H}_4-$  for **3**). The  $[\text{Co}(\text{neo})(\text{RCOO})_2]$  molecules in the crystal structures of **1–3** adopt a rather distorted coordination environment, with the largest trigonal distortion observed for **1**, whereas **2** and **3** are similarly distorted from ideal octahedral geometry. The combined theoretical and experimental investigations of magnetic properties revealed that the spin Hamiltonian formalism was not a valid approach and the L-S Hamiltonian had to be used to reveal very large magnetic anisotropies for **1–3**. The measurements of AC susceptibility showed that all three compounds exhibited slow-relaxation of magnetization in a weak external static magnetic field, and thus can be classified as field-induced single-ion magnets. It is noteworthy that **1** also exhibits a weak AC signal in a zero-external magnetic field.

**Keywords:** single-ion magnets; magnetic anisotropy; cobalt(II)



**Citation:** Nemeč, I.; Fellner, O.F.; Indruchová, B.; Herchel, R. Trigonally Distorted Hexacoordinate Co(II) Single-Ion Magnets. *Materials* **2022**, *15*, 1064. <https://doi.org/10.3390/ma15031064>

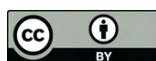
Academic Editor: Piotr Smoleński

Received: 4 December 2021

Accepted: 26 January 2022

Published: 29 January 2022

**Publisher's Note:** MDPI stays neutral with regard to jurisdictional claims in published maps and institutional affiliations.



**Copyright:** © 2022 by the authors. Licensee MDPI, Basel, Switzerland. This article is an open access article distributed under the terms and conditions of the Creative Commons Attribution (CC BY) license (<https://creativecommons.org/licenses/by/4.0/>).

## 1. Introduction

Hexacoordinate Co(II) complexes often tend to possess very large magnetic anisotropies arising from the direct contribution of spin orbit coupling to the ground state. If the coordination geometry is regular octahedron, the ground state is  ${}^4\text{T}_{1g}$ . Then, angular momentum is the main contributor to the zero-field splitting (ZFS), because the spin-orbit coupling operator transforms under  $t_{1g}$ , thus it directly mixes with the ground state. Magnetic anisotropy is then very large and of the easy-plane type [1], the classic spin Hamiltonian description loses validity, and low-lying excited states appear [2]. The design of highly anisotropic magnetic molecules exploits changing of the regular octahedral geometry, which can be achieved either by elongation/compression of the metal–ligand bonds or by trigonal distortion. Both types of distortion can lead to double orbitally degenerate ground states ( ${}^4\text{E}_g$  for compressed octahedron,  $\text{D}_{4h}$ ,  ${}^4\text{E}''$  for trigonal prism,  $\text{D}_{3h}$ ), manifesting themselves again by a large contribution of spin-orbit coupling to the ground state. However, contrary to the  ${}^4\text{T}_{1g}$  state [3,4], the anisotropy of E-states is of the axial character [5]. Thus, Co(II) complexes with doubly degenerate ground states are highly interesting for synthesis of single-ion magnets (SIMs), which are a class of single molecule magnets (SMMs) [6] containing only one paramagnetic center [7]. Among all SIMs based on 3d transition metal ions [8–15], those with trigonal prismatic environment around the Co(II) center have a special position, because they often exhibit slow relaxation of magnetization in the absence of an external magnetic field [16–22]. It must be noted that so-called zero-field SIMs (ZF-SIMs) are still very rare for complexes of 3d transition metals, which is because of the rather specific requirements needed for occurrence of ZF-SIMs; i.e., large and axial magnetic anisotropy with negligible rhombicity [23]. Thus, in line with the

matter discussed above, the trigonal Co(II) complexes with doubly degenerate ground state are ideal candidates for ZF-SIMs. Besides this class of Co(II) compounds, there are only a few examples of 3d metal based ZF-SIMs: linear two-coordinate Fe(I) [24,25], Co(II) [10] complexes, pentacoordinate Fe(III) [26], or tetra-coordinate Co(II) complexes [27–32].

In this paper, we focused our attention on trigonal distortion and, as the object of our research, we used very common carboxylate complexes [33] with one bidentate N-donor chelating ligand. Recently, we reported on two [Co(neo)(PhCOO)<sub>2</sub>] polymorphs (neo stands for neocuproine), which differed in their trigonal distortion and magnetic properties. Both compounds behaved as SIMs in a weak external magnetic field ( $B = 0.1$  T), so-called field-induced SIMs [34]. In the present paper, we show that, for [Co(neo)(RCOO)<sub>2</sub>] complexes, we can achieve a significant change in the trigonality of the coordination polyhedron by variation of carboxylate ligands (RCOO<sup>−</sup>). We report on the synthesis, crystal structure, and thorough experimental and theoretical investigation of static and dynamic magnetic properties of three new carboxylate complexes with the general formula [Co(neo)(RCOO)<sub>2</sub>], where RCOO<sup>−</sup> represents carboxylate ligands (acetate (**1**), pivalate (**2**), and 4-hydroxybenzoate (**3**)).

## 2. Materials and Methods

### 2.1. Materials

Co(NO<sub>3</sub>)<sub>2</sub>·6H<sub>2</sub>O, Co(ac)<sub>2</sub>·4H<sub>2</sub>O, neocuproine, sodium pivalate hydrate, sodium 4-hydroxybenzoate, and solvents (MeOH, diethyl ether (Et<sub>2</sub>O)) were supplied by VWR International (Stříbrná Skalice, Czech Republic), Sigma-Aldrich (Prague, Czech Republic), Lach-Ner (Neratovice, Czech Republic), and Litolab (Chudobín, Czech Republic).

### 2.2. Synthesis

#### 2.2.1. Complex [Co(neo)(ac)<sub>2</sub>] (**1**)

To the solution of Co(ac)<sub>2</sub>·4H<sub>2</sub>O (0.48 mmol, 120 mg) in 5 mL of methanol, 100 mg of neocuproine (0.48 mmol) was added. The solution was ultrasonicated for 15 min. The violet solution was filtered through a paper filter and crystallized by slow diffusion of Et<sub>2</sub>O in a closed flask. Then, 130 mg of **1** was isolated by filtration (yield = 70%) as violet crystals, which were dried in a desiccator under reduced pressure (overnight). IR (ATR,  $\nu$ , cm<sup>−1</sup>): 408 w, 437 w, 550 w, 618 w, 675 m, 733 w, 778 w, 813 w, 846 w, 865 m, 937 w, 1007 w, 1037 w, 1162 w, 1226 w, 1299 w, 1383 m, 1421 s, 1440 s, 1501 m, 1556 s, 1593 m, 1617 w, 3001 w, 3055 w.

#### 2.2.2. Complexes [Co(neo)(piv)<sub>2</sub>] (**2**) and [Co(neo)(4OH-benz)<sub>2</sub>]·2CH<sub>3</sub>OH (**3**)

Compounds **2** and **3** were both prepared using the following method. To the solution of Co(NO<sub>3</sub>)<sub>2</sub>·6H<sub>2</sub>O (70 mg, 0.24 mmol) in 15 mL of methanol, 50 mg of neocuproine (0.24 mmol) was added. The solution was heated up to 50 °C, then 2 molar equiv. of the corresponding sodium salt was added (60 mg of sodium pivalate hydrate, **2**; 77 mg of sodium 4-hydroxybenzoate, **3**). The violet solution was filtered through a paper filter and crystallized isothermally. Then, 49 mg (yield = 43%) of **2** and 52 mg of **3** (yield = 36%) were obtained as violet crystals a couple of days later. The crystals were dried in a desiccator under reduced pressure (overnight).

**2**: IR (ATR,  $\nu$ , cm<sup>−1</sup>): 355 m, 407 w, 551 w, 609 w, 656 w, 681 w, 733 w, 776 w, 791 w, 810 w, 864 w, 900 w, 940 w, 1002 w, 1032 w, 1157 w, 1225 m, 1297 w, 1359 m, 1377 w, 1421 s, 1457 w, 1486 s, 1503 m, 1533 m, 1593 m, 2865 w, 2926 w, 2967 w.

**3**: IR (ATR,  $\nu$ , cm<sup>−1</sup>): 406 w, 504 w, 549 w, 630 m, 658 w, 701 w, 728 w, 783 m, 855 m, 1030 m, 1099 w, 1142 w, 1166 m, 1227 m, 1284 m, 1373 s, 1396 s, 1503 m, 1534 w, 1568 w, 1593 s, 2818 w, 2907 w, 2937 w, 3059 w, 3352 w, 3462 w.

Elemental analysis: **1**, Mr = 550.4, C<sub>18</sub>H<sub>18</sub>CoN<sub>2</sub>O<sub>4</sub>, found: C, 56.28; H, 4.74; N, 7.25, requires C, 56.11; H, 4.71; N, 7.27%, **2**, Mr = 567.9, C<sub>24</sub>H<sub>30</sub>CoN<sub>2</sub>O<sub>4</sub>, found: C, 61.38; H, 6.52; N, 5.90, requires C, 61.40; H, 6.44; N, 5.97%, **3** (composition calculated for [Co(neo)(4OH-

benz)<sub>2</sub>·1.8 CH<sub>3</sub>OH),  $M_r = 661.9$ , C<sub>30</sub>H<sub>30</sub>CoN<sub>2</sub>O<sub>7.8</sub>, found: C, 59.46; H, 4.56; N, 4.97, requires C, 59.74; H, 4.91; N, 4.68.

### 2.3. General Methods

Elemental analysis was performed by a Flash 2000 CHNS Elemental Analyzer (Thermo Scientific, Waltham, MA, USA). A Jasco FT/IR-4700 spectrometer (Jasco, Easton, MD, USA) was used for the collection of the infrared (IR) spectra in the range of 400–4000 cm<sup>-1</sup> using the attenuated total reflection (ATR) technique on a diamond plate. The static magnetic data were measured on powdered samples pressed into pellets using a PPMS Dynacool (Quantum Design Inc., San Diego, CA, USA). The dynamic magnetic data were measured on powdered samples pressed into pellets stabilized by eicosane using a MPMS XL-7 Quantum Design SQUID magnetometer (Quantum Design Inc., San Diego, CA, USA).

### 2.4. X-ray Crystallography

Data collection for **1–3** was done using the standard rotational method on a D8 Quest diffractometer equipped with a Photon 100 CMOS detector (Bruker, Billerica, MA, USA) using the Mo-K $\alpha$  radiation ( $\lambda = 0.71073$  Å). Data collection, data reduction, and cell parameters refinements were performed using the Bruker Apex III software package [35]. The structures were solved by SHELXT [36] and all non-hydrogen atoms were refined anisotropically on F<sup>2</sup> using the full matrix least-squares procedure with Olex2.refine [37] in OLEX2 (version 1.5) [38]. All hydrogen atoms were found in differential Fourier maps and their parameters were refined using a riding model with  $U_{\text{iso}}(\text{H}) = 1.2(\text{CH})$  or  $1.5(-\text{CH}_3, -\text{OH})$   $U_{\text{eq}}$ . The molecular structures and packing diagram were drawn with MERCURY [39].

Powder diffraction data (Supplementary information, Figures S1–S3) were collected using a MiniFlex600 (Rigaku) equipped with the Bragg–Brentano geometry, and with iron-filtered Cu K $\alpha_{1,2}$  radiation.

## 3. Results and Discussion

### 3.1. Synthesis and Crystal Structure

Compound **1** was prepared by a direct reaction between Co(ac)<sub>2</sub>·4H<sub>2</sub>O and neo (molar ratio 1:1) in methanol. Compounds **2** and **3** were prepared in a very similar way, but Co(NO<sub>3</sub>)<sub>2</sub>·6H<sub>2</sub>O was used as the starting Co(II) compound and the corresponding sodium salts (NaRCOO) were used as a source of the carboxylate ligands. The reaction mixtures were prepared by dissolving Co(NO<sub>3</sub>)<sub>2</sub>·6H<sub>2</sub>O, neo, and NaRCOO in methanol (molar ratio of 1:1:2). These procedures proved to be good for the preparation of the crystalline products including single crystals useful for X-ray diffraction; however, the reaction yields were relatively low (30–50%).

Compounds **1–3** were isolated as violet crystals, which diffracted rather well, and we were able to determine crystal structures by single-crystal X-ray diffraction. The basic crystallographic data are summarized in Table 1. All compounds consist of the [Co(neo)(RCOO)<sub>2</sub>] complex molecules, only in **3** are two additional co-crystallized methanol molecules present in the asymmetric unit. The complex molecules are hexacoordinate, and all the ligands coordinate to the Co atom in a bidentate manner. The Co–N bonds adopt bond lengths between 2.08 and 2.13 Å, whereas the lengths of the Co–O bonds are more variable: 2.04–2.20 Å (Figure 1). The shapes of the coordination polyhedrons were evaluated using SHAPE algorithm and continuous shape measures (CSMs) [40]. We revealed that all the complex molecules possessed very large distortions from the ideal geometries. The coordination polyhedrons of **2** and **3** are closer to regular octahedral (O<sub>h</sub>) than trigonal prismatic geometry (D<sub>3h</sub>), with the following CSMs (O<sub>h</sub>, D<sub>3h</sub>): **2**; 6.352, 10.110, **3**. Complex **1** possesses the largest trigonal distortion and coordination geometry close to trigonal prism (11.893, 3.761, ESI Table S1).

than trigonal prismatic geometry ( $D_{3h}$ ), with the following CSMs ( $O_h, D_{3h}$ ): 7.650, 9.801, 2; 6.352, 10.110, 3. Complex 1 possesses the largest trigonal distortion and coordination geometry close to trigonal prism (11.893, 3.761, ESI Table S1).

Table 1. Crystallographic data for 1–3.

	1	2	3
Formula	$C_{18}H_{18}CoN_2O_4$	$C_{24}H_{30}CoN_2O_4$	$C_{30}H_{30}CoN_2O_8$
Formula weight	385.27	469.43	605.49
Crystal system	monoclinic	triclinic	monoclinic
Space group	$C2/c$	$P\bar{1}$	$P2_1/c$
Cell parameters	$C_{18}H_{18}CoN_2O_4$	$C_{24}H_{30}CoN_2O_4$	$C_{30}H_{30}CoN_2O_8$
Cell parameters	385.27	469.43	605.49
Crystal system	14.0976(17) monoclinic	9.5282(13) triclinic	9.922(4) monoclinic
Space group	$C2/c$	$P\bar{1}$	$P2_1/c$
Cell parameters	9.4555(12)	9.8422(13)	19.083(7)
$a/\text{Å}$	25.255(4)	14.4559(16)	15.191(6)
$b/\text{Å}$	14.0976(17)	9.5282(13)	9.922(4)
$\alpha/\text{deg}$	90	87.490(4)	90
$\beta/\text{deg}$	95.643(12)	9.8422(13)	19.083(7)
$\gamma/\text{deg}$	90	80.364(4)	91.457(14)
$V/\text{Å}^3$	3350.15(8)	62.028(4)	909
$Z$	8	1179.5(3)	4
Density, $D_c/\text{g cm}^{-3}$	1.528	1.322	1.399
Abs. coefficient, $\mu/\text{mm}^{-1}$	1.050	0.759	0.659
Data/restraints/params	2947/0/230	4629/566/422	5057/0/378
$R_1$	0.0412	0.0594	0.1207
$wR_2$	0.0730	0.1068	0.1847
$R_1^a$	0.0296	0.0411	0.0611
$wR_2^b$	0.0700	0.0999	0.1614
Goodness of fit	1.073	1.034	1.064
CSD number	2,126,276	2,126,278	2,126,275

<sup>a</sup>  $R_1 = \sum (|F_o| - |F_c|) / \sum |F_o|$ ; <sup>b</sup>  $wR_2 = \sqrt{\sum [w(F_o - F_c)^2] / \sum w(F_o)^2}$

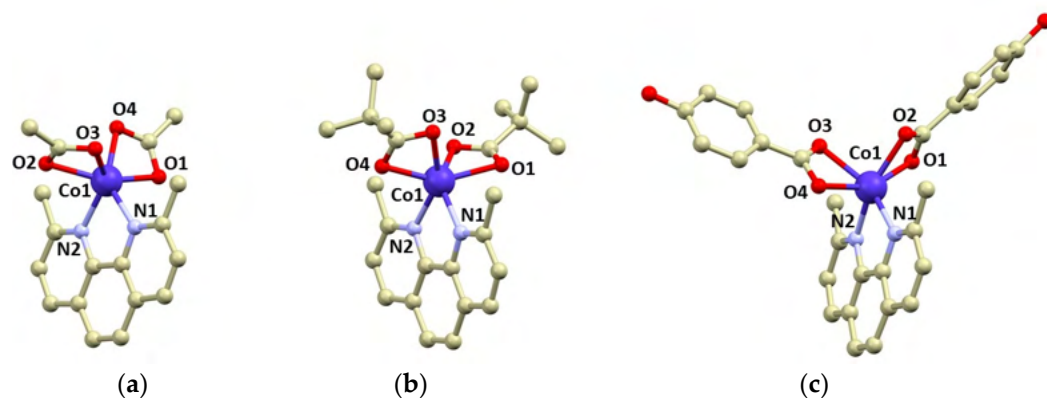


Figure 1. Molecular structures of complex molecules in the crystal structure of 1 (a), 2 (b) and 3 (c). Selected bond lengths (in Å): Co1–N1 = 2.105(2) in 1, 2.133(2) in 2, 2.130(4) in 3; Co1–N2 = 2.125(2) in 1, 2.118(2) in 2, 2.078(3) in 3; Co–O1 = 2.175(2) in 1, 2.198(9) in 2, 2.102(3) in 3; Co–O2 = 2.163(2) in 1, 2.150(9) in 2, 2.160(4) in 3; Co–O3 = 2.160(2) in 1, 2.149(3) in 2, 2.196(4) in 3; Co–O4 = 2.104(2) in 1, 2.119(6) in 2, 2.131(3) in 3.

The non-covalent interactions in 1–3 are mainly of weak nature, including C–H···O, C–H···π, and π···π interactions of the neo aromatic rings. Of note here is the crystal structure of 3, involving OH groups of the 4OH-benz ligands and co-crystallized molecules of methanol. These formed 2D networks of the molecules are interconnected by rather strong O–H···O hydrogen bonds with the donor–acceptor distances ranging between 2.65 and 2.85 Å (Figure S4) (Figure S4). Even such relatively strong non-covalent contacts did not sufficiently stabilize the crystal structure of 3. When the crystals were transferred outside of the mother-liquor, the solvent loss occurred upon drying and was accompanied by a loss of crystallinity and/or change in the unit cell parameters. Thus, at ambient conditions ( $T = 298\text{ K}$ ,  $p = 1\text{ atm}$ ), we were not able to unambiguously confirm the phase uniformity of 3, because the X-ray diffraction pattern of the dried 3 differed slightly from the pattern calculated from the single-crystal structure. Nevertheless, the experiments performed using grinded crystals of 3 immersed in a highly viscose crystallographic oil showed that, after



mother-liquor, the solvent loss occurred upon drying and was accompanied by a loss of crystallinity and/or change in the unit cell parameters. Thus, at ambient conditions ( $T = 298$  K,  $p = 1$  atm), we were not able to unambiguously confirm the phase uniformity of **3**, because the X-ray diffraction pattern of the dried **3** differed slightly from the pattern calculated from the single crystal structure. Nevertheless, the experiments performed using grinded crystals of **3** immersed in a highly viscose crystallographic oil showed that, after 1 h, the diffraction pattern underwent significant changes (Figure S3), which indicated that the batches of **3** we prepared were phase pure.

### 3.2. DC Magnetic Properties

The magnetic properties for **1–3** measured in a static magnetic field are depicted in Figure 2 as the temperature dependence of the effective magnetic moment and isothermal magnetization. Evidently, the profile of  $\mu_{\text{eff}}$  versus  $T$  is varied within the series owing to the variation of the geometry of the coordination polyhedra, and hence the ligand field. As there are negligible intermolecular interactions, the decrease in  $\mu_{\text{eff}}$  is attributed to the zero-field splitting/large magnetic anisotropy of these compounds. Indeed, this is also confirmed by the saturation values of  $M_{\text{mol}}$  of the isothermal magnetization curves well below the theoretical limit  $g \cdot S$ .

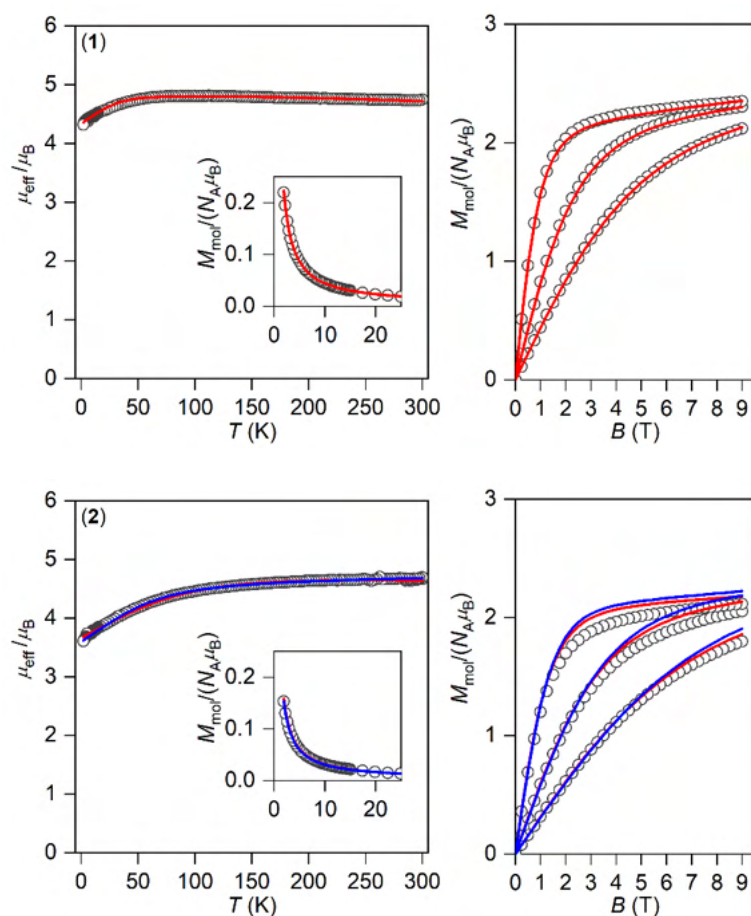
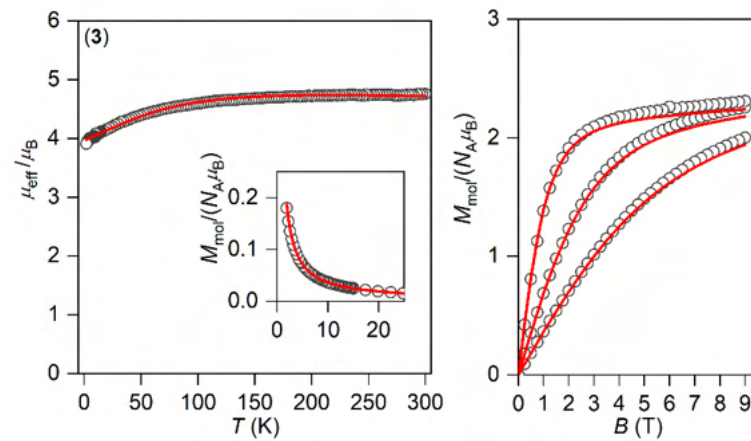


Figure 2. Cont.



**Figure 2.** The DC magnetic data for **1–3** shows the temperature dependence of the effective magnetic moment and isothermal molar magnetization measured at  $T = 2.75, 2.5, 5,$  and  $10$  K. The empty symbols represent the experimental data, the full lines represent the fitted data using Equation (1) with the Hamiltonian parameters in Table 2, and the red and blue lines correspond to the negative and positive value of  $\Delta_{ax}$ , respectively.

**Table 2.** The parameters of the Hamiltonian in Equation (1) derived from the experimental and calculated data.

Parameters	1	2 <sup>a</sup>		3
the analysis of DC data				
$\Delta_{ax}$ (cm <sup>-1</sup> )	-3317	the analysis of DC data		-1051
$\Delta_{rh}$ (cm <sup>-1</sup> )	-133	-23.6/32.5	523/810	-39.6
$\alpha$	1.66	1.04/1.25	1.04/1.25	1.21
$\lambda$ (cm <sup>-1</sup> )	-75.875.8	-167/-180	67/-180	-151
the analysis of CASSCF/NEVPT2 energy levels				
$\Delta_{ax}$ (cm <sup>-1</sup> )	-4322	-1703	-1703	-1641
$\Delta_{rh}$ (cm <sup>-1</sup> )	-465	-276	-276	-65.0
$\alpha; \lambda$ (cm <sup>-1</sup> )	-303	-251	-251	-256
the analysis of CASSCF/NEVPT2 magnetic data				
$\alpha$	1.98	1.55	1.55	1.67
$\lambda$ (cm <sup>-1</sup> )	-153	-162	-162	-153

<sup>a</sup> The parameters corresponds to the best-fit for the negative and positive value of  $\Delta_{ax}$ .

<sup>a</sup> The parameters corresponds to the best-fit for the negative and positive value of  $\Delta_{ax}$ .

Usually, the magnetic anisotropy is treated with the spin Hamiltonian comprising the zero-field splitting and Zeeman terms; however, hexacoordinate Co<sup>II</sup> complexes with the shape of the chromophore close to octahedron or trigonal prism possess orbital angular momentum, hence the spin Hamiltonian is inappropriate. This was confirmed by *ab initio* calculations that predicted magnetic behavior based on E ground state for **1** and low lying (below 1000 cm<sup>-1</sup>) excited states for **2** and **3**, both contradicting the use of spin Hamiltonian formalism [41] (*vide infra*).

Therefore, the DC magnetic data were analysed with the L-S Hamiltonian based on Griffith and Figgis [42–44], which describes the splitting of the <sup>4</sup>T<sub>1g</sub> term originating from the <sup>4</sup>F atomic term in lower symmetries than O<sub>h</sub> as follows:

$$\hat{H} = -\alpha \cdot \lambda \left( \vec{L} \cdot \vec{S} - \vec{L} \cdot \vec{L} \right) \lambda \left( \vec{S} \cdot \vec{L} \right) + \Delta_{ax} \left( \hat{L}_x^2 - \hat{L}_y^2 - \hat{L}_z^2 \right) + \Delta_{rh} \left( \hat{L}_x^2 - \hat{L}_y^2 \right) + \mu_B \vec{B} \cdot \left( g_L \vec{L} + g_S \vec{S} - \alpha \vec{L} \right) \quad (1)$$

The splitting of the <sup>4</sup>T<sub>1g</sub> term is described by  $\Delta_{ax}$  and  $\Delta_{rh}$  parameters;  $\alpha$  is an orbital reduction factor,  $\lambda$  is a spin-orbit coupling parameter, and  $g_S = 2.0023$ . Owing to the utilization of T<sub>1</sub>-P isomorphism, the angular orbital momentum  $L$  adopts the value of 1 with the effective Lande  $g$ -factor,  $g_L = -1$ . The Hamiltonian acts on  $|S, L, M_S, M_L\rangle$  functions with the effective Lande  $g$ -factor,  $g_L = -1$ . The Hamiltonian acts on  $|S, L, M_S, M_L\rangle$  functions

with  $M_L = 0, \pm 1$  and  $M_S = \pm 1/2, \pm 3/2$  [45]. Next, the orbital reduction factor embodies two parameters,  $\alpha = A\kappa$ , where  $A$  is the Figgis coefficient of the configuration interaction resulting from the admixture of the excited terms reflecting the ligand field strength, and  $\kappa$  describes the lowering orbital contribution due to covalency of the metal–ligand bond. Moreover, the spin-orbit coupling parameter  $\lambda$  can be reduced in comparison with its free-ion value  $\lambda_0 = -180 \text{ cm}^{-1}$ , which is attributable to the covalent character of the donor–acceptor bond.

The analysis encompasses both temperature- and field-dependent magnetic data and was done both for positive and negative values of  $\Delta_{ax}$  with the help of a program POLYMAGNET [46]. However, only in the case of compound **2** were reasonably good fits achieved for both signs of  $\Delta_{ax}$ , whereas the negative sign of  $\Delta_{ax}$  was found for **1** and **3**—Figure 2. The values of the fitted parameters are listed in Table 2. The negative values of the fitted  $\Delta_{ax}$  parameters resulted in the easy axis type of magnetic anisotropy, as visualized in the three-dimensional plots of molar magnetization—Figure S5. Such a type of magnetic anisotropy is essential for the formation of the spin reversal barrier needed for the observation of the Orbach type mechanism of the slow relaxation of magnetization. Moreover, the respective energy levels in the zero magnetic field are also plotted for **1–3** in Figure S5.

### 3.3. AC Magnetic Properties

The SMMs are generally characterized by the AC susceptibility measurements, evidencing the slow relaxation of magnetization. Therefore, first, the AC data were measured in the zero static magnetic field for **1–3**, but only in the case of **1** did we observe a very weak signal of the imaginary susceptibility ( $\chi''$ ). Thus, the data were also measured for a varying static magnetic field, which resulted in a clear observation of non-zero  $\chi''$  susceptibility—Figures S6–S8. Thus, the temperature and frequency AC susceptibility was measured at small  $B_{DC} = 0.1 \text{ T}$  to suppress the quantum tunneling of magnetization for **1–3**, which revealed frequency-dependent maxima of the imaginary susceptibility, thus confirming the slow relaxation of magnetization—Figures 3–5. The experimental data were analyzed with a program MIF&FIT [47] to the one component Debye’s model based on Equation (2):

$$\chi(\omega) = \frac{\chi_T - \chi_S}{1 + (i\omega\tau)^{1-\alpha}} + \chi_S \quad (2)$$

Such an analysis resulted in the values of isothermal ( $\chi_T$ ) and adiabatic ( $\chi_S$ ) susceptibilities, relaxation times ( $\tau$ ), and distribution parameters ( $\alpha$ ) for **1–3** (Tables S2–S4). For further analysis, only the data for which the fitted parameters were calculated with the standard deviation two times smaller than the value of the fitted parameter were considered. Afterwards, the temperature dependences of the relaxation times were analyzed with a model comprising the direct and Orbach mechanism:

$$\frac{1}{\tau} = AT + \frac{1}{\tau_0} \exp(U_{\text{eff}}/kT) \quad (3)$$

The fitted data are displayed in Figures 3–5 and the best-fit parameters are as follows:  $A = (6.52 \pm 0.62) \text{ K}^{-1}\text{s}^{-1}$ ,  $\tau_0 = (1.361 \pm 0.074) \times 10^{-7} \text{ s}$ , and  $U_{\text{eff}} = (37.7 \pm 0.25) \text{ K}$  for **1**;  $A = (471 \pm 29) \text{ K}^{-1}\text{s}^{-1}$ ,  $\tau_0 = (6.2 \pm 2.0) \times 10^{-6} \text{ s}$ , and  $U_{\text{eff}} = (19.0 \pm 0.74) \text{ K}$  for **2**;  $A = (2053 \pm 49) \text{ K}^{-1}\text{s}^{-1}$ ,  $\tau_0 = (1.04 \pm 0.31) \times 10^{-6} \text{ s}$ , and  $U_{\text{eff}} = (17.5 \pm 1.1) \text{ K}$  for **3**. The fitted values of  $U_{\text{eff}} = 26.2 \text{ cm}^{-1}$  for **1**,  $13.2 \text{ cm}^{-1}$  for **2**, and  $12.2 \text{ cm}^{-1}$  for **3** are smaller than the energy gaps between the first and the second Kramers doublets of  $\Delta = 82 \text{ cm}^{-1}$  for **1**,  $\Delta = 187/145 \text{ cm}^{-1}$  for **2**, and  $\Delta = 181 \text{ cm}^{-1}$  for **3** (Figure S5), but such a feature is typical for  $\text{Co}^{\text{II}}$  SMMs.

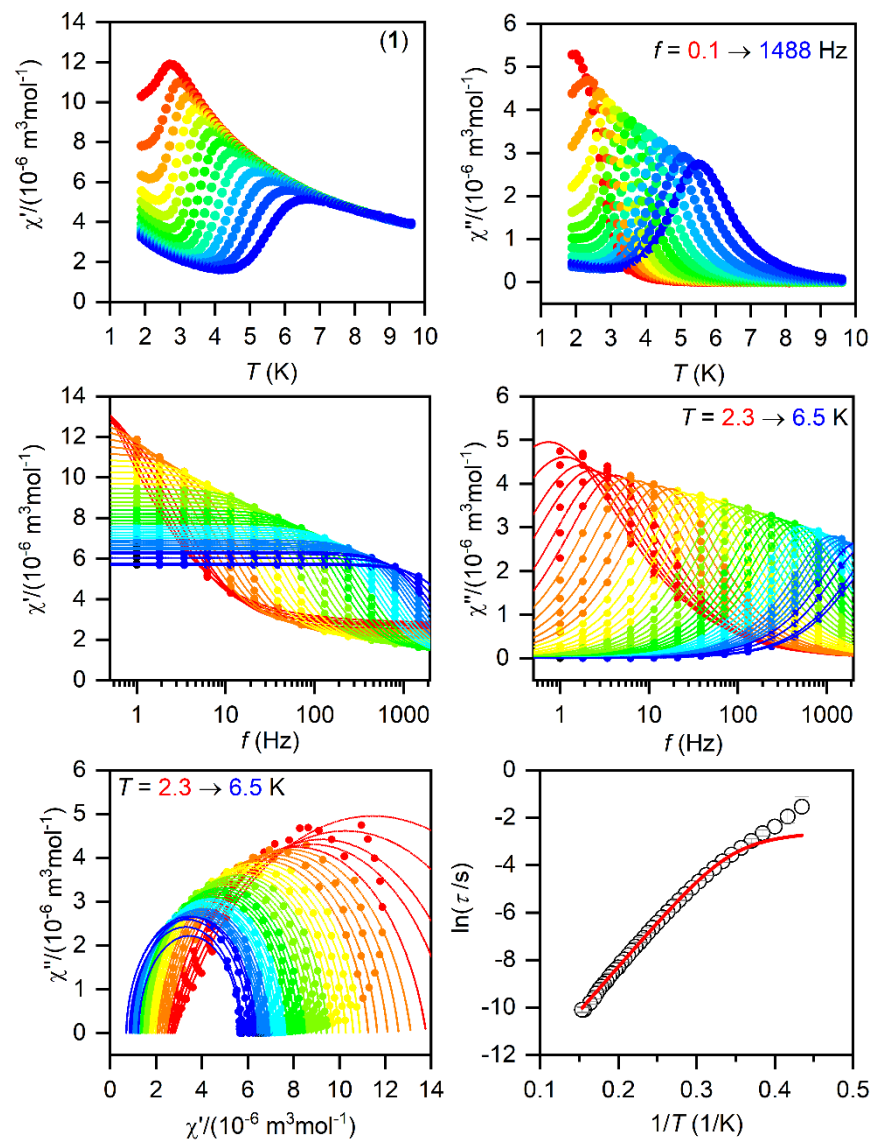


**Figure 3.** The AC magnetic data for **1**. Temperature dependence of the real ( $\chi'$ ) and imaginary ( $\chi''$ ) components of the AC susceptibility at the applied external magnetic field  $B_{DC} = 0.1$  T, for frequencies from 1 to 1500 Hz (full lines are only guides for eyes) (**top**). Frequency dependence of  $\chi'$  and  $\chi''$  components of the AC susceptibility at the applied external magnetic field  $B_{DC} = 0.1$  T, for frequencies from 1 to 1500 Hz (full lines are only guides for eyes) (**top**). Frequency dependence of molar susceptibilities fitted with one-component Debye's model using Equation (2) (full lines) (**middle**). The Argand (Cole-Cole) plot with full lines fitted with Equation (2) and, on the right, the fit of resulting relaxation times  $\tau$  with the direct + Orbach relaxation processes (red line) using Equation (3) (**bottom**).

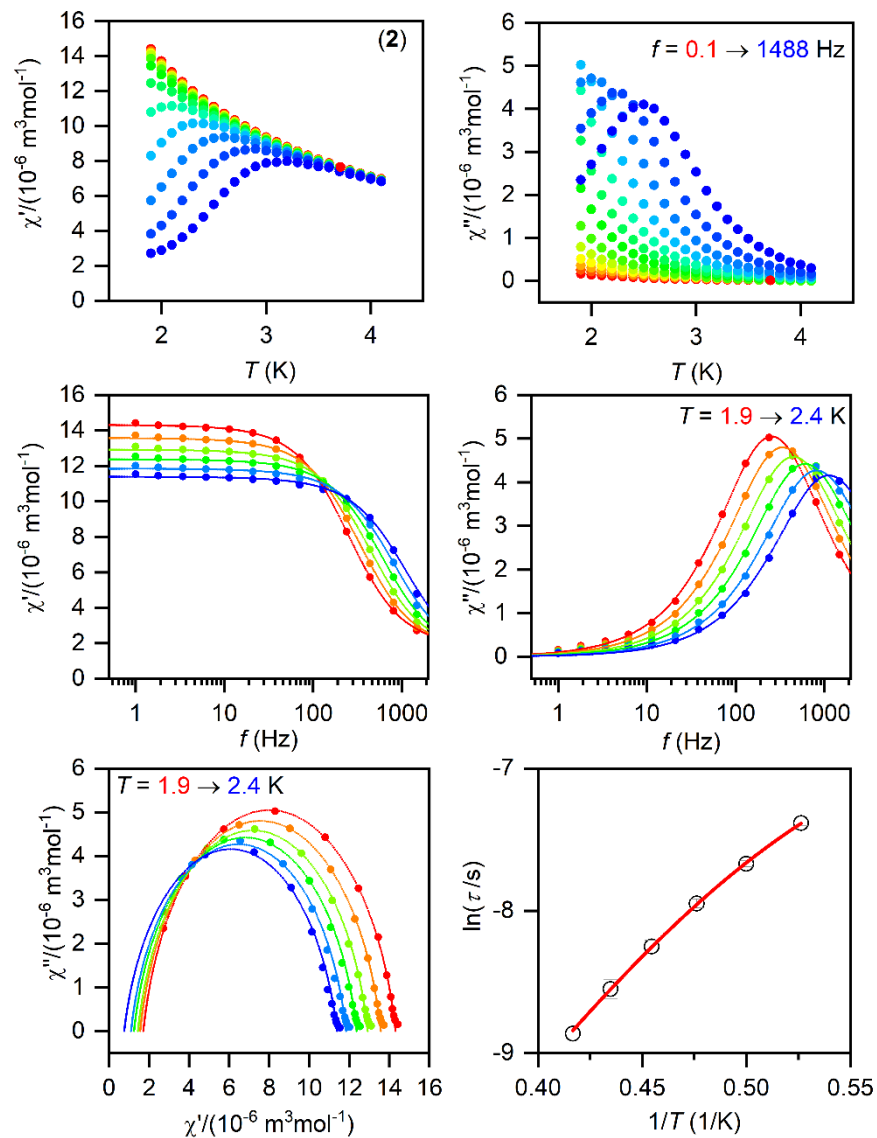


**Figure 4.** The AC magnetic data for 2. Temperature dependence of the real ( $\chi'$ ) and imaginary ( $\chi''$ ) components of the AC susceptibility at the applied external magnetic field  $B_{DC} = 0.1$  T for frequencies from 1 to 1500 Hz (full lines are only guides for eyes) (top). Frequency dependence of  $\chi'$  and  $\chi''$  molar susceptibilities fitted with one-component Debye's model using Equation (2) (full lines) (middle). The Argand (Cole-Cole) plot with full lines fitted with Equation (2) and, on the right, the fit of resulting relaxation times  $\tau$  with the direct + Orbach relaxation processes (red line) using Equation (3) (bottom).



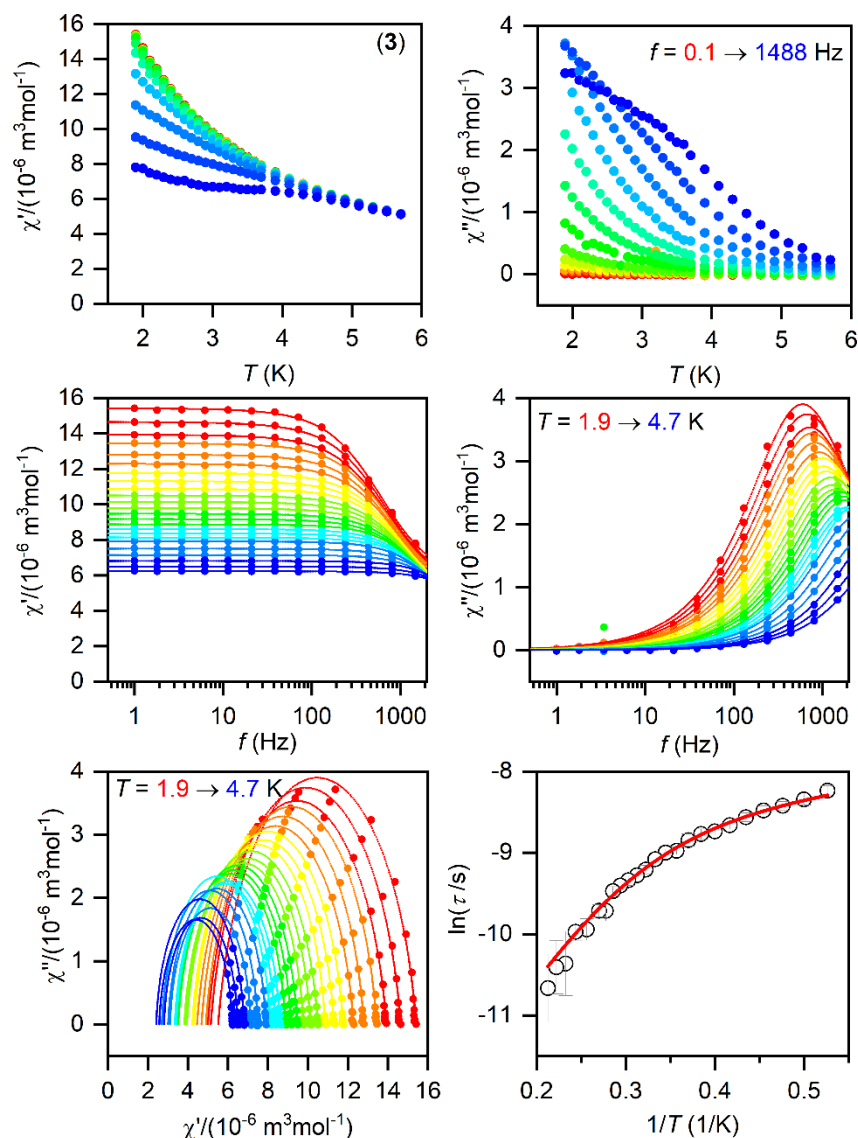


**Figure 5.** The AC magnetic data for **3**. Temperature dependence of the real ( $\chi'$ ) and imaginary ( $\chi''$ ) components of the AC susceptibility at the applied external magnetic field  $B_{DC} = 0.1$  T for frequencies from 1 to 1500 Hz (full lines are only guides for eyes) (**top**). Frequency dependence of  $\chi'$  and  $\chi''$  components of the AC susceptibility at the applied external magnetic field  $B_{DC} = 0.1$  T for frequencies from 1 to 1500 Hz (full lines are only guides for eyes) (**top**). Frequency dependence of molar susceptibilities fitted with one-component Debye's model using Equation (2) (full lines) (**middle**). The Argand (Cole-Cole) plot with full lines fitted with Equation (2) and, on the right, the fit of resulting relaxation times  $\tau$  with the direct + Orbach relaxation processes (red line) using Equation (3) (**bottom**).

### 3.4. Theoretical Calculations

#### 3.4. Theoretical Calculations

The electronic structure and magnetic properties of **1–3** were also studied by theoretical methods suitable for complexes with a multireference character. Therefore, the multireference calculations based on the state average complete active space self-consistent field (SA-CASSCF) [48] wave function method complemented by N-electron valence second-order perturbation theory (NEVPT2) [49,50] were conducted with an ORCA 5.0 computational package [51,52]. The experimental molecular structures were used, and just the positions of hydrogen atoms were normalized with Mercury software. The triple- $\zeta$  basis set def2-TZVP was used for all atoms except for carbon and hydrogen atoms, for which def2-SVP was applied [53]. The speed of the calculations was increased by using def2/J and def2-TZVP/C auxiliary basis sets [54,55], together with the chain-of-spheres (RJCOSX) approximation to exact exchange [56,57] as implemented in ORCA. The active space was defined by seven electrons in five d-orbitals of  $\text{Co}^{\text{II}}$  (CAS(7e,5o)), and all

possible in the d-orbitals of  $\text{Co}^{II}$  ( $d^7$ ), were all possible the multiplet sublevels and 40 of the levels were involved in the calculation [58,59] (equation (1) and the field theory (AHLFT) [58,59] was applied to calculate the splitting of d-orbitals for the case. Figure 6 is evident that splitting of d-orbitals for **1** is less the pattern typical for a trigonal prismatic ligand field, whereas the splitting for **2** resembles the gradual octahedral ligand field. This nicely demonstrates the gradual change in the ligand field symmetry within the series of **1-3**. Next, the deviations from ideal octahedral symmetry, but for **2** and **3** owing to their deviations from ideal  $O_h$  symmetry (0.930 in the case of **1** there is evidently a slightly ground term ( $0.930 \text{ cm}^{-1}$ ) belonging to  $D_{3h}$  as a symmetry (Figure 6 (middle)). It can be also interpreted as a large distortion of  $O_h$  symmetry, evidenced by the large splitting of the  $^4T_1$  also term spanning the energy interval of  $9 \times 10^3 \text{ cm}^{-1}$ . This is also interpreted in the splitting of the six lowest Kramers doublets (Figure 6, right), which is largest for **1**.

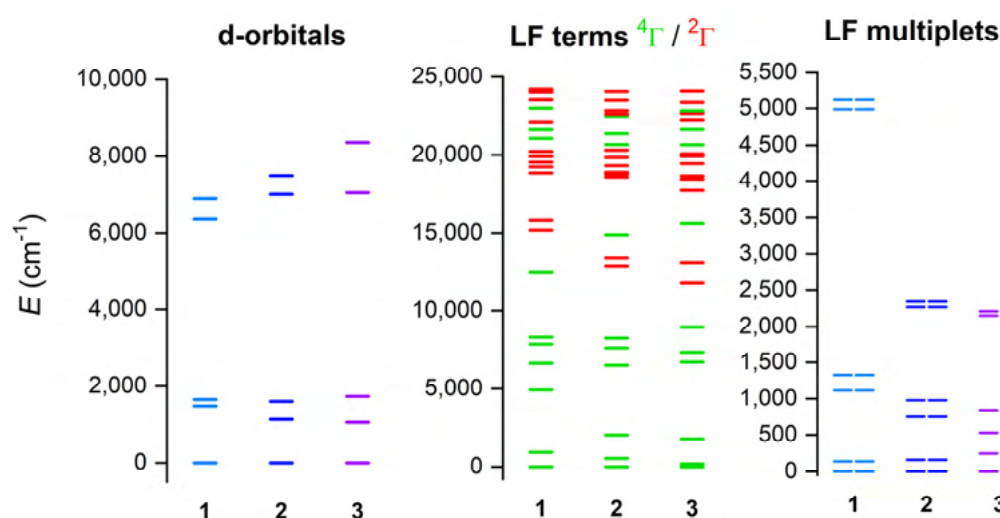


**Figure 6.** The outcome of the CASSCF/NEVPT2 calculations for complexes of **1-3**. Plot of d-orbital splitting, calculated by ab initio ligand field theory (AHLFT) (left), low-lying ligand-field terms (LFT) (middle), and ligand-field multiplets (LFM) (right). Note: different multiplicities of LFT are shown in a different color.

The energies of the six lowest Kramers doublets were used for the analysis of the parameters of the Hamiltonian in Equation (1). Such a procedure we applied for the first time in the investigation of the above mentioned  $\text{Co}^{II}$  (trigonal prismatic) complexes **1-3** and then also for other  $\text{Co}^{II}$  complexes [60]. This procedure resulted in the values of  $\Delta_{\text{ax}}$ ,  $\Delta_{\text{ax}}$ , which are listed in Table 2 graphically presented in Figure 9. However, this procedure has drawback as not possible to determine the values of  $\Delta_{\text{ax}}$  and  $\Delta_{\text{ax}}$  separately. To overcome this problem, calculated temperature and field dependent magnetization data directly in ORCA package resulting from CASSCF/NEVPT2 calculations and subsequently the magnetization data were fit to Equation (1), but fixed values of  $\Delta_{\text{ax}}$ ,  $\Delta_{\text{ax}}$ , which enable to determine the values of  $\Delta_{\text{ax}}$  and  $\Delta_{\text{ax}}$  listed in Table 2. The respective fits are depicted in Figure 10. There are clear trends visible from the calculated values:  $\Delta_{\text{ax}}$  and  $\Delta_{\text{ax}}$  are much larger for **1** than for **2-3**, evidencing the impact of the geometry change from the trigonal prismatic to the octahedral shape. We can also mention the possible source of discrepancy between the values of the Hamiltonian parameters derived from fitting of the experimental data and from CASSCF/NEVPT2 calculations. Firstly, the fitting of magnetic data is limited only to the temperature interval of 1.9–300 K, whereas the energy levels from Equation (1) span an interval of up to several thousand  $\text{cm}^{-1}/\text{K}$ , which means that the Boltzmann population of energetically higher Kramers doublets is negligible, and hence does not affect magnetic data. Secondly, the active space of theoretical calculations was limited to only five d-orbitals, thus, the ligand-based orbitals are missing

however, such calculations are usually not feasible for complexes with a large number of atoms.

Furthermore, the SINGLE\_ANISO module [63] now available in ORCA 5.0 was employed and the *ab initio* magnetization blocking barriers were computed for 1–3, as displayed in Figure 7. The corresponding matrix element of the transversal magnetic moment between the ground states with opposite magnetization is close to the value of 0.5 for 2–3 and thus is larger than 0.1, which suggests a large predisposition for the quantum tunneling of magnetization. On the contrary, the value of 0.088 for 1 is rather small. These results are in good agreement with the AC susceptibility data, where a weak non-zero out-of-phase signal in the zero magnetic field was observed only for 1, and applying the static magnetic field was necessary to observe the slow relaxation of magnetization for 2 and 3. The calculated energy barriers  $U$  are 140  $\text{cm}^{-1}$  for 1, 162  $\text{cm}^{-1}$  for 2, and 250  $\text{cm}^{-1}$  for 3, and reflect the alternation in the coordination polyhedron geometries.

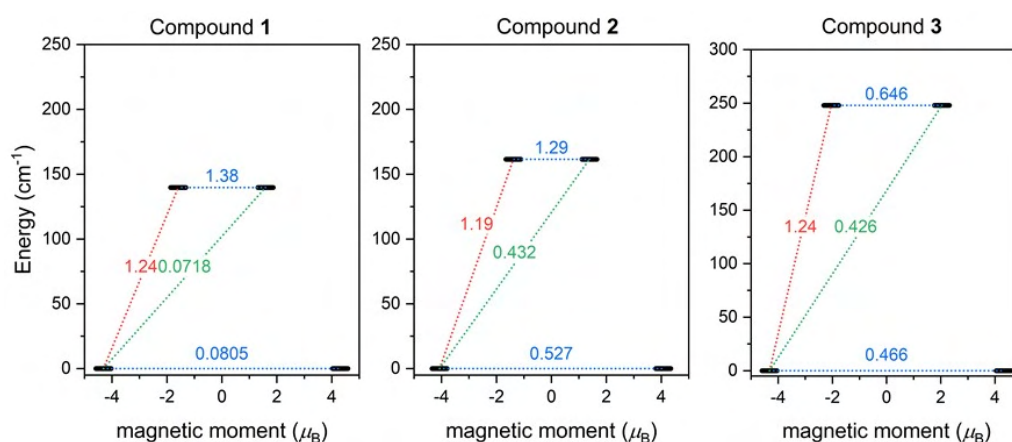


**Figure 7.** The outcome of SINGLE\_ANISO-CASSCF/NEVPT2 calculations for 1–3. The numbers presented in the plots represent the corresponding matrix element of the transversal magnetic moment (for values larger than 0.1, an efficient relaxation mechanism is expected). Dashed lines refer to (temperature-assisted) quantum tunneling (blue), Orbach/Raman mechanisms (red), and direct/Raman mechanisms (green) [64].

#### 4. Conclusions

In this report, we discussed the structure and magnetic properties of three compounds containing  $\text{Ce}(\text{OAc})_2(\text{RCOO})_2$  molecules (no. = neocuproine,  $\text{R} = \text{C}_6\text{H}_5$  for 1,  $\text{C}_6\text{H}_4$  for 2) and  $\text{Ce}(\text{OAc})_4$  for 3). All three complexes are hexacoordinate with distorted octahedral coordination environments rather distorted from ideal octahedron. Calculated continuous wave EPR spectra for 1 are close to trigonal prismatic geometry, whereas 2 and 3 adopt very distorted octahedral coordination environments. The magnetic properties were studied by AC and DC magnetometry, and it was revealed that very large magnetic anisotropy dominates the magnetic behavior of 1. *Ab initio* CASSCF/NEVPT2 calculations revealed that the origin of the large anisotropy in 1 is in the  $^4\text{F}_3$  ground state, whereas in 2 and 3, the large magnetic anisotropy arises from low-lying excited ligand field terms owing to the distorted hexacoordinate coordination geometry. The largest inter-Kramers doublet splitting was calculated for 3, the smallest was calculated for 1. This agrees rather well with the distorted regular octahedral geometry of the coordination polyhedra in these complexes (6.552 (763) (760) (1129) 931 (189)). AC susceptibility measurements revealed that the relaxation of magnetization in either the static or the dynamic field is observed as a weak signal in the out-of-phase component of the AC susceptibility for 1, and only for 2 and 3, and the slow relaxation of magnetization in the static magnetic field (DC field) and other slow relaxation time of magnetization in the AC field for 1 and 3. The field-induced single-ion magnetism in 1 and 3, largest  $U$  has 250  $\text{cm}^{-1}$ . SINGLE\_ANISO calculations revealed that



$|3/2, +3/2\rangle \leftrightarrow |3/2, -3/2\rangle$  quantum tunneling is the lowest for **1**, whereas in **2** and **3**, it should be the dominant relaxation process in the absence of the external magnetic field. This agrees rather well with the experimental observations presented in this report and, furthermore, it underlines the importance of trigonal coordination geometry (as in **1**) for the preparation of Co(II) zero-field SIMs.

**Supplementary Materials:** The following are available online at <https://www.mdpi.com/article/10.3390/ma15031064/s1>, Figure S1: XRPD data for (1); Figure S2: XRPD data for (2); Figure S3: XRPD data for (3); Figure S4: A perspective view on a 2D network; Figure S5: The three-dimensional plot of molar magnetization; Figure S6: In-phase  $\chi_{\text{real}}$  and out-of-phase  $\chi_{\text{imag}}$  molar susceptibilities for 1; Figure S7: In-phase  $\chi_{\text{real}}$  and out-of-phase  $\chi_{\text{imag}}$  molar susceptibilities for 2; Figure S8: In-phase  $\chi_{\text{real}}$  and out-of-phase  $\chi_{\text{imag}}$  molar susceptibilities for 3; Figure S9: The low-lying ligand-field multiplets originating from the  $^4T_{1g}$  state of 1–3; Figure S10: The analysis of the magnetic data calculated from CASSCF/NEVPT2 calculations; Table S1: The results of SHAPE calculation for 1–3; Table S2: Parameters of one-component Debye’s model for 1; Table S3: Parameters of one-component Debye’s model for 2; Table S4: Parameters of one-component Debye’s model for 3.

**Author Contributions:** Conceptualization, I.N.; methodology, I.N. and R.H.; formal analysis, I.N. and R.H.; investigation, I.N., O.F.F., B.I. and R.H.; writing—original draft preparation, I.N. and R.H.; writing—review and editing, I.N., O.F.F. and R.H. All authors have read and agreed to the published version of the manuscript.

**Funding:** This research was funded by the institutional sources of the Department of Inorganic Chemistry, Palacký University Olomouc, Czech Republic, LTAUSA19060 in the INTER-EXCELLENCE programme and the ERC under the European Union’s Horizon 2020 research and innovation programme (GA No 714850).

**Institutional Review Board Statement:** Not applicable.

**Informed Consent Statement:** Not applicable.

**Data Availability Statement:** All data contained within the article.

**Conflicts of Interest:** The authors declare no conflict of interest.

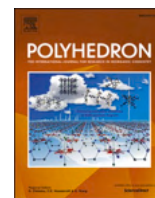
## References

1. Boča, R. *Theoretical Foundations of Molecular Magnetism*; Elsevier: Amsterdam, The Netherlands, 1999; p. 873.
2. Pavlov, A.A.; Nehrkor, J.; Zubkevich, S.V.; Fedin, M.V.; Holldack, K.; Schnegg, A.; Novikov, V.V. A Synergy and Struggle of EPR, Magnetometry and NMR: A Case Study of Magnetic Interaction Parameters in a Six-Coordinate Cobalt (II) Complex. *Inorg. Chem.* **2020**, *59*, 10746–10755. [[CrossRef](#)] [[PubMed](#)]
3. Matos, C.R.M.O.; Sarmiento, C.V.; Silva, H.C.; Ferreira, G.B.; Guedes, G.P.; Nunes, W.C.; Ronconi, C.M. Field-induced single-ion magnets exhibiting tri-axial anisotropy in a 1D Co (ii) coordination polymer with a rigid ligand 4,4'-(buta-1,3-diyne-1,4-diyl)dibenzoate. *Dalton Trans.* **2021**, *50*, 15003–15014. [[CrossRef](#)] [[PubMed](#)]
4. Świtlicka, A.; Palion-Gazda, J.; Machura, B.; Cano, J.; Lloret, F.; Julve, M. Field-induced slow magnetic relaxation in pseudooctahedral cobalt (II) complexes with positive axial and large rhombic anisotropy. *Dalton Trans.* **2019**, *48*, 1404–1417. [[CrossRef](#)] [[PubMed](#)]
5. Gómez-Coca, S.; Aravena, D.; Morales, R.; Ruiz, E. Large Magnetic Anisotropy in Mononuclear Metal Complexes. *Coord. Chem. Rev.* **2015**, *289–290*, 379–392. [[CrossRef](#)]
6. Ganzhorn, M.; Wernsdorfer, W. *Molecular Magnets*; Bartolome, J., Luis, F., Fernandez, J.F., Eds.; Springer: Berlin/Heidelberg, Germany, 2014; pp. 319–364.
7. Frost, J.M.; Harriman, K.L.M.; Murugesu, M. The Rise of 3-d Single-Ion Magnets in Molecular Magnetism: Towards Materials from Molecules? *Chem. Sci.* **2016**, *7*, 2470–2491. [[CrossRef](#)] [[PubMed](#)]
8. Craig, G.A.; Murrie, M. 3d Single-Ion Magnets. *Chem. Soc. Rev.* **2015**, *44*, 2135–2147. [[CrossRef](#)]
9. Yao, X.N.; Du, J.Z.; Zhang, Y.Q.; Leng, X.B.; Yang, M.W.; Jiang, S.; Wang, Z.X.; Ouyang, Z.W.; Deng, L.; Wang, B.W.; et al. Two-Coordinate Co (II) Imido Complexes as Outstanding Single-Molecule Magnets. *J. Am. Chem. Soc.* **2017**, *139*, 373–380. [[CrossRef](#)]
10. Bunting, P.C.; Atanasov, M.; Damgaard-Møller, E.; Perfetti, M.; Crassee, I.; Orlita, M.; Overgaard, J.; Slageren, J.; Neese, F.; Long, J.R. A Linear Cobalt (II) Complex with Maximal Orbital Angular Momentum from a Non-Aufbau Ground State. *Science* **2018**, *362*, eaat7319. [[CrossRef](#)]
11. Deng, Y.F.; Wang, Z.; Ouyang, Z.W.; Yin, B.; Zheng, Z.; Zheng, Y.Z. Large Easy-Plane Magnetic Anisotropy in a Three-Coordinate Cobalt (II) Complex [Li(THF)<sub>4</sub>][Co(NPh<sub>2</sub>)<sub>3</sub>]. *Chem. Eur. J.* **2016**, *22*, 14821–14825. [[CrossRef](#)]

12. Das, C.; Rasamsetty, A.; Tripathi, S.; Shanmugam, M. Magnetization Relaxation Dynamics of a Rare Coordinatively Unsaturated Co(II) Complex: Experimental and Theoretical Insights. *Chem. Comm.* **2020**, *56*, 13397–13400. [[CrossRef](#)]
13. Chen, Y.; Yang, Q.; Peng, G.; Zhang, Y.Q.; Ren, X.M. Influence of F-Position and Solvent on Coordination Geometry and Single Ion Magnet Behavior of Co (II) Complexes. *Dalton Trans.* **2021**, *50*, 13830–13840. [[CrossRef](#)] [[PubMed](#)]
14. Cui, H.H.; Lu, F.; Chen, X.T.; Zhang, Y.Q.; Tong, W.; Xue, Z.L. Zero-Field Slow Magnetic Relaxation and Hysteresis Loop in Four-Coordinate CoII Single-Ion Magnets with Strong Easy-Axis Anisotropy. *Inorg. Chem.* **2019**, *58*, 12555–12564. [[CrossRef](#)] [[PubMed](#)]
15. Tripathi, S.; Vaidya, S.; Ansari, K.U.; Ahmed, N.; Rivière, E.; Spillecke, L.; Koo, C.; Klingeler, R.; Mallah, T.; Rajaraman, G.; et al. Influence of a Counteranion on the Zero-Field Splitting of Tetrahedral Cobalt(II) Thiourea Complexes. *Inorg. Chem.* **2019**, *58*, 9085–9100. [[CrossRef](#)] [[PubMed](#)]
16. Novikov, V.V.; Pavlov, A.A.; Nelyubina, Y.V.; Boulon, M.-E.; Varzatskii, O.A.; Voloshin, Y.Z.; Winpenny, R.E.P. A Trigonal Prismatic Mononuclear Cobalt (II) Complex Showing Single-Molecule Magnet Behavior. *J. Am. Chem. Soc.* **2015**, *137*, 9792–9795. [[CrossRef](#)] [[PubMed](#)]
17. Pavlov, A.A.; Nelyubina, Y.V.; Kats, S.V.; Penkova, L.V.; Efimov, N.N.; Dmitrienko, A.O.; Vologzhanina, A.V.; Belov, A.S.; Voloshin, Y.Z.; Novikov, V.V. Polymorphism in a Cobalt-Based Single-Ion Magnet Tuning Its Barrier to Magnetization Relaxation. *J. Phys. Chem. Lett.* **2016**, *7*, 4111–4116. [[CrossRef](#)]
18. Gomez-Coca, S.; Cremades, E.; Aliaga-Alcalde, N.; Ruiz, E. Mononuclear Single-Molecule Magnets: Tailoring the Magnetic Anisotropy of First-Row Transition-Metal Complexes. *J. Am. Chem. Soc.* **2013**, *135*, 7010–7018. [[CrossRef](#)]
19. Ozumerzifon, T.J.; Bhowmick, I.; Spaller, W.C.; Rappé, A.K.; Shores, M.P. Toward Steric Control of Guest Binding Modality: A Cationic Co (II) Complex Exhibiting Cation Binding and Zero-Field Relaxation. *Chem. Comm.* **2017**, *53*, 4211–4214. [[CrossRef](#)]
20. Yao, B.; Deng, Y.-F.; Li, T.; Xiong, J.; Wang, B.-W.; Zheng, Z.; Zhang, Y.-Z. Construction and Magnetic Study of a Trigonal-Prismatic Cobalt (II) Single-Ion Magnet. *Inorg. Chem.* **2018**, *57*, 14047–14051. [[CrossRef](#)]
21. Zhu, Y.Y.; Cui, C.; Zhang, Y.Q.; Jia, J.H.; Guo, X.; Gao, C.; Qian, K.; Jiang, S.; Wang, B.W.; Wang, Z.M.; et al. Zero-Field Slow Magnetic Relaxation from Single Co (II) Ion: A Transition Metal Single-Molecule Magnet with High Anisotropy Barrier. *Chem. Sci.* **2013**, *4*, 1802–1806. [[CrossRef](#)]
22. Yao, B.; Singh, M.K.; Deng, Y.F.; Wang, Y.N.; Dunbar, K.R.; Zhang, Y.Z. Trigonal Prismatic Cobalt (II) Single-Ion Magnets: Manipulating the Magnetic Relaxation through Symmetry Control. *Inorg. Chem.* **2020**, *59*, 8505–8513. [[CrossRef](#)]
23. Feng, M.; Tong, M.-L. Single Ion Magnets from 3d to 5f: Developments and Strategies. *Chem. Eur. J.* **2018**, *24*, 7574–7594. [[CrossRef](#)] [[PubMed](#)]
24. Zadrozny, J.M.; Xiao, D.J.; Atanasov, M.; Long, G.J.; Grandjean, F.; Neese, F.; Long, J.R. Magnetic blocking in a linear iron (I) complex. *Nat. Chem.* **2013**, *5*, 577–581. [[CrossRef](#)] [[PubMed](#)]
25. Werncke, G.C.; Bunting, P.C.; Duhayon, C.; Long, J.R.; Bontemps, S.; Sabo-Etienne, S. Two-Coordinate Iron (I) Complex [Fe(N(SiMe<sub>3</sub>)<sub>2</sub>)<sub>2</sub>]: Synthesis, Properties, and Redox Activity. *Angew. Chem. Int. Ed.* **2015**, *54*, 245–248. [[CrossRef](#)] [[PubMed](#)]
26. Mossin, S.; Tran, B.L.; Adhikari, D.; Pink, M.; Heinemann, F.W.; Sutter, J.; Szilagyi, R.K.; Meyer, K.; Mindiola, D.J. A Mononuclear Fe (III) Single Molecule Magnet with a 3/2↔5/2 Spin Crossover. *J. Am. Chem. Soc.* **2012**, *134*, 13651–13661. [[CrossRef](#)] [[PubMed](#)]
27. Rechkemmer, Y.; Breitgoff, F.D.; van der Meer, M.; Atanasov, M.; Hakl, M.; Orlita, M.; Neugebauer, P.; Neese, F.; Sarkar, B.; van Slageren, J. A Four-Coordinate Cobalt (II) Single-Ion Magnet with Coercivity and a Very High Energy Barrier. *Nat. Commun.* **2016**, *7*, 10467. [[CrossRef](#)] [[PubMed](#)]
28. Fataftah, M.S.; Zadrozny, J.M.; Rogers, D.M.; Freedman, D.E. A Mononuclear Transition Metal Single-Molecule Magnet in a Nuclear Spin-Free Ligand Environment. *Inorg. Chem.* **2014**, *53*, 10716–10721. [[CrossRef](#)] [[PubMed](#)]
29. Vaidya, S.; Tewary, S.; Singh, S.K.; Langley, S.K.; Murray, K.S.; Lan, Y.; Wernsdorfer, W.; Rajaraman, G.; Shanmugam, M. What Controls the Sign and Magnitude of Magnetic Anisotropy in Tetrahedral Cobalt(II) Single-Ion Magnets? *Inorg. Chem.* **2016**, *55*, 9564–9578. [[CrossRef](#)] [[PubMed](#)]
30. Tu, D.; Shao, D.; Yan, H.; Lu, C. A Carborane-Incorporated Mononuclear Co(II) Complex Showing Zero-Field Slow Magnetic Relaxation. *Chem. Comm* **2016**, *52*, 14326–14329. [[CrossRef](#)]
31. Yao, X.N.; Yang, M.W.; Xiong, J.; Liu, J.J.; Gao, C.; Meng, Y.S.; Jiang, S.D.; Wang, B.W.; Gao, S. Enhanced Magnetic Anisotropy in a Tellurium-Coordinated Cobalt Single-Ion Magnet. *Inorg. Chem. Front.* **2017**, *4*, 701–705. [[CrossRef](#)]
32. Zadrozny, J.M.; Long, J.R. Slow Magnetic Relaxation at Zero Field in the Tetrahedral Complex [Co(SPh)<sub>4</sub>]<sub>2</sub><sup>-</sup>. *J. Am. Chem. Soc.* **2011**, *133*, 20732–20734. [[CrossRef](#)]
33. Ye, B.H.; Tong, M.L.; Chen, X.M. Metal-Organic Molecular Architectures with 2,2'-Bipyridyl-like and Carboxylate Ligands. *Coord. Chem. Rev.* **2005**, *249*, 545–565. [[CrossRef](#)]
34. Nemeč, I.; Herchel, R.; Trávníček, Z. Two polymorphic Co (ii) field-induced single-ion magnets with enormous angular distortion from the ideal octahedron. *Dalton Trans.* **2018**, *47*, 1614–1623. [[CrossRef](#)] [[PubMed](#)]
35. Bruker. APEX3; Bruker AXS Inc.: Madison, WI, USA, 2015.
36. Sheldrick, G.M. Crystal Structure Refinement with SHELXL. *Acta Crystallogr.* **2015**, *71*, 3–8. [[CrossRef](#)]
37. Bourhis, L.J.; Dolomanov, O.V.; Gildea, R.J.; Howard, J.A.K.; Puschmann, H. The Anatomy of a Comprehensive Constrained, Restrained Refinement Program for the Modern Computing Environment—Olex2. *Acta Crystallogr.* **2015**, *71*, 59–75. [[CrossRef](#)]
38. Dolomanov, O.V.; Bourhis, L.J.; Gildea, R.J.; Howard, J.A.K.; Puschmann, H. IUCr OLEX2: A Complete Structure Solution, Refinement and Analysis Program. *J. Appl. Crystallogr.* **2009**, *42*, 339–341. [[CrossRef](#)]



39. Macrae, C.F.; Sovago, I.; Cottrell, S.J.; Galek, P.T.A.; McCabe, P.; Pidcock, E.; Platings, M.; Shields, G.P.; Stevens, J.S.; Towler, M.; et al. Mercury 4.0: From Visualization to Analysis, Design and Prediction. *J. Appl. Crystallogr.* **2020**, *53*, 226–235. [[CrossRef](#)] [[PubMed](#)]
40. Alvarez, S. Polyhedra in (Inorganic) Chemistry. *Dalton Trans.* **2005**, 2209–2233. [[CrossRef](#)]
41. Misochko, E.Y.; Akimov, A.v.; Korchagin, D.v.; Nehrkorn, J.; Ozerov, M.; Pali, A.v.; Clemente-Juan, J.M.; Aldoshin, S.M. Purely Spectroscopic Determination of the Spin Hamiltonian Parameters in High-Spin Six-Coordinated Cobalt (II) Complexes with Large Zero-Field Splitting. *Inorg. Chem.* **2019**, *58*, 16434–16444. [[CrossRef](#)]
42. Figgis, B.N.; Gerloch, M.; Lewis, J.; Mabbs, F.E.; Webb, G.A. The Magnetic Behaviour of Cubic-Field 4T<sub>1g</sub> Terms in Lower Symmetry. *J. Chem. Soc. A.* **1968**, *57*, 2086–2093. [[CrossRef](#)]
43. Griffith, J.S. *The Theory of Transition-Metal. Ions*; Cambridge University Press and Assessment: Cambridge, UK, 2009; p. 455.
44. Mingos, D.M.P. *Magnetic Functions Beyond the Spin-Hamiltonian*; Springer: Berlin/Heidelberg, Germany, 2006; p. 278.
45. Boča, R. *A Handbook of Magnetochemical Formulae*; Elsevier: Amsterdam, The Netherlands, 2012; p. 1010.
46. Herchel, R.; Boča, R. *Program. Polymagnet*; Slovak Technical University: Bratislava, Slovakia, 2021.
47. Boča, R. *Program. MIF with FIT Module*; University of SS Cyril and Methodius: Trnava, Slovakia, 2019.
48. Malmqvist, P.Å.; Roos, B.O. The CASSCF State Interaction Method. *Chem. Phys. Lett.* **1989**, *155*, 189–194. [[CrossRef](#)]
49. Angeli, C.; Cimiraglia, R.; Malrieu, J.P. N-Electron Valence State Perturbation Theory: A Fast Implementation of the Strongly Contracted Variant. *Chem. Phys. Lett.* **2001**, *350*, 297–305. [[CrossRef](#)]
50. Angeli, C.; Cimiraglia, R.; Evangelisti, S.; Leininger, T.; Malrieu, J.-P. Introduction of N-Electron Valence States for Multireference Perturbation Theory. *J. Chem. Phys.* **2001**, *114*, 10252. [[CrossRef](#)]
51. Neese, F. Software Update: The ORCA Program System, Version 4.0. *Wiley Interdiscip. Rev. Comp. Mol. Sci.* **2018**, *8*, e1327. [[CrossRef](#)]
52. Neese, F.; Wennmohs, F.; Becker, U.; Riplinger, C. The ORCA Quantum Chemistry Program Package. *J. Chem. Phys.* **2020**, *152*, 224108. [[CrossRef](#)] [[PubMed](#)]
53. Weigend, F.; Ahlrichs, R. Balanced Basis Sets of Split Valence, Triple Zeta Valence and Quadruple Zeta Valence Quality for H to Rn: Design and Assessment of Accuracy. *Phys. Chem. Chem. Phys.* **2005**, *7*, 3297–3305. [[CrossRef](#)] [[PubMed](#)]
54. Weigend, F. Accurate Coulomb-Fitting Basis Sets for H to Rn. *Phys. Chem. Chem. Phys.* **2006**, *8*, 1057–1065. [[CrossRef](#)]
55. Hellweg, A.; Hättig, C.; Höfener, S.; Klopper, W. Optimized Accurate Auxiliary Basis Sets for RI-MP<sub>2</sub> and RI-CC<sub>2</sub> Calculations for the Atoms Rb to Rn. *Theor. Chem. Acc.* **2007**, *117*, 587–597. [[CrossRef](#)]
56. Izsák, R.; Neese, F. An Overlap Fitted Chain of Spheres Exchange Method. *J. Chem. Phys.* **2011**, *135*, 144105. [[CrossRef](#)]
57. Neese, F.; Wennmohs, F.; Hansen, A.; Becker, U. Efficient, Approximate and Parallel Hartree–Fock and Hybrid DFT Calculations. A ‘Chain-of-Spheres’ Algorithm for the Hartree–Fock Exchange. *Chem. Phys.* **2009**, *356*, 98–109. [[CrossRef](#)]
58. Mingos, D.M.P.; Day, P.; Dahl, J.P. *Molecular Electronic Structures of Transition Metal Complexes II*; Springer: Berlin/Heidelberg, Germany, 2012; p. 236.
59. Singh, S.K.; Eng, J.; Atanasov, M.; Neese, F. Covalency and Chemical Bonding in Transition Metal Complexes: An Ab Initio Based Ligand Field Perspective. *Coord. Chem. Rev.* **2017**, *344*, 2–25. [[CrossRef](#)]
60. Zoufalý, P.; Kliuikov, A.; Čížmár, E.; Císařová, I.; Herchel, R. Cis and Trans Isomers of Fe (II) and Co (II) Complexes with Oxadiazole Derivatives—Structural and Magnetic Properties. *Eur. J. Inorg. Chem.* **2021**, *2021*, 1190–1199. [[CrossRef](#)]
61. Drahoš, B.; Šalitroš, I.; Císařová, I.; Herchel, R. A Multifunctional Magnetic Material Based on a Solid Solution of Fe (II)/Co (II) Complexes with a Macrocyclic Cyclam-Based Ligand. *Dalton Trans.* **2021**, *50*, 11147–11157. [[CrossRef](#)] [[PubMed](#)]
62. Ghosh, S.; Kamilya, S.; Rouzières, M.; Herchel, R.; Mehta, S.; Mondal, A. Reversible Spin-State Switching and Tuning of Nuclearity and Dimensionality via Nonlinear Pseudohalides in Cobalt (II) Complexes. *Inorg. Chem.* **2020**, *59*, 17638–17649. [[CrossRef](#)] [[PubMed](#)]
63. Chibotaru, L.F.; Ungur, L. Ab Initio Calculation of Anisotropic Magnetic Properties of Complexes. I. Unique Definition of Pseudospin Hamiltonians and Their Derivation. *J. Phys. Chem.* **2012**, *137*, 064112. [[CrossRef](#)] [[PubMed](#)]
64. Dey, A.; Kalita, P.; Chandrasekhar, V. Lanthanide(III)-Based Single-Ion Magnets. *ACS Omega* **2018**, *3*, 9462–9475. [[CrossRef](#)] [[PubMed](#)]



# Weak antiferromagnetic interaction in Cu(II) complex with semi-coordination exchange pathway

Lubomir Havlíček<sup>a</sup>, Radovan Herchel<sup>b</sup>, Ivan Nemeč<sup>a,b,\*</sup>, Petr Neugebauer<sup>a</sup>

<sup>a</sup> Central European Institute of Technology, CEITEC BUT, Purkyňova 656/123, 61200 Brno, Czech Republic

<sup>b</sup> Department of Inorganic Chemistry, Faculty of Science, Palacký University, 17. listopadu 1192/12, 771 46 Olomouc, Czech Republic

## ARTICLE INFO

### Keywords:

Magnetic exchange interaction  
Non-covalent interaction  
Semi-coordination

## ABSTRACT

We present structural and magnetic studies of complex [Cu(dpt)(NCS)<sub>2</sub>], **1a**, dpt = bis(3-aminopropyl)amine. A weak antiferromagnetic interaction mediated by a Cu...π non-covalent interaction was identified by magnetometry measurements, and the exchange magnitude ( $J = -2.24 \text{ cm}^{-1}$ ,  $J$  stands for isotropic magnetic exchange constant) was determined. These results were supported by theoretical calculations (DFT) and the nature of the Cu...π interaction was studied by QT-AIM. It was confirmed that the Cu...π non-covalent interaction could be described as semi-coordination. The obtained results were compared to those previously reported for the isomorphous complex [Co(dpt)(NCS)<sub>2</sub>].

## 1. Introduction

Despite the absence of a formal definition, the term semi-coordination describes a situation in which the distance between a central atom (M) and a possible donor atom (X) is significantly longer than is typical for a covalent bond of the particular type [1], but still, the M...X distance adopts values consistent with non-covalent interaction. In other words, semi-coordination can be considered as an attractive non-covalent interaction involving a central atom. As the preliminary classification criterion, the M...X distance can be chosen and this "should be smaller than the sum of the van der Waals radii [2], but significantly longer than the typical coordination bond for the same formal oxidation states of both M and X." [3]. If we consider possible effects of semi-coordination on molecular magnetic properties, we can easily recognize weakening of the electrostatic interaction between M and X with their increasing distance. This could have important consequences for the overall ligand field strength in the complex molecule [4] and for its magnetic anisotropy [5,6], but reports addressing these issues are still lacking in the literature. On the other hand, there have been previous reports on the involvement of semi-coordination bonds in the mediation of magnetic exchange interactions. In 2012, Starodub et al. reported on the crystal structure and magnetic properties of a copper(II) complex with the 1,3-dithiole-2-thione-4,5-dithiolate ligand, which exhibited a weak antiferromagnetic interaction within a supramolecular dimer interconnected by a pair of weak Cu...S interactions ( $d(\text{Cu}\cdots\text{S}) =$

$3.144(1) \text{ \AA}$ ,  $\sum R_{\text{vdw}}(\text{Cu},\text{S}) = 3.8 \text{ \AA}$ ) [7]. In 2013, Nelyubina et al. proposed that even extremely long and weak Cu...O contacts ( $d(\text{Cu}\cdots\text{O}) = 3.5808(8) \text{ \AA}$ ,  $\sum R_{\text{vdw}}(\text{Cu},\text{O}) = 3.55 \text{ \AA}$ ) could be responsible for the mediation of weak antiferromagnetic exchange interactions in Na<sub>2</sub>Cu(CO<sub>3</sub>)<sub>2</sub> [8]. In 2016, we reported on the static and dynamic properties of pentacoordinate [Co(dpt)(NCS)<sub>2</sub>] complex (dpt = bis(3-aminopropyl)amine), which exhibited a weak ferromagnetic exchange interaction. The mediation of such exchange interaction was ascribed to the existence of the {[Co(dpt)(NCS)<sub>2</sub>]}<sub>2</sub> supramolecular dimers, which formed in the crystal structure due to weak intermolecular N—H...S hydrogen bonding between the amino groups of the dpt ligand and sulfur atoms from the NCS<sup>-</sup> ligands. Due to this special arrangement, the central atom is found in the proximity of the nitrogen atom from the NCS<sup>-</sup> ligand ( $d(\text{Co}\cdots\text{N}) = 3.451(1) \text{ \AA}$ ,  $\sum R_{\text{vdw}}(\text{Co},\text{N}) = 3.6 \text{ \AA}$ ) belonging to an adjacent complex molecule (Fig. 1). We confirmed the presence of ferromagnetic exchange experimentally and the assignment of the exchange pathway was supported by DFT calculations [9].

In this paper, we report the results obtained for analogous complex [Cu(dpt)(NCS)<sub>2</sub>], (**1a**), which is isomorphous with the Co complex [Co(dpt)(NCS)<sub>2</sub>], (**1b**). The synthesis and crystal structure of **1a** were previously reported by M. Cannas et al. in 1974 [10]. Here we report on redetermination of the crystal structure using aspherical scattering factors [11] and QT AIM (Quantum Theory of Atoms In Molecules) analysis of non-covalent interactions. Furthermore, to understand the magnetic properties of **1a** we performed magnetic measurements and

\* Corresponding author at: Department of Inorganic Chemistry, Faculty of Science, Palacký University, 17. listopadu 1192/12, 771 46 Olomouc, Czech Republic.  
E-mail addresses: [ivan.nemec@upol.cz](mailto:ivan.nemec@upol.cz), [ivan.nemec@ceitec.vutbr.cz](mailto:ivan.nemec@ceitec.vutbr.cz) (I. Nemeč).

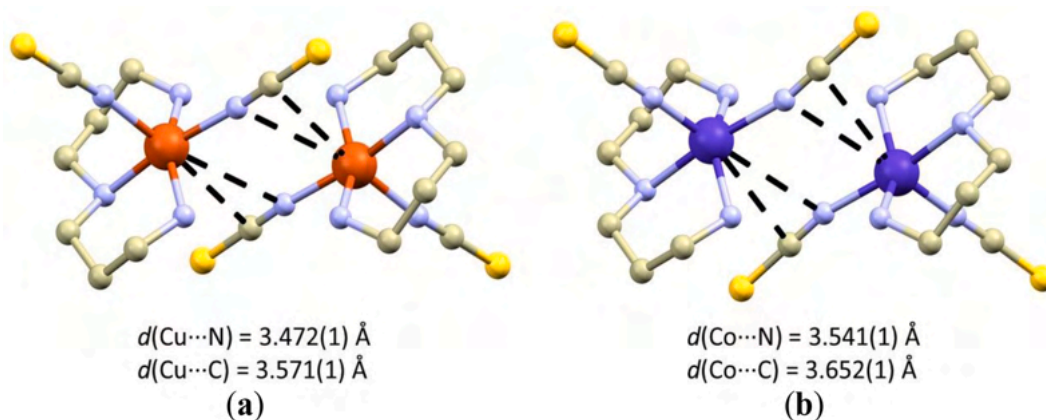


**Fig. 1.** A perspective view of the centrosymmetric supramolecular dimer in  $[\text{Cu}(\text{dpt})(\text{NCS})_2]$  (a) and  $[\text{Co}(\text{dpt})(\text{NCS})_2]$  (b). The hydrogen atoms were omitted for clarity. The Co/Cu...C/N interactions were depicted as black dashed lines. Color code: C (grey), Co (dark blue), Cu (orange), N (light blue), S (yellow).

electron paramagnetic resonance (EPR) spectroscopy. All the obtained results were supported by theoretical calculations and discussed in comparison to **1b**.

## 2. Experimental

### 2.1. Materials and methods

$\text{Cu}(\text{NO}_3)_2 \cdot 3\text{H}_2\text{O}$  was purchased from Lach-Ner (Neratovice, Czech Republic), other chemicals, i.e. potassium thiocyanate, bis(3-aminopropyl)amine (dpt), copper nitrate hydrate, from Sigma-Aldrich (Prague, Czech Republic), and the solvent used (methanol, MeOH) was purchased from Penta (Prague, Czech Republic).

Elemental analysis was performed by a Flash 2000 CHNS Elemental Analyzer (Thermo Scientific, Waltham, MA, USA). A Jasco FT/IR-4700 spectrometer (Jasco, Easton, MD, USA) was used for the collection of the infrared (IR) spectra of the studied ligand and complexes in the range of 400–4000  $\text{cm}^{-1}$  by using the attenuated total reflection (ATR) technique on a diamond plate. UV–VIS spectroscopy was performed using a Perkin-Elmer (Waltham, MA, USA) Lambda 35 spectrometer at 11.000–40.000  $\text{cm}^{-1}$ . The magnetometry was performed using Low Temperature Vibrating Sample Magnetometer Cryogenic Limited in the temperature range 2–300 K in the magnetic field of 0.2 T and the field dependent measurements from  $-9$  to 9 T.

Data collection for **1a** was done using an XtaLAB Synergy-I diffractometer with a HyPix3000 hybrid pixel array detector and microfocused PhotonJet-I X-ray source (Cu  $K\alpha$ ) at two temperatures: 100.0(2) K and 293(2) K. The structure was solved using SHELXT [12] program and refined by the full matrix least-squares procedure with Olex2.refine [13] in OLEX2 (version 1.5) [14]. The multi-scan absorption corrections were applied using the program CrysAlisPro 1.171.40.82a [15]. The molecular structures and packing diagram were drawn with MERCURY [16].

The non-spherical refinement of the structure was done by structure refinement method Hirshfeld atom refinement (HAR) [17,18] using NoSpherA2 software [10] incorporated in OLEX2 and with computational support of ORCA 4.2.1 computational package (functional: B3LYP, basis set: def2-TZVPP) [19]. Aspherical scattering factors were calculated at a high level of integration precision and anisotropic refinement of the hydrogen atoms were performed. The effect of HAR manifested itself by significant decrease of global descriptors of refinement quality (the value of  $R_1(I > 2\sigma(I))$  dropped from 0.0215 to 0.0146), but also in decrease of data to parameter ratio.

The selected crystallographic data for **1a**:

Crystal system: chemical formula:  $\text{C}_8\text{H}_{17}\text{CuN}_5\text{S}_2$ ,  $M_w = 310.94$  g/mol, **1a**@293 K: temperature of experiment = 293(2) K, monoclinic, space group:  $P2_1/n$ ,  $a = 7.59847(5) \text{ \AA}$ ,  $b = 14.15962(8) \text{ \AA}$ ,  $c = 12.70041(8) \text{ \AA}$ ,  $\beta = 100.2122(6) \text{ deg.}$ ,  $V = 1344.808(14) \text{ \AA}^3$ ,  $Z = 4$ ,  $D_c/g \text{ cm}^{-3} =$

$1.536$ ,  $\mu/\text{mm}^{-1} = 5.058$ ,  $F(000) = 644$ , Data/restraints/parameters = 2531/0/146, Goodness-of-fit (GOF) on  $F^2 = 1.065$ ,  $R_1$ ,  $wR_2$  ( $I > 2\sigma(I)$ ) = 0.0254, 0.0654,  $R_1$ ,  $wR_2$  (all data) = 0.0258, 0.0656, CCDC number = 2160407; **1a**@100 K, temperature of experiment 100.0(2) K, monoclinic, space group:  $P2_1/n$ ,  $a = 7.55240(10) \text{ \AA}$ ,  $b = 13.78360(10) \text{ \AA}$ ,  $c = 12.69370(10) \text{ \AA}$ ,  $\beta = 99.8500(10) \text{ deg.}$ ,  $V = 1301.93(2) \text{ \AA}^3$ ,  $Z = 4$ ,  $D_c/g \text{ cm}^{-3} = 1.586$ ,  $\mu/\text{mm}^{-1} = 5.225$ ,  $F(000) = 644$ , Data/restraints/parameters = 2437/0/145, Goodness-of-fit (GOF) on  $F^2 = 1.016$ ,  $R_1$ ,  $wR_2$  ( $I > 2\sigma(I)$ ) = 0.0215, 0.0606,  $R_1$ ,  $wR_2$  (all data) = 0.0220, 0.0609, CCDC number = 2160408, selected parameters after refinement with non-spherical atomic form factors:  $F(000) = 640.175$ , Data/restraints/parameters = 2437/0/298, Goodness-of-fit (GOF) on  $F^2 = 1.0889$ ,  $R_1$ ,  $wR_2$  ( $I > 2\sigma(I)$ ) = 0.0146, 0.0343,  $R_1$ ,  $wR_2$  (all data) = 0.0151, 0.0345.

### 2.2. Synthesis

The complex  $[\text{Cu}(\text{dpt})(\text{NCS})_2]$  **1a** was prepared as follows: 1 mmol (24.16 mg) of  $\text{Cu}(\text{NO}_3)_2 \cdot 3\text{H}_2\text{O}$  was dissolved in a mixture of 5 ml of distilled water and 5 ml of MeOH. The mixture was stirred until all copper nitrate was dissolved. To the stirring solution 2 mmol (16.22 mg) of solid KNCS was added. The mixture was then stirred and heated for 15 min. The deep blue solution was filtered and left for isothermal crystallization. Dark blue crystals were obtained after a week. The phase purity was confirmed by powder X-ray diffraction.

### 2.3. Theoretical calculations

The ORCA 4.2.1 computational package was used for all here reported calculations [17]. All the computations were based on the molecular fragments derived from the X-ray data, where only the positions of the hydrogen atoms were optimized using Density Functional Theory (DFT) with the triple- $\xi$  def2-TZVP basis functions for all atoms except for the carbon and hydrogen atoms, for which the def2-SVP basis set was applied [20]. The calculations used the resolution of identity approximation with the auxiliary basis created by an AutoAux generation procedure [21] and the chain-of-spheres approximation to exact exchange (RJCOSX) [22,23]. The integration grids were increased by setting Grid5 and Gridx5, and the convergence criteria were set to verytight SCF (self-consistent field) in all calculations. The QTAIM analysis was done using Multiwfn program [24,25]. The magnetic properties were studied with the ZORA relativistic approximation [26] with ZORA-def2-TZVP for all atoms [18], and the SARC/J Coulomb fitting basis set utilized as an auxiliary basis set [27]. Again, RJCOSX approximation was employed. Increased integration grids (Grid6 and Gridx6 in ORCA convention) and tight SCF convergence criteria were used in all calculations. Moreover, the radial integration accuracy around the heavy atoms (Co and Cu) was increased with using SpecialGridIntAcc set to 10.

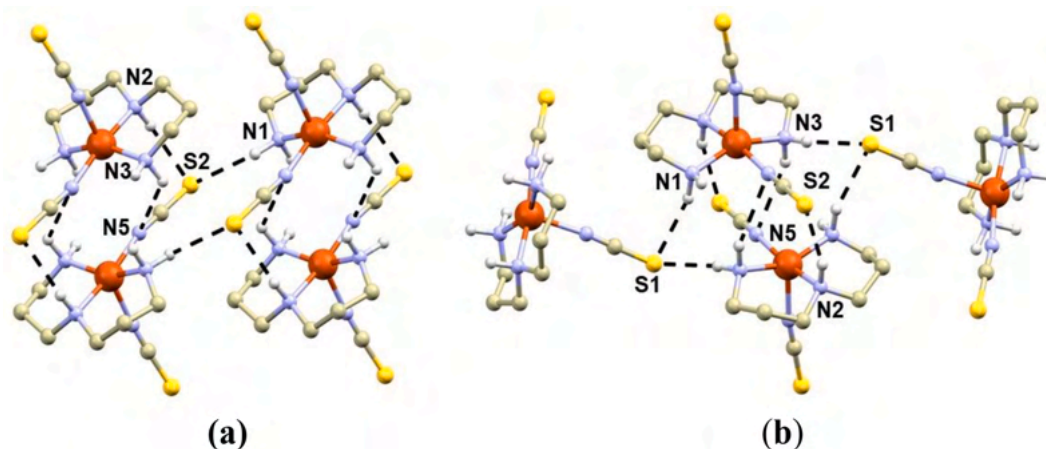


**Fig. 2.** A perspective view of the two fragments (a) and (b) in the crystal structure of **1a** with showed N—H...S hydrogen bonding (black dashed lines). Hydrogen atoms except for those belonging to amine groups were omitted for clarity. Color code: C (grey), Cu (orange), N (light blue), S (yellow). Donor...acceptor distances of hydrogen bonding:  $d(\text{N1}\cdots\text{S1}) = 3.672(1)$ ,  $d(\text{N2}\cdots\text{S2}) = 3.564(1)$ ,  $d(\text{N3}\cdots\text{S1}) = 3.420(1)$  Å.

The calculations of g-tensor parameters were performed with a state average complete active space self-consistent field (SA-CASSCF) wave functions method [28]. The dynamic electron correlation was treated with *N*-electron valence second-order perturbation theory (NEVPT2) [29–31]. Both spin–spin and spin–orbit coupling contributions were involved in the calculations through quasi-degenerate perturbation theory (QDPT) [32], where an approximation to the Breit–Pauli form of the spin–orbit coupling operator (SOMF) [33] and the effective Hamiltonian theory [34] were employed.

### 3. Results and discussion

#### 3.1. Crystal structures

We remeasured crystal structure of **1a** at two temperatures: 100.0(2) and 293(2) K. There was no structural transition observed between these two temperatures and obtained structures are very similar besides thermal contraction of the lattice parameters. In this paper we will describe crystal structure determined at 100 K. Compound **1a** crystallizes in the monoclinic space group  $P2_1/n$ . It consists of complex molecules  $[\text{Cu}(\text{dpt})(\text{NCS})_2]$  in which dpt acts as tridentate *N*-donor and isothiocyanate groups as terminal monodentate ligands. The metal center is thus pentacoordinate with coordination geometry close to square pyramidal ( $C_{4v}$ ) as can be judged from the value of Addison parameter ( $\tau = 0.33$ ,  $\tau = (\alpha - \beta)/60$ ,  $\alpha$  and  $\beta$  are two largest angles in the coordination polyhedron,  $\tau = 0$  for ideal square pyramidal and 1 for ideal trigonal bipyramidal geometries, [35]). This value is lower than in the case of Co analogue **1b** ( $\tau = 0.46$ ).

**Table 1**

Topological and energetic properties of  $\rho(r)$  calculated at the selected (3,-1) critical points.

	length/Å	$\nabla^2 \rho(r)/\text{a.u.}$	$h_e(r)/\text{a.u.}$	$V(r)/\text{a.u.}$	$G(r)/\text{a.u.}$	$E_{\text{int}}/\text{kcal.mol}^{-1}$	$ V(r) /G(r)$
Cu–N <sub>DPT</sub>	2.0280(13)	0.32961	−0.01712	−0.11664	0.09952	−36.60	1.17
	2.0757(13)	0.33313	−0.02267	−0.12862	0.10595	−40.36	1.21
	2.0145(13)	0.26143	−0.01924	−0.10383	0.08459	−32.58	1.23
Cu–N <sub>NCS</sub>	2.0373(14)	0.32395	−0.02115	−0.12329	0.10214	−38.68	1.21
	2.1458(14)	0.26757	−0.00927	−0.08544	0.07616	−26.81	1.12
N–H...S	3.564(1)	0.02967	−0.00011	−0.00764	0.00753	−2.40	1.01
	3.420(1)	0.03937	0.00034	−0.00917	0.00951	−2.88	0.96
	3.672(1)	0.0253	0.00017	−0.00598	0.00615	−1.88	0.97
Cu...N	3.472(1)	0.01613	0.00039	−0.00325	0.00364	−1.02	0.89
Co...N <sup>1</sup>	3.541(1)	0.012627	0.000323	−0.00251	0.00283	−0.79	0.89

<sup>1</sup> The crystal structure of **1b** was adopted from the article by Boeckman et al. [41].

The metal–ligand bond lengths between the nitrogen atoms of the dpt ligand and Cu central atom are shorter than the corresponding Co–N bonds in **1b**,  $d(\text{M–N}) = \mathbf{1a}$  [**1b**] in Å: 2.0145(13) [2.076(1)], 2.0757(13) [2.197(2)], 2.0280(13) [2.062(1)]. On the other hand, the M–N bonds with isothiocyanato ligands are longer in **1a**,  $d(\text{M–N}) = \mathbf{1a}$  [**1b**] in Å: 2.0373(14), 2.1458(14), [2.004(1), 2.120(2)]. Thus, both molecular structures of **1a** and **1b** are rather similar. However, there is one important difference when we check how the adjacent molecules in the crystal structure interact.

As we reported for **1b** previously [9], also in the crystal structure of **1a** (Fig. 1) the centrosymmetric supramolecular dimer  $\{[\text{Cu}(\text{dpt})(\text{NCS})_2]_2\}$  is stabilized by a weak N–H...S interaction between the secondary amine group of the dpt ligand and sulfur atom of the NCS ligand from an adjacent molecule:  $d(\text{N2}\cdots\text{S2}) = 3.564(1)$  Å (Fig. 2). Within this dimer rather short Cu...N ( $d(\text{Cu}\cdots\text{N}) = 3.472(1)$  Å,  $\sum R_{\text{vdw}}(\text{Cu}, \text{N}) = 3.60$  Å) or Cu...C ( $d(\text{Cu}\cdots\text{C}) = 3.571(1)$  Å,  $\sum R_{\text{vdw}}(\text{Cu}, \text{C}) = 3.70$  Å) possible non-covalent contacts can be recognized (Fig. 1). These distances are a bit shorter than those within the  $\{[\text{Co}(\text{dpt})(\text{NCS})_2]_2\}$  supramolecular dimer in **1b**.

Remarkably, an interesting difference between **1a** and **1b** is in the way how the NCS ligands providing the aforementioned interaction (NCS1) coordinate the metal atoms. In **1a**, the Cu–N<sub>NCS1</sub> distance is much shorter (2.0373(14) Å) than that for the other NCS ligand (2.1458(14) Å). On the contrary, in **1b**, the Co–N<sub>NCS1</sub> distance is the longer one (2.120(2) vs. 2.004(1) Å). The supramolecular dimers in the crystal structure are further stabilized mainly by weak N–H...S and C–H...S interactions with a rather long donor...acceptor distances (in Å):  $d(\text{N1}\cdots\text{S1}) = 3.672(1)$ ,  $d(\text{N2}\cdots\text{S2}) = 3.564(1)$ ,  $d(\text{N3}\cdots\text{S1}) = 3.420(1)$ ,



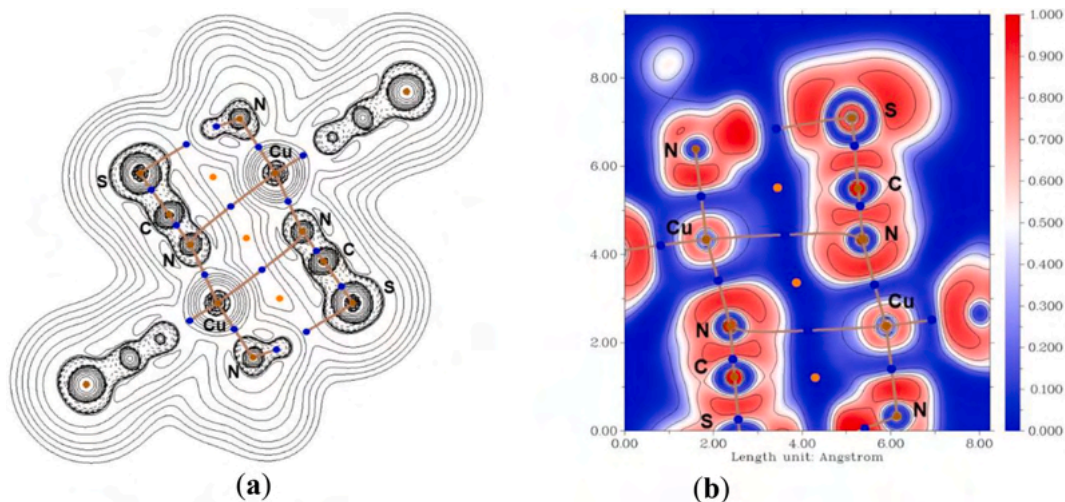


**Fig. 3.** The  $\nabla^2 \rho(\mathbf{r})$  contour plot in the  $\{\text{Cu-NCS1}\}_2$  plane of the dimeric fragment in the **1a** crystal structure (a). The calculated ELF isosurface plot for the  $\{\text{Cu-NCS1}\}_2$  fragment (b). Blue dots represent (3,-1) critical points, orange dots represent (3,+1) ring critical points and brown dots represents (3,-3) atomic critical points. Brown lines represent bond paths.

Fig. 2), the main motives for N—H...S contacts are shown in Fig. 2. Based on these hydrogen bonds two substructures can be recognized: a supramolecular chain along the a axis in which the dimers are interconnected by N1—H...S1 hydrogen bonds (Fig. 2a), interactions of the dimers via a bifurcated pair of the N1—H...S1 and N3—H...S1 hydrogen bonds, which form a supramolecular (−101) plane (Fig. 2b).

### 3.2. QT AIM analysis

The non-covalent interactions in both **1a** and **1b** were inspected using theoretical methods. Two fragments from the crystal structures of **1a** (centrosymmetric dimer and fragment showed in Fig. 2b) were chosen for topological analysis of electron density using QT AIM [36]. The wavefunctions were calculated by DFT using exchange–correlation functional B3LYP and single-point calculation. First, we investigated topology of electron density ( $\rho(\mathbf{r})$ ) for the centrosymmetric dimer. We focused our attention on density properties at (3, −1) critical points (CPs). For non-covalent interactions, it should be fulfilled that at corresponding CPs the Laplacian of the electron density ( $\nabla^2 \rho(\mathbf{r})$ ) and full energy density of electrons  $h_e(\mathbf{r})$  both adopt positive values. On the other hand, the coordination bonds and covalent bonds at their CPs adopt the following values:  $\nabla^2 \rho(\mathbf{r}) > 0$ ,  $h_e(\mathbf{r}) < 0$  (coordination bonds, so called intermediate type of interaction) or  $\nabla^2 \rho(\mathbf{r}) < 0$ ,  $h_e(\mathbf{r}) < 0$  (strong covalent bonds), respectively [1,3]. All the coordination bonds in **1a** fulfil the expected intermediate nature of the interaction having  $\nabla^2 \rho(\mathbf{r}) > 0$ ,  $h_e(\mathbf{r}) < 0$ . The estimation of contributions to the energy of the system based on the properties of topological descriptors at corresponding (3, −1) CPs revealed that the Cu–N bonds possess similar interaction energies ( $E_{\text{int}} = -33$  to  $-40$  kcal/mol, derived from virial at CP, [37]) except for the longest Cu–N<sub>NCS2</sub> bond ( $-26.8$  kcal/mol, Table 1). The N—H...S hydrogen bonds exhibit significantly smaller  $E_{\text{int}}$  ( $-1.8$  to  $-2.9$  kcal/mol, Table 1) corresponding with the weak nature of these contacts.

The topological and energetic properties at the (3, −1) CPs of these contacts also con-firmed their non-covalent character by positive values of  $\nabla^2 \rho(\mathbf{r})$  and  $h_e(\mathbf{r})$ . Moreover, we can utilize also the  $|V(\mathbf{r})|/G(\mathbf{r})$  criterium ( $V(\mathbf{r})$  is electron potential energy density,  $G(\mathbf{r})$  is electron kinetic potential energy) introduced by Espinosa et al. [38], which can be understood as a measure of stabilization of an interaction by a local concentration of charge. Thus, if  $|V(\mathbf{r})|/G(\mathbf{r}) > 1$ , then the contact/bond is considered as having a covalent component. For coordination Cu–N bonds this parameter adopts values in the range of 1.12–1.23. All the N—H...S hydrogen bonds possess  $|V(\mathbf{r})|/G(\mathbf{r}) \leq 1$ , which confirms their

purely non-covalent character.

Topological analysis of **1a** revealed that within the centrosymmetric dimer  $\{[\text{Cu}(\text{dpt})(\text{NCS})_2]_2\}$  the bond path and (3, −1) CP exists between the Cu atom and nitrogen atom of the NCS1 ligand from the adjacent complex molecule (Fig. 3a). Both  $\nabla^2 \rho(\mathbf{r})$  and  $h_e(\mathbf{r})$  are positive and small, which indicates a non-covalent character of this interaction and also interaction energy is very low ( $-1.02$  kcal/mol, Table 1). Furthermore, also the  $|V(\mathbf{r})|/G(\mathbf{r})$  indicator ensures a non-covalent character of the contact, since its value is rather low (0.89, Table 1). Thus, we may conclude that this contact is non-covalent and as such fulfils the criteria for semi-coordination. We investigated the nature of the similar Co...N contact also for **1b**. Again, the bond path and (3, −1) CP exists between the Co atom and nitrogen atom of the NCS1 ligand from the adjacent complex molecule. The topological and energetic properties calculated at this CP indicate that the contact is of a non-covalent character:  $\nabla^2 \rho(\mathbf{r}) > 0$ ,  $h_e(\mathbf{r}) < 0$ ,  $|V(\mathbf{r})|/G(\mathbf{r}) < 1$  (Table 1). The interaction energy ( $-0.79$  kcal/mol) is smaller than was calculated for **1a**.

To gain some insight into the nature of the Cu/Co...N contacts in **1a** and **1b** we utilized Electronic Localization Function [39,40], which was used to visualize electron density distribution. For both **1a** and **1b**, the calculation revealed that charge concentrations around the nitrogen atom of the NCS1 ligand are directed dominantly towards the neighboring carbon atom belonging to NCS1 and towards the Cu/Co atom with which this ligand forms a coordination bond (Fig. 3b). The Cu/Co...N contact clearly involves lower charge concentrations of the NCS1 ligand, and this supports our hypothesis that mainly the  $\pi$ -character of the electron density is involved in the formation of this contact, which we formulated in our previous report on magnetic properties of **1b** [9].

### 3.3. BS DFT

The DFT calculations were also utilized to estimate the magnetic exchange between the paramagnetic ions ( $\text{Cu}^{\text{II}}$  or  $\text{Co}^{\text{II}}$ ) within the supramolecular dimers of **1a** and **1b**. Therefore, the broken-symmetry DFT calculations were used with well-established B3LYP hybrid functional [42,43,44]. To account for weak van der Waals forces, DFT-NL variant was used in which the non-local part of VV10 was modified [45,46]. The isotropic exchange  $J$  was calculated for  $H = -J(S_1 S_2)$  spin Hamiltonian with the help of Ruiz and Yamaguchi formulas [47,48].

$$J^{\text{Ruiz}} = 2\Delta / [(S_1 + S_2)(S_1 + S_2 + 1)]$$

$$J^{\text{Yam.}} = 2\Delta / [\langle S^2 \rangle_{\text{HS}} - \langle S^2 \rangle_{\text{BS}}]$$



**Table 2**

The ZORA/B3LYP/ZORA-def2-TZVP calculated net Löwdin spin densities, the  $\langle S^2 \rangle$  values, the energy difference between the BS and HS states, and the isotropic exchange parameters for  $\{[\text{Cu}(\text{dpt})(\text{NCS})_2]_2\}$  of **1a** and  $\{[\text{Co}(\text{dpt})(\text{NCS})_2]_2\}$  of **1b**.

<b>1a</b>	HS	BS	<b>1b</b>	HS	BS
$\rho(\text{Cu})$	0.685	-0.685	$\rho(\text{Co})$	2.682	-2.682
$\rho(\text{N}_{\text{dpt}}^{2.0280})$	0.064	-0.063	$\rho(\text{N}_{\text{dpt}}^{2.082})$	0.046	-0.046
$\rho(\text{N}_{\text{dpt}}^{2.0757})$	0.091	-0.090	$\rho(\text{N}_{\text{dpt}}^{2.197})$	0.048	-0.047
$\rho(\text{N}_{\text{dpt}}^{2.0145})$	0.063	-0.063	$\rho(\text{N}_{\text{dpt}}^{2.076})$	0.047	-0.047
$\rho(\text{N}_{\text{NCS,ax}}^{2.1458})$	0.001	-0.001	$\rho(\text{N}_{\text{NCS,ax}}^{2.004})$	0.046	-0.046
$\rho(\text{N}_{\text{NCS,eq}}^{2.0373})$	0.055	-0.056	$\rho(\text{N}_{\text{NCS,eq}}^{2.120})$	0.036	-0.033
$\rho(\text{Cu}')$	0.685	0.685	$\rho(\text{Co}')$	2.682	2.682
$\rho(\text{N}_{\text{dpt}}^{2.0280})$	0.064	0.063	$\rho(\text{N}_{\text{dpt}}^{2.082})$	0.046	0.045
$\rho(\text{N}_{\text{dpt}}^{2.0757})$	0.091	0.091	$\rho(\text{N}_{\text{dpt}}^{2.197})$	0.048	0.047
$\rho(\text{N}_{\text{dpt}}^{2.0145})$	0.063	0.063	$\rho(\text{N}_{\text{dpt}}^{2.076})$	0.047	0.047
$\rho(\text{N}_{\text{NCS,ax}}^{2.1458})$	0.001	0.001	$\rho(\text{N}_{\text{NCS,ax}}^{2.004})$	0.046	0.046
$\rho(\text{N}_{\text{NCS,eq}}^{2.0373})$	0.055	0.056	$\rho(\text{N}_{\text{NCS,eq}}^{2.120})$	0.036	0.033
$\langle S^2 \rangle$	2.005	1.005		12.015	3.015
$\Delta(\text{cm}^{-1})$	-2.033			2.527	
$J^{\text{Ruiz}}(\text{cm}^{-1})$	-2.04			0.42	
$J^{\text{Yam}}(\text{cm}^{-1})$	-4.06			0.56	

$$^1 \Delta = \epsilon_{\text{BS}} - \epsilon_{\text{HS}}$$

The results are summarized in Table 2. It is evident that there is spin delocalization from the metal ion to the donor atoms, and this transfer of the spin density is more enhanced for **1a**. Remarkably, the spin density located on the nitrogen atom of the NCS1 ligand is at the closest distance from the spin density of the Cu atom from the adjacent molecules within the supramolecular dimer. This indicates the importance of the Cu... $\pi$  interaction for the mediation of the magnetic exchange. The three-dimensional plots of the spin density of the HS solution are showed in Fig. 4. The comparison of the energy difference  $\Delta$  between the BS and HS states resulted in prediction of weak antiferromagnetic exchange in **1a** and weak ferromagnetic exchange in **1b**.

Moreover, the non-orthogonal magnetic orbitals (single-occupied molecular orbitals, SOMOs) are visualized in Fig. 5. As expected for the square pyramid arrangement, the magnetic orbital for **1a** is a metal based  $3d_{x^2-y^2}$  orbital located in the equatorial plane (Fig. 5a). In the case of **1b** there are three magnetic orbitals: SOMO orbitals based on  $3d_{yz}$   $\text{Co}^{\text{II}}$  orbitals with the lowest overlap  $S_{\alpha\beta}$  (Fig. 5b), SOMO-1 orbitals based on

$3d_{x^2-y^2}$   $\text{Co}^{\text{II}}$  orbitals with the medium overlap  $S_{\alpha\beta}$  (Fig. 5c) and SOMO-2 orbitals based on  $3d_{z^2}$   $\text{Co}^{\text{II}}$  orbitals with the highest overlap  $S_{\alpha\beta}$  (Fig. 5d). The variations of  $S_{\alpha\beta}$  between the magnetic orbitals and the energy gap  $\Delta$  thus are the origins of the opposite signs of the isotropic exchange in **1a** and **1b**.

We investigated also the other possible exchange pathways in **1a** (ESI) within the structural fragments formed by the N—H...S hydrogen bonding between the complex molecules. A weak magnetic exchange between the complex molecules interacting via N—H...S hydrogen bonding (Fig. 2a) was proposed as the second possible exchange pathway. The comparison of the energy difference  $\Delta$  between BS and HS states resulted in prediction of weak antiferromagnetic exchange for the N1—H...S1 and N1—H...S2 hydrogen bond supramolecular fragments ( $J^{\text{Ruiz}} \approx -0.1 \text{ cm}^{-1}$ , Fig. S1), while weak ferromagnetic exchange was found in the N3—H...S1 hydrogen bond supramolecular fragment ( $J^{\text{Ruiz}} \approx 0.1 \text{ cm}^{-1}$ , Fig. S1). As we discussed, this fragment extends the supramolecular dimers into supramolecular coordination network along the a axis.

Furthermore, we applied CASSCF/NEVPT2 calculations to address properly the multideterminant character of this transition metal complex. The active space was defined by nine electrons in five d-orbitals, CAS(9e,5o), which resulted in five doublets originating from  $^2D$  atomic term. The ab initio ligand field theory (AFLT) was used to calculate the energy of the d-orbitals as depicted in Fig. 6. Ideal square pyramidal ligand field would result in the following splitting ( $d_{xz}$ ,  $d_{yz}$ ),  $d_{xy}$ ,  $d_{z^2}$  and  $d_{x^2-y^2}$ . The calculated d-orbitals show a very similar pattern, but  $d_{xz}$  and  $d_{yz}$  orbitals are no longer degenerate due to lower symmetry of the ligand field. Thus, the unpaired electron within the  $3d^9$  electron configuration resides in a  $d_{x^2-y^2}$  orbital. Subsequently, the ligand field terms and ligand field multiplets clearly show that the ground state is well separated from the excited states.

### 3.4. Magnetic properties

The magnetic properties of **1a** were measured in the temperature dependence (2–300 K) of the magnetic moment. The room temperature value of the effective magnetic moment ( $\mu_{\text{eff}}$ ) for the  $\{[\text{Cu}(\text{dpt})(\text{NCS})_2]_2\}$  supramolecular dimer has a value of  $2.5 \mu_{\text{B}}$  which very well fits the expected spin only value for two spins with  $S = 1/2$  and  $g_e = 2.0023$  ( $2.45 \mu_{\text{B}}$ ). The value of  $\mu_{\text{eff}}$  is constant down to ca. 10 K where it drops to  $1.8 \mu_{\text{B}}$ . This may be an indication of an antiferromagnetic interaction

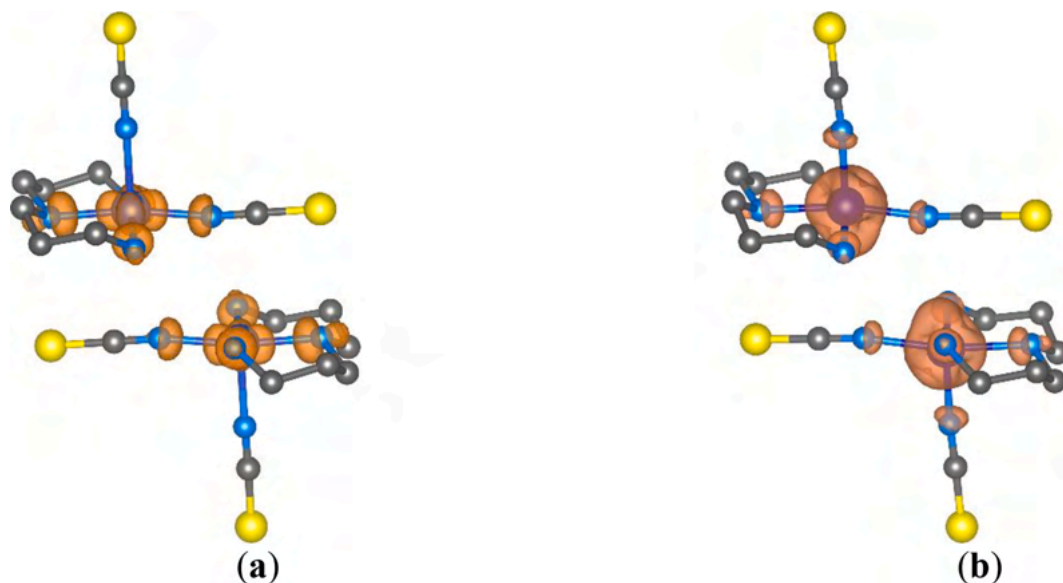


**Fig. 4.** The HS calculated spin density distribution using ZORA/B3LYP/ZORA-def2-TZVP for  $\{[\text{Cu}(\text{dpt})(\text{NCS})_2]_2\}$  of **1a** (a) and  $\{[\text{Co}(\text{dpt})(\text{NCS})_2]_2\}$  of **1b** (b). The spin densities are represented by dark orange surfaces calculated with a cutoff value of  $0.005 e \text{ bohr}^{-3}$ . Hydrogen atoms were omitted for clarity.

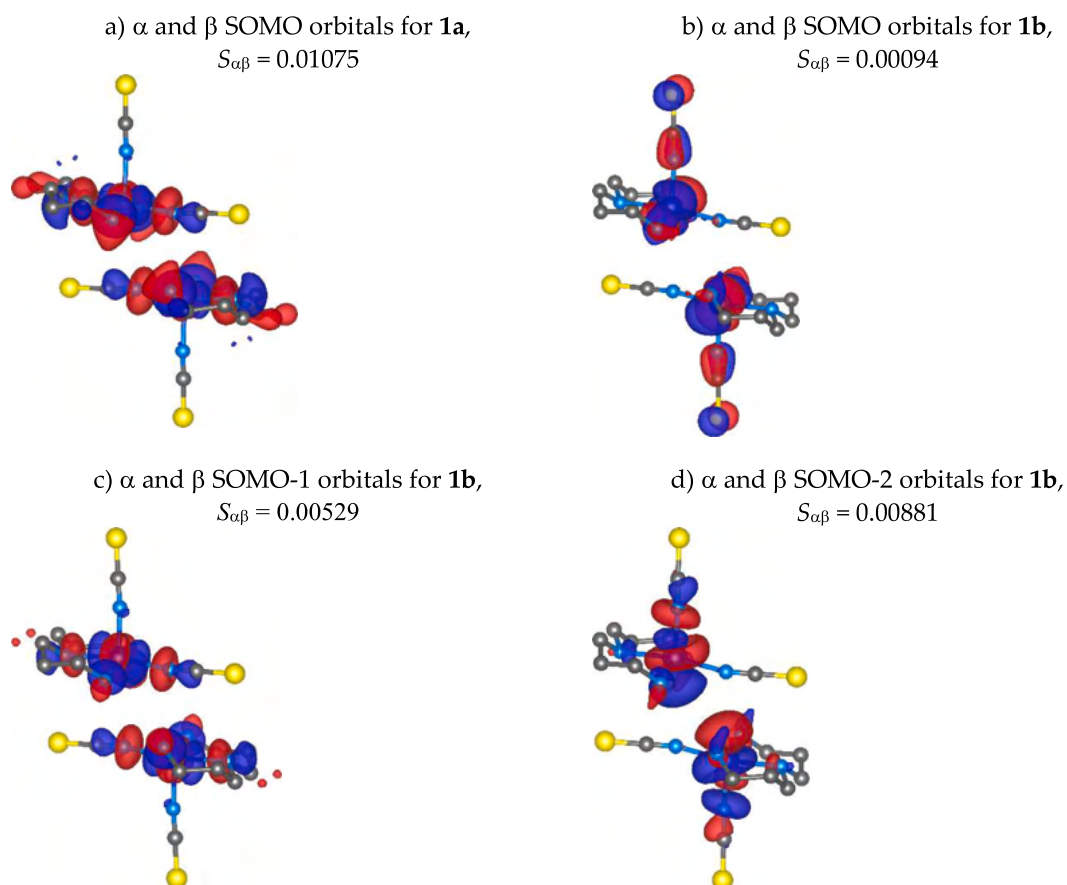


**Fig. 5.** The ZORA/B3LYP/ZORA-def2-TZVP non-orthogonal magnetic orbitals of the broken-symmetry spin state visualized for  $\{[\text{Cu}(\text{dpt})(\text{NCS})_2]_2\}$  of **1a** (a) and  $\{[\text{Co}(\text{dpt})(\text{NCS})_2]_2\}$  of **1b** (b). The values of overlap  $S_{\alpha\beta}$  between the corresponding orbitals are listed too. The molecular orbitals are represented by dark blue/red surfaces calculated with a cutoff value of  $0.02 \text{ e} \cdot \text{bohr}^{-3}$ . Hydrogen atoms were omitted for clarity.

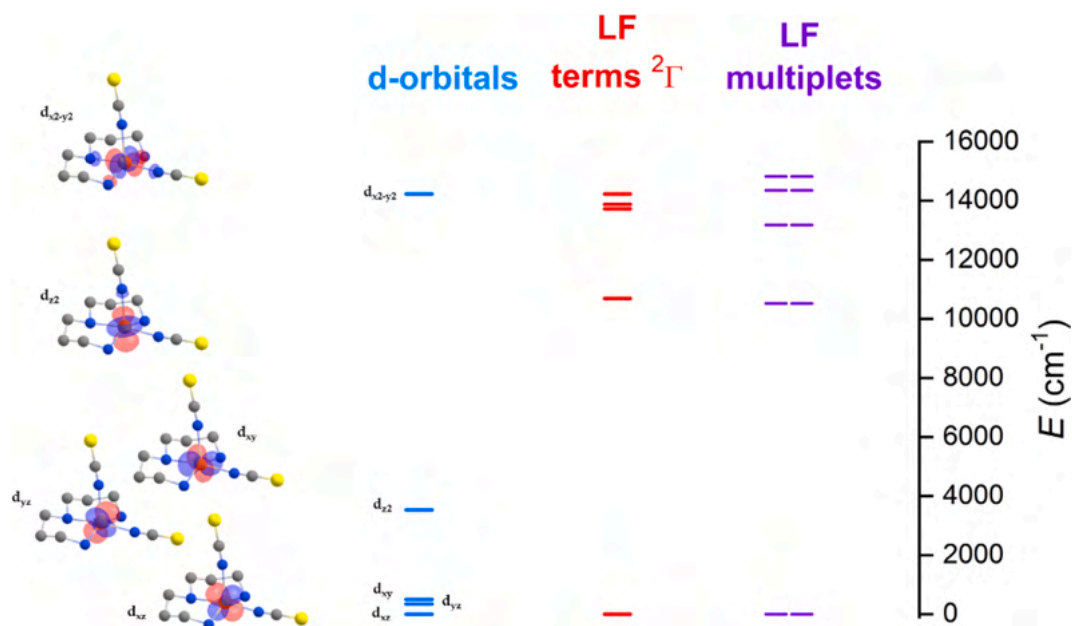


**Fig. 6.** The results of the theoretical CASSCF/NEVPT2 calculations for  $[\text{Cu}(\text{dpt})(\text{NCS})_2]$  of **1a**. Top: plot of the d-orbitals calculated by ab initio ligand field theory (AILFT) (left), ligand field terms (LFT) (middle), and ligand-field multiplets (LFM) (right).

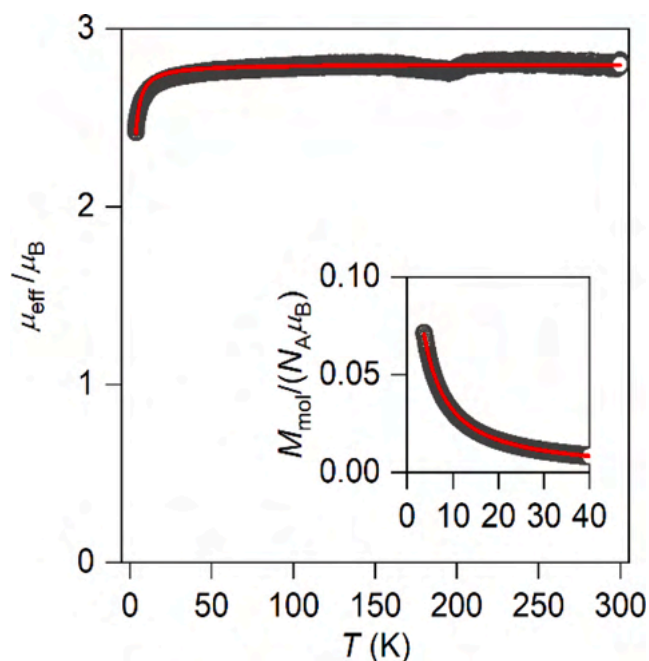


**Fig. 7.** The temperature dependence of the effective magnetic moment (calculated from magnetization measured at  $B = 0.2$  T) of **1a** with the low-temperature region expanded in the inset. Data are scaled per two Cu atoms. Circles - experimental data, full lines - calculated data.

between the Cu(II) atoms, which however, must be rather weak because no maximum on  $\chi$  vs  $T$  dependence was observed even at low temperatures (Fig. 7).

The magnetic data were fitted using the following spin Hamiltonian.

$$\hat{H} = -J(\mathbf{S}_1 \cdot \mathbf{S}_2) + \mu_B \sum_{i=1}^2 \mathbf{B} \cdot \mathbf{g}_i \cdot \mathbf{S}_i$$

for which a simple analytical formula can be derived as [49].

$$M_{\text{mol}} = N_A \mu_B g \frac{e^{(J+x)/kT} - e^{(J-x)/kT}}{1 + e^{(J+x)/kT} + e^{J/kT} + e^{(J-x)/kT}}$$

where  $x = \mu_B B g$ . The analysis of the experimental magnetization data was based on the minimizing the functional  $\sum_i (M_{\text{mol},i}^{\text{exp.}} - M_{\text{mol},i}^{\text{calc.}})^2$ , which resulted in  $J = -2.24 \text{ cm}^{-1}$ ,  $g = 2.29$  (Fig. 7), thus confirming the weak

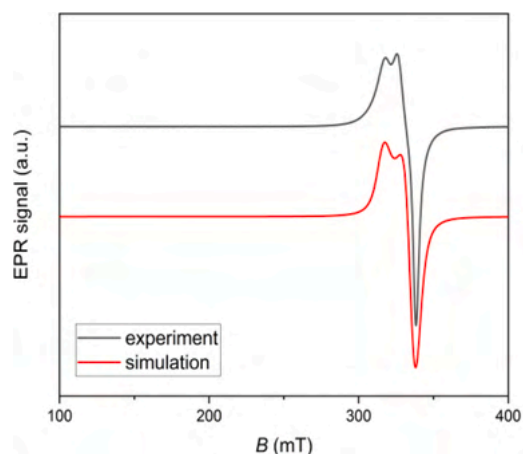


**Fig. 8.** (Left) X-band EPR powder spectrum of **1a** in the solid state at room temperature. The black dots represent experimental values, red line is a simulation for  $g_x = 2.012$ ,  $g_y = 2.013$  and  $g_z = 2.135$ . (Right): the molecular fragment overlaid with the principal axes of g-tensor (x/y/z-axes colored as red/green/blue arrows) calculated for the lowest Kramers doublet by theoretical CASSCF/NEVPT2 calculations.

antiferromagnetic exchange within the supramolecular dimer of **1a**.

The electronic structure of **1a** in the solid state was also probed by X-band EPR spectroscopy at room temperature (Fig. 8). The observed pattern corresponds with a rhombic distorted axial symmetry ( $g_x \approx g_y \neq g_z$ ). The fit of the experimental data was performed with EasySpin software [50], and provided following values of g-tensor:  $g_x = 2.012$ ,  $g_y = 2.013$  and  $g_z = 2.135$ . The g-tensor values predicted by the CASSCF/NEVPT2 calculations agrees qualitatively with the experimental results and confirmed distorted rhombic symmetry ( $g_x = 2.074$ ,  $g_y = 2.120$ ), however, the axial component was overestimated ( $g_z = 2.414$ ) by this approach.

#### 4. Conclusion

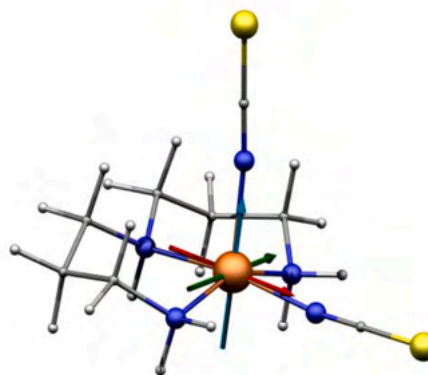
In this paper we reported on structural and magnetic investigations of the  $[\text{Cu}(\text{dpt})(\text{NCS})_2]$  complex (**1a**). The supramolecular dimers formed due to intermolecular N—H...S hydrogen bonding and a Cu... $\pi$  interaction between the Cu atom and thiocyanato ligand. We investigated the latter interaction by QT-AIM and we found it fulfills the criteria for classifying as semi-coordination, since it has non-covalent nature. The magnetic measurements revealed a weak antiferromagnetic interaction between the complex molecules. We investigated the possible magnetic exchange pathways by theoretical calculations (BS-DFT) and these proposed that the dominant exchange interaction is mediated among the supramolecular dimers via the Cu... $\pi$  pathway. By evaluation of the SOMO orbital overlaps we were able to explain the nature of the exchange interaction and we also explained why the magnetic exchange in similar isomorphous compound  $[\text{Co}(\text{dpt})(\text{NCS})_2]$  is of the opposite nature – weak ferromagnetic.

#### CRediT authorship contribution statement

**Lubomir Havlicek:** Validation, Formal analysis, Investigation, Data curation, Writing – original draft, Writing – review & editing, Visualization. **Radovan Herchel:** Methodology, Formal analysis, Investigation, Data curation, Writing – original draft, Writing – review & editing, Visualization. **Ivan Nemeč:** Conceptualization, Methodology, Formal analysis, Investigation, Data curation, Writing – original draft, Writing – review & editing, Visualization, Supervision, Project administration. **Petr Neugebauer:** Funding acquisition.

#### Declaration of Competing Interest

The authors declare that they have no known competing financial interests or personal relationships that could have appeared to influence



the work reported in this paper.

## Data availability

Data will be made available on request.

## Acknowledgements

This research was funded by Ministry of Education, Youth and Sports of the Czech Republic: LTAUSA19060 in the INTER-EXCELLENCE Programme, and by Specific Research Project no. CEITEC VUT-K-21-6867. R. H. and I.N. acknowledge the financial support from the institutional sources of the Department of Inorganic Chemistry, Palacký University Olomouc, Czech Republic.

We are grateful to Ondřej F. Fellner for measuring X-ray powder diffraction data. We acknowledge CzechNanoLab Research Infrastructure supported by MEYS CR (LM2018110).

## Appendix A. Supplementary data

Supplementary data to this article can be found online at <https://doi.org/10.1016/j.poly.2022.115962>.

## References

- I.V. Ananyev, N.A. Bokach, V.Y. Kukushkinc, Structure-directing sulfur metal noncovalent semicoordination bonding, *Acta Crystallogr. Sect. B Struct. Sci. Cryst. Eng. Mater.* 76 (2020) 436–449, <https://doi.org/10.1107/S2052520620005685>.
- S.S. Batsanov, Van der Waals radii of elements, *Inorg. Mater.* 37 (2001) 871–885, <https://doi.org/10.1023/A:1011625728803>.
- Z.M. Efimenko, A.S. Novikov, D.M. Ivanov, A.V. Piskunov, A.A. Vereshchagin, O. V. Levin, N.A. Bokach, V.Y. Kukushkin, The (Dioximate)Ni(II)/2 system: ligand oxidation and binding modes of triiodide species, *Inorg. Chem.* 59 (4) (2020) 2316–2327.
- S. Xue, A. Rotaru, Y. Garcia, Ligand field strength tuning in the model [Fe(H2Bpz2)2(bipy)] spin crossover complex, *Hyperfine Interact.* 240 (2019) 1–5, <https://doi.org/10.1007/s10751-019-1638-z>.
- D. Schweinfurth, J. Krzystek, M. Atanasov, J. Klein, S. Hohloch, J. Telsler, S. Demeshko, F. Meyer, F. Neese, B. Sarkar, Tuning magnetic anisotropy through ligand substitution in five-coordinate Co(II) complexes, *Inorg. Chem.* 56 (2017) 5253–5265, <https://doi.org/10.1021/acs.inorgchem.7b00371>.
- B. Drahoš, I. Čisárová, O. Laguta, V.T. Santana, P. Neugebauer, R. Herchel, Structural, magnetic, redox and theoretical characterization of seven-coordinate first-row transition metal complexes with a macrocyclic ligand containing two benzimidazolyl: N-pendant arms, *Dalt. Trans.* 49 (2020) 4425–4440, <https://doi.org/10.1039/d0dt00166j>.
- V.A. Starodub, S.V. Vitushkina, D. Kamenskyi, A.G. Anders, V.O. Cheranovskii, H. Schmidt, D. Steinborn, I. Potočňák, M. Kajňáková, A. Radvákova, A. Feher, Peculiarities of crystal structures and magnetic properties of Cu(II) and Ni(II) mixed-ligand complexes on the 1,3-dithiole-2-thione-4,5-dithiolate basis, *J. Phys. Chem. Solids* 73 (2012) 350–356, <https://doi.org/10.1016/j.jpcs.2011.10.001>.
- Y.V. Nelyubina, A.A. Korlyukov, I.V. Fedyanin, K.A. Lyssenko, Extremely long Cu...O contact as a possible pathway for magnetic interactions in Na2Cu(CO3)2, *Inorg. Chem.* 52 (2013) 14355–14363, <https://doi.org/10.1021/ic4024025>.
- I. Nemeč, R. Herchel, Z. Trávníček, Ferromagnetic coupling mediated by Co... $\pi$  non-covalent contacts in a pentacoordinate Co(II) compound showing field-induced slow relaxation of magnetization, *Dalt. Trans.* 45 (2016) 12479–12482, <https://doi.org/10.1039/c6dt01539e>.
- M. Cannas, G. Carta, A. Cristini, G. Marongiu, Crystal structures of thiocyanate polyamine copper(II) complexes. Part VI. Di-(3-aminopropyl)aminebis(isothiocyanato)copper(II), *J. Chem. Soc. Dalt. Trans.* (12) (1974) 1278.
- F. Kleemann, O.V. Dolomanov, M. Bodensteiner, N. Peyerimhoff, L. Midgley, L. J. Bourhis, A. Genoni, L.A. Malaspina, D. Jayatilaka, J.L. Spencer, F. White, B. Grundkötter-Stock, S. Steinhauer, D. Lentz, H. Puschmann, S. Grabowsky, Accurate crystal structures and chemical properties from NoSpherA2, *Chem. Sci.* 12 (2021) 1675–1692, <https://doi.org/10.1039/d0sc05526c>.
- G.M. Sheldrick, SHELXT – Integrated space-group and crystal-structure determination, *Acta Crystallogr. Sect. A Found. Crystallogr.* 71 (2015) 3–8, <https://doi.org/10.1107/S2053273314022670>.
- L.J. Bourhis, O.V. Dolomanov, R.J. Gildea, J.A.K. Howard, H. Puschmann, The anatomy of a comprehensive constrained, restrained refinement program for the modern computing environment - Olex2 dissected, *Acta Crystallogr. Sect. A Found. Crystallogr.* 71 (2015) 59–75, <https://doi.org/10.1107/S2053273314022207>.
- O.V. Dolomanov, L.J. Bourhis, R.J. Gildea, J.A.K. Howard, H. Puschmann, OLEX2: A complete structure solution, refinement and analysis program, *J. Appl. Crystallogr.* 42 (2009) 339–341, <https://doi.org/10.1107/S0021889808042726>.
- Rigaku Oxford Diffraction, CrysAlisPro 1.171.40.82a, (2020).
- C.F. MacRae, I. Sovago, S.J. Cottrell, P.T.A. Galek, P. McCabe, E. Pidcock, M. Platings, G.P. Shields, J.S. Stevens, M. Towler, P.A. Wood, Mercury 4.0: from visualization to analysis, design and prediction, *J. Appl. Crystallogr.* 53 (2020) 226–235, <https://doi.org/10.1107/S1600576719014092>.
- D. Jayatilaka, B. Dittrich, X-ray structure refinement using aspherical atomic density functions obtained from quantum-mechanical calculations, *Acta Crystallogr., Sect. A: Found. Crystallogr.* 64 (3) (2008) 383–393.
- S.C. Capelli, H.-B. Bürgi, B. Dittrich, S. Grabowsky, D. Jayatilaka, Hirshfeld atom refinement, *IUCr J* 1 (2014) 361–379.
- F. Neese, Software update: the ORCA program system, version 4.0, *Wiley Interdiscip. Rev. Comput. Mol. Sci.* 8 (2018) 1–6, <https://doi.org/10.1002/wcms.1327>.
- F. Weigend, R. Ahlrichs, Balanced basis sets of split valence, triple zeta valence and quadruple zeta valence quality for H to Rn: design and assessment of accuracy, *Phys. Chem. Chem. Phys.* 7 (2005) 3297–3305, <https://doi.org/10.1039/b508541a>.
- G.L. Stoychev, A.A. Auer, F. Neese, Automatic generation of auxiliary basis sets, *J. Chem. Theory Comput.* 13 (2017) 554–562, <https://doi.org/10.1021/acs.jctc.6b01041>.
- R. Izsák, F. Neese, An overlap fitted chain of spheres exchange method, *J. Chem. Phys.* 135 (14) (2011) 144105.
- F. Neese, F. Wennmohs, A. Hansen, U. Becker, Efficient, approximate and parallel Hartree-Fock and hybrid DFT calculations. A “chain-of-spheres” algorithm for the Hartree-Fock exchange, *Chem. Phys.* 356 (2009) 98–109, <https://doi.org/10.1016/j.chemphys.2008.10.036>.
- T. Lu, F. Chen, Multiwfn: a multifunctional wavefunction analyzer, *J. Comput. Chem.* 33 (2012) 580–592, <https://doi.org/10.1002/jcc.22885>.
- T. Lu, F. Chen, Quantitative analysis of molecular surface based on improved Marching Tetrahedra algorithm, *J. Mol. Graph. Model.* 38 (2012) 314–323, <https://doi.org/10.1016/j.jmgm.2012.07.004>.
- C. Van Wüllen, Molecular density functional calculations in the regular relativistic approximation: Method, application to coinage metal diatomics, hydrides, fluorides and chlorides, and comparison with first-order relativistic calculations, *J. Chem. Phys.* 109 (1998) 392–399, <https://doi.org/10.1063/1.476576>.
- F. Weigend, Accurate Coulomb-fitting basis sets for H to Rn, *Phys. Chem. Chem. Phys.* 8 (2006) 1057–1065, <https://doi.org/10.1039/b515623h>.
- P.Å. Malmqvist, B.O. Roos, The CASSCF state interaction method, *Chem. Phys. Lett.* 155 (1989) 189–194, [https://doi.org/10.1016/0009-2614\(89\)85347-3](https://doi.org/10.1016/0009-2614(89)85347-3).
- C. Angeli, R. Cimiraglia, J.P. Malrieu, N-electron valence state perturbation theory: a fast implementation of the strongly contracted variant, *Chem. Phys. Lett.* 350 (2001) 297–305, [https://doi.org/10.1016/S0009-2614\(01\)01303-3](https://doi.org/10.1016/S0009-2614(01)01303-3).
- C. Angeli, R. Cimiraglia, S. Evangelisti, T. Leininger, J.-P. Malrieu, Introduction of n-electron valence states for multireference perturbation theory, *J. Chem. Phys.* 114 (23) (2001) 10252–10264.
- C. Angeli, R. Cimiraglia, J.P. Malrieu, n-electron valence state perturbation theory: A spinless formulation and an efficient implementation of the strongly contracted and of the partially contracted variants, *J. Chem. Phys.* 117 (2002) 9138–9153, <https://doi.org/10.1063/1.1515317>.
- D. Ganyushin, F. Neese, First-principles calculations of zero-field splitting parameters, *J. Chem. Phys.* 125 (2) (2006) 024103.
- F. Neese, Efficient and accurate approximations to the molecular spin-orbit coupling operator and their use in molecular g-tensor calculations, *J. Chem. Phys.* 122 (3) (2005) 034107.
- R. Maurice, R. Bastardis, C. de Graaf, N. Suaud, T. Mallah, N. Guihéry, Universal theoretical approach to extract anisotropic spin hamiltonians, *J. Chem. Theory Comput.* 5 (2009) 2977–2984, <https://doi.org/10.1021/ct900326e>.
- A.W. Addison, T.N. Rao, J. Reedijk, J. van Rijn, G.C. Verschoor, Synthesis, structure, and spectroscopic properties of copper(II) compounds containing nitrogen-sulphur donor ligands, *J. Chem. Soc. Dalt. Trans.* 7 (1984) 1349–1356.
- R.F. Bader, *Atoms in Molecules*, Oxford University Press, 1994.
- E. Espinosa, E. Molins, C. Lecomte, Hydrogen bond strengths revealed by topological analyses of experimentally observed electron densities, *Chem. Phys. Lett.* 285 (1998) 170–173, [https://doi.org/10.1016/S0009-2614\(98\)00036-0](https://doi.org/10.1016/S0009-2614(98)00036-0).
- E. Espinosa, I. Alkorta, J. Elguero, E. Molins, From weak to strong interactions: a comprehensive analysis of the topological and energetic properties of the electron density distribution involving X-H...F-Y systems, *J. Chem. Phys.* 117 (2002) 5529–5542, <https://doi.org/10.1063/1.1501133>.
- A.D. Becke, K.E. Edgecombe, A simple measure of electron localization in atomic and molecular systems, *J. Chem. Phys.* 92 (1990) 5397–5403, <https://doi.org/10.1063/1.458517>.
- T. Lu, F.W. Chen, Meaning and functional form of the electron localization function, *Wuli Huaxue Xuebao, Acta Phys. – Chim. Sin.* 27 (2011) 2786–2792, <https://doi.org/10.3866/PKU.WHXB20112786>.
- J. Boeckmann, C. Näther, [Bis(3-aminopropyl)amine- $\kappa$  3N, N', N'']-bis-(thiocyanato- $\kappa$ N)cobalt(II), *Acta Crystallogr., Sect. E Struct. Rep.* 67 (8) (2011).
- C. Lee, W. Yang, R.G. Parr, Development of the Colle-Salvetti correlation-energy formula into a functional of the electron density, *Phys. Rev. B* 37 (1988) 785–789, <https://doi.org/10.1103/PhysRevB.37.785>.
- A.D. Becke, Density-functional exchange-energy approximation with correct asymptotic behavior, *Phys. Rev. A* 38 (1988) 3098–3100, <https://doi.org/10.1103/PhysRevA.38.3098>.
- P.J. Stephens, F.J. Devlin, C.F. Chabalowski, M.J. Frisch, Ab initio calculation of vibrational absorption and circular dichroism spectra using density functional force fields, *J. Phys. Chem.* 98 (1994) 11623–11627, <https://doi.org/10.1021/j100096a001>.



- [45] O.A. Vydrov, T. Van Voorhis, Nonlocal van der Waals density functional: the simpler the better, *J. Chem. Phys.* 133 (24) (2010) 244103.
- [46] W. Hujo, S. Grimme, Performance of the van der Waals density functional VV10 and (hybrid)GGA variants for thermochemistry and noncovalent interactions, *J. Chem. Theory Comput.* 7 (2011) 3866–3871, <https://doi.org/10.1021/ct200644w>.
- [47] E. Ruiz, J. Cano, S. Alvarez, P. Alemany, Broken symmetry approach to calculation of exchange coupling constants for homobinuclear and heterobinuclear transition metal complexes, *J. Comput. Chem.* 20 (1999) 1391–1400, [https://doi.org/10.1002/\(SICI\)1096-987X\(199910\)20:13<1391::AID-JCC6>3.0.CO;2-J](https://doi.org/10.1002/(SICI)1096-987X(199910)20:13<1391::AID-JCC6>3.0.CO;2-J).
- [48] T. Soda, Y. Kitagawa, T. Onishi, Y. Takano, Y. Shigeta, H. Nagao, Y. Yoshioka, K. Yamaguchi, Ab initio computations of effective exchange integrals for H-H, H-He-H and Mn 2 O 2 complex: comparison of broken-symmetry approaches, *Chem. Phys. Lett.* 319 (2000) 223–230, [https://doi.org/10.1016/S0009-2614\(00\)00166-4](https://doi.org/10.1016/S0009-2614(00)00166-4).
- [49] R. Boča, *A Handbook of Magnetochemical Formulae*, 1st ed., Elsevier, Amsterdam, 2012.
- [50] S. Stoll, A. Schweiger, *EasySpin, a comprehensive software package for spectral simulation and analysis in EPR*, *J. Magn. Reson.* 178 (1) (2006) 42–55.

## RESEARCH ARTICLE

[View Article Online](#)  
[View Journal](#) | [View Issue](#)

 Cite this: *Inorg. Chem. Front.*, 2023, **10**, 5406

# Neutral cobalt(II)-bis(benzimidazole)pyridine field-induced single-ion magnets for surface deposition†

 Jana Juráková,<sup>a</sup> Ondřej F. Fellner,<sup>b</sup> Sören Schlittenhardt,<sup>c</sup> Šárka Vavrečková,<sup>a</sup> Ivan Nemeč,<sup>a,b</sup> Radovan Herchel,<sup>b</sup> Erik Čížmár,<sup>d</sup> Vinicius Tadeu Santana,<sup>a</sup> Milan Orlita,<sup>e</sup> Denis Gentili,<sup>f</sup> Giampiero Ruani,<sup>f</sup> Massimiliano Cavallini,<sup>f</sup> Petr Neugebauer,<sup>a</sup> Mario Ruben<sup>c</sup> and Ivan Šalitros<sup>g</sup> \*<sup>a,g</sup>

Two novel hexacoordinated Co(II)-based single-ion magnets were prepared and characterised. Both neutral complexes feature metal-centred coordination with one terminal and one bidentate nitrate anions along with tridentate derivatives of a 2,6-bis(1*H*-benzimidazole-2-yl)pyridine ligand containing either *n*-octyl (complex **1**) or *n*-dodecyl (complex **2**) chains. The presence of long aliphatic chains ensures their solubility in low polarity and volatile solvents frequently used for lithography patterning. This enabled the preparation of microstructural layers and patterns on technologically relevant substrates by easy-to-handle and low-cost wet lithographic techniques. On the other hand, attempts at surface deposition *via* sublimation were not successful due to thermal instability. The electronic structure of complexes typically features an orbitally non-degenerate ground state well-separated from the lowest excited state, which allows one to analyse magnetic anisotropy by the spin Hamiltonian approach. Zero-field splitting parameters obtained from CASSCF-NEVPT2 calculations and from the analysis of magnetic data suggest that both compounds display positive axial *D* parameters within a range of 17–25 cm<sup>-1</sup>. Combined results from high-field electron paramagnetic resonance (X-band and HF-EPR) and Fourier-transform infrared magnetic spectroscopy (FIRMS) simulated with the spin Hamiltonian provided the axial and rhombic zero-field splitting terms *D* = +23.7 cm<sup>-1</sup> for complex **1** and *D* = +24.2 cm<sup>-1</sup> for complex **2**, together with pronounced rhombicity in the range of *E/D* ≈ 0.15–0.19 for both compounds. Dynamic magnetic investigations have revealed the field-induced slow relaxation of magnetisation, with maximal relaxation times ( $\tau$ ) of 7.6 ms for **1** and 0.8 ms for **2**. This relaxation is governed *via* a combination of several relaxation mechanisms, among which the quantum tunnelling was efficiently suppressed by the applied static magnetic field. The effective barriers of spin reversal  $U_{\text{eff}}$  = 77(4) K for **1** and  $U_{\text{eff}}$  = 70(2) K for **2** are consistent with the expected values calculated using the ZFS parameters.

 Received 19th May 2023,  
 Accepted 23rd July 2023

DOI: 10.1039/d3qi00931a

[rsc.li/frontiers-inorganic](https://rsc.li/frontiers-inorganic)
<sup>a</sup>Central European Institute of Technology, Brno University of Technology, Purkyňova 123, 61200 Brno, Czech Republic

<sup>b</sup>Department of Inorganic Chemistry, Faculty of Science, Palacký University, 17. listopadu 12, 771 46 Olomouc, Czech Republic

<sup>c</sup>Institute of Nanotechnology (INT), Karlsruhe Institute of Technology (KIT), Hermann-von-Helmholtz-Platz 1, 76344 Eggenstein-Leopoldshafen, Germany

<sup>d</sup>Institute of Physics, Faculty of Science, P.J. Šafárik University Park Angelinum 9, 04154 Košice, Slovakia

<sup>e</sup>LNCMI-EMFL, CNRS UPR3228, Univ. Grenoble Alpes, Univ. Toulouse, Univ. Toulouse 3, INSA-T, Grenoble and Toulouse, France

<sup>f</sup>Consiglio Nazionale delle Ricerche, Istituto per lo Studio dei Materiali Nanostrutturati (CNR-ISMN), Via P. Gobetti 101, 40129 Bologna, Italy

<sup>g</sup>Department of Inorganic Chemistry, Faculty of Chemical and Food Technology, Slovak University of Technology in Bratislava, Bratislava SK-81237, Slovakia.  
 E-mail: [ivan.salitros@stuba.sk](mailto:ivan.salitros@stuba.sk)

 † Electronic supplementary information (ESI) available. CCDC 2255669–2255672. For ESI and crystallographic data in CIF or other electronic format see DOI: <https://doi.org/10.1039/d3qi00931a>

## Introduction

Mononuclear single-molecule magnets (SMMs), also known as single-ion magnets (SIMs), offer a wide range of potential applications, including high-density data storage, quantum computing, and spintronic devices.<sup>1</sup> Unlike materials with long-range magnetic ordering, the magnetic bistability of SMMs is solely based on molecular properties and does not depend on intermolecular interactions. While initial studies have primarily focused on lanthanide SIMs, research in the last decade has revealed that mononuclear first-row transition metal complexes also exhibit interesting SIM properties. The first observation of slow relaxation of magnetisation (SRM) in mononuclear ferrous complexes by Long *et al.*<sup>2</sup> marked the beginning of a large body of research into first-row transition

metal SIMs.<sup>3</sup> High-spin Co(II) complexes are of particular interest due to their tendency to exhibit unsuppressed orbital angular momentum, resulting in significant single-ion magnetic anisotropy.<sup>4</sup> Furthermore, the non-integer ground spin state of Co(II) ions reduces the probability of quantum tunneling of magnetisation (QTM) under the applied static field, allowing a wide variety of Co(II) SIMs with various coordination numbers and geometries to be rapidly developed.

Exploring the technological applications of SIMs is challenging due to the fact that the prepared coordination compounds are typically in the form of single crystals or bulk powders, which are unsuitable for controlled manipulation and applications. Therefore, there is growing interest in fabricating nanostructured monolayers and thin films through substrate deposition. This approach combines the magnetic bistability of deposited SIMs with the electronic and/or magnetic properties of the substrate, resulting in hybrid structures that are better suited for desired applications.<sup>5</sup> Given this potential, current efforts are also focused on preparing Co(II) SIMs that are suitable for introduction on surfaces *via* sublimation<sup>6</sup> or wet deposition.<sup>7</sup> This could enable the investigation of SRM on layered or even sub-monolayered surfaces, particularly those that do not form strong covalent or non-covalent interactions with the substrates. Despite several reports proving the successful deposition by sublimation on various surfaces such as gold,<sup>8</sup> silver<sup>9</sup> and glass,<sup>10</sup> the deposited SIM molecules often exhibit diminished SMM behaviour or modified features of SRM due to interactions with the surface. Moreover, for some molecular systems, wet lithography may be a more reasonable option for maintaining their magnetic properties, as it allows for the transfer of the molecules onto substrates directly *via* chemical crafting from a solution.<sup>11</sup>

Co(II) complexes with 2,6-bis(benzimidazole-1-yl)pyridine (bbp) tridentate ligands are a well-known family of field-induced SIMs, where their rigid and aromatic ligand skeleton favours geometries supporting higher magnetic anisotropy, thus inducing a large zero-field splitting parameter  $D$ .<sup>12,13</sup> Furthermore, the rationalised introduction of aromatic or aliphatic substituents on the ligand skeleton has a significant impact on the relaxation mechanisms, which can be realized through single or multiple relaxation channels.<sup>7,14</sup> Our recent reports were focused on the pentacoordinate Co(II)-SIMs with bbp ligands functionalised by long aliphatic chains.<sup>7,15</sup> This modification enables good solubility in non-polar and volatile solvents used for lithographical deposition. Unfortunately, the weak halogenido coordination bonds are likely to have played a role in the thermal instability observed in the reported neutral pentacoordinate Co(II)-SIMs, ultimately hindering their successful surface deposition *via* sublimation. Therefore our current efforts are focused on the search for new neutral, thermally stable and sublimable Co(II)-SIMs consisting of functionalised bbp derivatives that also allow surface deposition by wet lithography approaches.

Herein we report the synthesis, and structural, spectral, magnetic and computational investigations of two neutral hexacoordinated field-induced Co(II)-SIMs (Fig. 1): complexes **1**

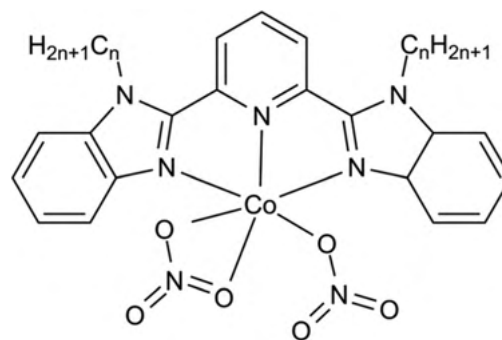


Fig. 1 Structure of reported Co(II)-SIMs **1** ( $n = 8$ ) and **2** ( $n = 12$ ).

and **2** of the general formula  $[\text{Co}(\text{L})(\text{NO}_3)_2]$ , where L corresponds to L1 = 2,6-bis(1-octyl-1*H*-benzimidazol-2-yl)pyridine and L2 = 2,6-bis(1-dodecyl-1*H*-benzimidazol-2-yl)pyridine for **1** and **2**, respectively. These complexes contain two coordinated nitrate anions, one acting as a monodentate chelating ligand and the other as a bidentate chelating ligand, and their coordination modes remain unchanged as the temperature varies. The magnetic anisotropy of the two analogues **1** and **2** was analysed by an *ab initio* theoretical approach and experimentally evaluated on the basis of static magnetic properties, X-band EPR spectroscopy and HF EPR/FIRMS spectroscopy. The alternating current (AC) susceptibility study confirmed that both complexes are field-induced SIMs and their SRM in the static magnetic field and temperature region is realised by a combination of several relaxation processes.

## Results and discussion

### Synthesis and spectral and structural properties

The detailed synthetic procedures of the hexacoordinate Co(II) complexes **1** and **2** are described in the Experimental section (see the ESI<sup>†</sup>). Their preparation is based on the reaction of  $\text{Co}(\text{NO}_3)_2 \cdot 6\text{H}_2\text{O}$  with previously reported tridentate ligands L1 and L2<sup>7</sup> in acetonitrile solution. The reactions yielded orange crystals suitable for single-crystal X-ray analysis after a few days of slow evaporation at room temperature. Their phase purity was confirmed by powder X-ray diffraction analysis before further spectroscopic and magnetic investigations were conducted (Fig. S2<sup>†</sup>). As the molecular structures of complexes **1** and **2** only differ in the length of aliphatic chains, their FT-IR (Fig. S3<sup>†</sup>) and UV-Vis (Fig. S4<sup>†</sup>) spectra are similar. The stretching vibrations of aliphatic C-H bonds were observed at intervals of 2922–2918  $\text{cm}^{-1}$  and 2854–2850  $\text{cm}^{-1}$  for asymmetric and symmetric valence vibrations, respectively. Medium vibrational bands corresponding to aromatic C-C or C-N stretching were observed in the range of 1599–1574  $\text{cm}^{-1}$ . Strong signals related to =C-H bending were found at 748  $\text{cm}^{-1}$  for both complexes. The solid-state UV-Vis absorption spectra of **1** and **2** revealed a broad band at an interval of 290–410 nm assigned to  $\pi \rightarrow \pi^*$  and  $n \rightarrow \pi^*$  transitions that split in the acetonitrile solution to  $\pi \rightarrow \pi^*$  transitions at

290 nm and to  $n \rightarrow \pi^*$  transitions at 375 nm. Furthermore, the solid-state spectra contain the second weaker band in the visible region of 500–575 nm related to d–d and MLCT transitions.

Single crystal X-ray diffraction analysis revealed that both compounds crystallise in the triclinic  $P\bar{1}$  space group at low temperatures (at 100 K for **1** and 90 K for **2**) as well as at 293 K (selected crystallographic parameters can be found in Table S1, see the ESI†). The asymmetric unit of each structure is neutral complex molecules, represented by the general formulas  $[\text{Co}(\text{L1})(\text{NO}_3)_2]$  and  $[\text{Co}(\text{L2})(\text{NO}_3)_2]$ , respectively (Fig. 2a and b). In both compounds, the Co(II) central atom is coordinated with three nitrogen atoms of the corresponding tridentate ligand and three oxygen atoms of one chelating and

one terminal nitrate anion. The structural analysis performed at two temperatures did not provide evidence for heptacoordination, which would involve the second oxygen atom of the terminal nitrate anion, as observed in similar systems previously.<sup>16</sup> At 100 K, the Co–N bond lengths of compounds vary within a tiny range of 2.088(1)–2.103(1) Å and heating to room temperature caused only small elongation to 2.100(3)–2.117(2) Å (Table S2†). Co–N bond lengths are preferably neither shorter nor longer due to coordination with the imidazole or pyridine moieties. On the other hand, Co–O coordination bonds of terminal  $\text{NO}_3^-$  anions ( $d_{\text{avg}} = 2.04$  Å for **1** and  $d_{\text{avg}} = 2.05$  Å for **2**) are notably shorter than those formed with chelating  $\text{NO}_3^-$  anions ( $d_{\text{avg}} = 2.11$  Å (O4) and 2.23 Å (O5) for **1**,  $d_{\text{avg}} = 2.10$  Å (O4) and 2.21 Å (O5) for **2**). Two oxygen donor atoms,

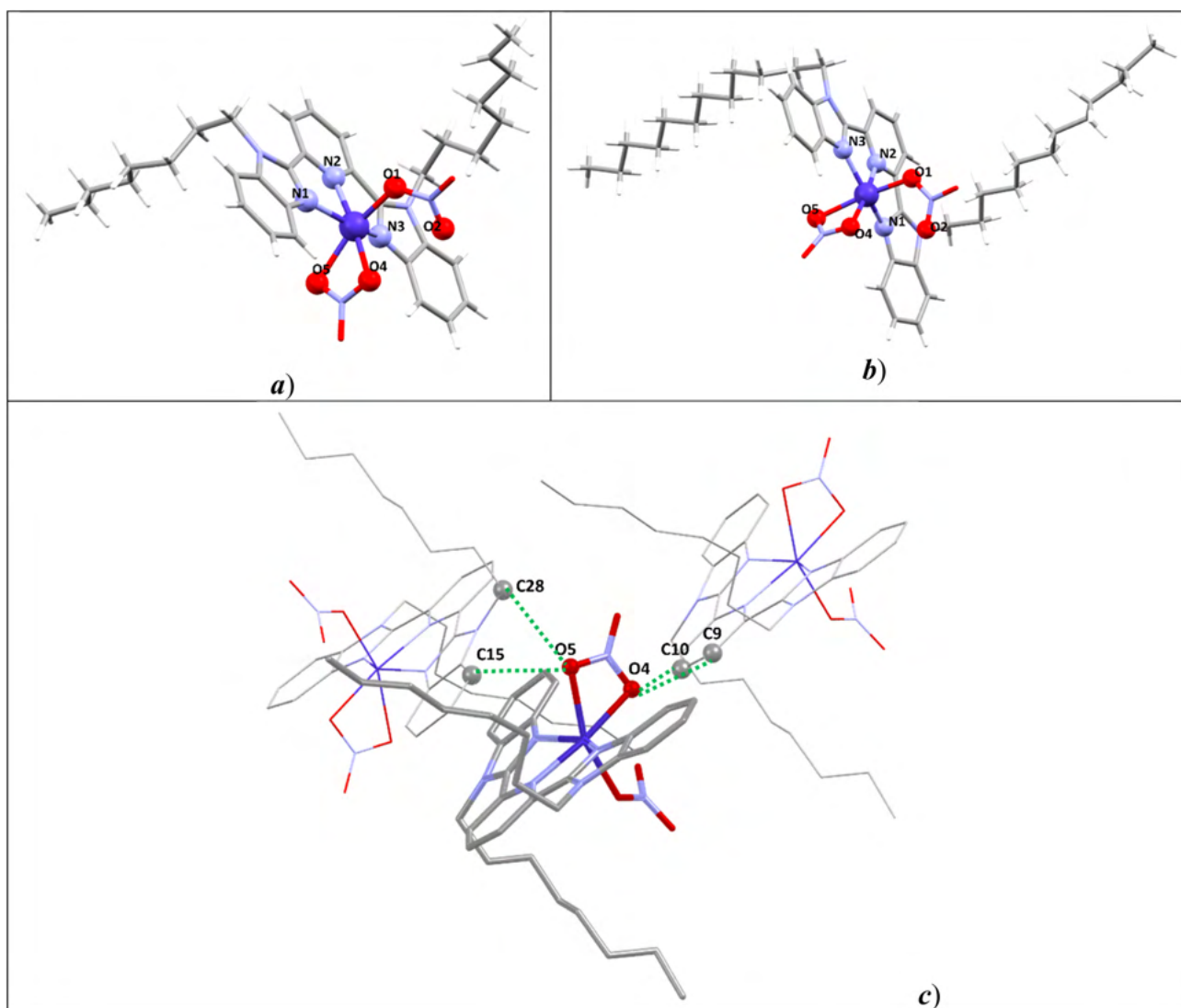


**Fig. 2** Molecular structures of **1** (a) and **2** (b). Visualisation of non-covalent interactions (green dashed lines) in compound **1** (c): O5...C15 = 3.125(2) Å, O5...C28 = 3.060(3) Å, O4...C9 = 3.183(2) Å, O4...C10 = 3.193(3) Å at 100 K; O5...C15 = 3.159(3) Å, O5...C28 = 3.195(4) Å, O4...C9 = 3.327(3) Å, and O4...C10 = 3.296(3) Å, at 293 K. Similar contacts have been found in compound **2** (Fig. S7†): O5...C5 = 3.097(2) Å, O5...C20 = 3.161(2) Å, O4...C10 = 3.132(2) Å, O4...C11 = 3.124(2) Å at 100 K; O5...C5 = 3.206(3) Å, O5...C20 = 3.210(3) Å, O4...C10 = 3.259(3) Å, and O4...C11 = 3.263(3) Å at 293 K.



O1 and O5, of the terminal and chelating  $\text{NO}_3^-$  ligand anions, respectively, lay on the axial axis of coordination polyhedra, and their *trans* angles present the most significant contribution to the deviation from ideal octahedral geometry (avg.  $159^\circ$  for **1** and avg.  $161^\circ$  for **2**, Table S3†). The equatorial plane is formed by three N-donor atoms of the corresponding tridentate ligand and by the remaining oxygen donor atom O4 of the chelating  $\text{NO}_3^-$  ligand anion. The symmetry measure parameters<sup>17a</sup> calculated using program SHAPE<sup>17b</sup> and the angular distortion parameter  $\Sigma^{18}$  suggest that the coordination polyhedra of all structures can be classified as severely distorted tetragonal bipyramids ( $S(\text{OC-6})_{\text{avg}} = 5.0$ ;  $\Sigma \approx 137^\circ$ ; Table S2 and Fig. S6†). Furthermore, the second oxygen atoms O2 of terminal  $\text{NO}_3^-$  anions create short intramolecular contacts with the Co(II) central atom with distances in the range 2.970(2)–3.013(2) Å. When those O2 oxygen atoms are hypothetically included in the coordination polyhedron, the continuous shape analysis suggests the capped octahedral ( $S(\text{COC-7})_{\text{avg}} = 5.6$ ) or capped trigonal prism ( $S(\text{CTPR-7})_{\text{avg}} = 6.3$ ) geometry.

Crystal structures of both compounds exhibit a similar motif of intermolecular interactions created by the O5 oxygen atom of chelating  $\text{NO}_3^-$  ligand anions of one complex with phenylene C15 and alkyl C28 carbon atoms of the second neighbouring molecule. Those intermolecular synthons with distances smaller than the sum of van der Waals radii of carbon and oxygen atoms (Fig. 2c and Fig. S7†) are responsible for the formation of intermolecular pseudodimers connected to each other *via* other short contacts between the second oxygen atom O4 of the chelating  $\text{NO}_3^-$  ligand and C9 and C10 aromatic carbon atoms of the neighbouring complex molecule.

### Surface deposition

The suitability of compounds **1** and **2** for film growth/deposition and patterning on silicon/ $\text{SiO}_2$  substrates *via* wet processes was investigated using drop-casting and lithographically controlled wetting. These methods are straightforward and provide essential information for wet processing. The films and patterned structures were characterised using bright-field and polarised optical microscopes to assess the material's birefringence. Raman spectroscopy was employed to identify the compounds on the deposited surfaces, thereby confirming their stability under wet processing.

When deposited by drop-casting, chloroform solutions of **1** and **2** form continuous films that cover the entire surface, with a marked accumulation of material at the boundaries of the film generated by the so-called “coffee stain effect”.<sup>19</sup> Optical microscopy shows that the films are formed by a continuous distribution of crystals, varying in size from a few microns at the centre of the film to tens of microns at the boundaries (Fig. S8†). As expected, larger crystals ( $>10 \mu\text{m}$ , Fig. S8b and d†) are preferentially located at the boundaries, while micrometric crystallites are located at the centre of the sample (Fig. S8a and c†). When observed by polarised optical microscopy, the large crystals exhibit a clear birefringence. However, except in a few rare cases, the crystals extinguish the

light at precise orientation only in some portions. The crystallites in the inner areas of the film show a less intense birefringence and do not extinguish the light by rotating the polarisers in any direction. This behaviour suggests the polycrystalline nature of investigated films. Drop-casting of more diluted solutions allows for preparing surfaces with randomly distributed, irregular and droplet-like formed agglomerates, each measuring a few microns in size. These agglomerates are composed of micrometre-sized crystallites that exhibit the same behaviour as the inner part of the continuous films. Despite some minor differences in the relative peak intensity (probably due to a slightly enhanced orientation of the crystals in the printed structure compared with the powder), Raman spectra confirm that compounds **1** and **2** are processable by drop casting (Fig. S9a and c†).

Compounds **1** and **2** were also patterned on optically accessible sub-micrometric structures by lithographically controlled wetting,<sup>20</sup> a well-known wet process widely used to pattern many functional materials (see the Experimental section and ref. 21 for more details). Lithography allows large-area patterning of soluble compounds exploiting the spatial confinement provided by the formation of menisci between the protrusions of a soft stamp and the surface of the substrate.

We printed both continuous parallel stripes (obtained by the replication of a blank compact disk) and isolated sub-micrometric “pits & lands” structures equivalent to the logical pattern used in compact disks. Surfaces prepared from both compounds **1** (Fig. 3) and **2** (Fig. S10†) have similar properties and are almost indistinguishable by optical microscopy or AFM. When observed by optical microscopy, the printed structures replicate the main features of the stamp protrusions, resulting in the formation of continuous or segmented parallel stripes. Printed structures appear variously coloured and show moderate birefringence. Upon conducting a thorough investigation using polarised optical microscopy, it was observed that individual stripes did not simultaneously block light around their entire perimeter. Instead, only specific areas were found to block light, and these areas changed depending on the rotation of the polarisers. Additionally, AFM investigation of the morphology within the printed structures revealed the presence of small crystal-like substructures inside the stripes. Both polarised optical microscopy and AFM suggest that surfaces of **1** and **2** were prepared by lithographically controlled wetting from polycrystalline structures. Also here, the Raman spectra confirmed the presence of **1** and **2** on the patterned surfaces (Fig. S9b and d†).

To obtain a comprehensive understanding of the deposition capabilities of the reported Co(II) complexes, we tested the surface deposition *via* thermal sublimation of **1** and **2** onto graphene, silicon wafers and gold substrates. To facilitate deposition, we utilized an in-house built high-vacuum sublimation chamber with an outfitted quartz crucible heated with a silicon nitride heater. Additionally, a thermocouple in thermal contact with the crucible is used to achieve precise temperature control. The base pressure inside the chamber is maintained at a low level of  $1 \times 10^{-6}$  mbar. Complexes **1** and **2**

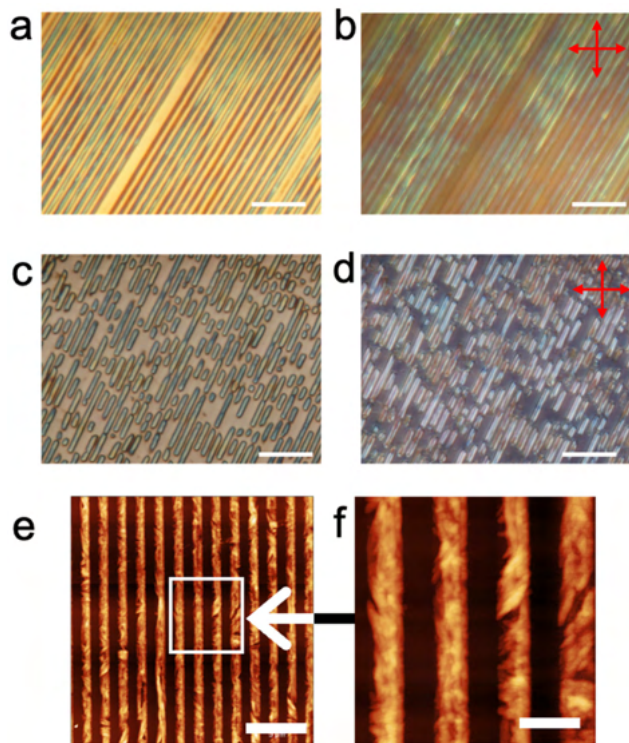


**Fig. 3** Printed structures of **1** fabricated by lithographically controlled wetting on a silicon surface: image of continuous stripes taken in bright field (a) and corresponding image under crossed polars (bar is 10  $\mu\text{m}$ ) (b). Image of microstructures taken in bright field (c) and corresponding image under crossed polars (bar is 10  $\mu\text{m}$ ) (d) AFM morphology of printed stripes (bar is 5  $\mu\text{m}$ , z scale 0–50 nm) (e); and zoomed-in (f) image of picture (e) with 1 bar = 1.5  $\mu\text{m}$ , z scale 0–45 nm.

began to sublime at temperatures of 270  $^{\circ}\text{C}$  and 310  $^{\circ}\text{C}$ , respectively, which are notably higher than their decomposition temperature (209  $^{\circ}\text{C}$  for **1**, 219  $^{\circ}\text{C}$  for **2**, Fig. S5†). This suggests that the complexes were unable to withstand the heating process and only the uncoordinated ligands were sublimed and deposited onto the selected surfaces. To determine whether the compounds remained intact after sublimation and deposition onto the surface, we employed X-ray photoelectron spectroscopy (XPS) as a surface-sensitive analytical technique. By comparing the as-synthesised bulk powder, powder after sublimation, and deposited samples, we aimed to investigate any potential degradation of the compounds. Additional information can be found in Fig. S11 and S12 in the ESI.† The absence of Co 2p and “NO<sub>3</sub><sup>−</sup>” nitrogen photoelectron peaks on the surfaces indicates that the complexes underwent partial decomposition during the sublimation and deposition process.

### Computational study and static magnetic investigation

To elucidate the connection between the magnetic anisotropy of the investigated compounds and their structural properties, we conducted a computational study with multiple objectives. First, we concentrated on the role of the nitrate ligand, which

coordinates the Co(II) atom in a monodentate manner. The second oxygen atom pointing towards the central atom adopts a rather large Co...O2 distance in both compounds (in  $\text{Å}$ , 3.013(1) in **1** and 2.997(1) in **2** at 100 K). Nevertheless, previously, we found that even such large distances can affect the static and dynamic magnetic properties of Co(II) complexes.<sup>22</sup> Therefore, to properly analyse structures of the complex molecules in **1** and **2** we performed single-point DFT calculations at the B3LYP def-TZVP level of theory using Orca 4.2.1 computational package.<sup>23</sup> The coordinates were taken from the corresponding crystal structures as determined by X-ray diffraction, and the positions of the hydrogen atoms were optimized (B3LYP and def2-SVP).<sup>24</sup> Then, Bader's QTAIM analysis<sup>25</sup> using the Multiwfn program<sup>26</sup> was performed to investigate the topology of electron density. The (3,−1) bond critical points were found only in the case of regular metal–ligand bonds and not for the above-mentioned possibly long Co...O2 contact. Therefore, as another option, we investigated the values of non-covalent interaction index,<sup>27</sup> which can determine whether the nature of non-covalent interactions is attractive or repulsive. However, in this case the interaction between the atoms has a weak van der Waals character. Therefore, we may conclude that the second oxygen atom should not affect the Co(II) centre directly and significantly.

In the next step, we focused our attention on the analysis of magnetic anisotropy of **1** and **2** and the calculation of the ZFS parameters by the state average complete active space self-consistent field (SA-CASSCF)<sup>28</sup> with the wave function method complemented by N-electron valence second-order perturbation theory (NEVPT2).<sup>29</sup> Again, the experimentally determined molecular structures with optimised positions of hydrogen atoms were used as input coordinates. The basis set used for the calculation consisted of def2-SVP basis for hydrogen and carbon atoms, while def2-TZVP was used for the remaining atoms. The costs of calculations were decreased by the use of the def2/J and def2-TZVP/C auxiliary basis sets<sup>30</sup> together with the chain-of-spheres (RJCOSX)<sup>31</sup> approximation to exact exchange as implemented in ORCA. The active space was defined by seven electrons in five d-orbitals of Co(II) (CAS (7e,5o)), and all possible multiplets, 10 quartets and 40 doublets, were involved in the calculations. Aiming at determining the ligand field parameters, we also performed *ab initio* ligand field theory (AILFT) calculations.<sup>32</sup>

The results obtained for both complexes are very similar. The splitting of d-orbitals reflects the distorted octahedral geometry of the coordination polyhedron with the close-lying orbitals  $d_{xz}$  and  $d_{xy}$  and with  $d_{yz}$  having slightly higher energy, by ca. 1000  $\text{cm}^{-1}$  (Fig. 4 left). The remaining d-orbitals have much higher energy:  $d_{z^2}$  ( $\sim 7700 \text{ cm}^{-1}$ ),  $d_{x^2-y^2}$  ( $\sim 9000 \text{ cm}^{-1}$ ). Thus, the electronic configuration of the d-valence shell for both complexes is  $d_{xz}^2, d_{xy}^2, d_{yz}^1, d_{z^2}^1, d_{x^2-y^2}^1$ . In such a configuration, relatively small energy of the first excitation between the orbitals with the same  $|m_l|$  value ( $d_{xz} \rightarrow d_{yz}$ ,  $|m_l| = \pm 1$ ) is a bit larger than the excitation involving a change of  $m_l$  by 1 ( $d_{xy} \rightarrow d_{yz}$ ). Therefore, a relatively large and positive  $D$  values can be expected for **1** and **2**.<sup>33</sup>

The SA-CASSCF/NEVPT2 calculations revealed that both complexes exhibit a similar splitting of the ligand-field terms

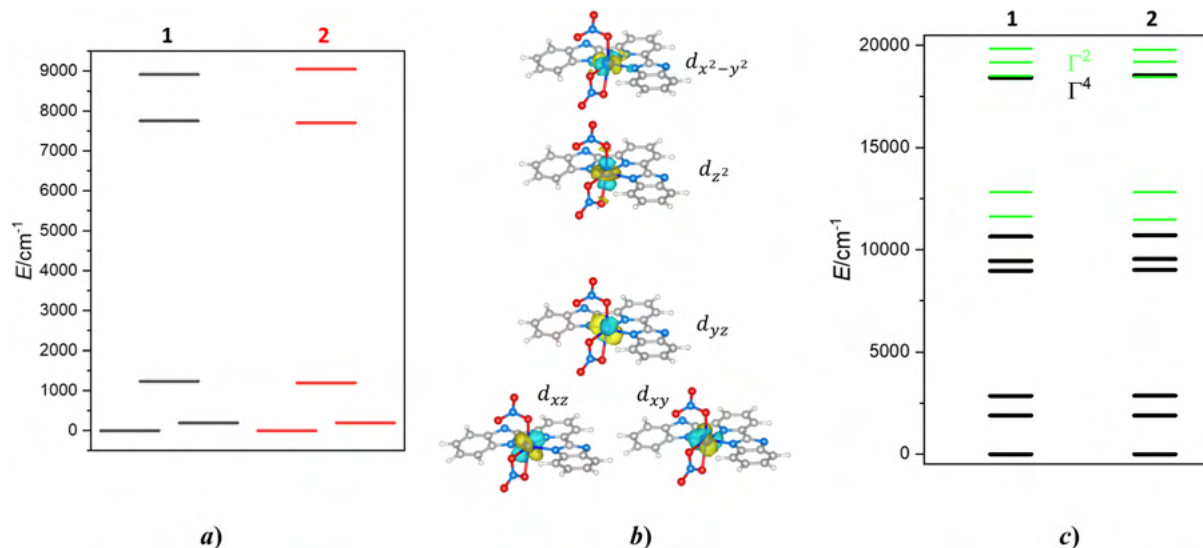


**Fig. 4** The outcome of the CASSCF/NEVPT2 calculations for complexes **1** and **2**. Plot of the d-orbital splitting calculated by *ab initio* ligand field theory (AILFT) (a), visualisations of the d-orbitals (b) and low-lying ligand-field terms (LFT) (c). Note: different multiplicities of LFT are shown in different colours.

(LFT) (Fig. 4 right). The  ${}^4T_{1g}$  LFT is split within the range of 0–3000  $\text{cm}^{-1}$  with the lowest excited state having energy greater than 1800  $\text{cm}^{-1}$  assuring applicability of spin Hamiltonian formalism.<sup>7,14,15</sup> The LFT's are split into ligand-field multiplets (LFM) due to spin-orbit coupling, resulting in ZFS as an energy separation between the two lowest Kramers doublets. The resulting ZFS parameters were found to be very similar for both complexes:  $D = +25.6$  (**1**) and  $+25.4$   $\text{cm}^{-1}$  (**2**) and  $E/D = 0.146$  (**1**),  $0.138$  (**2**). The effective spin Hamiltonian  $g$ -tensors calculated for **1** and **2** were practically identical, indicating easy-plane anisotropy ( $g_x \approx g_y \gg g_z$ ). This type of anisotropy in **1** and **2** was also deduced from the analysis of the first Kramers doublet using an effective spin  $S_{\text{eff}} = 1/2$ . The resulting effective  $g$ -factors are consistent with the easy-plane anisotropy ( $g_x \ll g_y \ll g_z$ ). The calculated parameters have been summarised in Table 1.

The theoretical calculations have confirmed the validity of employing the spin Hamiltonian formalism for  $S = 3/2$  in the subsequent analysis, as presented below:

$$\hat{H} = D(\hat{S}_z^2 - \hat{S}^2/3) + E(\hat{S}_x^2 - \hat{S}_y^2) + \mu_B B g \hat{S}_a \quad (1)$$

where the axial ( $D$ ) and rhombic ( $E$ ) parameters describing the zero-field splitting of quartet ground state are included

**Table 1** The theoretically calculated spin Hamiltonian parameters for complexes **1** and **2**

	$g_x, g_y, g_z, g_{\text{iso}}$	$g_{x,\text{eff}}, g_{y,\text{eff}}, g_{z,\text{eff}}$ ( $S_{\text{eff}} = 1/2$ ) <sup>a</sup>	$D/\text{cm}^{-1}$	$E/D$
<b>1</b>	2.442, 2.323, 2.097, <b>2.287</b>	1.986, 3.592, 5.815	+25.61	0.146
<b>2</b>	2.442, 2.323, 2.098, <b>2.287</b>	2.000, 3.654, 5.766	+25.41	0.138

<sup>a</sup> The  $g$ -parameters calculated for the ground state Kramers doublet for the effective spin  $1/2$ .

together with the Zeeman term defined for the  $a$ -direction of the magnetic field,  $B_a = B(\sin(\theta)\cos(\varphi), \sin(\theta)\sin(\varphi), \cos(\theta))$ .<sup>34</sup> Herein, we fitted both temperature and field-dependent magnetic data for **1** and **2** with the program POLYMAGNET.<sup>35</sup> Several attempts were made to analyse experimental data. Firstly, the data were fitted with the isotropic  $g$ -value and positive or negative  $D$ -parameter. Finally, the anisotropic  $g$ -tensor was also considered based on the theoretical calculations, where  $g_z$  was fixed to free electron value 2.0 and  $g_{xy}$  was allowed to vary. Here, only positive values of  $D$  were considered. The results of all three approaches are summarized in Table 2, Fig. 5 and Fig. S13, S14.† Generally, the  $|D|$  values were found in the range 15–25  $\text{cm}^{-1}$ , and it is evident that the model with anisotropic  $g$ -tensor provided higher positive values of  $D$ , which we also observed previously.<sup>36</sup> These values are also closer to those found by CASSCF/NEVPT2 calculations. Moreover, it is necessary to mention that in the case of compound **1**, the additional parameter  $\chi_{\text{TIP}}$  describing temperature-independent paramagnetism was needed to describe the steady increase of  $\mu_{\text{eff}}$  at higher temperatures. In contrast, it was revealed that the rhombic parameter  $E$  was not needed to fit magnetic data of **2** for models comprising positive  $D$ -parameter, which led to the reduction of the number of free parameters. Thus, the analysis of the static magnetic data revealed negligible differences in the magnetic anisotropy of **1** and **2**, suggesting that different relaxation properties of these compounds (*vide infra*) are not linked to their magnetic anisotropy.

### HF EPR and FIRMS spectroscopy

To corroborate the findings from the static magnetic measurements and computational studies, we utilised high-frequency electron paramagnetic resonance (HF EPR) and Fourier-trans-



**Table 2** The spin Hamiltonian parameters derived from the DC magnetic data of **1** and **2**<sup>a</sup>

Compound	$D$ (cm <sup>-1</sup> )	$E$ (cm <sup>-1</sup> )	$g$ -Factors	$\chi_{\text{TIP}}$ (10 <sup>-9</sup> m <sup>3</sup> mol <sup>-1</sup> )	RSS <sup>b</sup>
<b>1</b>	+19.5 (2.8)	+6.4 (1.7)	$g_{\text{iso}} = 2.253(18)$	5.8 (2.9)	0.000272
	-20.6 (2.4)	-5.0 (1.7)	$g_{\text{iso}} = 2.254(18)$	5.7 (2.9)	0.000296
	+24.0 (4.8)	+7.9 (2.3)	$g_{xy} = 2.335(24)$	7.3 (3.2)	0.00100
			$g_z = 2.0^c$		
<b>2</b>	+17.06 (27)	0	$g_{\text{iso}} = 2.3920(22)$	0	0.000477
	-14.46 (41)	-4.77(41)	$g_{\text{iso}} = 2.3919(36)$	0	0.000436
	+25.71 (30)	0	$g_{xy} = 2.5264(17)$	0	0.0000198
			$g_z = 2.0^c$		

<sup>a</sup>The standard deviation of fitted parameters are listed in parentheses. <sup>b</sup>The residual sum of squares, RSS, was calculated as  $\text{RSS} = \sum (M_{\text{calc.}} - M_{\text{exp.}})^2$ , where  $M_{\text{calc.}}$  and  $M_{\text{exp.}}$  are calculated and experimental values of molar magnetisation. <sup>c</sup>Value of  $g_z$  was fixed to 2.0.

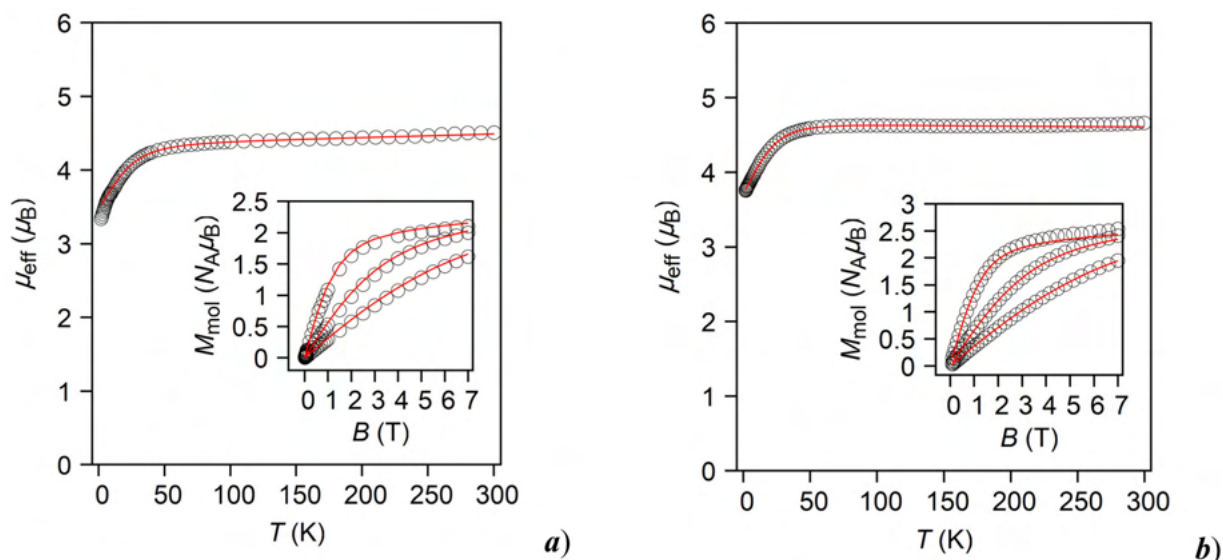


**Fig. 5** Temperature dependence of the effective magnetic moment and isothermal magnetisations measured at  $T = 2, 5$  and  $10$  K (shown in the inset) for **1** (a) and **2** (b). Empty symbols – experimental data, full lines – calculated data with  $D = +24.0$  cm<sup>-1</sup>,  $E = +7.9$  cm<sup>-1</sup>,  $g_{xy} = 2.335$ ,  $g_z = 2.000$ , and  $\chi_{\text{TIP}} = 7.3 \times 10^{-9}$  mol m<sup>-3</sup> for **1**, and  $D = +25.71$  cm<sup>-1</sup>,  $E = 0$  cm<sup>-1</sup>,  $g_{xy} = 2.5264$ , and  $g_z = 2.000$  for **2**.

form infrared magnetic spectroscopy (FIRMS) for complexes **1** and **2**. These techniques are accurate tools for determining the  $g$ -factors and ZFS in molecular magnets, especially those based on transition metals.<sup>37</sup> The results presented below can be compared in methodological aspects to several examples of quantitative ZFS determination in Co(II)-based complexes reported in the literature using a similar approach.<sup>38</sup> HFEPR spectra shown in Fig. 6 were obtained for both compounds at 5 K. Only three resonance peaks with typical effective  $g$ -factors of the Kramers doublet with  $m_s = \pm\frac{1}{2}$  were observed, suggesting a positive  $D$  in agreement with the theoretical predictions. This conclusion is further supported by the temperature dependence (shown for **1** in Fig. S15†), where the signal intensity decreases, indicating the depopulation of the ground state.<sup>38d,e</sup> Moreover, no other additional peaks for  $m_s = \pm\frac{3}{2}$  are observed. FIRMS spectra shown in Fig. 7 were processed as contour plots to help visualise the clear resonance shift with the magnetic field and facilitate the fitting of the frequency

versus magnetic field dependence of the magneto-optical transmissions. Furthermore, this type of plot helps in graphically visualising the ZFS values. In Fig. S16,† the raw FIRMS data divided by the reference show a very strong feature independent of the magnetic field, possibly a phonon mode, that hinders the adequate visualization of the magnetic absorption. Therefore, we used a different type of normalization, dividing the signal at a given magnetic field by the signal from the previous magnetic field, allowing us to get rid of the peaks that do not shift with magnetic field as described in the ESI.† It is a common practice to search for the normalization that evidences the shifting features. The samples of complexes **1** and **2** were prepared in a similar way and both had a reasonable transmission intensity; however, complex **2** displayed a less intense magnetic-related peak. The reason for the intensity is not related to the concentration and there is no trivial answer to why the magnetic features behave differently in each case. This type of behavior in magnetic FTIR among similar com-



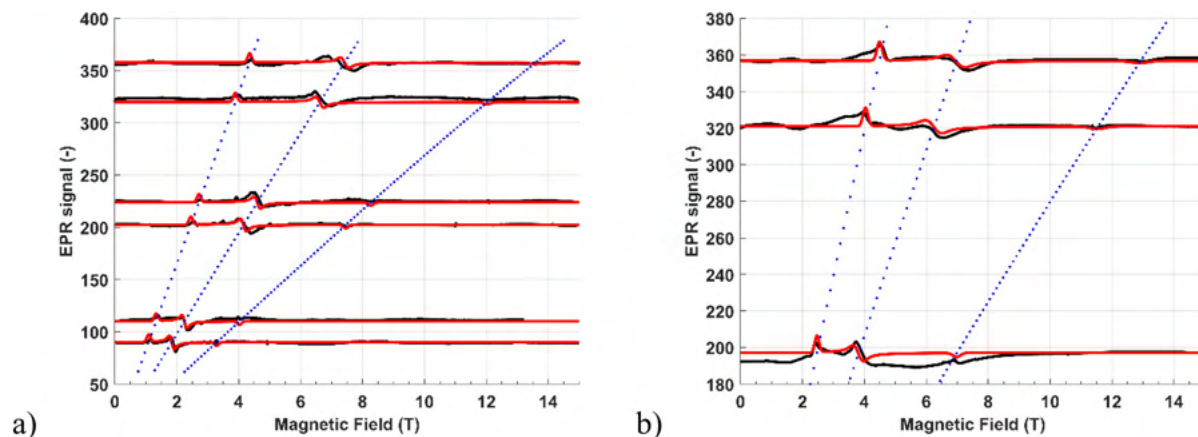


**Fig. 6** HFEPR spectra – red – using pressed powder pellets of **1** (a) and **2** (b) measured at  $T = 5.0$  K and several frequencies (y axis values correspond to the measurement frequency in GHz). Red lines are spectral simulations and blue dots are frequency-field dependence simulations using Easyspin with  $D = +23.7$   $\text{cm}^{-1}$ ,  $E/D = 0.184$ ,  $g_x = 2.45$ ,  $g_y = 2.38$ , and  $g_z = 2.16$  for **1**, and  $D = +24.2$   $\text{cm}^{-1}$ ,  $E/D = 0.162$ ,  $g_x = 2.48$ ,  $g_y = 2.35$ , and  $g_z = 2.19$  for **2**.

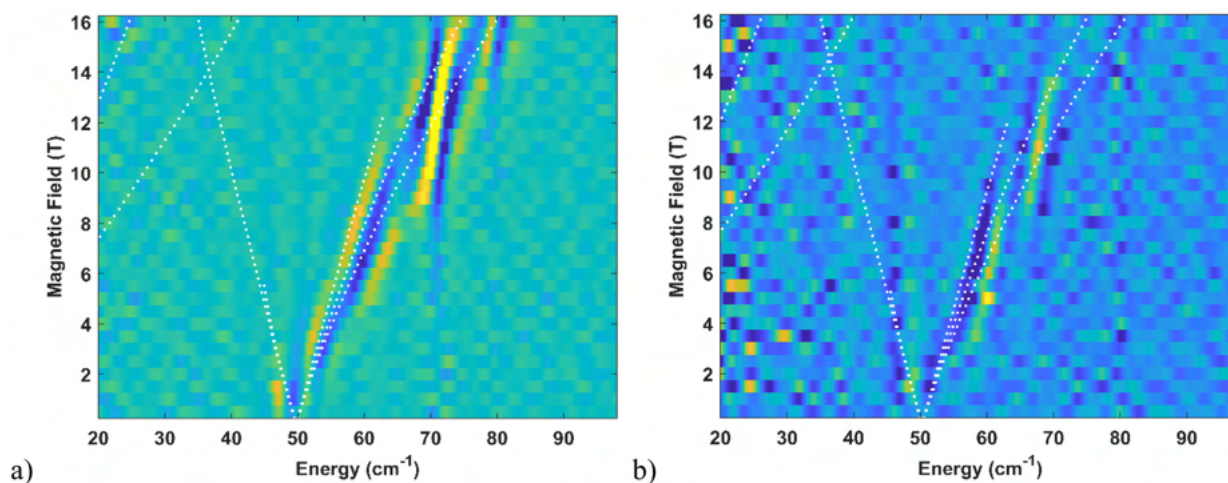


**Fig. 7** Contour plots of the derivative of the normalised FIRMS transmission spectra recorded for pressed powder pellets of **1** (a) and **2** (b) measured at  $T = 4.2$  K and a magnetic field of up to 16 T. The spectra were normalised by dividing them by the zero-field transmission spectrum, and at each magnetic field, by the spectrum from the previous magnetic field. The derivative highlights the shifts in magnetic field-dependent lines. Dots are simulation using Easyspin with  $D = +23.7$   $\text{cm}^{-1}$ ,  $E/D = 0.184$ ,  $g_x = 2.45$ ,  $g_y = 2.38$ , and  $g_z = 2.16$  for **1**, and  $D = +24.2$   $\text{cm}^{-1}$ ,  $E/D = 0.162$ ,  $g_x = 2.48$ ,  $g_y = 2.35$ , and  $g_z = 2.19$  for **2**.

pounds has also been observed in other materials in our previous studies.<sup>7,15</sup> Although we still do not have a satisfactory explanation yet, we are working to understand the influence of the spin-phonon coupling.<sup>39</sup> Indeed, as it will be shown in the dynamic magnetic investigation section, complex **1** has a much faster relaxation than complex **2** and this coincides with the fact that the magnetic peak has a stronger intensity in **1** compared to **2**. At this stage, there is not enough evidence to assure that this correlation implies any cause and effect. Therefore, this topic will be explored in our future works.

The results from HFEPR and FIRMS measurement techniques were analysed using the spin Hamiltonian approach for a high-spin Co(II) system with  $S = 3/2$  according to the theoretical predictions. The simulations were conducted using

Easyspin, an open-source MATLAB toolbox for simulating and fitting EPR spectra.<sup>38</sup> The parameters obtained from magnetisation and theoretical calculations were used as starting points for the fittings. The simulation of the HFEPR results was used to accurately determine the  $g$ -factors and the rhombic  $E$  values, as the available experimental frequency range was insufficient for ascertaining the axial  $D$  values. In contrast, FIRMS simulation was employed to obtain the precise ZFS as  $\Delta = 2\sqrt{D^2 + 3E^2}$ . Consequently, FIRMS simulations were conducted using the  $g$  and  $E$  values from HFEPR simulations to obtain the  $D$  values. These  $D$  values were then utilised to refine the HFEPR simulations. This iterative process was carried out for each sample until a satisfactory agreement between experimental and simulated data for both techniques was achieved.

**Table 3** Spin Hamiltonian parameters based on HFEPR and FIRMS simulation for complexes **1** and **2**

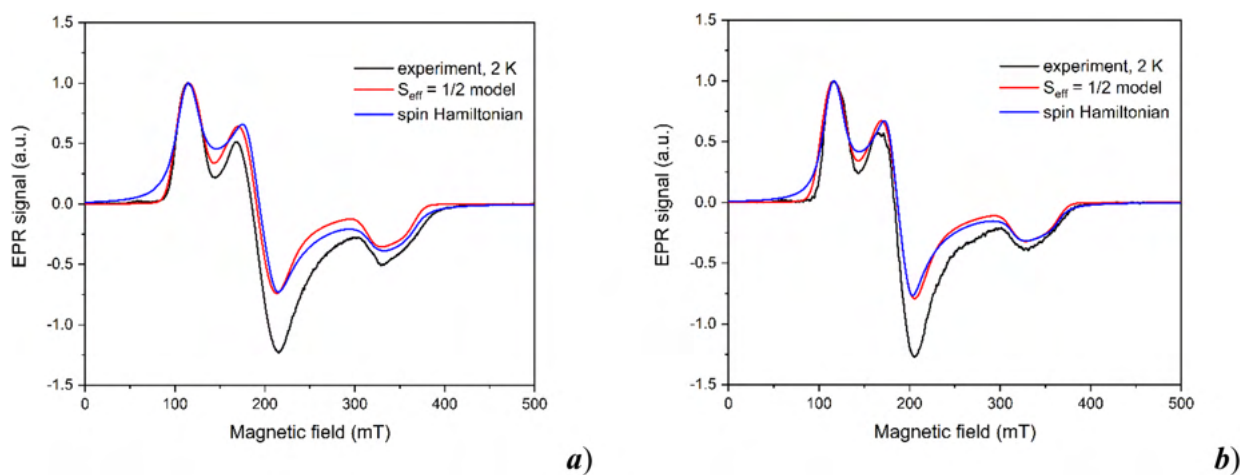
	$g_x, g_y, g_z, g_{iso}$	$D/\text{cm}^{-1}$	$E/D$
<b>1</b>	2.45, 2.38, 2.16, 2.33	+23.7	0.184
<b>2</b>	2.48, 2.35, 2.19, 2.34	+24.2	0.162

The results are shown in Fig. 6 and 7 for HFEPR and FIRMS, respectively. The common parameters obtained from the simulations are shown in Table 3.

### X-band EPR investigation

The X-band EPR spectra of compounds **1** and **2** were measured in the temperature range from 2 K to 60 K displaying a decrease of the signal intensity with a substantial line broadening with increasing temperature typical of large zero-field

splitting in Co(II) complexes (Fig. S17<sup>†</sup>). In this case, it is meaningful to use a simplified effective spin  $S_{\text{eff}} = 1/2$  model describing the ground Kramers doublet for the analysis of EPR at low temperatures. This model assumes the mixing of higher excited states with the ground Kramers doublet as the consequence of the spin-orbit coupling yielding highly anisotropic effective  $g$ -factors observed in the experimental data. The simulation of EPR spectra shown in Fig. 8 was performed using the EasySpin simulation package,<sup>40</sup> including the influence of the unresolved hyperfine interaction  $A$  and an anisotropic convolutional broadening  $\Delta B$  (full-width at half-height). The obtained parameter set is summarised in Table 4. The obtained values of effective  $g$ -factors of the ground Kramers doublet can be easily interpreted within the Griffith-Figgis formalism<sup>41</sup> as typical values stemming from the orbital singlet  $^4A_{2g}$  as the ground electronic state with the axial field parameter  $\Delta_{\text{ax}} > 1500 \text{ cm}^{-1}$  (easy-plane anisotropy) and substantial rhombic  $\Delta_{\text{rh}}$

**Fig. 8** The X-band EPR data of complexes **1** (a) and **2** (b) obtained at 2 K including the simulations using the effective spin  $S_{\text{eff}} = 1/2$  model (solid red lines) and spin Hamiltonian formalism (solid blue lines) with parameters summarised in Table 3.**Table 4** Parameters of the effective spin  $S_{\text{eff}} = 1/2$  model and spin Hamiltonian formalism estimated for the analysis of the X-band EPR for complexes **1** and **2**

Complex, approach	Parameters
<b>1</b> , $S_{\text{eff}} = 1/2$ model, estimated from data	$[g'_1, g'_2, g'_3] = [1.97, 3.47, 5.80]$ , $[A'_1, A'_2, A'_3] = [180, 200, 300]$ MHz $[\Delta B_1, \Delta B_2, \Delta B_3] = [20, 50, 50]$ mT
<b>1</b> , $S_{\text{eff}} = 1/2$ model, $x, y, z$ assignment <sup>40</sup>	$[g'_x, g'_y, g'_z] = [3.47, 5.8, 1.97]$ , $[A'_x, A'_y, A'_z] = [200, 300, 180]$ MHz $[\Delta B_x, \Delta B_y, \Delta B_z] = [50, 50, 20]$ mT
<b>1</b> , spin Hamiltonian, $x, y, z$ assignment <sup>40</sup>	$[g_x, g_y, g_z] = [2.341, 2.377, 2.136]$ , $[A_x, A_y, A_z] = [134, 74, 325]$ MHz $E/D = 0.178$
<b>1</b> , spin Hamiltonian, estimated from data	$[g_x, g_y, g_z] = [2.34, 2.38, 2.14]$ , $[A_x, A_y, A_z] = [130, 75, 190]$ MHz $E/D = 0.173$ $\Delta B = 25$ mT
<b>2</b> , $S_{\text{eff}} = 1/2$ model, estimated from data	$[g'_1, g'_2, g'_3] = [1.98, 3.56, 5.77]$ , $[A'_1, A'_2, A'_3] = [180, 200, 300]$ MHz $[\Delta B_1, \Delta B_2, \Delta B_3] = [20, 50, 50]$ mT
<b>2</b> , $S_{\text{eff}} = 1/2$ model, $x, y, z$ assignment <sup>40</sup>	$[g'_x, g'_y, g'_z] = [3.56, 5.77, 1.98]$ , $[A'_x, A'_y, A'_z] = [140, 280, 180]$ MHz $[\Delta B_x, \Delta B_y, \Delta B_z] = [50, 50, 20]$ mT
<b>2</b> , spin Hamiltonian, $x, y, z$ assignment <sup>40</sup>	$[g_x, g_y, g_z] = [2.342, 2.391, 2.123]$ , $[A_x, A_y, A_z] = [92, 74, 300]$ MHz $E/D = 0.154$
<b>2</b> , spin Hamiltonian, estimated from data	$[g_x, g_y, g_z] = [2.34, 2.39, 2.12]$ , $[A_x, A_y, A_z] = [100, 75, 190]$ MHz $E/D = 0.154$ $\Delta B = 20$ mT

parameter. The result is consistent with the predicted positive  $D$  parameter from SA-CASSCF/NEVPT2 calculations. Having the effective  $g$ -factor components  $g'_1$ ,  $g'_2$ , and  $g'_3$  of the ground Kramers doublet estimated for the EPR spectra, one can assign them correctly to  $g'_x$ ,  $g'_y$ , and  $g'_z$  and later to real  $g$ -factors  $g_x$ ,  $g_y$ , and  $g_z$  of spin Hamiltonian formalism using an approach outlined in ref. 42. First, all possible combinations of  $g'_1$ ,  $g'_2$ , and  $g'_3$  are used to calculate six dependencies of an average real  $g$ -factor on the  $E/D$  ratio, which are checked against the average  $g$ -factor obtained from the experimental room temperature value of the effective magnetic moment. This will eventually give a single assignment of  $x$ ,  $y$ , and  $z$  components instead of the 1, 2, and 3 components of the  $g$ -factors as well as the components of the anisotropic hyperfine interaction. At the same time, the correct value of  $E/D$  is estimated from the procedure, but the values of  $D$  and  $E$  directly cannot be estimated. It is sometimes cumbersome to obtain accurate values of the average real  $g$ -factor due to uncertainties in the subtraction of diamagnetic or temperature-independent paramagnetic susceptibility. In our case, we used the average  $g$ -values predicted from SA-CASSCF/NEVPT2 calculations in Table 1, and this approach showed an excellent consistency between calculations and analysis of EPR spectra. The results are also summarised in Table 4, yielding the  $E/D$  values 0.178 and 0.154 for **1** and **2**, respectively. It should be noted that the direct estimation of spin Hamiltonian parameters  $D$  and  $E$  from the X-band EPR is also not possible for Co(II) ions with  $D > 8 \text{ cm}^{-1}$ , only the  $E/D$  ratio can be obtained. Having the  $E/D$  ratio, real  $g$ -factors, and hyperfine interactions estimated from the aforementioned analysis, we used those values as starting parameters to simulate the experimental X-band EPR spectra using spin Hamiltonian formalism with the  $D$  parameter for simplicity fixed to  $25 \text{ cm}^{-1}$ . A very good agreement with the experimental spectra was obtained with only minor corrections of the starting parameters, yielding  $E/D$  values of 0.173 and 0.154 for **1** and **2**, respectively, as shown in Fig. 8. This result is in good agreement with the SA-CASSCF/NEVPT2, HF EPR and

FIRMS analysis, confirming slightly higher rhombic anisotropy in **1**. A slight difference in  $g$ -factors obtained from X-band EPR and HFEPR can be accounted for by the different sensitivity of the two methods to the influence of hyperfine coupling, which strongly affects the lineshape of X-band data.

### Dynamic magnetic investigation

In order to probe the SIM behaviour in reported compounds, the frequency dependence of the alternating current susceptibility was measured at various fields and temperatures (see the ESI† for a detailed experimental description of AC susceptibility measurements and data analysis). At 2 K and zero DC field, no significant out-of-phase component ( $\chi''$ ) of the AC susceptibility was observed for both complexes (Fig. S18 and S19, see the ESI†). This is a consequence of the fast relaxation of magnetisation resulting from the quantum tunnelling effect induced by hyperfine interactions with the nuclear spins. However, the applied DC field in the range of 0–0.5 T caused the suppression of the tunnelling effect, and the evolution of  $\chi''$  upon frequency change at 2 K proves the field-induced slow relaxation of magnetisation in **1** and **2**. Both compounds exhibit single-channel relaxation under a weaker DC field (<0.3 T), and two-channel relaxation under stronger DC fields (>0.3 T for **1** and >0.2 T for **2**; Tables S5 and S6†). Therefore, in-phase ( $\chi'$ ) and out-of-phase components of AC susceptibility were simultaneously fitted to extended one-set and two-set Debye models (eqn (S1)–(S4)†). The low-frequency (LF) channels appeared only above 0.3 T and were not analysed further.

The evolution of field-dependent relaxation time  $\tau$  for **1** and **2** is different (Fig. 9a). Compound **1** shows one order of magnitude longer  $\tau$  with the maximal value at 0.15 T (17.6 Hz,  $\tau_{\text{max}} = 9.1 \text{ ms}$ ), while **2** reaches the maximal value at 0.07 T (17.6 Hz,  $\tau_{\text{max}} = 0.76 \text{ ms}$ ). Given the closely similar coordination environment and values of ZFS splitting parameters in both compounds (*vide supra*), the noticeable discrepancies in the relaxation time could tentatively be attributed to the varying lengths of the aliphatic chains. It is plausible to consider that

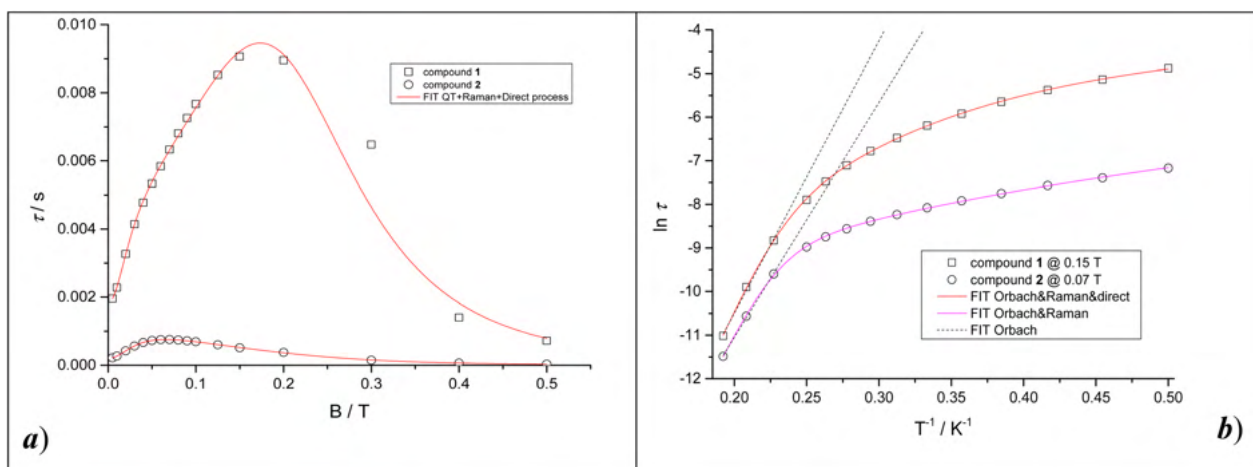


Fig. 9  $\tau$  vs.  $B$  (a) and  $\ln \tau$  vs.  $1/T$  (b) dependencies for compounds **1** and **2**.

the elongation of these chains may facilitate the interaction between the molecules and the environment through acoustic and/or optical vibrational modes, thereby influencing the relaxation dynamics. Both  $\tau$  vs.  $B$  dependencies were successfully fitted to relaxation eqn (2) which involves quantum tunnelling, direct and Raman relaxation processes.

$$\frac{1}{\tau} = \frac{b_1}{1 + b_2 B^2} + AB^m T + d \left( \frac{1 + eB^2}{1 + fB^2} \right) T^n \quad (2)$$

The fits were performed with fixed Raman and direct exponents to theoretical values  $m = 4$  and  $n = 9$ , expected for Kramer's ions.<sup>43</sup> Table S7† presents the obtained parameters  $b_1$ ,  $b_2$  (quantum tunnelling),  $A$  (direct process) and  $d$ ,  $e$ , and  $f$  (Raman process), which were used for the simulation of the individual relaxation rates and their contributions to the overall relaxation (Fig. S20†). For complex **1**, the major contribution to relaxation in the low field region is quantum tunnelling while the Raman relaxation becomes dominant with the increase of the field. Interestingly, quantum tunnelling is suppressed even at a very small field (0.005 T) for complex **2** and the Raman relaxation is the only dominant process up to ca. 0.2 T. Above 0.25 T, the major contribution to the relaxation of both compounds originates from the direct process.

The temperature-dependent dynamic studies were performed at  $B_{DC} = 0.15$  T for **1** and 0.07 T for **2**, where the slow relaxation of magnetisation lasts the longest (Fig. 9a).  $\chi''$  shows the single maxima shift from 76.3 Hz (for **1** at 1.8 K,  $\tau = 2.09$  ms) and from 331.6 Hz (for **2** at 2.0 K,  $\tau = 0.48$  ms), respectively, towards higher frequencies with the increase of the temperature (Tables S8 and S9†). The obtained frequency dependent  $\chi'$  and  $\chi''$  components of AC susceptibility were simultaneously fitted to a one-set Debye model (eqn (S1), (S2); Fig. S21, S22; and Tables S8, S9†). The obtained temperature dependencies of relaxation time  $\ln \tau$  vs.  $1/T$  were fitted with respect to relaxation eqn (3) involving the terms of direct, Raman and Orbach relaxation mechanisms, respectively

$$\frac{1}{\tau} = aTB^m + CT^n + \frac{1}{\tau_0} \exp\left(-\frac{U_{\text{eff}}}{kT}\right) \quad (3)$$

At first, the effective energy barrier of spin reversal  $U_{\text{eff}}$  was estimated by fitting the high-temperature region (4.4 K–5.2 K) to the Arrhenius-like equation of a single Orbach process, which resulted in  $U_{\text{eff}} = 62(4)$  K for **1** and  $U_{\text{eff}} = 54(2)$  K for **2** (Fig. 9b, dashed lines). The comprehensive analysis of  $\ln \tau$  vs.  $1/T$  dependencies in the whole temperature range however requires the combination of two or three relaxation mechanisms. The previous low-temperature analysis of  $\tau$  vs.  $B$  dependencies suggests that SRM in **1** is governed by Raman and direct mechanism at  $B_{DC} = 0.15$  T (Fig. S20,† solid vertical line), while for **2**, it is predominantly governed by a single Raman process at  $B_{DC} = 0.07$  T (Fig. S20,† dash-dotted vertical line). Therefore, the comprehensive fit of the  $\ln \tau$  vs.  $1/T$  dependencies was conducted using all three relaxation processes for **1**, and the combination of Orbach and Raman processes for **2**. Those two approaches resulted in relaxation parameters  $U_{\text{eff}} =$

77(4) K,  $\tau_0 = 7(2) \times 10^{-12}$  s,  $C = 0.6(1) \text{ K}^{-n} \text{ s}^{-1}$ ,  $n = 5.8(2)$ , and  $A = 1.00(4) \times 10^5 \text{ s}^{-1} \text{ T}^{-4} \text{ K}^{-1}$  for **1** and  $U_{\text{eff}} = 70(2)$  K,  $\tau_0 = 1.6(5) \times 10^{-11}$  s,  $C = 264(9) \text{ K}^{-n} \text{ s}^{-1}$ , and  $n = 2.28(3)$  (Fig. 9b solid lines; Table S10†). The obtained relaxation parameters indicate that subtle structural differences between **1** and **2** cause a slight decrease of the energy barrier of spin reversal  $U_{\text{eff}}$  and accelerate the Raman relaxation. On the other hand, the relaxation governed *via* the direct process seems to be relevant only in complex **1** with a shorter *n*-octyl aliphatic chain. It is interesting to note that the values of the effective energy barriers  $U_{\text{eff}}$  are close to the theoretical ones  $U = 69$  K and  $U = 74$  K, calculated by the equation for Kramer's ions  $U = (S^2 - \frac{1}{4})|D|$  using the axial ZFS parameters obtained from the fit with anisotropic *g*-tensor (Table 2). The Raman exponents acquire smaller values than the expected value of 9 for Kramer's ions,<sup>44</sup> but when optical and acoustic phonons are considered, values in the range of 1–6 are acceptable.<sup>38</sup>

## Summary

In this paper, we report on the synthesis, crystal structure, magnetic properties and field-induced single-molecule magnetic behaviour of two structurally similar hexacoordinated Co (II) complexes with tailor-made organic ligands for wet depositions on surfaces. Both compounds have been successfully deposited onto silicon surfaces as sub-micrometric structures through drop casting and lithographically controlled wetting, mimicking the logical patterns utilized in compact disks, such as parallel stripes or isolated "pits & lands". Although the neutral molecular structure of the complexes makes them suitable for sublimation, their thermal instability rendered this approach unsuccessful. The structural analysis unveiled the distorted octahedral shape of coordination polyhedra consisting of three nitrogen donor atoms of the corresponding tridentate ligand and three oxygen donor atoms of two nitrate anions, one of which is coordinated in a bidentate fashion and the other in a monodentate fashion. The role of the fourth oxygen atom of the monodentate nitrate ligand has been inspected in detail and it has been shown that the formed Co (II)⋯O noncovalent interactions do not affect the electronic structure of the central atom significantly. The comprehensive analysis of the electronic structure and magnetic properties of reported complexes **1** and **2** demonstrates their positive axial *D* parameters, easy-plane anisotropy, and applicability of the spin Hamiltonian formalism for  $S = 3/2$ . Combining *ab initio* calculations, static magnetic data, HF and X-band EPR, and FIRMS measurements, the study highlights the similarities and differences in magnetic anisotropy between the two complexes, which also influence their relaxation properties. AC susceptibility investigations demonstrated field-induced SIM behaviour in both complexes. At very low temperatures, the SRM is governed by a combination of quantum tunnelling, direct relaxation, and Raman relaxation processes. The effect of quantum tunnelling was effectively suppressed by an increased static magnetic field, which, in turn, activated relax-



ation *via* the direct mechanism. As the temperature increased, the Orbach relaxation process was also activated, with effective energy barriers that match the predicted values from the ZFS parameters.

## Author contributions

J. J.: synthesis, formal analysis, data curation, writing – original draft, and writing – review & editing; O. F. F.: formal analysis and data curation; S. S.: data curation; S. V.: data curation; I. N.: data curation, investigation, visualization, writing – original draft, and writing – review and editing; R. H.: investigation, visualization, writing – original draft, and writing – review and editing; E. Č.: data curation, investigation, visualization, writing – original draft, and writing – review & editing; V. T. S.: data curation, investigation, visualization, writing – original draft, and writing – review and editing; M. O.: data curation; D. G.: data curation and visualization; G. R.: data curation and visualization; M. C.: investigation, visualization, writing – original draft, and writing – review and editing; P. N.: conceptualization, resources, and writing – review & editing; M. R.: conceptualization, resources, and writing – review & editing; and I. Š.: conceptualization, funding acquisition, resources, supervision, data curation, writing – original draft, visualization, and writing – review & editing.

## Conflicts of interest

There are no conflicts to declare.

## Acknowledgements

Slovak grant agencies (APVV-19-0087, APVV-22-0172, DS-FR-22-0010 and VEGA 1/0029/22) are acknowledged for the financial support. J. J., I. N. V. T. S. and I. Š. acknowledge the financial support from the Grant Agency of the Czech Republic grant no. 22-23760S. This article was written with the generous support under the Operational Program Integrated Infrastructure for the project: “Strategic Research in the Field of SMART Monitoring, Treatment and Preventive Protection against Coronavirus (SARS-CoV-2)”, project no. 313011ASS8, co-financed by the European Regional Development Fund. J. J. acknowledges financial support from an internal grant from Brno University of Technology CEITEC VUT-J-22-8049. Furthermore, we acknowledge CzechNanoLab Research Infrastructure supported by MEYS CR (LM2023051). O. F. F., I. N. and R. H. acknowledge the financial support from the institutional sources of the Department of Inorganic Chemistry, Palacký University Olomouc, Czech Republic. O. F. F. acknowledges the support of MSTC Danube 8X23030 project.

## References

- 1 D. Gatteschi, R. Sessoli and J. Villain, *Molecular Nanomagnets*, Oxford University Press, Oxford, 2007.
- 2 (a) D. E. Freedman, W. H. Harman, T. D. Harris, G. J. Long, C. J. Chang and J. R. Long, Slow Magnetic Relaxation in a High-Spin Iron(II) Complex, *J. Am. Chem. Soc.*, 2010, **132**, 1224; (b) W. H. Harman, T. D. Harris, D. E. Freedman, H. Fong, A. Chang, J. D. Rinehart, A. Ozarowski, M. T. Sougrati, F. Grandjean, G. J. Long, J. R. Long and C. J. Chang, Slow Magnetic Relaxation in a Family of Trigonal Pyramidal Iron(II) Pyrrolide Complexes, *J. Am. Chem. Soc.*, 2010, **132**, 18115.
- 3 (a) A. K. Bar, C. Pichon and J.-P. Sutter, Magnetic anisotropy in two- to eight-coordinated transition-metal complexes: Recent developments in molecular magnetism, *Coord. Chem. Rev.*, 2016, **308**, 346; (b) J. M. Frost, K. L. M. Harriman and M. Murugesu, The rise of 3-d single-ion magnets in molecular magnetism: towards materials from molecules?, *Chem. Sci.*, 2016, **7**, 2470.
- 4 (a) J. Juráková and I. Šalitrš, Co(II) single-ion magnets: synthesis, structure, and magnetic properties, *Monatsh. Chem.*, 2022, **153**, 1001; (b) P. K. Sahu, R. Kharel, S. Shome, S. Goswami and S. Konar, Understanding the unceasing evolution of Co(II) based single-ion magnets, *Coord. Chem. Rev.*, 2023, **475**, 214871.
- 5 T. Blachowicz and A. Ehrmann, New Materials and Effects in Molecular Nanomagnets, *Appl. Sci.*, 2021, **11**, 7510.
- 6 J. Hruby, S. Vavreckova, L. Masaryk, A. Sojka, J. Navarro-Giraldo, M. Bartos, R. Herchel, J. Moncol, I. Nemeč and P. Neugebauer, Deposition of Tetracoordinate Co(II) Complex with Chalcone Ligands on Graphene, *Molecules*, 2020, **25**, 5021.
- 7 J. Juráková, J. Dubnická-Midlíková, J. Hrubý, A. Kliuikov, V. T. Santana, J. Pavlik, J. Moncol, E. Čižmár, M. Orlita, I. Mohelský, P. Neugebauer, D. Gentili, M. Cavallini and I. Šalitrš, Pentacoordinate cobalt(II) single ion magnets with pendant alkyl chains: shall we go for chloride or bromide?, *Inorg. Chem. Front.*, 2022, **9**, 1179.
- 8 (a) E. Kiefl, M. Mannini, K. Bernot, X. Yi, A. Amato, T. Leviant, A. Magnani, T. Prokscha, A. Suter, R. Sessoli and Z. Zaher, Robust Magnetic Properties of a Sublimable Single-Molecule Magnet, *ACS Nano*, 2016, **10**, 5663; (b) L. Malavolti, V. Lanzilotto, S. Ninova, L. Poggini, I. Cimatti, B. Cortigiani, L. Margheriti, D. Chiappe, E. Otero, P. Sainctavit, F. Totti, A. Cornia, M. Mannini and R. Sessoli, Nanofilament Formation and Regeneration During Cu/Al<sub>2</sub>O<sub>3</sub> Resistive Memory Switching, *Nano Lett.*, 2015, **15**, 535.
- 9 J. Hellerstedt, A. Cahlík, M. Švec, B. de la Torre, M. Moro-Lagares, T. Chutora, B. Papoušková, G. Zoppellaro, P. Mutombo, M. Ruben, R. Zbořil and P. Jelinek, On-surface structural and electronic properties of spontaneously formed Tb<sub>2</sub>Pc<sub>3</sub> single molecule magnets, *Nanoscale*, 2018, **10**, 15553.
- 10 F. Ciccullo, M. Glaser, M. S. Sättele, S. Lenz, P. Neugebauer, Y. Rechkemmer, J. van Slageren, M. B. Casu

- and M. B. Casu, Thin film properties and stability of a potential molecular quantum bit based on copper(II), *J. Mater. Chem. C*, 2018, **6**, 8028.
- 11 J. Hrubý, D. Dvořák, L. Squillantini, M. Mannini, J. van Slageren, R. Herchel, I. Nemeč and P. Neugebauer, Co(II)-Based single-ion magnets with 1,1'-ferrocenediyl-bis(diphenylphosphine) metalloligands, *Dalton Trans.*, 2020, **49**, 11697.
  - 12 A. K. Mondal, T. Goswami, A. Misra and S. Konar, Probing the Effects of Ligand Field and Coordination Geometry on Magnetic Anisotropy of Pentacoordinate Cobalt(II) Single-Ion Magnets, *Inorg. Chem.*, 2017, **56**, 6870.
  - 13 T. Jurca, A. Farghal, P. H. Lin, I. Korobkov, M. Murugesu and D. S. J. Richeson, Single-Molecule Magnet Behavior with a Single Metal Center Enhanced through Peripheral Ligand Modifications, *J. Am. Chem. Soc.*, 2011, **133**, 15814.
  - 14 B. Brachňaková, S. Matejová, J. Moncol, R. Herchel, J. Pavlik, E. Moreno-Pineda, M. Ruben and I. Šalitroš, Stereochemistry of coordination polyhedra vs. single ion magnetism in penta- and hexacoordinated Co(II) complexes with tridentate rigid ligands, *Dalton Trans.*, 2020, **49**, 1249.
  - 15 N. Malinová, J. Juráková, B. Brachňaková, J. Dubnická-Midlíková, E. Čižmár, V. T. Santana, R. Herchel, M. Orlita, I. Mohelský, J. Moncol, P. Neugebauer and I. Šalitroš, Magnetization Slow Dynamics in Mononuclear Co(II) Field-Induced Single-Molecule Magnet, *Cryst. Growth Des.*, 2023, **23**, 2430.
  - 16 S. Q. Su, S. Q. Wu, M. L. Baker, P. Bencok, N. Azuma, Y. Miyazaki, M. Nakano, S. Kang, Y. Shiota, K. Yoshizawa, S. Kanegawa and O. Sato, Quenching and Restoration of Orbital Angular Momentum through a Dynamic Bond in a Cobalt(II) Complex, *J. Am. Chem. Soc.*, 2020, **142**, 11434.
  - 17 (a) S. Alvarez, D. Avnir, M. Llunell and M. Pinsky, Continuous symmetry maps and shape classification. The case of six-coordinated metal compounds, *New J. Chem.*, 2002, **26**, 996; (b) M. Llunell, D. Casanova, J. Cirera, P. Alemany and S. Alvarez, *SHAPE version 2.0*, Universitat de Barcelona, Barcelona, 2010.
  - 18 M. G. B. Drew, C. J. Harding, V. McKee, G. G. Morgan and J. Nelson, Geometric control of manganese redox state, *J. Chem. Soc., Chem. Commun.*, 1995, **10**, 1035.
  - 19 (a) R. D. Deegan, O. Bakajin, T. F. Dupont, G. V. Huber, S. R. Nagel and T. A. Witten, *Nature*, 1997, **389**, 827; (b) M. Cavallini, *J. Mater. Chem.*, 2009, **19**, 6085.
  - 20 (a) M. Cavallini, D. Gentili, P. Greco, F. Valle and F. Biscarini, Capillary flow as the cause of ring stains from dried liquid drops, *Nat. Protoc.*, 2012, **7**, 1668; (b) T. Mallah and M. Cavallini, Surfaces, thin films and patterning of spin crossover compounds, *C. R. Chim.*, 2018, **21**, 1270.
  - 21 D. Gentili, P. Sonar, F. Liscio, T. Cramer, L. Ferlauto, F. Leonardi, S. Milita, A. Dodabalapur and M. Cavallini, *Nano Lett.*, 2013, **13**, 3643.
  - 22 (a) I. Nemeč, R. Herchel and Z. Trávníček, *Dalton Trans.*, 2016, **45**, 12479; (b) L. Havlíček, R. Herchel, I. Nemeč and P. Neugebauer, Weak antiferromagnetic interaction in Cu(II) complex with semi-coordination exchange pathway, *Polyhedron*, 2022, **223**, 115962.
  - 23 (a) F. Neese, Software update: the ORCA program system, version 4.0, *Wiley Interdiscip. Rev.: Comput. Mol. Sci.*, 2018, **8**, e1327; (b) F. Neese, F. Wennmohs, U. Becker and C. Riplinger, *J. Chem. Phys.*, 2020, **152**, 224108.
  - 24 F. Weigend and R. Ahlrichs, The ORCA quantum chemistry program package, *Phys. Chem. Chem. Phys.*, 2005, **7**, 3297.
  - 25 R. F. W. Bader, Atoms in molecules, *Acc. Chem. Res.*, 1985, **18**, 9.
  - 26 (a) T. Lu and F. Chen, Multiwfn: A multifunctional wavefunction analyzer, *J. Comput. Chem.*, 2012, **33**, 580; (b) T. Lu and F. Chen, Quantitative analysis of molecular surface based on improved Marching Tetrahedra algorithm, *J. Mol. Graphics Modell.*, 2012, **38**, 314.
  - 27 E. R. Johnson, S. Keinan, P. Mori-Sánchez, J. Contreras-García, A. J. Cohen and W. Yang, Revealing Noncovalent Interactions, *J. Am. Chem. Soc.*, 2010, **132**, 6498.
  - 28 P.Å. Malmqvist and B. O. Roos, The CASSCF state interaction method, *Chem. Phys. Lett.*, 1989, **155**, 189.
  - 29 (a) C. Angeli, R. Cimiraglia and J. P. Malrieu, *Chem. Phys. Lett.*, 2001, **350**, 297; (b) C. Angeli, R. Cimiraglia, S. Evangelisti, T. Leininger and J. P. Malrieu, N-electron valence state perturbation theory: a fast implementation of the strongly contracted variant, *J. Chem. Phys.*, 2001, **114**, 10252.
  - 30 (a) F. Weigend, Accurate Coulomb-fitting basis sets for H to Rn, *Phys. Chem. Chem. Phys.*, 2006, **8**, 1057; (b) A. Hellweg, C. Hättig, S. Höfener and W. Klopper, Optimized accurate auxiliary basis sets for RI-MP2 and RI-CC2 calculations for the atoms Rb to Rn, *Theor. Chem. Acc.*, 2007, **117**, 587.
  - 31 (a) R. Izsák and F. Neese, An overlap fitted chain of spheres exchange method, *J. Chem. Phys.*, 2011, **135**, 144105; (b) F. Neese, F. Wennmohs, A. Hansen and U. Becker, Efficient, approximate and parallel Hartree-Fock and hybrid DFT calculations. A 'chain-of-spheres' algorithm for the Hartree-Fock exchange, *Chem. Phys.*, 2009, **356**, 98.
  - 32 (a) D. M. P. Mingos, P. Day and J. P. Dahl, *Molecular Electronic Structures of Transition Metal Complexes II*, Springer, Berlin/Heidelberg, 2012; (b) S. K. Singh, J. Eng, M. Atanasov and F. Neese, Covalency and chemical bonding in transition metal complexes: An ab initio based ligand field perspective, *Coord. Chem. Rev.*, 2017, **344**, 2.
  - 33 S. Gomez-Coca, E. Cremades, N. Aliaga-Alcalde and E. Ruiz, Mononuclear Single-Molecule Magnets: Tailoring the Magnetic Anisotropy of First-Row Transition-Metal Complexes, *J. Am. Chem. Soc.*, 2013, **135**(18), 7010.
  - 34 R. Boča, *A Handbook of Magnetochemical Formulae*, Elsevier, Amsterdam, 2012.
  - 35 R. Boča and R. Herchel, *POLYMAGNET*, 2006–2022.
  - 36 R. Herchel, L. Váhovská, I. Potočňák and Z. Trávníček, Slow Magnetic Relaxation in Octahedral Cobalt(II) Field-Induced Single-Ion Magnet with Positive Axial and Large Rhombic Anisotropy, *Inorg. Chem.*, 2014, **53**, 5896.
  - 37 J. Telser, EPR Interactions – Zero Field Splittings, *eMagRes*, 2017, **6**, 207.
  - 38 (a) J. van Slageren, S. Vongtragool, B. Gorshunov, A. A. Mukhin, N. Karl, J. Krzystek, J. Telser, A. Müller, C. Sangregorio, D. Gatteschi and M. Dressel, Frequency-

- domain magnetic resonance spectroscopy of molecular magnetic materials, *Phys. Chem. Chem. Phys.*, 2003, **5**, 3837; (b) A. A. Pavlov, D. Y. Aleshin, S. A. Savkina, A. S. Belov, N. N. Efimov, J. Nehrkom, M. Ozerov, Y. Z. Voloshin, Y. V. Nelyubina and V. V. Novikov, A Trigonal Prismatic Cobalt(II) Complex as a Single Molecule Magnet with a Reduced Contribution from Quantum Tunneling, *ChemPhysChem*, 2019, **20**, 1001; (c) J. Vallejo, M. Viciano-Chumillas, F. Lloret, M. Julve, I. Castro, J. Krzystek, M. Ozerov, D. Armentano, G. De Munno and J. Cano, Coligand Effects on the Field-Induced Double Slow Magnetic Relaxation in Six-Coordinate Cobalt(II) Single-Ion Magnets (SIMs) with Positive Magnetic Anisotropy, *Inorg. Chem.*, 2019, **58**, 15726; (d) E. Ya. Misochko, A. V. Akimov, D. V. Korchagin, J. Nehrkom, M. Ozerov, A. V. Pali, J. M. Clemente-Juan and S. M. Aldoshin, Purely Spectroscopic Determination of the Spin Hamiltonian Parameters in High-Spin Six-Coordinated Cobalt(II) Complexes with Large Zero-Field Splitting, *Inorg. Chem.*, 2019, **58**(24), 16434; (e) A. Landart-Gereka, M. M. Quesada-Moreno, I. F. Díaz-Ortega, H. Nojiri, M. Ozerov, J. Krzystek, M. A. Palacios and E. Colacio, Large easy-axis magnetic anisotropy in a series of trigonal prismatic mononuclear cobalt(II) complexes with zero-field hidden single-molecule magnet behaviour: the important role of the distortion of the coordination sphere and intermolecular interactions in the slow relaxation, *Inorg. Chem. Front.*, 2022, **9**, 2810.
- 39 D. H. Moseley, S. E. Stavretis, K. Thirunavukkuarasu, M. Ozerov, Y. Cheng, L. L. Daemen, J. Ludwig, Z. Lu, D. Smirnov, C. M. Brown, A. Pandey, A. J. Ramirez-Cuesta, A. C. Lamb, M. Atanasov, E. Bill, F. Neese and Z.-L. Xue, Spin-phonon couplings in transition metal complexes with slow magnetic relaxation, *Nat. Commun.*, 2018, **9**, 2572.
- 40 (a) S. Stoll and A. Schweiger, EasySpin, a comprehensive software package for spectral simulation and analysis in EPR, *J. Magn. Reson.*, 2006, **178**, 42; (b) J. Nehrkom, J. Telser, K. Holldak, S. Stoll and A. Schnegg, Simulating Frequency-Domain Electron Paramagnetic Resonance: Bridging the Gap between Experiment and Magnetic Parameters for High-Spin Transition-Metal Ion Complexes, *J. Phys. Chem. B*, 2015, **119**(43), 13816.
- 41 A. V. Pali, D. V. Korchagin, E. A. Yureva, A. V. Akimov, E. Y. Misochko, G. V. Shilov, A. D. Talantsev, R. B. Morgunov, S. M. Aldoshin and B. S. Tsukerblat, Single-Ion Magnet  $\text{Et}_4\text{N}[\text{Co}^{\text{II}}(\text{hfac})_3]$  with Nonuniaxial Anisotropy: Synthesis, Experimental Characterization, and Theoretical Modeling, *Inorg. Chem.*, 2016, **55**, 9696.
- 42 S. Gómez-Coca, A. Urtizberea, E. Cremades, P. J. Alonso, A. Camón, E. Ruiz and F. Luis, Origin of slow magnetic relaxation in Kramers ions with non-uniaxial anisotropy, *Nat. Commun.*, 2014, **5**, 4300.
- 43 (a) K. N. Shrivastava, Theory of Spin-Lattice Relaxation, *Phys. Status Solidi B*, 1983, **117**, 437; (b) A. Singh and K. Shrivastava, Optical-acoustic two-phonon relaxation in spin systems, *Phys. Status Solidi B*, 1979, **95**, 273.
- 44 R. L. Carlin, *Magnetochemistry*, Springer-Verlag, Berlin, 1986.


 Cite this: *Phys. Chem. Chem. Phys.*,  
 2023, 25, 29516

# Tetracoordinate Co(II) complexes with semi-coordination as stable single-ion magnets for deposition on graphene†

 Jorge Navarro Giraldo,<sup>a</sup> Jakub Hrubý,<sup>b</sup> Šárka Vavrečková,<sup>§ab</sup>  
 Ondřej F. Fellner,<sup>c</sup> Lubomír Havlíček,<sup>b</sup> DaVonne Henry,<sup>e</sup> Shehan de Silva,<sup>e</sup>  
 Radovan Herchel,<sup>c</sup> Miroslav Bartoš,<sup>a</sup> Ivan Šalitroš,<sup>d</sup> Vinicius T. Santana,<sup>a</sup>  
 Paola Barbara,<sup>e</sup> Ivan Nemeč,<sup>\*ac</sup> and Petr Neugebauer<sup>id</sup> \*<sup>a</sup>

We present a theoretical and experimental study of two tetracoordinate Co(II)-based complexes with semi-coordination interactions, *i.e.*, non-covalent interactions involving the central atom. We argue that such interactions enhance the thermal and structural stability of the compounds, making them appropriate for deposition on substrates, as demonstrated by their successful deposition on graphene. DC magnetometry and high-frequency electron spin resonance (HF-ESR) experiments revealed an axial magnetic anisotropy and weak intermolecular antiferromagnetic coupling in both compounds, supported by theoretical predictions from complete active space self-consistent field calculations complemented by N-electron valence state second-order perturbation theory (CAS-SCF-NEVPT2), and broken-symmetry density functional theory (BS-DFT). AC magnetometry demonstrated that the compounds are field-induced single-ion magnets (SIMs) at applied static magnetic fields, with slow relaxation of magnetization governed by a combination of quantum tunneling, Orbach, and direct relaxation mechanisms. The structural stability under ambient conditions and after deposition was confirmed by X-ray photoelectron spectroscopy (XPS) and Raman spectroscopy. Theoretical modeling by DFT of different configurations of these systems on graphene revealed n-type doping of graphene originating from electron transfer from the deposited molecules, confirmed by electrical transport measurements and Raman spectroscopy.

 Received 29th March 2023,  
 Accepted 3rd October 2023

DOI: 10.1039/d3cp01426f

rsc.li/pccp

## 1 Introduction

Hybrid materials combining single-molecule magnets (SMMs) and solid-state materials are attractive candidates for next-generation technologies, such as high-density magnetic memory devices,<sup>1</sup> qubits,<sup>2</sup> and spintronic devices.<sup>3–5</sup> The solid-state substrate, having metallic, semi-metallic, or insulating character, provides a platform for the deposition of SMMs in the form of thin films, allowing addressing or manipulation of the molecular magnetic and electric properties.<sup>4,6,7</sup> For their successful deposition, the molecular compounds must present an increased chemical, structural, and thermal stability that guarantees the preservation of their magnetic properties during and after the deposition process,<sup>4</sup> which often involves their sublimation at high temperatures and under high-vacuum conditions. These features pose considerable challenges to the design of sublimable SMMs, such that the number of demonstrated complexes suitable for deposition and spintronic applications remains small.<sup>4</sup>

Co(II)-based coordination compounds often exhibit interesting magnetic properties emerging from a large spin-orbit coupling

<sup>a</sup> Central European Institute of Technology, CEITEC BUT, Purkyňova 656/123, 61200 Brno, Czech Republic. E-mail: ivan.nemec@ceitec.vutbr.cz, petr.neugebauer@ceitec.vutbr.cz

<sup>b</sup> Institute of Physical Engineering, Faculty of Mechanical Engineering, Brno University of Technology, Technická 2, 61669 Brno, Czech Republic

<sup>c</sup> Department of Inorganic Chemistry, Faculty of Science, Palacký University, 17. listopadu 12, 77147 Olomouc, Czech Republic

<sup>d</sup> Institute of Physics of Materials, Czech Academy of Sciences, Žitkova 22, 61662 Brno, Czech Republic

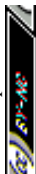
<sup>e</sup> Department of Physics, Georgetown University, Washington, DC, USA

<sup>f</sup> Department of Inorganic Chemistry, Faculty of Chemical and Food Technology, Slovak University of Technology in Bratislava, Bratislava SK-81237, Slovakia

† Electronic supplementary information (ESI) available. See DOI: <https://doi.org/10.1039/d3cp01426f>

‡ Present address: National High Magnetic Field Laboratory, Florida State University, 1800 E. Paul Dirac Drive Tallahassee, FL 32310, USA.

§ Present address: Institute of Applied Physics, Abbe Center of Photonics, Friedrich Schiller University, Albert-Einstein-Str. 15, 07745 Jena, Germany.





(SOC) inducing very large magnetic anisotropies in certain ligand field symmetries. For the preparation of SMMs, or their analogs with only one paramagnetic center, single-ion magnets (SIMs), it is important for the molecule to possess a large and preferably axial type of magnetic anisotropy ( $D < 0$ ), which is usually observed for low coordinate Co(II) complexes such as dicoordinate,<sup>8</sup> tetracoordinate,<sup>9–13</sup> pentacoordinate,<sup>14–20</sup> but also hexacoordinate with trigonal ligand field symmetry.<sup>21–27</sup>

To date, the most extensively investigated group of Co(II) SIMs consists of tetracoordinate complexes.<sup>28,29</sup> Within this class, the most intriguing results have been observed for SIMs that exhibit slow relaxation of magnetization in zero external magnetic fields, commonly known as zero-field SIMs (ZF-SIMs). There are only two groups of tetracoordinate Co(II) ZF-SIMs: those composed of monodentate ligands with S, Se, or Te donor atoms,<sup>30–32</sup> and those formed by bidentate ligands that create acute bite angles.<sup>33–37</sup> Our previous investigations strongly suggest avoiding the use of monodentate ligands in complexes intended for thermal depositions. Recently, we attempted to deposit two different types of tetracoordinate Co(II) complexes on various substrates, but found that the stability of the complex molecules during deposition was problematic under ambient conditions.<sup>38</sup> Even the use of a protective atmosphere was not sufficient to deposit intact tetracoordinate Co(II) molecules.<sup>39</sup> To enhance the stability of the Co(II) complexes intended for depositions we opted to use bidentate ligands instead of monodentate ligands. We decided to use bidentate Schiff base ligands which are well known for forming mononuclear Co(II) complexes exhibiting field-induced or zero-field slow relaxation of magnetization. Furthermore, we modified the Schiff base ligands by adding a 2-pyridyl substituent to ensure the high stability of the molecular complexes. This provides an additional nitrogen atom that is sterically hindered from forming a regular coordination bond with the metal atom. However, it can form a non-covalent interaction with the adjacent metal center. As we recently proposed,<sup>40</sup> non-covalent interactions between the donor atoms possessing free electron pairs such as N or O, and metal atoms can enhance the stability of the molecular complex without affecting the magnetic anisotropy of the metal centers significantly. Therefore, for depositions, we decided to utilize Co(II) compounds with a specific class of Schiff base ligands derived from the condensation of aromatic 2-hydroxy-benzaldehydes and 2-amino-6-picoline. The crystal structure of the Co(II) compound with the Hsalapi ligand (Hsalapi = 2-methyl-6-(2'-oxybenzylideneamino)pyridin) was reported previously.<sup>41</sup> In its crystal structure (Cambridge Structural Database code MIFWUU),<sup>42</sup> we see that two deprotonated salapi<sup>−</sup> ligands coordinate the Co(II) atom in a bidentate manner giving rise to the [Co(salapi)<sub>2</sub>] molecule (Fig. 1). Remarkably, the pyridine nitrogen atoms point towards the metal center, but the Co...N distances are relatively long (2.625(14) and 2.708(14) Å). Thus, from the perspective of structural coordination chemistry, these contacts could be classified as semi-coordinative because of their non-covalent nature and major electrostatic contribution.<sup>43–48</sup>

In this work, we opted to investigate whether the [Co(salapi)<sub>2</sub>] (hereafter **1**) and structurally related [Co(me-salapi)<sub>2</sub>] (hereafter

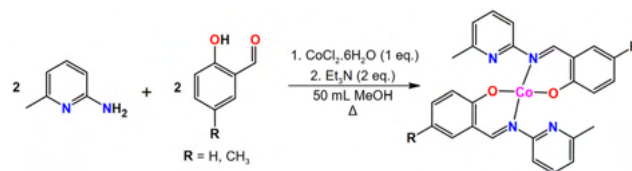


Fig. 1 Preparation scheme of compounds **1** (Co(salapi)<sub>2</sub>, R = H) and **2** (Co(me-salapi)<sub>2</sub>, R = CH<sub>3</sub>).

**2**, Hme-salapi = 2-methyl-6-(2'-oxy-4'-methyl-benzylideneamino)-pyridin) molecules can be magnetically considered to be tetracoordinate despite having relatively short Co...N non-covalent interactions. Furthermore, we investigated whether the Co...N interactions are stabilizing structures of molecules in **1** and **2** sufficiently enough for their utilization in depositions by wet chemistry and thermal sublimation. In this case, we performed molecular deposition on commercially available single-layer graphene.<sup>49</sup> Graphene offers interesting properties such as high electron mobility, spin transport, mechanical strength, and thermal conductivity.<sup>50–53</sup> Furthermore, in our vision, graphene serves as a good substrate for deposition when nanostructured into a quantum dot, which could be used as a bolometer for *in situ* spectroscopy of deposited compounds.<sup>54,55</sup> Graphene could also be used for the electrical addressing of SMMs, as it can be shaped and utilized for graphene transistors<sup>56</sup> that are commercially available nowadays.

Herein, we report on the synthesis, crystal structure, magnetic properties, and characterization of compounds **1** and **2** along with a theoretical study of their semi-coordination aspects, magnetic properties, and intermolecular exchange interactions. Direct current (DC) magnetometry and HF-ESR measurements demonstrated that the compounds present an axial magnetic anisotropy and a weak intermolecular antiferromagnetic exchange interaction, corroborated by broken-symmetry DFT (BS-DFT) calculations; while alternating current (AC) magnetometry showed that both compounds behave as field-induced SIMs. We also carried out a successful deposition of **1** and **2** on graphene and compared the results to a bulk reference. Raman spectroscopy, X-ray photoelectron spectroscopy (XPS), atomic force microscopy (AFM), and electrical transport measurements were used as characterization techniques supporting the theoretical predictions of molecular adsorption performed by DFT.

## 2 Materials and methods

Detailed information on the sample preparation, elemental analysis, characterization by infrared spectroscopy and X-ray diffraction (XRD), DC and AC magnetometry, electrical transport, and HF-ESR measurements is found in the ESI.†

### 2.1 Deposited samples

For both deposition processes (drop-cast and thermal sublimation) a chemical vapour deposition (CVD) grown monolayer graphene on a Si/SiO<sub>2</sub> substrate was used (300 nm thickness of



SiO<sub>2</sub>, Si (100), p-doped, 1–10 Ω cm from Graphenea, San Sebastian, Spain). The drop-cast sample was prepared by dissolving the bulk compound **1** or **2** in acetone (99%, Penta, Czech Republic) to make a final solution with a 1 mM concentration. The actual drop-casting was conducted in ambient conditions as 40 μL was drop-cast onto graphene. For the thermal sublimation, we used a home-built high-vacuum sublimation chamber equipped with a quartz crucible heated by a ceramic heater (BACH RC, Seefeld, Germany) with a thermocouple in thermal contact with the heater. The base chamber pressure during the sublimation was  $1 \times 10^{-6}$  mbar. The sublimations for **1** and **2** were performed at 270 and 283, respectively. The bulk powder from the crucible after sublimation was taken for further analysis. Optical images were acquired on a confocal Raman microscope WITec Alpha300 R+ (WITec, Ulm, Germany). All topography images and profiles were obtained with the scanning probe microscope Dimension Icon (Bruker, Billerica, USA) in tapping mode. X-ray photoelectron (XPS) measurements were carried out with Kratos Axis Supra (Kratos Analytical, Manchester, United Kingdom).

## 2.2 Computational details

The zero-field splitting (ZFS) terms were computed using Gaussian-basis DFT in the ORCA 4.2.1 and 5.0 electronic structure packages,<sup>57,58</sup> using the state average-CASSCF,<sup>59</sup> complemented by NEVPT2.<sup>60,61</sup> The input coordinates for the calculations were obtained from experimentally determined molecular structures refined by Hirshfeld atom refinement<sup>62</sup> incorporated in Olex2 (ver. 1.5).<sup>47</sup> The basis sets for the ZFS calculations were used as follows: def2-SVP for hydrogen and carbon atoms, triple- $\zeta$  def2-TZVP for the remaining atoms.<sup>63</sup> The calculation costs were decreased by using the def2/J and def2-TZVP/C auxiliary basis sets<sup>64,65</sup> together with the chain-of-spheres (RIJCOSX)<sup>66,67</sup> approximation to the exact exchange as implemented in ORCA. The active space was defined by seven electrons in five d-orbitals of Co(II) (CAS(7,5)), and all possible multiplets, 10 quartets, and 40 doublets, were involved in the calculations. The ligand field parameters were obtained using the *ab initio* ligand field theory (AIFLT) calculations.<sup>68</sup>

BS-DFT calculations in ORCA 5.0 were carried out to estimate the isotropic exchange interaction. Two DFT hybrid functionals, B3LYP<sup>69–71</sup> and PBE0,<sup>72</sup> were selected based on their good performance on previously studied coordination compounds.<sup>73–78</sup> Moreover, the calculations were performed with Ahlrichs triple- $\zeta$  basis sets def2-TZVP and also with their relativistic analogs ZORA-def2-TZVP.<sup>63</sup> Furthermore, the non-local density-dependent dispersion correction to DFT was accounted for in two ways, as non-self-consistent (DFT-NL) and as self-consistent (DFT-SCNL) implementation.<sup>79,80</sup>

The quantum theory of atoms in molecules<sup>81</sup> (QT-AIM) calculations were performed using ORCA 4.2.1, employing single-point DFT calculations utilizing the B3LYP functional and bases as described above (def2-TZVP). Then, the wavefunctions were used for the QT-AIM calculations using the Multiwfn program.<sup>82,83</sup> ELF calculations for Co(II) complexes, which visualize electron pairs, were compared to those for diamagnetic Zn(II) analogues, revealing no significant differences.

Molecular adsorption on graphene was calculated using plane-wave DFT performed on the Vienna Ab-Initio Simulation Package (VASP)<sup>84–87</sup> version 5.4.4, which uses a plane-wave basis for the Kohn–Sham orbitals, the Projector Augmented Wave method,<sup>87,88</sup> and pseudopotentials. The exchange–correlation was accounted for by the PBE functional,<sup>89,90</sup> with van der Waals corrections included by the D3 method with Becke–Johnson damping.<sup>91,92</sup> Collinear spin polarization and electric dipole corrections<sup>93,94</sup> were also included. In all calculations, the kinetic energy cut-off for the plane waves was 520 eV, and the cut-off energy of the plane wave representation of the augmentation charges was 644.9 eV. The threshold for electronic self-consistency loops was  $10^{-6}$  eV, and ionic relaxation was performed until residual forces on each ion were below 0.02 eV Å<sup>-1</sup>, unless stated otherwise.

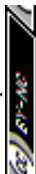
For calculations of the ground-state energy, ionic relaxation of isolated molecules, and ionic relaxation of the molecules on graphene, the reciprocal space was sampled using only one point at the Brillouin zone center ( $\Gamma$ -point calculation). For charge density calculations, a  $\Gamma$ -centered  $2 \times 2 \times 1$  Monkhorst–Pack mesh<sup>95</sup> was used to sample the Brillouin zone of all configurations. The obtained charge densities were used and kept constant in the density of states calculations, where the reciprocal space was sampled with a  $\Gamma$ -centered  $4 \times 4 \times 1$  Monkhorst–Pack mesh. Reciprocal space integration used Gaussian smearing of  $k$ -points equal to 0.1 eV. To generate the partial density of states (Fig. 7a), and the planar average of the charge density difference (Fig. 7b, c and ESI† Fig. S41, S42), we used the VASPKIT code.<sup>96</sup> We used the VESTA software<sup>97</sup> to plot Fig. 6a–d, f–i, 7b, c and ESI† Fig. S40–S42.

To model the monolayer graphene substrate, we first performed ionic relaxation of the  $10 \times 10$  graphene superlattice by plane-wave DFT until the interatomic forces were below 0.001 eV Å<sup>-1</sup>. ( $1 \times 1$  corresponds to a graphene unit cell containing two carbon atoms with an interatomic distance of 1.424 Å.) During the relaxation, the supercell's volume was kept constant, and the ionic positions were relaxed within the graphene's plane. The molecules were modeled taking as a basis their XRD structure. Then, ionic relaxation of the isolated molecules (gas phase) was performed using a parallelepiped unit cell of dimensions  $24.67 \times 24.67 \times 30$  Å<sup>3</sup> (ESI† Fig. S40). To simulate molecular adsorption on graphene, four different configurations (orientations) of each molecular complex were placed on the  $10 \times 10$  graphene substrate. A supercell height of 30 Å in the direction perpendicular to the graphene plane ( $z$  direction), guaranteed at least a 15 Å vacuum above the molecule on the substrate, minimizing the interaction between supercells in the  $z$  direction. Electric dipole corrections along the  $z$  direction were applied to reduce this interaction further. The supercell size and shape were kept the same in all calculations.

## 3 Results and discussion

### 3.1 Synthesis and structure

Compounds **1** and **2** can be prepared using the previously reported procedure.<sup>41</sup> However, we synthesized both compounds



by *in situ* reaction of 2-amino-6-methylpyridine, salicylaldehyde (or 5-methylsalicylaldehyde for preparation of **2**),  $\text{CoCl}_2 \cdot 6\text{H}_2\text{O}$  and triethylamine in methanolic solution (molar ratio 2:2:1:2, Fig. 1). The mixture was refluxed after the addition of all reagents and then filtered. Red-orange crystals suitable for single-crystal XRD were obtained by slow diffusion of  $\text{Et}_2\text{O}$  into the solution. The purity of both compounds was confirmed by elemental analysis and powder XRD experiments (ESI† Fig. S1). The thermal stability was investigated using thermogravimetric analysis (ESI† Fig. S2 and S3), and it was revealed that compounds **1** and **2** are stable up to 290 and 310 °C, respectively, and with melting temperatures 263–265 and 301 °C, respectively.

Compounds **1** and **2** adopt very similar crystal structures although they are not isostructural. **1** crystallizes in the monoclinic  $I2/a$  space group, whereas **2** in the orthorhombic  $Pbcn$  space group. The basic crystallographic and refinement data are summarized in the ESI† Table S1. Both crystal structures consist solely of the molecular complex (Fig. 2a and ESI† Fig. S4, S5). In both structures, the cobalt atom sits at a two-fold rotational axis, and thus only half of the complex molecule is symmetrically independent. Two bidentate ligands coordinate the central  $\text{Co(II)}$  atom, each by one phenolate oxygen atom ( $d_{\text{Co1-O1}} = 1.9527(16)$  Å and  $1.9613(7)$  Å in **1** and **2**, respectively) and by an imine nitrogen atom (N1 in Fig. 2a,  $d_{\text{Co1-N1}} = 1.9913(18)$  Å and  $1.9923(9)$  Å in **1** and **2**, respectively). The  $\text{Co} \cdots \text{N}$  distance of the pyridine nitrogen atoms (N2) is longer:  $2.6908(19)$  Å and  $2.6951(9)$  Å in **1** and **2**, respectively, therefore, both **1** and **2** can be formally considered to be tetracoordinate. According to the SHAPE algorithm and continuous shape measurements (CSMs), the shape of the coordination polyhedron corresponds to a distorted tetrahedron (CSMs( $T_d$ ): 2.857 and 2.531, respectively), however, distortion from the see-saw geometry is relatively small: (CSMs( $C_{2v}$ ): 3.800 and 4.723, respectively, ESI† Table S2). The complex molecules form extensive networks of  $\pi$ - $\pi$  aromatic stacking interactions organized in supramolecular layers parallel to (00l) planes (in **1**) or chains along the *c*-axis (in **2**, ESI† Fig. S4 and S5).

To investigate the nature of the  $\text{Co} \cdots \text{N}$  interaction we utilized the topological analysis of electron density by QT-AIM. Firstly, we performed single-point DFT calculations using the coordinates of the complex molecules **1** and **2** obtained from XRD experiments. To ensure reliable positions of the hydrogen atoms we applied the Hirshfeld atom refinement for both structures (for details see the ESI† Section S1). Then, we performed topological analysis of the electron density ( $\rho(r)$ ) using Multiwfn software.<sup>82,83</sup> As a result, we did not find any bond critical point (BCP) between the Co1 and N2 atoms, as seen from the Laplacian of electron density ( $\nabla^2\rho(r)$ , ESI† Fig. S6). This can be attributed to the orientation of the pyridyl moiety, which modulated the topology of  $\nabla^2\rho(r)$  between the Co and N atoms, preventing the formation of bond path or BCP (ESI† Fig. S6). Next, we analyzed this interaction using the non-covalent interaction (NCI) method.<sup>98</sup> This method utilizes the analysis of  $\rho(r)$  using the reduced density gradient function to distinguish between attractive and repulsive non-covalent interactions by determining the sign of the eigenvalue of the electron density Hessian matrix, defined as  $\lambda_2$ . We visualized the interactions within molecules using VMD software<sup>99</sup> (Fig. 2b). The  $\text{Co} \cdots \text{N}$  interaction was found to be a combination of steric effect (repulsion between the neighboring nitrogen atoms, red color) and attraction between the pair of the Co and N atoms (blue color). To better visualize this interaction, we also computed the electron localization function (ELF), which depicts the probability of finding an electron pair in multielectronic systems.<sup>100,101</sup> Fig. 2c shows that the pyridine electron pair is well localized, pointing towards the more electro-positive cobalt atom (ESI† Fig. S6). In summary, despite the absence of BCP, we show that the  $\text{Co} \cdots \text{N}$  interaction exhibits an attractive non-covalent character due to the interaction between the pyridyl electron pair and the cobalt atom. Therefore, we classify this interaction as semi-coordination.<sup>44</sup>

### 3.2 Magnetic properties and HF-ESR

We employed magnetometry to perform DC magnetic measurements, including temperature- (2–300 K) and field- (0–7 T at 2 K)

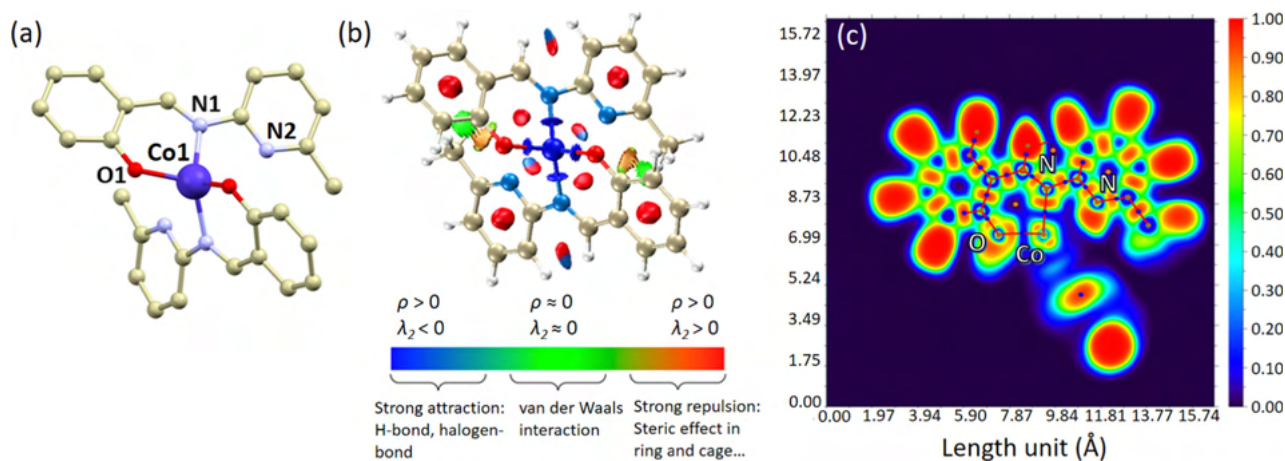


Fig. 2 (a) A perspective view on the structure of the molecular complex in the crystal structure of **1**, hydrogen atoms were omitted for clarity. Color code: carbon (light brown), cobalt (dark blue), nitrogen (light blue), and oxygen (red). Selected bond lengths (in Å): **1**,  $d_{\text{Co1-N1}} = 1.9970(8)$ ,  $d_{\text{Co1-O1}} = 1.9579(7)$ ; **2**,  $d_{\text{Co1-N1}} = 1.9923(9)$ ,  $d_{\text{Co1-O1}} = 1.9613(7)$ . (b) NCI plot calculated for **1**. (c) Visualization of the ELF for **1**.





dependence of the magnetic moment (Fig. 3a and ESI† Fig. S27). The crystal structures of **1** and **2** consist of isolated complexes that interact through  $\pi$ - $\pi$  stacking interactions, which are well-known non-covalent magnetic exchange pathways.<sup>102</sup> To appropriately analyze the magnetic data, we first performed theoretical calculations. We selected dimeric structural fragments (Fig. 3d) and conducted BS-DFT calculations following the procedure of Section 2.2 to estimate the isotropic exchange of the spin Hamiltonian defined as  $\hat{H} = -J\hat{S}_1\cdot\hat{S}_2$ , with  $\hat{S}_1$  and  $\hat{S}_2$  corresponding to the spin operator of each molecule in the dimer. The comparison of the energy difference between the high-spin (HS,  $S_{1\uparrow}\cdot S_{2\uparrow}$ ) and broken-symmetry spin states (BS,  $S_{1\uparrow}\cdot S_{2\downarrow}$ ),  $\Delta = \varepsilon_{\text{BS}} - \varepsilon_{\text{HS}}$ , was utilized to calculate  $J$  according to the formulas of Ruiz<sup>103</sup> and Yamaguchi:<sup>104</sup>

$$J^{\text{R}} = \frac{2\Delta}{(S_1 + S_2)(S_1 + S_2 + 1)}, \quad J^{\text{Y}} = \frac{2\Delta}{\langle S^2 \rangle_{\text{HS}} - \langle S^2 \rangle_{\text{BS}}} \quad (1)$$

All approaches predicted a weak antiferromagnetic coupling within the dimer for compounds **1** and **2** using all tested functionals and bases (see the ESI† Tables S8 and S9); for example, using the functional B3LYP + NL we find  $J^{\text{Y}} = -0.247 \text{ cm}^{-1}$  and  $-0.268 \text{ cm}^{-1}$  for **1** and **2**, respectively. A slightly

stronger antiferromagnetic exchange was predicted for **2**, which is consistent with its shorter C...C and C...N distances between the  $\pi$ - $\pi$  stacked ligands of the neighboring molecules compared to those in compound **1**. The magnetic exchange interaction between neighboring molecules is expected to be weak due to the relatively large Co...Co distances being 5.94479(9) and 5.82467(7) Å in compounds **1** and **2**, respectively.

Since the magnetic measurements for both compounds were very similar, we provided a more detailed description of the properties of **1**. The effective magnetic moment  $\mu_{\text{eff}}/\mu_{\text{B}}$  measured for **1**, where  $\mu_{\text{B}}$  is the Bohr magneton, adopts a value of 4.3 at room temperature, which is consistent with a large contribution of SOC. Thus, the Landé  $g$ -factor ( $g_{\text{iso}} = 2.20$ ) is larger than that of the free electron ( $g = 2.0023$ ). The  $\mu_{\text{eff}}/\mu_{\text{B}}$  values stayed approximately constant down to 30 K, where we observed a drop starting from 4.1 to 3.7 at 2 K suggesting the presence of intermolecular magnetic exchange interactions or ZFS. Since we did not observe maxima in the susceptibility curve ( $\chi = f(T)$ ), we may conclude that the intermolecular magnetic interactions among molecules are weak. Nevertheless, we were unable to fit the magnetic data in the absence of exchange coupling, and due to this fact as well as taking into account the results of BS-DFT calculations, we applied a spin Hamiltonian including axial ( $D$ ) and rhombic ( $E$ ) single-ion ZFS

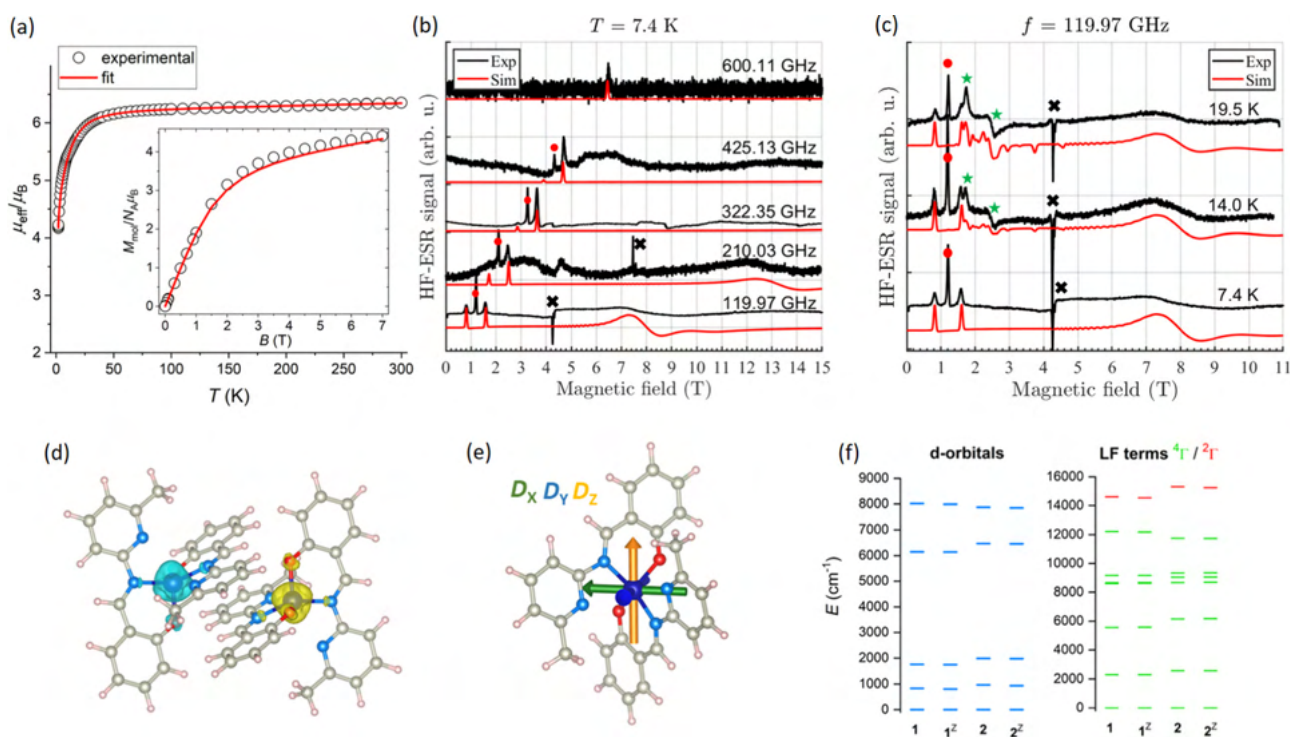
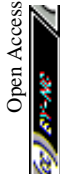


**Fig. 3** (a) Temperature dependence of  $\mu_{\text{eff}}/\mu_{\text{B}}$  acquired for **1** in the range from 2 K to 300 K with an external magnetic field 0.1 T, and the isothermal magnetization data measured at 2 K shown in the inset. The empty circles represent experimental data, while the red lines represent fittings to eqn (2)–(4). (b) Frequency dependence of the HF-ESR spectra of compound **1** at 7.4 K. (c) Temperature dependence of the HF-ESR spectra of compound **1** at 119.97 GHz. The parameters in the simulated spectra (with offset for more clarity) were  $D = -20 \text{ cm}^{-1}$ ,  $g_x = 2.20$ ,  $g_y = 2.15$ ,  $g_z = 2.40$ ,  $E/D = 0.122$ , and  $J = -0.3 \text{ cm}^{-1}$ . Green stars correspond to thermally-activated transitions ascribed to the excited  $S = 1/2$  doublet, black crosses indicate an ESR signal from an impurity in the sample holder's mirror, and red dots indicate a spurious signal not considered in the simulation. (d) The outcome of the BS-DFT calculations for **1** with visualization of the spin density isosurface. (e) Visualization of the  $D$ -tensor axes overlaid over the molecular structure of **1**. (f) AILFT-calculated d-orbital splitting (left) and ligand field terms (right).





terms and exchange coupling for the supramolecular dimer:

$$\hat{H} = -J(\hat{S}_1 \cdot \hat{S}_2) + D\left(\hat{S}_z^2 - \frac{S^2}{3}\right) + E(\hat{S}_x^2 - \hat{S}_y^2) + \mu_B B g \hat{S}_a, \quad (2)$$

together with the Zeeman term defined in the direction of the magnetic field as  $B_a = B(\sin \theta \cos \phi, \sin \theta \sin \phi, \cos \theta)$ , where  $\theta$  and  $\phi$  are the polar and azimuthal angles of the field. The molar magnetization in the  $a$ -direction of the magnetic field was numerically calculated from the partition function,  $Z$ , built from the energy levels of the spin Hamiltonian as follows:

$$M_a = N_A k_B T \frac{d \ln Z}{d B_a}, \quad (3)$$

where  $k_B$  and  $N_A$  are the Boltzmann and Avogadro constants, respectively. Then, the averaged molar magnetization of the powder sample was calculated as the orientational average:

$$M_{\text{mol}} = \frac{1}{4\pi} \int_0^{2\pi} \int_0^\pi M_a \sin \theta d\theta d\phi. \quad (4)$$

The experimental magnetic data were fitted using EasySpin,<sup>105</sup> analyzing both temperature- and field-dependent measurements simultaneously. The best fit was obtained with the following sets of parameters: for **1**,  $J = -0.19 \text{ cm}^{-1}$ ,  $g_{\text{iso}} = 2.272$ ,  $D = -15.3 \text{ cm}^{-1}$  and  $E/D = 0.012$ ; for **2**,  $J = -0.27 \text{ cm}^{-1}$ ,  $g_{\text{iso}} = 2.213$ ,  $D = -17.5 \text{ cm}^{-1}$  and  $E/D = 0.044$  (Fig. 3a and ESI† Fig. S27). This confirmed the presence of a relatively large and axial magnetic anisotropy.

ZFS was studied theoretically using the procedure outlined in Section 2.2, using ORCA 5.0. The calculations indicate that the  $^4\text{F}$  atomic term is split into seven ligand field multiplets as expected due to the low symmetry of the coordination polyhedron in **1** and **2**. Additionally, the energy of the first excited state is above  $1000 \text{ cm}^{-1}$ , making the spin Hamiltonian formalism suitable for analyzing magnetic data.<sup>106</sup> The splitting of the d-orbitals reflects the distorted tetrahedral geometry with the lowest  $d_{x^2-y^2}$  orbital. The configuration of the d-orbitals is for both complexes as follows:  $d_{x^2-y^2}$ ,  $d_{z^2}$ ,  $d_{xy^1}$ ,  $d_{xz^1}$ ,  $d_{yz^1}$  (ESI† Fig. S21 and S22). In this configuration, the energy of the first excitation between the d-orbitals with the same  $|m_l|$  value ( $d_{x^2-y^2} \rightarrow d_{xy^1}$ ,  $|m_l| = 2$ ) is smaller than the first excitation with  $\Delta|m_l| = 1$  ( $d_{z^2} \rightarrow d_{xz^1}$ ). This indicates a relatively large and axial magnetic anisotropy.<sup>23</sup> CASSCF-NEVPT2 calculations of the ZFS parameters confirmed this assumption:  $D = -25.3 \text{ cm}^{-1}$  and  $E/D = 0.084$  for **1**;  $D = -28.3 \text{ cm}^{-1}$  and  $E/D = 0.107$  for **2** (ESI† Tables S10 and S11). The obtained ZFS parameters were markedly different from those obtained by magnetometry. Therefore, we investigated if the used basis sets can help to diminish the difference between the calculated and experimentally derived ZFS parameters. We included relativistic effects by introducing relativistic analogs of Ahlrichs double- and triple- $\zeta$  basis sets (ZORA-def2-SVP for hydrogen and carbon atoms). The calculated  $D$  values were slightly lower than those resulting from non-relativistic calculations, but their absolute values are still significantly larger than those derived from magnetometry (ESI† Tables S10 and S11).

We investigated the impact of the pyridine nitrogen atoms on the electronic structure and magnetic anisotropy of compounds **1** and **2** by replacing the 6-methyl-pyridine groups with phenyl rings. Using DFT calculations (B3LYP and def2-SVP in ORCA 5.0) we optimized the positions of these new groups while keeping the positions of other atoms fixed, resulting in the **1'** and **2'** input structures. This method allowed us to maintain the ligand field strength and symmetry from the regular donor atoms ( $\{\text{NO}\}_2$ ) while eliminating any influence of the pyridine nitrogen atoms. The CASSCF-NEVPT2 calculations for **1** and **2** yielded very similar ligand field term structures as in **1** and **2**. However, the energy of the lowest quartet was found to be lower in **1** and **2** compared to **1** and **2** (ESI† Fig. S23–S25). The resulting ZFS parameters are different from those obtained for **1** and **2**; the  $|D|$  values were found to be larger ( $-40.3 \text{ cm}^{-1}$  for **1** and  $-38.1 \text{ cm}^{-1}$  for **2**) while the  $E/D$  values were significantly lower ( $E/D = 0.055$  in **1**,  $0.039$  in **2**).

Thus, the anisotropy of **1** and **2** is larger and less rhombic than calculated for **1** and **2**. The larger  $|D|$  values can be explained by the d-orbital splitting. Despite having the same splitting pattern and similar orbital energies as **1** and **2**, the observed changes in **1** and **2** are most pronounced for the  $d_{xy}$  orbital, which experiences the greatest decrease in energy (ESI† Fig. S25). This aligns with the orientation of this orbital in relation to the position of the pyridyl rings. In **1** and **2**, the pyridyl nitrogen atoms point towards the lobes of the  $d_{xy}$  orbital (ESI† Fig. S25). However, in **1** and **2**, the orientation of the orbital remains unchanged even without the pyridyl nitrogen atoms. It is worth noting that the decrease of the  $d_{xy}$  energy is larger in **2** than in **1** which correlates with the shorter Co...N distance (and thus larger destabilization of  $d_{xy}$ ) in **2** ( $2.6592(9) \text{ \AA}$ ) than in **1** ( $2.6901(11) \text{ \AA}$ ). As a result, the lower energy of the  $d_{xy}$  orbital leads to a smaller  $d_{x^2-y^2} \rightarrow d_{xy^1}$  excitation, resulting in larger  $|D|$  values. In summary, the CASSCF-NEVPT2 calculations revealed that while the interaction between the Co(II) atom and pyridyl nitrogen atoms does not induce significant changes in the overall ligand field, the interaction between the  $d_{xy}$  orbital and lone pairs of the nitrogen atoms produce smaller  $|D|$  values in complexes with the Co...N interactions.

The magnetization blocking barriers in **1** and **2** were calculated using the SINGLE\_ANISO module<sup>107</sup> incorporated in ORCA 5.0.<sup>58</sup> The results strongly indicate that quantum tunneling is the dominant relaxation process since the matrix element of the transversal magnetic moment between the ground states with opposite magnetizations is greater than 0.1 (0.23 for **1**, 0.18 for **2**, ESI† Fig. S26). Therefore, it is expected that **1** and **2** will behave as field-induced SIMs. Notably, changing the basis from non-relativistic to relativistic (def2-TZVP vs. ZORA-def2-TZVP) did not affect the matrix elements of any of the calculated magnetic moments (ESI† Fig. S26).

Further analysis of the magnetic properties of **1** was performed by HF-ESR. Although measurements were taken on compounds **1** and **2** both in powder form and deposited on graphene, only the powder spectra of **1** showed satisfactory results. HF-ESR measurements on the deposited compounds on graphene did not show a clear signal due to the low



deposited amounts, as evidenced in the ESI† Fig. S30 for compound **1**. Fig. 3b and c show the HF-ESR powder spectra of **1** at different frequencies and temperatures, respectively. (HF-ESR spectra at other frequencies are shown in the ESI† Fig. S28.) From the temperature-dependent spectra, we observed strong thermally-activated transitions ascribed to the  $S = 1/2$  doublet, indicated by green stars in the spectra, confirming that the ground state has spin  $3/2$ , and thus  $D$  is negative. Nevertheless, transitions between the ground-state  $S = 3/2$  and the excited state  $S = 1/2$  were not observed in the energy range accessible in our experiments. Therefore, we set a bound for the ZFS such that the mentioned transition does not appear in the simulated spectrum, being equal to  $|D| > 600 \text{ GHz} = 20 \text{ cm}^{-1}$ . Simulations with the parameters  $g_x = 2.20$ ,  $g_y = 2.15$ ,  $g_z = 2.40$ ,  $D = -20 \text{ cm}^{-1}$ ,  $E/D = 0.122$ , and an exchange term  $J = -0.3 \text{ cm}^{-1}$  reproduce most of the spectral features successfully and suggest intermolecular antiferromagnetic coupling, in agreement with BS-DFT calculations ( $J^X = -0.247 \text{ cm}^{-1}$ , B3LYP-NL method), and similar to the one found by DC magnetometry ( $J = -0.19 \text{ cm}^{-1}$ ). The ZFS parameters  $g$ -factors are in agreement with the ones calculated for **1** in bulk configuration by CASSCF-NEVPT2, as shown in Section 3.4 and Table 3. Although weak, the exchange coupling has a noticeable effect on the HF-ESR spectra, since it is responsible for the emergence of a second peak in the low magnetic field region (the first two peaks in the simulated spectra of Fig. 3b). The separation between those peaks indicates the strength of the exchange coupling, such that at  $J = 0$  there is only one peak in the low magnetic field region. Of the spectral features not captured in the simulation, the ones indicated by black crosses correspond to a signal coming from the mirror in the sample holder, while for the ones indicated by red dots, we do not have a conclusive explanation. From the simulations, we can infer that they do not come from plausible values of the spin Hamiltonian parameters for compound **1**.

To probe the slow relaxation of magnetization behavior in **1** and **2**, the AC susceptibility was measured at low temperatures (see the ESI† Section S7 for a detailed experimental description of AC susceptibility measurements and data analysis). At 2 K, a static magnetic field ( $B_{\text{DC}}$ ) scan revealed the absence of an out-

of-phase signal  $\chi''$  at  $B_{\text{DC}} = 0 \text{ T}$  for both compounds (ESI† Tables S13, S21 and Fig. S31, S35), which is a consequence of fast relaxation of magnetization resulting from the quantum tunneling (QT) effect induced by hyperfine interactions with nuclear spins. However, the applied  $B_{\text{DC}}$  field suppressed the tunneling, allowing us to map the AC susceptibility and find the optimal  $B_{\text{DC}}$  field for further temperature-dependent dynamic magnetic investigations. The frequency-dependent in-phase  $\chi'$  and out-of-phase  $\chi''$  components of the AC susceptibility were satisfactorily fitted to the extended one-set Debye model (ESI† eqn. (S1), (S2), Tables S13, S21 and Fig. S31, S35), by which the isothermal  $\chi_T$  and adiabatic  $\chi_S$  susceptibilities along with the relaxation time  $\tau$  (Fig. 4a) and its distribution parameter  $\alpha$  were determined at given  $B_{\text{DC}}$  fields.

The global relaxation rate  $\tau^{-1}$  is usually described by Orbach, Raman, direct, and QT relaxation processes as follows:

$$\frac{1}{\tau} = \frac{1}{\tau_{\text{Orbach}}} + \frac{1}{\tau_{\text{Raman}}} + \frac{1}{\tau_{\text{direct}}} + \frac{1}{\tau_{\text{QT}}} \\ = \frac{1}{\gamma_0} \exp\left(\frac{U}{k_B T}\right) + d \left(\frac{1 + eH^2}{1 + fH^2}\right) T^n + aH^m T + \frac{b_1}{1 + b_2 H^2}. \quad (5)$$

At very low temperatures (*i.e.* at 2 K), the Raman, direct or QT terms of eqn (5) usually participate in the relaxation of magnetization; therefore, the  $\tau$  vs.  $B_{\text{DC}}$  dependencies for both compounds were analyzed with the respective combinations of direct & QT or direct & Raman mechanisms. No combination of these mechanisms was appropriate for the  $\tau$  vs.  $B_{\text{DC}}$  analysis of **1** (ESI† Fig. S31d and Table S16), while a combination of direct & Raman processes gave satisfactory results in the low field region 0–0.1 T of **2** (ESI† Fig. S35d and Table S24).

The longest relaxation times were observed at  $B_{\text{DC}} = 0.06 \text{ T}$  for **1** and  $B_{\text{DC}} = 0.09 \text{ T}$  for **2** (Fig. 4a) and these static fields were used for further temperature-dependent dynamic magnetic studies. Additionally, slightly higher static fields ( $B_{\text{DC}} = 0.09 \text{ T}$  for **1** and  $B_{\text{DC}} = 0.125 \text{ T}$  for **2**) were used to record the same acquisition of dynamic magnetic measurements upon the change of temperature, enabling a comprehensive analysis of the slow relaxation of magnetization in both investigated SIMs

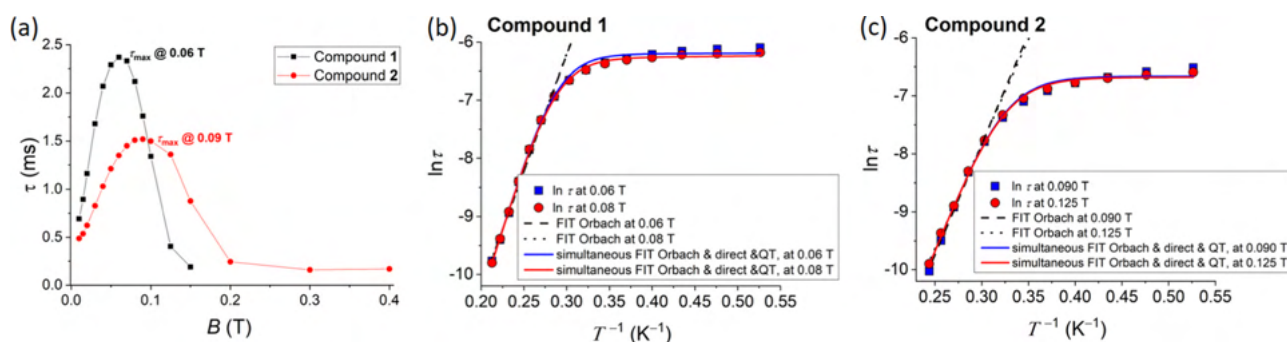
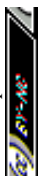


Fig. 4 (a)  $\tau$  vs.  $B_{\text{DC}}$  dependencies for compounds **1** and **2**. (b) and (c)  $\ln \tau$  vs.  $1/T$  plots for compounds **1** and **2**, respectively, obtained from AC susceptibility measurements recorded at two different DC magnetic fields. The blue and red solid lines result from simultaneous fits of two  $\ln \tau$  vs.  $1/T$  dependencies at two different DC magnetic fields for each compound.



(*vide infra*). Frequency-dependent in-phase ( $\chi'$ ) and out-of-phase ( $\chi''$ ) components of the magnetic susceptibility measured as a function of the frequency of an alternating magnetic field,  $B_{AC}$ , for a set of temperatures (1.9–4.9 K for **1** and 1.9–4.1 K for **2**; ESI† Fig. S32, S33, S36, S37 and Tables S14, S15, S22, S23) suggest a single relaxation channel. The out-of-phase components  $\chi''$  for **1** and **2** show the maximum shift from 69 Hz (at 1.9 K and 0.06 T,  $\tau \approx 2.3$  ms) and from 106 Hz (at 1.9 K and 0.09 T,  $\tau \approx 1.5$  ms), respectively, towards higher frequencies upon a temperature increase (ESI† Tables S14, S15, S22 and S23). This indicates a typical feature of SMMs – the maxima of  $\chi''$  are frequency and temperature dependent, and the relaxation time  $\tau$  shortens as the temperature increases. The temperature-dependent AC susceptibility measurements were fitted using an extended one-set Debye model (ESI† eqn (S1) and (S2)), which enabled us to obtain the relaxation time  $\tau$  at the corresponding temperatures and static magnetic fields. The analysis of temperature dependencies  $\ln \tau$  vs.  $1/T$  at a given  $B_{DC}$  was carried out with respect to various combinations of relaxation processes involved in the following relaxation equation:

$$\frac{1}{\tau} = \frac{1}{\tau_{\text{Orbach}}} + \frac{1}{\tau_{\text{Raman}}} + \frac{1}{\tau_{\text{direct}}} + \frac{1}{\tau_{\text{QT}}} \quad (6)$$

$$= \frac{1}{y_0} \exp\left(-\frac{U}{k_B T}\right) + CT^n + aH^m T + \frac{1}{\tau_{\text{QT}}},$$

where the corresponding terms represent Orbach, Raman, direct, and QT relaxation mechanisms, respectively. The most successful fits with the reliable values of relaxation parameters involve the combination of Orbach, direct, and QT mechanisms for **1** (ESI† Tables S17 and S18) and Orbach, direct, and Raman mechanisms for **2** (ESI† Tables S25 and S26). A more comprehensive analysis was focused on the simultaneous fitting of  $\ln \tau$  vs.  $1/T$  functions at two static  $B_{DC}$  fields. Thus, two  $\ln \tau$  vs.  $1/T$  dependencies recorded at 0.06 and 0.08 T for **1** and at 0.09 and 0.125 T for **2** were simultaneously analyzed using combinations of various relaxation mechanisms. The most accurate fits involve the combination of Orbach, direct, and QT processes for each compound (Fig. 4b, c and ESI† Tables S19, S27). The Orbach energy barriers ( $U_{\text{eff}}$ ) and relaxation time at infinite temperature ( $\tau_0$ ) are comparable to the previously reported tetracoordinated Co(II) field-induced SIMs with a similar degree of tetrahedral distortion and magnetic anisotropy (see the ESI† Table S28 for a comparison with similar compounds in other studies). Furthermore, the obtained relaxation parameters suggest that the presence of methyl substituents introduced on the tridentate Schiff base ligand accelerates the slow relaxation of magnetization governed *via* QT and Orbach relaxation, while the direct relaxation seems to be unaffected by such subtle structural variation. Table 1 summarizes the main results from the AC susceptibility analysis.

### 3.3 Deposition and charge transfer

Depositions on CVD graphene on Si/SiO<sub>2</sub> by drop-cast and thermal sublimation were performed to test the stability of both compounds. Optical images of deposited compounds **1** and **2** can be seen in Fig. 5a and Fig. S7, S14 (ESI†). The

**Table 1** Relaxation parameters for the reported compounds. Fits considering only the Orbach relaxation process were obtained by fitting the high-temperature parts of  $\ln \tau$  vs.  $1/T$  at the corresponding  $B_{DC}$  fields. Comprehensive fitting analysis of  $\ln \tau$  vs.  $1/T$  involves simultaneous fittings at two  $B_{DC}$  fields

Compound, Model	$U$ (K)	$\tau_0$ (ns)	$\tau_{\text{QTM}}$ (ms)	$a$ ( $T^m \text{ K s}$ ) <sup>-1</sup>	
				$m$	
<b>1</b> , Orbach <sup>a</sup> at 0.06 T	40	12	—	—	—
<b>1</b> , Orbach <sup>a</sup> at 0.08 T	40	11	—	—	—
<b>1</b> , Orbach & direct & QT <sup>b</sup>	48.2	2.0	2	$4 \times 10^4$	4 (fixed)
<b>2</b> , Orbach <sup>c</sup> at 0.09 T	38	4	—	—	—
<b>2</b> , Orbach <sup>c</sup> at 0.125 T	36	8	—	—	—
<b>2</b> , Orbach & direct & QT <sup>d</sup>	41	2.2	1.3	$4 \times 10^4$	4 (fixed)

<sup>a</sup> For data in the range 3.5–4.7 K. <sup>b</sup> At 0.06 T and 0.08 T. <sup>c</sup> For data in the range 3.3–4.1 K. <sup>d</sup> At 0.09 T and 0.125 T.

topography of both samples was investigated by AFM (Fig. 5(b, c) and Fig. S7, S14, ESI†), revealing that drop-cast depositions led to the formation of crystals a few micrometers high, while thermal sublimation resulted in islands with heights up to 150 nm for **1** (Fig. 5c), and 50 nm for **2** (ESI† Fig. S13). Raman spectroscopy and XPS confirmed that the chemical identity of the molecules was preserved upon the deposition by both drop-cast and thermal sublimation, a detailed comparison of XPS and Raman spectroscopy on the deposited samples with a bulk reference is found in the ESI† Sections S3 and S4. Raman spectra revealed a consistent shift of graphene's 2D peak ( $\sim 2690 \text{ cm}^{-1}$ ) towards lower energy values after the deposition of both compounds (Fig. 5d and ESI† Fig. S8, S15), which, considering that graphene was initially p-doped due to the contact with impurities under ambient conditions, suggests n-doping of graphene arising from electron transfer from the compounds.<sup>108,109</sup> n-Doping was further confirmed in transport measurements on samples deposited on graphene field-effect transistors (GFETs). To assess the charge transfer characteristics, **1** and **2** were drop-cast onto GFETs, following the procedure in the ESI† Section S8. The conductance through the devices was monitored as the gate voltage was varied from zero to 100 V, as shown in Fig. 5e and Fig. S39 (ESI†). As fabricated, the charge neutrality point (conductivity minimum) of the devices was approximately 95 V. With **2** deposited, the charge neutrality point shifted by  $-23$  V, indicating significant electron transfer to the graphene. Charge transfer was less apparent in devices coated with **1** (ESI† Fig. S39). The charge transfer effect may be much weaker with **1**, or a lower coverage of the devices may have muted the effect.

### 3.4 Theoretical calculations of molecular deposition and their magnetic properties

To simulate the molecular adsorption on graphene, we followed the procedure described in Section 2.2. For each molecular complex, we considered four different molecule orientations relative to the graphene substrate, based on the





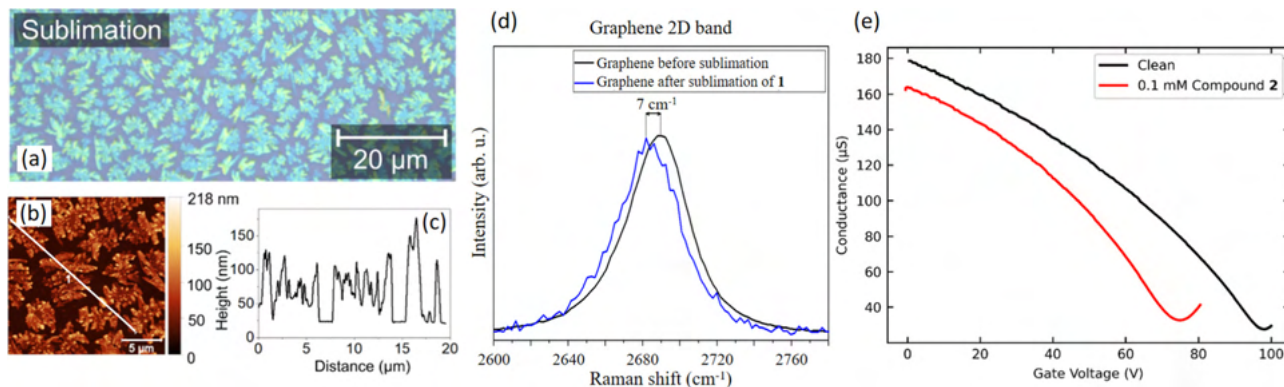


Fig. 5 (a) Optical image of deposited compound **1** (in green) on CVD graphene (dark blue) by thermal sublimation. (b) AFM image of deposited compound **1** on CVD graphene by sublimation. (c) The height profile along the white line indicated in the AFM image. (d) Raman spectra of the 2D band of graphene before and after sublimation of compound **1**. The wavelength of the laser source was 532 nm. (e) Gate-dependent conductivity through GFETs before and after deposition of compound **2** by drop-casting.

possible enhancement of hydrogen–carbon and carbon–carbon interactions between the molecule and substrate, as shown in Fig. 6a–d and f–i. Then, the molecules in each configuration were placed on top of the substrate, such that the ground state energy of the whole system was calculated, but without performing ionic relaxation. By varying the relative distance between the molecule and substrate, we generated the energy profiles in Fig. 6e and j for each configuration. The presence of energy minima in the profiles confirms that there is an attractive interaction between the molecule and substrate, which allows estimating the equilibrium distance of each system. We performed a third-degree polynomial fit to each curve to estimate the equilibrium distances,  $d_{eq}$ , and the results are found in Table 2. The distance between molecule and substrate was defined as the distance between the closest H atom to the graphene plane. We found that the equilibrium distances are in the range 2.50–2.72 Å for **1**, and 2.24–2.65 Å for **2**.

To determine the binding energies and equilibrium geometries of the molecules on graphene, we positioned the molecule in each configuration at the equilibrium distance and performed ionic relaxation of all ions (molecule and substrate) by plane-wave DFT. After obtaining the relaxed structure, we took the resulting molecule and substrate separately and computed a DFT self-consistent cycle for each of them to obtain the total energy of the individual systems. In this procedure, the binding energies were computed as

$$E_{bin} = E_{mol+subs} - E_{mol} - E_{subs}, \quad (7)$$

where  $E_{mol+subs}$ ,  $E_{mol}$ , and  $E_{subs}$  are the total energies of the molecule + substrate, isolated molecule, and isolated substrate, respectively. Table 2 shows the binding energies and changes in the relative distances between the Co center and its nearest neighbors. We found that both compounds have comparable equilibrium distances and binding energies, with **Conf. 4**

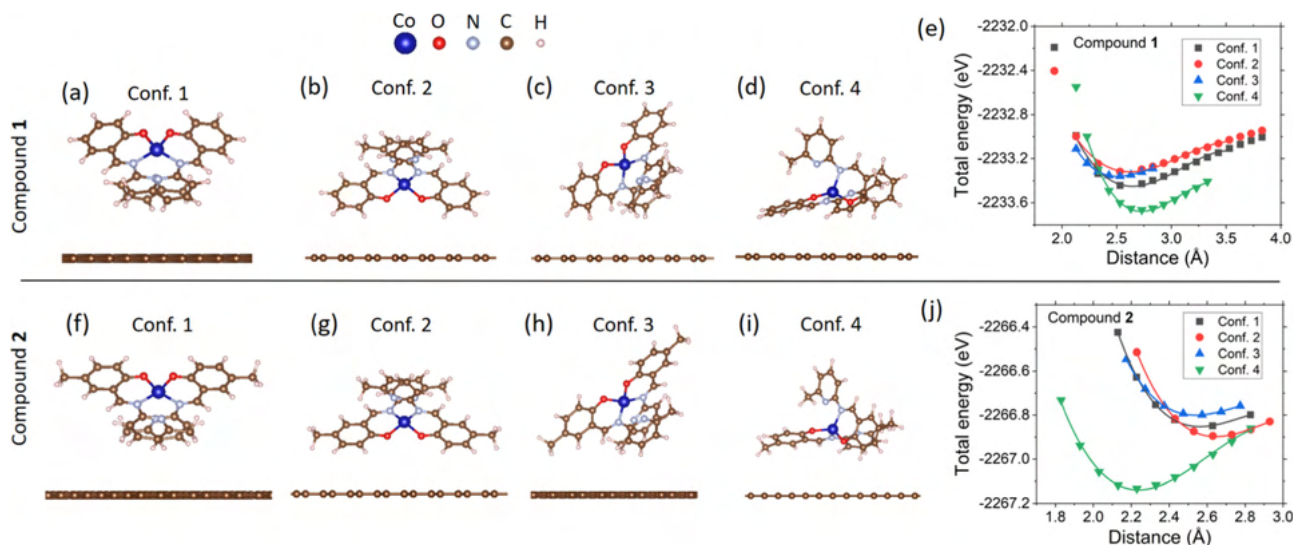
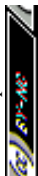


Fig. 6 Model systems used for plane-wave DFT calculations. (a)–(d) Configurations **1** to **4** of compound **1** with different orientations relative to the substrate. (e) Energy profile of compound **1** on graphene in all configurations, as a function of the distance to the graphene plane. The distance is defined as the distance between the closest hydrogen atom of the molecule to the substrate. Continuous lines represent fittings to a third-degree polynomial. (f)–(i) Configurations **1** to **4** of compound **2**. (j) Energy profile of compound **2** on graphene in all configurations.





**Table 2** Equilibrium distances ( $d_{\text{eq}}$ ) of the molecules on graphene in each configuration as determined from the energy profiles of Fig. 6e and j, binding energies ( $E_{\text{bin}}$ ), distances between the Co center and its neighbors ( $d_{\text{Co1-X}}$ ), HOMO–LUMO gap ( $\Delta E_{\text{HOMO-LUMO}}$ ), electron transfer from molecule to substrate ( $\Delta q$ , in units of number of electrons), and total magnetization of each configuration of molecule on the surface ( $\mu$ ), as calculated by plane-wave DFT

System	$d_{\text{eq}}$ (Å)	$E_{\text{bin}}$ (eV)	$d_{\text{Co1-N1}}$ (Å)	$d_{\text{Co1-N2}}$ (Å)	$d_{\text{Co1-O1}}$ (Å)	$\Delta E_{\text{HOMO-LUMO}}$ (eV)	$\Delta q$ ( $e^-$ )	$\mu$ ( $\mu_{\text{B}}$ )
1 XRD (exp.)	—	—	1.991	2.691	1.953	0.64	—	3.000
1 Isolated, DFT relax.	—	—	1.954	2.860	1.918	0.85	—	3.000
1 Conf. 1	2.61	−0.83	1.955	2.856	1.917	0.76	0.065	3.078
1 Conf. 2	2.59	−0.70	1.957	2.858	1.917	0.73	0.003	3.006
1 Conf. 3	2.50	−0.73	1.955	2.816	1.917	0.76	0.056	3.075
1 Conf. 4	2.72	−1.08	1.955	2.811	1.919	0.74	0.016	3.020
2 XRD (exp.)	—	—	1.992	2.695	1.961	0.65	—	3.000
2 Isolated, DFT relax.	—	—	1.954	2.776	1.918	0.84	—	3.000
2 Conf. 1	2.56	−0.90	1.955	2.768	1.921	0.75	0.084	3.099
2 Conf. 2	2.65	−0.92	1.955	2.782	1.917	0.74	0.014	3.020
2 Conf. 3	2.54	−0.80	1.954	2.772	1.917	0.76	0.078	3.095
2 Conf. 4	2.24	−1.15	1.957	2.768	1.921	0.73	0.033	3.045

having the highest binding energy (in absolute value) in both complexes. Nevertheless, we cannot conclude at this point that this is the preferred molecular orientation on graphene since the binding energies of the other configurations are comparable in value. The relatively low binding energy ( $|E_{\text{bin}}| \approx 1.2$  eV per molecule) of the studied configurations suggests that the binding mechanism is through van der Waals forces and could explain the tendency of the molecules to form clusters on graphene due to the low interaction with the substrate, as observed by optical microscopy and AFM images (Fig. 5a, b and ESI† Fig. S7, S14). With the aim of comparing the deposited molecules with the bulk structure (the initial experimental configuration found by XRD) and the isolated molecule relaxed by plane-wave DFT without substrate, in Table 2 we include the

distances from the Co center to the immediate coordination atoms ( $d_{\text{Co1-N1}}$ ,  $d_{\text{Co1-O1}}$ ), and the pyridyl nitrogen ( $d_{\text{Co1-N2}}$ ). The highest deviation in the relative distances was found between the initial XRD structure and the isolated, DFT-relaxed molecule; the distances from the Co center to the coordination ions N1 and O1 were slightly reduced in both compounds, while the distance to the pyridyl nitrogen N2 increased by 0.169 Å and 0.081 Å for **1** and **2**, respectively. These changes are expected since the effects of neighboring molecules in the crystal structure are present in the bulk compound, and subjecting the molecule to external forces that are absent in the isolated configuration. After adsorption, DFT calculations show only small deviations from the isolated configuration, consistent with the weak van der Waals interaction between molecule and substrate.

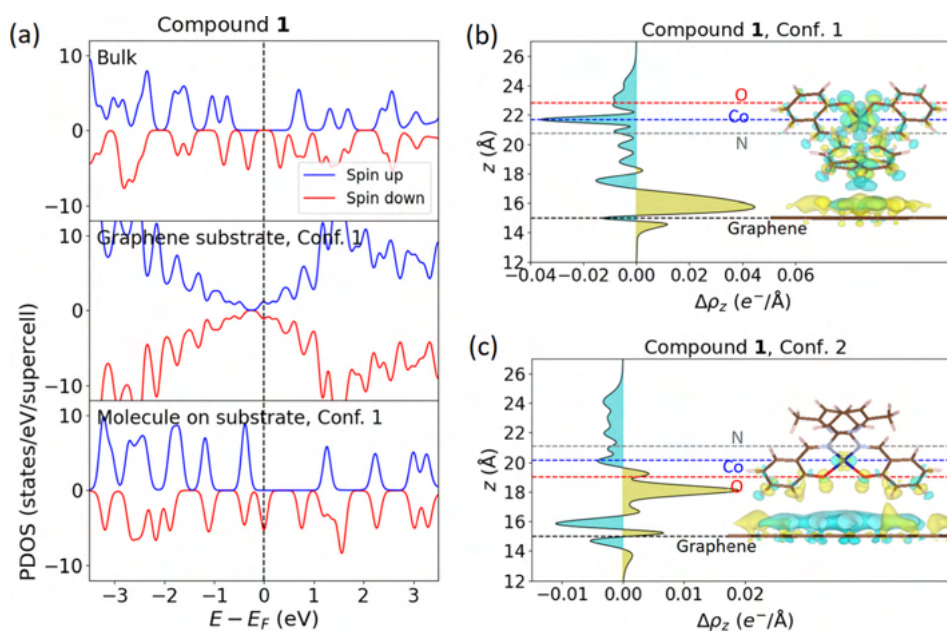
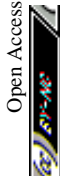


**Fig. 7** (a) Comparison between the DOS of **1** in the bulk (XRD) structure, the PDOS of graphene in **Conf. 1**, and the PDOS of compound **1** on graphene in **Conf. 1**. The dashed vertical line indicates the Fermi energy. (b) and (c) Planar average of the charge density difference of compound **1** in **Conf. 1** and **2**, respectively. Superimposed on them are isosurface plots of the charge density difference,  $\Delta\rho$ . The isosurface level is  $1.01 \times 10^{-3} e^- \text{Å}^{-3}$ ; yellow and cyan colors represent the accumulation and depletion of electrons, respectively. Dashed lines indicate the location of graphene, Co atom, and coordination N and O atoms.



We now study the changes in the highest occupied and lowest unoccupied molecular orbitals (HOMO and LUMO, respectively) after deposition. In the bulk structure and isolated, DFT-relaxed molecules, the HOMO–LUMO gap ( $\Delta E_{\text{HOMO-LUMO}}$ ) was obtained from the total density of states (DOS), while in the molecule + substrate system, it was obtained from the partial density of states (PDOS), selecting only the molecule's electronic orbitals. Fig. 7a shows a comparison between the DOS of **1** in the bulk structure and the PDOS of graphene and molecule in **Conf. 1** after deposition (ESI† Fig. S43 and S43 show the PDOS of all systems). The results of the HOMO–LUMO gap, shown in Table 2, indicate a noticeable change in the quantity in all considered systems. In particular, graphene affects the HOMO–LUMO gap of the deposited molecules, decreasing it by around 0.1 eV, considering that the initial system for plane-wave DFT calculations of molecular adsorption was the isolated, DFT relaxed molecules, which have a HOMO–LUMO gap of 0.85 eV and 0.84 eV for **1** and **2**, respectively. In Fig. 7a, we observe a depopulation of the molecules HOMO after deposition, leading to a population of graphene conduction bands and consequently, to n-doping of graphene. This is consistent in all studied configurations of both molecular complexes, as shown in the ESI† Fig. S43 and S44. Transport measurements (Fig. 5e and Fig. S39, ESI†) and Raman spectroscopy (Fig. 5d and ESI† Fig. S8, S15) confirmed electron transfer from the molecule to graphene, leading to n-doping of graphene.

To obtain a better understanding of the electron transfer behavior between the molecule and substrate, we performed Bader charge analysis<sup>81</sup> as implemented by Henkelman *et al.*<sup>110,111</sup> The results, shown in Table 2 for each configuration, indicate a consistent electron transfer from molecule to substrate, in agreement with the results from DOS analysis. Although such electron transfer is below 0.1 e<sup>−</sup>, it is observed that it has a direct effect in increasing the total magnetization of the system, compared to a value of 3.00  $\mu_{\text{B}}$  for isolated molecules, corresponding to three unpaired electrons of Co(II). The increase in magnetization is consistent with electron transfer from the molecule's HOMO to graphene, which has spin-down polarization as observed in Fig. 7a, and consequently, increasing the spin polarization of the molecules charge density (difference between spin up and spin down charge densities).

To analyze further the charge transfer behavior, we computed the charge density difference, defined as

$$\Delta\rho = \rho_{\text{mol+subs}} - \rho_{\text{mol}} - \rho_{\text{subs}}, \quad (8)$$

where  $\rho_{\text{mol+subs}}$ ,  $\rho_{\text{mol}}$ , and  $\rho_{\text{subs}}$  are the charge densities of the molecule + substrate, isolated molecule, and isolated substrate, respectively. Fig. 7b and c show the isosurface plots and planar average of the charge density difference ( $\Delta\rho_z$ , with  $\Delta\rho$  averaged over the *xy* plane) of compound **1** in **Confs. 1 and 2** (plots of all configurations are found in the ESI† Fig. S41 and S42). For both compounds, **Confs. 1 and 3** show a clear charge accumulation near graphene, while in **Confs. 2 and 4** regions of charge accumulation appear in the molecule. These charge accumulation regions in the molecule are near the locations of the O and N ions, which in **Confs. 2 and 4** are closer to graphene than in

**Table 3** Spin Hamiltonian parameters found by CASSCF-NEVPT2 for each system, compared to the experimental results obtained by HF-ESR and DC magnetometry

System	<i>D</i> (cm <sup>−1</sup> )	<i>E/D</i>	<i>g<sub>x</sub></i>	<i>g<sub>y</sub></i>	<i>g<sub>z</sub></i>	<i>g<sub>iso</sub></i>
<b>1</b> XRD (exp.) <sup>a</sup>	−25.3	0.084	2.185	2.126	2.462	2.258
<b>1</b> Isolated <sup>b</sup>	−18.5	0.009	2.139	2.141	2.368	2.216
<b>1 Conf. 1</b> <sup>b</sup>	−18.5	0.011	2.139	2.142	2.368	2.216
<b>1 Conf. 2</b> <sup>b</sup>	−18.6	0.014	2.139	2.143	2.370	2.217
<b>1 Conf. 3</b> <sup>b</sup>	−18.4	0.010	2.139	2.141	2.367	2.216
<b>1 Conf. 4</b> <sup>b</sup>	−18.4	0.016	2.139	2.144	2.368	2.217
<b>1</b> HF-ESR	<−20	0.122	2.20	2.15	2.40	2.25
<b>1</b> DC magn	−15.3	0.012	—	—	—	2.272
<b>2</b> XRD (exp.) <sup>a</sup>	−28.3	0.107	2.201	2.119	2.501	2.274
<b>2</b> Isolated <sup>b</sup>	−18.2	0.040	2.129	2.152	2.364	2.215
<b>2 Conf. 1</b> <sup>b</sup>	−18.9	0.030	2.131	2.151	2.373	2.218
<b>2 Conf. 2</b> <sup>b</sup>	−18.5	0.033	2.131	2.151	2.368	2.217
<b>2 Conf. 3</b> <sup>b</sup>	−18.4	0.038	2.129	2.152	2.367	2.216
<b>2 Conf. 4</b> <sup>b</sup>	−19.2	0.034	2.131	2.152	2.378	2.220
<b>2</b> DC magn.	−17.5	0.044	—	—	—	2.213

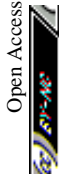
<sup>a</sup> CASSCF-NEVPT2 def2-TZVP method in ORCA 5.0. <sup>b</sup> CASSCF-NEVPT2 def2-TZVP method in ORCA 4.2.1.

**Confs. 1 and 3**, and act as electron sinks due to their high electronegativity. For this reason, **Confs. 2 and 4** have a lower charge transfer, as evidenced in Table 2. Transport measurements revealed higher electron transfer from the deposited compound **2** than from compound **1** to graphene, which might indicate that orientations with low electron transfer are preferred in compound **1**. Notably, higher or lower charge transfer is not correlated with higher or lower binding energy between a molecule and substrate.

We focus now on the ZFS terms and *g*-factors of the deposited structures, as calculated by CASSCF-NEVPT2 in ORCA 4.2.1. The results are summarized in Table 2. In all systems, we obtained a negative *D*, in agreement with DC magnetometry and HF-ESR measurements. Additionally, the calculations suggest an anisotropy of the *g*-factors before and after adsorption. Overall, a discrepancy between the calculated parameters for the bulk structures and the deposited configurations is found, which is more evident in the ZFS terms *D* and *E*. This result is a direct consequence of the geometrical changes in the molecule in the gas phase after DFT relaxation. Furthermore, the parameters of the isolated and adsorbed molecules are practically the same in both compounds due to the negligible geometrical change after deposition.

## 4 Conclusions and outlook

We have presented a theoretical and experimental study on the structure, stability, magnetic properties, and deposition properties on graphene of compounds **1** and **2**. DFT calculations and analysis of the topology of the electron density by QT-AIM confirmed that the Co center and the pyridine nitrogens N2 interact through attractive non-covalent interactions, thus exhibiting a semi-coordination character. We claim that such interaction is the source of the stability of the complexes under ambient conditions and after deposition on graphene, as confirmed by XPS and Raman spectroscopy. DC magnetometry showed that the compounds



present an axial magnetic anisotropy, with an axial ZFS term of  $D = -15.3 \text{ cm}^{-1}$  and  $-17.5 \text{ cm}^{-1}$  for **1** and **2**, respectively, while HF-ESR set the bound  $|D| > 20 \text{ cm}^{-1}$  on compound **1**. Both experimental methods confirm a weak intermolecular antiferromagnetic exchange interaction, in agreement with BS-DFT predictions. Dynamic magnetic investigations confirmed that the compounds are field-induced SIMs with maximum relaxation times of 2.3 ms (at 0.06 T, 1.9 K) and 1.5 ms (at 0.09 T, 1.9 K) for **1** and **2**, respectively. Theoretical modeling of the compounds on graphene by DFT shows an attractive interaction between them with a relatively small binding energy, with the highest one (in absolute value) corresponding to  $-1.15 \text{ eV}$  per molecule for compound **2** in **Conf. 4**. DOS and charge transfer analysis revealed an electron transfer from the molecule's HOMO to graphene, confirmed by transport measurements on GFETs and Raman spectroscopy, which increases the molecules' magnetic moment due to an increase in their spin density. This suggests the possibility of tuning the molecule's magnetic moment by electrostatic gating of the graphene substrate, which could be done by depositing them directly onto graphene quantum dot bolometers,<sup>54,55</sup> taking advantage of their high sensitivity that enables an *in situ* spectroscopic investigation.

## Author contributions

Writing original draft preparation, plane-wave DFT, CASSCF-NEVPT2 calculations, J. N. G.; writing original draft preparation, XPS, depositions, J. H.; AFM, Raman, and depositions, Š. V.; chemical synthesis and analytical characterization of ligand and complex, O. F. F.; DC magnetometry experiments and preliminary analysis, L. H.; deposition on GFETs, transport measurements, D. H.; GFETs fabrication, S. d. S.; BS-DFT, CASSCF-NEVPT2 calculations, R. H.; graphene sample preparation, M. B.; AC magnetometry analysis, writing original draft preparation, I. Š.; HF-ESR experiments and analysis, V. T. S.; transport measurements, GFETs fabrication, supervision, P. B.; XRD analysis, DFT-topology and ELF calculations, DC magnetometry analysis, writing review and editing, I. N.; supervision, P. N. All authors have agreed to the published version of the manuscript.

## Conflicts of interest

There are no conflicts to declare.

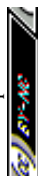
## Acknowledgements

We gratefully acknowledge the projects and grant agencies that supported this work. O. F. F., R. H., and I. N. acknowledge support from the Grant Agency of the Czech Republic (GAČR 23-07175S); J. N. G. acknowledges the Grant Agency of the Czech Republic (GAČR 23-05578S), a student grant of the Brno University of Technology (CEITEC-J-21-7508), and the Brno PhD Talent Scholarship – Funded by the Brno City Municipality; J. N. G., J. H., and L. H. acknowledge the MEYS CR INTER-

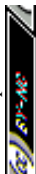
EXCELLENCE Programme (grant LTAUSA19060); O. F. F. acknowledges Palacky University's student grant DSGC-2021-0032 financed from the funds of the Operational Program Research, Development and Education under the project "Improving schematics of Doctoral student grant competition and their pilot implementation", Reg. No. CZ.02.2.69/0.0/0.0/19\_073/0016713; M. B. acknowledges funding from the ESF under the project CZ.02.2.69/0.0/0.0/20\_079/0017436; I. Š. acknowledges the grants from Slovak grant agencies DS-FR-22-0010, APVV-22-0172, APVV-19-0087, VEGA 1/0029/22; V. T. S. acknowledges funding from the EXPRO grant of the Grant Agency of the Czech Republic (GAČR 21-20716X); P. N. acknowledges the ERC Starting Grant (No. 714850) under the European Unions Horizon 2020 Research and Innovation Program. J. N. G., J. H., Š. V., and L. H. gratefully acknowledge the CzechNanoLab Research Infrastructure supported by MEYS CR (LM2018110). This article was written thanks to generous support through the Operational Program Integrated Infrastructure for the project: "Strategic research in the field of SMART monitoring, treatment and preventive protection against coronavirus (SARS-CoV-2)", Project No. 313011ASS8, co-financed by the European Regional Development Fund.

## Notes and references

- 1 D. Tanaka, N. Aketa, H. Tanaka, S. Horike, M. Fukumori, T. Tamaki, T. Inose, T. Akai, H. Toyama, O. Sakata, H. Tajiri and T. Ogawa, *Dalton Trans.*, 2019, **48**, 7074–7079.
- 2 A. Ardavan, O. Rival, J. J. Morton, S. J. Blundell, A. M. Tyryshkin, G. A. Timco and R. E. Winpenny, *Phys. Rev. Lett.*, 2007, **98**, 057201.
- 3 M. Urdampilleta, S. Klyatskaya, J. P. Cleuziou, M. Ruben and W. Wernsdorfer, *Nat. Mater.*, 2011, **10**, 502–506.
- 4 E. Coronado, *Nat. Rev. Mat.*, 2020, **5**, 87–104.
- 5 J. Dugay, M. Aarts, M. Gimenez-Marqués, T. Kozlova, H. W. Zandbergen, E. Coronado and H. S. Van Der Zant, *Nano Lett.*, 2017, **17**, 186–193.
- 6 T. S. Rahman, R. S. Berkley, Z. Hooshmand, T. Jiang, D. Le and A. F. Hebard, *J. Phys. Chem. C*, 2020, **124**, 28186–28200.
- 7 R. J. Holmberg and M. Murugesu, *J. Mater. Chem. C*, 2015, **3**, 11986–11998.
- 8 P. C. Bunting, M. Atanasov, E. Damgaard-Møller, M. Perfetti, I. Crassee, M. Orlita, J. Overgaard, J. Van Slageren, F. Neese and J. R. Long, *Science*, 2018, **362**, eaat7319.
- 9 F. Yang, Q. Zhou, Y. Zhang, G. Zeng, G. Li, Z. Shi, B. Wang and S. Feng, *Chem. Commun.*, 2013, **49**, 5289–5291.
- 10 T. Wu, Y. Q. Zhai, Y. F. Deng, W. P. Chen, T. Zhang and Y. Z. Zheng, *Dalton Trans.*, 2019, **48**, 15419–15426.
- 11 M. Böhme, S. Ziegenbalg, A. Aliabadi, A. Schnegg, H. Görls and W. Plass, *Dalton Trans.*, 2018, **47**, 10861–10873.
- 12 S. Vaidya, P. Shukla, S. Tripathi, E. Rivière, T. Mallah, G. Rajaraman and M. Shanmugam, *Inorg. Chem.*, 2018, **57**, 3371–3386.
- 13 Y. Q. Zhai, Y. F. Deng and Y. Z. Zheng, *Dalton Trans.*, 2018, **47**, 8874–8878.



- 14 T. Jurca, A. Farghal, P. H. Lin, I. Korobkov, M. Murugesu and D. S. Richeson, *J. Am. Chem. Soc.*, 2011, **133**, 15814–15817.
- 15 I. Nemeč, H. Liu, R. Herchel, X. Zhang and Z. Trávníček, *Synth. Met.*, 2016, **215**, 158–163.
- 16 R. Ruamps, L. J. Batchelor, R. Guillot, G. Zakhia, A. L. Barra, W. Wernsdorfer, N. Guihéry and T. Mallah, *Chem. Sci.*, 2014, **5**, 3418–3424.
- 17 D. Schweinfurth, J. Krzystek, M. Atanasov, J. Klein, S. Hohloch, J. Telser, S. Demeshko, F. Meyer, F. Neese and B. Sarkar, *Inorg. Chem.*, 2017, **56**, 5253–5265.
- 18 D. Schweinfurth, M. G. Sommer, M. Atanasov, S. Demeshko, S. Hohloch, F. Meyer, F. Neese and B. Sarkar, *J. Am. Chem. Soc.*, 2015, **137**, 1993–2005.
- 19 F. El-Khatib, B. Cahier, F. Shao, M. López-Jordà, R. Guillot, E. Rivière, H. Hafez, Z. Saad, J. J. Girerd, N. Guihéry and T. Mallah, *Inorg. Chem.*, 2017, **56**, 4601–4608.
- 20 J. Juráková, J. Dubnická Midlíková, J. Hrubý, A. Kliuikov, V. T. Santana, J. Pavlik, J. Moncol, E. Čižmár, M. Orlita, I. Mohelský, P. Neugebauer, D. Gentili, M. Cavallini and I. Šalitroš, *Inorg. Chem. Front.*, 2022, **9**, 1179–1194.
- 21 V. V. Novikov, A. A. Pavlov, Y. V. Nelyubina, M. E. Boulon, O. A. Varzatskii, Y. Z. Voloshin and R. E. Winpenny, *J. Am. Chem. Soc.*, 2015, **137**, 9792–9795.
- 22 A. A. Pavlov, Y. V. Nelyubina, S. V. Kats, L. V. Penkova, N. N. Efimov, A. O. Dmitrienko, A. V. Vologzhanina, A. S. Belov, Y. Z. Voloshin and V. V. Novikov, *J. Phys. Chem. Lett.*, 2016, **7**, 4111–4116.
- 23 S. Gomez-Coca, E. Cremades, N. Aliaga-Alcalde and E. Ruiz, *J. Am. Chem. Soc.*, 2013, **135**, 7010–7018.
- 24 T. J. Ozumerzifon, I. Bhowmick, W. C. Spaller, A. K. Rappé and M. P. Shores, *Chem. Commun.*, 2017, **53**, 4211–4214.
- 25 B. Yao, Y. F. Deng, T. Li, J. Xiong, B. W. Wang, Z. Zheng and Y. Z. Zhang, *Inorg. Chem.*, 2018, **57**, 14047–14051.
- 26 Y. Y. Zhu, C. Cui, Y. Q. Zhang, J. H. Jia, X. Guo, C. Gao, K. Qian, S. D. Jiang, B. W. Wang, Z. M. Wang and S. Gao, *Chem. Sci.*, 2013, **4**, 1802–1806.
- 27 B. Yao, M. K. Singh, Y. F. Deng, Y. N. Wang, K. R. Dunbar and Y. Z. Zhang, *Inorg. Chem.*, 2020, **59**, 8505–8513.
- 28 J. M. Frost, K. L. Harriman and M. Murugesu, *Chem. Sci.*, 2016, **7**, 2470–2491.
- 29 J. Juráková and I. Šalitroš, *Monatsh. Chem.*, 2022, **153**, 1001–1036.
- 30 J. M. Zadrozny and J. R. Long, *J. Am. Chem. Soc.*, 2011, **133**, 20732–20734.
- 31 E. A. Sutura, J. Nehr Korn, J. M. Zadrozny, J. Liu, M. Atanasov, T. Weyhermüller, D. Maganas, S. Hill, A. Schnegg, E. Bill, J. R. Long and F. Neese, *Inorg. Chem.*, 2017, **56**, 3102–3118.
- 32 J. M. Zadrozny, J. Telser and J. R. Long, *Polyhedron*, 2013, **64**, 209–217.
- 33 S. Vaidya, S. Tewary, S. K. Singh, S. K. Langley, K. S. Murray, Y. Lan, W. Wernsdorfer, G. Rajaraman and M. Shanmugam, *Inorg. Chem.*, 2016, **55**, 9564–9578.
- 34 M. S. Fataftah, J. M. Zadrozny, D. M. Rogers and D. E. Freedman, *Inorg. Chem.*, 2014, **53**, 10716–10721.
- 35 Y. Rechkemmer, F. D. Breitgoff, M. Van Der Meer, M. Atanasov, M. Hakl, M. Orlita, P. Neugebauer, F. Neese, B. Sarkar and J. Van Slageren, *Nat. Commun.*, 2016, **7**, 1–8.
- 36 S. Ziegenbalg, D. Hornig, H. Görls and W. Plass, *Inorg. Chem.*, 2016, **55**, 4047–4058.
- 37 X. N. Yao, M. W. Yang, J. Xiong, J. J. Liu, C. Gao, Y. S. Meng, S. D. Jiang, B. W. Wang and S. Gao, *Inorg. Chem. Front.*, 2017, **4**, 701–705.
- 38 J. Hrubý, Š. Vavrečková, L. Masaryk, A. Sojka, J. Navarro-Giraldo, M. Bartoš, R. Herchel, J. Moncol, I. Nemeč and P. Neugebauer, *Molecules*, 2020, **25**, 5021.
- 39 J. Hrubý, D. Dvořák, L. Squillantini, M. Mannini, J. Van Slageren, R. Herchel, I. Nemeč and P. Neugebauer, *Dalton Trans.*, 2020, **49**, 11697–11707.
- 40 I. Nemeč, O. F. Fellner, L. Havlíček and R. Herchel, *Acta Crystallogr., Sect. A: Found. Adv.*, 2021, **77**, C344.
- 41 L. Xu, Y. V. Mironov, X. Qi and S. J. Kim, *J. Struct. Chem.*, 2006, **47**, 998–1001.
- 42 C. R. Groom, I. J. Bruno, M. P. Lightfoot and S. C. Ward, *Acta Crystallogr. B*, 2016, **72**, 171–179.
- 43 Z. M. Efimenko, A. S. Novikov, D. M. Ivanov, A. V. Piskunov, A. A. Vereshchagin, O. V. Levin, N. A. Bokach and V. Y. Kukushkin, *Inorg. Chem.*, 2020, **59**, 2316–2327.
- 44 I. V. Ananyev, N. A. Bokach and V. Y. Kukushkin, *Acta Crystallogr., Sect. B: Struct. Sci., Cryst. Eng. Mater.*, 2020, **76**, 436–449.
- 45 L. J. Bourhis, O. V. Dolomanov, R. J. Gildea, J. A. Howard and H. Puschmann, *Acta Crystallogr., Sect. A: Found. Adv.*, 2015, **71**, 59–75.
- 46 G. M. Sheldrick, *Acta Crystallogr., Sect. C: Struct. Chem.*, 2015, **71**, 3–8.
- 47 O. V. Dolomanov, L. J. Bourhis, R. J. Gildea, J. A. Howard and H. Puschmann, *J. Appl. Crystallogr.*, 2009, **42**, 339–341.
- 48 C. F. MacRae, I. Sovago, S. J. Cottrell, P. T. Galek, P. McCabe, E. Pidcock, M. Platings, G. P. Shields, J. S. Stevens, M. Towler and P. A. Wood, *J. Appl. Crystallogr.*, 2020, **53**, 226–235.
- 49 A. K. Geim and K. S. Novoselov, *Nat. Mater.*, 2007, **6**, 183–191.
- 50 X. Du, I. Skachko, E. Y. Andrei and A. Barker, *Nat. Nanotechnol.*, 2008, **3**, 491–495.
- 51 C. Lee, X. Wei, J. W. Kysar and J. Hone, *Science*, 2008, **321**, 385–388.
- 52 J. H. Seol, I. Jo, A. L. Moore, L. Lindsay, Z. H. Aitken, M. T. Pettes, X. Li, Z. Yao, R. Huang, D. Broido, N. Mingo, R. S. Ruoff and L. Shi, *Science*, 2010, **328**, 213–216.
- 53 P. Neugebauer, M. Orlita, C. Faugeras, A. L. Barra and M. Potemski, *Phys. Rev. Lett.*, 2009, **103**, 136403.
- 54 A. El Fatimy, R. L. Myers-Ward, A. K. Boyd, K. M. Daniels, D. K. Gaskill and P. Barbara, *Nat. Nanotechnol.*, 2016, **11**, 335–338.
- 55 L. S. Marie, A. El Fatimy, J. Hrubý, I. Nemeč, J. Hunt, R. Myers-Ward, D. K. Gaskill, M. Kruskopf, Y. Yang, R. Elmquist, R. Marx, J. van Slageren, P. Neugebauer and P. Barbara, *J. Phys. Mater.*, 2020, **3**, 014013.

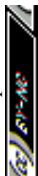




- 56 B. Zhan, C. Li, J. Yang, G. Jenkins, W. Huang and X. Dong, *Small*, 2014, **10**, 4042–4065.
- 57 F. Neese, *Wiley Interdiscip. Rev. Comput. Mol. Sci.*, 2018, **8**, e1327.
- 58 F. Neese, *Wiley Interdiscip. Rev. Comput. Mol. Sci.*, 2022, **12**, e1606.
- 59 P. Å. Malmqvist and B. O. Roos, *Chem. Phys. Lett.*, 1989, **155**, 189–194.
- 60 C. Angeli, R. Cimiraglia, S. Evangelisti, T. Leininger and J. P. Malrieu, *J. Chem. Phys.*, 2001, **114**, 10252.
- 61 C. Angeli, R. Cimiraglia and J. P. Malrieu, *Chem. Phys. Lett.*, 2001, **350**, 297–305.
- 62 F. Kleemiss, O. V. Dolomanov, M. Bodensteiner, N. Peyrerimhoff, L. Midgley, L. J. Bourhis, A. Genoni, L. A. Malaspina, D. Jayatilaka, J. L. Spencer, F. White, B. Grundkötter-Stock, S. Steinhauer, D. Lentz, H. Puschmann and S. Grabowsky, *Chem. Sci.*, 2021, **12**, 1675–1692.
- 63 F. Weigend and R. Ahlrichs, *Phys. Chem. Chem. Phys.*, 2005, **7**, 3297–3305.
- 64 F. Weigend, *Phys. Chem. Chem. Phys.*, 2006, **8**, 1057–1065.
- 65 A. Hellweg, C. Hättig, S. Höfener and W. Klopper, *Theor. Chem. Acc.*, 2007, **117**, 587–597.
- 66 R. Izsák and F. Neese, *J. Chem. Phys.*, 2011, **135**, 144105.
- 67 F. Neese, F. Wennmohs, A. Hansen and U. Becker, *Chem. Phys.*, 2009, **356**, 98–109.
- 68 *Molecular Electronic Structures of Transition Metal Complexes II*, ed. D. M. P. Mingos, P. Day and J. P. Dahl, Springer Berlin Heidelberg, Berlin, Heidelberg, 2012, vol. 143.
- 69 A. D. Becke, *Phys. Rev. A: At., Mol., Opt. Phys.*, 1988, **38**, 3098–3100.
- 70 C. Lee, W. Yang and R. G. Parr, *Phys. Rev. B: Condens. Matter Mater. Phys.*, 1988, **37**, 785–789.
- 71 P. J. Stephens, F. J. Devlin, C. F. Chabalowski and M. J. Frisch, *J. Phys. Chem.*, 1994, **98**, 11623–11627.
- 72 C. Adamo and V. Barone, *J. Chem. Phys.*, 1999, **110**, 6158–6170.
- 73 S. M. Hossain, S. Kamilya, S. Ghosh, R. Herchel, M. A. Kiskin, S. Mehta and A. Mondal, *Cryst. Growth Des.*, 2023, **11**, 42.
- 74 L. Havlíček, R. Herchel, I. Nemeč and P. Neugebauer, *Polyhedron*, 2022, **223**, 115962.
- 75 A. N. Gusev, I. Nemeč, R. Herchel, Y. I. Baluda, M. A. Kryukova, N. N. Efimov, M. A. Kiskin and W. Linert, *Polyhedron*, 2021, **196**, 115017.
- 76 A. Bhanja, L. Smythe, R. Herchel, I. Nemeč, M. Murrie and D. Ray, *Dalton Trans.*, 2021, **50**, 5023–5035.
- 77 B. Rybničková, J. Kuchár, P. Antal and R. Herchel, *Inorg. Chim. Acta*, 2020, **509**, 119689.
- 78 I. Šalitroš, R. Herchel, O. Fuhr, R. González-Prieto and M. Ruben, *Inorg. Chem.*, 2019, **58**, 4310–4319.
- 79 O. A. Vydrov and T. Van Voorhis, *J. Chem. Phys.*, 2010, **133**, 244103.
- 80 W. Hujo and S. Grimme, *J. Chem. Theory Comput.*, 2011, **7**, 3866–3871.
- 81 R. F. W. Bader, *Atoms in Molecules: A Quantum Theory*, Oxford University Press, 1994.
- 82 T. Lu and F. Chen, *J. Mol. Graphics Modell.*, 2012, **38**, 314–323.
- 83 T. Lu and F. Chen, *J. Comput. Chem.*, 2012, **33**, 580–592.
- 84 G. Kresse and J. Hafner, *Phys. Rev. B: Condens. Matter Mater. Phys.*, 1993, **47**, 558–561.
- 85 G. Kresse and J. Furthmüller, *Computational Mater. Sci.*, 1996, **6**, 15–50.
- 86 G. Kresse and J. Furthmüller, *Phys. Rev. B: Condens. Matter Mater. Phys.*, 1996, **54**, 11169–11186.
- 87 G. Kresse and D. Joubert, *Phys. Rev. B: Condens. Matter Mater. Phys.*, 1999, **59**, 1758–1775.
- 88 P. E. Blöchl, *Phys. Rev. B: Condens. Matter Mater. Phys.*, 1994, **50**, 17953–17979.
- 89 J. P. Perdew, K. Burke and M. Ernzerhof, *Phys. Rev. Lett.*, 1996, **77**, 3865–3868.
- 90 J. P. Perdew, K. Burke and M. Ernzerhof, *Phys. Rev. Lett.*, 1997, **78**, 1396.
- 91 S. Grimme, J. Antony, S. Ehrlich and H. Krieg, *J. Chem. Phys.*, 2010, **132**, 154709.
- 92 S. Grimme, S. Ehrlich and L. Goerigk, *J. Comput. Chem.*, 2011, **32**, 1456–1465.
- 93 J. Neugebauer and M. Scheffler, *Phys. Rev. B: Condens. Matter Mater. Phys.*, 1992, **46**, 16067–16080.
- 94 G. Makov and M. C. Payne, *Phys. Rev. B: Condens. Matter Mater. Phys.*, 1995, **51**, 4014–4022.
- 95 H. J. Monkhorst and J. D. Pack, *Phys. Rev. B: Solid State*, 1976, **13**, 5188–5192.
- 96 V. Wang, N. Xu, J.-C. Liu, G. Tang and W.-T. Geng, *Comput. Phys. Commun.*, 2021, **267**, 108033.
- 97 K. Momma and F. Izumi, *J. Appl. Crystallogr.*, 2008, **41**, 653–658.
- 98 E. R. Johnson, S. Keinan, P. Mori-Sánchez, J. Contreras-García, A. J. Cohen and W. Yang, *J. Am. Chem. Soc.*, 2010, **132**, 6498–6506.
- 99 W. Humphrey, A. Dalke and K. Schulten, *J. Mol. Graphics*, 1996, **14**, 33–38.
- 100 A. D. Becke and K. E. Edgecombe, *J. Chem. Phys.*, 1990, **92**, 5397–5403.
- 101 T. Lu and F. W. Chen, *Acta Phys. Chim. Sin.*, 2011, **27**, 2786–2792.
- 102 Y. H. Chi, J. M. Shi, H. N. Li, W. Wei, E. Cottrill, N. Pan, H. Chen, Y. Liang, L. Yu, Y. Q. Zhang and C. Hou, *Dalton Trans.*, 2013, **42**, 15559–15569.
- 103 E. Ruiz, J. Cano, S. Alvarez and P. Alemany, *J. Comput. Chem.*, 1999, **20**, 1391–1400.
- 104 T. Soda, Y. Kitagawa, T. Onishi, Y. Takano, Y. Shigeta, H. Nagao, Y. Yoshioka and K. Yamaguchi, *Chem. Phys. Lett.*, 2000, **319**, 223–230.
- 105 S. Stoll and A. Schweiger, *J. Magn. Reson.*, 2006, **178**, 42–55.
- 106 E. Y. Misochko, A. V. Akimov, D. V. Korchagin, J. Nehr Korn, M. Ozerov, A. V. Pali, J. M. Clemente-Juan and S. M. Aldoshin, *Inorg. Chem.*, 2019, **58**, 16434–16444.
- 107 L. F. Chibotaru and L. Ungur, *J. Chem. Phys.*, 2012, **137**, 64112.





- 108 J. Yan, Y. Zhang, P. Kim and A. Pinczuk, *Phys. Rev. Lett.*, 2007, **98**, 166802.
- 109 A. C. Ferrari and D. M. Basko, *Nat. Nanotechnol.*, 2013, **8**, 235–246.
- 110 W. Tang, E. Sanville and G. Henkelman, *J. Phys.: Condens. Matter*, 2009, **21**, 084204.
- 111 G. Henkelman, A. Arnaldsson and H. Jónsson, *Comput. Mater. Sci.*, 2006, **36**, 354–360.



Article

# Spin Crossover in Three Mononuclear Iron (III) Schiff Base Complexes

Ivan Nemeč<sup>1,2,\*</sup>, Ingrid Svoboda<sup>3</sup> and Radovan Herchel<sup>1</sup>

<sup>1</sup> Department of Inorganic Chemistry, Faculty of Science, Palacký University, 17. listopadu 1192/12, 771 46 Olomouc, Czech Republic

<sup>2</sup> Central European Institute of Technology, CEITEC BUT, Technická 3058/10, 61600 Brno, Czech Republic

<sup>3</sup> Material sciences, Darmstadt University of Technology, D-64287 Darmstadt, Germany

\* Correspondence: ivan.nemec@upol.cz; Tel.: +420-585-634-354

Received: 10 July 2019; Accepted: 31 July 2019; Published: 2 August 2019



**Abstract:** The synthesis, crystal structure, and magnetic properties of three new mononuclear complexes  $[\text{Fe}(\text{R-LA})(\text{L1})](\text{BPh}_4)$ , where  $\text{R-LA}^{2-}$  is a doubly deprotonated pentadentate Schiff base ligand and L1 is a monodentate benzimidazole or furopyridine ligand, are reported. Ligand- and anion-driven changes in crystal structures and magnetic behavior were investigated in terms of the magnetic susceptibility measurements and theoretical calculations.

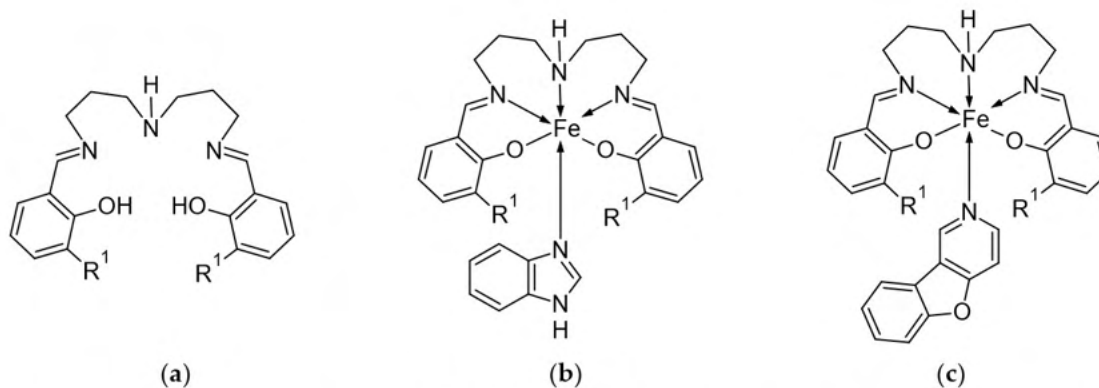
**Keywords:** spin crossover; Schiff base ligands; iron (III) complex; structure; magnetism

## 1. Introduction

Spin crossover (SCO) of (pseudo)octahedral complexes of iron(III) manifests as spin transition between  $S = 1/2$  (low-spin, LS) and  $S = 5/2$  (high-spin, HS) states [1]. Typically, the iron(III) complexes exhibit SCO for several types of coordination environments such as  $\{\text{FeO}_6\}$ ,  $\{\text{FeO}_3\text{S}_3\}$ ,  $\{\text{FeS}_6\}$ ,  $\{\text{FeN}_2\text{O}_2\text{S}_2\}$ ,  $\{\text{FeN}_3\text{O}_3\}$ , or  $\{\text{FeN}_6\}$ , but the most explored are the  $\{\text{FeN}_4\text{O}_2\}$  complexes with tri-, tetra-, penta-, or hexadentate Schiff base ligands [2]. For the last decade our attention focused predominantly on the Fe(III) complexes with pentadentate Schiff bases originating from reactions between derivatives of various ortho-hydroxy salicylaldehydes and aliphatic triamines [3–7]. In these compounds, two basic types of SCO complexes can be recognized due to different kinds of amine used in the synthesis of Schiff base ligands: so-called symmetric ones in which derivatives of bis(3-aminopropyl)amine are used ( $\text{H}_2\text{R-LA}$ , R- substituted compounds of 4-azaheptamethylene-1,7-bis(salicylideneimine),  $\text{H}_2\text{LA}$ ) and asymmetric ones with *N*-(2-aminoethyl)-1,3-propanediamine ( $\text{H}_2\text{R-LB}$ , R- substituted compounds of 4-azahexamethylene-1,7-bis(salicylideneimine),  $\text{H}_2\text{LB}$  Scheme 1). Initially, SCO was observed only for compounds with the general formula  $[\text{Fe}(\text{R-LA})(\text{L1})](\text{BPh}_4)$  [8] or  $[\{\text{Fe}(\text{R-LA})\}_2(\mu\text{-L2})](\text{BPh}_4)$  [9], and the observed transitions were of gradual or even spin equilibrium character. One exception was found in the case of a mononuclear compound with  $\text{R-LA} = \text{bis}(3\text{-methoxysalicylideneiminopropyl})\text{methylamine}$  and  $\text{L1} = 4\text{-aminopyridine}$ , which exhibited rather cooperative SCO, possibly due to its crystal packing involving  $\text{N-H}\cdots\text{O}$  and  $\text{N-H}\cdots\pi$  non-covalent interactions between the complex cations [10]. Other interesting results were obtained for compounds  $[\text{Fe}(\text{LA})(\text{L1A})][\text{M}(\text{dmit})_2]\text{-CH}_3\text{CN}$ ,  $\text{M} = \text{Ni, Pd, Pt}$ , in which L1A (1-(pyridin-4-yl)-2-(*N*-methylpyrrol-2-yl) ethane) is a photoisomerable ligand and  $[\text{M}(\text{dmit})_2]^-$  anions can act as molecular conductors [11]. Compounds of the general formula  $[\text{Fe}(\text{LA})(\text{L1B})](\text{BPh}_4)$  also contain photoisomerable ligands  $\text{L1B} = 3\text{-phenylazopyridine}$  or 4-phenylazopyridine [12]. Nevertheless, these complexes are not very interesting from a magnetic point of view because they exhibit only gradual spin transitions. This changed with the introduction of the shorter aliphatic chain in Schiff base ligands by substitution of the derivatives of bis(3-aminopropyl)amine by *N*-(2-aminoethyl)-1,3-propanediamine. Increased rigidity of the resulting



ligands (supported also by the introduction of naphthyl instead of benzene rings) led to preparation of the  $[\text{Fe}(\text{LB})(\text{LP})]$  complexes (where LP stands for (1) pseudohalido ligand), which exhibited cooperative spin transitions, in some cases even accompanied by thermal hysteresis [3].



**Scheme 1.** Structural formulas of (a) ligands H<sub>2</sub>LA (R<sup>1</sup> = H) and H<sub>2</sub>3EtO-LA (R<sup>1</sup> = O-CH<sub>2</sub>-CH<sub>3</sub>) and (b) complex cations  $[\text{Fe}(3\text{EtO-LA})(\text{L1}^{\text{a}})]^+$  in **1a** (R<sup>1</sup> = O-CH<sub>2</sub>-CH<sub>3</sub>) and (c)  $[\text{Fe}(3\text{EtO-LA})(\text{L1}^{\text{b}})]^+$  in **2a** (R<sup>1</sup> = O-CH<sub>2</sub>-CH<sub>3</sub>) or  $[\text{Fe}(\text{LA})(\text{L1}^{\text{b}})]^+$  in **2b** (R<sup>1</sup> = H).

Inspired by the abovementioned results we decided to attempt preparation of the  $[\text{Fe}(\text{LA})(\text{L1})](\text{BPh}_4)$  complexes exhibiting cooperative SCO by using monodentate ligands, which could increase the rigidity and the number of significant non-covalent interactions in the resulting complexes. Therefore, we decided to use two different bulky monodentate ligands, benzimidazole (L1<sup>a</sup>) and 1-benzofuro[3,2-c]pyridine (L1<sup>b</sup>), together with two slightly different pentadentate ligands, H<sub>2</sub>LA and H<sub>2</sub>3EtO-LA (4-azaheptamethylene-1,7-bis(3-thoxy-salicylideneimine), Scheme 1). We were successful in the preparation of three compounds:  $[\text{Fe}(3\text{EtO-LA})(\text{L1}^{\text{a}})](\text{BPh}_4)$  (**1a**),  $[\text{Fe}(3\text{EtO-LA})(\text{L1}^{\text{b}})](\text{BPh}_4) \cdot \text{CH}_3\text{OH}$  (**2a**), and  $[\text{Fe}(\text{LA})(\text{L1}^{\text{b}})](\text{BPh}_4)$  (**2b**). Here, we report their crystal structure and magnetic properties.

## 2. Materials and Methods

Chemicals were purchased from commercial sources (Sigma-Aldrich) and used as received. 1-benzofuro[3,2-c]pyridine was prepared according to a previously reported procedure [13,14]. Elemental analysis was carried out on a Flash 2000 (ThermoFisher Scientific, Waltham, MA, USA).

Magnetic susceptibility and magnetization measurements were done using a SQUID magnetometer (Quantum Design Inc., San Diego, CA, USA) from  $T = 2$  K at  $B = 0.1$  T. The magnetization data were taken at  $T = 2.0$  and 4.6 K, respectively. Raw susceptibility was corrected, and diamagnetic corrections of the constituent atoms were estimated from Pascal constants. The effective magnetic moment was calculated as usual:  $\mu_{\text{eff}}/\mu_{\text{B}} = 798(\chi' T)^{1/2}$  when SI units are employed.

Single-crystal X-ray diffraction data were collected on an Oxford diffractometer Xcalibur2 (Oxford Diffraction Ltd., Oxford, UK) with a Sapphire CCD detector and fine-focused sealed tube (Mo K $\alpha$  radiation,  $\lambda = 0.71073$  Å) source and equipped with an Oxford Cryosystem nitrogen gas-flow apparatus. All structures were solved and refined (full-matrix least-squares on  $F_o^2 - F_c^2$ ) by using SHELXS2014 software [15].

### 2.1. Synthesis

#### 2.1.1. Ligands

Neutral, pentadentate ligands H<sub>2</sub>LA and H<sub>2</sub>3EtO-LA were prepared by mixing the appropriate aldehyde and amine in a 2:1 molar ratio. Synthesis of all Schiff base ligands is analogous; therefore, only synthesis of H<sub>2</sub>LA is presented in detail [9]. A methanol solution of salicylaldehyde (2.44 g,



20 mmol in 50 cm<sup>3</sup>) was combined with di(3-aminopropyl)amine (1.31 g, 10 mmol) and the mixture was refluxed for 60 min. The ligand was obtained as a yellow solution ready for subsequent use.

### 2.1.2. Mononuclear Precursors

Synthesis of all precursors was very similar [9]; therefore, only the synthesis of [Fe(LA)Cl] is described. The methanol solution of ligand H<sub>2</sub>LA (10 mmol in 50 cm<sup>3</sup>) was combined with a solution of iron(III) chloride hexahydrate (2.70 g, 10 mmol) in 40 cm<sup>3</sup> of methanol. The mixture was refluxed for 20 min, and then triethylamine (2.22 g, 22 mmol) was added to complete deprotonation of the Schiff base ligand. The resulting violet solution was refluxed for 30 min and left to cool slowly to room temperature when a dark violet micro-crystalline powder precipitated. This was filtered off using a fritted funnel, washed with methanol and diethylether, and dried.

### 2.1.3. Mononuclear Complexes **1a**, **2a**, and **2b**

The complexes were prepared in the same manner by mixing 100 mg of the [Fe(LA)Cl] or [Fe(3EtO-LA)Cl] (0.193 mmol in the preparation of **1a** and **2a**, 0.233 mmol in the preparation of **2b**) precursor complexes with a heterocyclic derivate (23 mg of L1<sup>a</sup> for the preparation of **1a**, 33/38 mg of L1<sup>b</sup> for the preparation of **2a/2b**) in a molar ratio of 1:1. After 30 min of reflux, the solution was filtered through paper filter into an equimolar amount of solution of NaBPh<sub>4</sub>.

As an example, the synthesis of [Fe(3EtO-LA)(L1<sup>a</sup>)](BPh<sub>4</sub>) is described in detail. To a solution of [Fe(3EtO-LA)Cl] (100 mg in 30 cm<sup>3</sup> of methanol), L1<sup>a</sup> was added. The resulting violet solution was refluxed for 30 min and filtered into a solution of NaBPh<sub>4</sub> (66 mg in 5 cm<sup>3</sup>). Black crystals precipitated overnight. They were collected, washed with methanol and diethyl ether, and dried.

### 2.1.4. Elemental Analysis

**1a**: calcd (%) for C<sub>55</sub>B<sub>1</sub>Fe<sub>1</sub>H<sub>57</sub>N<sub>5</sub>O<sub>4</sub>, M<sub>w</sub> = 918.7 g·mol<sup>-1</sup>, C, 71.9; H, 6.3; N, 7.6. Found: C, 71.5; H, 6.1; N, 7.3. Yield = 67%.

**2a**: calcd (%) for C<sub>60</sub>B<sub>1</sub>Fe<sub>1</sub>H<sub>62</sub>N<sub>4</sub>O<sub>6</sub>, M<sub>w</sub> = 1001.8 g·mol<sup>-1</sup>, C, 71.9; H, 6.2; N, 5.6. Found: C, 71.6; H, 6.0; N, 5.2. Yield = 48%.

**2b**: calcd (%) for C<sub>55</sub>B<sub>1</sub>Fe<sub>1</sub>H<sub>50</sub>N<sub>4</sub>O<sub>3</sub>, M<sub>w</sub> = 881.7 g·mol<sup>-1</sup>, C, 74.9; H, 5.7; N, 6.4. Found: C, 74.5; H, 5.8; N, 6.1. Yield = 55%.

## 2.2. Theoretical Calculations

The theoretical calculations were carried out using the ORCA 4.1 computational package [16]. Three density functional theory (DFT) functionals, B3LYP [17–19], OPBE [20,21], and TPSSh [22,23], were used to optimize the molecular structures together with the polarized triple- $\zeta$  quality basis set def2-TZVP proposed by Ahlrichs and co-workers [24], where “verytightopt” optimization criteria were used in ORCA. The calculations utilized the RI approximation with the decontracted auxiliary def2/J Coulomb fitting basis set [25] and the chain-of-spheres (RIJCOSX) approximation to exact exchange [26,27] as implemented in ORCA. Increased integration grids (Grid5 and Gridx5 in ORCA convention) and tight SCF convergence criteria were used in all calculations. Moreover, the SCF stability test as implemented in ORCA was done for all final optimized geometries to verify whether the SCF solution was at a local minimum and not in a saddle point [28,29].

## 3. Results and Discussion

### 3.1. Crystal Structures

The crystal structures were determined by single-crystal X-ray diffraction for all three presented compounds **1a**, **2a**, and **2b**, and these crystallized in triclinic (*P*-1 for **1a** and **2a**) and monoclinic (*P*2<sub>1</sub>/*c* for **2b**) space groups (Table 1). All three compounds consist of complex Fe(III) cations charge balanced by BPh<sub>4</sub><sup>-</sup> anions. In **2a**, the additional methanol molecule is in its asymmetric unit, which is heavily

disordered. It was not possible to model it reasonably; therefore, the SQUEEZE procedure [30] was used to subtract the corresponding electronic density.

**Table 1.** Crystal data and details of structure determination.

Compound	1a	2a	2b
Formula	C <sub>55</sub> H <sub>57</sub> BFeN <sub>5</sub> O <sub>4</sub>	C <sub>59</sub> H <sub>58</sub> BFeN <sub>4</sub> O <sub>5</sub>	C <sub>55</sub> H <sub>50</sub> BFeN <sub>4</sub> O <sub>3</sub>
Formula weight	918.71	969.75	881.65
Crystal system	Triclinic	Triclinic	Monoclinic
Space group	<i>P</i> -1	<i>P</i> -1	<i>P</i> 2 <sub>1</sub> / <i>c</i>
Cell parameters			
<i>a</i> /Å	10.1648(7)	13.2869(4)	19.1978(10)
<i>b</i> /Å	15.2130(10)	13.6926(5)	11.7562(13)
<i>c</i> /Å	16.2320(10)	16.4083(6)	21.381(2)
$\alpha$ /°	81.990(6)	70.732(3)	90
$\beta$ /°	72.359(6)	78.232(3)	110.458(8)
$\gamma$ /°	86.049(6)	67.395(3)	90
<i>V</i> /Å <sup>3</sup>	2367.7(3)	2591.29(17)	4521.2(8)
<i>Z</i>	2	2	4
<i>T</i> /K	100(2)	190(2)	293(2)
Density, <i>D</i> <sub>c</sub> /g cm <sup>-3</sup>	1.289	1.243	1.295
Abs. coefficient/mm <sup>-1</sup>	0.371	0.344	0.384
Data/restraints/param	8326/0/601	6630/3/644	7931/0/577
<i>R</i> <sub>1</sub> <sup>a</sup> , <i>wR</i> <sub>2</sub> <sup>b</sup> (all data)	0.0660, 0.1073	0.0545, 0.0867	0.0618, 0.0810
<i>R</i> <sub>1</sub> <sup>a</sup> , <i>wR</i> <sub>2</sub> <sup>b</sup> [ <i>I</i> > 2σ( <i>I</i> )]	0.0379, 0.0978	0.0355, 0.0829	0.0340, 0.0763
Goodness of fit	1.049	1.028	0.954
CSD number	1939657	1939658	1939656

$$^a R_1 = \sum (|F_o| - |F_c|) / \sum |F_o|. \quad ^b wR_2 = \{ \sum [w(F_o^2 - F_c^2)^2] / \sum [w(F_o^2)] \}^{1/2}.$$

The complex cations in **1a**, **2a**, and **2b** consist of a pentadentate Schiff base ligand (3EtO-LA<sup>2-</sup> in **1a** and **2a**, LA<sup>2-</sup> in **2b**) coordinated to the central Fe(III) atom, and the sixth coordination site is occupied by a monodentate N-donor heterocyclic ligand (L1<sup>b</sup> in **2a** and **2b**, L1<sup>b</sup> in **1a**). The pentadentate Schiff base ligands coordinate iron centers in a *cis*-conformation of the oxygen atoms, which is typical for compounds with [Fe(R-LA)]<sup>+</sup> cations (Figure 1) [31]. The monodentate ligand is in a *trans*-position to the secondary amine group of the pentadentate ligand.

The metal–ligand bond lengths (Figure 1) are close to the values typical for the LS state with the longest bonds observed between the iron atoms and secondary nitrogen atoms of the pentadentate ligands (in Å, 2.0293(19) in **1a**, 2.0539(16) in **2a**, 2.0843(15) in **2b**) or the nitrogen atom of the heterocyclic monodentate ligand (in Å, 2.0105(18) in **1a**, 2.0497(15) in **2a**, 2.0990(16) in **2b**). The Fe–N bonds involving the imino nitrogen atoms are rather shorter and similar for all three structures, ranging between 1.98 to 2.01 Å. The Fe–O bonds are even shorter: 1.87–1.89 Å. The angular distortion parameter Σ is rather small [32]: 17.4° (**1a**), 23.7° (**2a**), and 30.3° (**2b**).

The crystal structures of **1a**, **2a**, and **2b** do not contain hydrogen bonding of significant strength. In **1a**, the secondary amine group from the complex cation forms offset N–H⋯π non-covalent contact with the aromatic ring of the BPh<sub>4</sub><sup>-</sup> anion. The shortest N⋯C distance is 3.446(3) Å (Figure S1 in supplementary materials). The N–H group from benzimidazole also forms N–H⋯π interaction with the aromatic ring of the BPh<sub>4</sub><sup>-</sup> anion—the N⋯C<sub>g</sub> distance is 3.227(4) Å (where C<sub>g</sub> stands for the ring centroid).

In **2a**, the interaction between complex cations is provided by very offset ring–ring interactions with a shortest C⋯C distance of 3.192(3) Å. Other non-covalent interactions include weak C–H⋯O and C–H⋯π contacts (Figure S2).

In **2b**, the secondary amine group from the complex cation forms weakly offset N–H⋯π interaction with the aromatic ring of the BPh<sub>4</sub><sup>-</sup> anion (the shortest N⋯C distance is 3.713(3) Å). Other non-covalent interactions in **2b** are weak C–H⋯O and C–H⋯π contacts (Figure S3).



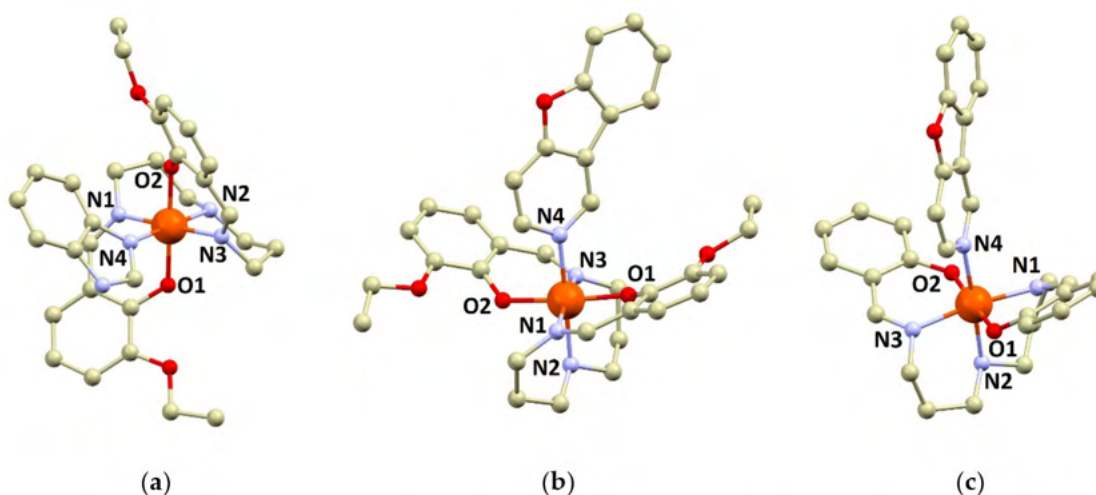


**Figure 1.** Depiction of the molecular structures of  $[\text{Fe}(3\text{EtO-LA})(\text{L1}^{\text{a}})]^+$  in **1a** (a),  $[\text{Fe}(3\text{EtO-LA})(\text{L1}^{\text{b}})]^+$  in **2a** (b) and  $[\text{Fe}(\text{LA})(\text{L1}^{\text{b}})]^+$  in **2b** (c). Selected bond lengths (in Å): in **1a**, Fe1–O1 = 1.8896(15), Fe1–O2 = 1.8951(15), Fe1–N1 = 1.9608(19), Fe1–N2 = 2.0293(19), Fe1–N3 = 1.971(2), Fe1–N4 = 2.0105(18); in **2a**, Fe1–O1 = 1.8719(12), Fe–O2 = 1.8796(12), Fe1–N1 = 1.9787(15), Fe1–N2 = 2.0539(16), Fe1–N3 = 1.9840(15), Fe1–N4 = 2.0497(15); in **2b**, Fe1–O1 = 1.8885(13), Fe1–O2 = 1.8892(13), Fe1–N1 = 1.9997(17), Fe1–N2 = 2.0843(15), Fe1–N3 = 2.0099(16), Fe1–N4 = 2.0990(16).

### 3.2. Magnetic Properties

The temperature dependence of the effective magnetic moment for **1a**, **2a**, and **2b** is shown in Figure 2. All three compounds undergo spin crossover from the LS to the HS state ( $S = 1/2 \rightarrow 5/2$ ), which start above ca. 150 K. Evidently, the spin crossover is incomplete until 300 K, because room temperature values of the effective magnetic moment are less than the spin-only value for  $S = 5/2$  and  $g = 2.0$  ( $5.93 \mu_{\text{B}}$ ). Moreover, the low temperature values of  $\mu_{\text{eff}}$  vary in the range  $\approx 2\text{--}3 \mu_{\text{B}}$ , which suggests that a small portion of iron(III) complexes stay in the HS state. This is also supported by the field dependence of molar magnetization measurements (measured at 2 and 4.6 K, Figure S4), which unequivocally confirm the LS ground state with a larger contribution of non-converted HS molecules in **1a** and **2a** ( $M_{\text{mol}}/N_{\text{A}}\mu_{\text{B}} = 1.5$  in **1a**, 1.4 in **2a** at 2 K and 7 T) than in **2b** ( $M_{\text{mol}}/N_{\text{A}}\mu_{\text{B}} = 1.1$  at 2 K and 7 T).

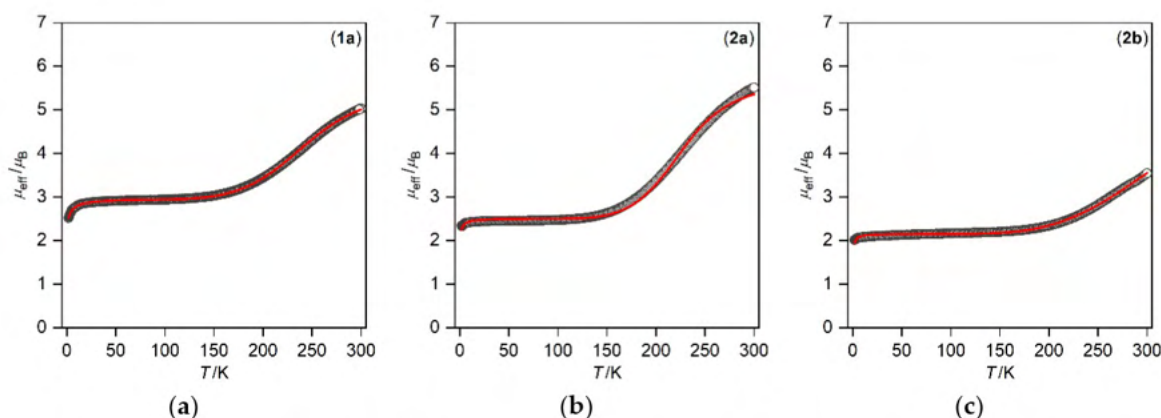


**Figure 2.** The temperature dependence of the effective magnetic moment for **1a** (a), **2a** (b), and **2b** (c). The experimental data are displayed as empty circles, calculated data are displayed as full lines.

The experimental data were analyzed with the help of the Ising-like model [33,34] having following Hamiltonian

$$\hat{H} = \frac{\Delta}{2} \hat{\sigma} - \gamma \langle \sigma \rangle \hat{\sigma} \quad (1)$$

where  $\sigma$  is fictitious spin with eigenvalues  $-1$  for LS and  $+1$  for HS states,  $\Delta$  is the energy difference between HS and LS states,  $\gamma$  stands for the cooperativeness of the system ( $\gamma > 0$ ), and  $\langle\sigma\rangle$  is the thermal average of the fictitious spin, which is calculated by solving the implicit equation

$$\langle\sigma\rangle = \frac{-1 + r_{\text{eff}} \exp[-(\Delta - 2\gamma\langle\sigma\rangle)/kT]}{+1 + r_{\text{eff}} \exp[-(\Delta - 2\gamma\langle\sigma\rangle)/kT]} \quad (2)$$

where  $r_{\text{eff}}$  is the effective degeneracy ratio of HS and LS states, and it incorporates both the spin and vibrational degeneracies of the respective spin states [35]. Then, the molar fraction of HS species,  $x'_{\text{HS}}$ , is computed as

$$x'_{\text{HS}} = \frac{1}{2}(1 + \langle\sigma\rangle). \quad (3)$$

In order to fit the experimental magnetic data, the overall susceptibility was calculated as

$$\chi_{\text{mol}} = (x''_{\text{HS}} + x_{\text{rHS}})\chi_{\text{HS}} + (1 - x''_{\text{HS}} - x_{\text{rHS}})\chi_{\text{LS}} \quad (4)$$

where  $x_{\text{rHS}}$  is the mole fraction of the residual high-spin state at low temperature,  $x''_{\text{HS}}$  is the rescaled high-spin fraction calculated from the Ising-like model as  $x''_{\text{HS}} = x'_{\text{HS}}(1 - x_{\text{rHS}})$ , and the molar susceptibility values for LS and HS states were calculated by the Curie–Weiss law as

$$\chi_{\text{LS}} = \frac{N_{\text{A}}\mu_0\mu_{\text{B}}^2 S_{\text{LS}}(S_{\text{LS}} + 1)}{3k} \frac{g_{\text{LS}}^2}{T - \Theta_{\text{LS}}} \quad (5)$$

$$\chi_{\text{HS}} = \frac{N_{\text{A}}\mu_0\mu_{\text{B}}^2 S_{\text{HS}}(S_{\text{HS}} + 1)}{3k} \frac{g_{\text{HS}}^2}{T - \Theta_{\text{HS}}}. \quad (6)$$

To summarize, the variation of Ising-like model parameters ( $\Delta$ ,  $\gamma$ ,  $\rho_{\varepsilon\phi\phi}$ ) leads to temperature variation of the HS mole fraction, which is subsequently utilized to calculate the temperature variation of the overall molar susceptibility and, hence, the effective magnetic moment. Due to the fact that the spin crossover is not finished until 300 K, the  $g_{\text{HS}}$  value was fixed to 2.0, which is a typical value for HS octahedral iron(III) complexes. Also, the Weiss constant of the HS state was set to zero, because the low temperature data are dominated by the LS fraction. Then, we are left with these additional free parameters:  $g_{\text{LS}}$ ,  $x_{\text{rHS}}$ , and  $\Theta_{\text{LS}}$ . Finally, a fitting procedure was applied to find the best parameters describing the experimental magnetic data, and the values of the parameters are listed in Table 2. The spin transition temperatures  $T_{1/2}$  are increasing in the following order: **2a** < **1a** < **2b**.

**Table 2.** The magnetic parameters for **1a**, **2a**, and **2b**<sup>a</sup>.

Compound	$g_{\text{LS}}$	$\Theta_{\text{LS}}$	$x_{\text{rHS}}$	$\Delta$ (K)	$\gamma$ (K)	$r_{\text{eff}}$	$\Delta H$ (J mol <sup>-1</sup> )	$\Delta S$ (J K <sup>-1</sup> mol <sup>-1</sup> )	$T_{1/2}$ (K)
<b>1a</b>	2.34	-4.3	0.15	930	116	35.0	7730	29.6	262
<b>2a</b>	2.01	-1.5	0.10	1200	95	150	9975	41.7	239
<b>2b</b>	2.01	-0.8	0.05	1033	127	17	8592	23.6	365

<sup>a</sup> the thermodynamic parameters were calculated as  $\Delta H = N_{\text{A}}\Delta$ ,  $\Delta S = R \ln r_{\text{eff}}$ , and  $T_{1/2} = \Delta H / \Delta S$ .

### 3.3. Theoretical Calculations

In order to evaluate the impact of various coordinated heterocyclic ligands on the spin crossover properties of pentacoordinate Schiff base iron(III) complexes, density functional theory (DFT) calculations were employed. Here, we tested three DFT functionals, B3LYP, OPBE, and TPSSh, which were selected by benchmark studies to be suitable functionals for the study of spin crossover phenomena [36–38]. The molecular geometries of the complex cations  $[\text{Fe}(\text{R-LA})(\text{L1})]^+$  of **1a**, **2a**, and **2b** were optimized for LS (doublet) and HS (sextet) states. Furthermore, we added another three analogous SCO complexes, namely, DAVCEJ, DETBEJ, and KISJUS, to address the robustness of this



theoretical approach. The respective donor–acceptor distances calculated with the TPSSh functional are summarized in Table 3; for other functionals, please see Tables S1 and S2. The experimental X-ray data are available for the low-spin state of **1a**, DAVCEJ, and KISJUS, whereas DAVCEJ01 is only available in a high-spin state structure because the reported room temperature X-ray data of DETBEJ and KISJUS01 correspond to incomplete spin transition at this temperature with respect to the magnetic data.

**Table 3.** The interatomic donor–acceptor distances for density functional theory (DFT)-optimized geometries of  $[\text{Fe}(\text{R-LA})(\text{L1})]^+$  of **1a**, **2a**, and **2b** and DAVCEJ, DETBEJ, and KISJUS using the TPSSh functional <sup>a</sup>.

Method	Compound	Fe–O	Fe–N <sub>im</sub>	Fe–N <sub>am</sub>	Fe–N <sub>hetero</sub>
X-ray analysis	<b>1a</b> (LS)	1.8896/1.8951	1.9608/1.971	2.0293	2.0105
	DAVCEJ (LS)	1.869/1.880	1.961/1.974	2.091	2.000
	DAVCEJ01 (HS)	1.908/1.920	2.072/2.096	2.257	2.146
	KISJUS (LS, 100 K)	1.863/1.880	1.946/1.954	2.023	1.982
TPSSh (LS)	<b>1a</b>	1.875/1.892	1.949/1.972	2.047	2.010
	<b>2a</b>	1.872/1.880	1.979/1.984	2.054	2.050
	<b>2b</b>	1.888/1.889	2.000/2.010	2.084	2.099
	DAVCEJ	1.875/1.890	1.953/1.968	2.105	2.008
	DETBEJ	1.872/1.899	1.953/1.978	2.044	2.016
	KISJUS	1.867/1.896	1.949/1.972	2.044	1.991
	<b>1a</b> (HS)	1.931/1.950	2.104/2.113	2.282	2.201
TPSSh (HS)	<b>2a</b> (HS)	1.934/1.936	2.105/2.109	2.281	2.229
	<b>2b</b> (HS)	1.939/1.942	2.104/2.107	2.276	2.225
	DAVCEJ (HS)	1.938/1.945	2.095/2.098	2.345	2.202
	DETBEJ (HS)	1.938/1.939	2.105/2.109	2.276	2.228
	KISJUS (HS)	1.935/1.945	2.107/2.109	2.286	2.174

<sup>a</sup> distances in Å.

Figure 3 shows a comparison of DFT-optimized donor–acceptor distances with the experimental data. It is evident that none of these DFT functionals provided perfect results: both B3LYP and OPBE overestimated Fe–N<sub>am</sub> and Fe–N<sub>het</sub> distances; Fe–N<sub>im</sub> was overestimated by B3LYP and underestimated by OPBE. Moreover, the Fe–N<sub>am</sub> distance of DAVCEJ (HS) is extremely long. It seems to us that the best results were provided by the TPSSh functional. Indeed, only this functional correctly predicted the LS ground state for the studied compounds according to the energy comparison of HS and LS isomers depicted in Figure 4. However, there is large variation in the energy difference,  $E_{\text{HS}}-E_{\text{LS}}$ , between 1.92 kcalmol<sup>-1</sup> for **2a** and 12.91 kcalmol<sup>-1</sup> for DETBEJ. Obviously, the  $E_{\text{HS}}-E_{\text{LS}}$  energy difference does not correlate with the  $T_{1/2}$  value of the studied compounds, and this inconsistency could also be ascribed to variation of the entropy within this series. However, all the studied compounds have a very similar composition of the Fe<sup>III</sup> complex cation and have BPh<sub>4</sub><sup>-</sup> as the counterion; thus, it can be anticipated that variation of the entropy for the whole series should be minute. Thus, it is most likely that the large variation in the  $E_{\text{HS}}-E_{\text{LS}}$  energy difference is due to imperfectness of the DFT functional and/or due to neglect of the crystal packing and non-covalent intermolecular interactions in the solid state, which cannot be reproduced with geometry optimization of  $[\text{Fe}(\text{R-LA})(\text{L1})]^+$  cations in vacuum.

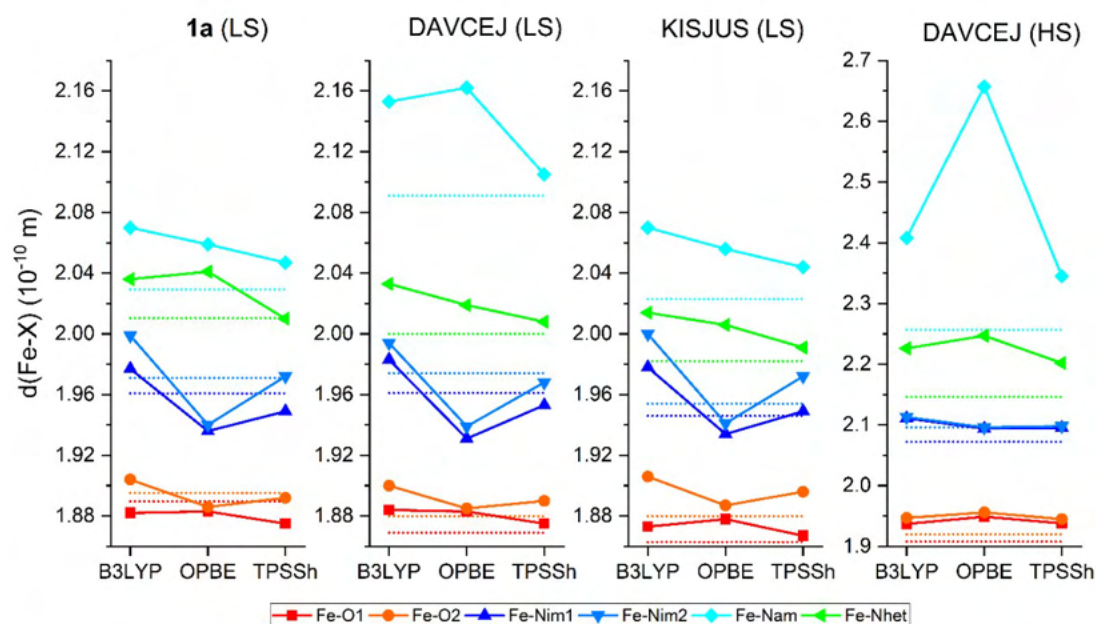


**Figure 3.** The variation of the donor–acceptor distances in DFT-optimized geometries (full lines + symbols) compared to the experimental X-ray data (dotted lines).

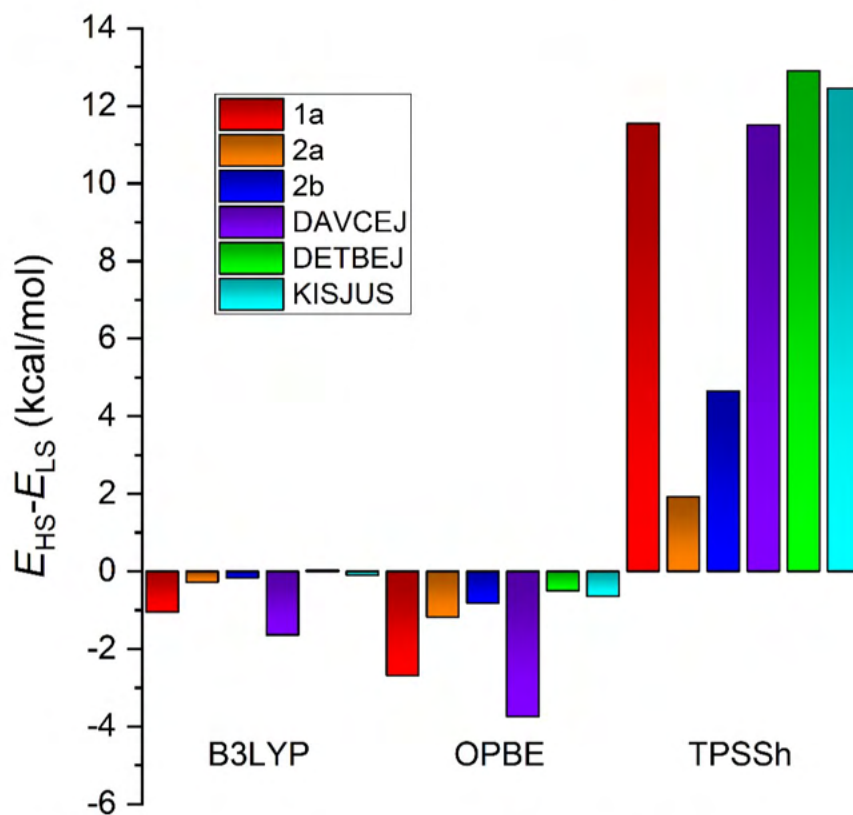


**Figure 4.** The energy separation of HS and LS states of **1a**, **2a**, and **2b** and DAVCEJ, DETBEJ, and KISJUS calculated using B3LYP, OPBE, and TPSSh with the def2-TZVP basis set.

#### 4. Conclusions

In this article we reported the synthesis, crystal structure, and magnetic properties of three new iron(III) complexes with two different pentadentate Schiff base ligands and monodentate heterocyclic ligands. The main motivation for this research was to increase the rather low cooperativity of



spin crossover behavior which was typically observed for this group of compounds previously. In general, it is well established that by introducing stacking interactions, the cooperativity of SCO systems might be enhanced. Therefore, relatively large, rigid, monodentate ligands (benzimidazole or 1-benzofuro[3,2-c]pyridine) capable of forming stacking interactions were deliberately introduced into the synthesis of the reported compounds. However, the prepared compounds did not exhibit any regular patterns of significant stacking interactions. The magnetic properties of the compounds showed that our attempt to increase SCO cooperativity was not successful, and the compounds exhibited weakly cooperative SCO without thermal hysteresis but with rather high critical SCO temperatures ( $T_{1/2} = 262$  (**1a**), 239 (**2a**), 365 (**2b**) K). DFT calculations were also employed in the study using three functionals, B3LYP, OPBE, and TPSSh. The best agreement with the experimental structures was found for the TPSSh functional, and also, only this functional identified LS isomers lower in energy than HS isomers. However, the general trend in the energy separation of HS and LS isomers and the spin crossover transition temperature  $T_{1/2}$  found from the experimental data was not fully recovered, which most probably points to the importance of the intermolecular interactions.

**Supplementary Materials:** The following are available online at <http://www.mdpi.com/2075-4701/9/8/849/s1>, Figure S1: The N–H... $\pi$  non-covalent interactions in **1a**, Figure S2: The non-covalent interactions in **2a**, Figure S3: The non-covalent interactions in **2b**, Table S1: The interatomic donor–acceptor distances for DFT-optimized geometries, Table S2: The interatomic donor–acceptor distances for DFT-optimized geometries.

**Author Contributions:** Conceptualization, I.N.; methodology, I.N. and R.H.; validation, I.N. and R.H.; formal analysis, R.H.; investigation, I.N., R.H. and I.S.; writing—original draft preparation, I.N. and R.H.; writing—review and editing, I.N. and R.H.; visualization, I.N. and R.H.

**Funding:** This research was funded by the institutional sources of the Department of Inorganic Chemistry, Palacký University Olomouc, Czech Republic (I.N. and R.H.), project CEITEC 2020 (LQ1601) with financial support from the Ministry of Education, Youth and Sports of the Czech Republic under the National Sustainability (I.N.).

**Acknowledgments:** Ivan Nemeč would like to acknowledge Jozef Miklovič for providing a small amount of 1-benzofuro[3,2-c]pyridine.

**Conflicts of Interest:** The authors declare no conflict of interest.

## References

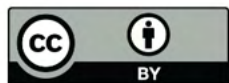
1. Van Koningsbruggen, P.J.; Maeda, Y.; Oshio, H. Iron(III) spin crossover compounds. In *Spin Crossover in Transition Metal Compounds I*; Gülich, P., Goodwin, H.A., Eds.; Springer: Berlin, Germany, 2004; pp. 259–324.
2. Harding, D.J.; Harding, P.; Phonsri, W. Spin crossover in iron(III) complexes. *Coord. Chem. Rev.* **2016**, *313*, 38–61. [[CrossRef](#)]
3. Nemeč, I.; Boča, R.; Herchel, R.; Trávníček, Z.; Gembický, M.; Linert, W. Dinuclear Fe(III) complexes with spin crossover. *Monatshfte Chem. Chem. Mon.* **2009**, *140*, 815–828. [[CrossRef](#)]
4. Herchel, R.; Boča, R.; Gembický, M.; Kožíšek, J.; Renz, F. Spin Crossover in a Tetranuclear Cr(III)–Fe(III)3 Complex. *Inorg. Chem.* **2004**, *43*, 4103–4105. [[CrossRef](#)] [[PubMed](#)]
5. Nemeč, I.; Herchel, R.; Boča, R.; Trávníček, Z.; Svoboda, I.; Fuess, H.; Linert, W. Tuning of spin crossover behaviour in iron(III) complexes involving pentadentate Schiff bases and pseudohalides. *Dalton Trans.* **2011**, *40*, 10090–10099. [[CrossRef](#)] [[PubMed](#)]
6. Nemeč, I.; Herchel, R.; Trávníček, Z. The relationship between the strength of hydrogen bonding and spin crossover behaviour in a series of iron(III) Schiff base complexes. *Dalton Trans.* **2015**, *44*, 4474–4484. [[CrossRef](#)] [[PubMed](#)]
7. Pogány, L.; Brachňaková, B.; Moncol, J.; Pavlik, J.; Nemeč, I.; Trávníček, Z.; Mazúr, M.; Bučinský, L.; Suchánek, L.; Šalitroš, I. Impact of substituent variation on the presence of thermal spin crossover in a series of mononuclear iron(III) schiff base complexes with terminal pseudohalido co-ligands. *Chem. A Eur. J.* **2018**, *24*, 5191–5203. [[CrossRef](#)] [[PubMed](#)]
8. Matsumoto, N.; Ohta, S.; Yoshimura, C.; Ohyoshi, A.; Kohata, S.; Okawa, H.; Maeda, Y. Studies on spin-equilibrium iron(III) complexes. Part 1. Syntheses and magnetic properties of a new family of spin cross-over iron(III) complexes with a unidentate ligand over a wide range of the spectrochemical series and a quinquadentate ligand derived. *J. Chem. Soc. Dalt. Trans.* **1985**, *12*, 2575. [[CrossRef](#)]



9. Boča, R.; Fukuda, Y.; Gembický, M.; Herchel, R.; Jaroščiak, R.; Linert, W.; Renz, F.; Yuzurihara, J. Spin crossover in mononuclear and binuclear iron(III) complexes with pentadentate Schiff-base ligands. *Chem. Phys. Lett.* **2000**, *325*, 411–419. [[CrossRef](#)]
10. Tanimura, K.; Kitashima, R.; Bréfuel, N.; Nakamura, M.; Matsumoto, N.; Shova, S.; Tuchagues, J.-P. Infinite chain structure and steep spin crossover of a Fe III Complex with a N<sub>3</sub>O<sub>2</sub> pentadentate schiff-base ligand and 4-aminopyridine. *Bull. Chem. Soc. Jpn.* **2005**, *78*, 1279–1282. [[CrossRef](#)]
11. Faulmann, C.; Dorbes, S.; De Bonneval, B.G.; Molnár, G.; Bousseksou, A.; Gomez-Garcia, C.J.; Coronado, E.; Valade, L. Towards molecular conductors with a spin-crossover phenomenon: Crystal structures, magnetic properties and Mössbauer spectra of [Fe(salten)mepepy][M(dmit)<sub>2</sub>] complexes. *Eur. J. Inorg. Chem.* **2005**, 3261–3270. [[CrossRef](#)]
12. Bannwarth, A.; Schmidt, S.O.; Peters, G.; Sönnichsen, F.D.; Thimm, W.; Herges, R.; Tuczek, F. Fe<sup>III</sup> spin-crossover complexes with photoisomerizable ligands: Experimental and theoretical studies on the ligand-driven light-induced spin change effect. *Eur. J. Inorg. Chem.* **2012**, *2012*, 2776–2783. [[CrossRef](#)]
13. Bobošík, V.; Krutošíková, A.; Jordis, U. Synthesis and reactions of 2,3-dimethylfuro[3,2-c]pyridines. *Monatshefte für Chemie Chem. Mon* **1995**, *126*, 747–752. [[CrossRef](#)]
14. Bencková, M.; Krutošíková, A. Synthesis of pyrrolo[2',3':4,5]furo[3,2-c]pyridines. *Monatshefte Chem. Chem. Mon.* **1995**, *126*, 753–758. [[CrossRef](#)]
15. Sheldrick, G.M. Crystal structure refinement with SHELXL. *Acta Crystallogr. Sect. C Struct. Chem.* **2015**, *71*, 3–8. [[CrossRef](#)]
16. Neese, F. Software update: The ORCA program system, version 4.0. *Wiley Interdiscip. Rev. Comput. Mol. Sci.* **2018**, *8*, e1327. [[CrossRef](#)]
17. Becke, A.D. Density-functional exchange-energy approximation with correct asymptotic behavior. *Phys. Rev. A* **1988**, *38*, 3098–3100. [[CrossRef](#)]
18. Lee, C.; Yang, W.; Parr, R.G. Development of the Colle-Salvetti correlation-energy formula into a functional of the electron density. *Phys. Rev. B* **1988**, *37*, 785–789. [[CrossRef](#)]
19. Stephens, P.J.; Devlin, F.J.; Chabalowski, C.F.; Frisch, M.J. Ab Initio calculation of vibrational absorption and circular dichroism spectra using density functional force fields. *J. Phys. Chem.* **1994**, *98*, 11623–11627. [[CrossRef](#)]
20. Handy, N.C.; Cohen, A.J. Left-right correlation energy. *Mol. Phys.* **2001**, *99*, 403–412. [[CrossRef](#)]
21. Perdew, J.P.; Burke, K.; Ernzerhof, M. Generalized gradient approximation made simple. *Phys. Rev. Lett.* **1996**, *77*, 3865–3868. [[CrossRef](#)]
22. Perdew, J.P.; Kurth, S.; Zupan, A.; Blaha, P. Accurate density functional with correct formal properties: A step beyond the generalized gradient approximation. *Phys. Rev. Lett.* **1999**, *82*, 2544–2547. [[CrossRef](#)]
23. Perdew, J.P.; Tao, J.; Staroverov, V.N.; Scuseria, G.E. Meta-generalized gradient approximation: Explanation of a realistic nonempirical density functional. *J. Chem. Phys.* **2004**, *120*, 6898–6911. [[CrossRef](#)] [[PubMed](#)]
24. Weigend, F.; Ahlrichs, R. Balanced basis sets of split valence, triple zeta valence and quadruple zeta valence quality for H to Rn: Design and assessment of accuracy. *Phys. Chem. Chem. Phys.* **2005**, *7*, 3297–3305. [[CrossRef](#)]
25. Weigend, F. Accurate Coulomb-fitting basis sets for H to Rn. *Phys. Chem. Chem. Phys.* **2006**, *8*, 1057–1065. [[CrossRef](#)] [[PubMed](#)]
26. Neese, F.; Wennmohs, F.; Hansen, A.; Becker, U. Efficient, approximate and parallel Hartree-Fock and hybrid DFT calculations. A “chain-of-spheres” algorithm for the Hartree-Fock exchange. *Chem. Phys.* **2009**, *356*, 98–109. [[CrossRef](#)]
27. Izsák, R.; Neese, F. An overlap fitted chain of spheres exchange method. *J. Chem. Phys.* **2011**, *135*, 144105. [[CrossRef](#)] [[PubMed](#)]
28. Seeger, R.; Pople, J.A. Self-consistent Molecular Orbital Methods. XVIII. Constraints and Stability in Hartree-Fock Theory. *J. Chem. Phys.* **1977**, *66*, 3045–3050. [[CrossRef](#)]
29. Bauernschmitt, R.; Ahlrichs, R. Stability Analysis for Solutions of the Closed Shell Kohn-Sham Equation. *J. Chem. Phys.* **1996**, *104*, 9047–9052. [[CrossRef](#)]
30. Spek, A.L. Platon Squeeze: A tool for the calculation of the disordered solvent contribution to the calculated structure factors. *Acta Crystallogr. Sect. C Struct. Chem.* **2015**, *71*, 9–18. [[CrossRef](#)] [[PubMed](#)]
31. Nemeč, I.; Boča, R.; Gembický, M.; Dlháň, L.; Herchel, R.; Renz, F. High-spin Schiff-base dinuclear iron(III) complexes bridged by N-oxide ligands. *Inorg. Chim. Acta* **2009**, *362*, 4754–4759. [[CrossRef](#)]



32. Guionneau, P.; Marchivie, M.; Bravic, G.; Letard, J.F.; Chasseau, D. Structural aspects of spin crossover. Example of the [(FeLn)-L-II(NCS)(2)] complexes. *Top. Curr. Chem.* **2004**, *234*, 97.
33. Bari, R.A.; Sivardière, J. Low-spin-high-spin transitions in transition-metal-ion compounds. *Phys. Rev. B* **1972**, *5*, 4466–4471. [[CrossRef](#)]
34. Wajnflasz, J. Etude de la transition “Low Spin”-„High Spin” dans les complexes octaédriques d’ion de transition. *Phys. Status Solidi* **1970**, *40*, 537–545. [[CrossRef](#)]
35. Boča, R.; Linert, W. Is There a Need for New Models of the Spin Crossover? *Monatshefte Chem. Chem. Mon.* **2003**, *134*, 199–216. [[CrossRef](#)]
36. Siig, O.S.; Kepp, K.P. Iron(II) and Iron(III) spin crossover: Toward an optimal density functional. *J. Phys. Chem. A* **2018**, *122*, 4208–4217. [[CrossRef](#)] [[PubMed](#)]
37. Cirera, J.; Via-Nadal, M.; Ruiz, E. Benchmarking density functional methods for calculation of state energies of first row spin-crossover molecules. *Inorg. Chem.* **2018**, *57*, 14097–14105. [[CrossRef](#)] [[PubMed](#)]
38. Swart, M.; Groenhof, A.R.; Ehlers, A.W.; Lammertsma, K. Validation of exchange–correlation functionals for spin states of iron complexes. *J. Phys. Chem. A* **2004**, *108*, 5479–5483. [[CrossRef](#)]



© 2019 by the authors. Licensee MDPI, Basel, Switzerland. This article is an open access article distributed under the terms and conditions of the Creative Commons Attribution (CC BY) license (<http://creativecommons.org/licenses/by/4.0/>).



Cite this: *New J. Chem.*, 2019, 43, 4937

# Ion-pair complexes of Schiff base Fe(III) cations and complex anions†

 Ivan Nemeč, <sup>a,b</sup> Pavel Zoufalý, <sup>a</sup> Paweł Jewula, <sup>b</sup> Peter Antal, <sup>a</sup>  
Wolfgang Linert <sup>c</sup> and Radovan Herchel <sup>a</sup>

Compound  $[\text{Fe}(\text{H}_2\text{-4OH-L}^6)]\text{Cl}$  was used for preparation of four new ion-pair complexes with general formula:  $[\text{Fe}(\text{H}_2\text{-4OH-L}^6)]\text{M}(\text{L}^3)_2 \cdot \text{H}_2\text{O}$  ( $\text{M} = \text{Co}^{\text{III}}$  (**3a**),  $\text{Cr}^{\text{III}}$  (**3b**) and  $\text{Fe}^{\text{III}}$  (**3c**)) and  $[\text{Fe}(\text{H}_2\text{-4OH-L}^6)]\text{-}[\text{Ag}(\text{CN})_2]$  (**3d**), where  $\text{H}_4\text{-4OH-L}^6 = N,N'$ -bis[2,4-dihydroxy-(benzylideneamino)ethyl]ethane-1,2-diamine and  $\text{H}_2\text{L}^3 = 2\text{-}[(E)\text{-}[(2\text{-hydroxyphenyl})\text{imino}]\text{methyl}]\text{phenol}$ . Furthermore, two  $[\text{Fe}(\text{H-4OH-L}^6)]$  complexes (**1a** and **1b**) with monodeprotonated hexadentate ligands were prepared. The crystal structures were determined by single-crystal X-ray measurements for all the above-mentioned complexes excluding **3c**. Its isostructurality with **3a–b** was confirmed by powder X-ray diffraction. The magnetic properties were investigated by static magnetic measurements and they are dominated by the high spin ground state of the complex cations and anions and at a smaller scale by the intermolecular interactions present among the molecules. The susceptibility and magnetization data were fitted simultaneously using the model for monomeric complexes including the zero-field splitting and the molecular field correction and these studies were supported also by CASSCF/NEVPT2 and BS-DFT calculations.

Received 11th January 2019,  
Accepted 19th February 2019

DOI: 10.1039/c9nj00192a

rsc.li/njc

## Introduction

Magnetic materials with two or more distinct properties – so-called multifunctional magnetic materials – attract a lot of attention due to their potential technological applications.<sup>1</sup> In order to achieve a combination of functional properties a convenient synthetic method is to assemble two diverse species possessing properties of interest. This can be done *via* a supramolecular approach or simply by assembling cations and anions with desired properties. This approach has proved to be successful when bistable spin-crossover (SCO) cations are used as molecular switches, modulating the physical response of their anionic counterparts in the crystal lattice of the hybrid material: *e.g.*, the SCO phenomenon affecting the luminescence of counter anions in solution,<sup>2</sup> or the conductivity of nickel bithiolene anions in the solid state,<sup>3</sup> or the magnetic properties of compounds composed of SCO cations inserted between the

anionic layers of ferrimagnetic oxalate polymers, or layered ferromagnets.<sup>4</sup> Furthermore, the combination of the  $\text{Co}^{\text{II}}$  and  $\text{Fe}^{\text{III}}$  complex ions led to the preparation of a coordination polymer exhibiting single-chain magnet (SCM) behaviour and an electron-transfer coupled spin transition.<sup>5</sup> In the case of the  $[\text{Mn}_2(\text{saltmen})_2\text{-Fe}(\text{LN5})(\text{CN})_2](\text{ClO}_4)_2$  chain polymer (saltmen =  $N,N'$ -(1,1,2,2-tetramethylethylene)bis(salicylideneimine), LN5 = 2,13-dimethyl-3,6,9-12,18-pentaazabicyclo[12.3.1]octadeca-1(18),2,12,14,16-pentaene) the SCM behaviour is induced by photo-switching of the  $\text{Fe}^{\text{II}}$  bridging unit.<sup>6</sup> Co-crystallization of the  $\text{Cr}^{\text{III}}$  single-ion magnet with the dinuclear  $\text{Fe}^{\text{II}}$  supramolecular host led to the preparation of a magnetic multifunctional material exhibiting SCO and slow relaxation of magnetization simultaneously.<sup>7</sup>

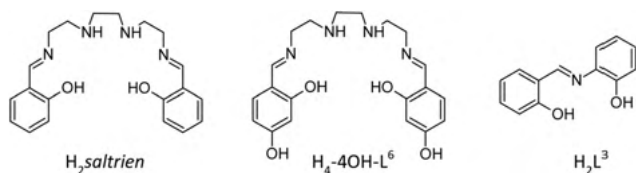
The SCO phenomenon has been well documented for the mononuclear and polynuclear  $\text{Fe}^{\text{III}}$  compounds with pseudo-octahedral  $\text{FeN}_4\text{O}_2$  coordination polyhedra<sup>8</sup> and several interesting ferric compounds with cooperative SCO accompanied by thermal hysteresis or exhibiting light-induced spin-state trapping have been previously reported.<sup>9</sup> The group of such compounds with saltrien ligands ( $\text{H}_2\text{saltrien} = N,N'$ -bis[2-hydroxy-(benzylideneamino)ethyl]ethane-1,2-diamine) is a popular example of  $\text{Fe}^{\text{III}}$  SCO complexes,<sup>8,10</sup> because these ligands are well-known for providing the appropriate ligand-field strength for the  $\text{Fe}^{\text{III}}$  ions to exhibit SCO. The modification of the saltrien ligand with peripheral hydroxyl groups at the fourth position of its phenyl rings results in  $\text{H}_4\text{-4OH-L}^6$  ( $N,N'$ -bis[2,4-dihydroxy-(benzylideneamino)ethyl]ethane-1,2-diamine, Scheme 1), which can act more diversely in formation of intermolecular contacts of significant

<sup>a</sup> Department of Inorganic Chemistry, Faculty of Science, Palacký University, 17. listopadu 1192/12, 771 46 Olomouc, Czech Republic.  
E-mail: ivan.nemec@upol.cz, ivan.nemec@ceitec.vutbr.cz

<sup>b</sup> Central European Institute of Technology, CEITEC BUT, Technická 3058/10, 61600, Brno, Czech Republic

<sup>c</sup> Institute of Applied Synthetic Chemistry, Vienna University of Technology, 1060 Vienna, Austria

† Electronic supplementary information (ESI) available: Powder diffraction patterns, results of BS-DFT calculations and crystal structure parameters and refinements. CCDC 1890216–1890219. For ESI and crystallographic data in CIF or other electronic format see DOI: 10.1039/c9nj00192a



Scheme 1 Structural formulas of ligands  $H_2saltrien$  (left),  $H_4-4OH-L^6$  (middle), and  $H_2L^3$  (right).

strength than non-substituted saltrien. The peripheral hydroxyl groups of  $H_4-4OH-L^6$  can act as hydrogen bonding acceptors or donors. Furthermore, similarly to the saltrien ligand, secondary amine groups are possible donors and phenolic oxygen atoms acceptors of hydrogen bonding. Another type of non-covalent contacts often formed by the complexes with both types of ligands are ring–ring stacking interactions –  $\pi$ – $\pi$  stacking. To sum up, the  $[Fe(H_2-4OH-L^6)]^+$  cations can be interesting building blocks for construction of supramolecular assemblies and the resulting crystal structures can be stabilized by a plethora of significant non-covalent contacts.

The presented work has two basic goals: (a) to investigate possible utilization of  $[Fe(H_2-4OH-L^6)]^+$  cations in the construction of ion-pair complexes; and (b) to investigate the magnetic properties of the prepared compounds with the aim to elucidate weak magnetic exchange interactions mediated by non-covalent contacts.

In our previous paper we have reported the presence of magnetic exchange interactions in the mononuclear  $[Fe(4OH-L^6)]X$  complexes ( $X = Cl^-$ ,  $Br^-$ ,  $I^-$ ), which were mediated between the low-spin (LS)  $[Fe(H_2-4OH-L^6)]^+$  cations through intermolecular interactions, despite the fact that all of the potential exchange pathways were unusually long.<sup>11</sup> In order to clarify and explore this phenomenon, we have decided to study another model system, where the non-covalent interactions would interconnect the  $[Fe(H_2-4OH-L^6)]^+$  cations with the complex anions carrying a different magnetic ground state. Therefore, we prepared a series of trivalent Schiff base anionic complexes of general formula  $K[M(L^3)_2] \cdot H_2O$ , where  $H_2L^3 = 2-[(E)-[2-hydroxyphenyl]imino]methylphenol$  and  $M = Co^{III}$  (**2a**),  $Cr^{III}$  (**2b**), and  $Fe^{III}$  (**2c**). By using these precursor complexes, we prepared an isostructural series of the  $[Fe(H_2-4OH-L^6)][M(L^3)_2] \cdot H_2O$  complexes ( $M = Co^{III}$  (**3a**),  $Cr^{III}$  (**3b**) and  $Fe^{III}$  (**3c**)). As another diamagnetic complex counter-anion, but with a linear shape, the potassium salt of  $[Ag(CN)_2]^-$  was used to obtain  $[Fe(H_2-4OH-L^6)][Ag(CN)_2]$  (**3d**). Furthermore, deprotonation of the parent precursor compound  $[Fe(H_2-4OH-L^6)]Cl$  (**1**) was studied. A possibility of mono-deprotonation to  $[Fe(H-4OH-L^6)] \cdot nH_2O$  compounds was revealed and the existence of two solvatomorphs  $[Fe(H-4OH-L^6)] \cdot (1a)$  and  $[Fe(H-4OH-L^6)] \cdot 2H_2O$  (**1b**) was confirmed. The detailed investigation of the magnetic properties of compounds **1a** and **3a–d** is reported.

## Results and discussion

### Synthesis

Our interest to study  $Fe^{III}$  complexes involving the  $H_4-4OH-L^6$  ligand was not only because of possible SCO behaviour of such

compounds but also due to the possibility of deprotonation of the peripheral hydroxyl groups of the ligand followed by preparation of compounds involving  $[Fe(4OH-L^6)]^-$  anions. These could be highly interesting, because  $Fe^{III}$  SCO compounds composed of complex anions are very rare<sup>8,12</sup> and could be further used for the preparation of multifunctional materials in which the anionic part would be switchable. Therefore, we focused our attention on deprotonation of the  $[Fe(H_2-4OH-L^6)]Cl$  compound. Soon it was confirmed that even for very basic methanolic solutions, we can obtain only mono-deprotonated complex  $[Fe(H-4OH-L^6)]$  (**1a**) which is rather stable. Remarkably, this complex does not decompose even in a solution with molar ratio  $1:KOH = 1:10$  and again, compound **1a** can be isolated as a single product. Compound  $[Fe(H-4OH-L^6)] \cdot 2H_2O$  (**1b**) was prepared as a side product in deprotonation of **1** by weak bases such as 4,4'-bipyridine or pyrazine, but the attempts for preparation of **1b** as a pure phase failed. Note: the phase purity of deprotonated compounds was always confirmed by XPRD (Fig. S1 in the ESI†).

Three compounds with general formula  $[Fe(H_2-4OH-L^6)][M(L^3)_2] \cdot H_2O$  ( $M = Co^{III}$  (**3a**),  $Cr^{III}$  (**3b**),  $Fe^{III}$  (**3c**)) were prepared by substitution of the chloride anion (elimination of  $KCl$ ) from the precursor  $[Fe(H_2-4OH-L^6)]Cl$  complex with the  $[M(L^3)_2]^-$  complex anions ( $K[M(L^3)_2] \cdot H_2O$ ,  $M = Co^{III}$  (**2a**),  $Cr^{III}$  (**2b**),  $Fe^{III}$  (**2c**)). The  $Cr^{III}$  and  $Co^{III}$  complexes are kinetically inert in terms of reactivity; therefore, they can be easily used for the preparation of the bimetallic supramolecular frameworks without side products. In a similar manner, the compound  $[Fe(H_2-4OH-L^6)][Ag(CN)_2]$  (**3d**) was prepared by substitution of the chloride anion by the  $[Ag(CN)_2]^-$  anion in methanolic solution.

### Crystal structures

**$[Fe(H-4OH-L^6)]$  compounds.** The crystal structures of both mono-deprotonated compounds **1a** and **1b** were determined using single-crystal X-ray diffraction. First, it must be noted that the crystallinity of **1a** is poor and despite numerous tries, the collected X-ray data are of very bad quality and the refined structure does not fulfill IUCr standards. However, the structural information is important for the analysis of its magnetic properties and therefore, it will be briefly discussed in this article, while the structural file was submitted to the Cambridge Structural Database (CSD) as a Privat Comm.<sup>13</sup>

Compound **1a** crystallizes in a monoclinic lattice with the space group  $P2_1/c$  (Table S1 in the ESI†). The central  $Fe^{III}$  atom is coordinated by four nitrogen and two oxygen atoms from the  $[H-4OH-L^6]^{3-}$  ligand and these atoms form together a distorted octahedral coordination environment (Fig. 1). The bond lengths in the coordination polyhedron correspond well with the high-spin (HS) state,<sup>14</sup> with the longest metal–ligand (M–L) bond lengths observed between the  $Fe^{III}$  and secondary amine atoms ( $d(Fe-N_{am}) = 2.209(17)$  and  $2.252(17)$  Å), while the imine nitrogen atoms form shorter Fe– $N_{im}$  bonds ( $2.052(17)$  and  $2.087(17)$  Å). The shortest M–L bonds are found for phenolic oxygen atoms:  $d(Fe-O) = 1.893(14)$  and  $1.919(14)$  Å.

The angular distortion parameter  $\Sigma$  is adopting the value of  $90.2^\circ$ , which is rather large but still typical for the HS



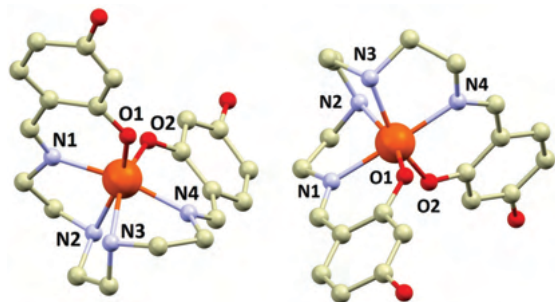


**Fig. 1** The drawing of the molecular structure of the  $[\text{Fe}(\text{H-4OH-L}^6)]$  complex in **1a** (left) and **1b** (right). The hydrogen atoms are omitted for clarity. Selected bond lengths (in Å): **1a**:  $\text{Fe1-N1} = 2.052(17)$ ,  $\text{Fe1-N2} = 2.209(17)$ ,  $\text{Fe1-N3} = 2.252(17)$ ,  $\text{Fe1-N4} = 2.087(17)$ ,  $\text{Fe1-O1} = 1.893(14)$ ,  $\text{Fe1-O2} = 1.919(14)$ , **1b**:  $\text{Fe1-N1} = 2.087(5)$ ,  $\text{Fe1-N2} = 2.182(6)$ ,  $\text{Fe1-N3} = 2.201(6)$ ,  $\text{Fe1-N4} = 2.078(5)$ ,  $\text{Fe1-O1} = 1.915(5)$ ,  $\text{Fe1-O2} = 1.911(4)$ .

$[\text{Fe}(\text{saltrien})]^+$  derivatives.<sup>11</sup> Previously, it was shown that the shape of the  $[\text{Fe}(\text{saltrien})]^+$  molecules might play a non-negligible role in the occurrence of SCO.<sup>15</sup> The parameter used for shape characterization is the dihedral angle  $\alpha$  measured between the least-square planes of the aromatic rings of the coordinated saltrien<sup>2-</sup> ligand. In **1a** this angle adopts a value of  $105.4^\circ$ , which is more typical for purely HS than SCO complexes.<sup>15</sup>

Compound **1b** crystallizes in an orthorhombic lattice with the space group  $P2_12_12_1$ . The asymmetric unit of **1b** contains one  $[\text{Fe}(\text{H-4OH-L}^6)]$  molecule and two lattice water molecules.

A distorted octahedral polyhedron is formed by the coordinated  $\text{H-4OH-L}^6$  ligand. The  $\text{Fe-N}_{\text{am}}$  bond lengths are a little bit shorter than in **1a**:  $2.182(6)$  and  $2.201(6)$  Å. The  $\text{Fe-N}_{\text{im}}$  and  $\text{Fe-O}$  bond lengths are very similar to those observed for **1a**:  $d(\text{Fe-N}_{\text{im}}) = 2.078(5)$  and  $2.087(5)$  Å,  $d(\text{Fe-O}) = 1.915(5)$  and  $1.911(4)$  Å. The  $\Sigma$  parameter is smaller ( $85.2^\circ$ ) than in **1a** indicating slightly smaller angular distortion. The  $\alpha$  angle ( $114.0^\circ$ ) is wider than in **1a**.

Despite a rather large similarity of their molecular structures the compounds **1a** and **1b** differ significantly in their crystal packing arrangements. In **1a**, the  $[\text{Fe}(\text{H-4OH-L}^6)]$  molecules are arranged into chain substructures *via*  $\text{O-H}\cdots\text{O}$  hydrogen bonding between the protonated and deprotonated peripheral hydroxy groups of the adjacent  $[\text{Fe}(\text{H-4OH-L}^6)]$  molecules (Fig. 2a), which is rather strong as can be indicated by the short donor $\cdots$ acceptor distance ( $2.504(3)$  Å). The secondary amine groups form weaker  $\text{N-H}\cdots\pi$  non-covalent contacts with aromatic rings of the neighbouring  $[\text{Fe}(\text{H-4OH-L}^6)]$  molecules (the shortest  $\text{N}\cdots\text{C}_{\text{g}}^{\text{b}}$  distance is  $3.630(3)$  Å, where  $\text{C}_{\text{g}}^{\text{b}}$  represents the centroid of the C-C bond from the aromatic ring closest to the donor group).

In **1b**, the  $[\text{Fe}(\text{H-4OH-L}^6)]$  molecules are assembled in helices in the direction of the *a* axis. This is again due to  $\text{O-H}\cdots\text{O}$  hydrogen bonding between the protonated and deprotonated peripheral hydroxy groups of the helically ordered  $[\text{Fe}(\text{H-4OH-L}^6)]$  molecules. This hydrogen bond adopts a bit longer donor $\cdots$ acceptor distance ( $2.606(7)$  Å) than the similar one in **1a**.

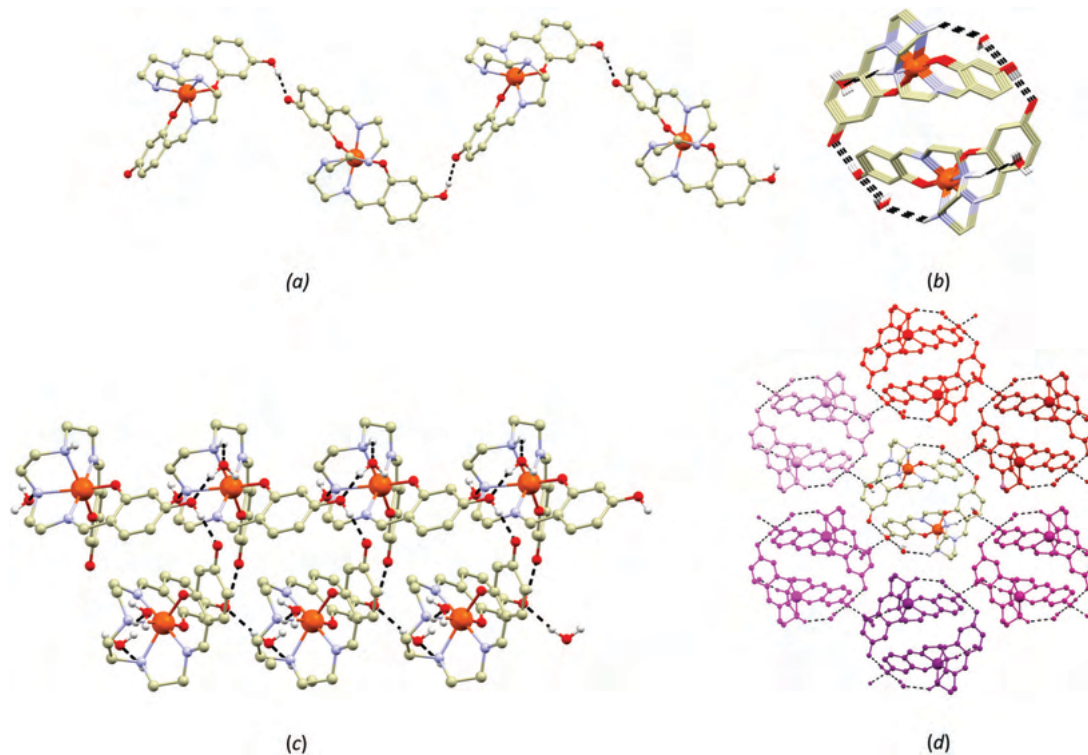


**Fig. 2** (a) A perspective view of the chain crystal packing motif in **1a**. A top view along the *a* axis (b) and side view along the *c* axis (c) of the helical supramolecular chain substructure in **1b**. A perspective view of interconnections of the supramolecular helices in **1b** (d). The hydrogen atoms (except for those involved in hydrogen bonding) are omitted for clarity and hydrogen bonding is displayed as black dashed lines.

Furthermore, the protonated peripheral hydroxy group acts also as an acceptor of two O–H···O hydrogen bonds with the lattice water molecules ( $d(\text{O} \cdots \text{O}) = 2.728(8)$  and  $2.832(8)$  Å). Remarkably, both lattice water molecules form regular hydrogen bonds only by involving only one of their hydrogen atoms, while the remaining form O–H··· $\pi$  contacts with aromatic rings of the adjacent complex molecules (the O···C<sub>g</sub><sup>b</sup> distances are  $3.728(9)$  and  $3.373(9)$  Å).

Two secondary amine groups of the [Fe(H-4OH-L<sup>6</sup>)] molecules form N–H···O hydrogen bonds with the lattice water molecules. One is involved in stabilization of the helix substructure ( $d(\text{N} \cdots \text{O}) = 3.355(9)$  Å, Fig. 2b and c) and it is significantly weaker than the second one, which provides a N–H···O(H)–H···O(H)–R type of interconnection between the neighbouring helices ( $d(\text{N} \cdots \text{O}) = 3.022(9)$  Å, Fig. 2d).

**[Fe(H<sub>2</sub>-4OH-L<sup>6</sup>)]<sup>+</sup> compounds.** For compounds with general formula [Fe(H<sub>2</sub>-4OH-L<sup>6</sup>)]<sup>+</sup>[M(L<sup>3</sup>)<sub>2</sub>]<sup>−</sup>·H<sub>2</sub>O, M = Co<sup>III</sup> (**3a**), Cr<sup>III</sup> (**3b**) and Fe<sup>III</sup> (**3c**), the crystal structures were determined by single-crystal X-ray crystallography for **3a** and **3b** and it was revealed that they are isostructural, crystallizing in the triclinic *P* $\bar{1}$  space-group (Table S1 in the ESI<sup>†</sup>). The isostructurality of **3c** to **3a–b** was confirmed by X-ray powder diffraction measurements (Fig. S2 in the ESI<sup>†</sup>).

Complex **3d** crystallizes in the orthorhombic space group *Iba*2. The crystal structures of the compounds **3a**, **3b** and **3d** were measured at different temperatures: **3a** and **3d** at 100 K, and **3b** at ambient temperature (293 K). In all three cases, the M–L bond lengths correspond to the HS state and are similar to those observed for the [Fe(H-4OH-L<sup>6</sup>)] compounds **1a** and **1b** (in Å):  $d(\text{Fe–N}_{\text{am}}) = 2.17\text{--}2.20$ ,  $d(\text{Fe–N}_{\text{im}}) = 2.09\text{--}2.12$ ,  $d(\text{Fe–O}) = 1.90\text{--}1.93$  (Fig. 3). Also, the ligand geometry, as described by  $\alpha$ , is very similar to that reported for the HS [Fe(saltrien)]<sup>+</sup> derivatives ( $\alpha = 98.7^\circ$  (**3a**),  $100.2^\circ$  (**3b**),  $113.7^\circ$  (**3d**)).<sup>16</sup> The angular distortion also corresponds to the HS state of the complex cations well ( $\Sigma = 97.2^\circ$  in **3a**,  $97.9^\circ$  in **3b**,  $95.2^\circ$  in **3d**).

The crystal packing will be described for **3a–c** and **3d** separately. In **3a–c** the [Fe(H<sub>2</sub>-4OH-L<sup>6</sup>)]<sup>+</sup> cations form centrosymmetric {[Fe(H<sub>2</sub>-4OH-L<sup>6</sup>)]<sup>+</sup>]<sub>2</sub> dimers (*R*<sub>2</sub><sup>2</sup>(16) synthon, Fig. 4a)

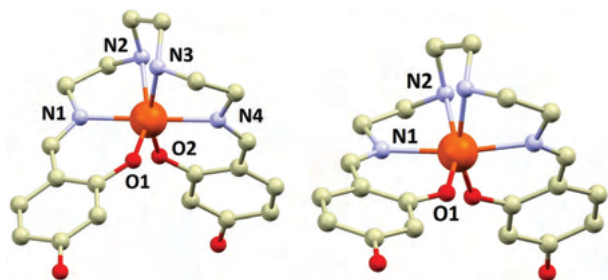


**Fig. 3** The drawing of the molecular structure of the [Fe(H<sub>2</sub>-4OH-L<sup>6</sup>)]<sup>+</sup> complex cations in **3a** and **3b** (left) and **3d** (right). The hydrogen atoms are omitted for clarity. Selected bond lengths (in Å): **3a**: Fe1–N1 = 2.107(2), Fe1–N2 = 2.179(2), Fe1–N3 = 2.197(2), Fe1–N4 = 2.095(2), Fe1–O1 = 1.9295(17), Fe1–O2 = 1.9124(17), **3b**: Fe1–N1 = 2.093(4), Fe1–N2 = 2.186(3), Fe1–N3 = 2.184(3), Fe1–N4 = 2.100(4), Fe1–O1 = 1.921(3), Fe1–O2 = 1.906(3), **3d**: Fe1–O1 = 1.911(2), Fe1–N1 = 2.116(2), Fe1–N2 = 2.178(2).

stabilized by the offset  $\pi$ – $\pi$  stacking interaction (with the shortest C···C distance  $3.766(3)$  Å in **3a** and  $3.709(6)$  in **3b**) and N–H···O hydrogen bonding between the secondary amine group and phenolic oxygen atoms. The N–H···O hydrogen bond is of medium strength with  $d(\text{N} \cdots \text{O}) = 3.027(3)$  Å (**3a**) and  $3.085(5)$  Å (**3b**). The same kind of supramolecular synthon was previously observed also in the crystal structures of the [Fe(H<sub>2</sub>-4OH-L<sup>6</sup>)]X compounds (X = Cl<sup>−</sup>, Br<sup>−</sup>, I<sup>−</sup>), where the *R*<sub>2</sub><sup>2</sup>(16) synthon is propagated by both secondary amine groups of the [Fe(H<sub>2</sub>-4OH-L<sup>6</sup>)]<sup>+</sup> molecules and thus a 1D chain is formed.<sup>11</sup> In **3a–c** the second amino group forms a N–H··· $\pi$  non-covalent interaction with the aromatic ring of co-crystallized complex anion [M(L<sup>3</sup>)<sub>2</sub>]<sup>−</sup> (the N···C<sub>g</sub><sup>r</sup> distances are  $3.251(3)$  Å in **3a** and  $3.346(6)$  Å in **3b**, where C<sub>g</sub><sup>r</sup> stands for the centroid of the corresponding aromatic ring). Similarly to [Fe(H<sub>2</sub>-4OH-L<sup>6</sup>)]X, both peripheral hydroxyl groups in the crystal structure of **3a–c** form hydrogen bonding with anions – in this case, with phenolic oxygen atoms of the L<sup>3</sup><sup>2−</sup> ligands from the complex anions [M(L<sup>3</sup>)<sub>2</sub>]<sup>−</sup> (Fig. 4b). The O–H···O hydrogen bonds are rather strong:  $d(\text{O–H} \cdots \text{O}) = 2.604(2)$  and  $2.664(2)$  Å in **3a**,  $2.633(4)$  and  $2.673(4)$  Å in **3b**. The overall supramolecular structure can be described as ladder-like with [Fe(H<sub>2</sub>-4OH-L<sup>6</sup>)]<sup>+</sup> rungs. The infinite “ladders” are interconnected by the N–H··· $\pi$  contacts. In the cavities between the ladders the co-crystallized water molecules are attached to the phenolic oxygen atoms of the [Fe(H<sub>2</sub>-4OH-L<sup>6</sup>)]<sup>+</sup> cations by the O–H···O hydrogen bonds with  $d(\text{O} \cdots \text{O}) = 2.871(3)$  Å in **3a** and  $3.014(8)$  Å in **3b**.

In **3d**, the [Fe(H<sub>2</sub>-4OH-L<sup>6</sup>)]<sup>+</sup> cations are organized into two interpenetrating supramolecular networks (Fig. 4). Each network is formed by N–H···N and O–H···N hydrogen bonds in which the secondary amine and peripheral hydroxyl groups of the [Fe(H<sub>2</sub>-4OH-L<sup>6</sup>)]<sup>+</sup> molecules act as hydrogen bonding donors (Fig. 4c and d), while the nitrogen atoms from the cyanido ligands act as acceptors of the bifurcated hydrogen bond. The O–H···N hydrogen bond is significantly stronger than N–H···N ( $d(\text{N–H} \cdots \text{N}) = 3.178(3)$  Å,  $d(\text{O–H} \cdots \text{N}) = 2.753(3)$  Å).

### Magnetic properties

The magnetic properties of the compounds **1a** and **3a–d** were studied by simultaneous analysis of the temperature dependence (1.9–300 K) of the magnetic susceptibility and the field dependence (0–7 T) of the magnetization. All the studied compounds do not exhibit SCO behaviour and the Fe<sup>III</sup> ions in [Fe(H<sub>2</sub>-4OH-L<sup>6</sup>)]<sup>+</sup> or [Fe(H-4OH-L<sup>6</sup>)] molecules stay in the HS state ( $S = 5/2$ ) over the whole measured temperature range. In compounds with one spin carrier such as **1a** ([Fe(H-4OH-L<sup>6</sup>)]<sup>+</sup>) or **3a** and **3d** ([Fe(H<sub>2</sub>-4OH-L<sup>6</sup>)]<sup>+</sup>) the magnetic behaviour is dominated by the ground spin state of the central Fe<sup>III</sup> atoms and the value of the effective magnetic moment ( $\mu_{\text{eff}}/\mu_{\text{B}}$ ) at 300 K is close to the theoretical value of 5.9 and stays approximately constant down to 20 K where a sharp decrease of  $\mu_{\text{eff}}/\mu_{\text{B}}$  starts (Fig. 5). The compounds with paramagnetic complex cations and complex anions, **3b** and **3c**, have similar behaviour and their room temperature values of  $\mu_{\text{eff}}/\mu_{\text{B}}$  adopt values for two unpaired spins  $5/2\text{--}3/2$  for **3b** and  $5/2\text{--}5/2$  for **3c**, respectively. The observed decrease of  $\mu_{\text{eff}}/\mu_{\text{B}}$  at the lowest temperatures for

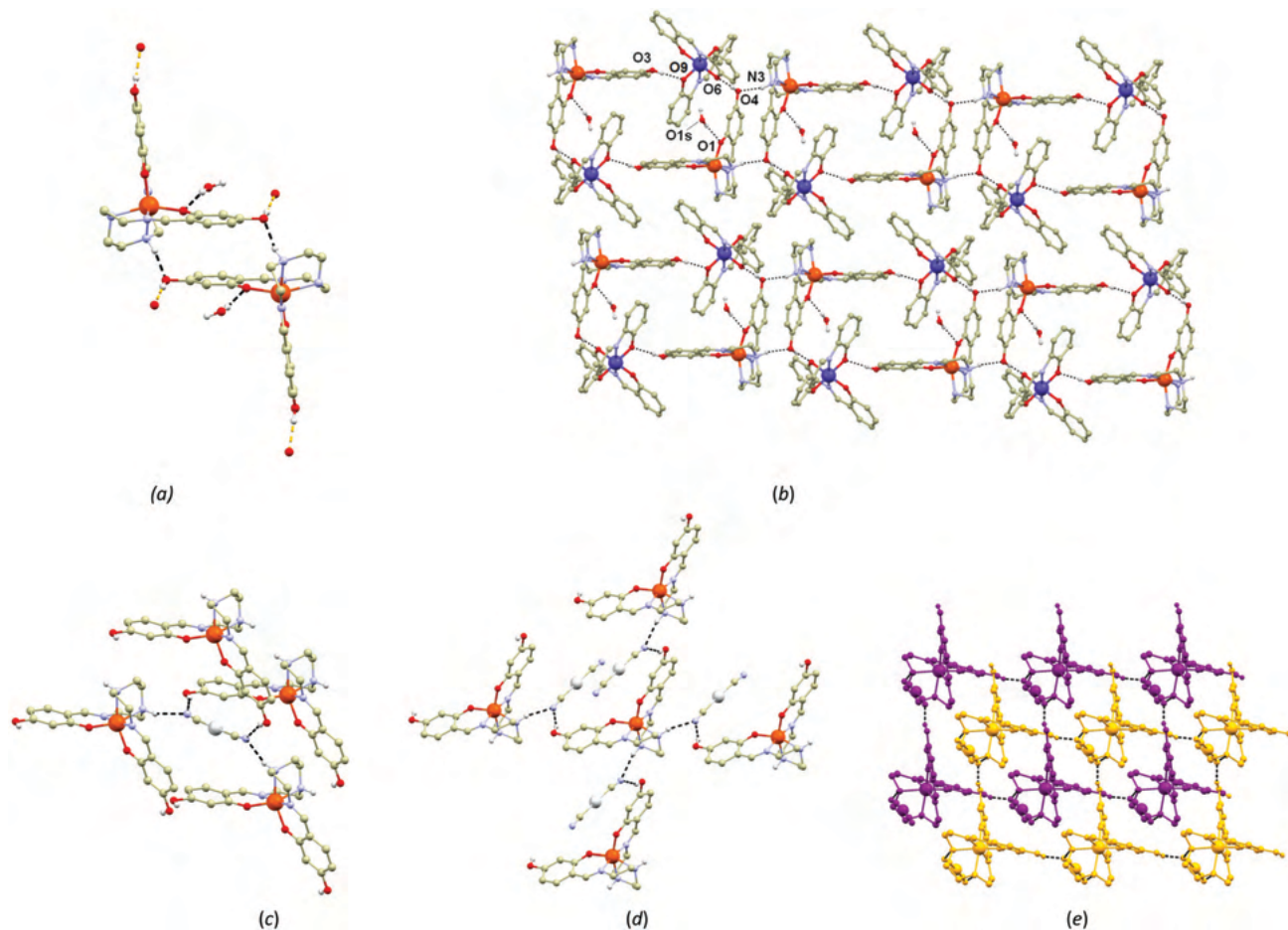


Fig. 4 (a) A perspective view of (a) the supramolecular dimer  $\{[\text{Fe}(\text{H}_2\text{-4OH-L}^6)]_2\}^{2+}$  and its hydrogen bonding interactions in **3a–c**; (b) of a fragment of the crystal structure of the compounds **3a–c**; and of non-covalent interactions provided by the  $[\text{Ag}(\text{CN})_2]^-$  anion (c) and  $[\text{Fe}(\text{H}_2\text{-4OH-L}^6)]^+$  cations (d) in **3d**. Depiction of two interpenetrating 2D networks (differentiated by orange and purple colors) in **3d** (e). The hydrogen atoms (except for those involved in hydrogen bonding) are omitted for clarity and hydrogen bonding is displayed as black dashed lines.

all compounds can be ascribed to zero-field splitting (ZFS) and/or to the intermolecular interactions providing weak anti-ferromagnetic magnetic exchange interactions between the neighbouring molecules in the crystal lattice. However, these intermolecular magnetic interactions should be weak because there are no maxima in the temperature dependence of the molar susceptibility. Indeed, the theoretical calculations (*vide infra*) suggest only weak anti-ferromagnetic exchange among paramagnetic complex ions. Therefore, the magnetic data were treated with a spin Hamiltonian involving the zero-field splitting terms – the axial and rhombic terms ( $D$  and  $E$ ) and the intermolecular magnetic interactions were described by the molecular field correction ( $zj$ ) as

$$\hat{H} = \sum_{i=1}^N D_i (\hat{S}_{z,i}^2 - \hat{S}_i^2 / 3) + E_i (\hat{S}_{x,i}^2 - \hat{S}_{y,i}^2) + \mu_{\text{B}} B g_i \hat{S}_{a,i} - zj \langle \hat{S}_a \rangle \hat{S}_a \quad (1)$$

where  $N = 1$  for **1a**, **3a**, and **3d** and  $N = 2$  for **3b** and **3c**. Then, the molar magnetization in the  $a$ -direction of the magnetic field,

$M_a$ , was numerically calculated as

$$M_a = -N_{\text{A}} \frac{\sum_i \left( \sum_k \sum_l C_{ik}^+ (Z_a)_{kl} C_{li} \right) \exp(-\varepsilon_{a,i}/kT)}{\sum_i \exp(-\varepsilon_{a,i}/kT)} \quad (2)$$

where  $Z_a$  is the matrix element of the Zeeman term for the  $a$ -direction of the magnetic field and  $C$  are the eigenvectors resulting from the diagonalization of the complete spin Hamiltonian matrix. The presence of  $zj$  means that an iterative procedure must be applied. The final calculated molar magnetization was calculated as an integral average to properly simulate the powder sample signal.

$$M_{\text{mol}} = 1/4\pi \int_0^{2\pi} \int_0^{\pi} M_a \sin \theta d\theta d\varphi \quad (3)$$

Both temperature and field dependent magnetic data were fitted simultaneously to obtain a consistent set of parameters, which are listed in Table 1. In order to not over-parametrize the fitting procedure, we assumed  $D_{\text{Fe}} = D_{\text{Cr}} = D$  and  $E_{\text{Fe}} = E_{\text{Cr}} = E$  for **3b** taking into account the results from CASSCF/NEVPT2



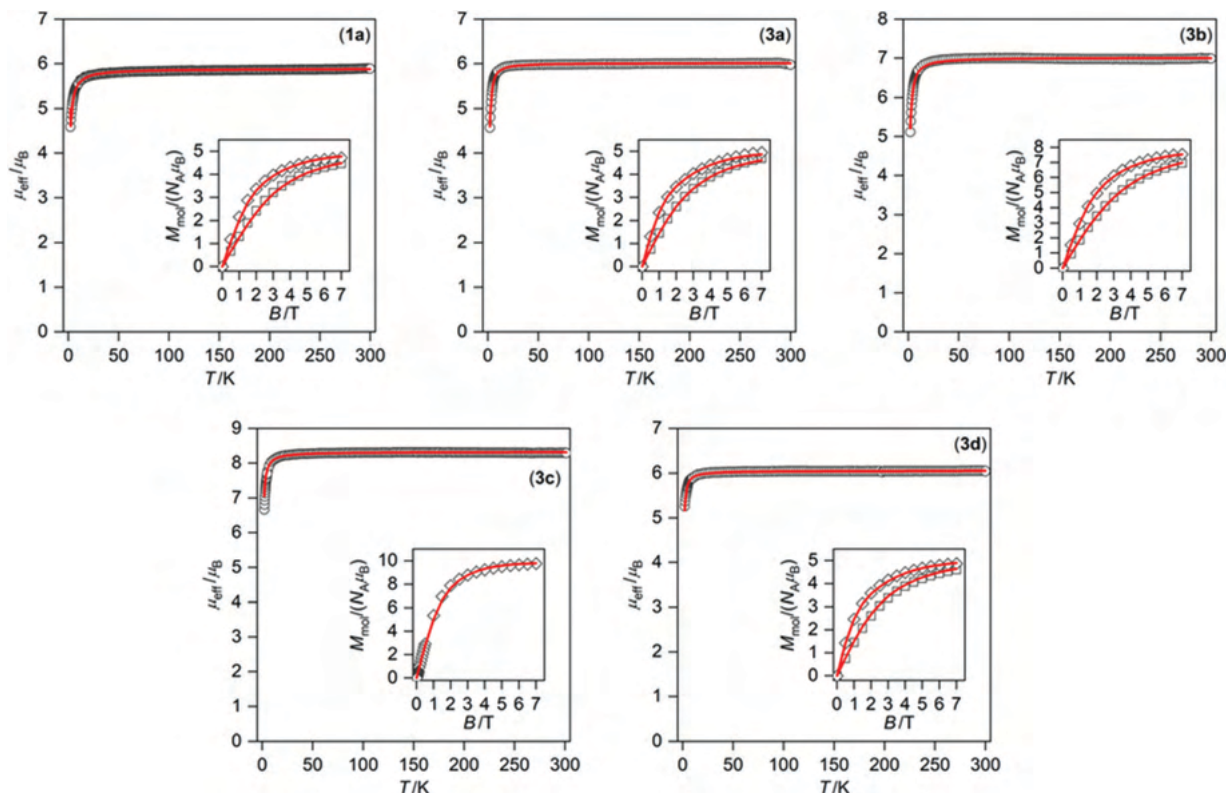


Fig. 5 Magnetic properties of compounds **1a–3d**. Each plot shows the temperature dependence of the effective magnetic moment and in the inset, the isothermal magnetizations measured at  $T = 2.0$  ( $\diamond$ ) and  $4.6$  K ( $\square$ ) are given. Experimental data – empty symbols, full red lines – the best fit calculated with parameters listed in Table 1.

Table 1 Comparison of theoretically calculated and fitted spin Hamiltonian parameters for complexes **1a–3d**

Compound	<b>1a</b>	<b>1b</b>	<b>3a</b>	<b>3b</b>	<b>3c</b>	<b>3d</b>
Metal ions	Fe <sup>III</sup>	Fe <sup>III</sup>	Fe <sup>III</sup> -Co <sup>III</sup>	Fe <sup>III</sup> -Cr <sup>III</sup>	Fe <sup>III</sup> -Fe <sup>III</sup>	Fe <sup>III</sup> -Ag <sup>I</sup>
Spins	5/2	5/2	5/2-0	5/2-3/2	5/2-5/2	5/2-0
CASSCF/NEVPT2 calculated parameters						
$D$ (cm <sup>-1</sup> )	-0.476	-0.555	-0.423	-0.459/-0.382	—	-0.332
$E/D$	0.242	0.200	0.077	0.088/0.170	—	0.203
$g_{1-3}$	1.999	1.999	1.999	1.999/1.969	—	1.999
	1.999	1.999	1.999	1.999/1.972	—	1.999
	1.999	1.999	1.999	1.999/1.973	—	1.999
$B$ (cm <sup>-1</sup> )	982	993	995/1131	996/997	—	985
$C$ (cm <sup>-1</sup> )	3772	3753	3800/3793	3788/3120	—	3793
$\zeta$ (cm <sup>-1</sup> )	442	442	444/551	443/257	—	443
Analysis of the experimental magnetic data						
$D$ (cm <sup>-1</sup> )	-0.88		-1.04	-1.15	-0.43	-1.03
$E/D$	0.13		0.00	0.22	0.33	0.14
$g$	1.99		2.03	1.98	1.99	2.04
$zj$ (cm <sup>-1</sup> )	-0.27		-0.12	-0.16	-0.15	-0.086
$\chi_{\text{TIP}}$ (10 <sup>-9</sup> m <sup>3</sup> mol <sup>-1</sup> )	0.26					0.65

calculations (*vide infra*) and also both  $g$ -factors were assumed equal and isotropic,  $g_{\text{Fe}} = g_{\text{Cr}} = g_{\text{iso}}$ . A similar simplification was also applied to **3c**. The  $D$ -parameter for Fe<sup>III</sup> was fitted in the range from  $-0.4$  to  $-1.2$  cm<sup>-1</sup> and  $g$ -factors are close to 2.0 as expected (Table 1). The molecular field correction parameter  $zj$  was found to be between  $-0.09$  and  $-0.3$  cm<sup>-1</sup>, confirming

weak antiferromagnetic exchange interactions among paramagnetic complex ions in the solid state.

### Theoretical calculations

The ORCA 4.0 software was utilized for Density Functional Theory (DFT) calculations of the isotropic exchange parameters



$J$  to assess the intermolecular magnetic exchange interactions in the studied complexes following our previous studies.<sup>17</sup> Thus, the well-known B3LYP functional was utilized in combination with the def2-TZVP basis set to calculate  $J$ -parameters based on the following Heisenberg spin Hamiltonian

$$\hat{H} = -J(\vec{S}_1 \cdot \vec{S}_2) \quad (4)$$

The broken-symmetry method was used to evaluate the energy difference between high-spin (HS) and broken-symmetry (BS) spin states,  $\Delta = E_{\text{BS}} - E_{\text{HS}}$ , and subsequently, the  $J$ -parameter was calculated by Yamaguchi's approach as

$$J = 2\Delta / (\langle S^2 \rangle_{\text{HS}} - \langle S^2 \rangle_{\text{BS}}) \quad (5)$$

The calculated  $J$ -parameters are listed in Fig. S3 (ESI<sup>†</sup>) for selected supramolecular dimers extracted from the experimental structures of **1b–3d** together with the plots of the spin density of BS states. These calculations showed the presence of weak antiferromagnetic exchange in these complexes.

Furthermore, post-Hartree–Fock multireference calculations based on the complete active space self-consistent field method (CASSCF) complemented with  $n$ -electron valence state perturbation theory (NEVPT2) were applied to mononuclear geometries extracted from the experimental X-ray data. The active space was defined by the metal  $d$ -orbitals and all multiplets arising from the  $3d^n$  electronic configuration were considered. These calculations correctly predicted the low spin state of Fe<sup>III</sup> in **1** and Co<sup>III</sup> in **3a**, whereas the high-spin state of Fe<sup>III</sup> in **1a–3d** – Fig. 6. Moreover, the splitting of  $d$ -orbitals evaluated by *ab initio* ligand field theory (AILFT) is also depicted in Fig. 6 showing the small variation of the  $d$ -orbital splitting in high-spin Fe<sup>III</sup> complexes. Next, the ZFS parameters and  $g$ -tensors were also calculated and the respective values of these parameters are listed in Table 1. The  $D$ -parameters were found to be all negative and small, the  $g$ -tensors of Fe<sup>III</sup> ions were isotropic, and the  $g$ -tensor of Cr<sup>III</sup> has almost negligible anisotropy too.

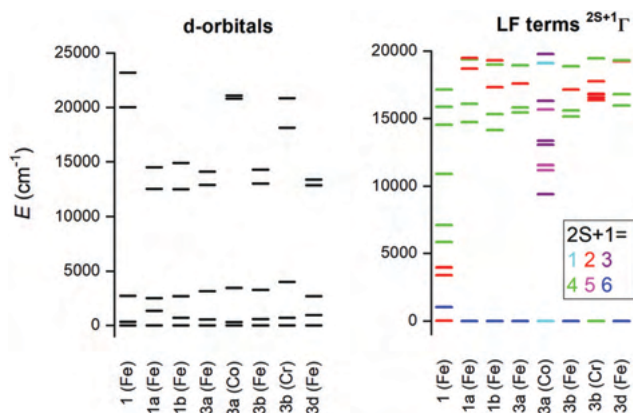


Fig. 6 The CASSCF/NEVPT2 calculations with CAS( $n$ ,5) active space for **1–3d**. Left: The energies of  $d$ -orbitals calculated by *ab initio* ligand field theory (AILFT). Right: The lowest ligand field terms with given multiplicities in colour.

## Conclusion

In the present manuscript we reported on the synthesis, crystal structures and magnetic properties of six new compounds prepared by (i) deprotonation of precursor complex  $[\text{Fe}(\text{H}_2\text{-4OH-L}^6)]\text{Cl}$ , which resulted in isolation of two solvatomorphs  $[\text{Fe}(\text{H-4OH-L}^6)]$  (**1a**) and  $[\text{Fe}(\text{H-4OH-L}^6)] \cdot 2\text{H}_2\text{O}$  (**1b**), and (ii) substitution of the chloride anion by complex anions:  $[\text{Fe}(\text{H}_2\text{-4OH-L}^6)][\text{M}(\text{L}^3)_2] \cdot \text{H}_2\text{O}$ ,  $\text{M} = \text{Co}^{\text{III}}$  (**3a**),  $\text{Cr}^{\text{III}}$  (**3b**) and  $\text{Fe}^{\text{III}}$  (**3c**) and  $[\text{Fe}(\text{H}_2\text{-4OH-L}^6)][\text{Ag}(\text{CN})_2]$  (**3d**). Crystal structures were determined for compounds **1a–b**, **3a–b**, and **3d** and it was revealed that the observed bond lengths and other structural parameters correspond with the HS state of the Fe<sup>III</sup> central atom. This was confirmed also by magnetic measurements which showed that compounds **1a** and **3a–d** do not exhibit SCO behavior, and this is also in agreement with the theoretical prediction calculated by the CASSCF/NEVPT2 method. The analysis of magnetic data and DFT calculations revealed that only weak antiferromagnetic interactions between the complex molecules are present. Despite the high spin nature of the final complexes, we might conclude that we proved the  $[\text{Fe}(\text{H}_2\text{-4OH-L}^6)]^+$  cations are appropriate building blocks for preparation of ion-pair complexes consisting of complex ions with different metal centers and, furthermore, the resulting compounds are rich in significant intermolecular interactions stabilizing their crystal structures.

## Experimental

All reagents and solvents were purchased from commercial sources (Sigma Aldrich) and used as received. Elemental analysis was carried out on a Flash EA 1112, ThermoFinnigan. Powder diffraction patterns were acquired with a Philips X'Pert in Bragg–Brentano geometry, using Ni-filtered Cu  $K_{\alpha 1,2}$  radiation.

Compound  $[\text{Fe}(\text{H}_2\text{-4OH-L}^6)]\text{Cl}$  was prepared by a procedure reported previously.<sup>11</sup> Compounds  $\text{K}[\text{Cr}(\text{L}^3)_2] \cdot \text{H}_2\text{O}$  (**2b**)<sup>18</sup> and  $\text{K}[\text{Fe}(\text{L}^3)_2] \cdot \text{H}_2\text{O}$  (**2c**)<sup>17a</sup> were prepared as reported previously;  $\text{K}[\text{Co}(\text{L}^3)_2] \cdot \text{H}_2\text{O}$  (**2a**) was prepared in the same fashion, but instead of  $\text{CrCl}_3 \cdot 6\text{H}_2\text{O}$  or  $\text{FeCl}_3 \cdot 6\text{H}_2\text{O}$  a stoichiometric amount of  $\text{CoCl}_2 \cdot 6\text{H}_2\text{O}$  was used.

## Synthesis

**Preparation of  $[\text{Fe}(\text{H-4OH-L}^6)]$  (**1a**).** 475 mg (1 mmol) of  $[\text{Fe}(\text{H}_2\text{-4OH-L}^6)]\text{Cl}$  was dissolved in 40 cm<sup>3</sup> of hot  $\text{CH}_3\text{OH}$ . Then, 100 mg (1.78 mmol) of KOH (in 4 cm<sup>3</sup> of  $\text{H}_2\text{O}$ ) was added and the dark violet solution was refluxed for 1 h, filtered, and set for controlled crystallization at room temperature. Brown crystals were obtained after 1 week and were isolated by filtration, washed with  $\text{CH}_3\text{OH}$  and dried first in a vacuum and then in the oven for 1 h at 50 °C.

Elemental analysis calcd (%) for  $\text{C}_{20}\text{FeH}_{23}\text{N}_4\text{O}_4$ ,  $M_w = 439.3$ : C, 54.7; H, 5.3; N, 12.7. Found: C, 54.2; H, 5.5; N, 12.3.

**Preparation of  $[\text{Fe}(\text{H}_2\text{-4OH-L}^6)][\text{M}(\text{L}^3)_2] \cdot \text{H}_2\text{O}$  ( $\text{M} = \text{Co}$  in **3a**,  $\text{Cr}$  in **3b**,  $\text{Fe}$  in **3c**).** 100 mg (0.21 mmol) of  $[\text{Fe}(\text{H}_2\text{-4OH-L}^6)]\text{Cl}$  was dissolved in boiling  $\text{CH}_3\text{OH}$  (40 cm<sup>3</sup>) and then 0.21 mmol of  $\text{K}[\text{M}(\text{L}^3)_2] \cdot \text{H}_2\text{O}$  (113 mg of **2a**, 113 mg of **2b**, 112 mg of **2c**) was added. The reaction mixture was then stirred for 30 min without

heating and then the solution was filtered through a paper filter and set for controlled crystallization at room temperature. Dark brown crystals were obtained after 2 days and were isolated by filtration, washed with CH<sub>3</sub>OH and dried in a vacuum.

Elemental analysis calcd (%) for **3a** C<sub>46</sub>CoFeH<sub>44</sub>N<sub>6</sub>O<sub>9</sub>, *M<sub>w</sub>* = 939.7: C, 58.8; H, 4.7; N, 8.9. Found: C, 58.7; H, 4.7; N, 8.8; for **3b**: C<sub>46</sub>CrFeH<sub>44</sub>N<sub>6</sub>O<sub>9</sub>, *M<sub>w</sub>* = 932.7: C, 59.2; H, 4.8; N, 9.0. Found: C, 59.4; H, 4.8; N, 8.8; for **3c**: C<sub>46</sub>Fe<sub>2</sub>H<sub>44</sub>N<sub>6</sub>O<sub>9</sub>, *M<sub>w</sub>* = 936.6: C, 59.0; H, 4.7; N, 9.0. Found: C, 59.1; H, 4.8; N, 8.9.

**Preparation of [Fe(H<sub>2</sub>-4OH-L<sup>6</sup>)]Ag(CN)<sub>2</sub> (**3d**).** 100 mg (0.21 mmol) of [Fe(H<sub>2</sub>-4OH-L<sup>6</sup>)]Cl was dissolved in boiling CH<sub>3</sub>OH (40 cm<sup>3</sup>) and then 0.23 mmol of K[Ag(CN)<sub>2</sub>] (45 mg in 4 cm<sup>3</sup> of water) was added. The mixture was stirred for 30 min without heating and then the solution was filtered through a paper filter and set for controlled crystallization at room temperature. The resulting solution was left to evaporate slowly. After 1 day, red block crystals of X-ray quality were isolated by filtration, washed with CH<sub>3</sub>OH and dried in a vacuum.

Elemental analysis calcd (%) for **3d** AgC<sub>22</sub>Fe<sub>1</sub>H<sub>24</sub>N<sub>6</sub>O<sub>4</sub>, *M<sub>w</sub>* = 600.2: C, 44.0; H, 4.0; N, 14.0. Found: C, 39.6; H, 3.8; N, 13.6.

### Magnetic data

Magnetic susceptibility and magnetization measurements were done using a SQUID magnetometer (MPMS, Quantum Design) in the temperature range *T* = 2–300 K at *B* = 0.1 T. The isothermal magnetization data were taken at *T* = 2.0 and 4.6 K, respectively, up to 7 T. The effective magnetic moment was calculated as usual:  $\mu_{\text{eff}}/\mu_{\text{B}} = 798(\chi' T)^{1/2}$  when SI units are employed.

### X-ray crystallography

Single crystal X-ray diffraction data were collected on an Oxford diffractometer Xcalibur2 with the Sapphire CCD detector and a fine-focused sealed tube (Mo K<sub>α</sub> radiation,  $\lambda = 0.71073 \text{ \AA}$ ) source and equipped with an Oxford Cryosystem nitrogen gas-flow apparatus. All structures were solved and refined (full-matrix least-squares on  $F_o^2 - F_c^2$ ) by using SHELXS-2014<sup>19</sup> incorporated into the WinGX program package.<sup>20</sup> For each structure its space group was checked by the ADSYMM procedure of the PLATON<sup>21</sup> software. All non-hydrogen atoms were refined anisotropically. The hydrogen atoms were placed into the calculated positions and they were included in the riding-model approximation with *U*<sub>iso</sub> = 1.2 or 1.5*U*<sub>eq</sub> (atom of attachment). All the crystal structures were visualized using the Mercury software.<sup>22</sup> Non-routine aspects of the structure refinement are as follows: unfortunately, crystals of **1b**, **3a** and **3b** were of poor quality with weak crystallinity causing their weak diffraction power. This resulted in troubles with the quality of collected data, such as low bond precision and a poor data/parameter ratio. Furthermore, some fragments of the complex molecules in the aforementioned compounds (aliphatic chain in **1b**, L3<sup>2-</sup> ligands in **3a** and **3b**) were positionally disordered. The best way to deal with these problems would be to model them as whole chain (**1b**) or molecule (**3a** and **3b**) disorders, but this was not possible due to the quality of the collected data. The structures of **3a** and **3b** contain also lattice water molecules,

which form only one significant hydrogen bond, while the second hydrogen atom forms a weak O–H··· $\pi$  contact. This led to significant thermal motion of the oxygen atoms and elongation of thermal ellipsoids. We tried to address these issues in the crystallographic information files.

### Theoretical calculations

All theoretical calculations were carried out with the ORCA 4.0 computational package.<sup>23</sup> The B3LYP DFT functional<sup>24</sup> was used for calculations of the isotropic exchange parameter *J* according to the Yamaguchi approach,<sup>25</sup> by comparing the energies of high-spin (HS) and broken-symmetry spin (BS) states. The polarized triple- $\zeta$  quality basis set def2-TZVP proposed by Ahlrichs and co-workers was used for all atoms.<sup>26</sup> The calculations utilized the RI approximation with the decontracted auxiliary def2/J Coulomb fitting basis set<sup>27</sup> and the chain-of-spheres (RIJCOSX) approximation to exact exchange<sup>28</sup> as implemented in ORCA. Increased integration grids (Grid6 and Gridx6 in the ORCA convention) and tight SCF convergence criteria were used in all calculations. The molecular fragment used in the calculations was extracted from the experimental X-ray structures. The calculated spin density was visualized with the VESTA 3 program.<sup>29</sup> The calculations were based on the state average complete active space self-consistent field (CASSCF)<sup>30</sup> wave functions complemented by N-electron valence second-order perturbation theory (NEVPT2)<sup>31</sup> using again the def2-TZVP basis set for all atoms. In the state-averaged approach, all multiplets for the given electron configuration were equally weighted. The ZFS parameters based on dominant spin-orbit coupling contributions from excited states were calculated through quasi-degenerate perturbation theory (QDPT),<sup>32</sup> in which an approximation to the Breit–Pauli form of the spin-orbit coupling operator (SOMF approximation)<sup>33</sup> and the effective Hamiltonian theory<sup>34</sup> were utilized. The calculations utilized the RIJCOSX approximation with the auxiliary coulomb basis def2/JK.<sup>35</sup> Increased integration grids (Grid6 and GridX6 in the ORCA convention) and tight SCF convergence criteria were used in all calculations. Additionally, *ab initio* ligand field analysis (AIFT) was done as implemented in ORCA, which resulted in the Racah parameters (*B* and *C*), the spin-orbit coupling constant  $\zeta$  and d-orbital energies.<sup>36</sup>

### Conflicts of interest

There are no conflicts to declare.

### Acknowledgements

The authors would like to thank to Dr Franz Werner for the XPRD measurements and their analysis. We are also grateful to Ľubor Dlháň (STU BA) for acquiring some of the magnetic data and to Prof. Hartmut Fuess (TU Darmstadt) for allowing I. N. to acquire single crystal data in his laboratory. This research was carried out under the project CEITEC 2020 (LQ1601) with financial support from the Ministry of Education, Youth and Sports of the Czech Republic under the National Sustainability

Programme II. I. N. and R. H. acknowledge financial support from the Grant Agency of the Czech Republic (GACR 17-08992S).

## Notes and references

- (a) A. B. Gaspar, V. Ksenofontov, M. Seredyuk and P. Gütllich, *Coord. Chem. Rev.*, 2005, **249**, 2661; (b) K. Senthil Kumar and M. Ruben, *Coord. Chem. Rev.*, 2017, **346**, 176.
- H. Matsukizono, K. Kuroiwa and N. Kimizuka, *Chem. Lett.*, 2008, **37**, 446.
- C. Faulmann, S. Dorbes, J. A. Real and L. Valade, *J. Low Temp. Phys.*, 2006, **142**, 265.
- (a) M. Clemente-León, E. Coronado, M. C. Giménez-López, A. Soriano-Portillo, J. C. Waerenborgh, F. S. Delgado and C. Ruiz-Pérez, *Inorg. Chem.*, 2008, **47**, 9111; (b) S. Floquet, S. Salunke, M. L. Boillot, R. Clément, F. Varret, K. Boukheddaden and E. Rivière, *Chem. Mater.*, 2002, **14**, 4164–4171; (c) M. Clemente-León, E. Coronado, M. López-Jordà and J. C. Waerenborgh, *Inorg. Chem.*, 2011, **50**, 9122–9130; (d) M. Clemente-León, E. Coronado, M. López-Jordà, J. C. Waerenborgh, C. Desplanches, H. Wang, J.-F. Létard, A. Hauser and A. Tissot, *J. Am. Chem. Soc.*, 2013, **135**, 8655–8667; (e) M. Clemente-León, E. Coronado, M. López-Jordà, G. Mínguez Espallargas, A. Soriano-Portillo and J. C. Waerenborgh, *Chem. – Eur. J.*, 2010, **16**, 2207–2219.
- N. Hoshino, F. Iijima, G. N. Newton, N. Yoshida, T. Shiga, H. Nojiri, A. Nakao, R. Kumai, Y. Murakami and H. Oshio, *Nat. Chem.*, 2012, **4**, 921.
- R. Ababei, C. Pichon, O. Roubeau, Y.-G. Li, N. Bréfuel, L. Buisson, P. Guionneau, C. Mathonière and R. Clérac, *J. Am. Chem. Soc.*, 2013, **135**, 14840.
- M. Darawsheh, L. A. Barrios, O. Roubeau, S. J. Teat and G. Aromí, *Angew. Chem., Int. Ed.*, 2018, **57**, 13509.
- P. J. van Koningsbruggen, Y. Maeda and H. Oshio, *Top. Curr. Chem.*, 2004, **233**, 259.
- (a) S. Hayami, K. Hiki, T. Kawahara, Y. Maeda, D. Urakami, K. Inoue, M. Ohama, S. Kawata and O. Sato, *Chem. – Eur. J.*, 2009, **15**, 3497; (b) D. J. Harding, D. Sertphon, P. Harding, K. S. Murray, B. Moubaraki, J. D. Cashion and H. Adams, *Chem. – Eur. J.*, 2013, **19**, 1082; (c) W. Phonsri, P. Harding, L. Liu, S. G. Telfer, K. S. Murray, B. Moubaraki, T. M. Ross, G. N. L. Jameson and D. J. Harding, *Chem. Sci.*, 2017, **8**, 3949; (d) I.-R. Jeon, C. Mathonière, R. Clérac, M. Rouzières, O. Jeannin, E. Trzop, E. Collet and M. Fourmigué, *Chem. Commun.*, 2017, **53**, 10283; (e) N. Phukkaphan, D. L. Cruickshank, K. S. Murray, W. Phonsri, P. Harding and D. J. Harding, *Chem. Commun.*, 2017, **53**, 9801; (f) L. Pogány, J. Moncol, J. Pavlik and I. Šalitroš, *New J. Chem.*, 2017, **41**, 5904; (g) B. Brachňáková and I. Šalitroš, *Chem. Pap.*, 2018, **72**, 773; (h) I. Nemeč, R. Herchel and Z. Trávníček, *Dalton Trans.*, 2015, **44**, 4474.
- See e.g.: (a) M. F. Tweedle and L. J. Wilson, *J. Am. Chem. Soc.*, 1976, **98**, 4824–4834; (b) R. H. Petty, E. V. Dose, M. F. Tweedle and L. J. Wilson, *Inorg. Chem.*, 1978, **17**, 1064–1071; (c) C. Gandolfi, C. Moitzi, P. Schurtenberger, G. G. Morgan and M. Albrecht, *J. Am. Chem. Soc.*, 2008, **130**, 14434–14435; (d) A. J. Fitzpatrick, H. M. O'Connor and G. G. Morgan, *Dalton Trans.*, 2015, **44**, 20839–20842; (e) A. Abhervé, T. Grancha, J. Ferrando-Soria, M. Clemente-León, E. Coronado, J. C. Waerenborgh, F. Lloret and E. Pardo, *Chem. Commun.*, 2016, **52**, 7360–7363; (f) S. Floquet, X. Ottenwaelder and M.-L. Boillot, *Inorg. Chem. Commun.*, 2007, **10**, 1549–1553.
- I. Nemeč, R. Herchel, I. Šalitroš, Z. Trávníček, J. Moncol, H. Fuess, M. Ruben and W. Linert, *CrystEngComm*, 2012, **14**, 7015.
- (a) S. Kang, Y. Shiota, A. Kariyazaki, S. Kanegawa, K. Yoshizawa and O. Sato, *Chem. – Eur. J.*, 2016, **22**, 532–538; (b) K. Takahashi, K. Kawamukai, M. Okai, T. Mochida, T. Sakurai, H. Ohta, T. Yamamoto, Y. Einaga, Y. Shiota and K. Yoshizawa, *Chem. – Eur. J.*, 2016, **22**, 1253–1257.
- Ivan Nemeč CCDC 1890122: Experimental Crystal Structure Determination, 2019, DOI: 10.5517/ccdc.csd.cc21ftp0.
- D. J. Harding, P. Harding and W. Phonsri, *Coord. Chem. Rev.*, 2016, **313**, 38.
- M. A. Halcrow, *Chem. Soc. Rev.*, 2011, **40**, 4119.
- R. Pritchard, S. A. Barrett, C. A. Kilner and M. A. Halcrow, *Dalton Trans.*, 2008, 3159.
- (a) R. Herchel, I. Nemeč, M. Machata and Z. Trávníček, *Inorg. Chem.*, 2015, **54**, 8625; (b) I. Nemeč, R. Herchel, T. Šilha and Z. Trávníček, *Dalton Trans.*, 2014, **43**, 15602.
- M. K. Koley, S. C. Sivasubramanian, B. Varghese, P. T. Manoharan and A. P. Koley, *Inorg. Chim. Acta*, 2008, **361**, 1485.
- G. M. Sheldrick, *Acta Crystallogr., Sect. A: Found. Crystallogr.*, 2008, **64**, 112.
- L. J. Farrugia, *J. Appl. Crystallogr.*, 1999, **32**, 837.
- (a) A. L. Speck, *PLATON, a multipurpose crystallographic tool*, Utrecht University, Utrecht, The Netherlands, 2001; (b) Y. Le Page, *MISSYM1.1 – a flexible new release*, *J. Appl. Crystallogr.*, 1988, **21**, 983.
- C. F. Macrae, P. R. Edgington, P. McCabe, E. Pidcock, G. P. Shields, R. Taylor, M. Towler and J. van de Streek, *J. Appl. Crystallogr.*, 2006, **39**, 453.
- (a) F. Neese, *Wiley Interdiscip. Rev.: Comput. Mol. Sci.*, 2012, **2**, 73; (b) F. Neese, *Wiley Interdiscip. Rev.: Comput. Mol. Sci.*, 2018, **8**, e1327.
- (a) A. D. Becke, *Phys. Rev. A: At., Mol., Opt. Phys.*, 1988, **38**, 3098; (b) C. Lee, W. Yang and R. G. Parr, *Phys. Rev. B: Condens. Matter Mater. Phys.*, 1988, **37**, 785; (c) P. J. Stephens, F. J. Devlin, C. F. Chabalowski and M. J. Frisch, *J. Phys. Chem.*, 1994, **98**, 11623.
- (a) K. Yamaguchi, Y. Takahara and T. Fueno, in *Applications of Quantum Chemistry*, ed. V. H. Smith, Reidel, Dordrecht, 1986, p. 155; (b) T. Soda, Y. Kitagawa, T. Onishi, Y. Takano, Y. Shigeta, H. Nagao, Y. Yoshioka and K. Yamaguchi, *Chem. Phys. Lett.*, 2000, **319**, 223.
- F. Weigend and R. Ahlrichs, *Phys. Chem. Chem. Phys.*, 2005, **7**, 3297–3305.
- F. Weigend, *Phys. Chem. Chem. Phys.*, 2006, **8**, 1057.

- 28 (a) F. Neese, F. Wennmohs, A. Hansen and U. Becker, *Chem. Phys.*, 2009, **356**, 98; (b) R. Izsák and F. Neese, *J. Chem. Phys.*, 2011, **135**, 144105.
- 29 K. Momma and F. Izumi, *J. Appl. Crystallogr.*, 2011, **44**, 1272.
- 30 P.-Å. Malmqvist and B. O. Roos, *Chem. Phys. Lett.*, 1989, **155**, 189.
- 31 (a) C. Angeli, R. Cimiraglia and J.-P. Malrieu, *Chem. Phys. Lett.*, 2001, **350**, 297; (b) C. Angeli, R. Cimiraglia, S. Evangelisti, T. Leininger and J.-P. Malrieu, *J. Chem. Phys.*, 2001, **114**, 10252; (c) C. Angeli, R. Cimiraglia and J.-P. Malrieu, *J. Chem. Phys.*, 2002, **117**, 9138.
- 32 D. Ganyushin and F. Neese, *J. Chem. Phys.*, 2006, **125**, 024103.
- 33 F. Neese, *J. Chem. Phys.*, 2005, **122**, 034107.
- 34 R. Maurice, R. Bastardis, C. de Graaf, N. Suaud, T. Mallah and N. Guihéry, *J. Chem. Theory Comput.*, 2009, **5**, 2977.
- 35 F. Weigend, *J. Comput. Chem.*, 2008, **29**, 167.
- 36 (a) M. Atanasov, D. Ganyushin, K. Sivalingam and F. Neese, *Molecular Electronic Structures of Transition Metal Complexes II*, ed. D. M. P. Mingos, P. Day and J. P. Dahl, Springer Berlin Heidelberg, Berlin, Heidelberg, 2012, pp. 149–220; (b) S. K. Singh, J. Eng, M. Atanasov and F. Neese, *Coord. Chem. Rev.*, 2017, **344**, 2.



# Variation of Spin-Transition Temperature in the Iron(III) Complex Induced by Different Compositions of the Crystallization Solvent

Published as part of a *Crystal Growth and Design virtual special issue on Molecular Magnets and Switchable Magnetic Materials*

Ivan Nemeč,\* Lucie Kotásková, and Radovan Herchel\*



Cite This: *Cryst. Growth Des.* 2023, 23, 1323–1329



Read Online

ACCESS |



Metrics & More

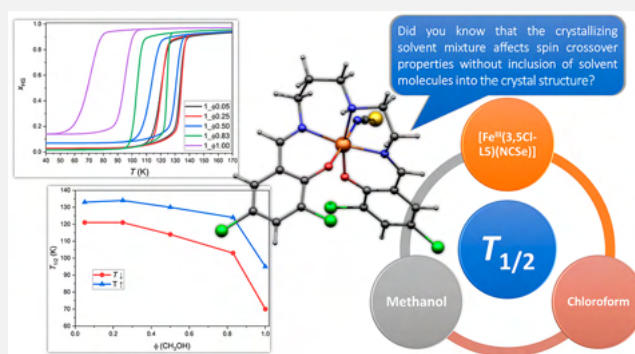


Article Recommendations



Supporting Information

**ABSTRACT:** We crystallized the Schiff-base iron(III) spin-crossover complex  $[\text{Fe}(3,5\text{Cl-L5})(\text{NCSe})]$  from different two-component solvent mixtures containing methanol and chloroform ( $\Phi = V(\text{CH}_3\text{OH})/V(\text{solvent}) = 0.05, 0.25, 0.50, 0.83,$  and  $1.00$ ). The obtained crystalline products were characterized by X-ray diffraction, and it was confirmed that they are all composed of the same crystalline phase, and they do not contain any crystal solvent. However, significant differences in magnetic properties were observed, and thermal hysteresis changed from (in K)  $121T_{\downarrow}$  and  $134T_{\uparrow}$  for  $\Phi = 0.05$  and  $0.25$ , down to  $72T_{\downarrow}$  and  $96T_{\uparrow}$  for  $\Phi = 1.00$ . The crystal structures of the low-spin and high-spin phases were studied theoretically and experimentally.



The tunability of the spin-crossover (SCO) behavior is an important assumption for versatile applications of SCO materials. Beneficially, SCO parameters such as thermal hysteresis width, transition temperature ( $T_{1/2}$ ), cooperativity degree, curve abruptness, and completeness can be manipulated by sample modifications. The effect of the presence<sup>1–3</sup> and loss<sup>4</sup> of a solvent molecule in the lattice, the selection of an anion,<sup>5,6</sup> as well as the choice of a side substituent<sup>6–8</sup> are well-known strategies for modifying the SCO behavior. Also, metal dilution represents a sophisticated approach for modification of the SCO behavior and observing of the cooperativity degree and transition temperature of SCO materials. The SCO behavior can be also tuned by a postsynthetic modification as was manifested by solid state performed anion metathesis.<sup>9</sup>

Our ongoing interest in the magnetic behavior of Fe(III) complexes with pentadentate Schiff base ligands has brought remarkable results on distinct magnetic behaviors of polymorphs within this class of compounds,<sup>10</sup> or hydrogen bonding induced modification of  $T_{1/2}$ .<sup>11</sup> Recently, a new report on SCO with broad thermal hysteresis observed for an Fe(III) complex with a pentadentate Schiff base ligand  $\text{H}_2\text{3,5Cl-L5}$  ( $N,N'$ -bis(1-hydroxy-3,5-dichloro-2-benzyliden)-1,6-diamino-4-azahexane) has been reported by Renz et al. which naturally caught our attention.<sup>12</sup> Complex  $[\text{Fe}(3,5\text{-Cl-L5})(\text{NCSe})]$  (**1**) exhibits thermally induced SCO with 24 K wide thermal hysteresis ( $T_{1/2} = 99\downarrow$  and  $129\uparrow$  K). From the comparison of the low-spin (LS,  $S = 1/2$ ) and high-spin (HS,  $S = 5/2$ ) crystal structures, it is apparent that reorganization of noncovalent interactions ( $\text{H}\cdots\text{Cl}$  and  $\text{Cl}\cdots\text{Cl}$ ) happens upon spin transition.

This, if significant, could explain the observation of the wide thermal hysteresis. In the original report,<sup>12</sup> the authors did not investigate this possibility in greater detail, and therefore, our original motivation for studying this system was to extensively theoretically and experimentally investigate the LS and HS crystal structures of **1**.

For the preparation of **1** we used a procedure similar to that in the original report,<sup>12</sup> but instead of an ultrasonic bath we used a standard magnetic stirrer. The reaction between  $[\text{Fe}(3,5\text{-Cl-L5})\text{Cl}]$  and  $\text{KNCSe}$  in pure methanol led to precipitation of a brown microcrystalline powder, which was filtered off using a paper filter. For the preparation of the single-crystals suitable for X-ray diffraction experiments we used the remaining mother liquor which was crystallized isothermally. After several days thin needle-like crystals were obtained. First, we collected the diffraction data for the HS state (150 K), and then we attempted to measure the LS state crystal structure at 90 K as was done in the original report.<sup>12</sup> To our surprise, the measurement revealed the crystal structure with the very same metal–ligand bond lengths and unit cell parameters as was observed for the HS phase. Obviously, this

Received: December 1, 2022

Revised: February 14, 2023

Published: February 16, 2023



did not match the previously reported magnetic properties.<sup>12</sup> Therefore, we measured the temperature dependence of the magnetic moment ( $\mu_{\text{eff}}/\mu_{\text{B}}$ ) for two obtained fractions, needle-like crystals (**1\_Φ1**) and microcrystalline powder precipitate (**1\_Φ1p**). The measurements confirmed the presence of SCO with thermal hysteresis for both batches; however, the critical temperatures and profiles of magnetic functions were different (Figure 1). The **1\_Φ1** batch exhibited much lower  $T_{1/2}$  (72↓

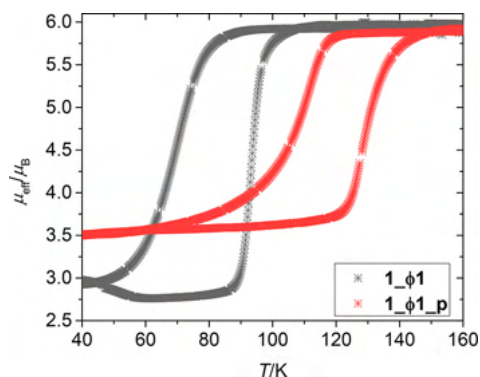


Figure 1. Temperature dependence of  $\mu_{\text{eff}}/\mu_{\text{B}}$  for **1\_Φ1** and **1\_Φ1p**.

and 96↑ K,  $\Delta T = 24$  K) than **1\_Φ1\_p** (106↓ and 129↑ K,  $\Delta T = 23$  K, Figure 1). Powder X-ray diffraction undoubtedly confirmed that both samples were the same crystallographic phase identical to the HS structure of **1** (Supporting Information, Figure S6–S7).

Inspired by this intriguing inconsistency, we investigated this phenomenon in greater detail. From magnetic measurements it is apparent that the low  $T_{1/2}$  was observed for the batch composed of crystals which grew more than 5 days, whereas the high  $T_{1/2}$  was observed for the precipitate. Therefore, one of the tested hypotheses was that different critical temperatures were related to the crystallinity of the samples, which is related to the time of the crystallization. In an attempt to prepare crystals, whose crystallization spans different time periods, we modified the composition of crystallization solutions from pure  $\text{CH}_3\text{OH}$  to solutions with a growing portion of  $\text{CHCl}_3$ .  $\text{CHCl}_3$  was chosen as the second solvent because it dissolves **1** very well; it does not enter the crystal structure of **1** (does not form a solvate) and has a similar boiling temperature as  $\text{CH}_3\text{OH}$ . Therefore, it could be expected that the crystallization of **1** will be governed by slow evaporation of the solvent mixture. This mixture gradually loses slightly more  $\text{CHCl}_3$  than  $\text{CH}_3\text{OH}$  molecules (because of higher vapor pressure of  $\text{CHCl}_3$ ), and thus the solubility of **1** should be continuously decreasing. Four different crystallization mixtures with a different volume fraction  $\Phi$  of  $\text{CH}_3\text{OH}$  were prepared ( $\Phi = 0.83, 0.50, 0.25$  and  $0.05$ ), and the corresponding crystalline samples (**1\_Φ0.83**, **1\_Φ0.50**, **1\_Φ0.25**, **1\_Φ0.05**) were obtained. In the case of the solutions with  $\Phi > 0.5$  also microcrystalline precipitates **1\_Φ0.83p** (besides already prepared **1\_Φ1\_p**) were obtained and were included into this study. The purity of all the prepared samples was confirmed by X-ray powder diffraction. It must be noted that in the case of one of the precipitates (**1\_Φ1\_p**), the presence of KCl impurity was detected as this is a side product of the ligand metathesis ( $\text{Cl}^-$  ligand was substituted by  $\text{KNCSe}$ ). We decided not to wash the precipitates with water (which would dissolve the impurity), because it would introduce a third solvent into the studied

system. Furthermore, the presence of the diamagnetic KCl should not affect the SCO temperatures.

**1** crystallizes as very thin needle-shaped crystals. The symmetry of the crystals is monoclinic with the  $P2_1/n$  space group (see Supporting Information, Table S1). The crystal structures of LS and HS phases were well described in the original report,<sup>12</sup> and we will not add a new structural description here.

The best quality crystals were obtained for the batch **1\_Φ0.25**. Again, we opted to measure the LS and HS crystal structures using a selected single crystal from this batch. We monitored SCO using diffraction methods. Therefore, we started the single crystal X-ray diffraction experiments at 140 K, and we collected sets of diffraction data at selected temperatures on cooling and also on heating. At 116 K (on cooling), a dramatic change in the quality of diffractions occurred as this was the  $T_{1/2}$  temperature. The crystal structure of **1\_Φ0.25@↓116K** shows metal–ligand (ML) bond lengths significantly shorter (Table S2) than observed at higher temperatures and in very good agreement with the LS structure of **1** reported in the original paper.<sup>12</sup> Upon further cooling (down to 108 K), neither the M–L bond lengths nor the unit cell parameters changed significantly, and therefore, we can conclude that the full HS → LS spin conversion occurred between 116 and 117 K (Figure 2). Upon heating, we

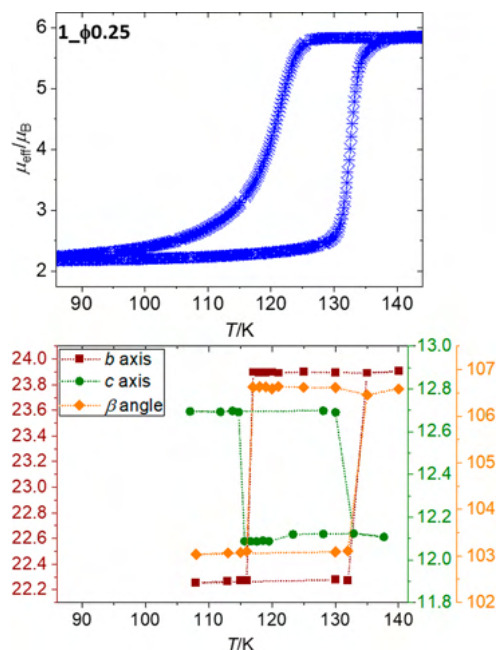


Figure 2. Temperature dependence of  $\mu_{\text{eff}}/\mu_{\text{B}}$  for **1\_Φ0.25** (top) and the temperature dependence of the selected unit cell parameters as determined from the single crystal X-ray diffraction experiment for **1\_Φ0.25** (bottom).

detected the LS → HS transition between 133 (LS) and 135 K (HS structure), whereas we were not able to get reasonable data from the measurement at 134 K. We attempted to also measure another SCO thermal cycle, but the crystal cracked upon another cooling. Here, we may conclude that the single crystal X-ray diffraction measurements confirmed that **1\_Φ0.25** exhibits thermally induced SCO with hysteresis wide 18 K (if we assume  $T_{1/2}$ ↑ to be 134 K). This is not in agreement with the magnetic data reported in the original

paper,<sup>12</sup> but it is also not in good agreement with the magnetic data measured for **1\_Φ1p**. Of note here is that the coordinates of the non-hydrogen atoms in the HS crystal structure of **1\_Φ1** (at 90 K) are almost identical with those determined for **1\_Φ0.25** (at 130 K, see Supporting Information, Figure S1) and thus, the difference in  $T_{1/2}$  cannot be assigned to changes in the crystal structures.

We performed magnetic measurements for all the prepared batches. The results showed that all the samples show thermally induced spin crossover (Figure S2 and Figure S3). Remarkably, it is obvious that the batches prepared from the mixture with the largest content of methanol showed hysteretic loops shifted to lower temperatures, whereas the batches from the higher  $\text{CHCl}_3$  content had hysteretic loops shifted to higher temperatures (Figure S2). The shift of hysteretic loops is observable also between **1\_Φ0.83** and **1\_Φ1**; however, the data for their precipitates **1\_Φ0.83p** and **1\_Φ1p** did not show a significant difference in  $T_{1/2}$  (Figure S3). The hysteretic loops for the batches with the highest  $\text{CHCl}_3$  content (**1\_Φ0.25** and **1\_Φ0.05**) are very similar, and they exhibit the highest  $T_{1/2}$ . The magnetic behavior of **1\_Φ0.25** fits the temperature dependence of the unit cell parameters rather well (Figure 2). The observed behavior is reproducible.

The magnetic data were analyzed by using an Ising-like model (ISM) with Gaussian distribution of the cooperativity parameter derived by Boča et al.<sup>13</sup> Within the ISM defined by the Hamiltonian

$$\hat{H} = \frac{\Delta}{2} \hat{\sigma} - \Gamma \langle \sigma \rangle \hat{\sigma} \quad (1)$$

the transition between two spin states,  $\sigma = -1$  for LS and  $\sigma = +1$  for HS states, is governed by the energy difference between HS and LS states ( $\Delta$ ) and the cooperativeness of the system ( $\Gamma$ ). Such a model can be modified to also include the distribution of the cooperativity parameter  $\Gamma$  in order to deal with the imperfections of the crystalline/powder samples by varying the standard deviation parameter  $\sigma$  of the Gaussian distribution function. The main advantage of such a model is its ability to reproduce the slope of the hysteresis loops, and hence better agreement with the experimental data can be achieved. Thus, the magnetic data were fitted by varying  $\Delta$ ,  $\Gamma$ ,  $r_{\text{eff}}$  and  $\sigma$  parameters within ISM, and subsequently calculated  $x'_{\text{HS}}$  for given temperature was used to calculate total molar susceptibility as

$$x''_{\text{HS}} = x'_{\text{HS}}(1 - x_{r\text{HS}}) \quad (2)$$

$$\chi_{\text{mol}} = (x''_{\text{HS}} + x_{r\text{HS}})\chi_{\text{HS}} + (1 - x''_{\text{HS}} - x_{r\text{HS}})\chi_{\text{LS}} \quad (3)$$

where  $x_{r\text{HS}}$  is the residual molar fraction of the HS state at a low temperature due to incomplete spin crossover, and  $x''_{\text{HS}}$  is rescaled high-spin fraction calculated from ISM resulting in the total high-spin mole fraction  $x_{\text{HS}}$  equal to  $x_{\text{HS}} = x''_{\text{HS}} + x_{r\text{HS}}$ . The molar susceptibility of the HS and LS species was calculated by the Curie law. The fitted parameters are listed in Table S3 and plotted in Figure 3 for crystal samples and in Figure S4 for microcrystalline precipitates. Evidently, there is small variation of the cooperativity  $\Gamma$  and entropy parameter  $r_{\text{eff}}$  within the prepared crystal batches of **1**, and variations of  $T_{1/2\downarrow}$  and  $T_{1/2\uparrow}$  are mainly due to a variation of  $\Delta$ . Furthermore, there is a significant increase of the distribution parameter  $\sigma$  for the microcrystalline precipitates, Table S3.

We also theoretically attempted to investigate the impact of different solvents on the molecular geometry and the energies

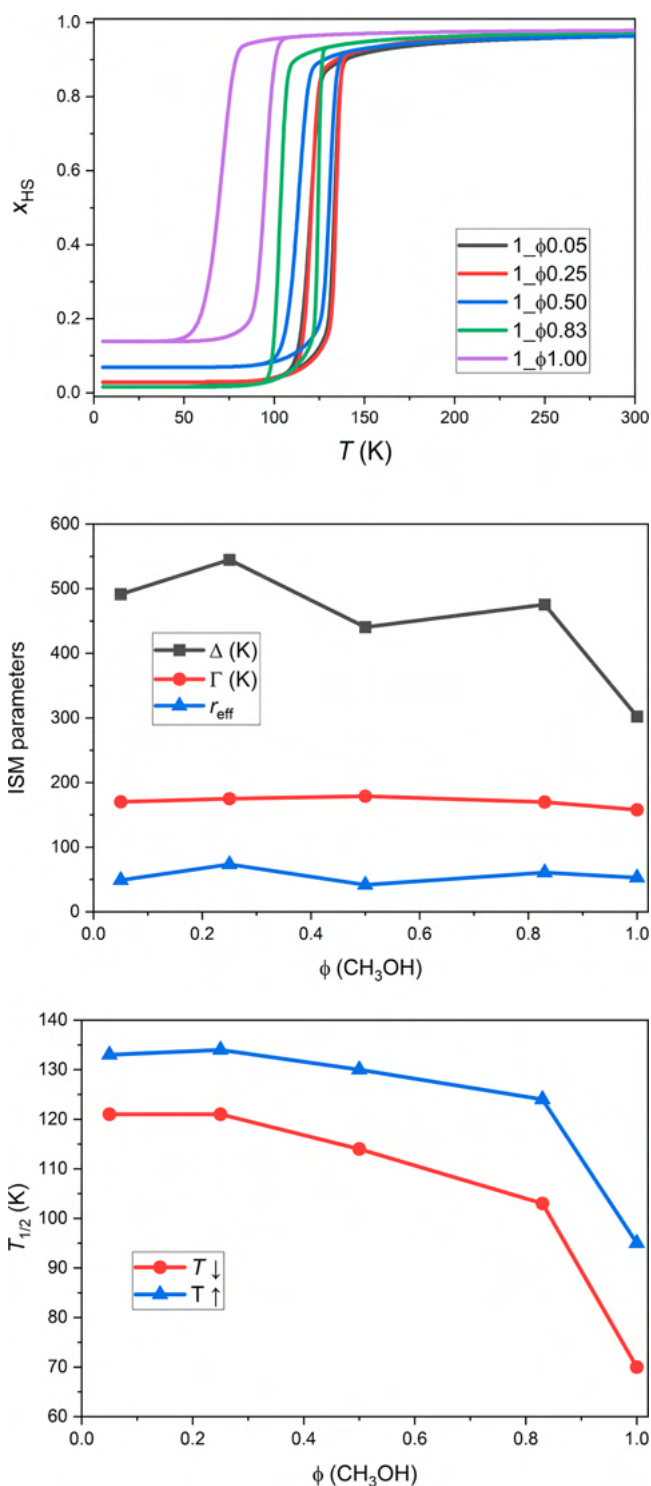


**Figure 3.** Temperature dependence the high-spin molar fraction  $x_{\text{HS}}$  according to ISM (top), the ISM parameters (middle), and transition temperatures (bottom) for crystalline samples of **1**.

of the LS and HS isomer of **1** using density functional theory (DFT) and utilizing ORCA 5.0 software.<sup>14</sup> We selected three functionals based on published benchmark studies,<sup>15–17</sup> namely, OPBE,<sup>18</sup>  $r^2\text{SCAN}$ ,<sup>19</sup> and B3LYP\* (B3LYP with reduced Hartree–Fock exchange to 15%)<sup>20</sup> and also included the atom-pairwise dispersion correction (D4).<sup>21</sup> The optimization was done in a vacuum, chloroform, and methanol with the C-PCM implicit solvation model.<sup>22,23</sup> Impact of



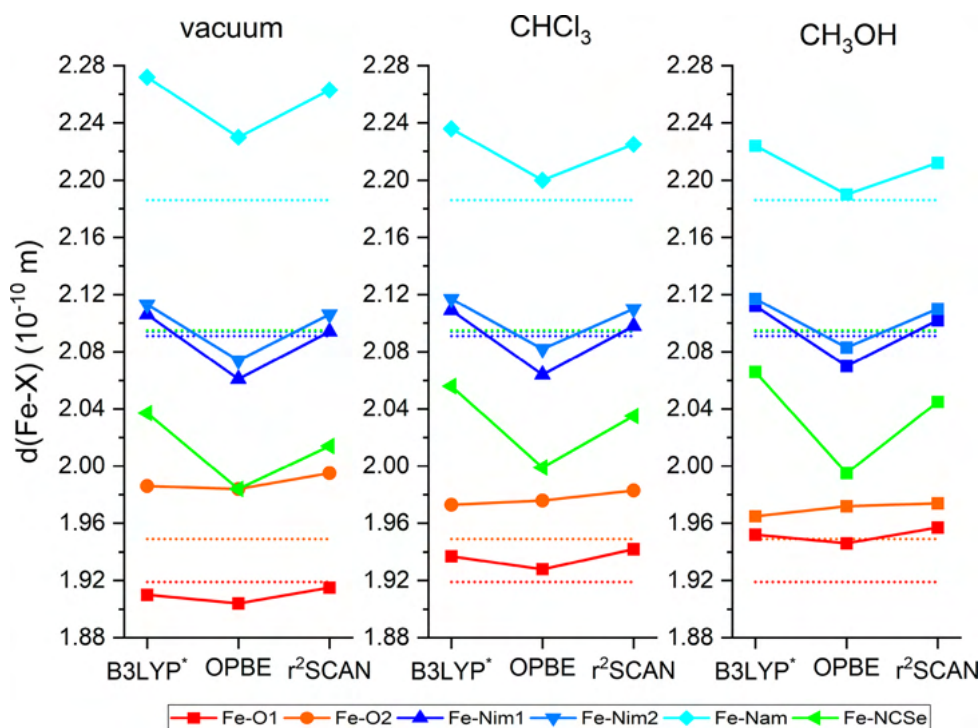


**Figure 4.** Graphical comparison of the donor–acceptor bond distances between X-ray data (dotted lines) and the respective DFT methods (B3LYP\*, OPBE, and  $r^2$ SCAN) for the high-spin state of **1**.

solvents is demonstrated for the HS state of [Fe(3,5-Cl-L5)(NCSe)] in Figure 4. It seems that OPBE underestimates the Fe–NCSe bond, whereas B3LYP\* and  $r^2$ SCAN overestimates the bond lengths to amino-nitrogen of 3,5-Cl-L5. In the case of the LS molecular geometries, OPBE heavily underestimates all Fe–N bond lengths (Figure S5). Moreover, there is also significant variation in bond lengths induced by the implicit solvation model, which points to the importance of intermolecular interactions.

The analysis of the electronic energy differences between the HS and LS isomers revealed positive values of  $\Delta E_{el} = E_{el}^{HS} - E_{el}^{LS}$  for all three DFT functionals, and thus these functionals properly found the LS state with lower electronic energy ( $E_{el}$ ), Table S4. As the molecular vibrations have a significant impact on the SCO properties, a better description is achieved with the energy difference corrected by the zero-temperature vibrational energy from the frequency calculation,  $\Delta E_{el+ZPE}$ , which is depicted in Figure 5.

Apparently,  $\Delta E_{el+ZPE}$  is significantly affected by applying the implicit solvation model, and both B3LYP\* and  $r^2$ SCAN provided reasonable values of the HS–LS separation. Moreover, it seems that a more polar solvent like CH<sub>3</sub>OH tends to increase  $\Delta E_{el+ZPE}$ , and thus it stabilizes the LS state. This is in contradiction to the experimental finding (Figure 3 and Table S3), for which higher  $\Phi(\text{CH}_3\text{OH})$  yielded lower  $\Delta$  and  $T_{1/2}$  values. We can speculate that this discrepancy is caused by the implicit solvation approach which cannot grasp the effect of all intermolecular interactions properly, or the properties of **1** in the solid state simply cannot be encompassed by such an approach at all.

However, if the presented theoretical calculations are not deceptive, perhaps it most likely leads to the conclusion that the reported phenomenon is not governed by thermodynamics, but by the kinetics of the crystal growth of **1** under various contents of chloroform and methanol in crystallizing

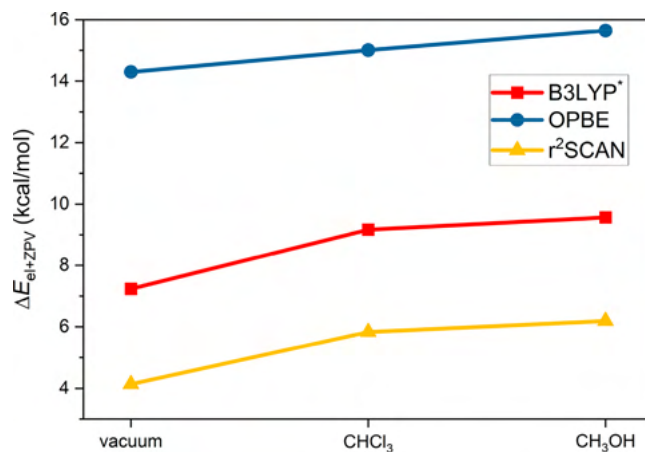


**Figure 5.** Graphical comparison the energy difference corrected by the zero-temperature vibrational energy from the frequency calculation  $\Delta E_{el+ZPE}$  between the HS and LS states for different DFT methods applied to **1**.

solutions. Hence, the quality of the crystalline material and SCO properties are affected by a solvent mixture, but the solvent molecules do not cocrystallize. One of the possible approaches to test this hypothesis is to correlate parameters such as crystal mosaicity with the observed magnetic behavior. Therefore, we decided to prepare several batches of **1** crystallized at different crystallization rates. As was mentioned above, the best crystals were obtained in the batch of **1**  $\Phi$ 0.25. However, the batches crystallized from solutions with a major chloroform fraction ( $\Phi$ 0.25 and  $\Phi$ 0.05) have practically the same magnetic properties (Figure 3). Thus, we decided to crystallize **1** from  $\Phi$ 0.5 and  $\Phi$ 0.83 solutions, because **1**  $\Phi$ 0.5 and **1**  $\Phi$ 0.83 differ in  $T_{1/2\downarrow}$  (114 K for **1**  $\Phi$ 0.5 and 103 K for **1**  $\Phi$ 0.83), and their spin transition on



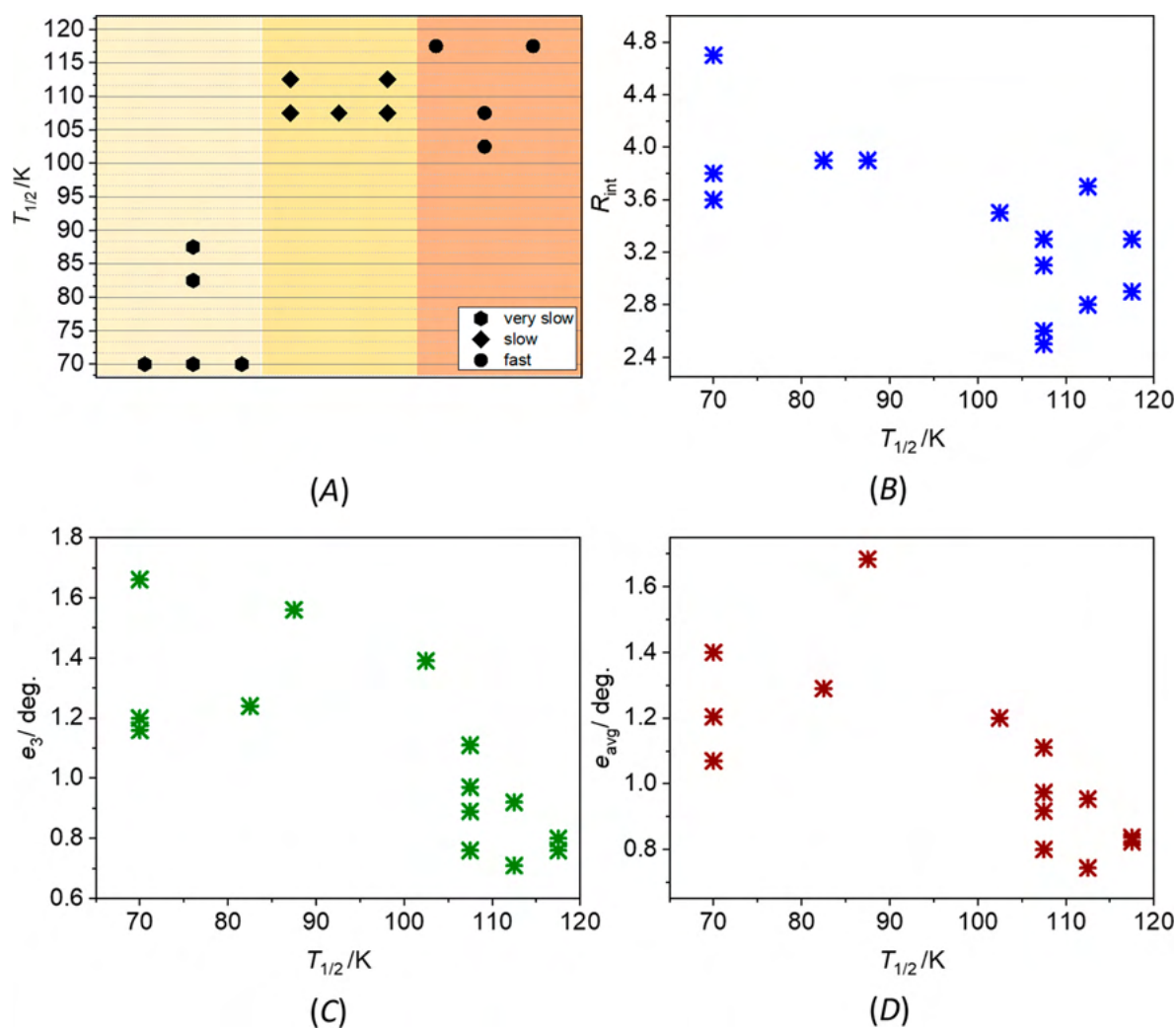


**Figure 6.** Plot of  $T_{1/2}\downarrow$  versus crystallization rate (A). The colored boxes are used to highlight the crystallization rate, with a lighter color indicating slower crystallization. The plots of  $R_{int}$  vs  $T_{1/2}\downarrow$  (B),  $e_3$  vs  $T_{1/2}\downarrow$  (C), and  $e_{avg}$  vs  $T_{1/2}\downarrow$  (D). The value of  $e_{avg}$  was calculated as the arithmetic average of components  $e_1$ ,  $e_2$ , and  $e_3$ . In all plots, the  $T_{1/2}\downarrow$  value of crystals that remained in the high spin phase down to 80 K was assigned as 70 K for visualization purposes.

cooling is still accessible using standard commercial cryogenic devices (above 80 K). For preparation of the batches, we used the same reaction procedures as are described in [Supporting Information](#), but the mother liquors were crystallized using three different crystallization rates: fast ( $\approx 1$  day), slow (up to 4 days), and very slow ( $\geq 7$  days). The majority of the used single crystals were obtained for all the batches crystallized from  $\Phi 0.5$  solutions regardless of the rate of crystallization used. However, also very slow crystallization from the  $\Phi 0.83$  solutions resulted in the production of a few suitable single crystals.

The crystal mosaicity was determined taking into consideration the results of previous work on mosaicity in SCO complexes.<sup>24</sup> We set experimental conditions to be as identical as possible for all the investigated specimens. The experiment was conducted at 150 K, which is well above the highest  $T_{1/2}\downarrow$  (Table S3). The data were collected using  $\omega$ -scans (width 0.5 deg), and the exposition time was adjusted for each crystal based on its size, aiming for 0.83 Å resolution, completeness above 99%, data redundancy  $> 3$ , and  $I/\sigma > 10$ . As was already mentioned, the crystals of **1** are very thin (typically  $\approx 0.05$  mm in two dimensions), needle-like shaped growing in clumps of

overlapping specimens, which makes it challenging to investigate the statistically relevant number of crystallites within a reasonable measurement time. Thus, we were capable of performing measurements for a limited number (14) of single crystals. It is important to note that the vast majority of the prepared crystals were not suitable for single-crystal experiments, and thus the results obtained only represent those crystals that met the necessary criteria.

After collecting each set of data at 150 K, we determined  $T_{1/2\downarrow}$  for each crystal by measuring unit cell parameters starting from 125 K down to 80 K in decrements of 5 K. The occurrence of the SCO phenomenon was recorded between two measured temperature points, and the average of these values was used for visualization purposes. The  $T_{1/2}\downarrow$  value of crystals that remained in the high spin phase at 80 K was set to 70 K for visualization purposes. The distribution of the determined  $T_{1/2\downarrow}$  values is shown (Figure 6A). The results supported our hypothesis that the speed of crystallization affects the quality of crystals and the  $T_{1/2\downarrow}$  value. Crystals crystallized in the "fast" and "slow" modes showed  $T_{1/2\downarrow}$  values above 100 K. Crystals that crystallized "very slowly" showed

$T_{1/2\downarrow}$  values below 90 K with most of them having  $T_{1/2\downarrow}$  even below 80 K.

The results of the X-ray diffraction measurements were evaluated in the CrysAlisPro software.<sup>25</sup> As a first indication of the crystal quality, we inspected the equivalency of symmetry equivalent reflections ( $R_{\text{int}}$ ) in the studied crystals. There is no strong correlation between  $T_{1/2\downarrow}$  and  $R_{\text{int}}$  but apparently, the crystals with lower  $T_{1/2\downarrow}$  values tend to have larger  $R_{\text{int}}$  and *vice versa* (Figure 6B).

The CrysAlisPro software provides the mosaicity in three directions ( $e_1$ ,  $e_2$ , and  $e_3$ ) by fitting a Gaussian function to the peak.<sup>26,27</sup> Although these parameters do not measure the mosaicity directly, variations in the values of  $e_1$ ,  $e_2$ , and  $e_3$  can indicate changes in the mosaicity of the studied crystals and thus their quality.<sup>28</sup> Some authors only use the  $e_3$  parameter due to its correlation with mosaicity values obtained from other data integration methods.<sup>26</sup> The results revealed that the  $e_2$  component varied slightly among the measurements (0.76–0.96°), while larger variations were observed for  $e_1$  (0.75–2.61°) and  $e_3$  (0.71–1.66°). As per previous reports, for evaluation of mosaicity, we considered the values of  $e_3$  and the arithmetic average ( $e_{\text{avg}}$ )<sup>29</sup> of all three components  $e_1$ ,  $e_2$ , and  $e_3$  (Figure 6C–D, Table S5). As with  $R_{\text{int}}$  the results for  $e_{\text{avg}}$  and  $e_3$  did not show a strong linear correlation; however, crystals with higher  $T_{1/2\downarrow}$  values tend to have lower values of  $e$  and  $e_3$  and *vice versa*.

In summary, to the best of our knowledge, such an unprecedented solvent-induced variation of SCO spin-transition temperature as was discussed for **1** has not been reported yet. We showed that the different crystallization rates produced crystals exhibiting different SCO critical temperatures. Very slow crystallization ( $\geq 7$  days) of the **Φ0.5** and **Φ0.83** solutions resulted into crystals exhibiting low SCO critical temperatures ( $T_{1/2\downarrow} < 90$  K), while faster crystallization (shorter than 4 days) led to larger  $T_{1/2\downarrow}$  values ( $> 100$  K). The performed diffraction experiments indicate that crystals with low  $T_{1/2\downarrow}$  values tend to have larger mosaicity parameters and  $R_{\text{int}}$  and thus they are of lower quality than those with larger  $T_{1/2\downarrow}$  values.

## ■ ASSOCIATED CONTENT

### Supporting Information

The Supporting Information is available free of charge at <https://pubs.acs.org/doi/10.1021/acs.cgd.2c01411>.

Synthesis, crystallographic data, magnetic measurements, DFT calculation details, and powder diffraction patterns (PDF)

### Accession Codes

CCDC 1909057 and 2223462–2223463 contain the supplementary crystallographic data for this paper. These data can be obtained free of charge via [www.ccdc.cam.ac.uk/data\\_request/cif](http://www.ccdc.cam.ac.uk/data_request/cif), or by emailing [data\\_request@ccdc.cam.ac.uk](mailto:data_request@ccdc.cam.ac.uk), or by contacting The Cambridge Crystallographic Data Centre, 12 Union Road, Cambridge CB2 1EZ, UK; fax: +44 1223 336033.

## ■ AUTHOR INFORMATION

### Corresponding Authors

Ivan Nemeč – Central European Institute of Technology, Brno University of Technology, 61200 Brno, Czech Republic; Department of Inorganic Chemistry, Palacký University, 77900 Olomouc, Czech Republic; [orcid.org/0000-0003-3231-7849](https://orcid.org/0000-0003-3231-7849); Email: [ivan.nemec@upol.cz](mailto:ivan.nemec@upol.cz)

Radovan Herchel – Department of Inorganic Chemistry, Palacký University, 77900 Olomouc, Czech Republic; [orcid.org/0000-0001-8262-4666](https://orcid.org/0000-0001-8262-4666); Email: [radovan.herchel@upol.cz](mailto:radovan.herchel@upol.cz)

### Author

Lucie Kotásková – Central European Institute of Technology, Brno University of Technology, 61200 Brno, Czech Republic; [orcid.org/0000-0003-4825-3616](https://orcid.org/0000-0003-4825-3616)

Complete contact information is available at: <https://pubs.acs.org/10.1021/acs.cgd.2c01411>

### Author Contributions

The manuscript was written through contributions of all authors. All authors have given approval to the final version of the manuscript.

### Notes

The authors declare no competing financial interest.

## ■ ACKNOWLEDGMENTS

The authors (I.N. and R.H.) acknowledge financial support from institutional sources of the Department of Inorganic Chemistry and Palacký University Olomouc, Czech Republic. We also acknowledge the CzechNanoLab Research Infrastructure supported by MEYS CR (LM2018110) for the measurement of some of the magnetic data. I.N. is grateful to Jakub Wojciechowski for discussions about mosaicity evaluation in CrysAlisPro software.

## ■ REFERENCES

- (1) Bari, R. A.; Sivardière, J. Low-Spin-High-Spin Transitions in Transition-Metal-Ion Compounds. *Phys. Rev. B* **1972**, *5* (11), 4466–4471.
- (2) Wajnflasz, J. Etude de La Transition “Low Spin”-“High Spin” Dans Les Complexes Octaédriques d’ion de Transition. *Phys. status solidi* **1970**, *40* (2), 537–545.
- (3) Boča, R.; Linert, W. Is There a Need for New Models of the Spin Crossover? In *Molecular Magnets Recent Highlights*; Springer Vienna: Vienna, 2002; pp 83–100.
- (4) Shakirova, O. G.; Lavrenova, L. G.; Kurat’eva, N. V.; Naumov, D. Y.; Daletskii, V. A.; Sheludyakova, L. A.; Logvinenko, V. A.; Vasilevskii, S. F. Spin Crossover in Iron(II) Complexes with Tris(Pyrazol-1-Yl)Methane. *Russ. J. Coord. Chem.* **2010**, *36* (4), 275–283.
- (5) Halcrow, M. A. Structure:Function Relationships in Molecular Spin-Crossover Complexes. *Chem. Soc. Rev.* **2011**, *40* (7), 4119.
- (6) Roubeau, O. Triazole-Based One-Dimensional Spin-Crossover Coordination Polymers. *Chem. - A Eur. J.* **2012**, *18* (48), 15230–15244.
- (7) Arcis-Castillo, Z.; Zheng, S.; Siegler, M. A.; Roubeau, O.; Bedoui, S.; Bonnet, S. Tuning the Transition Temperature and Cooperativity of Babpby-Based Mononuclear Spin-Crossover Compounds: Interplay between Molecular and Crystal Engineering. *Chem. - A Eur. J.* **2011**, *17* (52), 14826–14836.
- (8) Feltham, H. L. C.; Johnson, C.; Elliott, A. B. S.; Gordon, K. C.; Albrecht, M.; Brooker, S. “Tail” Tuning of Iron(II) Spin Crossover Temperature by 100 K. *Inorg. Chem.* **2015**, *54* (6), 2902–2909.
- (9) Askew, J. H.; Shepherd, H. J. Post-Synthetic Anion Exchange in Iron(II) 1,2,4-Triazole Based Spin Crossover Materials via Mechanochemistry. *Dalt. Trans.* **2020**, *49* (9), 2966–2971.
- (10) Krüger, C.; Augustín, P.; Dlháň, L.; Pavlík, J.; Moncol’, J.; Nemeč, I.; Boča, R.; Renz, F. Iron(III) Complexes with Pentadentate Schiff-Base Ligands: Influence of Crystal Packing Change and Pseudohalido Coligand Variations on Spin Crossover. *Polyhedron* **2015**, *87*, 194–201.

- (11) Nemeč, I.; Herchel, R.; Trávníček, Z. The Relationship between the Strength of Hydrogen Bonding and Spin Crossover Behaviour in a Series of Iron(III) Schiff Base Complexes. *Dalt. Trans.* **2015**, *44* (10), 4474–4484.
- (12) Rajnak, C.; Mičová, R.; Moncol, J.; Dlháň, L.; Krüger, C.; Renz, F.; Boča, R. Spin-Crossover in an Iron(III) Complex Showing a Broad Thermal Hysteresis. *Dalton Trans.* **2021**, *50* (2), 472–475.
- (13) Boča, R.; Boča, M.; Dlháň, L.; Falk, K.; Fuess, H.; Haase, W.; Jaroščíak, R.; Papánková, B.; Renz, F.; Vrbová, M.; Werner, R. Strong Cooperativeness in the Mononuclear Iron(II) Derivative Exhibiting an Abrupt Spin Transition above 400 K. *Inorg. Chem.* **2001**, *40* (13), 3025–3033.
- (14) Neese, F. Software Update: The ORCA Program System - Version 5.0. *WIREs Comput. Mol. Sci.* **2022**, *12*, e1606.
- (15) Cirera, J.; Ruiz, E. Assessment of the SCAN Functional for Spin-State Energies in Spin-Crossover Systems. *J. Phys. Chem. A* **2020**, *124* (24), 5053–5058.
- (16) Cirera, J.; Via-Nadal, M.; Ruiz, E. Benchmarking Density Functional Methods for Calculation of State Energies of First Row Spin-Crossover Molecules. *Inorg. Chem.* **2018**, *57* (22), 14097–14105.
- (17) Siig, O. S.; Kepp, K. P. Iron(II) and Iron(III) Spin Crossover: Toward an Optimal Density Functional. *J. Phys. Chem. A* **2018**, *122* (16), 4208–4217.
- (18) Perdew, J. P.; Burke, K.; Ernzerhof, M. Generalized Gradient Approximation Made Simple. *Phys. Rev. Lett.* **1996**, *77* (18), 3865–3868.
- (19) Furness, J. W.; Kaplan, A. D.; Ning, J.; Perdew, J. P.; Sun, J. Accurate and Numerically Efficient r 2 SCAN Meta-Generalized Gradient Approximation. *J. Phys. Chem. Lett.* **2020**, *11* (19), 8208–8215.
- (20) Reiher, M. Theoretical Study of the Fe(Phen)2(NCS)2 Spin-Crossover Complex with Reparametrized Density Functionals. *Inorg. Chem.* **2002**, *41* (25), 6928–6935.
- (21) Caldeweyher, E.; Ehlert, S.; Hansen, A.; Neugebauer, H.; Spicher, S.; Bannwarth, C.; Grimme, S. A Generally Applicable Atomic-Charge Dependent London Dispersion Correction. *J. Chem. Phys.* **2019**, *150* (15), 154122.
- (22) Garcia-Ratés, M.; Neese, F. Effect of the Solute Cavity on the Solvation Energy and Its Derivatives within the Framework of the Gaussian Charge Scheme. *J. Comput. Chem.* **2020**, *41* (9), 922–939.
- (23) Barone, V.; Cossi, M. Quantum Calculation of Molecular Energies and Energy Gradients in Solution by a Conductor Solvent Model. *J. Phys. Chem. A* **1998**, *102* (11), 1995–2001.
- (24) Lakhroufi, S.; Tailleur, E.; Guo, W.; Le Gac, F.; Marchivie, M.; Lemée-Cailleau, M.-H.; Chastanet, G.; Guionneau, P. Mosaicity of Spin-Crossover Crystals. *Crystals* **2018**, *8* (9), 363.
- (25) *CrysAlisPro*, 1.171.42.49; Rigaku Oxford Diffraction, 2020.
- (26) Harrison, K.; Wu, Z.; Juers, D. H. A Comparison of Gas Stream Cooling and Plunge Cooling of Macromolecular Crystals. *J. Appl. Crystallogr.* **2019**, *52* (5), 1222–1232.
- (27) Kabsch, W. Integration, Scaling, Space-Group Assignment and Post-Refinement. *Acta Crystallogr. Sect. D Biol. Crystallogr.* **2010**, *66* (2), 133–144.
- (28) Madsen, S. R.; Overgaard, J.; Stalke, D.; Iversen, B. B. High-Pressure Single Crystal X-Ray Diffraction Study of the Linear Metal Chain Compound Co3(Dpa)4Br2·CH2Cl2. *Dalt. Trans.* **2015**, *44* (19), 9038–9043.
- (29) Farley, C.; Burks, G.; Siegert, T.; Juers, D. H. Improved Reproducibility of Unit-Cell Parameters in Macromolecular Cryocrystallography by Limiting Dehydration during Crystal Mounting. *Acta Crystallogr. Sect. D Biol. Crystallogr.* **2014**, *70* (8), 2111–2124.

## Recommended by ACS

### Spin-Crossover Behaviors of Iron(II) Complexes Bearing Halogen Ligands in Solid State and Solution

Ju Wang, Jun Tao, *et al.*

JANUARY 12, 2023

INORGANIC CHEMISTRY

READ 

### High-Temperature Spin Crossover in Fe<sup>III</sup> N<sub>4</sub>O<sub>2</sub> Complexes Incorporating an [R-sal,323] Backbone

Kyle J. Howard-Smith, Feng Li, *et al.*

JANUARY 11, 2023

CRYSTAL GROWTH & DESIGN

READ 

### Elastic Properties of the Iron(II)–Triazole Spin Crossover Complexes [Fe(Htrz)<sub>2</sub>trz]BF<sub>4</sub> and [Fe(NH<sub>2</sub>trz)<sub>3</sub>]SO<sub>4</sub>

Damian Paliwoda, Azzedine Bousseksou, *et al.*

FEBRUARY 10, 2023

CRYSTAL GROWTH & DESIGN

READ 

### Push and Pull Effect of Methoxy and Nitro Groups Modifies the Spin-State Switching Temperature in Fe(III) Complexes

Bijoy Dey, Vadapalli Chandrasekhar, *et al.*

OCTOBER 17, 2022

ACS OMEGA

READ 

Get More Suggestions >